Advances in Geophysical and Environmental Mechanics and Mathematics

AGEM²

Kolumban Hutter *Editor*

Nonlinear Internal Waves in Lakes

Springer

Advances in Geophysical and Environmental Mechanics and Mathematics

Series Editor: Professor Kolumban Hutter

For further volumes:
http://www.springer.com/series/7540

Board of Editors

Kolumban Hutter
Editor

Nonlinear Internal Waves in Lakes

Springer

Editor
Prof. Dr. Kolumban Hutter
ETH Zürich
c/o Versuchsanstalt für Wasserbau
Hydrologie und Glaziologie
Gloriastr. 37/39
8092 Zürich
Switzerland
hutter@vaw.baug.ethz.ch

ISSN 1866-8348 e-ISSN 1866-8356
ISBN 978-3-642-23437-8 e-ISBN 978-3-642-23438-5
DOI 10.1007/978-3-642-23438-5
Springer Heidelberg Dordrecht London New York

Library of Congress Control Number: 2011942325

Preface

INTAS has been an international association for the promotion of collaboration between scientists from the European Union, Island, Norway, and Switzerland (INTAS countries) and scientists from the new independent countries of the former Soviet Union (NUS countries). The program was founded in 1993, existed until 31 December 2006 and is since 01 January 2007 in liquidation. Its goal was the furthering of multilateral partnerships between research units, universities, and industries in the NUS and the INTAS member countries. In the year 2003, on the suggestion of Dr. V. Vlasenko, the writer initiated a research project on "Strongly nonlinear internal waves in lakes: generation, transformation and meromixis" (Ref. Nr. INTAS 033-51-3728) with the following partners:

INTAS

Prof. K. Hutter, PhD, Department of Mechanics, Darmstadt University of Technology, Darmstadt, Germany

Dr. V. Vlasenko, Institute of Marine Studies, Plymouth University, Plymouth, United Kingdom

Prof. Dr. E. Pelinovsky, Institute of Applied Physics, Laboratory of Hydrophysics, Russia, Academy of Sciences, Nizhni Novgorod, Russia

Prof. Dr. N. Filatov, Northern Water Problems Institute, Karelian Scientific Centre, Russian Academy of Sciences, Petrozavodsk, Russia

Prof. Dr. V. Maderich, Institute of Mathematical Machines and System Modeling, Ukrainian Academy of Sciences, Kiev, Ukraine

Prof. Dr. V. Nikishov, Institute of Hydrodynamics, Department of Vortex Motion, Ukrainian Academy of Sciences, Kiev, Ukraine

The joint proposal was granted with commencement on 01 March 2004 and it lasted until 28 February 2007. The writer was research and management coordinator; annual reports were submitted.

The final report, listing the administrative and scientific activities, submitted to the INTAS authorities quickly passed their scrutiny; however, it was nevertheless decided to collect the achieved results in a book and to extend and complement the

results obtained at that time with additional findings obtained during the 4 years after termination of the INTAS project. Publication in the Springer Verlag series "Advances in Geophysical and Environmental Mechanics and Mathematics" was arranged. The writer served as Editor of the book, now entitled "Nonlinear Internal Waves in Lakes" for brevity. The contributions of the six partners mentioned above were collected into four chapters. Unfortunately, even though a full chapter on the theories of weakly nonlinear waves was planned, Professor E. Pelinovsky, a world-renowned expert in this topic, withdrew his early participation. The remaining chapters contain elements of it, and the referenced literature makes an attempt of partial compensation. Strongly nonlinear waves are adequately covered in Chap.4. Writing of the individual chapters was primarily done by the four remaining groups; all chapters were thoroughly reviewed and criticized professionally and linguistically, sometimes with several iterations. We hope the text is now acceptable.

Internal waves and oscillations (seiches) in lakes are important ingredients of lake hydrodynamics. A large and detailed treatise on "Physics of Lakes" has recently been published by Hutter et al. [1, 2]. Its second volume with the subtitle "Lakes as Oscillators" deals with *linear* wave motions in homogeneous and stratified waters, but only little regarding *nonlinear* waves is treated in these books. The present book on "Nonlinear Internal Waves in Lakes" can well serve as a complementary book of this treatise on topics which were put aside in [1, 2].

Indeed, internal wave dynamics in lakes (and oceans) is an important physical component of geophysical fluid mechanics of 'quiescent' water bodies of the globe. The formation of internal waves requires seasonal stratification of the water bodies and *generation* by (primarily) wind forces. Because they propagate in basins of variable depth, a generated wave field often experiences *transformation* from large basin-wide scales to smaller scales. As long as this fission is hydrodynamically stable, nothing dramatic will happen. However, if vertical density gradients and shearing of the horizontal currents in the metalimnion combine to a Richardson number sufficiently small ($< ¼$), the light epilimnion water mixes with the water of the hypolimnion, giving rise to vertical diffusion of substances into lower depths. This *meromixis* is chiefly responsible for the ventilation of the deeper waters and the homogenization of the water through the lake depth. These processes are mainly formed because of the physical conditions, but they play biologically an important role in the trophicational state of the lake.

- Chapter 1 on *Internal waves in lakes: Generation, transformation, meromixis – an attempt of a historical perspective* gives a brief overview of the subjects treated in Chaps.2–4. Since brief abstracts are provided at the beginning of each chapter, we restrict ourselves here to state only slightly more than the headings.
- Chapter 2 is an almanac of *Field studies of nonlinear internal waves in lakes on the Globe*. An up-to-date collection of nonlinear internal dynamics is given from a viewpoint of field observation.
- Chapter 3 presents exclusively *Laboratory modeling of transformation of large-amplitude internal waves by topographic obstructions*. Clearly defined driving mechanisms are used as input so that responses are well identifiable.

- Chapter 4 presents *Numerical simulations of the non-hydrostatic transformation of basin-scale internal gravity waves and wave-enhanced meromixis in lakes*. It rounds off the process from generation over transformation to meromixis and provides an explanation of the latter.

As coordinating author and editor of this volume of AGEM^2, the writer thanks all authors of the individual chapters for their patience in co-operating in the process of various iterations of the drafted manuscript. He believes that a respectable book has been generated; let us hope that sales will corroborate this.

It is our wish to thank Springer Verlag in general and Dr. Chris Bendall and Mrs. Agata Oelschläger, in particular, for their efforts to cope with us and to do everything possible in the production stage of this book, which made this last iteration easy.

Finally, the authors acknowledge the support of their home institutions and extend their thanks to the INTAS authorities during the 3 years (2004–2007) of support through INTAS Grant 3-51-3728.

For all authors,
Zurich, Switzerland K. Hutter

References

1. Hutter, K, Wang, Y, Chubarenko I.: Physics of Lakes, Volume 1: Foundation of the Mathematical and Physical Background, Springer Verlag, Berlin, etc. 2011.
2. Hutter, K, Wang, Y, Chubarenko I.: Physics of Lakes, Volume 2: Lakes as Oscillators, Springer Verlag, Berlin, etc. 2011.

Contents

List of Acronyms

ACIT	Autonomous current and temperature device (Soviet analogue to RCM)
ADC	Analog–digital converter
ADC(P), ADP	Acoustic Doppler current (profiler)
APE	Available potential energy
APEF	Flux of available potential energy
ASAR	Advanced synthetic aperture radar
BBL	Bottom boundary layer
BITEX	(Lake) Biwa transport experiment
BO	Benjamin-Ono (equation, theory)
BOM	Bergen ocean model
BPE	Background potential energy
BVF	Brunt-Väisälä frequency
CFD	Computational fluid dynamics
CT	Conductivity-temperature
CTD	Conductivity-temperature-density (profiler)
CWT	Continuous wavelet transform
DIL	Depth of isotherm location
DNS	Direct numerical simulation
2D, 3D	Two-dimensional, three-dimensional
ELCOM	Estuary, lake and coastal ocean model
eK-dV	Extended Korteweg-de Vries (equation)
EMS	Meteostation 'EMSet' – Environmental meteostation
ENVISAT	'Environmental Satellite' is an Earth-observing satellite
ENVISAT ASAR	ASAR is equipment installed in the ENVISAT
ESA	European space agency
FFT	Fast Fourier transforms
Fr	Froude number
ID	Isotherm depth
IHM	Institute of hydromechanics (of the NASU)

INTAS	International association for the promotion of co-operation with scientists from the new independent states of the former Soviet Union
IR	Infrared radiometer
ISW	Internal solitary wave
JKKD	Joseph-Kubota-Ko-Dobbs (model)
K-dV	Korteweg-de Vries (equation, theory)
K-dV-mK-dV	Korteweg-de Vries-modified Korteweg-de Vries (model, theory)
KE	Kinetic energy
KEF	Flux of kinetic energy
KH	Kelvin-Helmholtz (instability)
LADEX	Lake Ladoga experiment
LES	Large eddy simulation
LIDAR	Light identification, detection and ranging
LU	Product of a lower triangular matrix and an upper triangular matrix
MAC	Marker and cell method
MCC	Miyata-Choi-Camassa (solitary wave, solution)
MEM	Maximum entropy method
mK-dV	Modified Korteweg-De Vries (equation)
MODIS	Moderate resolution-imaging-spectra radiometer
NASA	National Space Agency of the USA
NASU	National Academy of Sciences of the Ukraine
NIERSC	Nansen International Environmental Scientific Center
NOAA	National Oceanic and Atmospheric Organization of the USA
NS	Navier-Stokes (equation)
NWPI	Northern Water Problems Institute (of RAS if Russia)
PE	Potential energy
PFP	Portable flux profiler
PIFO	Polar Institute of Fishery and Oceanography (in Murmansk)
PIV	Particle image velocimetry
POM	Princeton ocean model
PSE	Pseudo-energy
PSD	Power spectral density
PSEi, PSEin	Pseudo-energy of incoming wave
PSEr, PSEref	Pseudo-energy of reflected wave
PSEtrans	Pseudo-energy of transmitted wave
PWF	Work done by pressure perturbations
R=PSEr/PSEi	Reflection coefficient
RADARSAT	Official name of a Canadian Satellite
RANS	Reynolds averaged Navier-Stokes (equations)
RAS	Russian Academy of Science
RCM	Portable current meter

Ri	Richardson number
Re	Reynolds number
ROMS	Regional ocean model system
r.w.	Reflected wave
r.r.w	Re-reflected wave
SAR	Synthetic aperture radar satellite
SeaWiFS	SeaWiFS stands for Sea-viewing Wide Field-of-view Sensor. It is the only scientific instrument on GeoEye's OrbView-2 (AKA SeaStar) satellite
SGS	Subgrid (scale) stress
SPOT	Satellite pour l' observation de la terre (French)
STN	Measuring station
TELEMAC	Unstructured mesh finite element modeling system for free surface waters
THREETOX	Three-dimensional hydrostatic free-surface model
TL	Thermo chain
TR	Temperature recorder
VOF	Volume of fluid (method)

Chapter 1
Internal Waves in Lakes: Generation, Transformation, Meromixis – An Attempt at a Historical Perspective

K. Hutter

Abstract We review experimental and theoretical studies of linear and nonlinear internal fluid waves and argue that their discovery is based on a systematic development of thermometry from the early reversing thermometers to the moored thermistor chains. The latter (paired with electric conductivity measurements) allowed development of isotherm (isopycnal) time series and made the observation of large amplitude internal waves possible. Such measurements (particularly in the laboratory) made identification of solitary waves possible and gave rise to the emergence of very active studies of the mathematical description of the motion of internal waves in terms of propagating time-dependent interface motions of density interfaces or isopycnal surfaces. As long as the waves remain stable, i.e., do not break, they can mathematically be described for two-layer fluids by the Korteweg-de Vries equation and its generalization. When the waves break, the turbulent analogs of the Navier–Stokes equations must be used with appropriate closure conditions to adequately capture their transformation and flux of matter to depth, which is commonly known as meromixis.

1.1 Thermometry

The following analysis begins with the study of thermometry. Its study and success of instrument development turned out to be the crucial element disclosing the internal dynamics of the ocean and of lakes.

"Bearing in mind that changes in the distribution of water temperature delineate the seasonal cycle of warming and cooling in lakes and also that temperature is a relatively conservative label of water movements on time scales of days or less, the

K. Hutter (✉)
c/o Laboratory of Hydraulics, Hydrology and Glaciology, Gloriastr. 37-39, ETH, CH-8092 Zurich, Switzerland
e-mail: hutter@vaw.baug.ethz.ch

K. Hutter (ed.), *Nonlinear Internal Waves in Lakes*,
Advances in Geophysical and Environmental Mechanics and Mathematics,
DOI 10.1007/978-3-642-23438-5_1,

history of internal waves may be said to begin with attempts to measure the subsurface distribution of temperature, for example with heavily insulated thermometers in 1799 (Saussure 1799). The subsequent story of thermometry in limnology and oceanography (McConnell 1982) provides examples of the profound influence, which advances in instrument design exerted on progress. Maximum and minimum thermometers provided the first demonstration of a thermocline (Bèche, de la 1819)... Other early observations of lake stratification were reviewed by Geistbeck (1885); and the thermocline was first so named by Birge (1897)... Negretti's and Zarembra's reversing thermometer (McConnell 1982) was probably the first used in a lake by Forel (1895)... With care in calibration and use, the modern standard instrument measures in situ temperature with an error of less than $\pm 0.01^{\circ}$C. For measurement near the bottom of deep lakes, Strom (1939) had a special thermometer constructed by Richter and Wiese (Berlin) with a range from $+2^{\circ}$C to $+5^{\circ}$C divided in 0.01°C intervals and with a claimed error of less than 1/5 division" (Mortimer 1984).

Mortimer continues: "If such accuracy were needed today, it would be more conveniently achieved by electrical resistance thermometry. This method (along with the thermocline technique) also has a long history (Mortimer 1963)... Electrical resistance thermometry, introduced by Siemens to oceanography (McConnell 1982), was first applied in a lake by Warren and Whipple in 1895. The advent of thermistors after the Second World War considerably simplified the technique of electrical resistance thermometry, although platinum wire coils remained in use where the highest precision was required. First described for lake use, in 1950 (Mortimer and Moore 1953; Platt and Shoup 1950), the thermistor probes are now standard equipment. The first thermistor "chain", a powerful tool for continuous simultaneous recording of temperature at selected fixed depths, was developed by the writer [Mortimer, ed.] (Mortimer 1952a, 1952b; Mortimer 1955) to record temperatures in Windermere in 1950 and in Loch Ness 2 years later. The earliest device for continuous recording (but at a single depth) was Wedderburn's ingenious underwater thermograph (Wedderburn and Young 1915), later borrowed from the Royal Scottish Museum (Mortimer 1952a) ... to record internal seiches in Windermere.

Much more extensive and detailed surveys in lakes, yielding quasi-synoptic pictures of temperature distribution, became possible with the invention of temperature/depth profilers deployed from moving vessels, the bathythermograph (Spilhaus and Mortimer 1977) and depth undulating probes and towed thermistor chains (Boyce and Mortimer 1977). In fact, the first detailed three-dimensional study of the seasonal cycle of warming and cooling (stratification/destratification) was made by Church (1942, 1945). With a bathythermograph in 1942 from Lake Michigan railroad ferries".

This much for Mortimer's text (Mortimer 1984) on thermometry! Today, synoptic field studies are conducted, in which thermistor chains encompass the metalimnion region, and current meters at epilimnion and (several) hypolinion depths are deployed for some weeks to months, e.g., (Hollan 1974), (Horn 1981), (Hutter 1983), (Hutter et al. 1983), (Stocker and Salvadè 1986), (Roget 1992),

(Roget et al. 1997), (Appt et al. 2004), and (Mortimer 1979). They yield thermometric time series data in whole basin dynamic studies but are logistically practically only possible in small lakes of at most several tens of kilometers of horizontal extent. In large lakes (e.g., the Great Lakes in America or Lakes Ladoga and Onego and the Caspian Sea), distances between moored instruments are too large for effective synoptic maintenance. In these cases, detailed thermometry is generally local, reserved to bays or selected shore regions. Moreover, often economic constraints limit the scope of whole-view synoptic campaigns.

1.2 Internal Oscillatory Responses

The study of rhythmic periodic fluctuations in lake level preceded corresponding studies of temperature oscillations and corresponding vertical thermocline motions. In fact, measurement and theoretical understanding of the former was needed for a proper understanding of internal wave dynamics. As Mortimer says, "the first detailed set of observations of lake level oscillations (Duillier,[1] on Lake Geneva, 1730, introducing the word 'seiche') and their occurrence in many lakes (Vaucher 1833) were. . .preceded by systematic observations and conjectures by a Jesuit missionary (André, Father Louis, 1671) in 1671, describing the large but irregular 'tides' at the head of Green Bay (a gulf which opens onto Lake Michigan) and attributing them to a combination of lunar tidal influence and to the influence of the main lake. Three centuries elapsed before those conjectures were confirmed by spectral analysis and numerical modeling (Heaps 1961; 1975; Heaps et al. 1982)".

Regarding theory, fluid mechanics helped to gain a more complete understanding of the measured seiche oscillations. Forel's lifetime study of Léman seiches and temperatures (Forel 1895) and their interpretation with Merian's equation (Merian 1885) for the rectangular basin, followed by Chrystal's (Chrystal 1905) channel equation applied to basins of simple elongated geometry, and Defant's (Defant 1918) simple one-dimensional finite difference procedure, which allowed computation of seiche periods and structures, provided first interpretations, which later were widely applied, e.g., (Marcelli 1948; Caloi 1954; Maurer et al. 1996; Servais 1975; Tison and Tison Jr 1969).

The effect upon seiches of the rotation of the Earth due to the Coriolis force was first theoretically treated by Taylor (1920) in a rectangular basin and by Jeffreys (1923) and Goldstein (1929) in an elliptical basin of constant depth. The influence of the Coriolis effect on seiche oscillations was theoretically analyzed by Proudman (1928) and then first applied for the Baltic Sea by Neumann (1941), for Lake Michigan by F. Defant (the son of A. Defant) (1953), using his father's method (Defant 1918), for the ocean and their basins by Platzman (1970; 1975; 1984), for

[1] Duillier F (1730) Remarques sur l'histoire du lac de Genève. In: Spo Histoire de Genève 2**:** p 463.

Lake Erie by Platzman in (1963) and by Platzman and Rao in (1964b), the world ocean by (Platzman 1984), and later almost routinely by many others, e.g., (Mortimer and Fee 1976; Platzman 1972; Raggio and Hutter 1982a; b; c; Rao and Schwab 1976; Rao et al. 1976; Lemmin and Mortimer 1986; Lemmin et al. 2005; Antenucci et al. 2000; Antenucci and Imberger 2001a,b).

Of significance for internal seiche dynamics in constant depth containers, which are layered in a light epilimnion and heavy hypolimnion, is Charney's (Charney 1955) equivalent depth description, later generalized by Lighthill to N layers (Lighthill 1969). According to this description, the seiche eigenvalue problem of the N-layer fluid with free surface and non-mixing interfaces can be reduced to N independent (virtual) single-layer models for a formally homogeneous fluid with their own equivalent depths. In this restricted sense of the equivalence of the fluid basins to which the equivalence is applied, must be bounded by vertical walls which extend over all layers. The barotropic and baroclinic quasi-static oscillations are then equivalent mathematical problems. In this context, the role played by the Earth's rotation is expressed by the external and internal equivalent depths $h_{\text{ext/int}}$, phase speeds $c_{\text{ext/int}}$, and external and internal Rossby radii of deformation $R_{\text{ext/int}}$, given by

$$h_{\text{ext}} = H = H_1 + H_2, \quad h_{\text{int}} = \frac{H_1 H_2}{H} = \frac{H_1 H_2}{H_1 + H_2},$$

$$c_{\text{ext}} = \sqrt{\mathrm{g}\, h_{\text{ext}}}, \quad c_{\text{int}} = \sqrt{\frac{\Delta\rho}{\rho}\mathrm{g} h_{\text{int}}},$$

$$R_{\text{ext}} = \frac{c_{\text{ext}}}{f} = \frac{\sqrt{g\, h_{\text{ext}}}}{f}, \quad R_{\text{int}} = \frac{c_{\text{int}}}{f} = \frac{1}{f}\sqrt{\frac{\Delta\rho}{\rho} g h_{\text{int}}},$$

in which H is the water depth and H_1 and H_2 are the layer depths. For the two-layer baroclinic wave, R_{int} is a factor $\sqrt{(\Delta\rho/\rho)h_{\text{int}}/h_{\text{ext}}}$ smaller than for the corresponding barotropic case. This difference gives rise to a subtle definition of the notion whether a lake is to be considered "large" or "small" (see Chap. 2), the distinction depending on whether processes are barotropic and baroclinic, respectively.

The equivalent depth description for constant depth-layered fluids has widely been used also for real lakes of variable depth with reasonable success, as demonstrated by results with the two- and three-layer models and the corresponding equivalent depth models, (Bäuerle 1981; 1985; 1994; Heaps et al. 1982; Stocker et al. 1987; Hüttemann and Hutter 2001; Hutter 1983; Hutter et al. 1983; 2011; Kanari 1975; Mortimer 1952a,b; Mortimer 1974; Roget 1992; Roget et al. 1997; Saggio and Imberger 1998; 2001; Schwab 1977). The restriction of the equivalent depth model to the innermost region, which is fully occupied by all layers is a severe disadvantage for lakes with shallow slopes. In these cases, two- and three-layer

models have occasionally been employed, in which the near-shore regions with only two or a single layer are included in the computational domain (Hutter et al. 2011; Roget 1992; Roget et al. 1997; Salvadè et al. 1988). For continuous stratification, a more detailed division of the metalimnion into several layers may, in this case, still be advantageous. The computational procedure is then best done by applying full three-dimensional software accounting for such layering; see Chap. 4 of this book.

The above model hierarchy is based on linear equations of lake hydrodynamics; nevertheless, results, deduced from the models allow a fair to good reproduction of observed data, provided that the driving mechanisms are moderate, such that, e.g., large amplitude excursions of the thermocline do not reach the free surface and thus do not destroy a given stratification; or that fluid instabilities do not lead to mixing and thus do not transform a given stratification to a different one and thus change the conditions under which a theoretical linear model is valid. By contrast, complex evolutionary models must necessarily be based on nonlinear formulations that, beyond the short time-scale processes, allow changes in seasonal stratification to be captured.

To deepen the description of the physical processes in this regime, note that stratification in lakes, i.e., the formation of a more or less distinct density interface that is commonly identified with the thermocline is a consequence of the seasonally changing and storm-episodic interaction of mechanical (wind-driven) and radiative (sun-driven) fluxes: "The mechanical flux generates currents and (most importantly) shears which promote turbulence (Schmidt 1917), while the positive (or negative) radiative fluxes create (or destroy) vertical density gradients and their associated buoyancy forces, which suppress turbulence (Richardson 1925). The ever-shifting balance between promotion and suppression, expressed as the Richardson number (Richardson 1925), determines the short-term (storm episodic) and long-term (seasonal) response of lakes to the forcing actions of wind and sun", (Mortimer 1984). Mortimer draws attention to review articles (Hutchinson 1957; Mortimer 1956; Mortimer 1974; Ruttner 1952) and mentions that reference (Mortimer 1956) "is a historical account of the pioneering work of Birge and Juday, including their study of the penetration of radiation into lakes (Birge and Juday 1929), see also (Sauberer and Ruttner 1941) and of work of the wind in transporting heat downward (Birge 1916)".

More specifically, consider a linearly stratified fluid layer in two-dimensional space and let (x, z) be Cartesian coordinates (x horizontal, z vertical against gravity). Let $(-\mathrm{d}\rho/\mathrm{d}z) > 0$ be the constant vertical density gradient; moreover, assume the layer to be subject to a steady horizontal velocity field $U(z)$ with vertical gradient $\mathrm{d}U/\mathrm{d}z = constant$. With these quantities and the acceleration due to gravity, g, two squared frequencies can be formed, namely

$$N^2 = \frac{g\left(-\frac{\mathrm{d}\rho}{\mathrm{d}z}\right)}{\rho}, \text{(buoyancy frequency)},$$

$$S^2 = \left(\frac{\mathrm{d}U}{\mathrm{d}z}\right)^2, \quad \text{('shear' frequency)}.$$

Their ratio

$$Ri = \frac{N^2}{S^2}$$

defines the Richardson number. Miles (1961) in his seminal paper "On the stability of heterogeneous shear flows" proved by a linear instability analysis for a Boussinesq fluid that perturbations (u, v, ρ') to $(U, 0, \rho)$ decay exponentially if $Ri > ¼$, but grow exponentially if $Ri < ¼$. When $\mathrm{d}\rho/\mathrm{d}z$ and $\mathrm{d}U/\mathrm{d}z$ are not constant but vary smoothly, then $Ri = ¼$ is taken by physical oceanographers and limnologists as the local critical Richardson number characterizing the transition from stable to unstable flow on a local scale. More correctly, there is a value of Ri in the vicinity of ¼ below which a shear flow in a heterogeneous fluid becomes unstable.

It transpires that in the regime $Ri > ¼$ propagating or standing waves in lakes or the ocean maintain to stably exist when conditions of linearity are no longer fulfilled. This is the regime of *weakly* nonlinear waves and theoretical accounts of it are given by Ablowitz and Segur (1981), Lamb (1980), and Mysak (1984), Helfrich and Melville (2006) and others. When $Ri < ¼$, or for nonlinear waves in the vicinity of this value, the waves become unstable, leading to mixing and, consequently, *transformation* of the wave forms and the propagation properties. These mixing processes are typical as results of *strongly* nonlinear waves; they contribute to the thermocline destruction and the rapid transport of species (nutrients, phosphate, oxygen, etc.) into the hypolimnion. This mechanism is referred to as *meromixis*.

To understand the properties of the nonlinear equations, (Hutter 1986), it is helpful to address the rudiments of the theory of long shallow-water finite-amplitude *surface waves*. In their derivation, two nondimensional parameters arise:

$$\varepsilon = \frac{a}{H}, \qquad \mu = \left(\frac{H}{\lambda}\right)^2,$$

where a and λ are, respectively, the wave amplitude and a horizontal length scale, H is the undisturbed water depth, ε measures nonlinear wave steepening, and μ linear phase dispersion, while the Ursell number

$$U = \frac{3\varepsilon}{\mu}$$

gives the relative significance of the two effects. Generally, ε and μ are small and of the same weight, and waves traveling in the positive x-direction are governed by the Korteweg-de Vries equation (1894; 1895):

$$\zeta_t + c_0\zeta_x + c_1\ \zeta\zeta_x + c_2\,\zeta_{xxx} = 0,$$

$$c_0 = \sqrt{gH}, \quad c_1 = \frac{3c_0}{2H}, \quad c_2 = \frac{1}{6}c_0 H^2.$$

In his historical account on the *K*–d*V* equation, Miles (1981) states that "Boussinesq (1871b; 1872; 1877) obtained two implicit equivalents of the *K*–d*V* equation . . . but missed the simpler and more important (as it proved to be) form of Korteweg and de Vries (1895). Kruskal (1978) and Miura (1976) discuss its mathematical properties. For strongly nonlinear waves, c_1 is large and c_2 small; the wave solutions steepen ahead of their crests and a hydraulic jump or shock wave is formed. For weak nonlinear waves, c_1 is small, but c_2 large; then wave dispersion is significant.

The solitary wave solution of the *K*–d*V* equation is given by

$$\zeta = a \operatorname{sec} \mathrm{h}^2 \frac{x - ct}{L},$$

$$c = c_0 + \frac{1}{3}ac_1 = c_0\left(1 - \frac{a}{2H},\right)$$

$$L = \sqrt{\frac{12c_2}{ac_1}} = \sqrt{\frac{4H^3}{3a}},$$

which represents a symmetric hump of permanent form, Fig. 1.1. For a sufficiently smooth and localized initial wave form $\zeta(x, 0)$, the asymptotic solution for $t \to \infty$ will consist of a group of solitons, trailed by a linear wave train. The leading soliton always has the largest amplitude and travels fastest, the second soliton has the second largest amplitude and so on, and the soliton group tends to spread, Fig 1.2. The number of solitons that emerges from any initial profile can be obtained from a Schrödinger equation in which the potential well is given by the initial profile; see Gardiner (1967) and Osborne and Burch (1980). Asymptotic soliton groups develop from initial wave humps; initial troughs develop into oscillatory wave trains.

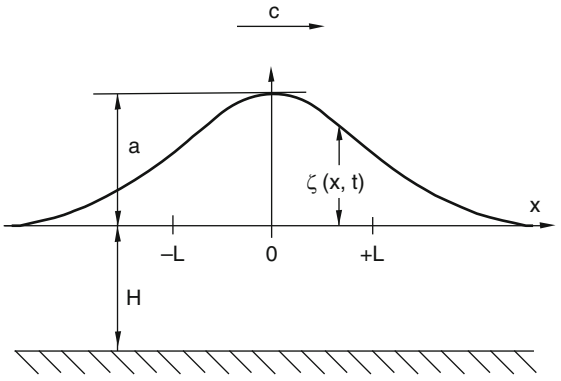

Fig. 1.1 Surface solitary wave with amplitude *a* moving to the right with phase speed *c* in water of depth *H*. (The amplitude *a* is exaggerated relative to *H*)

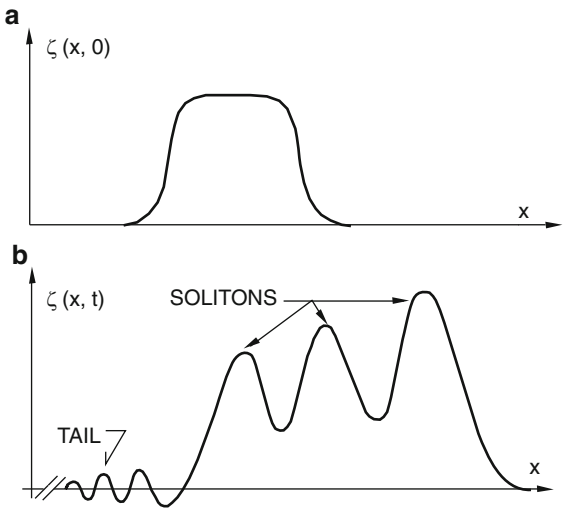

Fig. 1.2 A sufficiently localized initial wave profile $\zeta(x, 0)$, shown in (**a**) evolves into (**b**), a group of solitons and a dispersive wave train

Nonlinear *internal* water waves lead to similar descriptions: Keulegan (1953) and Long (1956) gave an account of long solitary waves in a two-layer fluid; Benjamin (1966; 1967), Davis and Acrivos (1967), Ono (1975), Joseph (1977), Kubota et al. (1978), Grimshaw (1978; 1979; 1981a; b; c; 1983), and others studied the continuously stratified fluid in which the wavelength λ, the total depth H, and a stratification scale height h (the thickness of the metalimnion) are crucial parameters. Three limiting cases are distinguished:

1. Shallow-water theory: $\lambda/H >> 1$, $h/H < \mathrm{O}(1)$,
2. Deep-water theory: $\lambda/H \to 0$, $\lambda/h >> 1$,
3. Finite-depth theory $\lambda/h >> 1$, $h/H << 1$, (i.e. $\lambda \sim H$)

and all can be derived from a generalized evolution equation due to Whitham (1967):

$$\frac{\partial \zeta}{\partial t} + c_1 \zeta \frac{\partial \zeta}{\partial x} + \frac{\partial}{\partial x} \int_{-\infty}^{\infty} \zeta(x', t) \left\{ \frac{1}{2\pi} \int_{-\infty}^{\infty} c(k) e^{ik(x-x')} \mathrm{d}k \right\} dx' = 0,$$

where ζ measures the internal wave displacement field (e.g., $\zeta = \int w \mathrm{d}t$, where w is the vertical velocity component, or ζ is the interfacial displacement at a density discontinuity) and $c(k)$ is the linear phase speed. Shallow-water internal waves (Benjamin 1966; 1967) have $c(k) = c_0(1 - Bk^2)$ and are thus governed by the K–dV equation. For a continuously stratified fluid, a countable infinite number of eigenspeeds exists, which corresponds to the different vertical baroclinic modes; in each of these cases, c_0, c_1 and c_2 take on their respective values. In a two-layer fluid, they are

$$c_0 = \sqrt{g' \frac{(H_1 H_2)}{H}},$$

$$c_1 = -3c_0 \frac{H_2 - H_1}{H_1 H_2},$$

$$c_2 = c_0 \frac{H_1 H_2}{6},$$

where $g' = g(\rho_2 - \rho_1)/\rho_1)$ is the reduced gravity and H_1, H_2 are the epi- and hypolimnion depths, respectively. Evidently, for $H_1 = H_2, c_1 = 0,;$ hence, the nonlinear term vanishes in this case. When $H_2 > H_1$, then $c_1 < 0$ and the solitary wave solution is a depression wave (Fig 1.3); alternatively, when $H_2 < H_1$,the wave travels as a hump. Explicitly, the solution reads

$$\zeta = -a \sec \mathrm{h}^2 \frac{x - ct}{L},$$

$$H_1 u_1 = -H_2 u_2 = c_0 a \sec \mathrm{h}^2 \frac{x - ct}{L},$$

$$c = c_0 - \frac{1}{3} a c_1,$$

$$L = \sqrt{-\frac{12 c_2}{a c_1}}$$

and implies that with $c_1 < 0$, the phase is enhanced by nonlinearities.

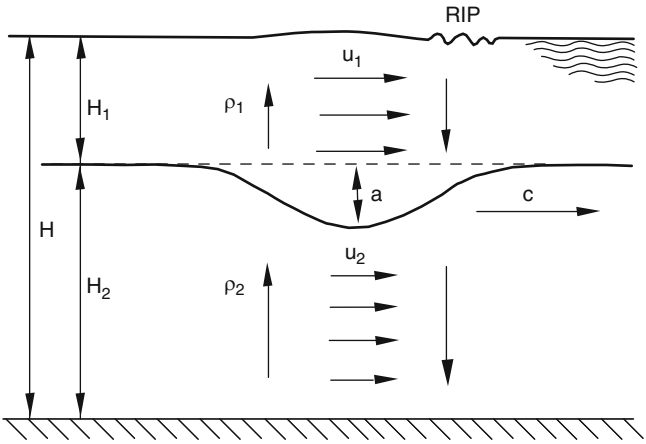

Fig. 1.3 Internal solitary wave in a two-layer fluid with $H_1 < H_2$. Arrows indicate current pattern within the internal wave. This gives rise to the surface rip which leads the wave. When $H_1 > H_2$, the solitary wave is a wave of elevation rather than a wave of depression

Long internal waves in *deep* water are governed by the Benjamin-Davis-Ono equation; it can be deduced from Whitham's equation by substituting the dispersion law $c = c_0(1 - \gamma\|\gamma\|)$. For the special case of a two-layer fluid with a deep lower layer, the solitary wave solution reads (Benjamin 1967)****

$$\zeta = \frac{aL^2}{(x - ct)^2 + L^2},$$

$$c = c_0 + \frac{1}{4}ac_1, L = -4a\frac{c_2}{c_1} > 0,$$

$$c_0 = \sqrt{g'H_1}, \quad c_1 = -3\frac{c_0}{H_1}, \quad c_2 = -\frac{c_0\rho_1 H_1}{2\rho_2}.$$

The finite depth equation for intermediate wavelengths is treated by Joseph (1977) and Koop and Butler (1981). All these cases apply under the limiting situation of a quiescent fluid. Additional complexities are *mean shear* (Lee and Bearsley 1974; Maxworthy 1979; Tung et al. 1981), *slowly varying topography* (Grimshaw 1981a; b; c), *changes in topography in the direction of propagation* (Farmer 1978; Farmer and Carmack 1981; Farmer and Smith 1978; Grimshaw 1978), *attenuation due to energy dissipation* (Grimshaw 1981a; Koop and Butler 1981), *radiation damping* (Grimshaw 1979; Maslowe and Redekopp 1980), *fission* (Djordjevic and Redekopp 1978), and *second order effects* (Gear and Grimshaw 1983; Grimshaw 1981c; Segur and Hammak 1982). In this list, effects of the rotation of the Earth and the transverse tilting of the thermocline in a nonlinear internal surge are still ignored.

1.3 Observations of Nonlinear Internal Waves

Nonlinear internal solitary waves in nature have been observed in the ocean, primarily in the continental shelf regions and in fjords and straits, in the atmosphere, and in lakes (Mysak 1984). Prominent examples are internal waves in the Andaman Sea (Osborne and Burch 1980), in the Strait of Georgia (Gargett 1976), and in Knight Inlet (Farmer and Carmack 1981; Farmer and Smith 1978). Laboratory experiments have been conducted, among others, by (Davis and Acrivos 1967) (Church 1945), Benjamin (1967), Maxworthy (1979; 1980), Kao and Pao (1980), Koop and Butler (1981), and Segur and Hammak (1982).

Our own experimental work, done in the laboratory of the Department of Mechanics of Darmstadt University of Technology, concerned weak and strong nonlinear waves of a two-layer fluid in a rectangular channel with constant or variable basal topography. It resulted in MSc and PhD dissertations (Hüttemann 1997; Maurer 1993; Schuster 1991; Wessels unpublished), summarized in Diebels

et al. (1994), Maurer et al. (1996), Hüttemann and Hutter (2001), Vlasenko et al. (2005a; 2003), Vlasenko and Hutter 2001; 2002a; b), and (Wessels and Hutter 1996), describing the fission of an internal soliton when approaching an obstruction. Substantial, painstaking extensions of these types of experiments are presented in detail by Gorogedtka et al. in Chap. 3 of this book. Interpretations of some of these – not in terms of nonlinear wave equations (e.g., the K–de$V$ equation) but by solutions of the (turbulent) Navier–Stokes (Reynolds) equations – are given by Vlasenko and Hutter (2002a; b), Vlasenko et al. (2005a; 2003), Stashchuk et al. (2005a; 2005b), and by Maderich et al. in Chap. 4 of this book. Among others, a collection of observational studies of nonlinear internal waves in lakes worldwide is given in Table 1.1.

As an example, we quote from Mysak (1984). "What is observed in many long lakes is that following a strong gust of along shore winds, the thermocline at one end of the lake is depressed and an internal surge is formed. Initially, the surge steepens owing to nonlinear effects, but as it propagates down the lake it evolves with a train of shorter period waves which often tend to have the appearance of a group of solitons or solitary waves [. . .]. In very long lakes (e.g., Babine Lake) the waves tend to disappear at the far end because of dissipation or dispersion. However, in some of the shorter lakes, the surges are seen to travel back and forth along the lake several times."

Table 1.1 Collection of lakes on Earth, where experimental campaigns on internal waves have been conducted

Lake name	References
Babin	Farmer (1978), Farmer and Carmack (1981), Farmer and Smith (1978)
Baikal	Granin (1984), Verbolev et al. (1984), Shimaraev et al. (1994), Chensky et al. (1998), and Lovcov et al. (1998)
Baldegg	Lemmin (1987) and Boegman et al. (2005)
Banyoles	Roget (1992) and Roget et al. (1997)
Biwa	Boegman et al. (2003) and Shimizu et al. (2007), Shimizu and Imberger (2008)
Chapla	Filonov and Thereshchenko (1999)
Constance	Chubarenko et al. (2003) and Appt et al. (2004)
Geneva	Thorpe et al. (1996) and Thorpe and Lemmin (1999)
Kinneret	Imberger (1998), Saggio and Imberger (1998; 2001), Antenucci and Imberger (2001a), Boegman et al. (2003), Gomes-Giraldo et al. (2008)
Ladoga	Filatov et al. 1981 (1981), Filatov (1983, 1990), Filatov (1991), Kochkov (1989), Rukhovets and Filatov (2009)
Loch Ness	Thorpe (1974, 1977)
Lugano	Hutter (1983, 1986, 1991)
Michigan	Mortimer (2004)
Onego	Filatov et al. (1990), Rukovets and Filatov (2009), Hutter et al. (2007)
Ontario	Mortimer (2006)
Seneka	Huntkins and Fliegel (1973)
Zurich	Horn (1981), Mortimer and Horn (1982), and Horn et al. (1986)

Figure 1.4 shows such a situation for Lake Zurich for an episode 11.-14.04.1978. Following the very strong eastward blowing wind, the thermocline became tilted, downward at the southeastern end and upward at the western end. When the wind stopped, the thermocline relaxed and began to oscillate with a 44-h fundamental seiche period. However, as the thermocline was depressed downward at the southeastern end, its encounter with the shallow bathymetry produced a large surge marked A in Fig. 1.4 (as an upwelling of the isotherm-depth-time series for mooring (4) and a downwelling for mooring (11)). This surge then traveled to the other end of the lake (~24 km) in about 1 day, seen in Fig. 1.4 as downstrokes ABCD at (11), (9), (6), and (4) and return propagation EFGH at (4), (6), (9), and (10). The surge seems to be locked to the gravest seiche mode, repeatedly newly generated at the western end by the downstroke of the thermocline in its gravest seiche mode; for more see (Horn et al. 1986; Mortimer and Horn 1982).

Field observations also suggest that the rate of decay from basin-scale internal waves to small-scale internal waves is due to several identifiable mechanisms, namely (1) nonlinear steepening and ensuing disintegration of long internal waves or solitons; (2) shear instabilities caused by energy transfer from the mean flow or basin-scale seiches to the small-scale motion; (3) shoaling at and reflection from slopes; (4) effects of localized constrictions stimulating the development of wave instability; and (5) interaction with topography (Horn et al. 2001; Vlasenko and Hutter 2002b). The laboratory experiments in Chap. 3 deal with the propagation and interaction of internal waves with underwater obstacles, slopes, and the effect of localized constrictions of channels with rectangular cross-sections. Table 1.2 summarizes the studied configurations of obstructing elements in an otherwise rectangular flume with constant depth; see also Fig. 1.5.

In the experiments discussed in Chap. 3, the upper-layer depth was consistently smaller than the lower layer depth; so, solitons approach submerged bodies as interface *depressions*. Depending on the value of the ratio h^*/H_2 of the obstruction height to the lower-layer depth, a soliton encounter with the obstacle is recognized as follows:

1. When $h^*/H_2 << 1$ as a *transformation* of the approaching solitary wave to a transmitted signal (often with undulating tail) and no visible reflected wave and no recognizable turbulent eddies due to the encounter.
2. When $h^*/H_2 < 1$ as an *interaction* of the wave with the obstacle in which the soliton is transformed and split into a transmitted and a reflected signal. Because of the often observed formation of a pair of turbulent eddies in front of the obstacle, energy is dissipated in this fission into a smaller scale transmitted signal and a reflected solitary wave which together are not energy conserving.
3. When $h^*/H_2 \leqslant 1$ (h^* is very close to H_2), the interactions of the approaching wave with the obstacle give rise to wave instabilities, high turbulence and *mixing* with low-energy signal transmitted, some reduced reflected wave signal and large turbulent activity into smaller scale motion. This is the regime where nonlinear two-layer modeling ceases to reliably reproduce the true interactions, and nonhydrostatic turbulent modeling is becoming necessary.

The detailed description of these interaction regimes is given in Chaps. 3 and 4.

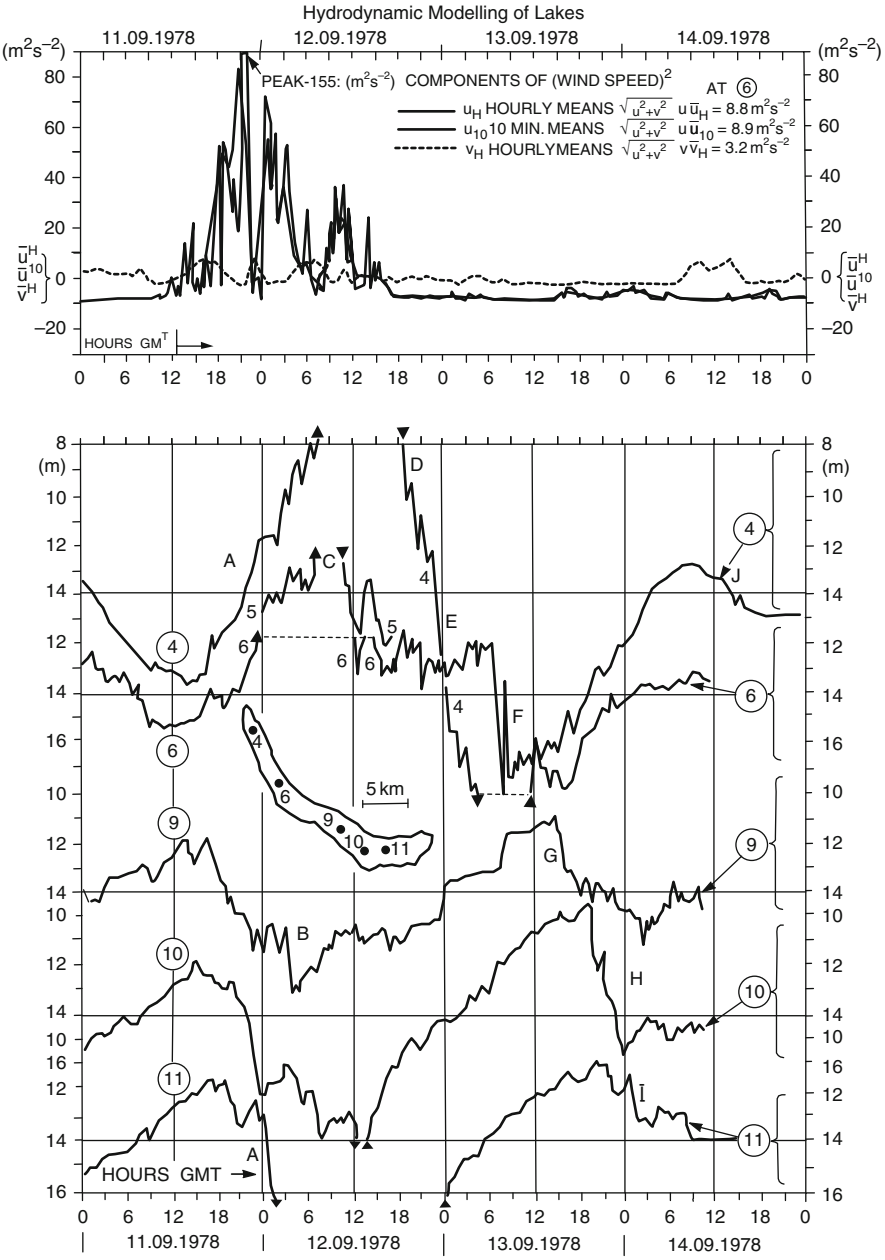

Fig. 1.4 Depth variation of the 10°C isotherm at mooring stations 4, 6, 9, 10, and 11 from 11.–14. 09. 1978, in Lake Zurich. Mooring station numbers, placed near the corresponding traces, are *circled*. Letters A to I refer to the passage of an internal surge past the indicated stations. The *upper panel* displays the *u* (EW) and *v* (NS) components of the wind speed squared, 3 m above the lake surface at station 6, reproduced from (Mortimer and Horn 1982), ©Vierteljahresschrift der Natforsch. Ges. Zürich

Table 1.2 Types of encounters of an internal soliton (trough) with topographic obstructions in a two-layer system (see also Fig. 1.5)

Form of obstacle	Remarks/References
– Triangular or trapezoidal obstructionwith $h^* < h_2$ and $H_1 < H_2$ – Geometry, see Fig. 1.4a – Soliton as an interface depression	Guo et al. (2004), Hüttemann and Hutter (2001) Maurer et al. (1996), Wessels and Hutter (1996), Sveen et al. (2002) Sveen et al. (2002)
– thin plate or cuboid obstructionwith $h^* < H_2$, $H_1 < H_2$– Obstruction length L with $L \approx 0$ or $L > h^*$ – Geometry, see Fig. 1.5b – Approaching soliton as interface depression	This book, Chap. 3 for experiments, Chapter 4 for numerical modeling and comparison with experiments
– Cylindrical lateral obstruction of Gaussian form covering both layers – Geometry, see Fig. 1.5c – $H_1 < H_2$ for a solitary depressing wave	This book, Chap. 3 for experiments
– Reflection of an internal wave at a slope or a slope–shelf combination – Slope angle $0° < \beta < 90°$ – Shelf angle $0° < \alpha << 90°$ – Geometry, see Fig. 1.5d	This book, Chap. 3 for experiments; Chaps. 1 and 4 for numerical modeling Vlasenko and Hutter (2002a, b) Vlasenko et al. (2005a, b)) Thorpe (1997)

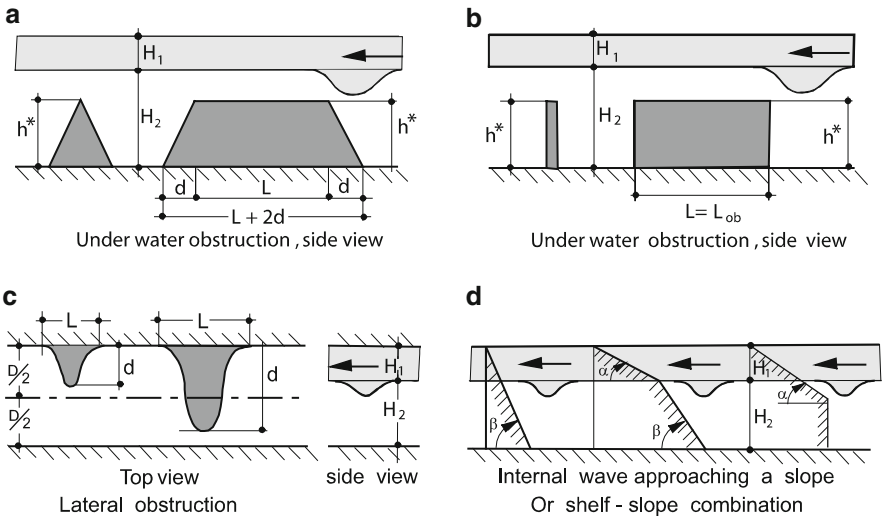

Fig. 1.5 Sketches of obstructions in a two-layer fluid in a rectangular duct: (**a**) Underwater *triangle* or trapezoid, *side view*; (**b**) plate or cube, *side view*; (**c**) Gaussian cylinders covering both layers, *top view*; (**d**) slope or slope shelf combination, *side view*

Analytical description of nonlinear wave motion in stratified fluids (e.g., expressed by the K–dV equation) follows a judicious balance between nonlinear advection (responsible for nonhydrostatic wave steepening) and linear dispersion

(responsible for smoothing). When nonlinear advection is small, hydrostatic conditions prevail and the shallow water approximation applies; however, when advection is dominant, nonlinear steepening develops and instabilities may ensue. This is the case, e.g., in all those situations when bathymetric variations or underwater obstructions cause wave breaking and form turbulent eddies, which may break long basin-scale waves and split them into a whole spectrum of small-scale internal processes. It is obvious that this post-critical motion must be modeled by nonhydrostatic multi-layered numerical models, which account for the internal mixing of matter from near-surface layers down to large depths (known as meromixis).

A large number of numerical software exists which integrates the turbulent Navier–Stokes equations. In Chap. 4, some are briefly reviewed, and Maderich et al. present their own formulation on the basis of large eddy closure schemes and precursors of their software, (Kanarska and Maderich 2003; 2004; Kanarska et al. 2007; Maderich et al. 2008; 2009; 2010); they apply it to some of the experiments, discussed in Chap. 3.

References

Ablowitz M and Segur H (1981) Solitons and the inverse scattering transform Soc. Industrial and Applied Mathematics, p 425

André, Father Louis, quoted and translated in Relation of 1671–72, and in Relation of 1676–77; Thwaites RG: The Jesuit Relations and Other Documents, 60, Burrow, Cleveland, Ohio 1671, 1676

Antenucci JP, Imberger J and Saggio A (2000) Seasonal evolution of the basin scale internal wave field in a large stratified lake. Limnol Oceanogr 45(7):1621–1638

Antenucci JP, Imberger J (2001) On internal waves near the high-frequency limit in an enclosed basin. J Geophys Res106:22465–22474

Antenucci JP and Imberger J (2001) Energetics of long internal gravity waves in large lakes. Limnol Oceanogr 46(7):1760–1773

Appt J, Imberger J and Kobus H (2004) Basin-scale motion in stratified Upper Lake Constance. Limnol Oceanogr49(4):919–933

Bäuerle E (1981) Die Eigenschwingungen abgeschlossener, zweigeschichteter Wasserbecken bei variabler Bodentopographie. Bericht aus dem Institut für Meereskunde, Christian Albrechts Universität

Bäuerle E (1985) Internal free oscillations in the Lake of Geneva. Annales Geophysicae 3:199–206

Bäuerle E (1994) Transverse baroclinic oscillations in Lake Überlingen. Aquatic Sciences 56 (2): 145–149

Bèche HT, de la (1819) Sur la profondeur et la temperature du Lac de Genève. Bibl Univ Sci Arts, Genève

Benjamin, TB (1966) Internal waves of finite amplitude and permanent form. J Fluid Mech 25: 241–270

Benjamin, TB (1967) Internal waves of permanent form in fluids of great depth. J Fluid Mech 29: 559–592

Birge EA (1897) Plankton studies on Lake Mandota: II, The crustacea of the plankton from July 1894 to December 1896. Trans WisconsinAcad Sci Arts Lett, II, p 274

Birge EA (1916) The work of the wind in warming a lake. Trans Wis Acad Sci Arts Lett18**:** 341, 429, 495, 508
Birge EA and Juday C (1929) Transmission of solar radiation by the waters of inland lakes. Trans Wis Acad Sci Arts Lett24: p 509
Boegman L, Imberger J, Ivey GN, Antenucci JP (2003) High-frequency internal waves in large stratified lakes. Limnol Oceanogr 48:895–919
Boegman L, Ivey GN, Imberger J (2005) The degeneration of internal waves in lakes with sloping topography. Limnol Oceanogr 50:1620–1637
Boussinesq J (1871a) Théorie de l'intumescence liquide, appelée onde solitaire ou de translation, se propegant dans un canal rectangulaire. C R Acad Sci Paris 72: 755–759
Boussinesq J (1871b) Théorie génerale des mouvements qui sont propagés dans un canal rectangulaire horizontal. C R Acad Paris 73: 256–260
Boussinesq J (1872) Théorie des ondes et des ramous qui se propagent le long d'un canal rectangulaire horizontal, en communicant au liquide continue dans ce canal des vitesses sensiblement pareilles de la surface au fond. J Math Pure Appl 17(2): 55–108
Boussinesq J (1877) Essai sur la théorie des eaux courantes. Mém.présentés par divers Savants à L'Acad. Sci.Inst. France (series 2) 23: 1–680 (see also 24: 1–64)
Boyce FM and Mortimer CH (1977) IFYGL temperature transects, Lake Ontario, 1972. Environment Canada, Tech Bull 100
Caloi P (1954) Oscillationi libre del Lago di Garda. Arch Met Geophys Bioklim A7: p 434
Charney JG (1955) Generation of oceanic currents by wind. J Mar Res 14: 477–498
Chensky AG, Lovtsov SV, ParfenovYuV, Rastegin AE, Rubtzov VYu (1998) On the coastal-trapped waves in the southern area of Lake Baikal. Oceanic Fronts and Related Phenomena, Konstantin Fedorov Memorial Symposium. St.-Petersburg: RSHMU Publishers, 29–30
Chrystal G (1905) On the hydrodynamical theory of seiches (with a biographical sketch). TransRoy Soc Edinburgh 41: p 599
Chubarenko I Chubarenko B, Bäuerle E, Wang Y, and Hutter K (2003) Autumn Physical Limnological Experimental Campaign in the Island Mainau Littoral Zone of Lake Constance. J Limnol 62: 115–119
Church PE (1942) The annual temperature cycle of Lake Michigan, I. Cooling from late autumn to the terminal point, 1941–1942. Univ Chicago Inst Meteorol, Misc, Rept 4
Church PE (1945) The annual temperature cycle of Lake Michigan, II Spring warming and summer stationary periods 1942 Cooling. Univ Chicago Inst Meteorol, Misc, Rept 18
Davis RE and Acrivos, A (1967) Solitary internal waves in deep water. J Fluid Mech 29: 593–607
Defant A (1918) Neue Methode zur Ermittlung der Eigenschwingungen (seiches) von abgeschlossenen Wassermassen (See, Buchten, usw.).Ann Hydrogr, Berlin 46: p 78
Defant F (1953) Theorie der Seiches des Michigansees und ihre Abwandlung durch Wirkung der Corioliskraft. Arch Met Geophys Bioklim, Vienna A6: p 218
De Vries, G (1894) Bijdrage toto de kennis der lange goven. Doctoral Dissertation University of Amsterdam.
Diebels S, Schuster B and Hutter K (1994) Nonlinear internal waves over variable topography. Geophys Astrophys Fluid Dyn 76: 165–192
Djordjevic VD and Redekopp LD (1978) The fission and disintegration of internal solitary waves moving over two-dimensional topography. J Phys Oceanogr 8: 1016–1024
Farmer DM (1978) Observations of long nonlinear internal waves in a lake. J Phys Oceanogr 8: 63–73
Farmer DM and Carmack EC (1981) Wind mixing and restratification in a lake near the temperature of maximum density. J Phys Oceanogr 11: p 1516
Farmer DM and Smith JD (1978) Nonlinear internal waves in a fjord. In: Hydrodynamics of Estuaries and Fjords (JCJ Nihoul, ed), Elsevier: 465–493
Filatov NN (1983) Dynamics of lakes. Leningrad, Gidrometeoizdat Press, 166 [In Russian]
Filatov NN (1991) Hydrodynamics of Lakes. St.-Petersburg: Nauka Press, 191 [In Russian with English summary]

Filatov NN, Beletsky DV, Zaitsev LV (1990) Variability of hydrophysical fields in Lake Onego. "Onego" experiment.Water Problems Department, Karelian Scientific Centre AS USSR, Petrozavodsk, 110 [In Russian]
Filatov NN, Ryanzhin SV, Zaitsev LV (1981) Investigation of turbulence and Langmuir circulation in Lake Ladoga. J Great Lakes Res 7(1): 1–6
Filonov AE, Thereshchenko, IE (1999) Thermal lenses and internal solitons in Chapla Lake, Mexico. Chin J Oceanol Limnol 17(4): 308–314
Forel FA (1895) Lac Léman. Monographie Limnologique, 2, Lausanne
Gardiner CS (1967) Method for solving the Kortweg-de Vries equation. Phys Rev Lett 19: 1095–1097
Gargett AE (1976) Generation of Internal Waves in the Strait of Georgia, British Columbia. Deep Sea Res 23**:** 17–32
Gear JA and Grimshaw R (1983) A second order theory for solitary waves in shallow fluids. Phys Fluids 26: 14–29
Geistbeck a (1885) Die Seen der deutschen Alpen. Mitt Ver Erdkunde, Leipzig
Goldstein S (1929) Tidal motion in a rotating elliptic basin of constant depth. MonthlyNotes Royal Astronom Soc (Geophys Suppl) 2: 213–231
Gomez-Giraldo A, Imberger J, Antenucci J, Yeates P (2008) Wind-shear-generated high-frequency internal waves as precursors to mixing in a stratified lake. Limnol Oceanogr 53: 354–367
Granin N (1984) Some results of internal wave measurements in Lake Baikal. In: Hydrology of Lake Baikal and other water bodies. Nauka, Novosibirsk: 67–71 [In Russian]
Grimshaw R (1978) Long nonlinear internal waves in channels of arbitrary cross sections. J Fluid Mech 86: 415–431
Grimshaw R (1979) Slowly varying solitary waves I. Korteweg-de Vries equation. Proc Roy Soc, London A368**:** 359–375
Grimshaw R (1981a) Evolution equations for long, nonlinear internal waves in stratified shear flows. Studies Appl Math 65: 159–188
Grimshaw R (1981b) Slowly varying solitary waves in deep fluids. Proc Royal Soc London A376: 319–332
Grimshaw R (1981c) A second order theory for solitary waves in deep fluids. Phys Fluids 24**:** 1611–1618
Grimshaw R (1983) Solitary waves in density stratified fluids. In*:* Nonlinear deformation waves. IUTAM Symposium, Tallin, 1982 (U Nighel and J Engelbrecht, eds), 431–447, Springer Verlag, Berlin etc.
Guo Y, Sveen JK, Davies PA, Grue J, Dong, P (2004) Modelling the motion of an internal solitary wave over a bottom ridge in a stratified fluid. Environ Fluid Mech4: 415–441
Heaps NS (1961) Seiches in a narrow lake, uniformly stratified in three layers. Geophys Supp J Roy Astronom Soc London5**:** p 134
Heaps N (1975) Resonant tidal co-oscillations in a narrow gulf. Arch Met Geophys Bioklim A24: p 361
Heaps NS, Mortimer CH and Fee EJ (1982) Numerical models and observations of water motion in Green Bay, Lake Michigan. Phil Trans Roy Soc, London A306: p 371
Helfrich K, Melville W (2006) Long nonlinear internal waves. Ann Rev Fluid Mech 38: 395–425
Hollan E (1974) Strömungsmessungen im Bodensee. Ber Arbeitsgem Wasserwerke Bodensee-Rhein, (AWBR) 6: p 111–187
Horn W (1981) Zürichsee 1978: Physikalisch-limnologisches Messprogramm und Datensammlung. Internal Report Nr 50**.** Versuchsanstalt für Wasserbau, Hydrologie und Glaziologie, Eidg Tech Hochschule, Zürich (unpublished)
Horn W, Mortimer CH, Schwab D J (1986) Wind-induced internal seiches in Lake Zurich observed and modeled. Limnol Oceanogr 31(6): 1232–1254
Horn DA, Imberger J, Ivey GN (2001) The degeneration of large-scale interfacial gravity waves in lakes. J Fluid Mech 434: 181–207

Horn DA, Imberger J, Ivey GN, Redekopp LG (2002) A weakly nonlinear model of long internal waves in closed basins. J Fluid Mech 467: 269–287
Hunkins K, Fliegel M (1973) Internal undular surges in Seneca Lake: a natural occurrence of solitons. J Geophys Res 7: 539–548
Hutchinson GE (1957) A treatize on limnology. Vol 1 Geography, Physics and Chemistry, Wiley, New York: p 10015
Hüttemann, H (1997) Modulation interner Wasserwellen durch Variation der Bodentopographie. Diplomarbeit am Fachbereich Mechanik, Darmstadt University of Technology, 110 p. (unpublished)
Hüttemann H and Hutter K (2001) Baroclinic solitary water waves in a two-layer fluid system with diffuse interface.Experiments in Fluids 30: 317–326
Hutter K (1983) Strömungsdynamische Untersuchungen im Zürich und Luganersee. Ein Vergleich von Feldmessungen mit Resultaten theoretischer Modelle. SchweizZ Hydrol 45: 101–144
Hutter K (1986) Hydrodynamic modeling of lakes. Encyclopedia of Fluid Mechanics 6, Gulf Publishing: 897–998
Hutter K (1991) (with contributions by Bäuerle, E., Salvadè, G., Spinedi, C. and Zamboni, F.), Large scale water movements in lakes.Aquatic Sciences 53: 100–135
Hutter K, Salvadè G and Schwab DJ (1983) On internal wave dynamics in the northern basin of the Lake of Lugano. Geophys Astrophys Fluid Dyn 27: 299–236
Hutter K, Wang Y and Chubarenko I (2011) Physics of Lakes. Vol 2, Lakes as oscillators, Springer Verlag, Berlin etc.
Hutter K, Filatov N, Maderich V, Nikishov V, Pelinovsky E, Vlasenko V (2007) 'Strongly nonlinear internal waves in lakes: Generation, transformation, meromixis' Final report of INTAS project No 03-51-3778
Imberger J (1998) Flux paths in a stratified lake: A review: 1–17. In: Physical processes in lakes and oceans. (Imberger J, Ed.), Coastal and Estuarine Studies. American Geophysical Union
Jeffreys H (1923) The free oscillations of water in an elliptical lake. Proc Lond Math Soc 2nd Ser: p 455
Joseph RI (1977) Solitary waves in a finite depth fluid. J Phys A10: L225–227
Kanari S (1975) The long internal waves in Lake Biwa. Limnol Oceanogr 20: 544–553
Kanarska Y, Maderich V (2003) A non-hydrostatic numerical model for calculating free-surface stratified flows. Ocean Dynamics 53: 6–18
Kanarska Y, Maderich V (2004) Strongly non-linear waves and gravitational currents in rectangular basin. Applied Hydromechanics 6(78) No 2: 75–78
Kanarska Y, Shchepetkin A, McWilliams JC (2007) Algorithm for non-hydrostatic dynamics in the Regional Oceanic Modeling System. Ocean Modelling 18: 143–174
Kelvin Thomson, Lord, W (1871) Hydrokinetic solutions and observations. Philosophical Magazine 42: 362–377
Kao TW and Pao HP (1980) Wake collapse in the thermocline and internal solitary waves. J Fluid Mech 97: 117–127
Keulegan GK (1953) Characteristics of internal solitary waves. J Res Nat Bureau of Standards 51: 133–140
Kochkov NV (1989) The patterns of generation, evolution and destruction of internal waves in lakes. Doctoral Dissertation. Institute of Limnology, Leningrad [In Russian]
Koop CG and Butler G (1981) An investigation of internal solitary waves in a two fluid system. J Fluid Mech 112: 225–251
Korteweg DJ and de Vries G (1895) On the change of form of long waves advancing in a rectangular channel and on a new type of long stationary waves. Phil Mag 39: 422–443
Kruskal MD (1978) The birth of the soliton. In: Nonlinear evolution equations solvable by the spectral transform (F. Calogero, ed), Pitman: 1–8
Kubota T, Ko DRS nad Dobbs LD (1978) Weakly nonlinear, long internal gravity waves in stratified fluids of finite depth. AIAA J Hydronautics 12: 157–165
Lamb GL, Jr (1980) Elements of soliton theory. John Wiley and Sons, New York

Lee CY and Bearsley RC (1974) The generation of long nonlinear internal waves in a weakly stratified shear flow. J Geophys Res 79: 453–462

Lemmin U (1987) The structure and dynamics of internal waves in Baldeggersee. Limnol Oceanogr 32: 43–61

Lemmin U and Mortimer CH (1986) Tests of an extension to internal seiches of Defant's procedure for determination of surface seiche characteristics in real lakes. Limnol Oceanogr 31(6): 1207–1231

Lemmin U, Mortimer H and Bäuerle E (2005) Internal seiche dynamics in Lake Geneva. Limnol Oceanogr 50(1): 207–216

Lighthill J (1969) Dynamic response of the Indian Ocean to onset of the southwest monsoon. Phil Trans Roy Soc London A265: 45–92

Long RR (1956) Solitary waves in one- and two-fluid systems. Tellus 8: 460–470

Lovcov SV, Parfenov JuV, Rastegin AE, Rubcov V Ju, Chensky AG (1998) Macro-scale variability of water temperature and internal waves in Lake Baikal. Astrofisika I Fisika mikromira Proceed. School of Basic Physics**,** Irkursk Univ: 279–285 [In Russian]

Maderich V, Heling R, Bezhenar R, Brovchenko I, Jenner H, Koshebutskyy V, Kuschan A, Terletska K (2008) Development and application of the 3D numerical model THREETOX to the prediction of cooling water transport and mixing in inland and coastal waters. Hydrological Processes 22: 1000–1013

Maderich V, Grimshaw R, Talipova T, Pelinovsky E, Choi B, Brovenchko I, Terletska K, Kim D (2009) The transformation of an interfacial solitary wave of elevation at a bottom step. Nonlinear Processes in Geophysics 16: 1–10

Maderich V, Talipova T, Grimshaw R, Brovenchko I, Terletska K, Pelinovsky E, Choi B (2010) Interaction of a large amplitude interfacial solitary wave of depression with a bottom step. Phys Fluids doi:10.1063/1.3455984

Marcelli L (1948) Sesse del Lago di Lugano. (Publ Ist Naz Geofis, Roma) Ann Geofis1: p 454

Maslowe SA and Redekopp LG (1980) Long nonlinear waves in stratified shear flows. J Fluid Mech 101: 321–348

Maurer J (1993) Skaleneffekte bei internen Wellen im Zweischichtenfluid mit topographischen Erhebungen. Diplomarbeit am Fachbereich Mechanik, Darmstadt University of Technology (unpublished)

Maurer J, Hutter K and Diebels S (1996) Experiments on scale effects in internal waves of two-layered fluids with variable depth. European Journal of Mechanics (B Fluids) 15: 445–470

Maxworthy T (1979) A note on internal solitary waves produced by tidal flow over a three-dimensional ridge. J Geophys Res 84: 338–346

Maxworthy T (1980) On the formation of nonlinear internal waves from the gravitational collapse of mixed regions in two and three dimensions. J Fluid Mech 96: 47–64

McConnell A (1982) No Sea too Deep: The History of Oceanographic Instruments. Holger, Bristol

Merian JR (1885) Über die Bewegungen tropfbarer Flüssigkeiten in Gefässen. Abhandl JR Merian, Basel. Attracted little attention until reproduced by Von der Mühl, Math Ann 28: p 575

Miles JW (1961) On the stability of heterogeneous flows. J Fluid Mech 10: 496–508

Miles JW (1981) The Korteweg-de Vries equation: A historical essay. J Fluid Mech 106: 131–147

Miura RM (1976) The Korteweg-de Vries equation: A survey of results. SIAM Review 18: 412–459

Mortimer CH (1952) Water movements in stratified lakes deduced from observations in Windermere and model experiments. Union Geod Geophys, Bruxelles, Assn Int Hydrol, C Rend Rapp 3: p 335

Mortimer CH (1952) Water movements in lakes during summer stratification; evidence from the distribution of temperature in Windermere. Phil Trans Roy SocLondon B236: p 355

Mortimer CH (1953) A review of temperature measurement in limnology. Mitt Int Ver Limnol1: p 25

Mortimer CH (1953) The resonant response of stratified lakes to wind. Schweiz Z Hydrol 15: 94–151

Mortimer CH (1955) Some effects of the Earth's rotation on water movement in stratified lakes. Verh Internat Ver Limnol 12: p 66
Mortimer CH (1956) E.H. Birge – an explorer of lakes, 163–211. In: E.A. Birge, a memoir, By CG Sellery, Madison University Wisconsin Press
Mortimer CH (1963) Frontiers in physical limnology with particular reference to long waves in rotating basins. Great Lakes Res Div Publ. (University of Michigan) 10:9–42
Mortimer CH (1974) Lake Hydrodynamics. Mitt Internat Verein Limnol 20: 124–197
Mortimer CH (1979) Strategies for coupling data collection and analysis with dynamic modeling of lake motions. In: Hydrodynamics of lakes (WH Graf and CH Mortimer Eds) Eslevier Sci Publ Comp, Amsterdam, etc.:183–231
Mortimer CH (1984) Measures and models in physical limnology. In: Hydrodynamics of Lakes (K. Hutter Ed) CISM Courses and Lectures Nr 286, Springer Verlag Vienna-New York: 287–322
Mortimer CH (2004) Lake Michigan in motion: Responses of an inland sea to weather, earth-spin and human activities. University of Wisconsin Press
Mortimer CH (2006) Inertial oscillations and related internal beat pulsations and surges in lakes Michigan and Ontario. Limnol Oceanogr 51(5): 1941–1955
Mortimer CH and Fee EJ (1976) free surface oscillation and tides of Lakes Michigan and Superior. Phil Trans Soc Lond A281: p 1
Mortimer CH, Horn W (1982) Internal wave dynamics and their implications for plankton biology in the Lake of Zurich. Vierteljahresschrift Natforsch Ges Zürich1 27: 299–318
Mortimer CH and Moore WH (1953) The use of thermistors for the measurement of lake temperatures. Mitt Int Ver Limno l2: p 42
Mysak LA (1984) Nonlinear internal waves. In: Hydrodynamics of Lakes. CISM Lecture Notes, Nr 286 [K. Hutter, ed.] Springer Verlag Vienna etc.: 129–152
Neumann G (1941) Eigenschwingungen der Ostsee. Archiv der Deutschen Seewarte, Mar Observat 61(4)
Ono H (1975) Algebraic solitary waves in stratified fluids. J Phys Soc Japan 39: 1082–1091
Osborne AR and Burch TL (1980) Internal solitons in the Andaman Sea. Science 208: 451–460
Platt RB and Shoup CS (1950) the use of a thermistor in a study of summer temperature conditions of mountain lake Virginia. Ecology 31: p 484
Platzman GW and Rao DB (1964) Spectra of Lake Erie water levels. J Geophys Res 69: p 2525
Platzman GW (1963) The dynamic prediction of wind tides on Lake Erie. Meteorol Monogr 4(26): p 44
Platzman GW (1970) Ocean tides and related waves. Amer Math So., Lecturesin Appl Math 14: p 239
Platzman GW (1972) Two-dimensional free oscillations in natural basins. J PhysOceanogr 2: 117–138
Platzman GW (1975) Normal modes of the Atlantic and Indian Ocean. J Phys Oceanogr 5: 201–221
Platzman GW (1984) Normal modes of the world ocean. Part III: A procedure for tidal synthesis. J Phys Oceanogr 14: 1521–1531
Platzman G and Rao DB (1964) The free oscillations of Lake Erie. In: Studieson Oceanography (Hidaka Volume) (ed. K. Yoshida) University of Washington Press: 359–382
Proudman J (1928) On a general expansion in the theory of the tides. Proc LondMath Soc 29: 527–236
Raggio G and Hutter K (1982a) An extended channel model for the prediction of motion in elongated homogeneous lakes, Part I: Theoretical introduction. JFluid Mech 121: 231–255
Raggio G and Hutter K (1982b) An extended channel model for the prediction of motion in elongated homogeneous lakes, Part II: First order model applied to ideal geometry. Rectangular basins with flat bottom. J Fluid Mech 121: 257–281
Raggio G and Hutter (1982c) An extended channel model for the prediction of motion in elongated homogeneous lakes, Part III: Free oscillations in natural basins. J Fluid Mech 121: 283–299

Rao DB and Schwab D (1976) Two-dimensional normal modes in arbitrary enclosed basins on the rotating Earth: Applications to Lakes Ontario and Superior. Phil Trans Roy Soc London A281: 63–96

Rao DB, Mortimer CH and Schwab DJ (1976) Surface normal modes of LakeMichigan: calculations compared with spectra of observed water level fluctuations. J Phys Oceanogr 6: 575–588

Richardson LF (1925) Turbulence and vertical temperature difference near trees. Phil Mag 49: p. 81

Roget E (1992) Internal Seiches and Barclinic Currents in Lake Banyoles. Ph. D.Thesis, Autonomous University, Barcelona,pp 287

Roget E, Salvadè G and Zamboni F (1997) Internal seiche climatology in a small lake where transversal and second vertical modes are usually observed. LimnolOceanogr 42(4): 663–673

Rukhovets L, Filatov N (Eds.) (2009) Ladoga and Onego - Great European Lakes:Modelling and Experiment. London. Springer-Praxis, pp 302

Ruttner F (1952) Grundriss der Limnologie, 2nd ed, Berlin Gruyter, 232, translated by Fry FEJ and Frey DG as Fundamentals of Limnology, Toronto University Press

Saggio A and Imberger J (1998) Internal wave weather in a stratified lake. Limnol Oceanogr 43(8): 1780–1795

Saggio A, Imberger J (2001) Mixing and turbulent fluxes in the metalimnion of a stratified lake. Limnol Oceanogr 46: 392–409

Salvadè G, Zamboni F and Barbieri A (1988) Three-layer model of the north basin of Lake of Lugano. Annales Geophysicae 5B: 247–259

Sauberer F and Ruttner F (1941) Die Strahlungsverhältnisse der Binnengewässer. Becker and Erler, Leipzig: p 240

Saussure HB, de (1799) Voyages dans les Alpes. Neuchatel

Schmidt W (1917) Wirkungen der ungeordneten Bewegungen im Wasser der Meere und Seen. Ann Hydrogr Mar Met 367: p 431

Schuster B (1991) Experimente zu nichtlinearen internen Wellen großer Amplitudein einem Rechteckkanal mit variabler Bodentopographie. Doctoral Dissertation, TH Darmstadt vii + (1–165) (unpublished)

Schwab DJ (1977) Internal free oscillations in Lake Ontario. Limnol Oceanogr 22: 700–708

Segur H and Hammak JL (1982) Soliton models of long internal waves. J Fluid Mech 118: 285–304

Servais F (1975) Etude théorique des oscillations libres (seiches) du Lac Tanganika. Explor Hydrobiol Lac Tanganika, 1946–1947. Inst Roy Sci Nat Belique, Bruxelles 2: p 3

Shimaraev MN, Verbolov VI, Granin NG, Sherstyankin PP (1994) Physical limnology of Lake Baikal: a review. Baikal International Center for Ecological Research, Print N2, Irkutsk-Okayama

Shimizu K and Imberger J (2008) Energetics and damping of basin-scale waves in a strongly stratified lake. Limnol Oceanogr 53(4): 1574–1588

Shimizu K, Imberger, J and Kumagai M (2007) Horizontal structure and excitation of primary motions in a strongly stratified lake. Limnol Oceanogr 52(6): 2641–2655

Spilhaus FM and Mortimer CH (1977) A bathythermograph. J Mar Res, Yale 1: p 95

Stashchuk N, Vlasenko V, Hutter K (2005) Numerical mechanisms of disintegration of basin-scale internal waves in a tank filled with stratified water. Nonlinear Processes in Geophysic 12: 955–964

Stashchuk N, Filatov NN, Vlasenko V, Petrov M, Terzhevik A, Zdorovennov R (2005) Transformation and disintegration of internal waves near lake boundary. Abstract EGU05-A-02701; SRef-ID: 1607–7962/gra/ EGU05-A-02701

Stocker K and Salvadè G (1986) Interne Wellen im Luganersee. Bericht Nr I/85 der Versuchsanstalt für Wasserbau, Hydrologie und Glazionlogie an der ETH Zürich (unpublished)

Stocker K, Hutter K, Salvadè G, Trösch J and Zamboni F (1987) Observations and analysis of internal seiches in the Southern Basin of Lake of Lugano. AnnGeophysicae 5B: 553–568

Strom KM (1939) A reversing thermometer by Richter and Wiese with 1/100°C graduation. Int Rev Hydrol 38: p 259
Sveen JK, Guo Y, Davies PA, Grue J (2002) On the breaking of internal solitary waves at a ridge. J Fluid Mech 469: 161–188
Taylor GI (1920) Tidal oscillations in gulfs and rectangular basins. Proc Lond Math Soc, 2nd Ser **20**: p 148
Thorpe SA (1974) Near-resonance forcing in a shallow two-layer fluid: a model for the internal surge in Loch Ness. J Fluid Mech 69: 509–527.
Thorpe SA (1977) Turbulence and mixing in a Scottish loch. Phil Trans R Soc London A286: 125–181
Thorpe SA (1997) On the interaction of internal waves reflecting from slopes. J Phys Oceanogr 27: 2072–2078
Thorpe SA, Keen JM, Jiang R, Lemmin U (1996) High-frequency internal waves in Lake Geneva. Phil Trans Royal Soc LondonA 354: 170, 237–257
Thorpe SA, Lemmin U (1999) Internal waves and temperature fronts on slopes. Ann Geophysicae 17: 1227–1234
Tison LJ and Tison G Jr (1969) Seiches et dénivellations causées par le vent dans les lacs, baies, estuaries. Note Technique No 102, Organisation Météorologique Mondiale, Genève, Suisse
Tung KK, Ko DRS and Chang JJ (1981) Weakly nonlinear internal waves in shear. Studies Appl Math 65: 189–221
Vaucher JPE (1833) Mémoire sur les seiches du Lac de Genève, composé de 1803 à 1804. Mem Soc Phys Genève6**:** p 35
Verbolov VI. (Ed.) (1984) Hydrology of Lake Baikal and other waters. In: Hydrology of Lake Baikal and other water bodies. Nauka, Novosibirsk [In Russian]
Vlasenko V and Hutter K (2001) Generation of second mode solitary waves by the interaction of a first mode soliton with a sill. Nonlinear Processes in Geophys 8: 223–239
Vlasenko V and Hutter K (2002a) Numerical experiments on the breaking of solitary internal waves over a slope-shelf topography, J Phys Oceanogr 32: 1779–1793
Vlasenko V and Hutter K (2002b) Transformation and disintegration of strongly nonlinear internal waves by topography in stratified lakes. Annales Geophysicae 20: 2087–2113
Vlasenko V, Filatov NN, Petrov M, Terzhevik A, Zdorovennov R, Stashchuk N (2005) Observation and modelling of nonlinear internal waves in Lake Onego. Proc 9-th Workshop on PPNW, Lancaster University: 39–46
Vlasenko V, Stashchuk N and Hutter K (2003)Baroclinic tides: mathematical aspects of their modelling. Recent Res Devel Phys Oceanography 2: 61–96
Vlasenko V, Stashchuk N and Hutter K (2005b) Baroclinic tides. Theoretical modelling and observational evidence. Cambridge University Press
Warren HW and Whipple GC (1895) The thermophone, a new instrument for determining temperature. Technol Quart 8: p 125
Wedderburn EM and Young AW (1915) Temperature observations in Loch Earn, Part II, Trans Royal Soc Edinburgh 50: p 741
Wessels, F Wechselwirkung interner Wellen im Zweischichtenfluid mit topographischen Erhebungen.Diplomarbeit am Fachbereich Mechanik, Darmstadt University of Technology, pp 69 (unpublished)
Wessels F and Hutter K (1996) Interaction of internal waves with a topographic sill in a two-layered fluid. J Phys Oceanogr 26(1): 5–20
Whitham G (1967) Nonlinear dispersive waves. Proc Royal Soc London A299: 6–25

Chapter 2
Field Studies of Non-Linear Internal Waves in Lakes on the Globe

N. Filatov, A. Terzevik, R. Zdorovennov, V. Vlasenko, N. Stashchuk, and K. Hutter

Abstract This chapter is devoted to the experimental techniques commonly applied in field studies of nonlinear internal waves in lakes of the world. It consists of four sections. The *first* attempts an overview of internal waves in many lakes on the globe and provides a summarising sketch of common measuring techniques and methods of graphical representation of collected results. The *second* takes a closer view on experimental methods of field observation, most being invasive, but we equally also address the modern remote-sensing techniques, which open promising, perhaps still challenging, procedures allowing a closer look at internal wave phenomena. More substantially, the specific features of the patterns of manifestation, i.e., generation and dissipation of nonlinear internal waves in lakes of different size and shape under various sets of environmental conditions, are considered. It is shown that planning experiments on nonlinear internal waves in large lakes are a far more challenging task than for smaller lakes since the range of thermodynamic processes and phenomena is much more complex, and so is the set of hydrometeorological conditions (forcing) in stratified lakes. The *third* section focuses on internal wave dynamics of Lake Onego and its internal wave response during the summers of 2004/2005 and presents an exploitation of the data during the two summer field campaigns in the context of internal wave processes. The field experiments performed with the intention to investigate the generation and dissipation of nonlinear internal waves in Lake Onego are described in detail. These data are in the *fourth* section compared with models of nonlinear waves, which rounds out this chapter on internal waves in Lake Onego.

N. Filatov (✉)
Northern Water Problems Institute, Karelian Research Center, Petrozavodsk, Russia
e-mail: nfilatov@rambler.ru

K. Hutter (ed.), *Nonlinear Internal Waves in Lakes*,
Advances in Geophysical and Environmental Mechanics and Mathematics,
DOI 10.1007/978-3-642-23438-5_2,

2.1 Overview of Internal Wave Investigations in Lakes on the Globe

2.1.1 Introduction

The history of investigations of internal waves in lakes dates back to more than 100 years. The first publications about field observations of internal waves in Loch Ness were provided by Watson (1904) and Wedderburn (1907). Early investigations of internal waves using long time series of measurements with moored thermistor chains were performed by Mortimer (1952) in Lake Windermere. He described the response to episodic wind forcing on internal seiches and showed that the main effect of the wind forcing in a stratified lake is to generate large, basin-scale, low-frequency internal seiches and, for large lakes where the Earth's rotation is important, to generate internal Kelvin and Poincaré waves. Several general overviews of hydrodynamics of lakes, including internal waves, are given by Mortimer (1974), Csanady (1977), Simons and Schertzer (1987), Imberger and Hamblin (1982), Hutter (1993, 1984), Filatov (1991), Imberger (1998) and Wüest and Lorke (2003). A recent account on internal waves in Lake Michgan with a wealth of data analysis is given by Mortimer in his book "Lake Michigan in Motion" (2004).

Despite the long history of research into internal waves in lakes, nonlinear internal waves are far less studied than larger-scale internal waves. The energy influx to the lake's depth is supplied by wind acting on the free surface. It drives the surface water and generates internal waves in the form of basin-scale standing waves (Mortimer 1952; Mortimer and Horn 1982) or propagating nonlinear waves (Farmer 1978). Experimental studies that yield descriptions of the patterns of manifestation, i.e., generation and dissipation of nonlinear internal waves, are more detailed in small lakes than in large and deep ones. Figure 2.1 demonstrates lakes on the globe where nonlinear internal waves were investigated and which are mentioned in this book.

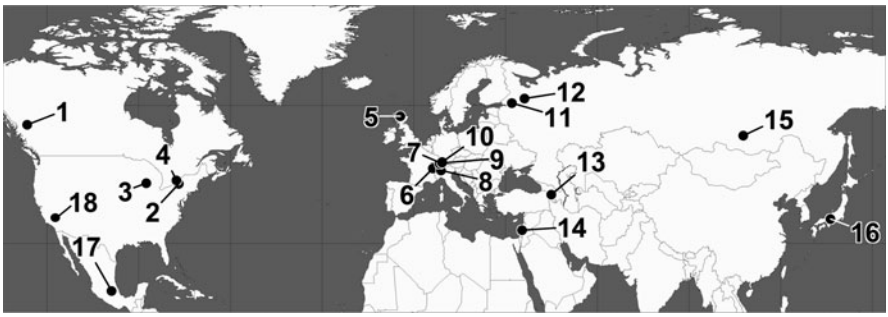

Fig. 2.1 Lakes on the globe where nonlinear internal waves were investigated and which are mentioned in this book:1 – Babine, 2 – Ontario, 3 – Michigan, 4 – Seneca, 5 – Loch Ness, 6 – Geneva (Léman), 7 – Zurich, 8 – Lugano, 9 – Baldegg, 10 – Constance-Bodensee, 11 – Ladoga, 12 – Onego, 13 – Sevan, 14 – Kinneret, 15 – Baikal, 16 – Biwa, 17 – Chapala, 18 – Mono

The reason why basin-wide linear internal waves have been studied more than nonlinear localised internal waves is that in lakes – such as the North American Great Lakes: Ontario, Erie, Huron, Michigan, Superior; the largest European lakes: Ladoga and Onego, and Lake Baikal – the contribution of large-scale internal (Kelvin and Poincaré) waves covering the entire lake or some of its parts, and related water circulations are greater than those of relatively high-frequency nonlinear internal waves.

Furthermore, planning experiments on nonlinear internal waves in large lakes are a far more challenging task than for smaller lakes since the range of thermodynamic processes and phenomena is much more complex, and so is the set of hydrometeorological conditions (forcing) in stratified lakes.

This chapter considers specific features of the manifestation of nonlinear internal waves in lakes of different sizes and shapes, under various sets of environmental conditions. Classifications of the lakes are, however, quite diverse. Since we mentioned classifications such as "great", "large", and "small", let us first classify lakes by size, as related to the characteristics of internal waves. A recent paper written by specialists in limnology (Noges et al. 2008) argued that "*. . .there exists no agreed definition of a lake being large*". The authors "*. . .did not present any numerical values but listed three main criteria that distinguish large lakes from smaller ones. But, for practical purposes, the Water Framework Directive considers a lake surface area of 10 km^2 as the boundary between medium-size and large lakes, and lakes with surface areas 100 km^2 and more as very large*". These definitions are unacceptable in terms of the manifestation of thermodynamic processes and events in lakes. Patterns of generation, dissipation and interaction of these events depend on the spatial size, depth and stratification of lakes. The main parameters for placing a lake into one class or another are dictated by physical processes and can be typified by dimensional analysis. For waves on the rotating Earth, they are given by the following characteristic numbers:

1. The *Rossby radius of deformation* R_{R}

$$R_{\mathrm{R}} = \frac{c}{f},$$

where c is the phase speed of barotropic or baroclinic waves, and f is the Coriolis parameter.

2. The *buoyancy* or *Brunt–Väisälä frequency* N (*rad s*$^{-1}$)

$$N^2(z) = g\frac{\partial \rho(z)}{\rho_0 \partial z},$$

where $[N] = [\mathrm{rad\ s^{-1}}]$, ρ_0 is a reference density [kg m^{-3}] and ρ is the local density [kg m^{-3}]. Together with the size and form of a lake, N is a very important parameter for internal waves in lakes.

3. Another important parameter for internal waves is the *Burger number* S_i. It is defined as the ratio of the internal (baroclinic) Rossby radius of deformation R_R to a length scale L that characterises the basin dimension:

$$S_i = \frac{\sqrt{gD_i}}{Lf} = \frac{c_i}{Lf},$$

where $_i$ stands for "internal", D is the depth and L represents the basin radius for a circular basin and the major axis as half-length for an ellipse, and for a real lake, is a typical horizontal half length of the lake. In Table 2.1, values are shown for the Burger number of different lakes with different sizes.

The Rossby radius of deformation and length (size) scales of lakes in near-shore hydrodynamics determine whether a basin is "large" or "small" for a particular wave category. For example, Lake Michigan is "fairly small" for barotropic Rossby and Kelvin waves, but "very large" for internal Kelvin and Poincaré type waves (Mortimer 2004). In the latter case, $R_R < L$. Thus, we shall classify lakes depending on manifestations of the baroclinic motions in them – very large or great and deep ones, such as the American Great Lakes, Lake Baikal, and the largest Lakes of Europe (Ladoga and Onego). In these lakes, the baroclinic Rossby radius of deformation R_R, during summer stratification, is a few kilometres, i.e., much smaller than the lake's horizontal extent ($R_R << L$), and the epilimnion thickness (h_1) is much smaller than the hypolimnion thickness h_2, $h_1 << h_2$. As regards geophysical hydrodynamics, examples of large and deep lakes are Lakes Biwa (Japan), Kinneret (Israel), Constance and Geneva (Alpine, Europe), whose average width is greater than the baroclinic Rossby radius of deformation ($R_R < L$). Effects

Table 2.1 Burger numbers (c_i/Lf) for several lakes. Lake Mono can be considered circular; Lakes Kinneret, Biwa, Michigan and Ladoga, Ontario and Onego are near ellipses with aspect ratios 2/3, 1/2, 1/3, and 1/4, respectively; Lake Babine is very long. L represents the basin radius for a circular basin and the major axis half-length for an ellipse (partly based on Table. 3 of Antenucci and Imberger 2001)

Lake	Latitude	c (ms^{-1})	L (m)	f (rad s^{-1})	S_i	Source
Mono (N.America)	38°01′ N	0.74	4,000	7.81E-5	2.07	MacIntyre et al. (1999)
Babine (N.America)	54°45′N	0.19	3,000	1.19E-04	0.53	Farmer (1978)
Kinneret (Middle East)	32°50′N	0.33	7,500	8.95E-5	0.56	Antennucci et al., (2000)
Biwa (Asia)	35°20′N	0.45	15,000	8.17E-5	0.37	Saggio and Imberge (1998)
Upper Lake Constance (Europe)	47°39′N	0.35	35,000	1.08E-04	0.09	Appt et al. (2004)
Ontario (N.America)	43°42′N	0.5	120,000	1.95E-4	0.04	Csanady (1973)
Michigan (N.America)	44°00′N	0.48	160,000	1.95E-4	0.03	Csanady (1973)
Ladoga (Europe)	61°00′N	0.5	120,000	1.27E-04	0.03	Filatov (1991)
Onego (Europe)	61°30′N	0.5	80,000	1.28E-04	0.05	Filatov (1991)

of the Earth's rotation on water hydrodynamics in such lakes are significant. Finally, the group of relatively small and, as a rule narrow, deep stratified lakes, where nonlinear internal waves were investigated, includes those lakes whose width is comparable to, or smaller than, the baroclinic Rossby radius of deformation ($R_R \geq L$), and the length of these lakes may be several kilometres to several dozens of kilometres. Examples are Lakes Seneca and Babine (North America), Loch Ness, Lake Baldegg, Zurich and Lugano in Europe. Typical scales of the spectral energy density $S(\omega)$ of internal waves in lakes of different size are demonstrated in Fig. 2.2.

These spectra were received from data on isotherm displacements and currents in lakes of different shapes and sizes, like Lakes Ontario, Erie, Ladoga, Onego, Balkhash, Sevan, Krasnoe (Murthy and Filatov 1983; Filatov 1991), and also from published information on internal wave spectra in other world lakes (e.g., Horn et al. 2002; Appt et al. 2004; Mortimer 2004).

For great and large stratified lakes with baroclinic Rossby radii of deformation R_R much smaller than the lake's horizontal extent ($R_R << L$), effects of the Earth's rotation on water hydrodynamics in such lakes are significant. The spectra of internal waves have maxima at low frequencies (Fig. 2.2a) which correspond to large-scale lake-wide Kelvin waves. Their amplitudes in great lakes are one to two

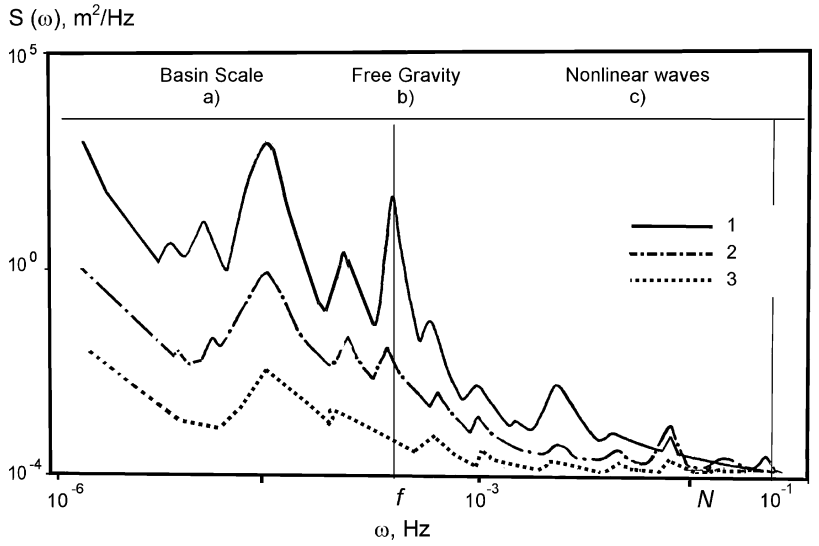

Fig. 2.2 Sketch of typical spectra of internal waves (isotherm displacement) dependent upon the size of lakes on the globe (1*) Great and Large stratified lakes* with baroclinic Rossby radii of deformation R_R much smaller than the lake's horizontal extent $R_R << L$; effects of the Earth's rotation on water hydrodynamics in such lakes are significant. (2) *Large Lakes* with $R_R < L$. In these lakes, effects of the Earth's rotation on water hydrodynamics are still significant; (3) *Relatively small lakes*, as a rule, narrow, deep stratified lakes, for those lakes whose width is comparable to, or smaller than, the baroclinic Rossby radius of deformation ($R_R \geq L$), and the length of these lakes may be several kilometres to several dozens of kilometres. f is the local inertial frequency, N is the Brunt-Väisälä frequency (Filatov 1991)

orders of magnitude larger than in medium-size lakes ($R_R < L$) where effects of the Earth's rotation on water hydrodynamics are still significant (Fig. 2.2b). In relatively small lakes, as a rule, narrow, deep and stratified, the width is comparable to, or smaller than, the baroclinic Rossby radius of deformation ($R_R \geq L$), and the length of these lakes may be several kilometres to several dozens of kilometres. At low frequencies, the maxima can be observed (Fig. 2.2c) and correspond to internal seiches. In such lakes, maxima of oscillations within a range from f (local inertial frequency) to N (the Brunt-Väisälä frequency) are absent, internal wave amplitudes are significantly smaller – two orders of magnitude compared to those of great lakes.

The first publications about solitary waves and internal surges were related to lakes of relatively small size: Loch Ness (Thorpe 1977), Lake Seneca (Hunkins and Fliegel 1973) and Babine Lake (Farmer 1978).

A clear presentation (or explanation) of nonlinear internal waves in lakes was made by Hutter 1993; Hutter et al. 1998 and Mortimer 2004. These authors showed that after a storm, internal waves in lakes may take the form of an internal surge or packets of internal solitons, generated by the nonlinear steepening of basin-scale finite-amplitude waves (Hutter 1993; Thorpe et al. 1972; Farmer 1978). When, in a two-layered system, the thickness h_1 of the upper layer is less than h_2, the thickness of the lower layer, the model response to strong forcing is usually a wave or surge of depression (rarely elevation) of the interface, accompanied by a much smaller elevation hump on the free surface. Sketches of an internal surge and an initial solitary wave of depression on the interface between two fluid layers of respective thicknesses h_1 and h_2 ($h_1 < h_2$) and densities ρ_1 and ρ_2 are shown in Fig. 2.3a, b, respectively, in which arrows indicate current directions in a wave moving to the right.

These solitons are much shorter in length than the wind-induced large-scale thermocline displacements (Vlasenko and Hutter 2002). 'When the wave amplitude is large compared with the upper layer thickness, the wave form deviates from the small-amplitude linear sinusoidal form. It steepens and acquires higher-frequency components as the wave travels and as the forcing increases' (Mortimer 2004). These are illustrated in numerical experiments (Hutter 1993; Hutter et al. 1998).

When the amplitude of the propagating waves is comparable with the epilimnion thickness, nonlinear dispersion plays a key role. In other cases, when the internal wave

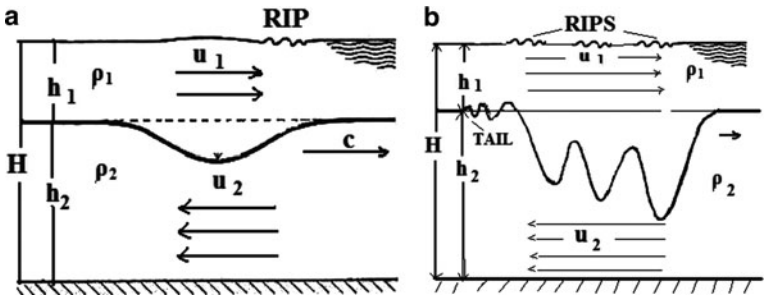

Fig. 2.3 Sketch of internal surge (**a**) and solitons (**b**). (from Hutter et al. 1998)

propagates from the deep part of a basin to a shallow boundary, a breaking event can arise. When, in a two-layered system, the thickness h_1 of the upper layer is less than h_2, the thickness of the lower layer, the model response to strong forcing is usually a wave or surge of depression (rarely elevation) of the interface, accompanied by a much smaller elevation hump on the free surface (Hutter et al. 1998). Hutter (1993) has shown that internal solitons usually evolve from waves of depression, i.e., when $h_1 < h_2$. Therefore, the largest and fastest-travelling solitons emerge at the head of their group, creating a distinct front. If the upper-layer currents induced by the internal solitons are sufficiently large, they interact with wind-generated waves on the surface to form "tide rips" (Fig. 2.3b). These can sometimes be seen in satellite images as parallel bands of differing reflectance (e.g., Brandt et al. 1997).

In-situ measurements in lakes show that the internal wave field has a continuous spectrum ranging from low-frequency basin-scale to maximum buoyancy-frequency waves. The range of thermohydro-dynamic processes and phenomena in lakes is far more complex than in laboratory tanks, and planning of field campaigns for the study of nonlinear internal waves is therefore more difficult.

Below, we consider some examples of nonlinear internal wave manifestations in various lakes around the world. Let us begin with describing observations and results of analysis of nonlinear internal waves in fairly narrow lakes where the internal Rossby radius of deformation is larger than the lake width. Nonlinear internal waves were first studied most comprehensively in such narrow lakes.

2.1.2 Examples of Nonlinear Internal Waves on Relatively Small Lakes

Loch Ness (Europe). Mortimer (1975) was the first who discovered an internal surge in Loch Ness. This is a very long, deep and narrow lake (Fig. 2.4a). The width of Loch Ness is a few kilometres and the effects of the rotation of the Earth are weak here, $R_R \geq L$. Loch Ness is small from a point of view of hydrodynamics. In 1955, Mortimer moored three thermistor chains in this lake. He described the internal surge, which returned after reflecting at the end of the lake and pointed out that "...the surge amplitude is noticeably greater on the basin side lying to the right of the direction of surge progression, a consequence of the rotation of the Earth". Thorpe et al. (1972) demonstrated "...that the internal surge in Loch Ness has the character of an internal undular bore, analogous to a tidal bore, propagating at a speed of about 35 cm s^{-1} with a steep leading front followed by a train of internal undulations" (Fig. 2.4b). The surges are generated by strong winds and these can occur throughout the ice-free season, but are most frequent and intense in autumn. The amplitude of a depression wave formed at the lake-head by a wind stress nearly Heaviside-type in time; it is inversely proportional to the phase speed and the initial slope of the wave is inversely proportional to the square of the phase speed.

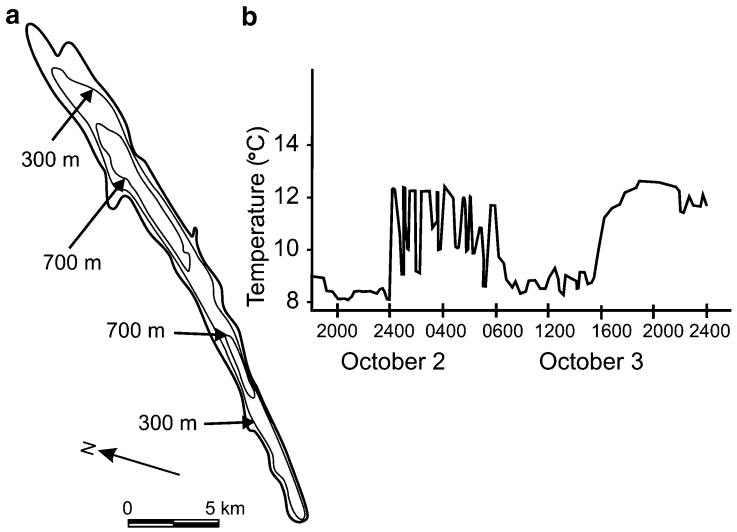

Fig. 2.4 Loch Ness bathymetry (**a**) and a sample of internal surge in the Lake (**b**) (assembled figure from Thorpe et al. 1972 and Mortimer 1975)

The observations demonstrated that the internal surge contains a packet of spatially coherent large-amplitude internal solitary waves which are followed by an oscillatory tail of irregular wavelength (Fig. 2.4). High-frequency solitary waves are expected to break on sloping topography at the basin perimeter leading to enhanced dissipation.

The surges in Loch Ness travelled in both directions, forth and back, along the lake with decreasing amplitude.

Lake Babine (North America). Farmer (1978) describes observations of large-amplitude, internal waves in Lake Babine (North America) which is 177 km long, deep and very narrow. The maximum depth of the southern basin is 235 m, the central basin depth is about 100 m, but extensive shoaling occurs. The width of Lake Babine is only a few kilometres and the effects of the rotation of the Earth are weak, $R_R \geq L$. From a point of view of lake hydrodynamics, this is a relatively small lake. At least 20 large-amplitude asymmetrical waves were observed in Babine Lake from June to October 1978 (Farmer 1978). Figure 2.5 displays water-temperature–time series from five stations showing the passage of an internal surge in Lake Babine from 5 to 7 July. Farmer explains the generation of nonlinear waves in a narrow lake as follows: "For long deep stratified lakes it is typical, that, following a strong gust of alongshore winds, the thermocline at one end of the lake is depressed and an internal surge is formed. On the first stage, the surge steepens owing to nonlinear effects, but as it propagates down the lake it evolves with a train of shorter period waves which often tend to have the appearance of a group of solitons or solitary waves".

At the first stage, the surge begins as a small depression wave on an otherwise tranquil thermocline, and then the leading edge of the wave steepens and the amplitude increases. The phase speed of the waves on Lake Babine, estimated

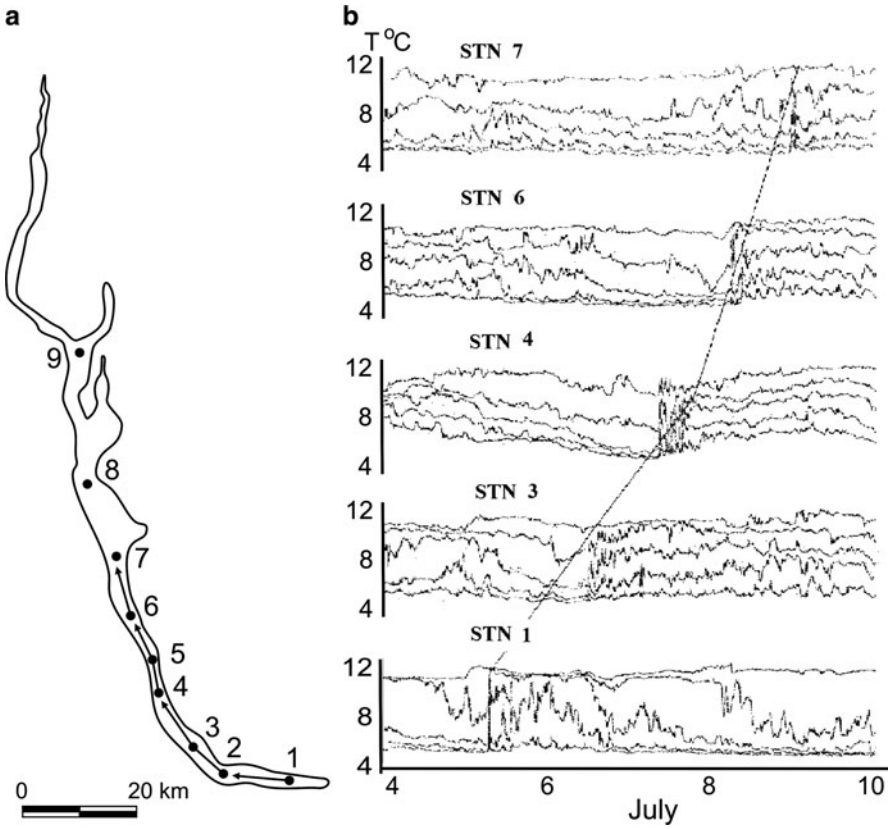

Fig. 2.5 Lake Babine top view (**a**) and water-temperature–time series from five stations (marked by numbers); indicated by the connecting line is also the passage of an internal surge on 5–7 July. Direction of the passage of the front is from STN1 to STN 7 (**b**) (assembled from Farmer 1978)

from observations, is 0.19 m s^{-1} and the wavelength is about 456 m. Consequently, the breaking distances in Lake Babine were about 25–32 km, implying that interaction between nonlinear effects and dispersion would begin between two stations. Strong steepening occurred without evidence of solitary waves and was observed at the final stage of the wave motion (Farmer 1978).

Finally, contrary to the surges in Loch Ness, where internal surges travelled in both directions several times along the lake with decreasing amplitude, in Lake Babine and Lake Seneca (both in North America), the surge travelled only in one direction (Hunkins and Fliegel 1973; Farmer 1978).

Lake Baldegg (Europe). Lake Baldegg is small ($R_R \geq L$), several km long, deep (max depth 65 m), and its surface area is about 5.2 km^2 (Lemmin 1987). The regular lake shape makes Lake Baldegg an excellent place for field study of internal waves (Fig.2.6a).

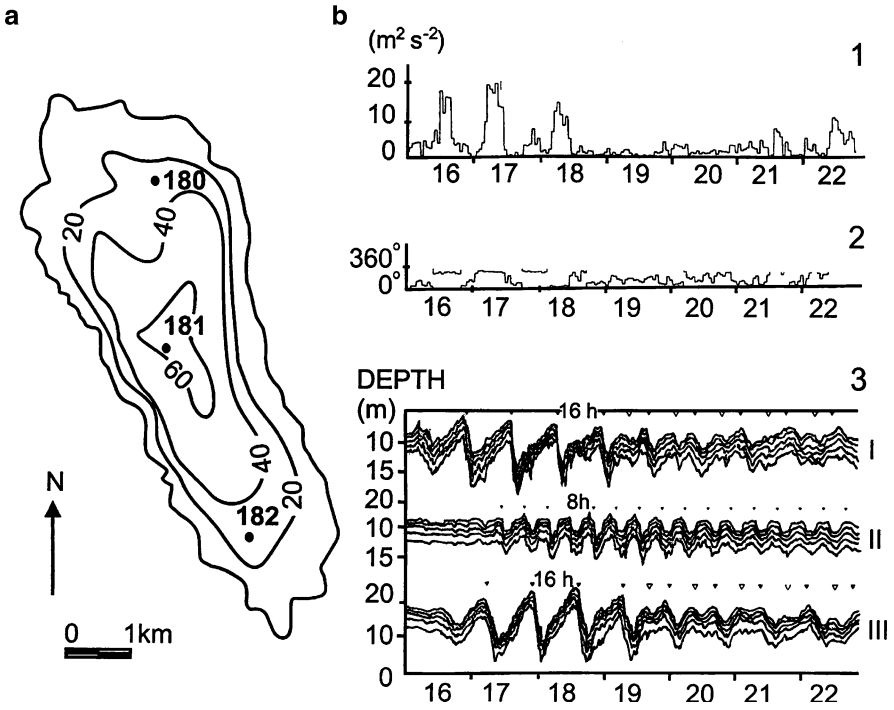

Fig. 2.6 (**a**) Lake Baldegg bathymetry. Points of observations of water temperature are shown by numbers 180, 181, 182; b) Wind speed squared (1) and wind direction (2); Isotherm-depth fluctuations (3) at stations 180 (I), 181 (II), and 182 (III), November 1978, small triangles mark an average period of 16 h (first basin mode) dominant at stations 180 and 182 and a period near 8 h dominant at station 181 (assembled from Lemmin 1987)

Analysis of long records of temperature/depth distributions determined at 10- or 20-min intervals at several stations and extending over three stratification seasons provides a detailed picture of the characteristics, dynamics, and seasonal variation activity of the internal waves in Lake Baldegg (Lemmin 1987). Reflected internal surges were observed about ten times during the field campaign and arise after wind pulses with speeds more than 4–5 m s^{-1}, blowing more than 3–4 h along the axis of the lake. Internal gravity waves may become unstable and break, thereby dissipating some of their energy if their amplitudes become too high. As a result, nonlinear features, such as asymmetry of the wave shapes and steep-fronted internal surges, are formed (Fig. 2.6b). Solitary wave packets were not observed by Lemmin's experiment, because the 20 min sampling period of the observations is too large for the time scales of these waves.

Boegman et al. (2005) compared the results obtained by mathematical modelling with Lemmin's field observations on Lake Baldegg for the estimation of the temporal distribution of the energy between the components of the internal wave modes. According to the numerical experiments, the distribution of the available

potential energy among internal seiches, surges and solitary waves is 70, 20 and 10%, respectively (Boegman et al. 2005).

Other Lakes. As was found by Stevens et al. (1996), on the basis of almost three years of field measurements in narrow but long stratified Lake Kootenay (British Columbia, Canada), more than 80% of the potential energy of basin-scale internal waves is lost, i.e., broken into smaller-scale internal waves and eventually dissipated into heat during only one inertial wave period.

Let us mention some other papers about nonlinear internal waves in other small lakes. Filonov and Thereshchenko (1999) reported observations of internal solitons in Lake Chapla, Mexico. The size of the lake is 75 $\times$ 25 km^2, with average depth 6 m, and maximum depth 11 m. From the point of view of hydrodynamics, Lake Chapla is small as $R_R \geq L$, and the Earth rotation effects are weak. Internal waves were registered in 1996 on the buoy station with thermistors. The internal thermal front near a buoy station was accompanied by intensive internal waves of bore and soliton type in the form of Korteweg–de Vries (K–dV) with amplitudes about 1 m. Didenkulova and Pelinovsky (2006) report on phenomena similar to tsunamis in some Russian lakes.

The results of observations demonstrated that in relatively small (or narrow) lakes, e.g., Baldegg, Seneca, Babine and Loch Ness, the basin-scale internal wave field may be composed of a standing seiche, a progressive nonlinear surge and a dispersive solitary wave.

2.1.3 Examples of Nonlinear Internal Waves in Medium- and Large-Size Lakes

Lake Zurich (Europe). Lake Zurich (Fig. 2.7a), a narrow basin relative to its length, is divided into three regions: a deep part (max. depth 136 m) in the western half of the "lower" basin and a shallow part (~20 m) in its eastern end, plus a dynamically separated "Obersee" ("upper" lake); the average depth of the "lower" lake is 51 m, its area 67 km^2, and its length about 30 km (Mortimer and Horn 1982). Because the internal Rossby radius of deformation approximately equals the basin width during the August–September interval, the influence of the rotation of the Earth on the motions considered here is not expected to be large and sometimes absent (Hutter 1984). A seiche-linked steep-fronted surge was described for Lake Zurich by Mortimer and Horn (1982) and Horn et al. (1986). In their works, a large volume of data from measurements of currents (31 current metres) and water temperature (120 temperature sensors) at 12 deployed moorings was analysed. Data analysis of the field observations demonstrated that the temperature and current records show that the subsequent response is a combination of several internal standing wave modes (Fig. 2.7b). Results of a multi-layered circulation model, driven by observed winds, are shown in Fig. 2.7b (2–4) by dotted lines. According to spectral analyses of temperature–time series, the principal energy

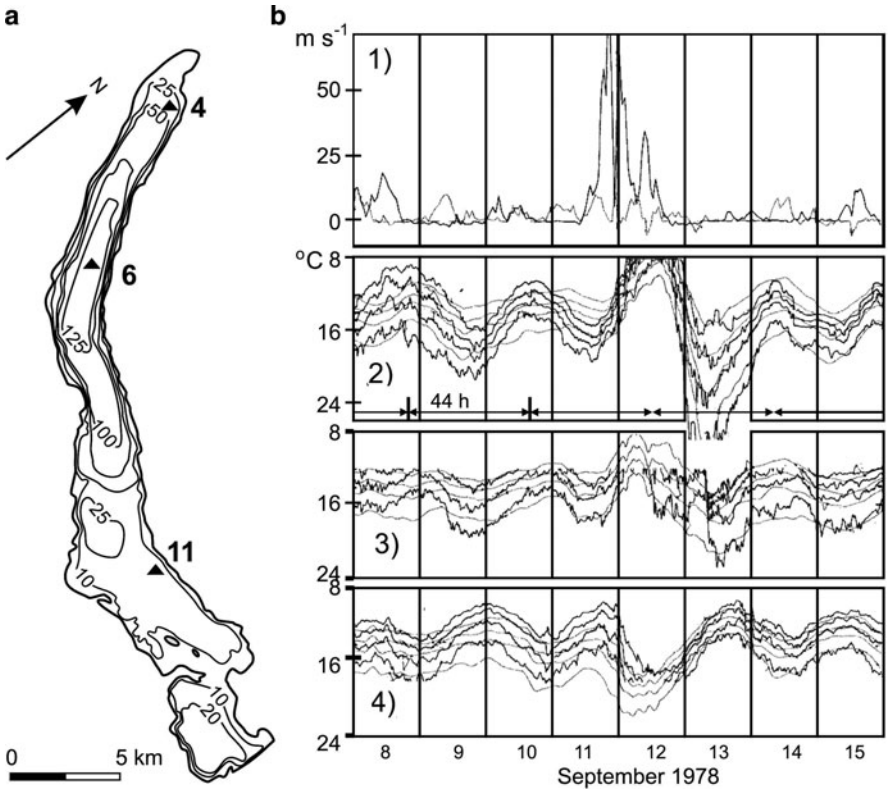

Fig. 2.7 (**a**) Lake Zurich bathymetry with points of observations of internal waves (shown by black triangles); (**b**) data of internal wave experiment: (1) wind speed components u (solid line) and v (dotted line) at mooring 6; Observed (solid lines) and modelled (dotted lines) 8°C , 10°C and 14°C variations of isotherms at moorings 4 (2), 6 (3), 11 (4) 8–15 September 1978 (assembled from Mortimer and Horn 1982)

maximum corresponds to the first seiche mode with a period near 44 h. Isotherm depth amplitudes of the responses may become large and nonlinear features may appear as steep-fronted internal surges during 12–13 September 1978 (Mortimer and Horn 1982).

Mortimer and Horn (1982) concluded that the surges are generated at the basin ends only by down-strokes of the thermocline and only if the down-stroke is sufficiently large to cause the internal wave to interact strongly with the bottom topography. The lake's internal response was principally dependent on the timing, strength, and duration of the wind impulse, relative to, and interacting with, internal seiche motions already in progress.

Lake Constance (Europe). Lake Constance is an example of a long stratified lake with somewhat complex topography. The lake consists of two dynamically isolated basins, the "upper" and the "lower" Lake Constance (Fig.2.8a). Two sub-basins

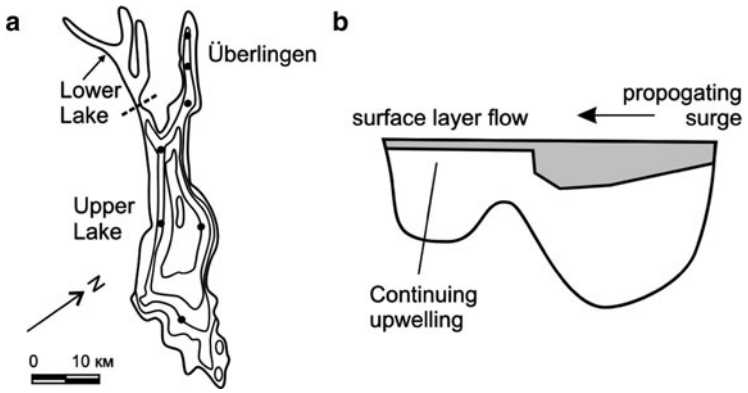

Fig. 2.8 (**a**) Lake Constance bathymetry and (**b**) schematic evolution of an internal surge in the Lake (assembled from Appt et al. 2004)

form the upper lake: the larger sub-basin is the main basin with a maximum water depth of 252 m and a mean depth of 101 m; the smaller sub-basin, called Lake Überlingen, has a maximum water depth of 147 m and a mean depth of 84 m (Bäuerle et al. 1998). The mean width of the main basin is 9.3 km, while Lake Überlingen has a mean width of 2.3 km. Basin-scale internal waves in Upper Lake Constance are significantly affected by the rotation of the Earth, as indicated by the Burger number S_i, i.e., the ratio of the internal Rossby radius R_R to a horizontal length scale LS (Antenucci and Imberger 2001). Defining LS as half of the respective mean, sub-basin width yields $S_i = 0.6$ for the main basin and $S_i = 2.4$ for Lake Überlingen. The basin-scale internal wave response is therefore modified by the rotation of the Earth into Kelvin-type waves, Poincaré-type waves, and topographic waves. The typical thermocline displacement is around 5–10 m in the larger part of the lake and about 10–12 m in Lake Überlingen.

The evolution of internal surges in Upper Lake Constance was observed after strong upwelling. Field campaigns with observations of internal surges were organised by Boehrer (2000); Antenucci and Imberger (2001) and Appt et al. (2004). The study of Appt et al. (2004) is an example for the possible extent to which numerical methods after validation and field measurements may be combined in order to gain a more coherent understanding of the behaviour of internal waves in large stratified lakes. In the above-mentioned papers, results of extensive field experiments, obtained with modern equipment, were analysed. In the field campaign described by Appt (2004), each station of observation was equipped with a single-cable thermistor chain of 100 m length, as well as with a wind anemometer and a wind direction sensor located at 2.4 m above water. Each thermistor chain consisted of 51 thermistors with an accuracy of 0.018°C and a resolution of 0.0018°C. The thermistors were placed at 0.75-m intervals in the upper 30 m and at increasing intervals of 1.00–15.00 m below. According to available data in the western part of Lake Überlingen, an internal surge was generated by upwelling. The

reflection of the surge from the northwestern boundary induced a vertical mode-two response, leading to an intrusion in the metalimnion that caused a three-layer velocity structure in the smaller sub-basin. Schematic evolution of an internal surge (Fig. 2.8b) is demonstrated by Appt et al. (2004).

Upwelling in the lake continued after cessation of the wind. As the surge approached the narrower and shallower western end of the main basin, its leading edge steepened. This agrees with the behaviour of surges in Babine Lake (Farmer 1978), where a decrease in cross section increased the wave amplitude, while nonlinear effects associated with their finite amplitude steepened their leading edge. The internal surge and its reflection in Lake Constance caused a two-step thermocline that can be easily identified in temperature profiles. It is, thus, a suitable indicator for the nonlinearity of the lake response (Boehrer 2000).

Lake Geneva (Europe). Lake Geneva is the largest lake in Western Europe, situated at approximately 47°N in the pre-alpine region at the border between Switzerland and France (Mortimer 1974). It consists of a 310-m-deep main basin, called the "Grand Lac" (Big Lake), and a smaller western part, about 25 km long and 4 km wide, called the Petit Lac (Little Lake) (Fig. 2.9a).

For most dynamical processes, the two sub-basins are, however, not decoupled. At the end of the summer season, an internal Rossby radius of approximately 4 km can be estimated. From the point of view of hydrodynamics, the Big Lake (Grand Lac) is a large lake, whereas the Little Lake (Petit Lac) is a small lake. Mortimer (1953, 1974) detected the surface "signature" of a cyclonically progressing internal wave in Lake Geneva. He provided a data analysis of summer records (July–August 1941–1944) of water-temperature time series in the lake. An observed period of 75 h of the presumed first internal seiche mode in Lac Leman was derived from a

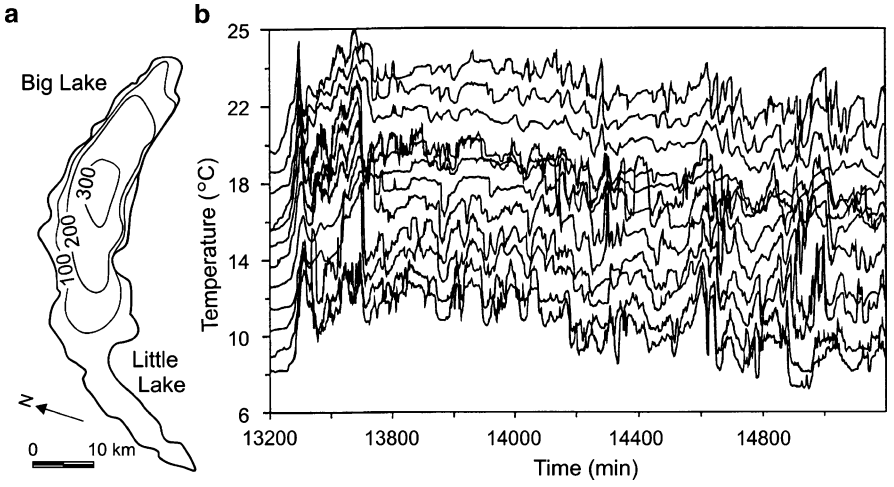

Fig. 2.9 (**a**) Lake Geneva bathymetry. (**b**) Water-temperature records in Lake Geneva in August 1997 deployed on the sloping subsurface side of Lake Geneva southeast of Big Lake (assembled from Thorpe and Lemmin 1999)

number of water-temperature data at 15-m depth. Mortimer also demonstrated the cyclonic progression of the internal wave (Mortimer 1963).

The coupling of the analysis of different types of field data (mostly temperature and isotherm depth and current time series) with numerical modelling proved to be a powerful approach to the understanding of the phenomena observed in Lake Geneva. The hydrodynamic studies conducted by Mortimer (1974), Bäuerle (1985), Thorpe et al. (1996), Thorpe and Lemmin (1999), and Lemmin et al. (2005) present a consistent picture of the lake, dominated by the presence of several modes of wind-forced long internal waves modified by the rotation of the Earth and by a broad spectrum of short internal waves, including solitons. Thorpe et al. (1996) described high-frequency internal waves in Lake Geneva. They discussed the generation of high-frequency waves in Lake Geneva after the passage of a large thermocline depression along the slope of the lake. The observed large thermocline depression was consistent with the arrival of a first mode baroclinic Kelvin wave at the sampling sites. Fig. 2.9b (taken from Thorpe and Lemmin 1999) demonstrates "a temperature rise of about 4°C occurring in 35 min... The abrupt temperature increase is characteristic of internal surges or non-linear Kelvin waves travelling cyclonically around the lake which appears to be the dominant response to changes in wind forcing".

Three possible mechanisms were proposed as sources of the observed trains of high-frequency waves:

- A soliton packet following an internal thermocline jump
- A jump generating local disturbances as it propagates over irregular and rough boundary topography
- A jump produced in a region of high shear and low Richardson number, resulting in a moving disturbance radiating internal waves

Thorpe (1992) also showed that currents along the slope flowing over rough topography can generate internal waves, but the present energy peaks were always associated with undular jumps. A possible mechanism of generation of nonlinear internal waves in the lake is flow interaction with boundaries. Frontal steepness of internal seiches has been observed after strong wind pulses. As time passes, the observed fronts in Lake Geneva evolve into regular seiches. Thorpe et al. (1996) suggest several ways in which Kelvin and short-internal waves may be linked and energy transferred from internal seiches to short internal waves. Observations suggest that high-frequency internal waves may be radiated into the lake interior from the sloping sides of the lake as internal surges travel cyclonically around it (Thorpe et al., 1992).

The slope in the spectra of internal waves in Lake Geneva closely corresponds to the ω^{-2}-power law within the frequency band between f and N (Thorpe et al. 1996).

Lake Kinneret (Asia, Middle East). Lake Kinneret (the Sea of Galilee) is located in Israel, has a size (22 × 15) km^2 and is oriented north–south with a maximum depth of 42 m and a surface area of 167 km^2. The lake shape is compact-regular (Fig. 2.10). The internal Rossby radius is typically half the basin width. From the

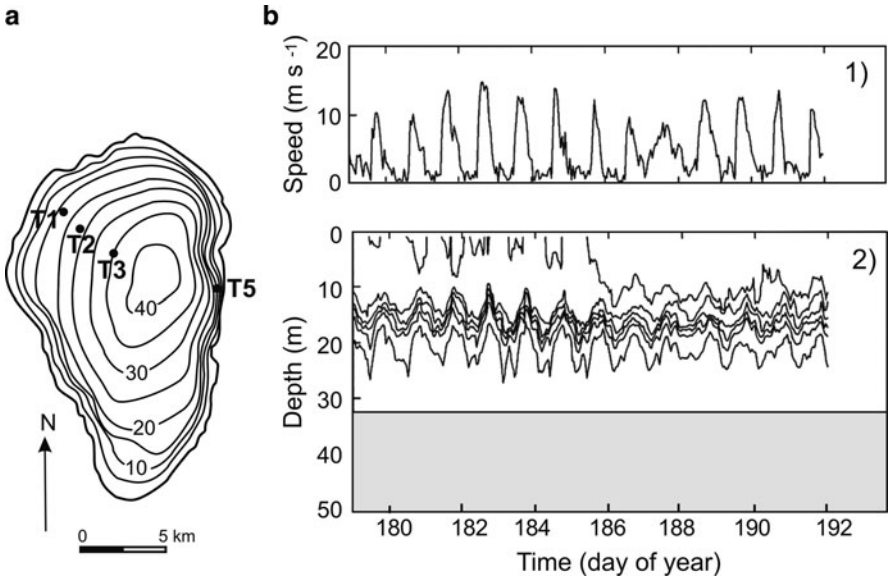

Fig. 2.10 (**a**) Lake Kinneret bathymetry and (**b**) data of observations of wind (1) and isotherm displacement (2) at point T3 in the field campaign (1998). (assembled from Antenucci et al. 2000)

point of view of hydrodynamics, Lake Kinneret is a large lake ($R_R < L$). The lake is stratified from late February through late December (Serruya 1975).

The demonstration of the existence of nonlinear internal waves in the lake was carried out in several papers by Imberger (1998); Antenucci and Imberger (2001); Boegman et al. (2003); Saggio and Imberger (1998, 2001) and Gomez-Giraldo et al. (2008). These authors described the sampling procedures and techniques of the identification of internal waves. The thermistor chain data were supplemented by microstructure data collected by using a portable flux profiler (PFP) equipped with temperature sensors (0.001°C resolution) and an orthogonal two-component laser Doppler velocimeter (0.001 m s^{-1} resolution). Profiling vertically through the water column at a speed of 0.1 m s^{-1} and a sampling frequency of 100 Hz, the PFP resolved the water-column structure with vertical scales as small as 1 mm.

Antenucci et al. (2001) suggest that "waves of high-frequency in lakes do not necessarily derive their energy from basin-scale internal waves through some form of energy cascade but from wind-induced shear in the surface layer. The coherent nature of high-frequency waves over the whole water column suggests that mixing due to basin-scale internal waves or intrusions, which are typically vertically localised, cannot be responsible for the generation of these waves". The observations suggest a steepening mechanism similar to that observed in long narrow lakes (Antenucci et al. 2001). Data analysis showed that in Lake Kinneret "... the leading edge of each Kelvin wave trough [...] steepened; each wave changed from a sinusoidal shape to one exhibiting a gradual rise in isotherm depth followed by an abrupt descent after the passage of the wave crest" (Boegman et al. 2003). The nonlinear steepening might be

influenced by the nonuniform bathymetry/topography of Lake Kinneret. It remains, however, unclear whether these high-frequency waves are generated through nonlinear steepening of the basin-scale internal waves (Horn et al. 2001) or boundary interaction, as suggested by Saggio and Imberge (1998). The 2-min sampling interval did not reveal internal solitary waves or other high-frequency waves in the lake. These authors analyse larger-resolution data with a 15-s sampling interval for Lake Biwa (Boegman et al. 2003).

According to estimations, internal solitary waves are not sinusoidal in character. It is suggested that localised shoaling of solitary and higher mode internal waves might result in significant energy flux from the basin-scale wave field to dissipation and mixing within the bottom boundary layer (BBL).

Lake Biwa (Asia). Lake Biwa is the largest stratified lake in Japan (Kumagai et al. 1998). It is 64 km long, with a maximum width of 20 km and a minimum width of only 1.4 km. The main basin has a maximum depth of 104 m and a typical internal Rossby radius of about 5 km. In this case, both sub-basins are large lakes (Fig. 2.11a).

Saggio and Imberge (1998), Boegman et al. (2003) and Shimizu et al. (2007) used the results of the Lake Biwa Transport Experiment (BITEX) 1992–1993. The experiments include records of water temperature by thermistor chains with a 15-s sampling interval.

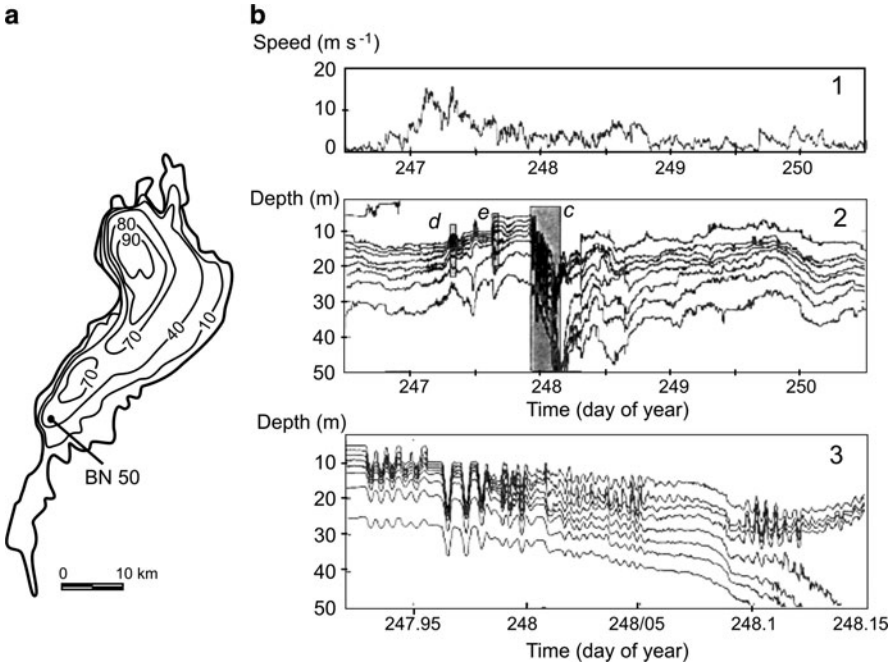

Fig. 2.11 (**a**) Lake Biwa bathymetry; BN 50 is a station of observation; (**b**) time series of observations: (1) wind speed, (2) isotherm depths for a 4-d observation period; (3) magnified view of shaded region in panel 2 showing isotherms (assembled from Boegman et al. 2003)

The high-resolution field experiments in Lake Biwa show "that the basin-scale waves play an important role in distributing and attenuating the energy of the wind impulses. The Kelvin and Poincaré waves are quickly increased in their potential energy after each typhoon, but then relax over a few days during which time their energy is cascaded to smaller scales and distributed throughout the lake. Attenuation of the internal wave energy occurs because of the interaction of the waves with boundaries" (Saggio and Imberger 1998).

Shimizu et al. (2007) investigated the horizontal structure and excitation of basin-scale internal waves and gyres in Lake Biwa using long-term data of observations and results of modelling. These authors showed that "these internal waves were damped within a few days, and the dynamics during calm periods were dominated by the gyres, illustrating the importance of internal waves on mixing and gyres on long-term horizontal transport".

Clear examples of the generation of high-frequency waves in Lake Biwa by the interaction between long waves and topography is given in a paper by Boegman et al. (2003). The rising of the thermocline observed during the afternoon and night of 4–5 September coincided with the passage of a mode-one Kelvin wave with a period of ~2 days as seen in the time series of isotherm displacement (Fig. 2.11b). Evidences of nonlinear waves after the passage of the typhoon in Lake Biwa are demonstrated by Boegman et al (2003). "The basin-scale waves are strongly energised by the wind, and the high-frequency waves are made up of trains of nonlinear waves, probably generated by the interaction of long waves with the bathymetry as described by Thorpe et al. (2001) or by nonlinear steepening of basin-scale waves (Horn et al. 1999). It is not clearly understood how these waves are generated and how high-frequency waves are generated through nonlinear steepening of basin-scale internal waves (Horn et al. 2001) or boundary interaction as suggested by Saggio and Imberger (1998)".

Frequency analysis of the temperature time series suggests that the slope of the internal wave spectrum in the broad range is probably the result of the composition of groups of waves with high intermittence. The internal waves play an important role in the energy cascade from large to small scales, providing an important link in the understanding of flux paths in stratified lakes (Saggio, Imberger 1998). All spectra of internal waves in Lake Biwa exhibit the ranges described above and keep the same (ω^{-2})–slope.

"The agreement of the shape of internal wave spectra in the ocean (Garrett 1975) and in a lake is an important result considering the large difference in scales between these two environments and the difference in the constraints offered by the boundaries in lakes. The shape and level of the observed internal wave spectrum in Lake Biwa appears to be due to a rapid redistribution of energy among the groups of waves by nonlinear interactions, resulting in the rapid relaxation of the distorted spectra toward a universal form" (Saggio, Imberger 1998). However, the reasons that the groups of waves which compound this regime are generated are not clearly understood (Imberger 1998). A possible explanation is that the interaction of low-frequency waves with the boundaries generates packets of waves of high frequencies.

2.1.4 *Examples of Nonlinear Internal Waves in Great Lakes: Lakes Michigan and Ontario, Baikal, Ladoga and Onego*

Lakes Michigan and Ontario (North America). Mortimer (2004) described internal beat pulsations and surges in the North American Great Lakes Michigan and Ontario. One of the focuses in Mortimer's work was the cross-basin Poincaré internal waves with internal seiche modes and whole basin shore trapped internal Kelvin waves. Seiche-linked internal surges were also observed in Lake Ontario during high-resolution, cross-basin temperature surveys (Mortimer 2006) (Fig. 2.12).

Mortimer (2006) showed that "[. . .] the surges did not propagate along but across the basin, away from a region of strong down-welling along the southern shore, i.e. the shore lying to the right of the wind direction during the storm, which produced the down-welling and initially set the internal seiche and surges in motion". The large-amplitude Poincaré waves and their precursor down-welling events generate surges similar to those seen in smaller lakes. Periodic release and radiation of internal surges from a down-welled front were described earlier by Mortimer (1979). A sample of internal surges in Lake Ontario was also shown by Mortimer (2006, Fig. 2.13).

Lake Baikal (Asia). Lake Baikal is 636 km long, has a maximum width of 79.5 km and a minimum width of 25 km, its maximum depth is 1,642 m, and the average depth is 758 m (Fig.2.14a).

The first references to the existence of internal waves in Lake Baikal were reported in papers by Shostakovich and Rossolimo in the 1930s (cited in Verbolov 1984) and Shimaraev et al. (1994). Focussed observations of internal gravity waves on Lake Baikal started in 1980 (Verbolov 1984). Granin (1984) also first mentioned the existence of nonlinear internal waves in Lake Baikal. Evidence of internal surges and packets of short internal waves which have a train character were measured for Lake Baikal at offshore and near-shore zones. Figure 2.14b demonstrates a train of solitons in the thermocline raised after the passage of the internal surge at the point of observation situated 1.5 km off shore of the north-west deep part of the lake. The amplitudes of these high-frequency waves reach several metres.

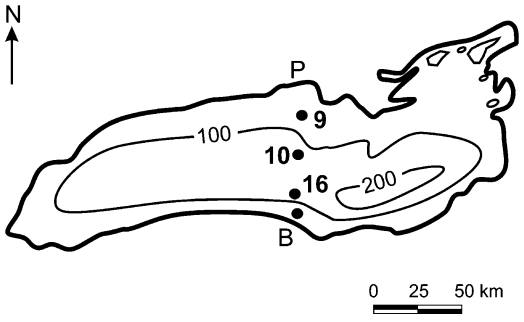

Fig. 2.12 Lake Ontario bathymetry. Transect B (Braddock) and P (Presqu'ile) of investigations of internal waves and points of observations (from Mortimer 2006)

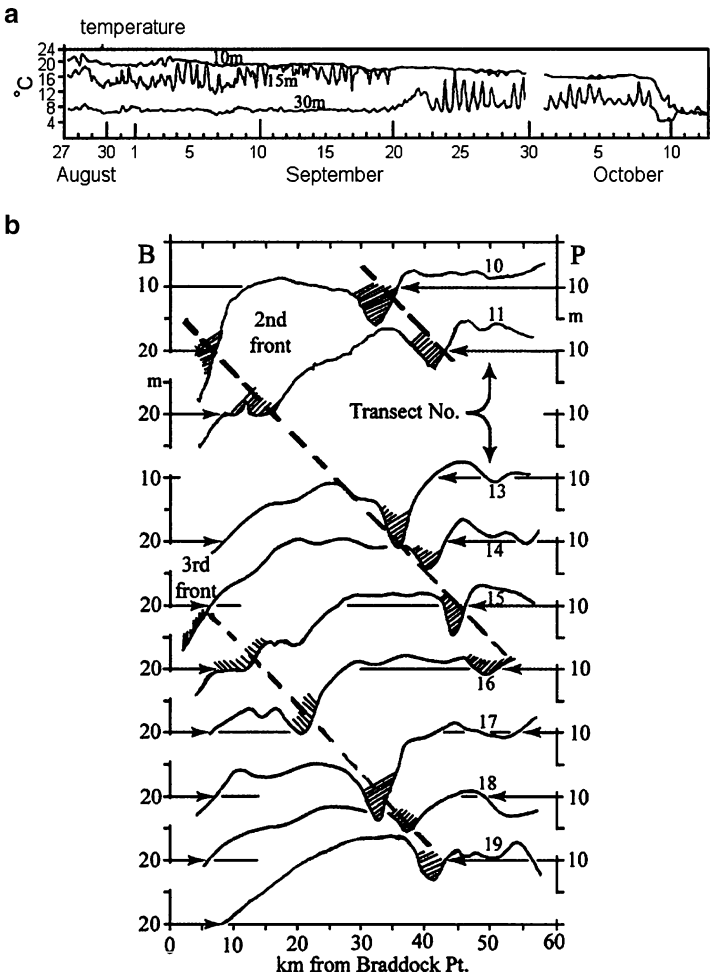

Fig. 2.13 (**a**) Water temperature fluctuations (at 10-, 15- and 30-m depth) at Station 9 in Lake Ontario (Fig. 2.12) from 27 August to 12 October 1972, responses to wind impulses and (**b**) migration of an internal surge (shown hatched), the individual isotherm depth traces measured across BP transects, points 10–19 (see on Fig. 2.12), stacked with vertical separation to simulate a time scale (assembled from Mortimer 2006)

Spectra of water temperature fluctuations were calculated and compared with the model developed by Garrett and Munk (1975) for the ocean. Seasonal variations of spectra of internal waves (Fig. 2.15) were also calculated for Lake Baikal (Shimaraev et al. 1994). The approximation of these spectra by the Garrett and Munk model (1975) discloses an ω^{-2} trend, shown in Fig. 2.15.

Another evidence of nonlinear internal waves in Lake Baikal was revealed by Chensky et al. (1998). In this paper, results of mathematical modelling of the coastal-trapped waves in the southern area of Lake Baikal are described. The

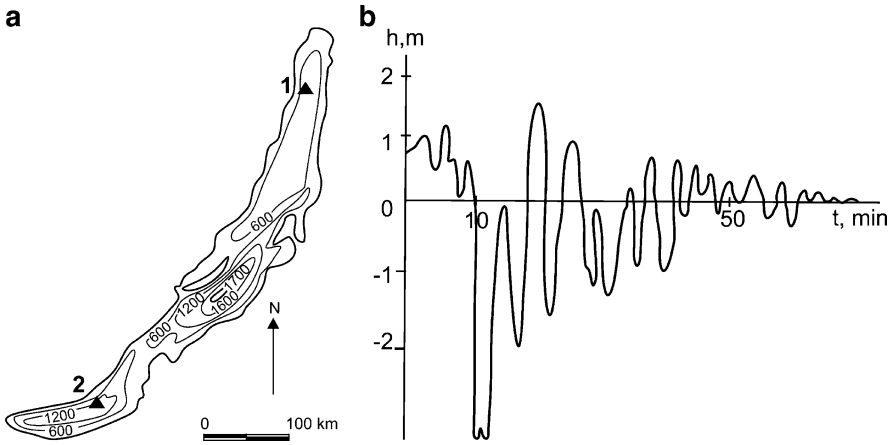

Fig. 2.14 (**a**) Lake Baikal bathymetry. Points of observation of internal waves shown by *triangles*: (1) in 1.5 km from the shore of the north-west deep part of the lake on 17.07.1980, (2) Seasonal observations of internal waves; (**b**) Isotherm depth fluctuations at the thermocline depth at point 1 of Lake Baikal demonstrated non-linear waves (assembled from Granin 1984, with permission of the author)

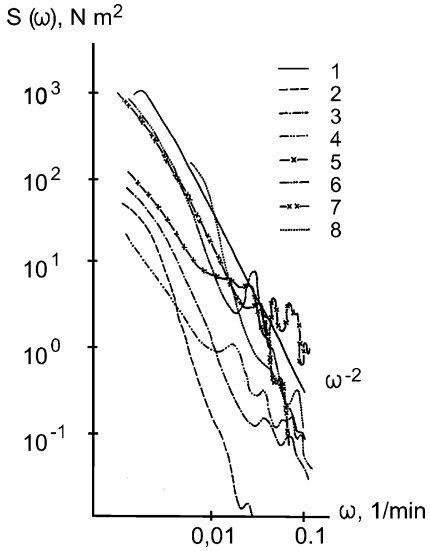

Fig. 2.15 Seasonal variations of internal wave spectra (water temperature in the thermocline) for Lake Baikal (point 2 on Fig. 2.14): 1 – Garret-Munk model (1975), 2 – March, 3 – June, 4 – July, 5 – August , 6 – September , 7 – October , 8 – November; (assembled from Shimaraev et al. 1994, with permission)

authors applied the K–dV model for weakly nonlinear internal Kelvin waves. However, the results of the experimental investigations of the nonlinear internal waves during winter seem to be oblique (see Chensky et al. 1998 and Lovcov et al. 1998). The authors supposed that the internal Rossby radius for winter stratification is about 3 km, the same as during the summer. Doubts are cast upon this presumption, because in this period the water in Lake Baikal is nearly homogeneous.

We could not find any better substantiated descriptions of field observations in the papers of these authors.

Lake Ladozhskoe [Ladoga] (Europe). Lake Ladoga is the greatest dimictic lake in Europe situated in Karelia, the north-western part of Russia. The surface area of Lake Ladoga is 17,891 km^2 and its volume is 908 km^3. The lake ranks among the top 15 of the world's freshwater lakes and is comparable in surface area with Lake Ontario. The latitude of the centre of the lake is about 61°N. The mean depth of the lake is 52 m; the maximum depth is approximately 230 m. The horizontal extent of the lake is much larger than the internal Rossby radius of deformation which equals ~4 km in summer. In the book "Ladoga and Onego – Great European Lakes: Data Analysis and Modeling" (Ed. L.Rukhovets and N. Filatov, 2009) these lakes are called the Great European Lakes. For surface seiches, the external Rossby radius is somewhat larger than a typical horizontal length ($R_{R(ext)} > L$), but the baroclinic Rossby radius is very small when compared with the horizontal dimension of the lake ($R_{R(int)} << L$). Figure 2.16 shows Lake Ladoga with its bathymetry and the locations of points where internal waves were observed (Δj, $j = 1,.. 5$).

During the LADEX physical experiment conducted in 1980–1984, a large set of hydro-physical and meteorological data was collected (Filatov et al. 1981; Filatov 1991). Field measurements of currents and water temperature were performed in the bays of the northwest part and at several locations in the offshore zones. In the stratified Jakkimvarsky Bay, three buoy stations for measurements of currents and water temperatures at several depths were deployed for three months for several years (points $\Delta 1$, $\Delta 2$, $\Delta 3$, in Fig. 2.16). High-frequency oscillations of currents were registered every few seconds from a 6-m tower using hot wire anemometers with temperature-compensated V-wire probes, and high-frequency oscillations of water temperature were measured by thermistors. In the offshore zones, currents and water temperature measurements were carried out at several depths from 5 to 70 m for a period of 3 months with a time step of 5 min (points $\Delta 4$, $\Delta 5$ in Fig. 2.16). A broad spectrum of internal waves, currents and mixing processes was discovered, which is reported by Filatov (1991).

The spectral structure of the currents for Lake Ladoga (Filatov et al. 1981) shows a 4-day modulation of inertial oscillations and a 15-day modulation of synoptic fluctuation of currents [see the double-frequency spectrum (a linear invariant of the symmetric part of the spectral tensor) in Figure 2.17].

The maxima in the spectra (Fig. 2.17b) correspond to synoptical oscillations of currents, with time scales approximately 2–4 days, inertial oscillations with a period of 13.5 h and high-frequency internal waves. Spectral analysis indicated the presence of internal Kelvin and Poincaré waves with phase shifts between the low-frequency oscillations (period about 4 days) and the inertial oscillations, which indicate the possibility of nonlinear interactions between spectral constituents; energy flows from one spectral band to another and high-frequency internal waves near the Brunt–Väisälä frequency. Nonstationary (time–frequency) spectra of the internal waves (isotherm displacement) in the metalimnion of Lake Ladoga

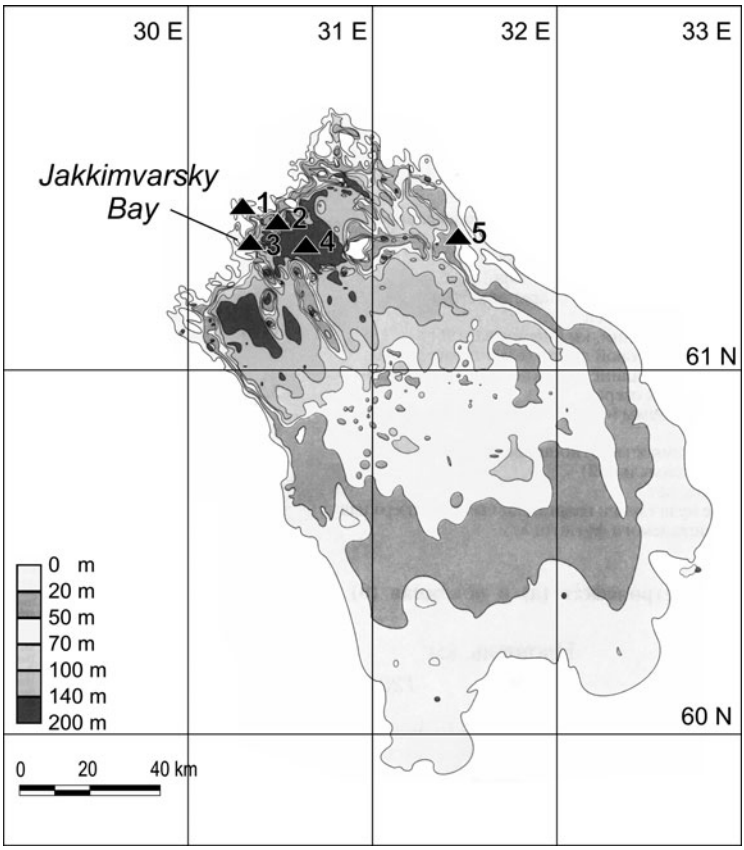

Fig. 2.16 Lake Ladoga bathymetry and locations of points of observation indicated by Δj, $j = 1,\ldots,5$

were calculated by Filatov (1983) and in the doctoral dissertation of Kochkov (1989), see Fig. 2.18a. The approximation of the spectra of isotherm-depth-time series of internal waves for Lake Ladoga by the Garrett and Munk model is shown in Fig. 2.18b. The agreement of the shapes of the internal wave spectra in the ocean (Garrett and Munk 1975) and in Lake Ladoga is an important result taking into account the large difference in scales between these two environments and the difference in the constraints offered by the boundaries of lakes (Filatov et al. 1981; Kochkov 1989).

The case of an internal surge in the offshore zone of Lake Ladoga (Fig. 2.19a) with an amplitude of about 10 m was observed in August, 1977 (Filatov, et al. 1981). This internal bore on the thermocline was generated by atmospheric pressure gradients after the passage of an atmospheric front (Fig. 2.19b). The wind speed at the time was about 11–12 m s^{-1}.

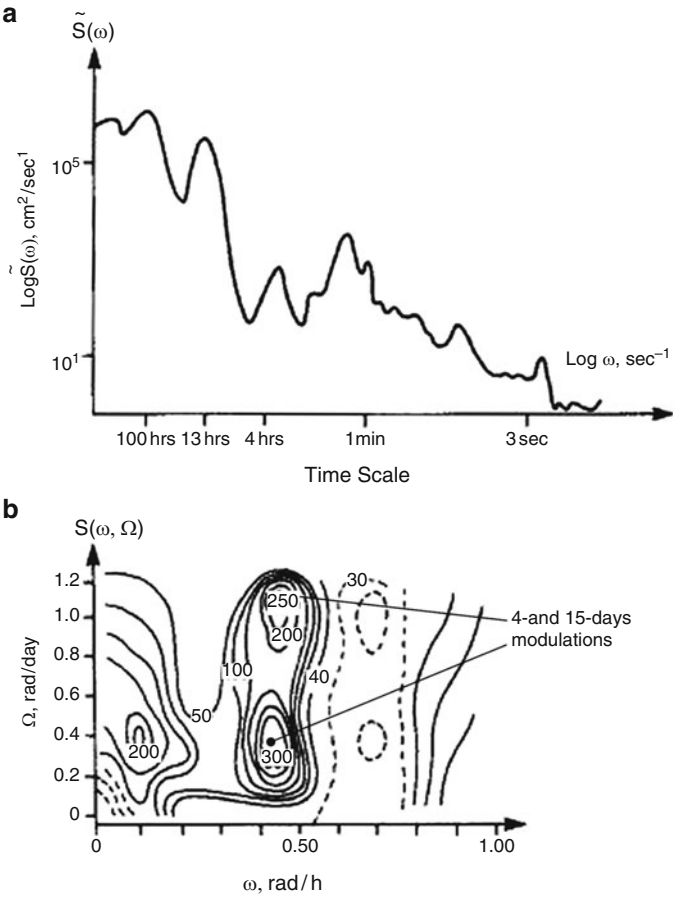

Fig. 2.17 (**a**) Power spectra of currents in the metalimnion of Lake Ladoga for the broad time scale from few seconds to several hundred hours and (**b**) double-frequency spectra (linear invariant of the symmetric part of the spectral tensor of currents) of horizontal currents at the 10-m depth of the offshore station on Lake Ladoga. Ω (in rad/day) corresponds to fluctuations of horizontal currents with frequency ω (rad/h). The inertial oscillations have variability with frequency 0.3 and 1.1 rad/day. The 4- and 15-day modulations of inertial oscillations and the 15-day modulation of synoptic fluctuation of currents are shown (from Filatov et al. 1981)

Lake Onezhskoe [Onego] (Europe). Lake Onezhskoe (Onego) has an average surface area of 9,943 km^2, a volume of 290 km^3, an overall length of 290 km and is, on average, 30-m deep with a maximum depth of 120 m. Lake Onego is the second largest lake in Europe after Lake Ladoga (Fig. 2.20). This is a very large, relatively deep lake with an internal Rossby radius of deformation of 3–5 km, which is almost two orders of magnitude smaller than a typical width of the lake.

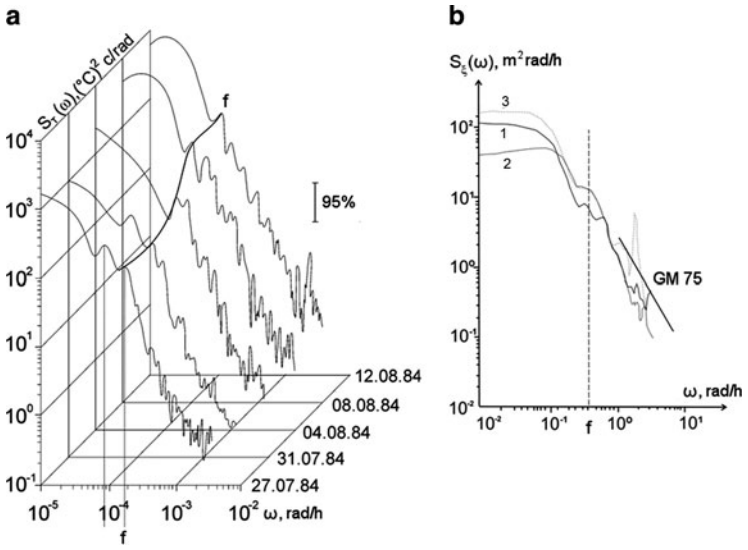

Fig. 2.18 (**a**) Nonstationary (time–frequency) water-temperature spectra of internal waves in the offshore zone of Lake Ladoga and (**b**) spectra of isotherm-depth-time series of internal waves before storm (1), after storm (2), from ensemble averages (3) and compared with the Garrett-Munk model (1975, GM75) in Lake Ladoga, July–August 1984 (from Filatov 1983; Kochkov 1989)

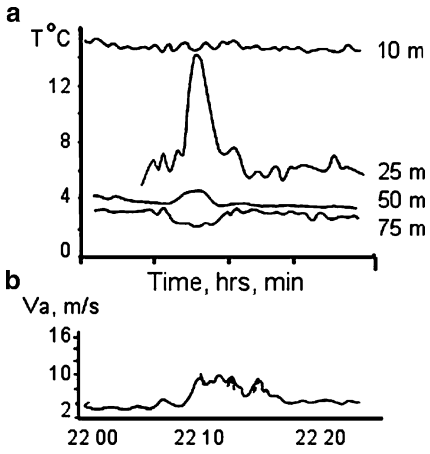

Fig. 2.19 (**a**) Internal surge (of the water temperature) in the offshore zone of Lake Ladoga (in Fig. 2.18, Δ4) was observed with an amplitude of about 10 m in August, 1977 after a relatively strong wind (**b**) with speed V_a ~12 m s^{-1} had blown, Filatov et al. (1981)

The earlier most intensive investigations of the hydrodynamics of Lake Onego were provided during the "experiment Onego" in 1986–1990; it revealed registrations of long-term time series of currents and water temperature data and remote-sensing observations (Boyarinov et al. 1994; Filatov et al. 1990; Filatov 1991; Beletsky et al. 1994). In the cited sources, a wide spectrum of internal waves has been studied, except nonlinear internal waves. Basin wide barotropic (external)

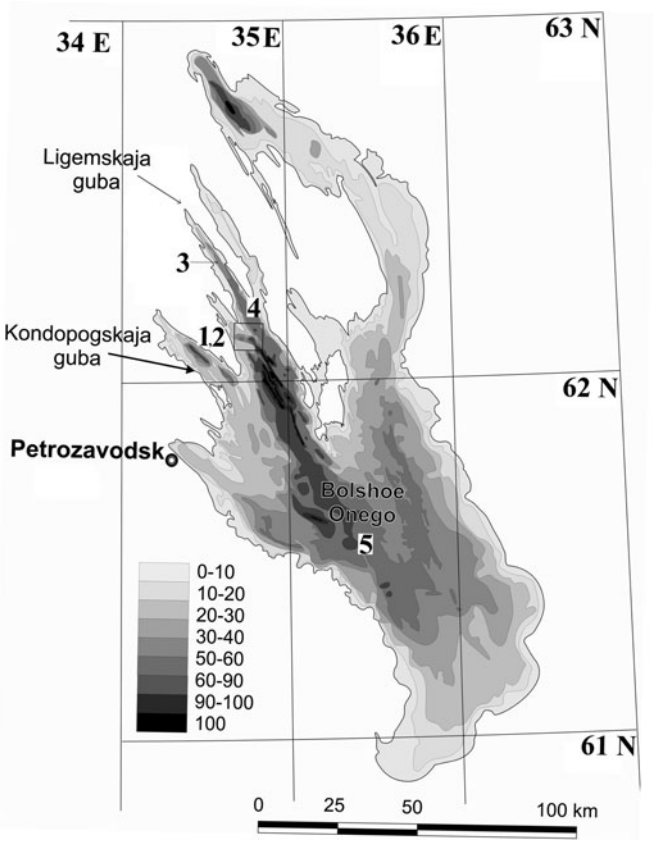

Fig. 2.20 *Lake* Onezhskoe (Onego) bathymetry. 1, 2 – Polygons of observation of internal waves in 2004–2005; 3, 4 – observations of internal waves in 1977 and 1987; 5 – "Onego experiment" 1986–1990 (Filatov et al. 1990)

gravity oscillations in Lake Onego were studied using long-term water level and current metre observations (Rudnev et al. 1995).

Special field campaigns on internal waves in Lake Onego were organised in 2004–2005 within the INTAS project No 03-51-3728 "Strongly non-linear waves in lakes: generation, transformation and meromixis". Particular attention was paid to the processes of degeneration of internal waves, their successive interaction with lake boundaries, transformation and disintegration during their shoaling near the lake boundaries and bottom slope, to interactions of nonlinear waves with the background stratification as well as wave breaking with the generation of spots of mixed water (Hutter et al. 2007). Internal surges and solitary waves were observed during this experiment. The data analysis of these experiments will be presented in Sects. 2.3 and 2.4.

2.1.5 *Some Remarks on the Overview of Nonlinear Internal Wave Investigations in Lakes*

Data analysis of numerous field experiments of internal waves for large and small lakes has shown that the resulting internal wave spectrum exhibits a continuous shape between the local inertial, f, and buoyancy, N, frequencies with an average slope of about ω^{-2}, where ω is the frequency. Garrett and Munk (1975) proposed a universal model for the frequency–wave number spectrum of internal waves. However, the reasons why the internal wave spectrum is nearly universal in lakes are not clearly understood.

Field observations in stratified lakes of different size of the globe revealed nonlinear internal waves: i.e., surges and solitons. Wind generates internal waves in lakes in the form of basin-scale waves (Mortimer 1952; Mortimer and Horn 1982; Hutter 1993) or propagating nonlinear waves (Thorpe et al. 1972). After a storm or strong winds, internal waves in lakes may take the form of an internal surge or packets of internal solitons, generated by the nonlinear steepening of a basin-scale finite-amplitude wave (Thorpe et al. 1972; Farmer 1978; Mortimer 1975; Hutter 1993). Since these solitons are much shorter in length than the wind-induced initial large-scale thermocline displacements, their generation results in a transfer of energy within the internal wave field from large to smaller scales:

- In small narrow stratified lakes, like Loch Ness, Lakes Baldegg, Seneca, Babine, where the effects of the Earth's rotation can be neglected, it is suggested that the basin-scale internal wave field may be decomposed into a standing seiche and a progressive nonlinear surge (bore) and solitary waves. In some lakes, for example, in Loch Ness and Lake Baldegg, nonlinear surges are repeated several times by reflection after their generation, and in other narrow lakes, for example, in Lakes Babine and Seneca, the nonlinear surge survived only through its initial forward path after its generation;
- In large lakes, where the effects of the rotation of the Earth are important, broad spectra of Kelvin- and Poincaré-type waves arise, paired with nonlinear internal waves. These seiches, Poincaré waves, and Kelvin waves appear to generate groups of waves at higher frequencies by interaction with the lake bathymetry or by nonlinear processes in the thermocline. The main action of the wind in the internal wave field is to energise low-frequency basin-scale waves.

Nonlinear internal waves in lakes are generated by nonlinear steepening and shoaling. The available data of observations on large lakes of the globe, however, are yet to provide answers to several important questions. For instance, what does occur if a solitary wave packet is impinging upon a sloping topography at the lake boundary? How is the energy contained within a solitary wave packet distributed in a single wave-sloping? How rapidly do these nonlinear waves dissipate their energy within the lake interior? What is the critical angle of the boundary slope where internal waves can shoal and will break? All waves that are generated in lakes must encounter inevitably variable bottom topography and interact with it simply because

lakes are closed basins (Vlasenko and Hutter 2002). The distribution and the flux of energy between basin-scale standing waves, internal surges and solitary waves, remains with few exceptions (Imberger 1998; Horn et al. 2001), poorly investigated. It is evident that the degeneration process of nonlinear internal waves remains a challenge to be captured by field-scale hydrodynamic models (Boegman et al. 2005).

Thorpe (1974) and Horn et al. (2000) noted that it needs "...a significant amount of integrated field, laboratory and numerical work to parameterise the interactions of non-hydrostatic internal waves, basin-scale internal waves and the turbulent benthic boundary layer where primarily mixing occurs".

2.2 Overview of Methods of Field Observations and Data Analysis of Internal Waves

2.2.1 Touch Probing Measuring Techniques

The principal parameters for internal wave measurements in lakes are water-temperature (density-) profiles and time series of observations of currents and water temperature. First investigations of internal waves using moored thermistor chains were performed by Mortimer (1953) in Windermere. Nowadays, many electronic high precision thermistors with loggers have been developed. The thermistors in thermistor chains are usually distributed with spacings from a few centimetres to a metre in the thermocline region and larger spacing in the epilimnion and toward the bottom where the stratification is generally weak. The depths of the isotherm location (DIL), or simply the isotherm depths (ID), are calculated from data registered by interpolation of temperature observations on depths measured by thermistors in the chains and by CTD (conductivity, temperature, density) profilers. Another way to measure IDs is to record internal waves by termistor strings or distributed probes (Konjaev and Sabinin 1992), or by towed thermo-probes and free-falling advanced microstructure probes as developed, e.g., at the Northern Water Problems Institute (Glinsky 1998). Vertical profiles of currents, measured by a shipboard broadband Acoustic Doppler Current Profiler (ADCP and ADP) or deployed to the bottom, and towed ADCP and moored current metres RCM (Recorder of Current Meters – Aanderaa company, Norway).

Planning field experiments of nonlinear internal waves in large stratified lakes is a far more challenging task than in small lakes since the range of thermodynamic processes and phenomena is much more complex, and so is the set of hydrometeorological conditions (forcing).

Modern instruments, such as (1) the free-falling microstructure profilers equipped with velocity, temperature and conductivity sensors, (2) the bottom devices with the ADCP (or ADP) recording devices for measuring the near-bottom currents, (3) the high-resolution thermistor chains, and (4) the towed profiling of in-situ probes, were used for investigations of internal waves and are now available for

modern investigations. Nowadays, one uses thermistor chains and portable flux profilers (PFPs) which are equipped with precision high-resolution temperature sensors (of a resolution of about 0.001°C) and orthogonal two- or three-component laser Doppler velocimeters or acoustic Doppler current profilers (Boegman et al. 2003). Modern data for internal waves can be obtained by using moored self-contained temperature loggers. On the one hand, the time step of measurements (readings) depends both on the task of investigation and on the time scales of the internal waves. The time step for measuring high-frequency internal pulses is only a few seconds. On the other hand, for basin-scale internal waves, the time scale of measurements is on the order of a few minutes to many hours in campaigns of several months' duration. Thermistors have an accuracy of 0.002°C and should have a response-time constant of less than 3 s. Thermistors are usually calibrated by the manufacturer before and after deployment. Data records for each thermistor are aligned by time, and the rate of change of the temperature between two fixed thermistor depths is used to solve for the depth of a desired temperature, thus constructing isotherm-depth-time series.

Observational studies which yield descriptions of the patterns of manifestation, generation and dissipation of nonlinear internal waves are generally more detailed in small than in large and deep lakes. To study the generation, interaction, and dissipation of internal waves in small narrow lakes like Loch Ness, Babine Lake, and Lake Seneca, several thermistor chains were deployed (Thorpe et al. 1972; Farmer 1978). As it was shown by the authors (see Fig. 2.21), to study nonlinear internal waves in relatively narrow lakes, the deployment of several thermistor chains along the main lake axis is sufficient.

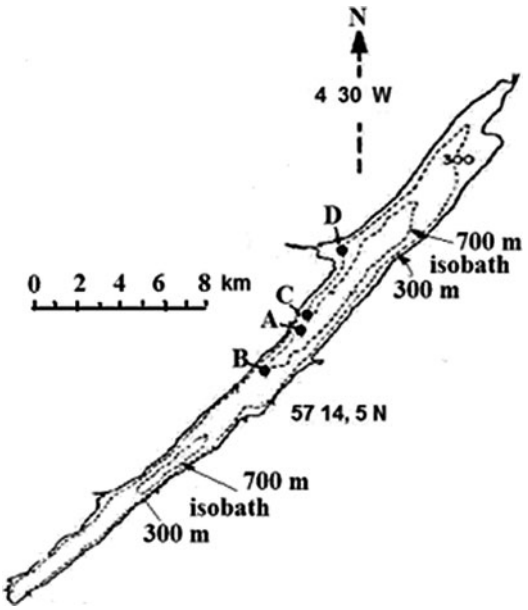

Fig. 2.21 Positions of thermistor chains (A–D) along approximately the thalweg of Loch Ness (from Thorpe et al. 1972)

In larger lakes, where the effect of the Coriolis force becomes significant, the thermistor chains and current measurement devices are usually deployed along and across the basin (Antenucci and Imberger 2001; Saggio and Imberger 2001; Mortimer 2006).

Depth-reaching studies of internal wave dynamics which are based on water-level records were demonstrated by Mortimer (1963) and Lemmin et al. (2005). The water level recorders, easily installed and maintained, can be operated during the whole year. In the paper, season-long water level records at 12 stations around Lake Geneva measured by the Swiss Federal Water Service along the shore in 1950 were analysed regarding the evidence of internal seiches, modified by the Coriolis force. To this end, the surface-elevation-time series were smoothed to eliminate the barotropic oscillation. The authors noted and used the fact that the thermocline oscillations were accompanied by oscillations at the lake-surface level, which are out-of-phase with, and typically about 100 times smaller in amplitude than, the oscillations of thermocline isotherms.

In the large Lakes Kinneret, Biwa, and Geneva, several extensive campaigns for investigations of internal waves were conducted. In these experiments, thermistor chains were deployed approximately perpendicular to the shore (Fig. 2.22a). Such deployment of measuring equipment allows description of a wide spectrum of internal waves – from basin-scale Kelvin and Poincaré to high-frequency waves, to reveal mechanisms of generation of nonlinear internal waves, such as surges and solitons. The physical parameters of the nonlinear internal waves (wave numbers, amplitudes, speed, and direction of propagation) were determined through direct

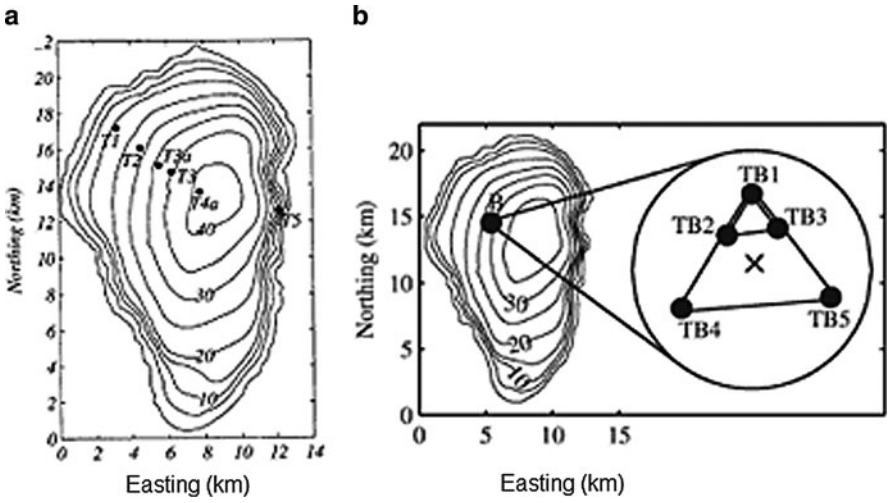

Fig. 2.22 (**a**) Locations of the thermistor chains (T1–T5) deployed across Lake Kinneret for investigations of a broad spectrum of internal waves and (**b**) scheme of setting thermistor chains for investigations of characteristics of high frequency internal waves in Lake Kinneret. (from Gomez-Giraldo et al. 2008)

measurements by three or more noncollinear thermistor chains. Direct observation gives an average crest-to-crest period. For analysis of high-frequency internal waves, an array of five closely spaced, high-temporal resolution thermistor chains was deployed in the form of a small and large triangle in Lake Kinneret (Fig. 2.22b) (Gomez-Giraldo et al. 2008).

The horizontal distances between the thermistor chains in the Lake-Kinneret experiment are equal to 9 m for the small triangle and 200 m for the larger triangle; the spacing was determined from wavelength estimates before the experiment (Boegman et al. 2003). Another kind of thermistor-chain positions was applied in Lake Biwa in the form of a cross and a line.

To register the vertical thermal structure during a probable shoaling of nonlinear internal waves in a bay of large Lake Onego, the thermistor chains was installed along a line (approximately perpendicular to the shore) with depths from 11.3 to 32.0 m in the northern part of the lake (Bolshoe Onego Bay, Fig. 2.23):

The sampling interval of the water temperature and currents depends on the possible time scales of the investigated internal waves. For high-frequency internal waves (solitons), the sampling interval of the measurements should lie in the range of few seconds to few minutes. The methodology, based on data from commonly available equipment, has proved to be a successful means to provide information that is essential for the calibration and verification of mathematical models of the internal water movement in the lake.

The set of equipment for the complex study includes deployed buoy stations for registrations of currents and water temperature; this equipment was used in Lake Onego during the INTAS experiment 2004–2005 (Hutter et al. 2007). These are AANDERAA current metres and water-temperature devices (ADP, CTD, TR, TL, ACIT) and a meteo-station installed on the board of the research vessel. Figure 2.24 demonstrates the measurement systems used on board of the research vessel of the Northern Water Problems Institute "R/V Ecolog".

To investigate the development of internal waves in the Great American Lakes, the researchers measured not only water temperature and currents with the use of autonomous buoy stations deployed along and perpendicular to the shore, but also

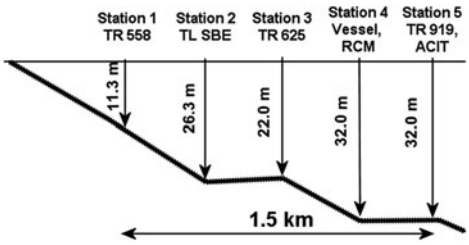

Fig. 2.23 Distribution of equipment for investigations of shoaling of nonlinear internal waves in Lake Onego during the INTAS experiment 2004 (see more about experiment 2004 in Sect. 2.3). Here, TR stands for temperature recorder, *TL* – thermochain, RCM –current metre AANDERAA, ACIT-Autonomous current and temperature device, Soviet analogue of RCM

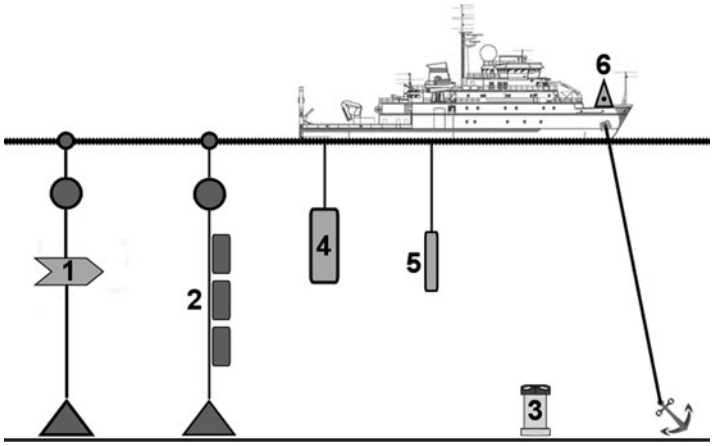

Fig. 2.24 Scheme of research instrumentation on board of "R/V Ecolog" in internal wave experiments 2004–2005: (1) Buoyant body with current metres RCM Aanderaa (Norway), (2) thermistor chains, (3) acoustic Doppler profiler (ADP) for current measurements, (4) profiler of Conductivity, Temperature, Depth (CTD), (5) free falling CTD, (6) Meteostation mEMSet on the boat

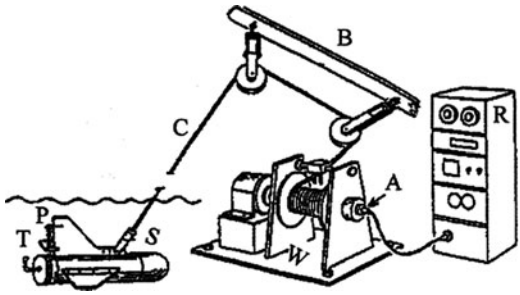

Fig. 2.25 Towed profiler of hydrophysical parameters: *T* temperature, *P* pressure, *S* commutating swivel, *A* winch axle, *C* conductor cable, beam with sheaves, *W* winch, *R* recorder (Mortimer 2006)

performed registrations along lake cross-sections. Such approaches, used on Lakes Ontario and Michigan, are described in Mortimer (2006). To "instantly" register the water-temperature profile in studying the propagation of an internal surge along the cross-section in Lake Ontario, a towed temperature profiler was used (Fig. 2.25). An analogous profiler batfish was developed at NWPI by Aleksander Glinsky and used in the field experiment "Onego" on Lake Onego (Filatov et al. 1990).

2.2.2 Remote-Sensing Techniques

In the last four decades, the combination of in situ field and *remote-sensing* observations has demonstrated that nonlinear internal solitary-like waves and surges are general features of the coastal oceans and of lakes (Apel et al. 1975; Kondratyev and Filatov 1999).

Internal waves can be observed with the use of high-resolution satellite images, e.g., SAR data (synthesis aperture radar satellite) and SPOT (French satellite with optical imaging "Satellite Pour 1'Observation de la Terre", with resolution 2.5, 5 and 10 m) and of lower-resolution satellite images, e.g., SeaWiFS and MODIS (Moderate Resolution-Imaging-Spectra radiometer). High-resolution satellite SAR images allow the estimation of a depression internal wave packet observed as a bright band, followed immediately by a dark band. In SPOT and MODIS, images with 1 km resolution have been measured in the optical bands. In these, internal waves become visible at the sun glint area, because the sun glint radiance associates with sea-surface roughness variations due to internal waves. Other possibilities to estimate internal wave parameters are colour image data from low-resolution radiometer from the SeaWiFS satellite using chlorophyll measurements (*chl*). A visible ocean colour sensor can observe the variation in the subsurface layer. SeaWiFS images indicate the variation of *chl* when an internal wave passes through. The technique of estimation of internal wave parameters is based on a well-known fact that large-amplitude nonlinear internal waves may significantly affect the distribution of the near-surface phytoplankton (Queguiner and Legendre 1986).

In some large lakes, complex studies of physical processes, including internal waves, were conducted by means of remote-sensing and sub-satellite hydrophysical measurements. Satellite data obtained from the USA National Space Agency (NASA) by the satellites "Aqua" and "NOAA", and from the European Space Agency (ESA), by the satellite "Envisat", were applied to analyse the spring thermal bar and internal waves in Lakes Ladoga and Onego (Malm and Jonsson 1994; Kondratyev and Filatov 1999). In Bogucki et al. (2005), SAR images were used for the analysis of nonlinear internal waves, in particular internal solitary waves (ISWs). A more effective band for internal wave observations is SAR imaging, which uses a modification of the surface gravity wave field, namely the coherent surface-strain rate induced by ISWs which travel along the wave guide of the thermocline. The pattern of short gravity waves can be detected by the radar backscatter system via Bragg scattering. Results of the analysis of RADARSAT sea-surface space images with manifestation of internal solitons in the New York Bight (Fig. 2.26) have been presented by Bondur et al. (2006).

The internal waves are visible as alternating light and dark bands. Figure 2.26 indicates the locations of several separate wave groups, visible in the SAR image. The number of wave packets, wave-packet distances, wavelengths and group velocity are determined by satellite image processing (Bondur et al. 2006). Amplitudes and energy fluxes of the internal wave in the area of wave generation have been estimated by two different methods; image processing, direct observation, and simulation yielded close agreement of the parameter values.

Target-oriented multi-level experiments using air and space facilities, realised on lakes Onego and Ladoga, were organised in the late 1980s (Kondratyev and Filatov 1999; Filatov et al. 1990; Karetnikov and Naumenko 1993). Observations within the "Onego" experiment, which had started in 1986 (Filatov et al. 1990), were carried out using buoy stations with thermistor chains and current metres; equipment on research

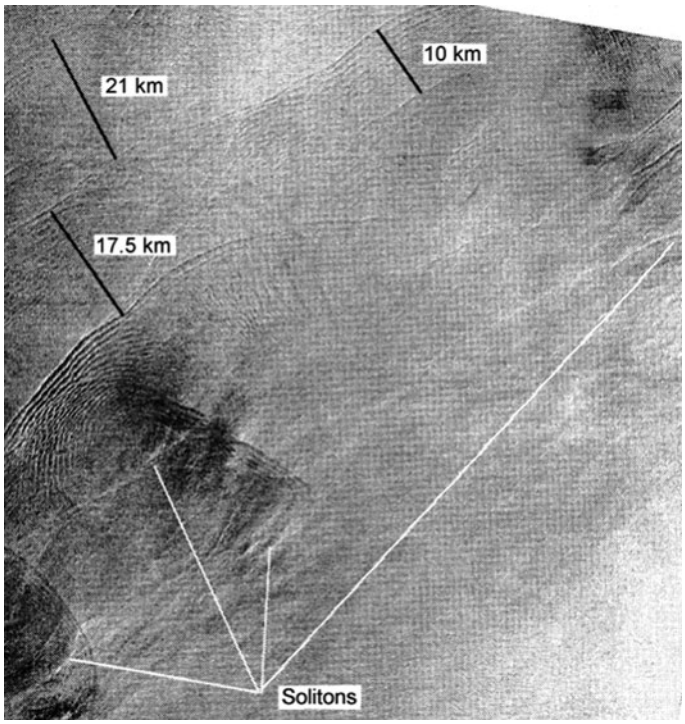

Fig. 2.26 Manifestation of solitons in the New York Bight by satellite radar image of RADARSAT. The size of the wave groups in km is shown on the figure (from Bondur et al. 2006)

vessels was similar to those shown in Fig. 2.24; stationary hydro-meteorological standard stations of observations were employed; a research laboratory on board an aircraft AN-28 (Polar Institute of Fishery and Oceanography – PIFO, Murmansk) was equipped by infrared radiometer, side looking radar, LIDAR (Light Identification, Detection and Ranging). Data were collected with aircraft-mounted lasers capable of recording concentration of *chl a*; and low-resolution (1,000 m) satellite data from "NOAA", "Meteor", medium and high-resolution data from Soviet satellites "Resourse-01" (several optical bands), "Kosmos-F1" (panchromatic data), "Almaz" (Soviet satellite with synthesis aperture radar data) were employed. The measurements with medium- and high-resolution data with resolution 170–45 m in the ranges 0.5–0.6, 0.6–0.7, 0.7–0.8, 0.8–1.1 mm from these satellites, as well as results of a multi-spectral scanner were used. Aircraft, research vessel and satellite observations were synchronised and allowed to synoptically study the physical processes and phenomena (Fig. 2.27).

All available information was used to reveal the nature of the characteristics in Lake Ladoga's and Lake Onego's water dynamics, including eddies and internal waves in the offshore and near-shore zones, as demonstrated by the satellite images. These data revealed considerable "patchiness" of the images pointing at corresponding variability of the phenomena occurring at the lake surface. Satellite

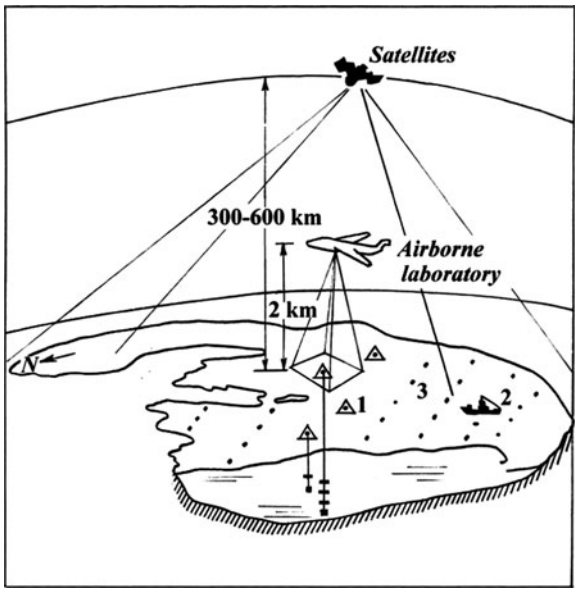

Fig. 2.27 Sketch of the multi-layered Lake Onego physical experiment during 1986–1990 using several satellites, aircraft laboratory, buoy stations with thermistor chains and current metres (1), research vessels (2), points of water temperature observations (3). (from Filatov 1991 and Kondratyev and Filatov 1999)

data from the Soviet satellite "Almaz" with SAR demonstrated surface-revealed streaks perpendicular to the shore of Lake Ladoga (Fig. 2.28). These streaks in lakes arise due to the appearance of internal gravity-wave packets on the surface. With these observation techniques, internal waves are best manifest on the lake surface with the thermocline located rather close to the surface, where the upper thermocline-metalimnion boundary is found at the 5–15 m depth. In this case, the currents, evoked by internal waves, are particularly strong in the epilimnion. Since internal waves are not directly visible, they can only be detected by their surface signature and by direct measurements of *in situ* hydrophysical parameters. Where the density interface is sufficiently shallow to permit the internal wave crests to interact with the sea surface, the waves can be detected by the resulting increased roughness of the lake surface. Surface roughness is best seen by the use of Synthetic Aperture Radar (SAR) imagery. Internal waves appear on the surface in the form of low-frequency surface signals with the periodicity of internal waves. SAR images of Lake Ladoga received from the satellite "Almaz" show manifestations of internal waves on the surface with wavelengths of a few hundred metres to kilometres (Kondratyev and Filatov 1999; Naumenko et al. 1992, Fig. 2.28)

This figure is a good example of internal wave manifestation with a group of tightly packed solitons; basin scale internal waves are shown in this image.

A survey, conducted by a side-looking radar from the satellite "ENVISAT" (radiometer ASAR – An Advanced Synthetic Aperture Radar) satellite, which was synchronised with ship-borne observations from R/V Ecolog, indicated that, according to the shade and texture of the surface layer, Lake Onego was divided

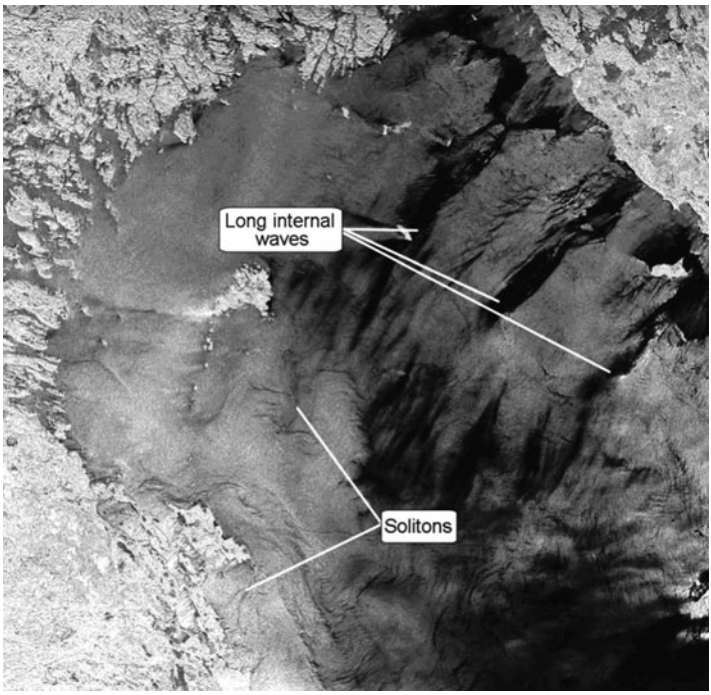

Fig. 2.28 Satellite "Almaz" SAR image of Lake Ladoga in summer 1995. In part of the Lake, manifestations of internal waves and other mesoscale structures are shown

into two parts with patches of dozens to hundreds of metres exhibiting manifestation of solitary waves (see Sect. 2.3. Fig. 2.40).

Another remote-sensing technique, applied for internal wave investigations in lakes and oceans, is acoustic echo-sounding. Farmer and Smith (1980) used echo-sounding observations from the boat to observe physical processes in natural waters. In the Lake Ladoga experiment (Filatov 1983), internal-wave observations were undertaken, combined with touch probing measuring techniques (thermistor chains, CTD, current measurement) with echo-sounders from the research vessel "Talan" of the Institute of Limnology of the Russian Academy of Sciences. Four acoustic surveys in Lake Ladoga by a dual-beam 400-kHz echo-sounder were performed. Figure 2.29a displays an image of the evolution of the flow (hydro-acoustic transect) which allows estimation of the thermocline fluctuations by internal waves (internal standing wave and surge) and vertical distribution of the water temperature and speed of sound in the water, as measured from the anchored board of the research vessel "Talan" in Lake Ladoga (Filatov 1983).

Such waves can be distinguished by the use of the phytoplankton distribution registered by echo-sounding. The upper mixed layer thickness was about 12 m with a local depth of 30 m. Fig. 2.29 illustrates the presence of fluctuations at the

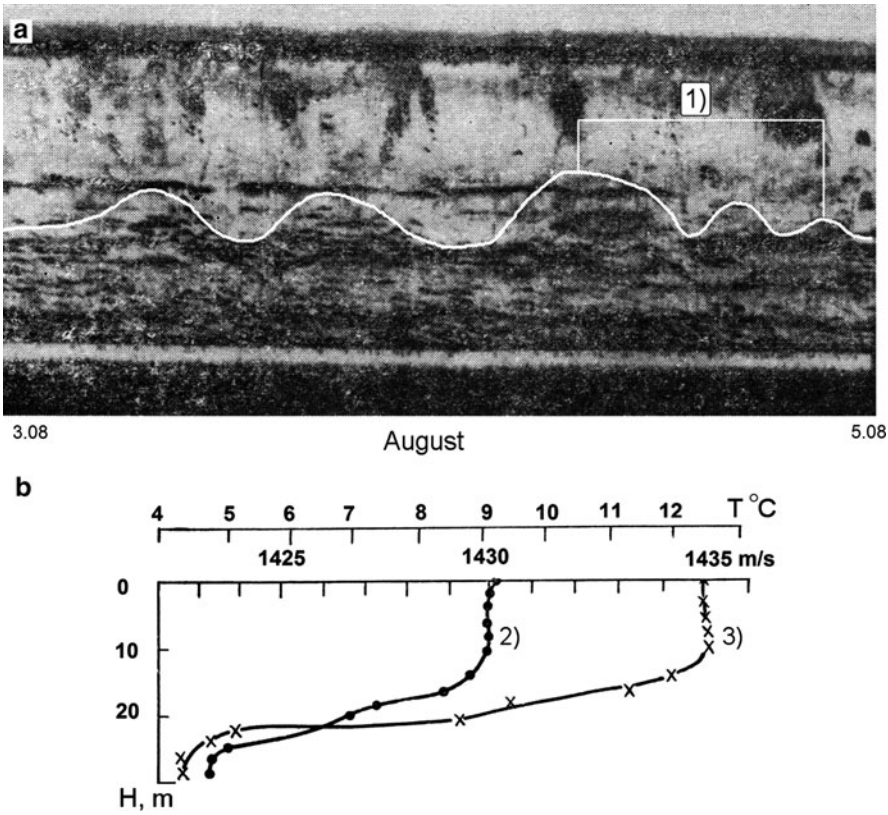

Fig. 2.29 (**a**) Acoustic image demonstrating the evolution of the flow in the near-shore zone of Lake Ladoga in August 1977 (station Δ1 on Fig. 2.11). The onsetting internal standing wave is shown by the white curved line indicated by (1); (**b**) Vertical distribution of the water temperature (2) and sound speed (3). Data obtained by Acoustic dual-beam 400-kHz echo-sounder from the anchored board of the research vessel

thermocline with a period of four hours, corresponding to that of the internal seiches in the Jakkimvarsky Bay of Lake Ladoga (see Fig. 2.16). The amplitudes of these internal waves were about 3–6 m. High-frequency nonlinear internal waves can also be seen in Fig. 2.29a; they are shown by the white curved line (1) (which demonstrates the capacity of this echo sounding approach). Another example of observations of internal waves and mixing is given in Moum et al. (2003). The acoustic backscatter records in the lake disclose Kelvin–Helmholtz billows growing from instabilities on the forward face of a solitary wave (Fig. 2.30).

There also exist several other methods of internal wave observations. For example, Michallet and Ivey (1999) applied ultrasonic probes and data processing to study interfacial solitary waves in layered waters.

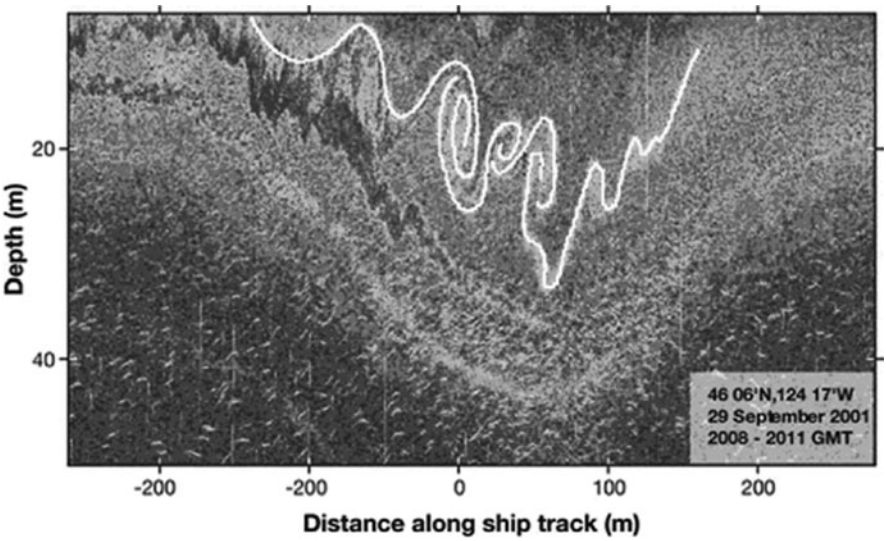

Fig. 2.30 Acoustic backscatter records showing Kelvin–Helmholtz billows growing from instabilities on the forward face of a solitary wave and billows (shown by the white curved line) (from Moum et al. 2003)

2.2.3 Data Analysis of Time Series of Observations of Internal Waves

The general data analyses of time series of observations of water temperatures (often in the form of IDs) and currents use standard statistical procedures applied in limnology and oceanography (Gonella 1972; Mooers 1976; LeBlond and Mysak 1978; Mortimer 1979; Konjaev and Sabinin 1992; Kondratyev and Filatov 1999; Rozhkov et al. 1983). The set of methods include auto- and cross-correlations and spectral analysis of time-series records and hydrophysical scalar and vector fields. The power spectral densities of internal waves are calculated by the use of the techniques of spectral analysis, which are obtained with the well-known method of Bendat and Piersol (1971), e.g., FFT (fast Fourier transforms) or MEM (maximum entropy method). These methods, applied to time series of scalar fields (water temperature records, water level fluctuations or IDs) and orthogonal components (projections in velocity vectors on to Cartesian axes) of 2-D vectors of currents, are well described in the literature (Rozhkov et al. 1983). However, as shown by three-dimensional progressive vector diagrams of currents (Fig. 2.31), measured by ADCP devices, the trajectories of water movements are more informative, even though also more complicated than 2-D progressive vector diagrams of U and V components of the currents are constructed.

The most general statistical model for the current–time series is their representation in the form of nonstationary nonhomogeneous vectorial stochastic functions with values in 3-D Euclidean space. For a joint data analysis of scalars (water

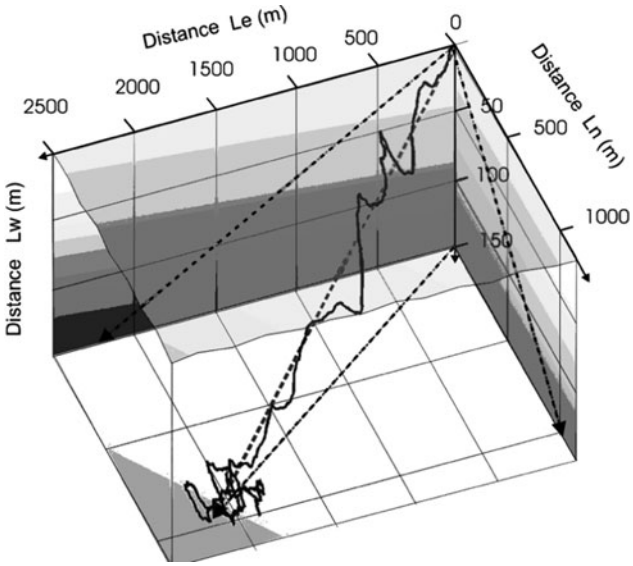

Fig. 2.31 3-D progressive-vector diagram of currents measured by ADCP (three components of current: U, V and W) (*solid line*) and mean water transport vector (*dotted line*). (from Bondur and Fialtov 2003)

temperature, isotherm depths) with vector processes (currents), special approaches should be applied (Rozhkov et al. 1983; Filatov 1991; Murthy and Filatov 1981).

At present, since a uniform, generally accepted technique of analysis of time series is still lacking, data processing for currents is performed on the basis of the representation of a velocity vector in terms of its projection in a two-dimensional (2D) Cartesian coordinate system (component method); complex-valued methods (Mooers 1976) in which the 2D vectors are represented as complex numbers with their real and imaginary parts being equal to the projections of the velocity vector to the Cartesian axis are also used as is the method of rotary-components (Gonella 1972). Rotary spectra display the frequency distribution of kinetic energy partitioned into clockwise- and anticlockwise-turning currents of the U and V components of the vector time series.

By comparative analyses of these methods, it can be shown that, due to the difference of the mathematical models of the current vector (and, therefore, because of the operations over these models), the probability characteristics of the currents calculated by the different methods are not equivalent to one another; sometimes, the different methods may cause illusive representations of the current variations. The most arguable approach to the processing of data of current measurements and this analysis is given by the vector-algebraic method worked out by Rozhkov et al. (1990). This method was applied for auto- and cross-data analysis of currents (vector valued) and water temperature (scalar valued) for the large Lakes Ladoga, Onego, Sevan and Nesijarvi (Filatov 1991).

The principal probability characteristics of the current velocities are the expectation vector V, the correlation tensor, defined as the expectation of the tensor product of vectors, and the spectral density tensors determined through Fourier transforms of the correlation function. The theory of the method was developed by Rozhkov et al. (1983) and was first applied for Lake Ladoga by Filatov (1983). The spectra $S_V(\omega)$ characterise the distribution by the frequency of oscillations of the current velocities and give a quantitative measure of the intensity of such oscillations and their orientation in the accepted system of coordinates and changes in time,

$$S_V(\omega) = \frac{1}{2\pi} \int_{-\infty}^{\infty} e^{-i\omega\tau} K_V(\tau) \mathrm{d}\tau,$$

where

$$S_V(\omega) = \begin{pmatrix} S_{V_1V_1} & S_{V_1V_2} \\ S_{V_2V_1} & S_{V_2V_2} \end{pmatrix},$$

and

$$S_{V_1V_2}(\omega) = C_{V_1V_2}(\omega) + iQ_{V_1V_2}(\omega),$$

$$S_{V_2V_1}(\omega) = C_{V_2V_1}(\omega) + iQ_{V_2V_1}(\omega),$$

$$C_{V_1V_2}(\omega) = C_{V_2V_1}(\omega) \quad Q_{V_1V_2}(\omega) = -Q_{V_2V_1}(\omega).$$

The above-mentioned probability characteristics are invariants and do not depend on the choice of the system of coordinates.

The properties of the correlation, $K_V(\tau)$, and the spectral tensor-functions $S_V(\omega)$ and, thus, the process properties $V(t)$ may be optimally disclosed through the set of invariant scalar functions, namely: $J_1(\omega)$ is the invariant spectrum of currents, $\lambda_{1,2}(\omega)$ are the axes of the ellipse, and $\alpha(\omega)$ is the angle (from North) to the principal axis of the current ellipse (see Fig. 2.33) .

The correlation function and spectral density estimates in a stationary approximation are calculated by averaging function values of time series of pertinent variables along the whole realisation length, and in nonstationary approximations by performing gliding averaging of separate parts of the realisation. For processes with strong nonstationarity, a spectral density estimation is produced by means of gliding auto-regression transforms.

These methods of time series analysis of vectors (currents) and scalars (IDs) were used for Lake Ladoga (Filatov 1983) and in the internal wave experiment for Lake Onego of the INTAS field study experiment in the summers of 2004–2005 (Hutter et al. 2007). Spectral analysis data of ID and currents (six tensor characteristics) in Lake Onego allow us to establish the dominant period in the currents of the internal

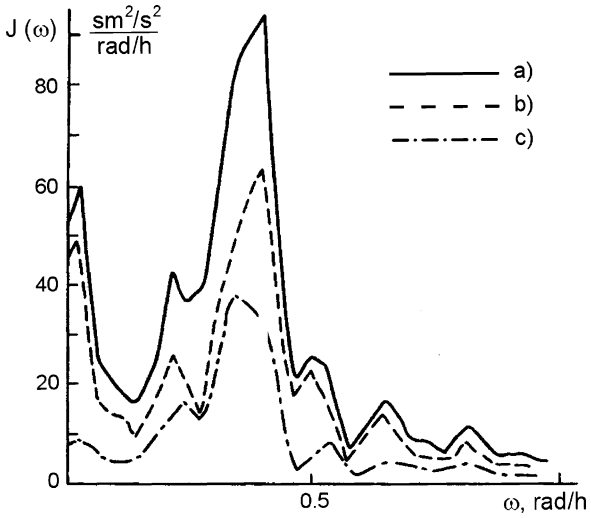

Fig. 2.32 Characteristics of the tensor spectral density of currents in the metalimnion of Lake Onego, 2004, point Δ5, horizont 15 m in the thermocline: $J_1(\omega)$ – linear invariant (or spectra) (**a**), $\lambda_1(\omega)$ – major axis of ellipse of currents (**b**), $\lambda_2(\omega)$ – minor axis of current ellipse (c)

wave near the local inertial frequency ($\omega \sim 0.5$ rad h^{-1}) in the offshore zone at stations Δ4 and Δ5 (Fig. 2.37). Small diurnal ($\omega \sim 0.26$ rad h^{-1}) long-period macro-scale internal Kelvin waves ($\omega < 0.1$ rad h^{-1}) and high-frequency fluctuations were also detected (Fig. 2.32). Tensor-data analysis of the currents allowed identification of the current ellipses; at the upper level, they exhibit a greater anisotropy when compared with those observed at depths below 30 m. The rotation indicator shows that in the low-frequency range, the rotation was clockwise (not demonstrated in Figure 2.33). This is typical for internal inertial oscillations of currents. The rotation of the current vectors with a semi-diurnal period is explained by the tendency of the direction of the main current to follow the steep depth gradient. The sizes and aspect ratios of the current ellipses provide a characterisation of the current.

Figure 2.33 shows the current ellipse at the thermocline, indicating a strong anisotropy. The main direction of the currents during the period of observation is 195°. Spectral analysis using the frequency–time approach and wavelet transforms have been conducted for data of internal waves in e.g., Lakes Kinneret (Antenucci et al. 2000), Onego (Hutter et al. 2007), Ladoga (Filatov et al., 1991), Michigan and Ontario (Mortimer 2006). Sampled data on the water temperature and IDs allow evaluation of the density spectrum of internal gravity–inertial waves in the period ranges from the local inertial band ($\omega \approx f$) to short-term intervals of a few minutes, typical for the local Brunt–Väisälä frequency. The spectrum of the internal waves (ID) has a dominant maximum at the local inertial frequency ($\omega \sim 0.5$ rad h^{-1}), and minor maxima in the high frequency range caused by short-period internal waves near N, where harmonics exist corresponding to the group of internal waves having random phases and amplitudes. On the basis of ID-data, a frequency-temporal spectrum $S(\omega, t)$ can be constructed by calculating the spectra of internal waves for several time spans belonging to the observation period of nonstationary spectra of internal waves for different time intervals.

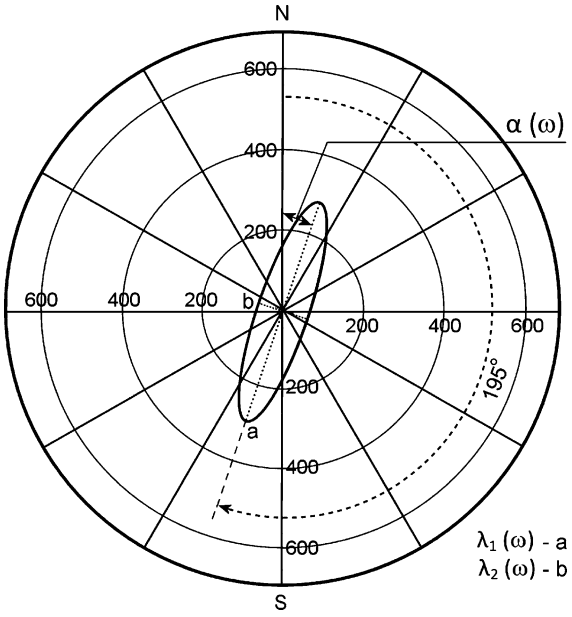

Fig. 2.33 Ellipse of currents in the metalimnion of Lake Onego, 2004, at station 5, at a depth of 15 m. (**a**) the major axis of the ellipse is $\lambda_1(\omega)$ and (**b**) the minor axis is $\lambda_2(\omega)$

Figure 2.34 shows a sample of wavelet analysis of the 12°C- isotherm depth–time series at a particular position in the Lake Onego-INTAS experiment 2005. It reveals the presence of the maxima at frequencies which correspond to the synoptical period (internal Kelvin wave through the whole period of measurements), the diurnal period to the inertial oscillations.

No evidence of an internal surge or of solitons is evident in this wavelet (Fig.2.34). The amplitude of the Kelvin wave (d_8 in the figure) is twice as large as that of internal Poincaré waves with period 13.5 h (d5 in the figure). Finally, we mention that Saggio and Imberger (1998) applied the wavelet analysis to investigations of internal waves in Lakes Biwa and Kinneret.

The nonstationary continuous wavelet time–frequency spectrum of internal waves for the 12°C–isotherm (station Δ5, Lake Onego, 2005) is shown in Fig. 2.35. Its spectra demonstrate an increasing value of the energy of the internal wave oscillations on the frequencies of internal Kelvin and Poincaré waves during the period of the stratification development.

It is interesting to note that various authors (Thorpe & Jiang, 1998; Imberger 1998; MacIntyre et al. 1999; Stevens 1999) found that the energy spectrum of internal waves exhibits high accuracy within the frequency band between f and N, as observed in the ocean (Garrett and Munk 1975). The agreement of the shape of the internal wave spectra in the ocean and in lakes is an important result, considering the large difference in scales between these two environments and the difference in the constraint offered by the boundaries of lakes. These characteristics also seem to be independent of the size of the lake, having been observed in other lakes

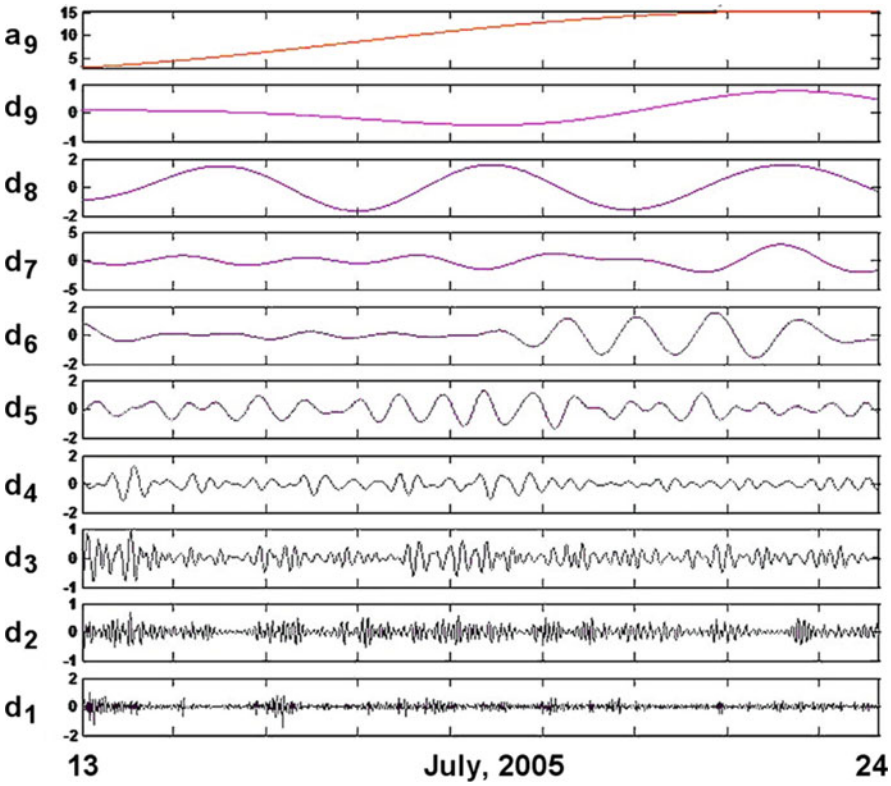

Fig. 2.34 Discrete wavelet decomposition at 9 levels (discrete Meyer wavelet) for the 12°C–isotherm depth variations at station Δ4 (Lake Onego, 2005). a9 – trend, d9 – 216 h, d8 – 108 h (Kelvin waves), d7 – 54 h, d6 – 27 h, d5 – 13.5 h (Poincaré), d4 – 6.75 h, d3 – 3.4 h, d2 – 1.7 h, d1– 0.85 h

too: Geneva (Thorpe et al. 1996), Kinneret (Imberger 1998) and Ladoga, Onego and Sevan and Krasnoe (medium- and small-size lakes in Europe) (Filatov 1991, Fig. 2.36). However, the mechanisms which create and distribute the energy throughout this universal power spectrum of Garrett and Munk (1975) according to ω^{-2}, are seemingly independent of the size and location of the aquatic system, but are not yet understood.

It is evident nowadays that coupling of the analysis of different types of measurements of field data with remote-sensing observations and numerical modelling has proven to be a powerful approach to better comprehend the internal wave characteristics observed in lakes.

It is worth noticing that the choice of methods in studying nonlinear internal waves strictly depends on the formulated hypotheses, typical lake size, extent of stratification and wave parameters in a range from basin scale to high frequency, and weather conditions.

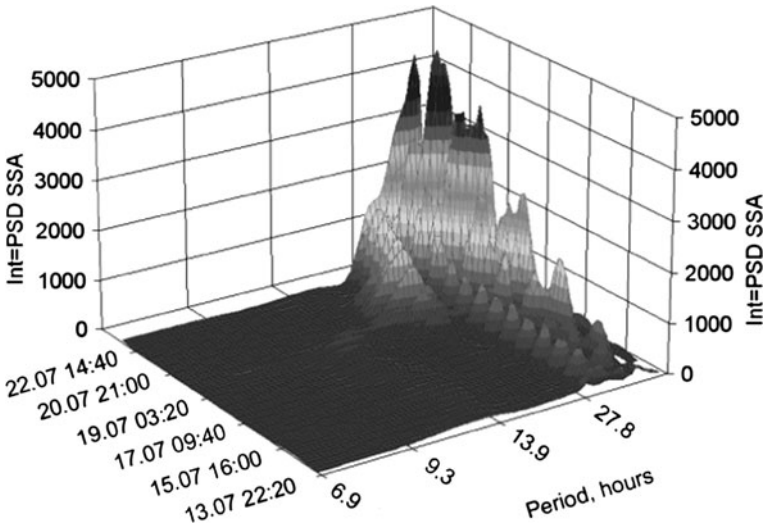

Fig. 2.35 Nonstationary continuous wavelet time–frequency spectrum of internal waves. (12°C–isotherm, station 5, INTAS experiment on Lake Onego 2005)

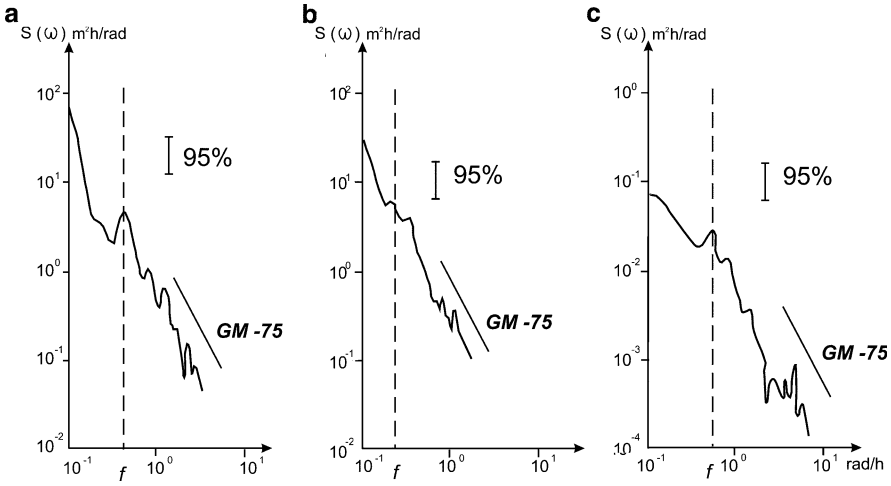

Fig. 2.36 Ensemble averages of spectra of internal waves (IDs in the middle of the metalimnion) in Lakes Ladoga, Sevan and Krasnoe. "GM-75" is the ω^{-2} law of Garett and Munk (1975)

2.3 Lake Onego Field Campaigns 2004/2005: An Investigation of Nonlinear Internal Waves

The Lake Onego experiment 2004–2005 was devoted to studies of nonlinear internal waves. It was a first special complex experiment performed in a large (or great, see Rukhovets and Filatov 2009) lake by means of field observations, remote-sensing data analysis from satellites, and mathematical and laboratory physical modelling (Hutter et al. 2007).

Particular attention was devoted to the processes of degeneration of basin-scale baroclinic movements into short-period internal waves, their successive interaction with lake boundaries, the transformation and disintegration of internal waves during their shoaling near lake boundaries and bottom slope, the interactions of nonlinear waves with the background stratification as well as breaking with the generation of spots of mixed water. In the framework of the INTAS project "Strongly nonlinear waves in lakes: generation, transformation and meromixis" (Hutter et al. 2007), internal wave processes were studied theoretically in conjunction with the use of experimental data obtained during the summer campaigns in Lake Onego in 2004–2005 and previous observations of internal waves (1977–1987 and 1986–1992) in gulfs of Lake Onego under complex hydrometeorological conditions. A fully nonlinear nonhydrostatic numerical model (Hutter et al. 2007; Vlasenko et al. 2005) was applied. It was important to analyse the climatology of the processes under study and to gain better knowledge about the development of its specific features related to the weather conditions, depth distribution, and angles of the slope of the shore of the lake.

2.3.1 Field Measurements

Two field campaigns were performed in the framework of the INTAS project in Lake Onego, Karelia, Russia in the periods 18–28 July 2004 and 13–24 July 2005. To register the vertical thermal structure during a probable shoaling of nonlinear internal waves, the following equipment was installed along a line roughly following the direction of steepest descent of the bathymetry and with depths from 10 to 32 m in the Bolshoe Onego Bay (see Fig. 2.37, Table 2.2 and Fig. 2.24): thermistor chains with 5–10 min sampling intervals were installed at stations 1, 3 and 5; currents were measured by RCM current metres with time intervals of 10 and 5 min, respectively, at stations 4 and 5 and by acoustic doppler profiler ADP with 1 min sampling interval; a free falling CTD profiler was used for every 20-min temperature-profile-measurement at station 4.

To evaluate the development of internal waves in Lake Onego, the observational data received at the same polygon in 1977 and in the narrow bay Lizhemskaya Guba in the Bay Bolshoe (Big) Onego in 1987 were also used. Figure 2.38 demonstrates locations of equipment deployment in 1977 (a) and 1987 (b).

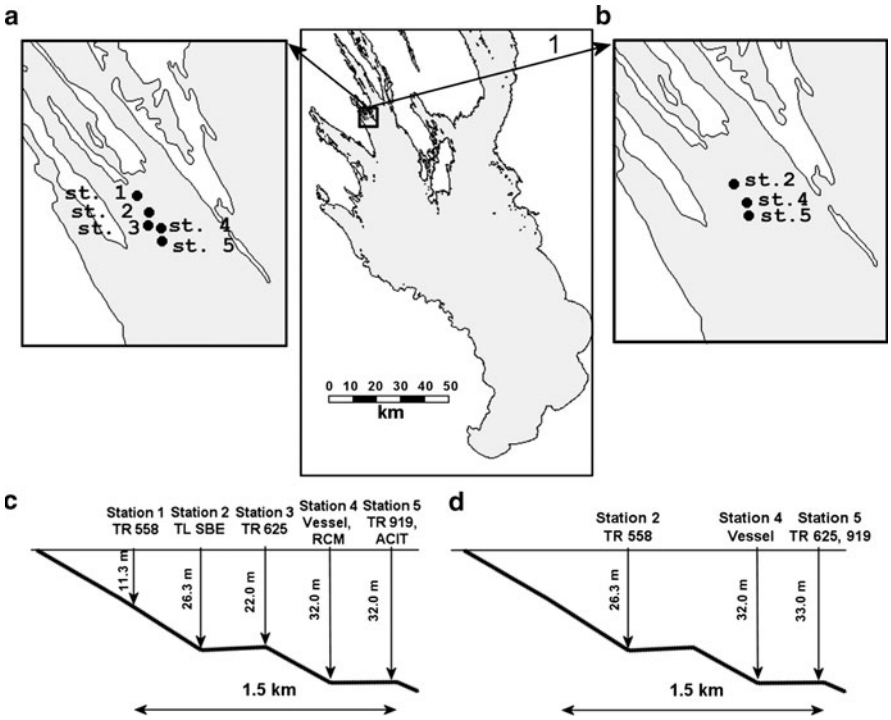

Fig. 2.37 Locations of the polygons of field campaign in the Bolshoe (Big) Onego Bay, Lake Onego in 2004–2005 (1). Locations of the points of observations during 18–28 July 2004 (**a**) and 13–24. July 2005 (**b**). Positions of hydrophysical stations with respect to the shore and to the entry of the bay, vertical profiles (sections) of observations in 2004 (**c**) and in 2005 (d)

The depth distribution at the measurement sites and locations of measurement devices are shown in Fig. 2.37 and Table 2.2. Instrumentation for exploration of the water dynamics on board of 'R/V "Ecolog" is shown in pictures in Sect. 2.2 (see Fig. 2.24).

Meteorological data during experiments were collected from the meteorological network of the Russian "Roshydromet" stationed around the lake and on board of R/V "Ecolog" of the Northern Water Problems Institute (NWPI) by the meteorological station mEMSet 99 with wind sensors, air temperature and humidity sensor EMS 33, and infrared (IR) radiometer. Hourly registrations were performed from the board of the anchored vessel "Ecolog" (station 4): wind speed [m s^{-1}]; wind direction [degrees]; wave height, Beaufort number; wave height direction [degrees]; total cloudiness [points[1]]; air temperature [°C (dry-bulb)]; air temperature [°C (wet-bulb); air pressure [mm Hg]; surface water temperature [°C]; water

[1] In Russia estimates of total cloudiness is in fractions from 1 to 10. Ten points are equal to 100% of cloudiness.

Table 2.2 Description of equipment used in the measurements performed in 2004/2005

CTD-90M Sea and Sun Technology (Germany)			
Sensors	Range	Accuracy	Resolution
Pressure	50 bar	±0.1% FS	0.002% FS
Temperature, °C	−2. . .+35	±0.005	0.001
Conductivity, mS/cm	0. . .6	±0.005	0.0001
Free-falling profiler (NWPI, Russia)			
Sensors	Range	Accuracy	Resolution
Temperature, °C	−2 ÷ 30	±0.2	0.01
TR-2 Aanderaa (Norway)			
Sensors	Range	Accuracy	Resolution
Temperature, °C	−2.46 ÷ +21.48	±0.15	0.02
Temperature recorder SBE 39 (USA)			
Sensors	Range	Accuracy	Resolution
Temperature, °C	−5 to 35	±0.002	0.0001
Automatic current and temperature recorder ACTR (Russia)			
Sensors	Range	Accuracy	
Temperature, °C	−2 ÷ 38	±0.03	
Current velocity, cm s^{-1}	3–200	±5%	
Direction, degrees	0–360	±5%	
ADP SonTek (USA)			
Sensors	Range	Accuracy	Resolution
Current speed, cm s^{-1}	±10	±0.5	0.1
Current direction, deg.	0–360	±1	0.1
RCM-4 Aanderaa (Norway)			
Sensors	Range	Accuracy	Resolution
Temperature, °C	−0.34 ÷ 32.17	±0.15	0.03
Conductivity, mS m s^{-1}	0 ÷ 70	2%	0.1%
Current velocity, cm s^{-1}	1.5 ÷ 200	±1.5	2%
Direction, degrees	0 ÷ 360	±3	3
Meteorological station mEMSet 99 (Czech Republic)			
Sensors			
Wind sensor Met One 034B	Starting threshold	0.28 m s^{-1}	
	Speed accuracy	0.1 m s^{-1}	
	Direction accuracy	±4°	
Air temperature and humidity sensor EMS 33	Operation range		
	• Relative humidity	0–100%	
	• Temperature	−40 ÷ +60°C	
	Accuracy		
	• Temperature	±0.3°C	
	• Relative humidity	±2%	
Pyranometer M-80 m (Russia)			
Sensitivity	Direct	0.0130 mV for 1 W m^{-2}	
	Reflect	0.0112 mV for 1 W m^{-2}	

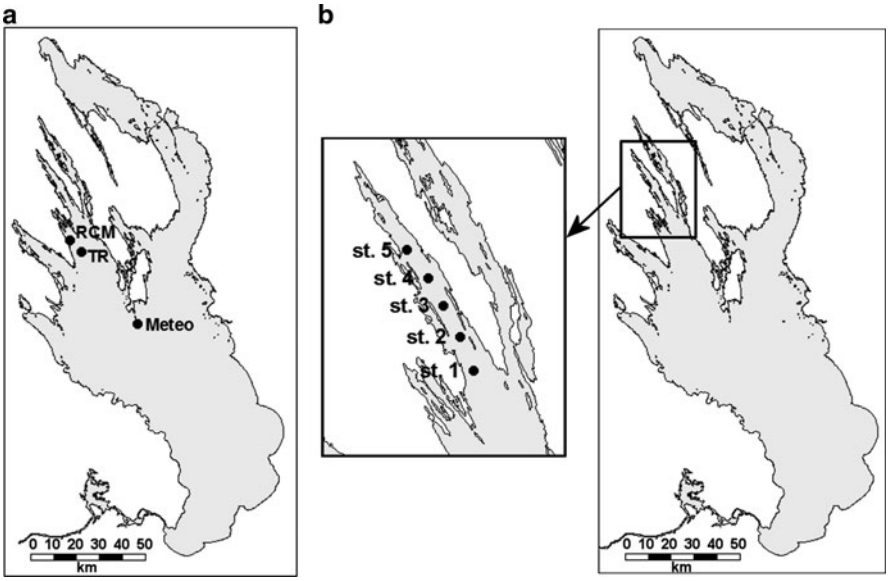

Fig. 2.38 Locations of the points of observation in the Bolshoe Onego Bay, Lake Onego 1977 (**a**), where *RCM* is an AANDERRA current metre position, *TR* is a temperature recorder of AANDERRA, *Meteo* is a meteostation; and (**b**) indicates positions of observation points in Lizhemskaya Guba (Gulf), Bolshoe Onego Bay, 1987b

transparency [m]. Weather conditions during the period of field measurements were close to calm with substantial cloudiness. Measured wind and current velocities are expressed in terms of *u*- and *v*-components at Station 4, 18–28.07. 2004 shown in Fig. 2.39.

Average wind velocity during the 2004 experiment was about 3 m s^{-1}, with a maximum up to 5–9 m s^{-1} (Fig. 2.39a). Average current speed at the depth of 5 m during the experiment in the year 2004 was about 5–8 cm s^{-1} with a maximum up to 35 cm s^{-1} (Fig. 2.39b).

The initial state of the thermal structure can be characterised as summer stratification. The upper mixed layer was 5 m thick, and its temperature was about 18°C. The water temperature in the bottom layers (~30 m) was close to 5–6°C.

To register the changes in the vertical thermal structure during a possible passage of nonlinear internal waves over the changing depth of the bottom, the equipment was employed along the profile with depths from 11 to 32°m in the Bolshoe Onego Bay (Fig. 2.37c, d). To perform the measurements of the currents and water temperature, the devices described below were used in the first experiment.

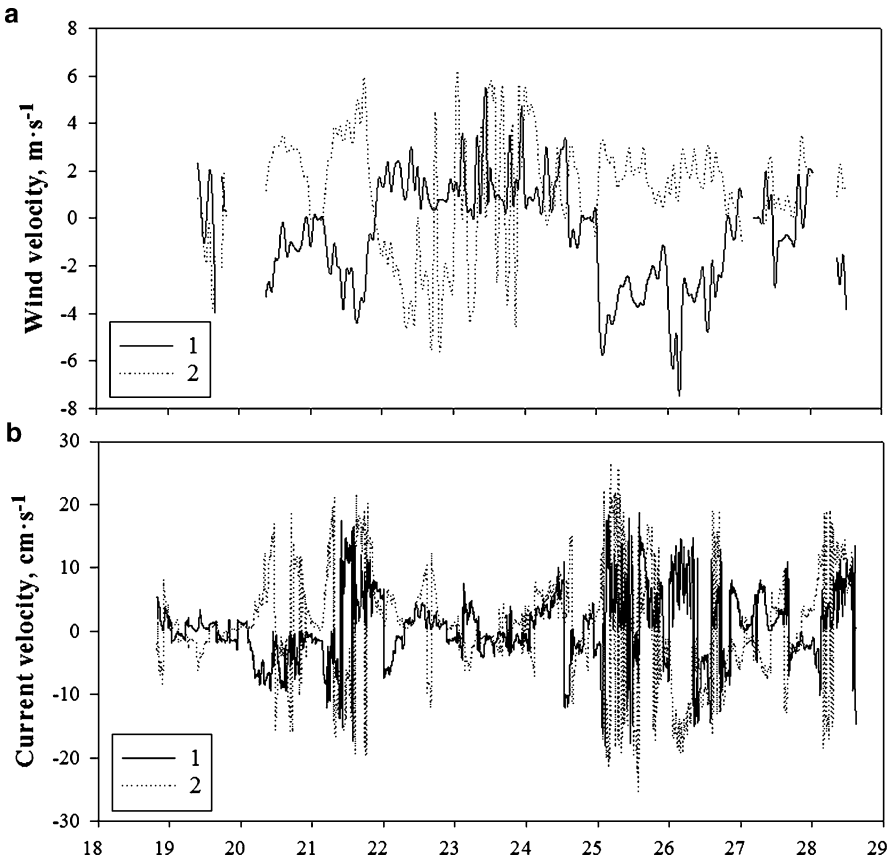

Fig. 2.39 Measured wind (**a**) and current (**b**) velocities (depth 5 m) expressed in terms of *u* (1)- and *v* (2)-components of the vector at Station 4, Lake Onego, 18–28.07.2004

2.3.2 Data Analysis

Data Analysis of Lake Onego INTAS Experiments 2004–2005.
Experiments 2004
Target-oriented satellite imagery was also used. During the field campaigns, satellite infrared (IR) and satellite aperture radar (SAR) images were received from NOAA (Fig. 2.40) and ENVISAT ASAR (Fig. 2.41). All available information from NOAA (surface temperature) for the period 13–24 July, 2004 and the ENVISAT ASAR image taken on 26.07.04 (Dr. D. Akimov from NIERSC – private communication) were used to reveal the nature of the distinctive features in the Lake Onego-water dynamics, including eddies, upwelling zones and internal waves.
Figure 2.40 displays the distribution of the average surface water temperature (after transformations of brightness values) with manifestation of upwelling along the

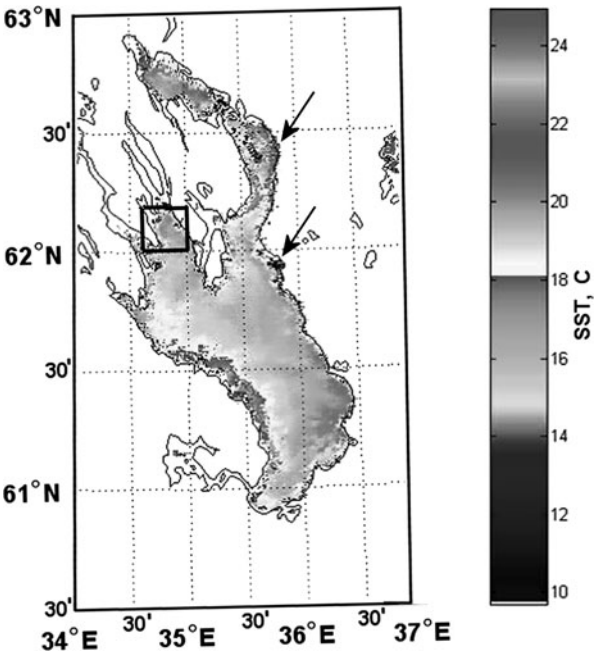

Fig. 2.40 Average surface water brightness temperature from NOAA satellite 13–24.07.2004 The location of the INTAS polygon is shown by the marked square. Black arrows show upwelling zones

east and west costs of the lake (black arrows indicate surface water with temperature around 16°C). Unfortunately, a low resolution of the NOAA satellite in the infrared band – only 1 km – did not allow resolving more detailed dynamics of the thermal structure in the area of the polygon. A survey by a side-looking radar from the satellite "ENVISAT" (radiometer ASAR – Advanced Synthetic Aperture Radar) synchronised with shipborne observations from R/V "Ecolog", indicated the presence of patches in Lake Onego, sized from dozens to hundreds of metres with the manifestation of stripes conditioned by internal waves with typical size from hundred metres to one kilometre.

These data revealed considerable "patchiness" of the phenomena occurring at the lake surface. Satellite data from "ENVISAT ASAR" satellite demonstrate streaks on the surface and coastal upwellings (Fig. 2.41). These streaks on the lake surface revealed internal gravity waves which appear as wave packets on the surface. Internal waves are best seen on the lake surface if the thermocline is located rather close to the surface when the upper thermocline–metalimnion boundary is found at the 5–15 m depth. The SAR image of Lake Onego shows the manifestation of several upwelling zones and internal waves on the surface with wavelengths of a few hundred metres (inserts 1 and 2 in Fig. 2.41).

Long internal shore-hugging Kelvin waves with periods of several days and Poincaré-wave modes occupying the whole lake with a time scale near the local inertial period of 13.5 h were observed. In the offshore regions, low-frequency oscillations with periods from days to weeks are usually caused by large-scale low-frequency oscillations of currents and temperatures. These waves are likely

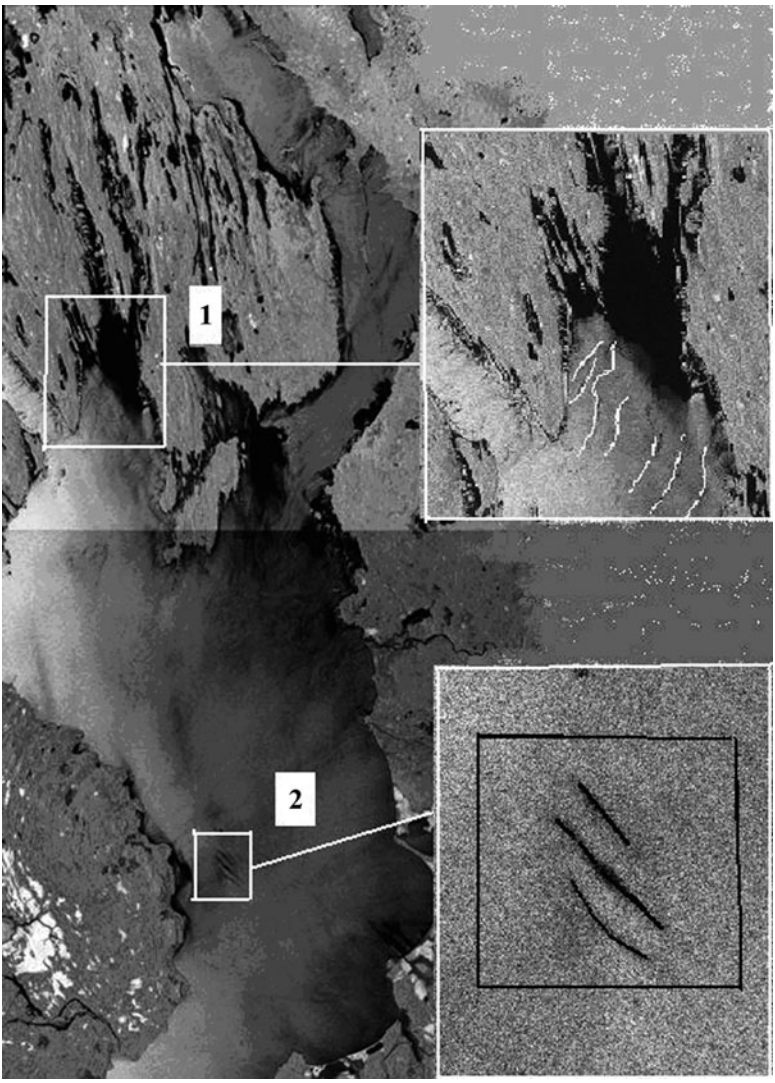

Fig. 2.41 "ENVISAT" ASAR image taken on 26.07.04. on Lake Onego. Insets in the frame show solitary wave manifestation by conspicuous lines. Internal waves in Bolshoe Onego, in INTAS polygon are shown in (1) by *white lines* and in the central part of the lake (2) by *black lines*

generated by wind and can persist long after the cessation of the initial wind impulse. Internal Poincaré waves occur in the lake distant from shore, exceeding the internal Rossby radius of deformation (3–5 km). During the INTAS experiment 2004–2005, their signals are seen at stations 4 and 5 (Fig. 2.37c–d). The wind-induced coastal upwellings and the broad counter-current in the deep part of the lake are among the main water circulation responses due to the wind. After the

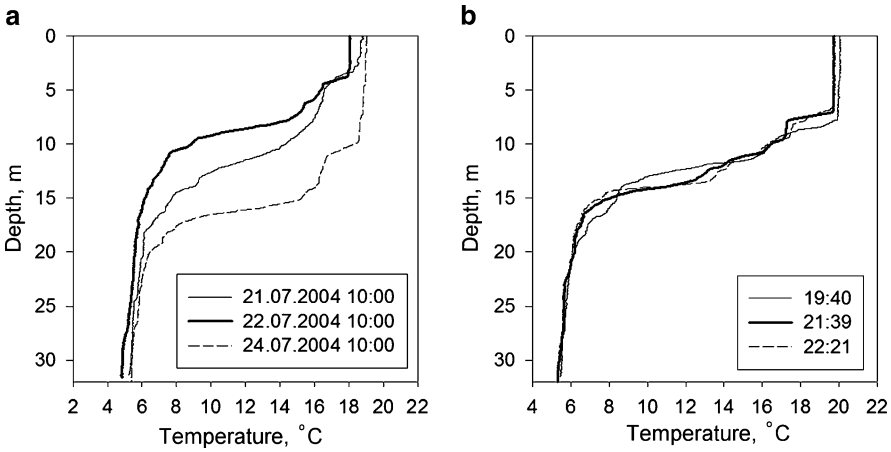

Fig. 2.42 Vertical temperature profiles at station 4. (**a**): profile 21.07, 10:00 presents the situation before the passage of the upwelling, 22.07, 10:00, during upwelling, 24.07, 10:00 and after upwelling. (**b**): all profiles taken on 25 July, in the evening during 2 h 41 min. (Experiment INTAS 2004)

cessation of the wind, upwelling relaxation begins. The irregular lake morphometry, however, prevents long internal Kelvin-wave propagation around the lake. According to observations and modeling (Filatov 1991; Beletsky et al. 1994), the upwelling front moved along the eastern coast to the north, in the direction which generally coincides with the propagation direction of the Kelvin waves which were periodically released from the front; internal surges, however, migrated across the basin through fields of inertially rotating response currents.

The initial state of the thermal structure of the lake can be characterised as summer stratification (Fig. 2.42) under an average wind velocity of about 3 m s^{-1}. Weather conditions during the experiment were close to calm.

The upper mixed layer was about 5-m thick, and its temperature was about 18°C in the beginning of the experiment 21.07.2004 (Fig. 2.42). The water temperature in the bottom layers (~30 m) was close to 5°C. The thermocline was initially quite fuzzy-edged (the water temperature at 22 m depth was 14°C). The thermo- and hydrodynamical processes registered during the experiment in the Bolshoe Onego Bay can be described in terms of the time series presented in Fig. 2.43.

The evolution of the temperature at the 10-m depth reveals a very weak water activity prior to 20/21 July. On 21–22 July 2004, a sharp change of the water temperature took place in the thermocline after the passage of the strong wind with speeds about 9 m s^{-1} (see Fig. 2.39a). This sharp change of the water temperature was similar to the passage of the internal surge (Fig. 2.43). The thermocline was raised, and the 10 m-water temperature changed from 16 to 6°C. We may suspect that the basin-scale Kelvin wave was transformed into an internal surge due to steepening, and its further passage led to the development of high-frequency solitons because of shoaling. The temperature gradients got stronger, being about

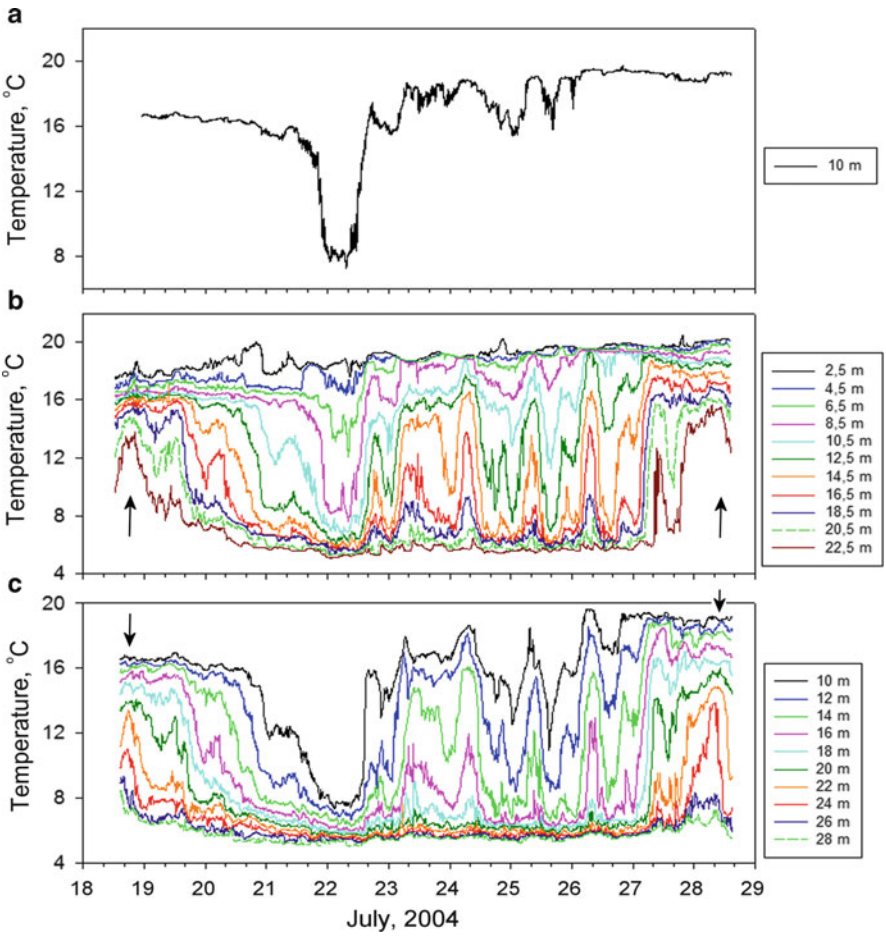

Fig. 2.43 Development of the water temperature with time: (**a**) St. 2, 18 July 2004, 23:07:00–28 July 2004, 14:33:43; (**b**) St. 3,18 July 2004, 12:25–28 July 2004, 14:20; (**c**) St. 5, 18 July 2004, 14:35–28 July 2004, 15:05. *Black arrows* mark a time period of the basin scale internal Kelvin wave in Lake Onego

2°C/m from 24 to 27 July 2004. Simultaneously, the upper mixed layer depth gradually grew. For the period from the middle of 22 July to 28 July, the depth of the 16°C-isotherm dropped from ~5 to ~21 m.

The daily heating effect at station 3 can be noticed only within the upper layer of 4–5 m (Fig. 2.44).

The temperature maximum in the upper layer, at 2.5 m, is related to the daily heating and was recorded in the evening hours; this is in good accordance with the existing knowledge of the daily dynamics of the water temperature during calm weather. Because of the daily heating, a small temperature jump, about a few tenth of a degree, was developed within the 2.5–4.5 m layer. At the same time, after

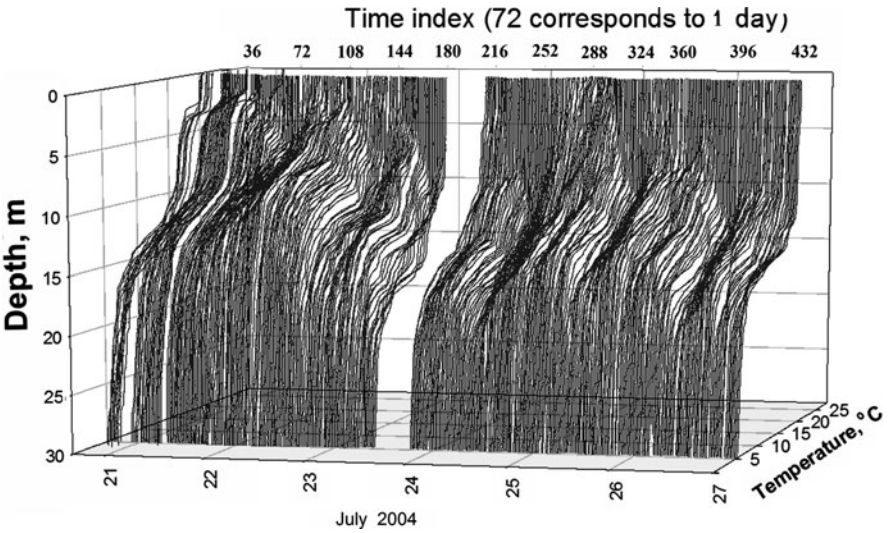

Fig. 2.44 Temporal evolution of the vertical thermal structure during the period of observation at station 3. The profiles taken from 23.07.04 9:20 to 17:40 were rejected as defective because of the CTD profiler power source malfunction

the upwelling event, strong variations of the water temperature (up to 6–8°C at the 12.5 m depth) were recorded with a period close to 1 day (Figs. 2.43 and 2.44). They can be seen within the whole water column. Such fluctuations were observed in previous studies of Lake Onego and were linked with the presence of one of the main lake seiches. Taking into account that these fluctuations reached their maxima mostly during the first half of the day, we assume that they have a wave nature. However, since these temperature fluctuations are present at depth, they are unlikely to be influenced by solar heating which bears witness in favour of our (wave) assumption. The average solar heating in 10 days resulted in the 2°C increase of the water temperature at the 2.5 m depth (station 3), with a nearly linear trend. The vertical temperature profiles (Fig. 2.44) demonstrate the presence of elements typical for the thin vertical structure, i.e., area with a sharp increase/decrease of the temperature gradients and so-called steps, see, e.g., patterns between spots 4 and 5, 6 and 7, 7 and 9 (Fig. 2.45).

An important parameter in analysing the thin vertical structure is the Brunt–Väisäla frequency (BVF). Using the data of vertical profiles at station 4 and the density formula proposed by Chen and Millero (1986), the density values and corresponding BVFs were calculated (see Fig. 2.46).

Figure 2.46 shows that a band of high frequencies is located at depths close to the lower boundary of the density jump and has a complicated wave-like shape. In time, it represents a sequence of intermittent spots. Sometimes, spots with low values appear (see, e.g., the area between profiles 372 and 380). The corresponding vertical temperature profiles (Fig. 2.44) demonstrate the presence of steps and

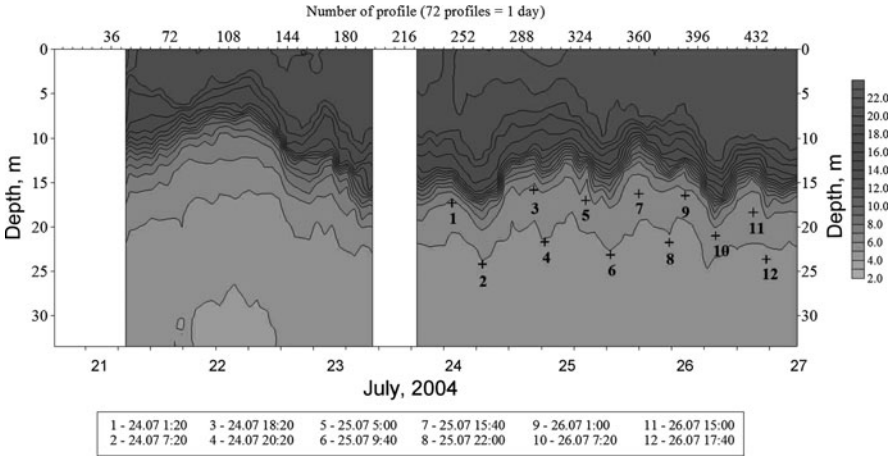

Fig. 2.45 Development of the vertical thermal structure in time (station 3, experiment 2004). The profiles from 23.07.04 9:20 to 17:40 are left blank because of the CTD profiler power source malfunction

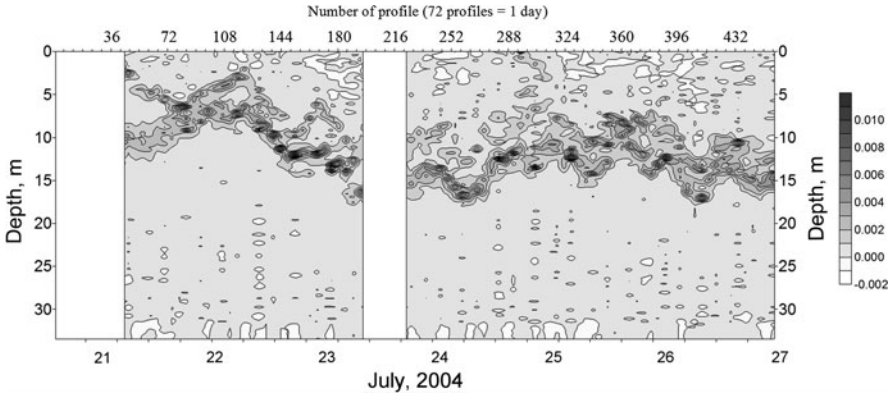

Fig. 2.46 Two-dimensional development of the Brunt–Väisäla frequency in time, from 21.07.2004, 06:00 (profile 43) to 26.07.2004, 23:59 (station 4). The gap 23.07.04 9:20 to 17:40 shows the time interval where data are likely defective because of a CTD profiler power source malfunction

decreasing gradients. Presumably, spots with low values of Brunt–Väisäla frequencies correspond to increasing mixing.

The most efficient approach in studying the effect of nonlinear internal waves by observational data is the analysis of temporal–spatial dynamics of isotherm displacements (IDs). To this end, data on water temperature at station 3 (experiment during 2004) were expressed in terms of isotherm-displacement–time series (Fig. 2.47).

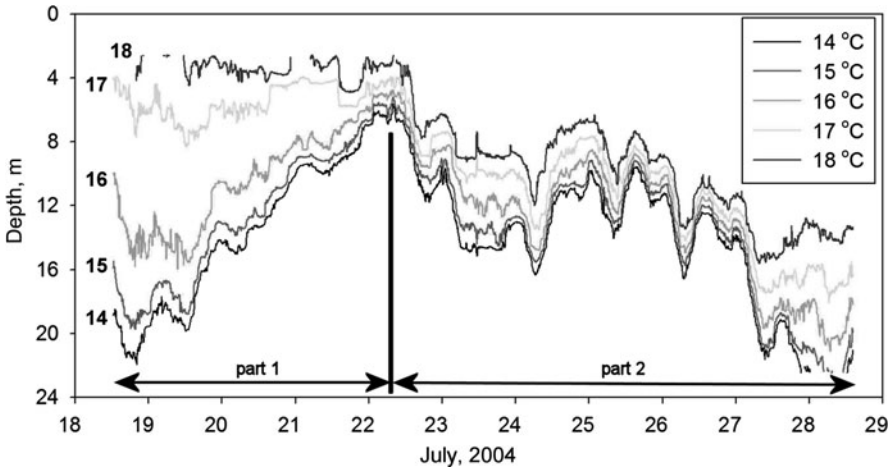

Fig. 2.47 Isotherm-displacement variations at station 3; INTAS experiment in July 2004

As evident, the episode of the measurements can be divided into two parts, one from the beginning of the field experiment to the middle of 22 July, and the other from 22 July to the end of the measurements on 28 July. The first part is characterised by a nearly monotonic decrease of the upper mixed layer depth (upwelling), and the second by its increase (downwelling). Notice that the latter is modulated by a wave-like phenomenon, with periods of fluctuations from several hours to one day. A sudden decrease of IDs 14–18°C took place early on 22 July 2004. The main reason for the event was the transformation of the basin-scale Kelvin wave into an internal surge due to steepening. The amplitude of the internal surge was about 10 m. The amplitude of the response became large, nonlinear features appeared as steep-fronted internal surges with periods close to 24 h. Its further passage led to the development of high-frequency solitons because of shoaling (Fig.2.47).

Power spectra of isotherm-displacement–time series and currents (not demonstrated here) were calculated with the use of FFT, the maximum entropy method (MEM) and by tensor analysis (Bendat and Piersol 1971; Rozhkov et al. 1983; Rogkov and Trapeznikov 1990). Calculations were performed after subtracting the mean and removing the linear trend for three cases, the whole series and its two parts corresponding to the period before and after the passage of the upwelling (Fig. 2.48). before the event (upwelling, passage of basin scale internal waves) for the period 19.07.2004, 13:20 – 21.07.2004, 23:40; 2) after the event for 22.07. 2004, 8:05 – 24.07. 2004, 18:20

It is also worth mentioning that the power spectra of the 16°C isotherm displacement for the period after upwelling and the passage of basin-scale internal waves shows an increase of energy at frequencies close to those of nonlinear internal waves (Fig. 2.48). For the data set of the 16°C isotherm-depth–time series (at station 3), the spectra for the episodes 19.07.2004, 13:20 – 21.07.2004, 23:40

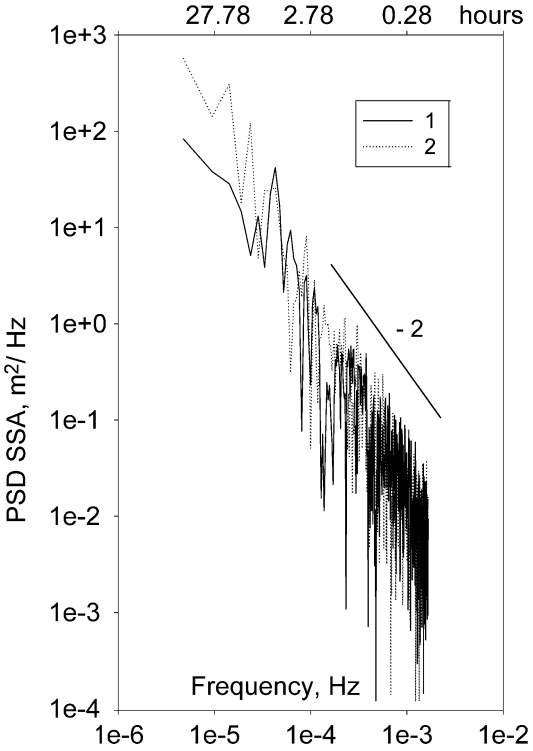

Fig. 2.48 Power spectra (16°C isotherm displacement at station 3): 1) before the event (upwelling, passage of basin scale internal waves) for the period 19.07.2004, 13:20 – 21.07.2004, 23:40; 2) after the event for 22.07. 2004, 8:05 – 24.07. 2004, 18:20

(before the passage of the wave) and 22.07.2004, 8:05 – 24.07.2004, 18:20 (after the passage of the wave) were calculated. As seen, after the passage of the upwelling, an energy increase occurs close to the periods of inertial waves (13–14 h), free gravity waves (2–3 h) and of nonlinear internal waves.

Within the frequency band between f and N, the energy spectrum of internal waves presented in Fig. 2.48 closely follows a power law with exponent –2, as observed in some lakes and in the ocean (Garrett and Munk 1975). Strong wind causes the development of Kelvin and Poincaré waves in Lake Onego, scales of which are comparable with the basin size. Interaction of these long waves with the bottom topography is accompanied by nonlinear effects and leads to the appearance of trains of short-period internal waves. The curves in Fig. 2.48 represent this fission process, which is likely evidence of the energy cascading from basin-scale baroclinic motions to short period waves and mixing.

According to Saggio and Imberger (1998), the increase of spectral energy within the frequency band at 10^{-2}–10^{-3} Hz in the spectrum of internal waves calculated for the fluctuations of the isotherm-displacement–time series before and after the strong wind can be explained by the energy transfer from the long-wave range to that of short-period nonlinear waves due to dissipation and breakdown along the inclined bottom.

For data analysis of the nonlinear internal waves (isotherm displacement – ID variations), the continuous wavelet transform (CWT) was applied to decompose a

signal into wavelets, small oscillations that are highly localised in time. Whereas the Fourier transform decomposes a signal into harmonics, effectively losing all time-localisation information, the CWT-basis functions are scaled and shifted versions of the time-localised mother wavelet. The CWT is used to construct a time–frequency representation of a signal that offers very good time and frequency localisations. This is an excellent tool for mapping the changing properties of nonstationary signals which look like solitons and surges. When a signal is judged as nonstationary, the CWT of isotherm–depth variations can be used to identify stationary sections of the data stream.

To better distinguish the distribution of the energy along certain frequencies within the power spectrum in time, the wavelet analysis (discrete transformation and continuous wavelet time–frequency spectrum) was applied (Fig. 2.49).

Figure. 2.49 shows a sample of wavelet analysis of the 16°C isotherm-depth–time series at a particular position in the Lake Onego INTAS experiment

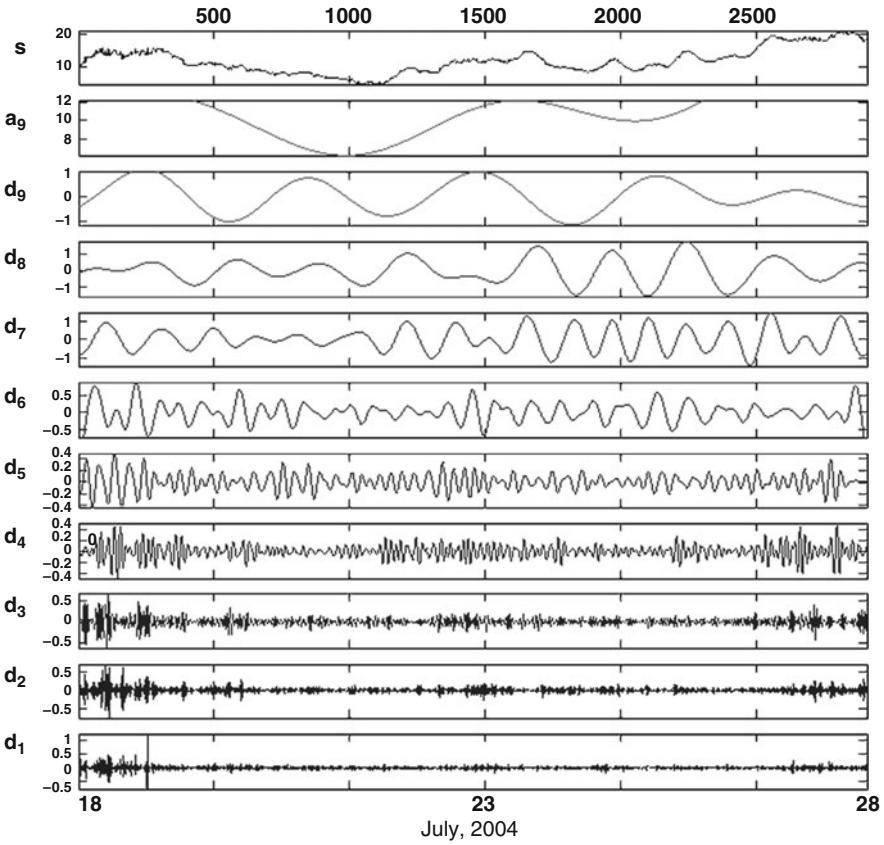

Fig. 2.49 Wavelet decomposition (discrete Meyer wavelet) for the 16°C isotherm-displacement variations at station 3 (Lake Onego, 2004). (a_9 – trend, d_9 – 236 h, d_8 – 118 h, d_7 – 59 h, d_6 – 29.5 h, d_5 – 14.75 h, d_4 – 7.4 h, d_3 – 3.7 h, d_2 – 1.85 h, d_1 – 0.92 h

2004; it reveals the presence of large scale internal waves which correspond to internal Kelvin wave. These are the waves d_9 and d_8 in Fig. 2.49. Inertial oscillations are also shown (d_5). High frequency oscillations arise after the event-passage of the basin scale waves. After this event at 22.07.2004, an internal surge and solitons arise. The amplitude of the Kelvin waves (d_8 on the figure) is larger than that of the internal Poincaré waves (d_5). It is worth mentioning also that the power spectra of the isotherm displacements for the period after upwelling show an increase of their amplitude at frequencies close to periods of nonlinear internal waves (Fig. 2.49, d1–d4).

Experiment-2005

Figures 2.50–2.53 demonstrate some results of the measurements performed in the INTAS experiment of 2005. In Fig. 2.50, the variability of the wind during the 2005 experiment is shown.

Data from registrations of meteorological parameters show the presence of diurnal and synoptical variations of air temperature, humidity and wind velocity. The latter were likely of breeze nature. Maximum wind velocities reached 8–11 m s^{-1} with average values of about 3–4 m s^{-1}.

At the beginning of the field measurements, the vertical thermal structure was close to a pattern that is typical of periods without wind mixing; this is indicated by the strongly stratified upper part of the water column. The remainder is characterised by a slow decrease of the water temperature (Fig. 2.51 showing a

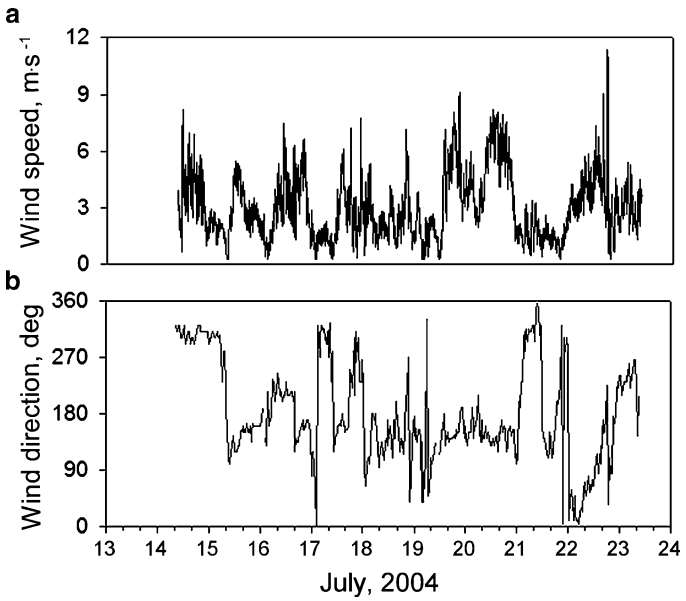

Fig. 2.50 Wind observations: wind speed (**a**) and direction (**b**), measured at station 4 during the field campaign 14–23 July, 2005

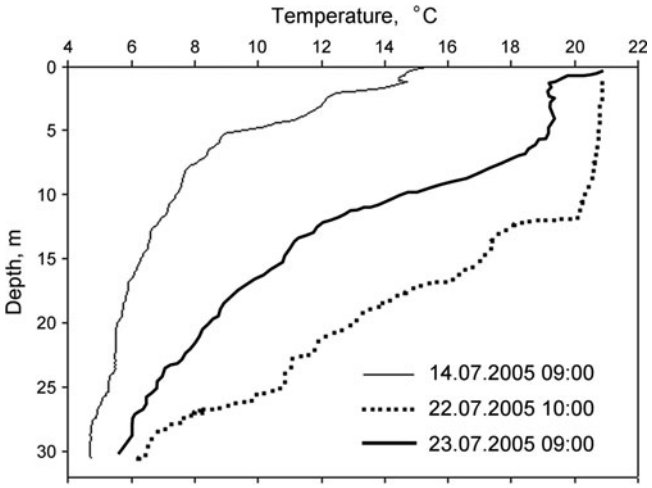

Fig. 2.51 Vertical temperature profiles in Lake Onego measured at station 4, 14.07, 22.07 and 23.07. 2005

profile registered on 14 July). In a day, the upper mixed layer was formed; afterwards its thickness varied quite strongly.

Figure 2.52a demonstrates the variability of the water temperature at station 2, whilst panel (b) displays the 14°C isotherm-displacement–time series calculated from the thermistor chain data for the same period.

The variability of the water temperature from the epilimnion to the hypolimnion at station 4 for the 2005 experiment is shown in Fig. 2.53. Using data of the vertical profile at station 4 and the density formula proposed by Chen and Millero (1986), the density values and corresponding Brunt–Väisäla frequencies were calculated. The results are shown in Fig. 2.54. Compared to those deduced from the data of 2004 (Fig. 2.46), the depth corresponding to the highest BVF-values was smaller, and its variability in time was not well pronounced.

The isotherm displacements (IDs) were calculated from data registered by the thermistor chains and by the CTD profiler (see Figs. 2.52 and 2.53). During the period of measurements, they oscillated (Fig. 2.53), with the most pronounced period close to one day; all of them show a strong trend to deepening, from 6.5 to 23.5 m, with a rate of 2 m d^{-1}, in the period from 13 to 22 July; thereafter follows a sharp depth decrease (to 14 m) in one day. Presumably, the beginning of an event of Kelvin waves was registered, the development of which was, unfortunately, not covered by the measurements.

Wavelet analysis of the isotherm-displacement–time series of the 11.5°C-isotherm (data of INTAS experiment 2005) reveals the presence of frequency maxima which likely correspond to an internal Kelvin-wave, the diurnal period, inertial oscillations and seiche fluctuations with periods from 2 to 3.5 h (see Fig. 2.36). Most of them correspond to the descending parts of the 11.5°C isotherm displacement, except the last event (22.07 10:45 – 23.07 09:00), when the isotherm displacement had gradually decreased. Nonstationary continuous wavelet

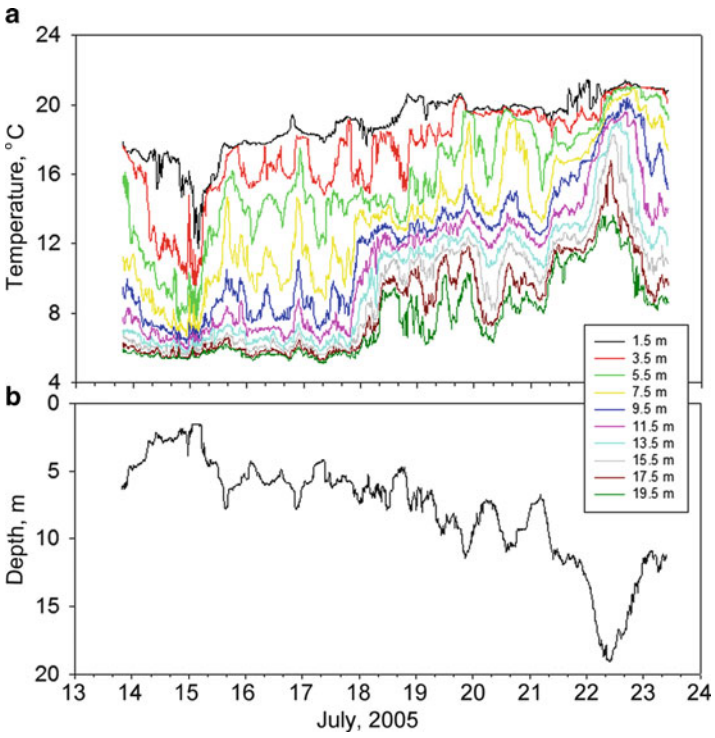

Fig. 2.52 (**a**) Development of the water temperature in time at Station 2, 13 July 2005, 19:50–23 July 2005, 09:50 for 10 thermistors per chain; (**b**) 14°C isotherm-displacement–time series calculated from the thermistor chain data for the same period

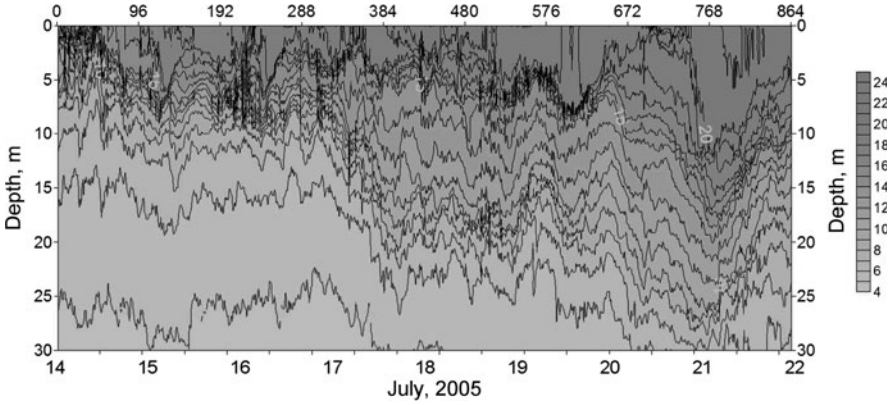

Fig. 2.53 Development of the water temperature (IDs) with time at Station 4, 14 July 2005, 09:00–23 July 2005, 09:00; the top abscissa axis shows the number of profiles (each corresponding to a time slice, of which 96 correspond to one day)

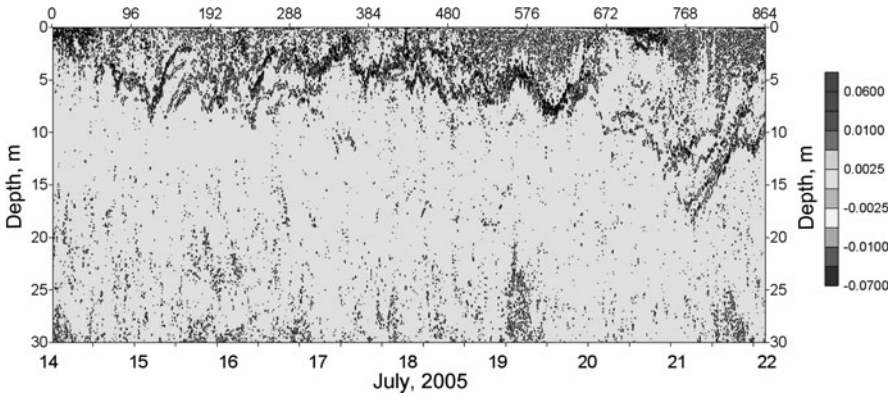

Fig. 2.54 2-D time development of the Brunt–Väisäla frequency at Station 4, 14 July 2005, 09:00–23 July 2005, 09:00

time–frequency spectra of the internal waves (Fig. 2.36) showed that the locations of high BVF values varied in a wave-like manner, and the vertical temperature profiles demonstrate the appearance of step-like patterns (Fig. 2.3.17).

The energy of internal waves increases with time, especially for large scale internal Kelvin waves during the deepening of the metalimnion during the episode 19–22.07.2005 at station 5 (12°C-isotherm displacement). No clear evidence of nonlinear internal surge-like waves during the internal wave experiment 2005 in Lake Onego was found.

2.3.2.1 Internal Wave Experiments 1977 and 1987 in Lake Onego

Experiment 1977. Other internal wave experiments were conducted in Lake Onego in 1977 and 1987. The principal aim of the experiment in 1977 was to describe the seasonal evolution of internal waves in a large stratified lake. The observational data were registered in the summer of 1977 during a five-month campaign from 27 May to 11 October in the south-western part of the Bolshoe Onego Bay, Osetrovskaya Banka [bank], at a depth of 30 m. The temporal evolution of the vertical thermal structure during the period from 27 May to 11 October 1977 is based on thermistor chain registrations and is displayed in Fig. 2.55.

In late September 1977, the vertical distribution of the water temperature was nearly uniform (Fig. 2.55). The horizontal current variability (u and v components) is shown in Fig. 2.56. The maximum velocities – up to 40 cm s^{-1} – were registered at depths from 1 to 15 m.

The 11.5°C isotherm-depth–time series was calculated and is shown in Fig. 2.57. As can be seen, the most dramatic event occurred in mid-July, when the isotherm-depth–time series abruptly changed within one day: it first dropped from 9 to 11 m, and subsequently rose to less than 2 m in depth and then fell again to more than 9 m. This event was followed by an oscillatory downwelling lasting until 20 July, which

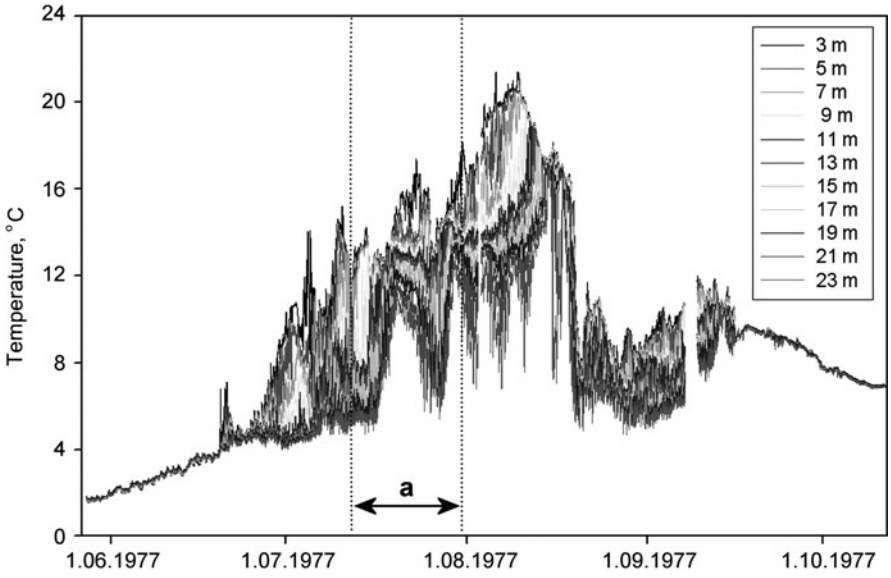

Fig. 2.55 Temporal evolution of the vertical thermal structure (temperature from 3 to 23 m) at the Osetrovskaya Banka of Bolshoe Onego during the period from 27 May to 11 October 1977 (data from thermistor chain registrations). The depth of the location is 30 m. The interval "a" identifies the water temperature variations from 09.07 to 30.07.1977 when an internal surge occurred

turns into an upwelling of approximately 6 days duration. The 11.5°C isotherm displacement on 09.07.–30.07.1977 demonstrates this internal surge development in Bolshoe Onego very well (Fig. 2.57).

The spectral analysis of this ID-time series allows identification of significant peaks of energy with frequencies corresponding to the inertial frequency, reminiscent of macro-scale whole-lake–internal Kelvin waves (Fig. 2.58). The wavelet analysis demonstrates that the energy peaks at frequencies close to the inertial frequency which corresponds to an episode of an abrupt isotherm displacement change.

The spectral analysis and continuous time–frequency wavelets demonstrate the presence of energy peaks at frequencies close to the local inertial frequency (Poincaré waves). As the increase of the energy at frequencies corresponding to Poincaré waves correlates with that corresponding to nonlinear internal waves, we may assume that Poincaré waves are related to the development of nonlinear internal waves.

Experiment 1987. Other complex studies of an internal wave experiment were organised in the summer of 1987 during the experiment "Fjord" (Boyarinov et al. 1994). It took place in a narrow bay in the northern part of the Bolshoe Onego Bay, Lizhemskaya Guba [bay], where the influence of the Coriolis parameter of the formation of water movements is weak because the internal Rossby radius is larger than the breadth of the bay (Fig.2.38b). The observational data were recorded from 19 August to 11 September 1987.

Figure 2.59 presents the variability of currents measured at several levels in Lizhemskaya bay.

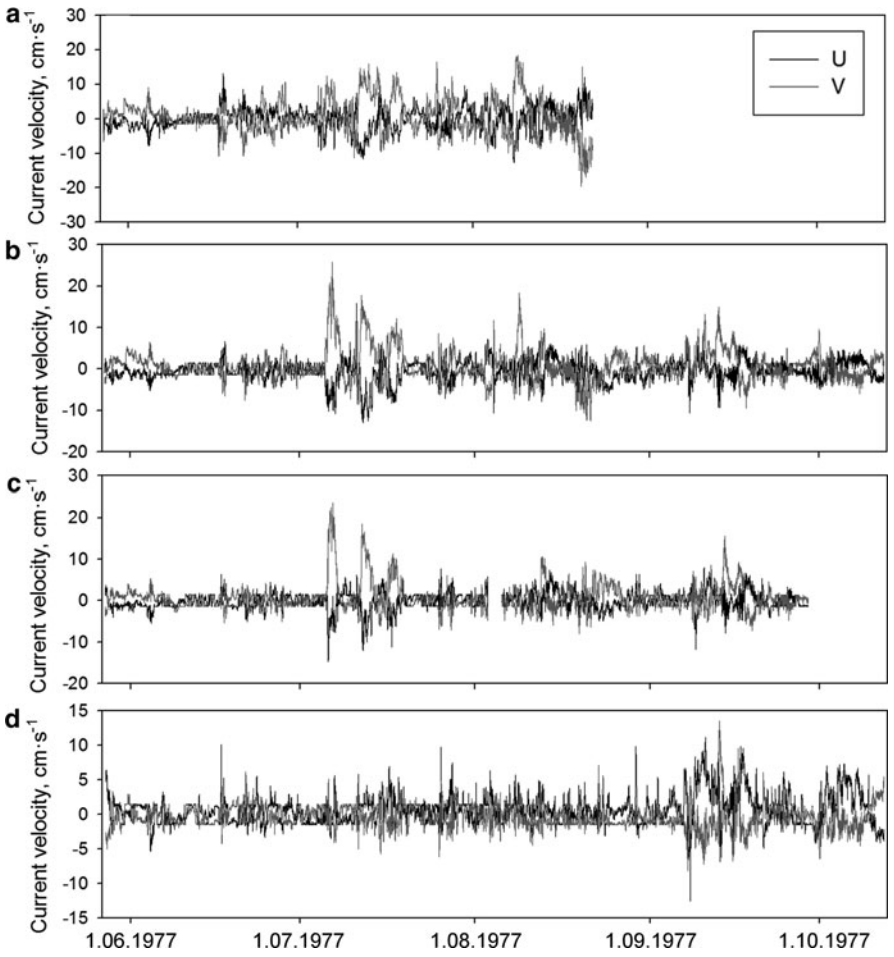

Fig. 2.56 Current components (u – *solid lines* and v – *dotted lines*) registered at the base station in the 1977 experiment in Bolshoe Onego (**a**) – 5 m, (**b**) – 10 m, (**c**) – 15 m, (**d**) – 25 m depths)

The currents in the water column of Lizhemskaya bay had an oscillating character with a decrease of the average velocity from surface to bottom that is typical for internal seiche-like movements. Let us examine the water temperature changes during the period of observation.

Thermistor chains and one current meter were deployed at four stations (see Fig. 2.38b). The temporal variations of the water temperature and horizontal current are shown in Fig. 2.60. As can be seen, at least one event – the passage of a long internal wave with a period of about 10 days – occurred during the measurement period. The isotherm displacements at Station 1 are shown in Fig. 2.61. As seen in Fig. 2.60, from 9 September 1987, it led to a sharp increase of the isotherm-

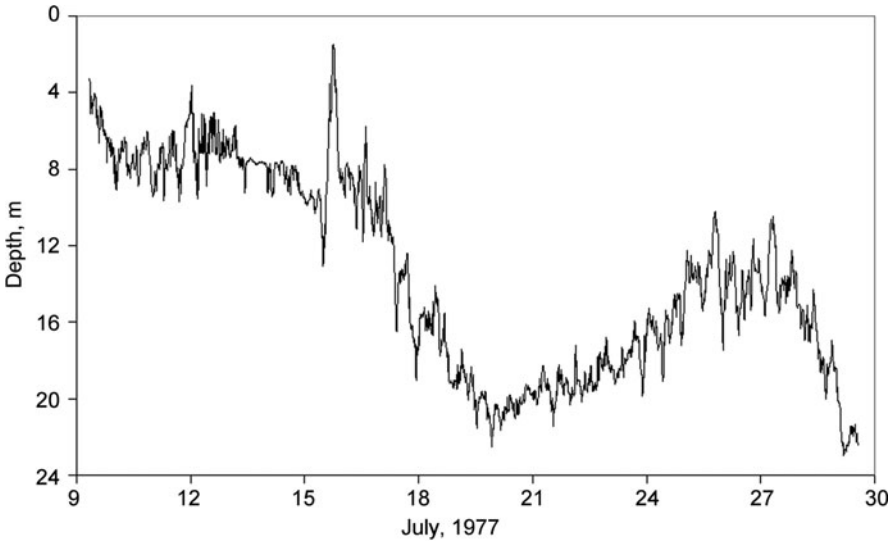

Fig. 2.57 11.5°C isotherm-depth variations at station TR (Lake Onego, 1977, see fig. 2.38)

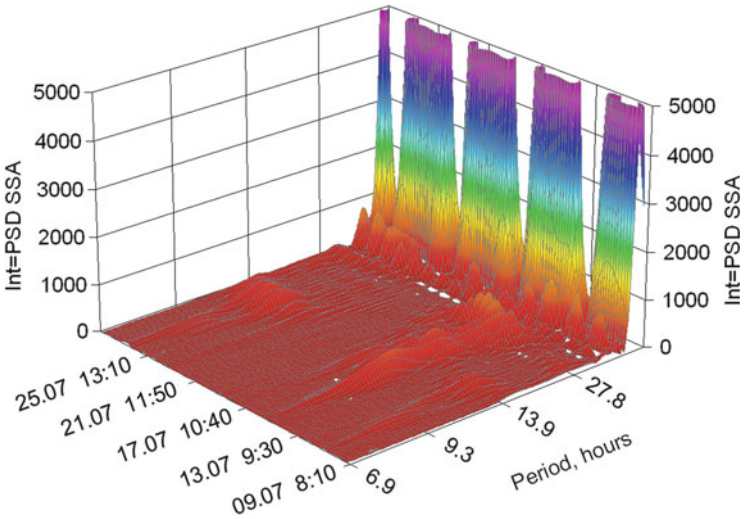

Fig. 2.58 Continuous time–frequency wavelet of the 11.5°C- isotherm displacement, Station TR, Lake Onego, July, 1977

displacement–time series. The vertical structure of the water temperature experienced certain changes, including an appearance of a step-like pattern along the thermocline. This is reminiscent of an internal surge on the thermocline, like that observed in Babine Lake.

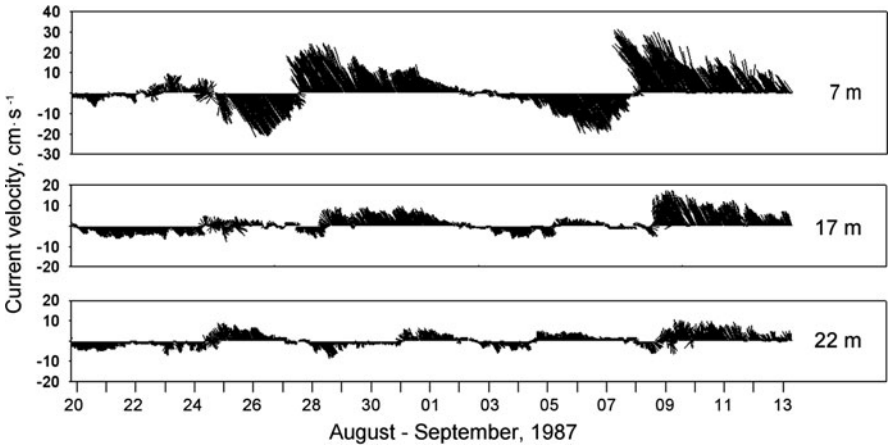

Fig. 2.59 Variability of the water currents at different depths in Lizhemskaya bay, Lake Onego, St. 3, 20.08 – 13.09.1987

As can be seen from observational data received during the experiment 25 – 29.08.1987, at least one event – a long nonlinear internal wave passage (surge) with amplitude about 30 m and high frequency solitons – occurred during the measurement period. It is demonstrated by the 9 and 10°C isotherm-displacement–time series (Fig. 2.61).

The wavelet analysis (not demonstrated here) reveals an increase of energy around the frequencies corresponding to the diurnal and short periods, starting gradually on 5 September 1987 to the end of the measurement period.

2.3.3 Summary of the Lake Onego Experiments

- Basin-scale internal (Kelvin and Poincaré) waves and nonlinear internal waves (surge or bore and solitons) and their interactions with the bottom topography (shoaling) were studied using observational data obtained during the field campaigns in Lake Onego in 2004–2005, and of historical long time records of water temperature, currents and wind speed registered in 1977 and 1987 in different parts of Lake Onego.
- The degeneration of basin-scale baroclinic internal waves into short-period internal waves, their successive interaction with lake boundaries, as well as their breaking with the generation of spots of mixed water have been studied with the aid of observational data obtained during the mentioned field campaigns.
- The performed analysis includes a phenomenological description of available observational data, and estimates of principal frequencies/periods dominating the nonstationary frequency spectra of the internal waves (see also results in Sect. 2.2).

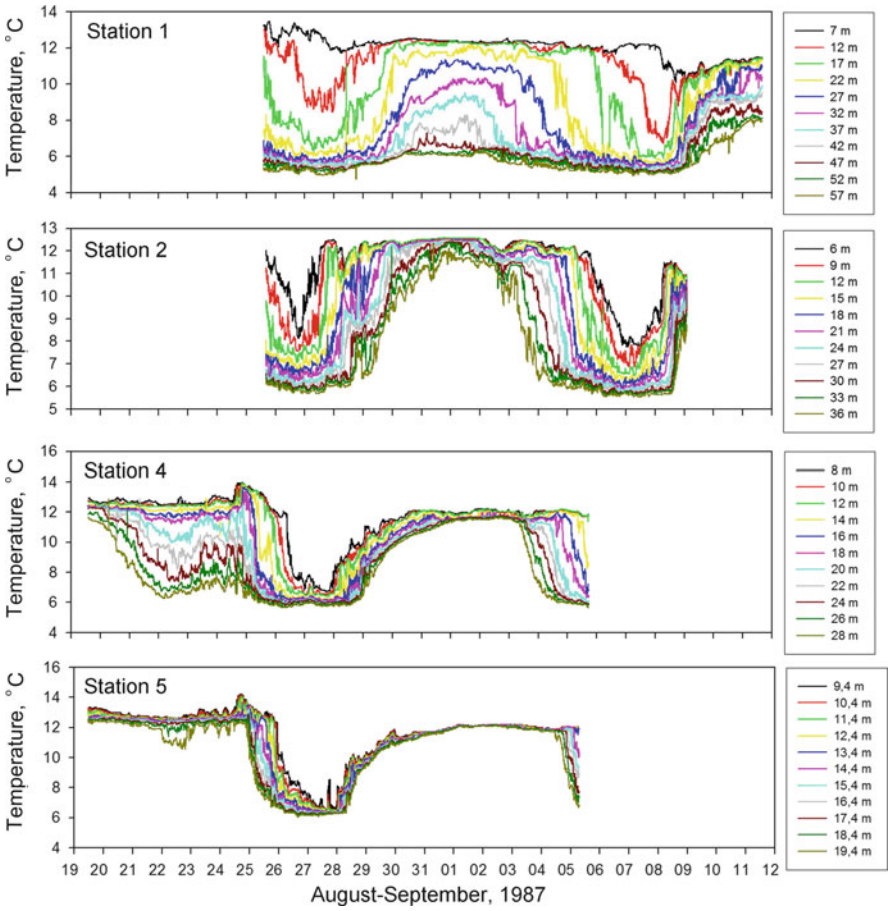

Fig. 2.60 Development of the water temperature in Lizhemskaya bay, Bolshoe Onego Bay, Lake Onego in the August–September 1987 "Fjord" experiment

- The observational data collected during earlier studies (1977 and 1987) in Lake Onego, were used for the analysis of parameters of nonlinear internal waves exhibited in the offshore zone of Bolshoe Onego, where effects of the rotation of the Earth is important (experiment 1977) and in a narrow deep bay (experiment "Fjord" 1987), where effects of the rotation of the Earth is weak.
- Particular attention was paid to the processes of transformation and disintegration of internal waves during their shoaling near the lake boundaries. It was demonstrated that strong nonlinear wave–topography interaction can affect the background stratification.
- The development of internal waves may deepen the upper mixed layer and lead to strong mixing processes.

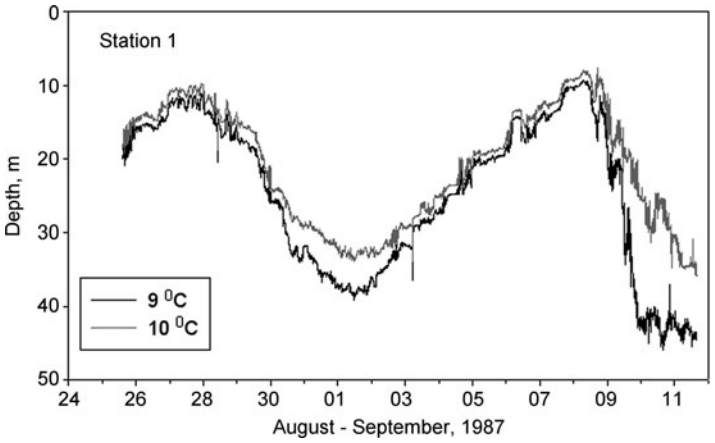

Fig. 2.61 9°C and 10°C isotherm-displacement variability calculated from vertical profiling data at Station 1, 24 August-11 September 1987 in Lizhemskaya Guba, Bolshoe Onego Bay (Fig. 2.38)

2.4 Comparison of Field Observations and Modelling of Nonlinear Internal Waves in Lake Onego[2]

2.4.1 Introduction

The degeneration of basin-scale baroclinic seiches into short-period internal waves, their successive interaction with lake boundaries, as well as breaking with the generation of spots of mixed water are studied theoretically on the basis of a fully nonlinear nonhydrostatic numerical model and with the use of experimental data obtained during the summer campaign in Lake Onego in 2004. Particular attention was paid to the processes of transformation and disintegration of internal waves during their shoaling near lake boundaries.

It is demonstrated that strong nonlinear wave–topography interaction can affect the background stratification. After storms, internal waves in lakes may take the form of an internal surge or packets of internal solitons, generated by the nonlinear steepening of a basin-scale finite-amplitude wave (Thorpe 1977; Farmer 1978; Wiegand and Carmack 1986). Since these solitons are much shorter in length than the wind-induced initial large-scale thermocline displacements, their generation results in a transfer of energy within the internal wave field from large to small scales. As a confirmation of such an energy sink, field observations show that wind forced basin-scale waves decay at a rate far greater than can be accounted for simply by internal dissipation (Imberger 1994; Stevens et al. 1996).

[2] In this section we partly use text and figures from Vlasenko V., Filatov N., Petrov M., Terzhevik A., Zdorovennov R., Stashchuk N. 2005.

Additional evidence of this pathway for energy from large to small scales was reported by Horn et al. (2001). In this paper, the authors concluded that one of the more probable scenarios of basin-scale wave disintegration in long narrow lakes is its nonlinear steepening and fission into a series of solitary waves. These waves must further inevitably encounter lake boundaries where they are eventually destroyed (Vlasenko and Hutter 2002). During the breaking event, the water stratification is changed at the place of wave breaking. In the present study, we apply the mathematical model to examine the effect of the bottom topography and nonlinearity on energy cascading from basin-scale internal waves to short-period internal waves and farther to turbulence and mixing. The model is applied to the conditions of Lake Onego where, during the summer campaign in 2004, some experimental data on the baroclinic response of the lake to wind forcing were collected.

2.4.2 *Data of Field Measurements in Lake Onego*

The field observations performed in Lake Onego during 18–28 July 2004 were applied for comparison with results of modelling. To register the vertical thermal structure during a probable shoaling of nonlinear internal waves, the following equipment was installed along the line with depths from 10 to 32 m in the Bolshoe Onego Bay (Fig. 2.62). Thermistor chains with 5 min sampling interval were installed at stations 1, 2, 3 and 5; currents were measured by current metres with

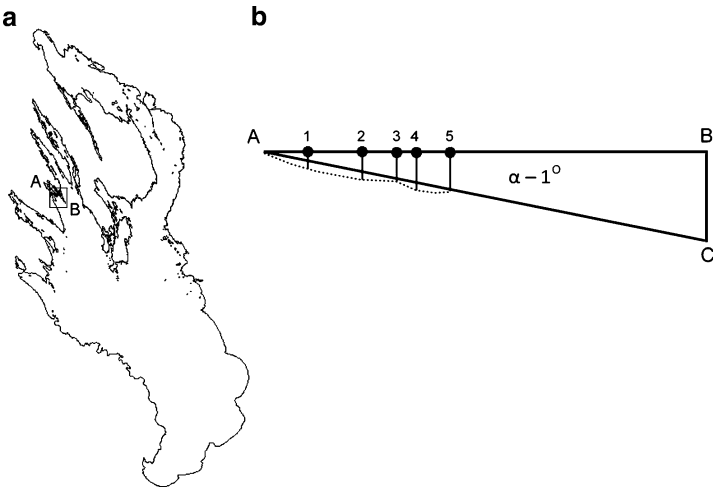

Fig. 2.62 (**a**) Position of the observational site on the main axis of Lake Onego (A–B) and (**b**) bottom profile in the experimental site shown by the dotted line, the ideal bottom profile shown by the *solid line* (not in scale). Numbers 1–5 are stations of observations in July 2004 (Fig. 2.37a); Distance AB is 5.0 km, Depth BC is 50 m; α is the angle of inclination of the bottom slope

time intervals of 10 and 5 min at stations 4 and 5, respectively; a free falling CTD profiler was used for every 20 min temperature profile measurements at station 4.

As is seen from Fig. 2.62a, the bottom profile in the experimental site is not monotonous. It includes several sections with greater and lesser inclinations with angles in the interval 0.8–2°.

The initial state of the thermal structure can be characterised as summer stratification. The upper mixed layer was 5 m thick, and its temperature was about 18°C. The water temperature in the bottom layers (~30 m) was close to 5–6°C (Fig. 2.42).

Dynamical processes registered during the experiment in the Bolshoe Onego Bay can be described in terms of the time series of the water temperature presented in Fig. 2.63.

Experiment INTAS 2004. Evolution of the temperature at the depth of 10 m reveals a very weak water activity during the time span 18–20 July. However subsequently, on 21 and 22 July, a sudden decrease of temperature took place, which could be the consequence of the near-shore upwelling developed in the north-west part of Lake Onego. Cold water remained near the free surface for about one day, and after that the thermocline slowly returned back to its undisturbed position (from the analysis of the thermistor-chain data not presented here). This descending was accompanied by vertical oscillations of the metalimnion with periods from several hours to one day. More high-frequency oscillations with periods of 10–20 min can also be identified in the time series of the thermistor chains (see, for instance, positions 1–5 in Fig. 2.63).

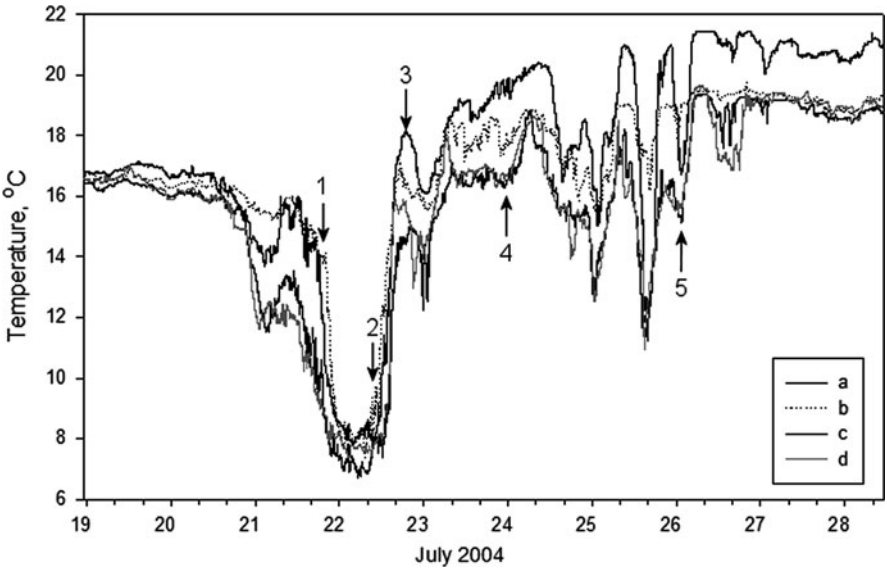

Fig. 2.63 Water temperature, at the 10 m depth, from 18.07.2004 23:15 to 28.07.2004 10:45 (sampling interval 5 min) at station 1 (**a**), 2 (**b**), 3 (**c**), 5 (**d**). Vertical oscillations of water temperature are shown by numbers 1–5

Our comparative analysis of the whole data set, obtained by all devices during the experiment, allows one to assume the following probable scenario of the registered event. The initial elevation of the pycnocline (up to 15 m) registered in the Bolshoe Onego Bay on 21–22 July was the manifestation of the local upwelling caused by either a basin-scale baroclinic seiche, or any other type of short baroclinic wave motion (we have no data to prove or reject the idea). The long-period disturbance was followed by shorter-period baroclinic oscillations with time scales from several hours to one day. These oscillations, in turn, were accompanied by even additional short-period disturbances with time-scales in the range between 10 and 20 min. The curves in Fig. 2.63 represent this fission process, which can provide evidence of the energy cascading from basin-scale baroclinic motions to short period waves and mixing. To check this hypothesis, a numerical model was developed and applied to the conditions of Lake Onego.

2.4.3 Model

We will restrict our analysis of internal waves to a two-dimensional case, bearing in mind that we do not describe the detailed structure, but mechanisms and tendencies. With such a stipulation, the two-dimensional system of the Reynolds equations in the Boussinesq approximation, written in Cartesian (x,z) coordinates in which the x and y-axes lie on the undisturbed free surface and the z-axis points upwards (opposite to the direction of gravity), takes the form

$$\begin{cases} \omega_t + J(\omega,\psi) = g\rho_x/\rho_a + (a_h\psi_{xz})_{xz} + (a_h\psi_{xx})_{xx} + (a_v\psi_{zz})_{zz} + (a_v\psi_{xz})_{xz}, \\ \rho_t + J(\rho,\psi) = (k_h\rho_x)_x + (k_v\rho_z)_z, \end{cases}$$

Here $\psi(u = \psi_z, w = -\psi_x)$ is the stream function, where u, w are the horizontal and vertical velocity components, and $\omega = \psi_{xx} + \psi_{zz}$ is the vorticity; ρ_a is the water density; k_v and k_h are the coefficients of vertical and horizontal turbulent diffusion, a_v and a_h are the coefficients of vertical and horizontal turbulent viscosity; $J(a,b) = a_x b_z - a_z b_x$ is the Jacobian operator.

Richardson number dependences were used for parameterisation of the coefficients of vertical turbulent exchange a_v and k_v. For the coefficients of horizontal turbulent exchange a_h and k_h, the gradient dependent parameterisation by Stacey and Zedel (1986) was used.

We are only interested in baroclinic motions, and thus use the 'rigid lid' conditions at $z = 0$. The bottom line $z = -H(x)$, is a streamline at which the "no-slip" condition and zero mass flux across the boundary is used, viz. $\psi_{\boldsymbol{n}} = \psi_x = \psi_z = 0$, where $\boldsymbol{n}$ is the unit normal vector to the bottom. Vorticity, at the boundaries was calculated from a previous temporal layer. The problem is solved numerically with the use of the alternative direction implicit method [more details on the numerical procedure are presented in Vlasenko et al. (2005)].

2.4.4 Results of Modelling

Two series of numerical experiments were performed to model the internal wave dynamics in Lake Onego. The first series was carried out for the whole model domain with a relatively coarse resolution (horizontal step 20 m, and 50 vertical steps). Such accuracy is not sufficient for the study of the wave-topography interaction in the shallow near-shore zone, but it is acceptable for modelling the disintegration of basin-scale oscillations into series of short-period waves. The second problem – shoaling of internal waves in a shallow-water zone on the final stage of the evolution, was studied on a fine-resolution grid with $x = 2$ m, and 150 vertical steps. Both problems are considered below.

Nonlinear Disintegration of a Baroclinic Seiche. The water stratification was taken close to that presented in Fig. 2.63. A smoothed profile of the bottom topography along the lake's longest axis (Fig. 2.62) was taken from the bathymetric map. It is assumed that the wave motions are generated by the initially tilted interface. The vertical deflection of the density jump from its initially undisturbed position at both sides of the lake comprises 5 m. This value is assumed to be typical of Lake Onego. As can be inferred from the analysis of the model results, the initially tilted interface, once being released, slowly returns to the undisturbed horizontal position. It is almost horizontal by day 5 (see Fig. 2.64).

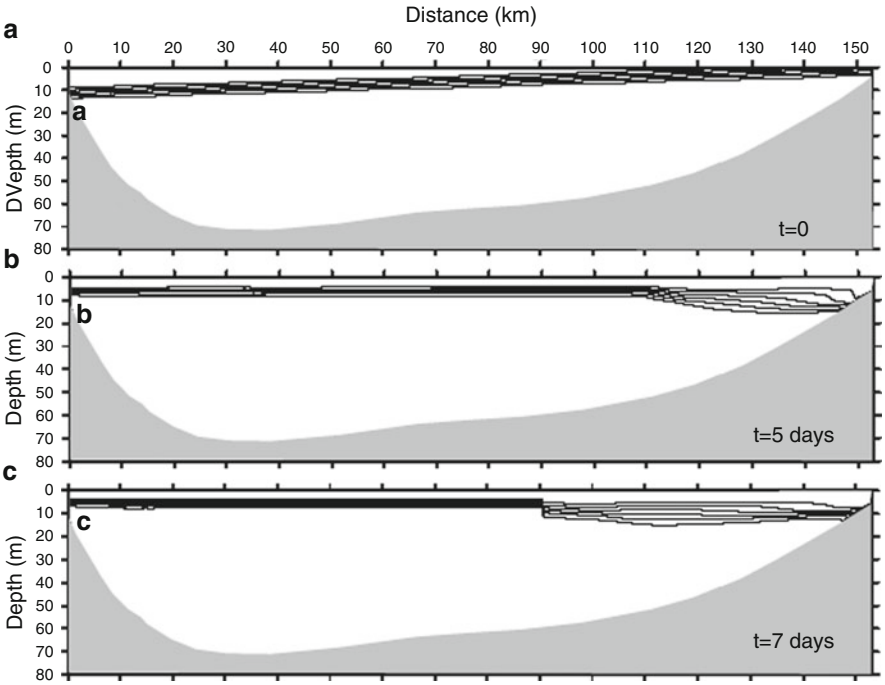

Fig. 2.64 Model predicted nonlinear evolution of basin-scale internal wave. Formation of a baroclinic bore is clearly seen after 7 days of the model time

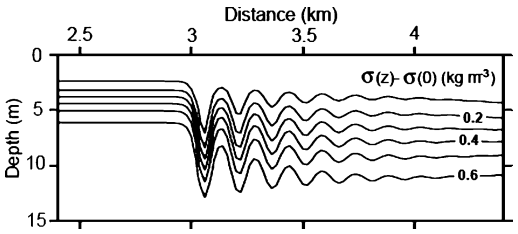

Fig. 2.65 Internal wave train produced in the course of the evolution of the baroclinic seiche. Isolines of density differences are plotted

However, the topography of the interface is not symmetrical with respect to the basin centre. Due to the nonlinear steepening, a progressive baroclinic bore at the right-hand side of the basin occurs. By day 7, this bore is fully developed (see Fig. 2.64c). In the course of propagation, the undulating bore gradually transforms into a series of short-period internal waves as illustrated in Fig. 2.65. At the final stage of its evolution, the baroclinic bore is disintegrated into a series of solitary waves propagating towards the shore. The maximum amplitude of the leading wave in the present case is approximately 7 m.

The results from other numerical runs with initial interface inclinations which are 'realistic' for Lake Onego have shown that amplitudes of internal solitary waves (ISWs) can lie in the range between 5 and 15 m. As a result, one can assume that the baroclinic response of the Bolshoe Onego Bay observed in the experiment was probably caused by one or several such incoming waves propagating from the deep part to the shore. Their interaction with the shallow water zone is considered below.

Shoaling of Internal Waves. Numerical experiments on shoaling of solitary internal waves in the area of the Bolshoe Onego Bay were performed for several incoming waves with amplitudes varying in the range between 5 and 15 m. From the viewpoint of internal wave shoaling, the experimental site turned out to be very interesting, because it includes the "turning point" where incoming solitary waves can change their polarity and transform from a wave of depression into a wave of elevation. In terms of the weakly nonlinear theory, this takes place when the density jump is located just in the middle between the free surface and the bottom, so that the coefficient of the quadratic nonlinearity in the Korteveg–de Vries equation goes trough zero. Analysing Fig. 2.63, one may conclude that the turning point is located somewhere between Stations 1 and 5 (Fig.2.62b). The process of wave decomposition near the "turning point" can also take the form of dispersive disintegration of incoming waves into a secondary wave train.

Finally, the most striking scenario of wave evolution over an inclined bottom is wave breaking, in case its amplitude becomes comparable with the total water depth. The breaking event leads to the formation of a turbulent pulsating jet and spots of mixed water. It was found from the analysis of the model results, that all these scenarios are very probable for the area under study. Figure 2.66 represents the shoaling of an ISW over the inclined bottom with an inclination angle of 1.3°. This value is close to the average values taken from the bathymetric map. In the deep part of the basin with a depth of 70 m, the amplitude of the ISW was 10 m (Fig. 2.66a). In the first stage of evolution over the inclined bottom, the incoming ISW becomes asymmetric (Fig. 2.66b) and further gradually transforms into a

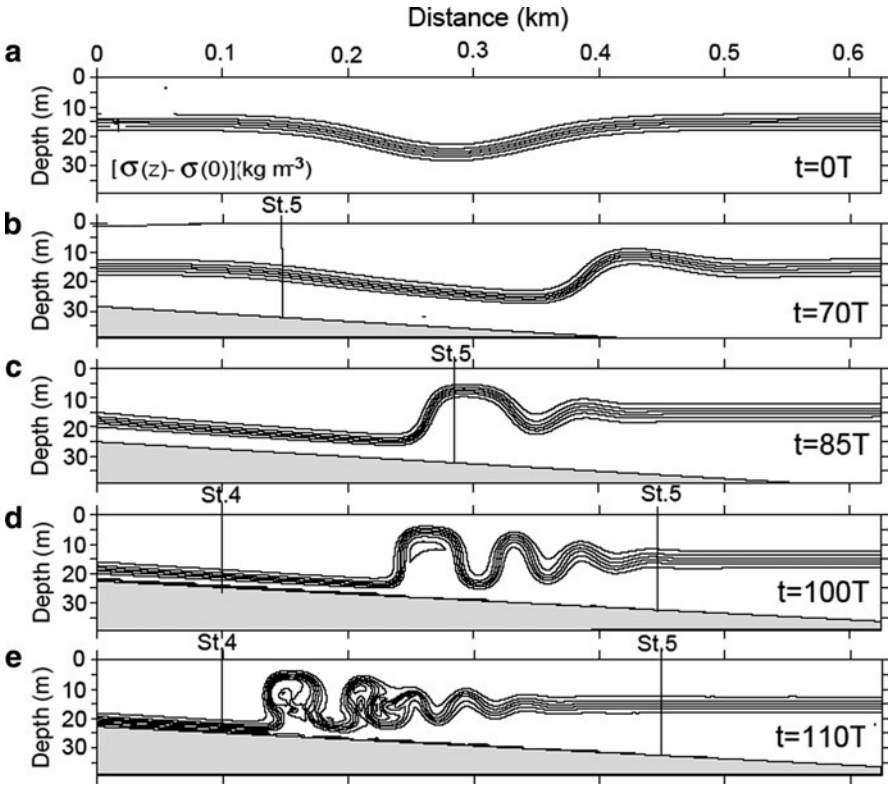

Fig. 2.66 Model predicted evolution of an internal solitary wave with an initial amplitude of 10 m over an inclined bottom. Inclination angle equals 1.3°, time scale $T = 75$ s

packet of short-period internal waves (Figs. 2.66c, d). Wave breaking does not take place at this stage because the steepening of the rear face of the wave over the slowly varying bottom (Fig. 2.66b) is compensated by the permanent leakage of wave energy into the dispersive wave tail (Fig. 2.66c). However, several leading waves are eventually destroyed when this balance is violated by the stronger nonlinearity in the more shallow part of the basin (see Fig. 2.66e). The breaking occurs between Stations 4 and 5, so that the resulting reconstruction of the vertical water stratification must be observed in the experiment, if the breaking events really took place. As seen from Fig. 2.63, the slope of the bottom profile in the experimental site is not monotonous. It includes several sections with inclinations different from those in the discussion of the above experiment. To check the sensitivity of the model results to the bottom inclination, several additional runs were performed.

Figure 2.67 illustrates the breaking regime of the wave evolution. It occurs when the inclination angle equals 2.3°. The initial stage of the breaking event is not shown in Fig. 2.67; it is similar to those described in Vlasenko and Hutter (2002).

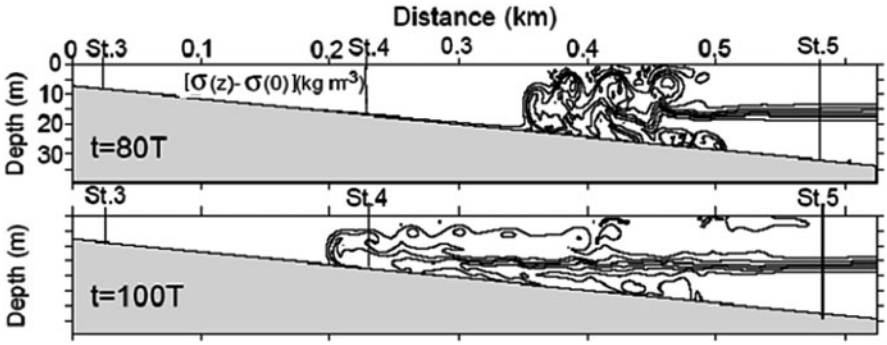

Fig. 2.67 Density field showing the result of internal wave breaking over relatively steep bottom topography (inclination angle equals 2.3°; Initial amplitude equals 10 m, $T = 75$ s) (from Vlasenko and Hutter 2002)

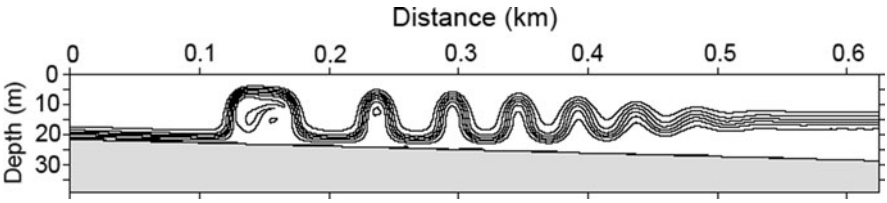

Fig. 2.68 Density field showing the result of dispersive disintegration of an ISW with initial amplitude of 10 m over the gently sloping topography with inclination angle 0.6° (from Vlasenko and Hutter 2002)

An important result from this run is that wave breaking is able to dramatically change the background stratification.

Quite a different scenario of wave evolution is expected for relatively gently sloping bottom profiles with inclination angles less than 1°. The dispersive fission of the incoming ISW into a series of short-period internal waves is the basic mechanism controlling the evolution. An example of the "dispersive" disintegration is shown in Figure 2.68. The cumulative effect of nonlinear steepening in the present case is not as fast as the dispersive disintegration.

The above results concern the evolution of a relatively large wave. Similar effects of breaking and dispersive fission also took place for all other considered waves, although for small-amplitude ISWs, they are not so pronounced. Figure 2.69 displays the evolution of a 5 m amplitude ISW propagating over the bottom topography with inclination angle of 1.3°. Dispersive disintegration, which is predominant at the first stage (upper panel), is changed into breaking and formation of a horizontal intrusion (middle panel).

Note that the breaking process is not as pronounced as it is for large-amplitude waves. Instead of a turbulent pulsating jet, an upstream propagating wave of elevation (or "bolus" is produced in the breaking area just as in the experimental work of Helfrich and Melville (2006)).

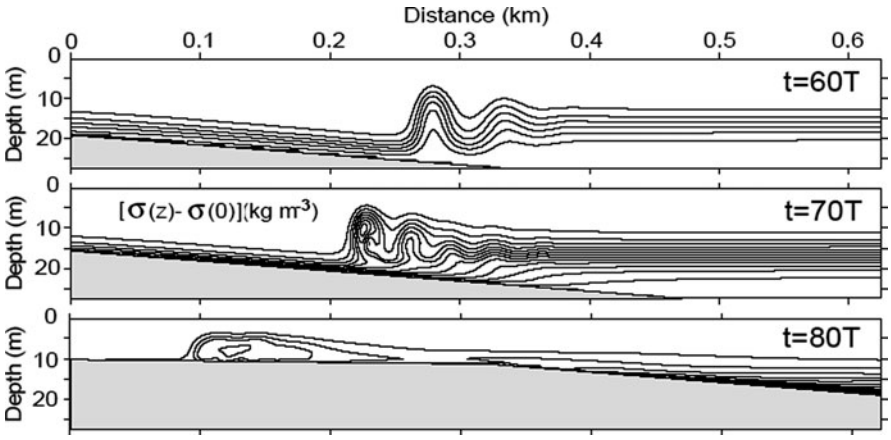

Fig. 2.69 Evolution of a 5 m amplitude solitary internal wave over bottom topography. Inclination angle equals 1.3°, time scale $T = 144$ s. (from Vlasenko and Hutter 2002)

2.4.5 Discussion and Conclusions

The results presented in this section indicate several possible scenarios for a wave energy sink from large-scale motions to smaller scales and further to turbulence. At the first stage of evolution, the basin-scale baroclinic seiche gradually transforms into a series of solitary internal waves. This fission occurs due to the nonlinear steepening and dispersive disintegration of the propagating baroclinic bore. The second important stage of the energy cascading is wave-topography interaction when propagating internal waves interact with lake boundaries. Depending on the wave amplitude, stratification and bottom profile, the process of wave–topography interaction can take a form of strong overturning and breaking, as is shown in Figures 2.67 and 2.68, or "soft" dispersive disintegration, as presented in Fig. 2.69. For wave breaking (even local, as in Fig.2.69) the background stratification can change dramatically during a quite short time span. It is very likely, that such a reconstruction of the vertical stratification was observed in Lake Onego during the summer 2004 campaign. Fig. 2.42b represents some changes of the temperature profile within 2 h. Vertical steps of an almost homogeneous fluid can be treated as areas of enhanced vertical mixing caused by internal wave breaking. Figure 2.42b also reveals high frequency wave activity on 25 July 2004.

We highlighted only one possible scenario of wave evolution in the lake and tried to identify the parameters controlling the wave process. Of course, such a scenario is somewhat conventional, and the real manifestation of internal wave dynamics can be more complicated (see experimental data on Lake Onego in Figs. 2.43 and 2.63). It can incorporate three-dimensional effects such as refraction, generation of Kelvin waves, influence of variable lake width or wave–wave interaction. Their influence on wave dynamics should also be studied. However, we do believe that the results obtained above can help to understand the basic features of energy transfer from large- to small-scale motions in lakes.

Acknowledgements The authors of this chapter thank their colleagues from NWPI: Mr. Mikhail Petrov for work in the two field campaigns in Lake Onego and for data analysis of internal waves; we thank Mr. Andrey Mitrochov and Drs. Alexey Tolstikov, Maksim Potakhin, Andrei Georgiev and Mr. Oleg Zimon for participation in the field campaigns. Our gratitude goes to Dr. Galina Zdorovennova for useful help with corrections of the text and to Mrs. Marija Bogdanova for redrawing some figures. Special thanks are conveyed to the organiser of the expedition Mr. Vasily Kovalenko and crew members of the research vessel of NWPI "Ecolog". Finally, we offer sincerest acknowledgements to the INTAS authorities for the Grant which made the experiments possible.

References

Antenucci JP, Imberger J (2001) On internal waves near the high-frequency limit in an enclosed basin. *J Geophys Res*. **106**: 22465-22474.

Apel J, Byrne H, Proni J, Charnell R (1975) Observations of oceanic internal and surface waves from the Earth resources technology satellite. *J Geophys Res*. **80**: 865-81.

Appt J, Imberger J, Kobus H (2004) Basin-scale motion in stratified Upper Lake Constance. *Limnol Oceanogr,* 4: 919-933.

Bäuerle E, Ollinger D, Ilmberger J (1998) Some meteorological, hydrological and hydrodynamical aspects of Upper Lake Constance. *Arch Hydrobiol Spec Issues Adv Limnol*, **53**: 31-83.

Beletsky D, Filatov NN, Lbraev R (1994) Hydrodynamics of Lakes Ladoga and Onego. In special issue. *Water pollution research journal of Canada*. **29**, 2-3:365-385.

Bendat JS, Piersol AG (1971) Random data: *Analysis and measurement procedures*. Wiley-Interscience.

Boegman L, Imberger J, Ivey GN, Antenucci JP (2003) High-frequency internal waves in large stratified lakes. *Limnol. Oceanogr*, **48**:895–919.

Boegman L, Ivey GN, Imberger J (2005) The degeneration of internal waves in lakes with sloping topography. *Limnol Oceanogr*, **50**:1620–1637.

Boehrer B (2000) Modal response of a deep stratified lake. *J Geophys Res*, C12, **105**: 28837-28845.

Bogucki D J, Redekopp LG, Baith J (2005) Internal solitary waves in the Coastal Mixing and Optics. *J Geophys Res* ,**110,** Co 2024. doi.:10.1029/2003JC002243.

Bondur VG, Morozov EG, Belchansky GI, Grebenyuk YuV (2006) Radar Imaging and Numerical Simulation of Internal Tidal Waves Nearby US North-Eastern Coast, *J of Earth Research from Space*, **2**: 51-64. [In Russian, translated to English].

Bondur VG., Fialtov NN (2003) Study of physical processes in coastal zone for detecting anthropogenic impact by means of remote sensing. In: Proc. *7-th Workshop on 'Physical Processes in Natural Waters'*, 2003 in Petrozavodsk, Russia, 98-103.

Boyarinov P, Palshin N, Petrov M (1994) Thermal processes in Lake Onego. In: special issue: *Water pollution research J of Canada*, 29,2-3: 403-422.

Brandt P, Rubino A, Alpers W and Backhaus JO (1997) Internal waves in the Straight of Messina studied by a numerical model and synoptic aperture radar images from the ERS satellites. *J Phys Oceanogr*, 27 (5): 648-663.

Chen CT, Millero FJ (1986) Precise thermodynamic properties for natural waters covering only limnological range. *Limnol Oceanogr*, **31**: 657-662.

Chensky AG, Lovtsov SV, ParfenovYuV, Rastegin AE, Rubtzov VYu (1998) On the coastal-trapped waves in the southern area of lake Baikal. Oceanic Fronts and Related Phenomena, *Konstantin Fedorov Memorial Symposium. St.-Petersburg*: RSHMU Publishers, 29-30.

Csanady GT (1977) Intermittent full upwelling in Lake Ontario. *J Geophys Res*, **82**: 397-419.

Didenkulova II, Pelinovsky EN (2006) Phenomena similar to tsunami in Russian internal basins. *Russ J Earth Sci*, **8**, ES6002, doi:10.2205/2006ES000211.

Farmer DM (1978) Observations of long nonlinear internal waves in a lake. *J Phys Oceanogr*, **8**: 63–73.

Filatov NN (1983) Dynamics of lakes. Leningrad, Gidrometeoizdat Press, 166 [In Russian].

Filatov NN (1991) *Hydrodynamics of Lakes*. St.-Petersburg: Nauka Press, 191 [In Russian with English summary].

Filatov NN, Beletsky DV, Zaitsev LV (1990) *Variability of hydrophysical fields in Lake Onego. 'Onego'* experiment, Water Problems Department, Karelian Scientific Centre AS USSR, Petrozavodsk, 110 [In Russian].

Filatov NN, Ryanzhin SV, Zaitsev LV (1981) Investigation of turbulence and Langmuir circulation in Lake Ladoga. *J Great Lakes Res*, **7** (1): 1-6.

Filonov, A.E., Thereshchenko, I.E. 1999. Thermal lenses and internal solitons in Chapla Lake, Mexico. *Chin J Oceanol & Limnol*, **17**, 4: 308-314.

Garrett CJR, Munk WH (1975) Space time scales of internal waves. *Progress report*, **80**: 281-297.

Glinsky A (1998) Current meters for measurement of low-speed velocities in ice-covered lakes. *Limnol Oceanogr* **43** (7): 1661-1668.

Gomez-Giraldo A, Imberge, J, Antenucci J, Yeates P (2008) Wind-shear–generated high-frequency internal waves as precursors to mixing in a stratified lake. *Limnol Oceanogr*, 1: 354–367.

Gonella J (1972) A rotary-component method for analyzing meteorological and oceanographic vector time series. *Deep-Sea Res*, **19**: 833-846.

Granin N (1984) Some results of internal waves measurements in Lake Baikal. In: *Hydrology of Lake Baikal and other water bodies*. Nauka, Novosibirsk, 67-71[In Russian].

Hamblin PF (1977) Short-period internal waves in the vicinity of a river-induced shear zone in a fiord lake. *J Geophys Res***. 82**: 3167–3174.

Helfrich K, Melville W (2006) Long nonlinear internal waves. Ann. Rev Fluid Mech**, 38**: 395–425.

Hodges B, Imberger J, Saggio A, Winters KB (2000) Modeling basin-scale interval waves in a stratified lake. *Limnol Oceanogr*, **45**: 1603–1620.

Horn W, Mortimer CH, Schwab D J (1986) Wind-induced internal seiches in Lake Zurich observed and modeled. Limnol. Oceanogr, **31** (6) : 1232-1254.

Horn DA, Imberger J, Ivey GN (1999) Internal solitary waves in lakes – a closure problem for hydrostatic models. In:_ *11th Aha Huliko Hawaiian Winter Workshop – Internal Gravity Waves II*, University of Hawaii.

Horn DA, Imberger J, Ivey GN (2001) The degeneration of large-scale interfacial gravity waves in lakes. *J Fluid Mech*, **434**: 181–207.

Horn DA, Imberger J, Ivey GN, Redekopp LG (2002) A weakly nonlinear model of long internal waves in closed basins. *J Fluid Mech*, **467**: 269–287.

Hunkins K, Fliegel M (1973) Internal undular surges in Seneca Lake: a natural occurrence of solitons. *J Geophys Res*, **78**: 539–548.

Hutter K., Filatov N, Maderich V, Nikishov V, Pelinovsky E, Vlasenko V (2007) 'Strongly nonlinear internal waves in lakes: Generation, transformation, meromixis' *Final report of INTAS project No. 03-51-3778*.

Hutter K (1984) Fundamental equations and approximations.(Hutter K. Ed.) *Hydrodynamics of lakes*. (Hutter, K. Ed.) CISM-Lectures. No **286** New York: Springer.

Hutter K (1993) Waves and Oscillations in the Ocean and in Lakes. In: *Continuum Mechanics in Environmental Sciences and Geophysics* (Hutter, K. and Wilmanski K., Eds) CISM Lectures Notes No. **337**, Springer Verlag, Vienna-New York, 79-240.

Hutter K, Bauer G, Wang Y, Güting P (1998) Forced motion response in enclosed lakes. Physical processes in Lakes and Oceans. In: *Coastal and Estuarine Studies* (Imberger, J., Ed.), **54**: 137-166.

Imberger J, Hamblin PM (1982) Dynamics of lakes, reservoirs, and cooling ponds. *Ann Rev Fluid Mech*, **14**: 153-187.

Imberger J (1994) Transport processes in lakes: A review. In: *Limnology now: A paradigm of planetary problems*, (Margalef R Ed.), Elsevier, 99-193.

Imberger J (1998) Flux paths in a stratified lake: A review, p. 1–17. In: Physical processes in lakes and oceans. (Imberger, J., Ed.), *Coastal and Estuarine Studies*, **54.** American Geophysical Union.
Karetnikov SG, Naumenko MA (1993) Using of IR satellite imageries for study of Lake Ladoga thermics. *J.Earth Study from Space* (Russia), **4**: 69-78 [In Russian].
Kochkov NV (1989) *The patterns of generation, evolution and destruction of internal waves in a lakes*. Doctoral Dissertation. Institute of Limnology, Leningrad [In Russian].
Kondratyev KJ, Filatov NN (1999) *Limnology and Remote Sensing. A contemporary approach*. London. Springer-Praxis, 406.
Kondratyev KJ, Filatov NN, Zaitsev LV (1989) Estimation water exchange and polluted water by remote sensing. *Report of Academy of Sciences of USSR*, 304: 829-832 [In Russian].
Konjaev KV, Sabinin KD (1992) *Waves inside the ocean*. S.Petersburg Gidrometeoizdat, 232 [In Russian].
Kumagai M, Asada Y, Nakano S (1998) Gyres measured by ADCP in Lake Biwa, In J. Imberger [ed.], *Physical processes in lakes and oceans*. American Geophysical Union. 199–208.
Laval B, Imberger J, Hodges BR, Stocker R (2003) Modeling circulation in lakes: Spatial and temporal variations. *Limnol Oceanogr*, **48**: 983–994.
LeBlond PH, Mysak LA (1978) *Waves in the ocean*. Elsevier.
Lemmin U (1987) The structure and dynamics of internal waves in Baldeggersee. *Limnol Oceanogr*, **32**: 43–61.
Lemmin U, Mortimer CH and Bäuerle E (2005) Internal seiche dynamics in Lake Geneva, *Limnol Oceanogr*, **50**: 207-216.
Lovcov SV, Parfenov JuV, Rastegin AE, Rubcov V Ju, Chensky AG (1998) Macro-scale variability of water temperature and internal wave in Lake Baikal. *Astrofisika I Fisika mikromira, Proceed. School of basic physics*, Irkursk Univ, 279-285 [In Russian].
Macintyre S, Flynn KM, Jellison R, Romero JR (1999) Boundary mixing and nutrient fluxes in Mono Lake, California. *Limnol. Oceanogr.* **4**: 512–529.
Malm J, Jonsson L (1994) Water surface temperature characteristics and thermal bar evolution during spring in Lake Ladoga. *J Remote Sens Environ*, **48**: 35-46.
Malm J, Mironov DV, Terzhevik A, Jonsson L (1994) Investigation of the spring thermal regime in Lake Ladoga using field and satellite data. *Limnol Oceanogr.* **39** (6): 1333-1348.
Michallet H, Ivey GN (1999) Experiments on mixing due to internal solitary waves breaking on uniform slopes. *J Geophys Res.* **104**: 13467–13477.
Mooers CNK (1976) Wind-driven currents on the continental margin. In: (Stanley, D.J. Swift, J. P. (eds.), *Marine sediment transport and environmental management*. Wiley, 29-52.
Mortimer CH (1952). Water Movements in lakes during Summer Stratification; Evidence from the Distribution of Temperature in Windermere. *Phil. Trans. Royal Soc. of London.* **B 236**, 635: 355-404.
Mortimer CH 1953 .The resonant response of stratified lakes. to wind. *Schweiz Z Hydrol.* **15**: 94-151.
Mortimer CH (1963) Frontiers in physical limnology with particular reference to long waves in rotating basins. *Great Lakes Res Div Publ. (University of Michigan),* **10**: 9-42.
Mortimer CH (1975) Lake hydrodynamics. *Mitt. Internat Verein Limnol*, **20**: 124–197.
Mortimer CH (1979) Strategies for coupling data collection and analysis with dynamic modelling of lake motions. In: *Hydrodynamics of Lakes*, (Graf, W.H. and Mortimer, C.H., Eds.), Elsevier Sci. Publ., Amsterdam-Oxford-New York, 183-222.
Mortimer CH (2004) *Lake Michigan in motion: Responses of an inland sea to weather, earth-spin and human activities*. Univ. Wisconsin Press.
Mortimer CH (2006) Inertial oscillations and related internal beat pulsations and surges in lakes Michigan and Ontario. *Limnol Oceanogr*, **51** (5): 1941–1955.
Mortimer CH, Horn W (1982) Internal wave dynamics and their implications for plankton biology in the Lake of Zurich. *Vierteljahresschrift Nat forsch Ges Zürich.* **127**: 299–318.
Moum J, Farmer D, Smyth W, Armi L, Vagle S (2003) Structure and generation of turbulence at interfaces strained by internal solitary waves propagating shoreward over the continental shelf. *J Phys Oceanogr* **33**: 2093–112.

Murthy CR, Filatov NN (1981) Variability of currents and horizontal turbulent exchange coefficients in Lakes: Ladoga, Huron, Ontario. *Oceanology*, **21**: 322-325 [In Russian].

Naumenko MA, Etkin VS, Litovchenko KT (1992) Investigation of radar signatures of lake surface with the «Kosmos -1870» («Almaz-0») SAR. *Proc. Int Geosc and Rem Sens Symp*. 'IGARS'92. Houston, **2**: 1774-1776.

Noges T et al (2008) (Ed) European Large Lakes: Ecosystem Changes and their Ecological and Socioeconomic Impact. *Developments in Hydrobiology*. Springer.

Queguiner B, Legendre L (1986) Phytoplankton photo synthetic adaptation to high frequency light fluctuations simulating those induced by sea surface waves. *Mar Biol*, **90**: 483–491.

Rogkov VA, Trapeznikov JA (1990) Probability models of oceanological processes. Leningrad. *Hydrometeorological Press*. [In Russian].

Rozhkov VA, Belishev AP, Klevantcov YuP (1983) Vector analysis of ocean currents. Leningrad. *Hydrometeorological Press*. [In Russian].

Rudnev S, Salvade G, Hutter K, Zamboni F (1995) External gravity oscillations in Lake Onega. *Ann. Geophysicea* **13**, Springer-Verlag, 893-906.

Rukhovets L, Filatov N (Eds.) (2009) *Ladoga and Onego - Great European Lakes:Modelling and Experiment*. London. Springer-Praxis, 302.

Saggio A, Imberge, J (1998) Internal wave weather in a stratified lake. *Limnol Oceanogr*, **43** (S): 1780-1795.

Saggio A, Imberger J (2001) Mixing and turbulent fluxes in the metalimnion of a stratified lake. *Limnol Oceanogr*. **46**, 392–409.

Serruya S (1975) Wind, water temperature and motions in Lake Kinneret: General pattern. *Int. Ver. Theor Angew Limnol Verh*. **19**: 73-87.

Shimaraev MN, Verbolov VI, Granin NG, Sherstyankin PP (1994) Physical limnology of Lake Baikal: a review.// Baikal International Center for Ecological Research, Print N 2, Irkutsk-Okayama.

Shimizu K, Imberger J, Kumagai M (2007) Horizontal structure and excitation of primary motions in a strongly stratified lake. Limnol Oceanogr, **52** (6): 2641–2655.

Simons TJ, Schertzer WM (1987) Stratification, currents and upwelling in Lake Ontario, summer 1982. *Can J Fish Aquat. Sci*, **44**: 2047-2058.

Stacey MW, Zedel LJ (1986) The time-dependent hydraulic flow and dissipation over the sill of observatory inlet. *J Phys Oceanogr*, **16**(6).

Stashchuk N, Filatov NN, Vlasenko V, Petrov M, Terzhevik A, Zdorovennov R (2005) Transformation and disintegration of internal waves near lake boundary. *Abstract EGU05-A-02701*; SRef-ID: 1607-7962/gra/ EGU05-A-02701.

Stashchuk N, Vlasenko V, Hutter K (2005) Numerical mechanisms of disintegration of basin-scale internal waves in a tank filled with stratified water. *Nonlinear Processes in Geophysics*, **12**: 955-966.

Stevens CL (1999) Internal waves in a small reservoir. *J Geophys Res*. **104**: 15777-15788.

Stevens C, Lawrence P, Hamblin P, Imberger J (1996) Wind forcing of internal waves in a long stratified lake. *Dyn Atmos Oceans*, **24**: 41-50.

Thorpe SA (1974) Near-resonant forcing in a shallow two-layer fluid: a model for the internal surge in Loch Ness? *J Fluid Mech*. **63**: 509–527.

Thorpe SA (1977) Turbulence and mixing in a Scottish Loch, *Phil. Trans Roy Soc London*, **A 286**: 125.

Thorpe SA, Hall A, Crofts I (1972) The internal surge in Loch Ness. *Nature* **237**: 96–98.

Thorpe SA (1992) The generation of internal waves by flow over the rough topography of a continental-slope. *Proc Royal Soc London* **A 439**, N 1905, 115–130.

Thorpe SA, Keen JM, Jiang R, Lemmin U (1996) High-frequency internal waves in Lake Geneva. *Phil Trans Royal Soc, London*, **A 354**, 170: 237-257.

Thorpe SA, Lemmin U (1999) Internal waves and temperature fronts on slopes. *Ann. Geophysicae* 17, 1227-1234.

Verbolov VI. (Ed.) (1984) Hydrology of Lake Baikal and other waters. In: *Hydrology of Lake Baikal and other water bodies*. Nauka, Novosibirsk [In Russian].

Vlasenko V, Hutter K (2002) Transformation and disintegration of strongly nonlinear internal waves by topography in stratified lakes. *Annales Geophysicae*, **20,** 2087.

Vlasenko V, Filatov NN, Petrov M, Terzhevik A, Zdorovennov R, Stashchuk N (2005) Observation and modelling of nonlinear internal waves in Lake Onega. *Proc. 9-th Workshop on PPNW*, Lancaster University, 39-46.

Watson ER (1904) Movements of the waters of Loch Ness, as indicated by temperature observations. *J. Geogr*, **24**: 430–437.

Wedderburn EM (1907) Temperature of the fresh-water lochs of Scotland. *Trans R Soc Edin*. **45**: 407–489.

Wiegand RC, Carmack EC (1986) The climatology of internal waves in a deep temperate lake. *J Geophys Res* **91**: 3951–3958.

Wüest A, Lorke A (2003) Small-scale hydrodynamics in lakes. *Ann Rev Fluid Mech* **35**:373–412.

Yeates PS, Imberger J (2003) Pseudo two-dimensional simulations of internal and boundary fluxes in stratified lakes and reservoirs. Int J River Basin Manag, **1**: 297–319.

Chapter 3
Laboratory Modeling on Transformation of Large-Amplitude Internal Waves by Topographic Obstructions

N. Gorogedtska, V. Nikishov, and K. Hutter

Abstract In this chapter, the results of laboratory investigations of the generation and propagation of large-amplitude solitary internal waves in two-layer systems with complex topography are presented. The influence of the shape and size of underwater obstacles and localized constrictions of the channel on the transformation, reflection, and fission of solitary waves is studied. Interaction of solitary wave with different types of slopes is analyzed.

3.1 Generation and Propagation of Internal Solitary Waves in Laboratory Tanks

3.1.1 Introduction

During the last 40–50 years, considerable attention has been devoted to the experimental study of internal solitary waves. Of specific interest are experimental investigations under controlled conditions; for these, the required parameters of the medium and the generated waves can be optimally set. Such conditions can be realized when the experiments are conducted in laboratory tanks. Data obtained in laboratory experiments possess a high degree of reliability, and they permit to focus on the different features of the dynamical processes, here concerning the propagation of internal solitary waves. The investigated results allow us to both extend our knowledge and understand the character of the nonlinear wave propagation in a stratified medium.

In recent years, numerical methods have been widely used when studying the generation and propagation of internal solitary waves in a stratified medium in

N. Gorogedtska (✉) • V. Nikishov (✉)
Institute of Hydromechanics of National Academy of Sciences of Ukraine, Kiev, Ukraine
e-mail: vinihm@gmail.com

K. Hutter (ed.), *Nonlinear Internal Waves in Lakes*,
Advances in Geophysical and Environmental Mechanics and Mathematics,
DOI 10.1007/978-3-642-23438-5_3,

general, and in lakes in particular. Increasingly, generated results are represented in the form of numerical models, which allow comprehensive descriptions of the studied processes. The models highly depend on the simplified assumptions used to simulate the complicated dynamical processes as they arise in lakes. They can be tested or complemented by field data for particular applications. However, the presence of uncontrolled natural perturbations in the latter brings in difficulties of the interpretation of the final results. An important role of data of laboratory experiments is therefore to provide detailed quantitative and qualitative information that is often inaccessible under natural conditions when performing field observations. Qualitative improvement of the numerical models and corroboration of their validity are achieved by verification using data of the laboratory measurements obtained under well-defined circumstances. Integration of numerical models and laboratory experiments are fruitful approaches to improve the predictions of specific features of the dynamical processes of energy transformation in lakes.

Characterization of solitary internal waves and problems of their generation under laboratory conditions were investigated in many experimental studies. First, works should be mentioned in which the characteristics of solitary internal waves are studied, and comparison with known dependences, obtained on the basis of corresponding theoretical models, must be accomplished. Many experimental studies are devoted to carry out research on the interaction of solitary internal waves with topographic features, e.g., with an inclined coast, a bottom construction, and so forth. The results of these studies are compared with those of theoretical analyses, but dominant attention is focused on studying the processes of the interaction of waves with topographic features.

The prevailing stratification in water areas such as seas and lakes is vertical. In freshwater lakes, it is primarily the temperature distribution that is responsible for the stratification; its variation with depth is caused by summer heating. As a rule, the summer stratification in lakes is stable: the upper layer density is smaller than that in lower layers. Realistic density distributions can be approximated in such situations by two-layer configurations with constant density in each layer. Fortunately, much attention in experimental works is paid to studying the propagation of solitary waves at the interface of two (miscible or immiscible) liquids of different densities. This is so because in seas and lakes the stratifications are similar; analysis of deduced results in these layered fluids provides insight into the properties of internal waves and the processes of transport of mass and energy in such stratified systems. Experimental findings may be compared with analytical results. Furthermore, interest in studying wave propagation is also associated with the relative simplicity of the creation of the two-layer stratification.

In the present section, we shall consider works of a general plan in which questions of the generation of internal solitary waves are studied; wave propagation over flat bottom along the interface of two liquids is investigated; comparison with results of theoretical works is carried out with the purpose to describe the characteristics of waves on the basis of the inferred dependences. Studies in

which laboratory modeling of processes of the interaction of internal solitary waves with topographic features is dealt with will be the focus in subsequent sections.

3.1.2 Dissipation Not in Focus

Experimental investigations of internal solitary waves propagating in a basin along the interface of two liquids with different densities have been carried out by Kao et al. (1985). The basin was 9.1 m long, 0.6 m deep, and 0.36 m wide. The fluids in the two layers are freshwater and saltwater, respectively. Features of the wave generation are considered in detail with the help of the "*step pool method*". Schematically, the essence of this method is represented in Fig. 3.1.

A watertight movable gate is positioned near the upstream wall of the basin. There is a small gap between the lower part of the gate and the bottom. If, after an initial filling of the entire tank with identical levels of the free and interface surfaces, additional freshwater is added from above into the part behind the gate, a lowering of the halocline level by the value h^+will be created in the separated part; this lowering is paralleled by a corresponding very small rise of the free surface (see Fig. 3.1). An analogous situation occurs in communicating vessels filled by fluids with different densities. Estimation shows that the difference between the levels of the free surface is about 1 mm when the salinity in the lower layer is 15 ppt and $h^+ = 10$ cm. Evidently, this value is small and comparable with a curvature radius of the meniscus arising near the plate. Waves that propagate in different directions along the free surface are generated by the lifting of the gate. They are caused by a small difference of the levels of the free surfaces and the perturbations of the free surface induced by the displacement of the plate. Then, the levels of the free surfaces on both sides of the location of the gate become equilibrated. However, the density (pressure) distribution with depth in the main part differs from that in the separated part of the basin. Heavier fluid located in the main part of the basin moves into the separated part under the action of a horizontal pressure gradient. Simultaneously, lighter (fresh) fluid travels into the main part of the basin. Subsequent displacement of lighter fluid results in the formation of a solitary wave. The process is accompanied by the generation of local vortices

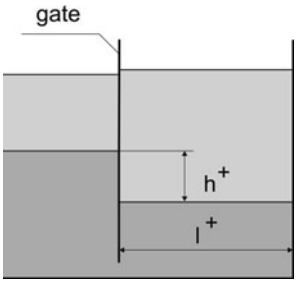

Fig. 3.1 Experimental setup, showing a movable gate at the right end of a wave tank ("step pool method")

induced by the removal of the gate. It is noted that the formation of solitary waves is also accompanied by different degrees of initial breaking, which restricts generation of waves with maximum amplitude. Furthermore, the distance l^+ between the end wall and the gate is adjusted in order to minimize the production of trailing waves.

In our own work, preliminary experiments were conducted to fathom the range of the parameters $|h^+|^{1/2}$ and l^+, at which single-hump solitary waves could be generated. It was found that a train of such waves could be generated for large values of these parameters.

We carefully filled the basin with the freshwater and saltwater. Ideal, sharp interfaces could not be produced. Our filling procedure with subsequent suction of mixed fluid resulted in a rather small thickness of an intermediate layer (0.5–1.3 cm). The form of the density profile can be adequately described by the expression

$$\rho(z) = \rho_0(1 - \kappa \tanh \alpha z), \tag{3.1}$$

$$\rho_0 = (\rho_1 + \rho_2)/2, \quad \kappa = (\rho_2 - \rho_1)/2\rho_0,$$

where ρ_1 and ρ_2 are the densities of the liquids of the upper and lower layers, respectively, z is the vertical coordinate, and $\alpha^{-1}$is half the thickness of the intermediate layer (pycnocline).

The intermediate layer position varied in the experiments of Kao et al. (1985) from 0.95 to 7.6 cm below the free surface. Their solitary waves have negative polarity corresponding to a wave of depression in this case because the thickness of the upper layer has always been less than that of the lower layer. Different methods of measurements have been used: visualization of currents by dyeing the layers and subsequent photographing; velocity measurement by employing a thermoanemometer; use of a special electric conduction probe, connected to a servomechanism which could trace the given electric conductivity, i.e., identify the position of the isopycnals; and use of the method of hydrogen bubbles, allowing one to measure an instant pattern of the flow field.

The first eigenmode and proper number c for the corresponding eigenvalue problem of the vertical velocity component of the baroclinic wave (a Sturm–Louiville eigenvalue problem) had been calculated numerically, and then the coefficients of the K-dV equation have been estimated. Comparison of the experimental data with the inferred parameters of the waves corresponding to the K-dV theory has shown good conformity of the experimental and theoretical results. In particular, the profile of the solitary waves is well described by the K-dV theory for different values of the ratio h_1 / H, where $h_1$is the thickness of the upper layer and H is the overall thickness. Other characteristics of the solitary waves also correlate well with the K-dV theory. This concerns the wave velocity and its amplitude, that is, the amplitude–wavelength relation describing the balance of the dispersive and

nonlinear effects. Differences with the K-dV theory were observed only for strongly nonlinear solitary waves for which the K-dV theory is inapplicable.

Experiments in which the characteristics of internal solitary waves were studied in basins filled with the two-layer system have been conducted by Grue et al. (1999). A basin measuring 0.5 m wide and either 6.2 m or 12.3 m long was used. In one run, a tank length of 21.4 m was also used. The thickness of the diffuse interface layer did not exceed 2 cm. Solitary waves were generated following the step pool method by Kao et al. (1985). The velocity field induced by the waves, the propagation velocities, and the shapes of the waves were measured in the experiments with the help of different techniques (particle tracking velocimetry and image analysis). The amplitudes of the generated waves changed from small to almost maximal (just before wave breaking). Analyses of theoretical models have also been carried out by the authors, including fully nonlinear models and K-dV models. Fully nonlinear problems in which the Laplace equation was solved for each layer with corresponding nonlinear kinematic and dynamic conditions at the interface, that is, for irrotational flows, were considered by Grue et al. (1999) and Grue (2005). The solution is obtained by using Cauchy's integral theorem and employing complex analysis. It was shown that the results of the calculations using the fully nonlinear model corresponded well with the experimental data. We emphasize that such coincidence of the results occurred even for washed-out pycnoclines. Vorticity rolls on the back edge of the waves were observed in experiments for waves with large amplitudes. They arose owing to Kelvin–Helmholtz instabilities that developed behind the maximum displacement. The form of the leading front was generally well described by the theory. Development of instabilities resulted in mixing and asymmetric shapes of the waves. In those cases, the pycnoclines were washed out. Estimates showed that the local Richardson number in the intermediate layer, close to the wave crest, was below 0.25. It indicates the existence of flow instabilities in accordance with the Miles and Howard theorem (Turner 1973; Drazin and Reid 2004).

Grue et al. (1999) found that the K-dV theory describes waves with amplitudes smaller than a fourth of the thinner layer thickness well. This theory is practically useful for all basin fillings when the amplitude of the waves is small. This conclusion agrees with those obtained earlier by Kao et al. (1985). Grue et al. (1999) emphasize that the model holds even when two layers differ strongly in thickness from one another, in particular, e.g., for $h_1/h_2 = 0.01$, where h_2 is the thickness of the lower layer. The authors revealed that waves of moderate and large amplitudes are described by the fully nonlinear theory, developed by them, and the results are in good agreement with the data of their laboratory measurements.

Koop and Butler (1981), using a "paddle" as *wave generator*, carried out experiments in a basin made of Plexiglass, with sizes $600 \times 45 \times 60$ cm. The liquids of different density that were used in the experiments were immiscible (Freon TF and distilled water). Configurations of the basin filling, which corresponded to the cases of "shallow" and "deep" water, were investigated to study the depth influence on the characteristics of propagating waves. Solitary waves were generated by moving a special paddle. Measurements of the amplitudes

of the propagating waves were taken by distributed capacity gauges. There are appreciable distortions of the interface with the use of such a wave generator, and the propagation velocity of the perturbations is much smaller than that of a solitary wave and eventually the solitary wave comes off "tail". It allows one to study the characteristics of solitary waves in isolation but requires rather long basins.

One of the important characteristics of solitary waves is the wavelength λ. Koop and Butler (1981) introduced two definitions of wavelength. The first, $\lambda_{0.5}$, represents the distance from the point corresponding to the wave crest, to the point corresponding to the half-amplitude. The second definition of the wavelength is expressed by the following integral formula:

$$L_{\mathrm{w}} = \frac{1}{a}\int_0^{\infty} \eta(x - ct)\mathrm{d}(x - ct), \tag{3.2}$$

where c is the wave velocity, η is the interface displacement, x is the coordinate along the direction of the wave, and a is the amplitude. This definition of the wavelength is connected with the "mass" of the wave. As the authors remark, the second definition corresponds better to the description of a wave as mass is an invariant of the wave movement. Attention in the work was focused on the study of the forms of the solitary waves and amplitude–wavelength parity relation $a/h = O(h^2/\lambda^2)$ expressing a balance between effects of nonlinearity and dispersion which is relevant to the K-dV model.

Koop and Butler (1981) derived a "second-order K-dV equation" in which terms of second order in the expressions describing nonlinear and dispersive effects are accounted for. Similar equations have also been derived by Lee and Beardsley (1974) and Gear and Grimshaw (1983). Corrections of the theoretical profile of the wave were made, and the ratio between wave amplitude and wavelength was improved. Profiles of the solitary wave have been measured, and it is shown that they correspond to the theoretical "sech^2"-profile when waves are rather weak (ratio of wave amplitude a to the bottom layer thickness $a/h_2 < 0.1$). Characteristics of stronger waves were in good agreement with the results obtained on the basis of an improved K-dV theory. It should be noted that in the case of "deep" water, when the parameters of the experiments correspond to the limits $\lambda/H \to 0$, $\lambda/h_2 \gg 1$, the Benjamin–Ono model (Benjamin, 1967, Ono, 1975) is a poor description of the measured data as is the Joseph–Kubota–Ko–Dobbs model, developed for the case of finite depth: $\lambda/h_2 \gg 1$, $h_2/H \ll 1$ (Joseph 1977, Kubota et al. 1978). Comprehensive descriptions of the K-dV and related models such as the Benjamin–Ono (BO) and Joseph–Kubota–Ko–Dobbs (JKKD) models are given by Ablowitz and Segur (1981).

Later, a second-order correction to the finite-depth theory JKKD was derived to identify the range of validity of the entire expansion due to Segur and Hammack (1982). It was shown that the experimental results of Koop and Butler (1981) are well reproduced by this improved theory. The authors also carried out experiments to study the forms of the solitary waves to check their description within the

framework of the K-dV and JKKD models of the first- and second-order expansion. The experimental wave tank was 30 m long, 60 cm deep, and 39.4 cm wide. The stratified liquid used in the experiments consisted of a layer of freshwater above a brine-water layer. The thickness of the intermediate layer was from 1 to 2 cm. Waves were generated by vertical movement of a piston, located close to the bottom near the upstream wall of the basin. It was found that for a two-layer system the solitary wave velocity was smaller than the K-dV theory predicts, and sometimes it was even below the phase velocity c_0 of the linear long-wave theory. This discrepancy is caused by the finite thickness of the intermediate layer between the liquids, when waves with comparatively small amplitudes were studied.

Experiments on the characteristics of solitary internal waves propagating in a two-layer system were also carried out by Walker et al. (2003). Experiments were conducted in a 6-m-long, 0.4-m-wide, and 0.6-m-deep basin. Stratification was created by filling the basin with freshwater; then, saltwater was supplied to the basin from below through an inlet port. Waves were generated by employing a D-shaped paddle of neutral buoyancy. The paddle was placed between the layers. Its nose was of streamline form to reduce the generation of separated vortices, which may trigger turbulent mixing. The density distribution was measured with the help of a microprobe, which consisted of four wires. A series of gauges intended to register the form and speed of the passing wave was installed in the basin. These gauges measured the resistance of the liquid volume between two vertical metal strips located at a distance of 10 mm from each other. To measure a velocity profile within the passing wave, the "particle image velocimetry" method was used. The range of changing the ratio of depths was $0.125 < h_1/h_2 < 0.5$, the nonlinearity parameter, a/h_1, was changed within the limits $0.2 < a/h_1 < 0.7$, and the thickness of the intermediate layer was from 1.2 cm to 8.0 cm.

Attention in the work was devoted to a comparison of the measured internal solitary waves with calculated values obtained by using theoretical models (two-layer K-dV, continuously stratified K-dV, and fully nonlinear theory (Evans and Ford 1996)). Basically, the study was concerned with consideration of the maximum horizontal velocity u in the wave trough. Comparison between these models and the data revealed that the K-dV theory can be used with a sufficient degree of accuracy at small values of a/h_1 (<0.4). At larger values of a/h_1 (>0.4), the calculations following the K-dV theory give values which strongly differ from the experimental data. It should be noted that the same limit of applicability of the K-dV theory was also found by Grue et al. (1999). On the whole, theoretical calculations overestimate velocities in comparison with the experimental data; in particular, for intensive waves this overestimation is as large as 65%.

Vertical uplift of a plate and suction through a perforated plate: An experimental investigation of the characteristics of internal solitary waves and comparison of the experimental data with theoretical results was also made by Bukreev and Gavrilov (1983). Experiments were carried out in a plexiglass basin; the basin was 220 cm long, 17 cm wide, and 15 cm high. It was filled with two immiscible liquids: water and kerosene. The authors used two methods to generate the internal solitary waves. In the first method, the solitary wave at the interface was generated

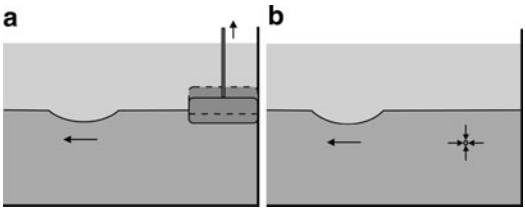

Fig. 3.2 Schematic view of the solitary wave generation by using two different methods: (**a**) by suddenly lifting a plate and (**b**) by sucking saltwater into a perforated tube located in the saltwater

by a plate which was displaced by a prescribed distance in the vertical direction (see Fig. 3.2a). An internal solitary wave of depression was also generated by short-time suction of saltwater through a perforated tube located at a given depth in the second method (see Fig. 3.2b). In other words, the waves were generated by short-time action of a sink which was uniformly distributed across the channel width. A solitary wave of elevation was generated by using these sources. The waves were recorded by electric conduction gauges. Measurements showed that the wave profile is in reasonable agreement with the theoretical results based on the K-dV theory. For waves with rather large amplitudes, appreciable deviations from the theoretical profile arise. A widening of the profile of the solitary wave occurs when the amplitude becomes larger; this effect was, however, not systematically studied. Other cases of discrepancies between experimental data and theoretical estimations also occurred. In particular, it was found for wave amplitudes in the interval $0.04 < a/h_2 < 0.6$ that the speeds of the solitary waves were usually smaller than those predicted by the K-dV theory. On the other hand, experimental data were in good agreement with those of the theory developed by Keulegan (1953). Solitary waves of positive and negative polarities were studied. Results are similar for both kinds.

Studies on the velocity fields near the bottom surface, caused by the passage of a solitary internal wave of depression in a two-layer fluid, were performed by Carr and Davies (2006). Experiments were made in a 6.4-m-long, 0.4-m-wide, and 0.6-m-deep basin. The waves were generated by using the "step pool method" of Kao et al. (1985) and are based on the results obtained by Kao et al. (1985) and Grue et al. (1999); the movable gate was positioned 0.27 m and 0.6 m distant from the face wall of the basin. Particle image velocimetry (PIV) and laser Doppler anemometry (LDA) methods were used to visualize the velocity distribution. The distributions of the horizontal and vertical velocity components and the cross-stream component of the vorticity were examined, depending on the change of the wave amplitude, a, the thickness ratio of the upper and lower layers $b = h_1/h_2$, and the thickness of the lower layer. The results revealed that an unsteady near-wall flow of jet-like shape arose directly near the bottom at the instance when the intensive nonlinear internal wave of depression passed the considered position. The near-wall flow velocity was rather small in comparison with the maximum speed of the liquid caused by the passing solitary wave, and the direction of this flow coincided with that of the wave motion, i.e., it was opposite to the direction of the flow velocity in the lower layer of the fluid. The near-wall flow formation was

connected with the appearance of a negative pressure gradient at the instance of the passage of the wave and the development of the boundary layer instability.

The propagation and reflection of internal solitary waves of depression from an *inclined slope* were simulated by Bourgault and Kelley (2007). They used a nonhydrostatic numerical model that integrates the laterally averaged Boussinesq–Navier–Stokes equations. The authors were able to both resolve a narrow area near the bottom and show precisely the existence of the separation of the boundary layer caused by the negative pressure gradient at the tailing edge of the solitary wave. They proposed to take into account the energy loss of the moving wave under the formation of the separation flow by introducing the corresponding form factor in the common drag coefficient.

Of interest is also the work of Michallet and Barthelemy (1998), in which the authors presented results of an experimental investigation of long waves propagating at an interface of two immiscible liquids of different densities. Experiments were carried out in a 3-m-long, 15-cm-high, and 10-cm-wide small flume. Waves were generated by using a *gate-type wave maker*, similar to that used in the step pool method of Kao et al. (1985). It was mentioned that a smooth and slow rise of the gate is preferable to a fast removal, since it minimizes barotropic perturbations. Parameters of solitary internal waves were measured using six ultrasonic probes installed along the central line of the basin. Experiments and nonlinear theories were compared in terms of wave profiles, phase velocities, and, mainly, frequency–amplitude relations. The authors emphasize that using the frequency, ω_k, is preferred for comparison with the experiments, since the data consist of recordings of the interface displacement at one location against time. The frequency $\omega_k$is determined by the ratio

$$\omega_k = \frac{2a}{\int_{-\infty}^{\infty} \eta(t, x_0)\mathrm{d}t} = \frac{c_k}{\lambda}, \tag{3.3}$$

where $\eta(t,\ x_0)$is the displacement of the interface in time, c_k is the phase speed, and λ is the characteristic length of the solitary wave.

For solitary internal waves with large amplitudes, comparison of experimental data with computed results was accomplished by Michallet and Barthelemy (1998). The so-called K-dV–mK-dV theory proposed in the works by Funakoshi (1985) and Funakoshi and Oikawa (1986) was used (see also Gardner's equation or the extended K-dV equation by Ostrovsky and Stepanyants 2005). The K-dV theory and modified K-dV theory were combined by also accounting the terms with cubic nonlinearity. Waves of which the amplitudes are in the range $0<a<\bar{h}$ were considered. Here, $\bar{h} = h_2 - h_c$ is the distance between the interface and the critical level, h_c, and represents the limiting amplitude of the waves. It was assumed that the amplitude had an order of magnitude $O(\bar{h})$, which was small in comparison with the general depth of the basin. Formulas describing key parameters of the solitary internal waves were described in the work. The free surface can be replaced by a rigid lid when the difference between the densities of the layers is small. For this

case, an expression describing the interface displacement caused by solitary waves was proposed.

Comparison of wave profiles, phase speeds, and frequency–amplitude ratios, obtained as a result of the executed experiments with theoretical relations, has shown that they strictly correspond to the K-dV theory for small amplitudes but practically apply for all relations of the layer thicknesses. The characteristics of the solitary waves with large amplitudes asymptotically tend to be predictable with the K-dV–mK-dV theory. Notice that the characteristics of the internal solitary waves were also studied in other works devoted to the investigations of wave interaction with topographic features of the bottom, slopes, ridges, etc. Results of these works will be discussed later.

There are also other methods of the generation of internal solitary waves that differ from the above-mentioned ones. A brief description of these methods for the generation of internal solitary waves is presented now.

Two-piston wave generator. A wave generator that consisted of two pistons, separated by a horizontal thin plate at the interface level, was constructed by Schuster (1992) and, later, used by Maurer (1993), Wessels (1993), and Hüttemann (1997). The corresponding results were discussed in detail and compared with the nonlinear theory by Diebels et al. (1994); Maurer et al. (1986); and Wessel and Hutter (1996). The soliton-like displacement of the interface, studied in these works, had negligible barotropicity; this wave was achieved by moving the pistons of the wave generator in opposite directions in such a manner that the displaced volumes were the same, and by using a linear ramp function in time to control the piston movement. The experiments were made in a 10-m-long wave tank with quadratic cross section and side length 0.33 m.

A '*flap-type*' *wave maker* was used by Helfrich and Melville (1986) to generate long nonlinear internal waves propagating along the interface in a two-fluid system in a wave tank 24 m long, 0.6 m high, and 0.38 m wide. Waves were generated by up-and-down oscillations of a small airfoil placed at the interface between the two fluids. A similar method was also used by Wallace and Wilkinson (1988) to generate internal waves in a two-layer system. The experiments were performed in an 18-m-long, 0.6-m-wide, and 0.75-m-deep tank. A periodic wave train was generated; it steepened and developed into a solitary-like wave before its final overturning on the slope. The internal waves were generated by a horizontal paddle which oscillated about its forward edge attached to a pivoting support. A bulbous nose of the forward edge prevented overturning and mixing in the halocline adjacent to the paddle. The structure of the internal waves during the shoaling and run-up phases was determined by means of conductivity probes and by different flow-visualization techniques. Notice, the mirror installed along the longitudinal axis of the tank at a given angle relative to the horizon was used to observe the pattern of the studied processes of the wave interaction with the slope simultaneously from above and from the side.

An analogous approach was realized by Umeyama (2002) to generate progressive internal waves propagating along the interface between freshwater and saltwater in a wave tank 6 m long, 0.15 m wide, and 0.35 m deep. A series of electronic

signals was produced by an arbitrary waveform synthesizer to control the motion of the internal waves. The author also used an oil-pressure-type wave-generating pump when the experiments were made in a wave tank of smaller size. Here, fluid is periodically ejected in the tank with a given frequency.

The "*tilting tube*" method was used by Horn et al. (2000, 2001) and Boegman et al. (2005) to study the degeneration of basin-scale interface gravity waves in enclosed basins, to quantify the temporal energy flux associated with the degeneration. The method is principally different from the above-mentioned ones. There are no moving gadgets within the wave tank. The laboratory experiments were carried out in a fully enclosed clear acrylic tank that was 600 cm long, 29 cm deep, and 30 cm wide. The tank could rotate about a horizontal axis approximately through its center so that the interface could be initially tilted. The tank was filled with a two-layer stratification: freshwater was in the upper layer and saline water in the lower layer. The tank was then tilted by a small angle to its initial horizontal position. The experiment begins when the tank is suddenly returned to the horizontal position, and baroclinic pressure gradients drive the flow in different directions above and below the pycnocline. The modeling of the development of a two-fluid system with tilted thermocline that arises in lakes after wind load cessation can be performed by using this method. At a large initial tilt, the initial basin-scale wave steepens into an internal surge, which subsequently evolves into a packet of solitons.

Mechanisms of breaking progressive internal waves were studied by Troy and Koseff (2005). Experiments were carried out in a 4.88-m-long, 0.61-m-high, and 0.3-m-wide wave tank. A two-layer profile of stratification was created by filling the tank with freshwater up to a given depth, and then injecting the heavier (salt) water below the fresh layer. Selective withdrawal was made before the experiments were started to make the intermediate layer thinner. This enabled the authors to maintain the thickness of the intermediate layer smaller than 1 cm. Progressive interfacial waves were generated by vertically oscillating a half-cylinder ("*plunger-type*" *wave maker*) placed at the density interface. It was asserted that the wave maker did not create surface waves or unwanted interfacial mixing. A personal computer was used to control the displacement of the half-cylinder that allowed generation of arbitrary waveforms, including sinusoids, and polychromatic wave trains with a nearly uniform spectrum (in the assigned spectrum window) at the upstream-most wave gauge location.

3.1.3 Influence of Dissipation

Another important problem considered in experimental investigations of internal waves is the influence of dissipation on the decay rate of waves. It is known that dissipation is present in all experimental investigations connected to the movement of liquids. In some cases, its influence is not too large; however, frequently it is one of the principal causes of the difference between experimental and theoretical results.

The influence of the viscosity on the propagation of internal waves was investigated by Koop and Butler (1981). The authors modified the known model (Keulegan 1948) for the estimation of the influence of viscosity on the damping of surface waves, and applied it to internal waves propagating in a two-layer environment. In the theory, it was assumed that energy dissipation occurred in the viscous boundary layer, formed at rigid boundaries and at the interface. The effect of dissipation resulted in a general reduction of the solitary wave amplitude. In their work, a dependence of the change of the wave amplitude a on the distance $(x - x_0)$ was obtained as

$$a(x) = a_0(x)\left[1 + Ka_0^{1/4}\frac{(x - x_0)}{h_1}\right]^{-4}, \tag{3.4}$$

where the coefficient K is determined by the thickness of the layers, $h_1$and h_2, the basin width B, acceleration of gravity g, the kinematic viscosity v, and a relative difference of the densities $\Delta = 1 - \rho_1/\rho_2$.

Experiments showed that the effects of viscous dissipation resulted in a reduction of the wave amplitude during its propagation. An amplitude reduction by 50% till the moment when the wave reached the end of the basin was observed. Measurements were continued after wave reflection from the face walls of the basin. It was found that the amplitude of the solitary wave was only 30% of that of the incident wave when the reflected wave had passed 3.5 m from the face wall and returned to the initial position of the measurement. It is concluded that the large attenuation is apparently connected with the fact that the bottom layer thickness in the experiments was small; hence, the influence of the viscosity was appreciable. Besides, immiscible liquids were used in the work. For this reason, the interface between the liquids was sharp, which resulted in an enhancement of the viscosity effects. However, the accuracy of the amplitude of the wave when it passed through the perturbed region, caused by the previous passage of the wave, was not considered.

Experimental data were compared with results of numerical modeling of the *generalized* K-dV equation; it possesses additional terms allowing for the viscosity influence. The experimental data of the measured wave form, obtained by using the gauge installed at only 20 cm from the wave generator, were used as initial conditions in the numerical modeling. Comparison of the calculated results with the data of the experiments has shown satisfactory correspondence. The conclusion was made that the influence of the viscosity on the attenuation amplitude, as well as on the solitary wave energy, was important.

The authors also considered the problem of the influence of the viscosity on the length of a solitary wave since the characteristics of a solitary wave should correspond to their amplitude–wavelength ratio. The influence of the viscosity on this ratio should be studied. Propagating solitary waves are characterized by the dynamic balance between nonlinear and dispersive effects, and such a ratio can be represented as $a\lambda^2/H^3 = \text{const}$. Obviously, the influence of the viscosity results in a

gradual decrease of the amplitude. Eventually, viscous effects become comparable with the nonlinear ones. From this point of view, the viscosity should appear in the above-mentioned ratio. With the aid of numerical calculation, the authors showed that when $a/h_2 < 0.2$, the influence of the viscosity diminished and resulted in a deviation of the characteristics of the solitary wave from its usual behavior, i.e., for rather weak waves, the deviation of the viscous from the inviscid theory is fairly insignificant.

A theoretical analysis of the influence of the viscosity on the attenuation of the amplitude of the solitary wave was conducted by Leone et al. (1982). The authors obtained a dependence describing a decrease of the amplitude a of an internal wave on the distance. The analysis was carried out on the basis of a series of simplifying assumptions: inviscid flow corresponds to the flow caused by the Korteveg–deVries soliton, moving with constant speed c; all lines of the current are flat and horizontal when viscous effects are taken into account; only a viscous shift of the velocity is taken into account at the interface; and viscous effects close to the free surface are neglected. The analytical form of the factor K in equation (3.4) is rather complicated even at specified simplified assumptions. In a limiting case of weak stratification when $\Delta = 1 - \rho_1/\rho_2 \ll 1$, the expression for this factor takes a simple form, namely

$$K = \frac{1}{12h_2(1+b)}\sqrt[4]{\frac{\nu^2|b-1|}{c_0^2 h_1^2 h_2}}\left[b + \frac{2h_2(1+b)}{B} + \frac{(1+b)^2}{2b}\right], \tag{3.5}$$

where $b = h_1/h_2$, and $c_0 = (g'((h_1h_2)/(h_1+h_2)))$ is the phase speed.

The authors remark that the expression for the factor K (Koop and Butler 1981), in which the approximate boundary condition on the interface was used, was incorrect and resulted in an overestimation of attenuation. They examined the validity of the obtained expression by comparison of their prediction with experimental data of the work of Segur and Hammack (1982). Appreciable differences between the theory and experiment emerged: in particular, calculations overestimated the attenuation of the internal wave when it moved from the generator toward the channel end and underestimated it, when it moved after reflection from the end face toward the generator. The authors explained that the difference was caused by the presence of "parasitic" wave movements. When using the above method, surface waves are generated simultaneously with internal waves. The surface wave speed is higher than that of the internal wave. It so happens that the first passing of the internal wave occurred on the background of the remaining perturbations near the free surface caused by the surface wave. So, the velocity shift at the surface was less when the internal wave moved to the end face and, hence, dissipation decreased. On the other hand, after reflection from the end face of the basin the internal wave moved on the background of the residual currents directed against its movement. It resulted in an appreciable increase of shear and dissipation. The authors considered these features of propagation of solitary waves to be due to

the limited length of the basin and introduced empirical corrections into their estimated relations describing the dissipation.

It is noticed that friction at the walls is also an important factor causing wave energy loss. This conclusion was confirmed by Troy and Koseff (2006). They theoretically and experimentally studied viscous damping of progressive waves propagating at an interface of two liquids of various densities. It was assumed that the motion caused by the waves was potential flow. Friction at the interfaces, at the bottom, and at the lateral walls was considered. It was shown that energy dissipation near the lateral walls was the dominating mechanism of wave damping. Friction at the bottom was poorly expressed because the interface was rather far from the bottom. It was remarked that to reduce the contribution of friction at the lateral walls below a level which is determined by the influence of the shearing caused by the wave on the interface, it is necessary to have a basin width at least three times as large as the overall thickness of the liquid layer in the experiments.

Attenuation of solitary internal waves under the effect of viscosity was also investigated by Gavrilov (1988). Experiments were carried out both for the free surface case and for the case of a cover (rigid lid conditions) for waves of elevation and depression. The author showed that calculations corresponded sufficiently well with the experimental data. Additional friction was taken into account when the rigid lid condition was used. It was also shown that calculations based on similar dependences (Koop and Butler 1981) correspond less with the experimental data.

One should also mention the work of Bukreev and Gavrilov (1983) in which attenuation of solitary waves propagating along an interface of two immiscible liquids was studied. It was found that the amplitude of the waves decreased approximately ℓ times at a distance $s/l = 100$, where s is the covered distance, l is the length of a rectangle with a height, equal to the wave amplitude a, and the area is equal to the wave area. The given dependence corresponds to a reflection of a wave from the face walls of the basin.

Data on viscous damping of solitary waves are especially important when studying their interaction with an inclined slope and when finding the coefficient of reflection because the recording equipment is installed at a certain distance from the slope. It was shown when studying the propagation of solitary waves of depression (Kao et al. 1985) that attenuation of waves in a liquid of constant depth made $4.3\%\ \mathrm{m}^{-1}$ at a distance of 3–6 m from the gate, and gradually increased to $6.2\%\,\mathrm{m}^{-1}$ at long distances from the gate and ratio of depths $h_1/H = 1/14$. This coefficient decreased with the growth of h_1/H. It was found that the attenuation was somewhat smaller than when inferred from theoretical calculations (Leone et al. 1982).

Rather appreciable attenuation of solitary waves was revealed by Michallet and Bartholemy (1998). The wave amplitude decreased by 3% when the wave was passing a distance of 30 cm. This attenuation had an order of magnitude close to that found experimentally by Koop and Butler (1981). Such a level of attenuation was connected, apparently, to the small size of the basin cross section, i.e., with appreciable influence of friction at the walls and the bottom of the basin. Besides,

the growth of the velocity shear on the interface of immiscible liquids also leads to attenuation.

A slightly smaller attenuation was recorded by Sveen et al. (2002). In a basin with cross section 0.4 m × 0.6 m, it made about 4.8% at a distance of 1 m; in a basin with cross section 0.5 m × 1.0 m, it was 1.3% by amplitude.

3.1.4 Summary

On the basis of the above review, it is possible to draw the following inferences:

1. Internal waves play a significant role in the processes of transport of mass and energy in stratified seas and lakes. A popular approximation of the density distribution is a two-layer configuration with an upper layer of a light fluid and a heavier fluid in a lower layer. The density jump interface is at the location of the thermocline. Such a two-layer configuration has modeled internal waves in real lakes rather successfully.
2. There are a number of methods of generation of internal waves propagating along an interface between two liquids of different density. Waves are typically generated by vertically oscillating a wave maker placed at the interface. Two basic types of such wave makers are primarily used in laboratory experiments. The first type is a *"flap" wave maker*. Waves are generated by oscillations of an airfoil around its tip that is hinged to a rod. The other rod end is attached to the front wall of the basin. The second type is a *"plunger" wave maker*, in which a submerged body, also placed at the density interface, oscillates up and down. An internal solitary wave is generated by a single displacement of a generating element (up or down) a given distance. This causes a localized vertical displacement of the interface, and its further development results in the formation of an internal solitary wave. Such an interface displacement can also be produced by the movement of a piston. A two-piston system can be used to generate internal solitary waves. In these methods, it is rather important not to generate a flow separation under the effect of the initiation of the wave motion. In fact, the motion of the moving elements ought to be such that formation of vortical structures and subsequent turbulence of the fluid, which result in undesirable perturbations, are avoided.

   A localized interface rise and consequential wave generation can also be generated by releasing *fluid trapped behind a gate with its subsequent elevation*. In this (*step pool*) *method,* it is necessary to determine precisely the depth and length of the interface level in the separated part of the basin to guarantee generation of a single solitary wave, but it does not avoid the occurrence of dispersive wave tails. It is important to provide a smooth elevation of the gate with the purpose to avoid mixing of fluids.
3. An important problem is concerned with the creation of a distinct boundary between layers in order to compare the recorded data with theoretical results.

The basin should be filled with liquids as carefully as possible to achieve small thickness of the intermediate transition layer. This allows one to use rather simple dependences obtained for a two-layer liquid, to describe the characteristics of waves, instead of solving more complicated Sturm–Liouville problems for cases of continuous stratification.

4. In the majority of the executed works, the structure of the density field was measured with the help of *electric conductivity gauges*. The works did, however, not concentrate on such important questions as the operating frequency of the gauge. It is known that a double electric layer of dissolved ions is formed near the gauge electrodes. This layer can significantly influence the accuracy of the measurements; therefore, it is necessary to raise the gauge-work frequency for normally operating the equipment, thus allowing considerable diminishing of the effect of electric double layers.
5. In most works the measurement of the wave characteristics is carried out by *distributed electric conductivity gauges,* which have strongly nonlinear performance data. It is necessary to take special measures to achieve linearization of their operating characteristics.
6. Modern methods to measure velocity (*PIV, PTV, planar laser-induced fluorescence*, etc.) are promising techniques to determine the velocity distribution inside internal solitary waves that result in the best understanding of the processes of wave propagation.
7. Comparison of experimental data with theoretical dependencies demonstrates that the characteristics of internal solitary waves (speed of propagation, structure of the wave, and amplitude–wavelength or frequency–amplitude ratios) of small amplitude can be successfully described by the K–dV theory. Fully nonlinear theories are to be used to describe the waves with larger amplitudes. The extended K–dV theory can also be used for such description.

3.2 Transmission, Reflection, and Fission of Internal Waves by Underwater Obstacles

3.2.1 Transformation and Breaking of Waves by Obstacles of Different Height

Internal solitary waves propagating in a stratified fluid over a flat horizontal bottom have been extensively studied in recent years. A state-of-the-art report was given in the last section. A quick summary of the pertinent literature is as follows: The relatively dense coverage of the subject is motivated by its practical importance. There are many publications devoted to the theme. Characteristics of solitary internal waves were studied experimentally by Koop and Butler (1981); Segur and Hammack (1982); Bukreev and Gavrilov (1983); Kao et al. (1985); Michallet and Barthelemy (1997, 1998); Grue et al. (1999); Walker et al. (2003); and Carr and

Davies (2006). The current state of the art in experimental studies of internal waves and comparison with theoretical models are reviewed by Ostrovsky and Stepanyants (2005). It was established that the K–dV theory provided a valid description of the behavior of solitary internal waves for small-amplitude motions. When the amplitude increases, a more complicated theory should be used to describe the internal wave characteristics. For large-amplitude waves in a two-layer system, there is an alternative approximation that combines the K–dV and modified K–dV equations (this is the so-called K–dV–mK–dV equation or Gardner's equation). It includes quadratic and cubic nonlinear terms and exhibits solitary wave solutions. A fully nonlinear theory was recently developed. The results, obtained by using this theory, correspond to data of laboratory experiments.

In this section, we consider the propagation of internal solitary waves in a two-layer fluid of nonuniform depth. The shoaling, breaking, and run-up of such waves on a uniform slope were studied comprehensively by Kao et al. (1985); Helfrich and Melville (1986); Helfrich (1992); Michallet and Ivey (1999); Chen et al. (2007a, 2007b) and others. Only a few experimental investigations deal with the interaction of internal solitary waves with isolated, two-dimensional topography.

Laboratory investigations were made on fission of an internal wave in a two-layer fluid by a triangular obstruction, its "stability", that is, form preservation, of the transmitted wave, as well as the energy annihilated or dissipated by the vortex due to the obstruction were studied (Wessel and Hutter 1996). Experiments were carried out in a basin 10 m long, 0.33 m wide, and 0.33 m deep, filled by two layers of liquids of different density: freshwater and saltwater. Internal solitary waves of elevation were generated by two pistons which move horizontally in opposite directions; a thin separating plate is put between the two pistons of the liquids. The size of the pistons and speeds of their movement were selected so as to equalize the volumes moved by each piston. Measurements of the wave structure were performed by six distributed electric conductivity gauges. The obstacle had the form of a truncated triangle (the triangular obstruction is flat-topped (10 mm)). Experiments were also made with an obstacle of different form: a combination of a slope and a plateau. It was seen that the solitary wave impinging on an obstacle often fissions into reflected and transmitted waves. The authors introduced a parameter of blocking which represents the ratio between the obstacle height, h, and the bottom layer thickness, h_2:$B = h/h_2$ and called it the "degree of blocking". It was revealed that for large sizes of the parameter of blocking (for example, $B = 1.2$), a transmitted wave is not formed. In the opposite case, at small values of B (for example, $B \leq 0.6$), the wave passes above the obstacle, and no reflected waves are observed. Interesting results were obtained when studying the interaction of an internal solitary wave with an extended ridge. It has been shown in this case that a steepening of the leading face occurs while the wave is adjusting to the extended ridge. It is accompanied by a growth of the wave amplitude. At the same time, the back front extends considerably, and a cavity, which serves as the inducing reason of the beginning of generation of the oscillating tail, is formed on it. This cavity disappears later above the plateau and above the back slope of the ridge. Then, the form of the moving structure significantly changes in comparison

with the form of the incident wave: the forward front becomes very steep, its amplitude is large, and a long tail arises. It is remarked in the work that a change in amplitude of the wave during its motion and interaction with the bottom features is frequently used as a quantitative estimation of the wave attenuation. In this case, the dispersion effects can cause an expansion or narrowing of the wave and substantial change of wave form during the wave interaction with topographic features. To explain the wave attenuation, it is reasonable to use other wave characteristics, in particular its potential energy (Bogucki and Garrett 1993):

$$E = \frac{1}{2}(\rho_2 - \rho_1)g \int_{x_1}^{x_2} \eta^2(x,t)\mathrm{d}x. \tag{3.6}$$

For solitary waves of small amplitude, the potential energy is practically equal to the kinetic energy (Bogucki and Garrett 1993); for other wave forms, the energies are proportional to each other. It is shown in the work that the potential wave energy and its amplitude decay with distance, following an exponential law (Maurer 1993; Maurer et al. 1996).

It was found that an increase of the degree of blocking, B, results in a transformation of a solitary wave into a dispersive wave train. This process in essence is a consequence of wave breaking and formation of vortical structures above the obstacle. A certain part of the wave energy is dissipated. It is shown that a vortex is formed on the leeward side of the ridge. This process is accompanied by the formation of a narrow near-wall jet on the leeward side of the ridge. This jet penetrates more or less deeply into the bottom layer; as a consequence, lighter water is entrained from the upper layer. The vortex intensity grows when the degree of blocking increases. It is obvious that the formation of vortical structures, which break down as a result of the development of instability and consequential fluid turbulence, is an effective mechanism of wave energy dissipation that cannot be described within the framework of the existing theoretical models of nonlinear internal waves with large amplitude.

In subsequent works (Hüttemann 1997; Hüttemann and Hutter 2001; Vlasenko and Hutter 2001), attention was focused on studying the influence of the finite thickness of the intermediate layer on the character of the interaction of a solitary wave with an obstacle. Finiteness of the thickness of this interface is caused by natural processes of diffusion, which occur between the salty and fresh liquids. It is shown in these papers that finite thickness of the intermediate layer causes existence of baroclinic modes of higher order. The experimental equipment was adapted to the generation of a single solitary wave which corresponded to the baroclinic mode of a wave of a perfect two-layer system. During interaction with the ridge, this wave was split into a pair of reflected and transmitted waves having the form of solitary waves with finite amplitude and representing the first higher order wave mode of the two-layer system. Besides, during the interaction the second wave mode was generated because of the influence of the finite thickness of the intermediate layer.

Interaction of solitary internal waves of depression with an underwater obstruction has also been investigated experimentally (Sveen et al. 2002). Experiments were carried out in basins with the sizes: [25 × 0.5 × 1.0 m] and [6.4 × 0.4 × 0.6]. A number of experiments were carried out in channels of 15.3 m and 21.5 m length. The container was filled with two layers of (fresh and salty) liquids. The solitary internal waves were generated using the step pool method (Kao et al. 1985). Four kinds of ridges were used. They had different heights and inclinations. Particle tracking and particle image methods were used to measure the velocity field. The density was measured with the help of a conductivity meter and a fluid density gage. When studying the interaction of an internal solitary wave with a relatively wide ridge, it was found that a steepening of the back front of the wave takes place; this steepened part will eventually practically be perpendicular to the slope of the ridge. Then, the wave is transformed into a leading wave of depression and a subsequent wave of elevation. Such behavior is similar to the process of transformation of an internal solitary wave of depression over an inclined coast when the region above the point of return is considered. It has been noticed that the interface on the back front of the wave thickens and its boundaries are washed out. This proves that mixing of fluids takes place. In the presence of a narrow ridge, wave breaking occurs rather quickly in form of an overturn of liquid. In the beginning of the overturn process, a large jet of liquid moves downward, and vortical structures are formed in the space between the jet and the initial interface.

In studies of the formation of vortical structures, it was noticed that the vortices appear on the windward side of the ridge, and the place of their appearance and development is determined by the wave amplitude. Vortices are formed as a consequence of separation of the flow caused by the influence of a negative gradient of pressure connected with the passage of the wave. The separation starts as a splash-like flow directed upward which transforms into a flow containing one or more vortices. For moderate interaction between the wave and the ridge, the formed vortical structures move upward and dissipate near the top of the ridge. At strong interaction, vortex generation and break down were more pronounced. In the beginning, a vortex is formed due to the instability of the near-wall flow and its separation. Subsequently, it moves up and along the ridge and is combined with another vortex of higher intensity in the region located higher on the slope. The second vortex appears later than the first. As a result, the flow, separating at the ridge, occupies a large region. Moreover, the vortices cause the appearance of a smaller-scale flow and mixing of the liquids.

It is appropriate here to mention the work of Carr and Davies (2006) in which the separation of near-wall flow was studied for the motion of a solitary internal wave over a flat bottom. Analysis of the characteristics of the transmitted waves showed that they consist of a leading solitary wave-like pulse and a train of waves of smaller amplitude. For weak interaction, the form of the leading part is close to that of the solitary wave. When moderate interaction is considered, the overall form of the initial pulse is wider than that of the incident wave, and the tail is not separated from the wave train. The leading part of the wave form is close to the theoretical profile

of the solitary wave. At strong interaction, the form of the front of the pulse is close to the theoretical profile, but fluctuations in the tail look like a train of waves with large amplitude.

In the following work (Guo et al. 2004), experiments were carried out in a small basin (Sveen et al., 2002) with the same measuring equipment. The analysis of strong interaction of internal solitary waves with a ridge was carried out when the upper layer was stratified. It was shown that the velocity in the bottom layer considerably grows because of the decrease of the cross section due to the presence of the ridge. The back front of the wave steepens during the translation of the wave over the ridge, and a vortex is generated in this region. The separation of the near-wall current generates a vortex of opposite direction of the rotation. This conclusion is confirmed by the analysis of the profile of the vorticity distribution represented in the work. An intensive jet appears between the two vortices, which results in an amplification of wash-out layers. It is an established fact that these vortices are of almost the same intensity. Measurements of the change of the density field were made which confirmed that the strong interaction of an internal solitary wave with an obstacle results in strong mixing of the liquids.

In our own studies, we allow for the interaction of internal solitary waves with underwater features as a possible mechanism for the transformation of wave energy in lakes from larger to smaller scales. Our experimental research deals with the propagation and interaction of waves with underwater obstacles of rectangular form. They are a natural continuation of the above-mentioned works devoted to studying the interaction of internal solitary waves with smoother topographic obstructions. It is evident that the degree of wave interaction with a rectangular obstacle is stronger than with a triangular one. Our principal attention was drawn to studying strongly nonlinear internal solitary waves of large amplitude. Apart from this, more complicated conditions of experiments are useful from a viewpoint of examination of extreme situations of wave interaction with obstacles. In addition, situations are also essential in verification attempts of numerical models to calculate the scattering of internal solitary waves by topographic features, when the fix point of separation is on the obstacle.

Experimental Setup. Experiments were made in a basin 7 m long, 0.33 m wide, and 1.5 m high. The walls of the basin and its bottom were made of plexiglass. The basin was located in a basement room whose temperature was practically constant during the experiments, although seasonal changes of the temperature occurred there. An auxiliary tank of large size was filled with water before the experiments. After adjustment of the water temperature to that of the room, the wave basin was filled with saltwater (of salinity equal to 15 ppt) to a given depth. Subsequently, freshwater was added using the special arrangement given in Fig. 3.3 to create a two-layer system. The freshwater entered the reservoir from an inlet tube. The reservoir was installed on a wooden board floating on the water. There are two compartments at the ends of the board. The freshwater moved into these compartments from the reservoir through four to eight flexible tubes to achieve uniform inflow over the width of the compartments. The external walls of the

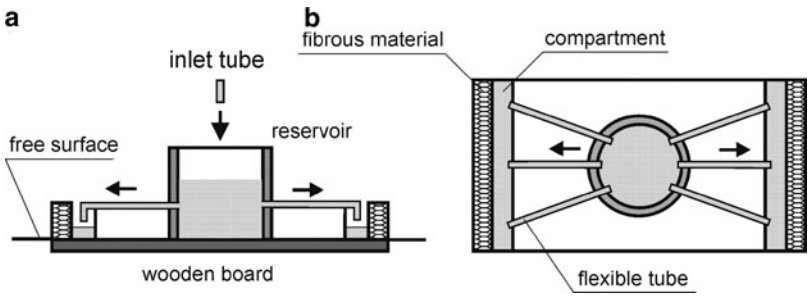

Fig. 3.3 Arrangement for filling the basin by freshwater: (**a**) – side view; (**b**) – top view

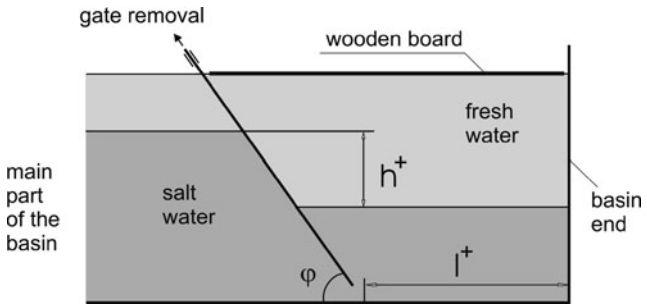

Fig. 3.4 Modified "generator" of internal solitary waves

compartments were made from fibrous material, and the freshwater moved slowly through this material that served as an energy dissipator to reduce the mixing of the liquids. The upper surface of the board was maintained at the level of the free surface (or somewhat lower), and the basin was filled very gradually by freshwater, especially in the beginning of the process. When the distance between the lower surface of the board and the upper boundary of the saltwater became sufficiently large, the filling rate could be increased. After termination of the filling operation, the intermediate layer was selectively withdrawn using a special vertical tube with dilated end that was placed at the boundary between the saltwater and freshwater. This allowed the thickness of the intermediate layer to decrease.

Solitary waves were generated following the modified step pool method by Kao et al. (1985). A sketch of the generator is presented in Fig. 3.4; its operation was described already in Sect. 3.1. Here, some peculiarities of the wave generation, which are connected with the modification of the construction, are considered. The gate was lifted and the lighter fluid contained in the separated compartment of the basin began to move forward to the main part of the basin. Very soon, a solitary wave was formed. Its motion was accompanied by local vortices, which were induced by the removal of the gate. It was noted already by Kao et al. (1985) that the solitary waves were also accompanied by different degrees of initial pulse breaking, which restricted the wave maximum. Another imperfection of such

a scheme of wave generation concerns also the movement of the heavier fluid in the opposite direction after gate removal, its reflection from the end wall, and consequential transfer of perturbations to the main part of the basin. These peculiarities of this wave maker are especially important when processes of wave reflection from topographic features are studied. It was suggested by Michallet and Ivey (1999) to use a slightly tilted gate (at 30° to the vertical) in order to improve the performance of wave generation. The interface incline after removal of the gate is better adjusted to the shape of the solitary wave. The angle of the gate incline was chosen by trial and error. A series of experiments were made with this modification in a basin of smaller size to choose the optimal angle φ of the gate and the length l^+ of the foot point of the gate from the end of the basin. It was found that a decrease of the angle φ (below 48°, see Fig. 3.4) results in an intensification of undesirable perturbations caused by the lengthening of the gate displacement path.

The observed internal solitary wave of depression was formed after lifting the gate, but simultaneously a wave of elevation connected with the motion of the heavier liquid was also formed – it propagated into the opposite direction and was reflected from the end wall. To avoid its motion into the main part of the basin, the gate was re-positioned to the initial state (before start), and the perturbations of the reflected wave of elevation were cut off. This is made at the instant when the leading front of the wave of elevation reaches the position of the gate. Such a procedure allows generation of solitary waves with very weak tailing perturbations. With this method, internal solitary waves of different amplitudes could be generated. The amplitude was controlled by varying the freshwater depth h^+ in the separated part of the basin. Note that the wooden board floating on the water and used for filling the separated part of the basin with freshwater was not removed and served to damp perturbations of the free surface during the wave-generation process.

The density profile was measured using a conductivity micro-probe with a sensor diameter of 0.8 mm. The probe was calibrated using a series of test reservoirs with prescribed salinity. The function describing the calibration curve was nonlinear. Regressive curves were used to obtain the formulas and calculate the density profiles. They were described as high-degree polynomials used for the approximation of separated overlapping segments of the curves. A typical salinity distribution is presented in Fig. 3.5.

Data of the profile measurement before run 1 are designed by squares and those of the measurement before run 2 are shown as triangles. The solid curves corresponding to these data are described by the expression

$$S = S_{0.5}\left[1 - \tanh\frac{(z - z_c)}{\delta}\right], \tag{3.7}$$

where the interface thickness is equal to 2δ. In the illustrated cases, the parameter z_c is equal to 27.3 cm and $\delta = 0.43$ cm for run 1 and $z_c = 27.1$ cm and $\delta = 0.48$ cm for run 2.

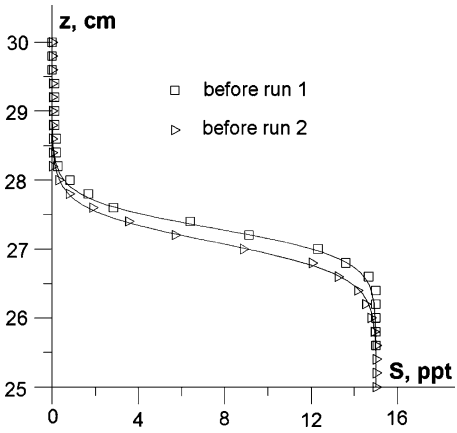

Fig. 3.5 Profiles of salinity before run 1 and run 2

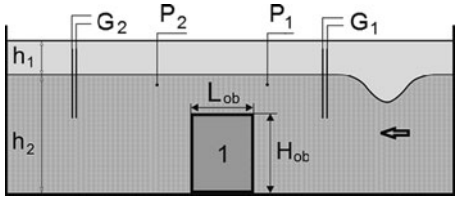

Fig. 3.6 The scheme of basin and equipment

We can see that the interface thickness increases somewhat after run 1 and the interface center shifts downward. Only two experiments were made with the same waters, and then the basin was re-filled. This was necessary because of the wash-out of the boundary between the layers, and because after some runs the use of the assumption of a two-layer system became doubtful.

Description of Results. The results of the experimental investigations dealing with the propagation of internal solitary waves (ISW) of depression in a two-layer fluid system are now presented. Attention was focused to the study of the interaction of ISW with obstacles of different sizes placed on the channel bottom. The obstacles were rectangular. A series of experiments was made with horizontal obstacles of size $L_{ob} = 52.5\,\text{cm}$; $L_{ob} = 17\,\text{cm}$ and a thin plate. Heights of the obstacles (H_{ob}) were changed for each L_{ob} to study the influence of the blocking effect on the interaction of waves with the obstacle. The scheme of the basin and equipment employed is presented in Fig. 3.6. Here, the length of the obstacle, designated as number 1, is L_{ob} and the height is H_{ob}, while h_1 and h_2 are the thicknesses of the upper and lower layers, respectively; the overall depth of the filling is $H = h_1 + h_2$. The arrow shows the direction of wave propagation. Measurements of the interfacial displacement caused by the moving solitary waves were conducted by distributed capacity gauges (G_1, G_2) that were completely submerged in the water. The gauges consist of two parallel thin electrically isolated wires. The capacity of this wire system depends upon the distance between the wires, the salinity (of the electrically conductive medium) of the lower

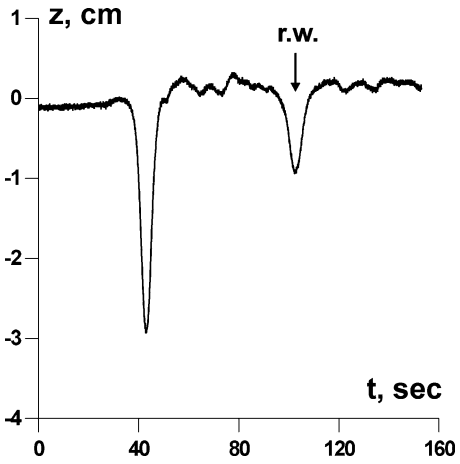

Fig. 3.7 Time series of the displacement at a fixed position of the interface caused by the incident and reflected (r.w.) internal waves (experiment 0902)

layer fluid, and the depth of submergence of the two wires into the lower layer. Therefore, variations in the vertical position of the interface will cause variations of the gauge capacity. The system for collection and processing of the experimental data allows executing fast polling of sensors, transforming signals into numerical form due with the analog–digital converter (ADC), and rapid analysis performance of the process using a PC. These gauges were calibrated using a reservoir with freshwater and a small reservoir with saltwater being placed in it. The calibration reservoir was electrically connected with the wave basin. Note that different from the electric conductivity gauges which have a nonlinear operating character, the regime of operation of the capacity gauges is close to linear.

An example of the interface displacement time series recorded by the capacity gauges, which was positioned ahead of the topographic obstructions, is presented in Fig. 3.7. The abscissa measures time, and the ordinate axis vertical displacement caused by the propagating waves. The distance from the gauge to the leading edge of the obstacle ($H_{ob} = 22$ cm; $L_{ob} = 52.5$ cm) was equal to 196 cm, and the overall depth was 30 cm. The salinity profile is described by equation (3.7) with the parameters $z_c = 26.5$ cm and $\delta = 0.75$ cm. Therefore, the thickness of the lower layer is $h_2 = 26.5$ cm. The registration at the gauge is clearly recording the incident solitary wave and the wave which is reflected from the topographic feature and propagated upstream.

The electric conduction probes, P_1 and P_2, were used to determine the moment of the passage of the solitary internal waves from which the wave speed can be estimated. The boundary between the layers (or at the upper layer) was dyed to visualize the processes of wave interaction with the obstacle. Digital cameras (video and photo) were used to record the visible information.

Theoretical Considerations. It is known that the K–dV theory adequately describes the characteristics of solitary waves with small amplitude (Koop and Butler 1981, Kao et al. 1985 and others). An interface displacement $\eta(x, t)$ obeying the K–dV equation possesses a solitary wave solution of the form

$$\eta(x,t) = a\,\mathrm{sech}^2\left(\frac{x - c^* t}{\lambda}\right), \tag{3.8}$$

where a, c^*, λ are the amplitude, phase velocity, and wavelength, respectively. The solitary wave is predicted to travel without a change of form at constant speed c^*. In a two-layer system, the speed c^* is described by the following expression (Bogucki and Garrett 1993):

$$c^* = c_0\left(1 + \frac{1}{2}\frac{a(h_2 - h_1)}{h_1 h_2}\right), \tag{3.9}$$

where c_0 is the speed of the infinitesimal wave,

$$c_0 = \left(g' \frac{h_1 h_2}{H}\right)^{1/2}. \tag{3.10}$$

Two definitions of the disturbance wavelength are used. The first definition, denoted by $\lambda_{0.5}$, simply represents the half-amplitude point and is defined by $\eta(x - ct)/a = 1/2$, whence $x - ct = \lambda_{0.5}$. The second definition,

$$L_\mathrm{W} = \frac{1}{a}\int_{-\infty}^{\infty} \eta(x)\mathrm{d}x \cong \frac{c}{a}\int_{t_0}^{t_1} \eta(t)\mathrm{d}t \ldots, \tag{3.11}$$

is also used (Koop and Butler, 1981; Michallet and Ivey 1999).

When the nonlinear coefficient in the K–dV equation becomes small (for example, if the interface is located near a critical level), higher-order nonlinear terms must be taken into account in the evolution equation. In this case, the model equation resembles the K–dV equation with an extra cubic nonlinear term (for example, Michallet and Barthelemy 1998). It was demonstrated that the equation can be successfully applied to the description of strongly nonlinear internal solitary waves. We will consider the frequency–amplitude characteristic that is directly defined with the wave profile $\eta(x_0, t)$ (Michallet and Barthelemy (1997, 1998)). It is preferable to use the dependence of the characteristic frequency ω_k that is defined with $\eta(x_0, t)$ as

$$\omega_k = \frac{a}{\int_0^\infty \eta(t)\mathrm{d}t} = \frac{c_k}{\lambda}, \tag{3.12}$$

which directly follows from (3.11).

An important wave characteristic that describes the energy transformation in the process of wave interaction with the underwater obstacle is the wave energy. The total energy of the wave is estimated as (Bogucki and Garrett 1993, Helfrich 1992)

$$E = g\Delta\rho \int_0^{\lambda} \eta^2(x)\mathrm{d}x = cg\Delta\rho \int_0^{\lambda} \eta^2(t)\mathrm{d}t. \tag{3.13}$$

The influence of the obstacle height on the scattering of the incident ISW has been studied. A parameter determining the degree of interaction of the internal solitary wave of depression with the obstacle (blocking parameter) is the ratio $k_{\text{int}} = a/(h_2 - H_{\text{ob}})$.

It was proposed by Wessel and Hutter (1996) to consider the blocking parameter in the form: $B = H_{\text{ob}}/h_2$. Here, h_2 is the thickness of the lower layer and H_{ob} is the obstacle height. The primary parameter determining the degree of interaction between the internal solitary wave and the topographic feature is the ratio between the wave amplitude and the distance from the interface to the obstacle top (Vlasenko and Hutter 2002a, b). In other words, it is the interaction parameter $k_{\text{int}} = a/(h_2 - H_{\text{ob}})$. A similar parameter was also considered by Helfrich and Melville (1986) and Helfrich (1992). In these works, the propagation of nonlinear internal waves over a slope was studied. It was found that waves move onto the shelf with no instability, when $a/d_{-S} < 0.3$, where d_{-S} is the depth of the lower layer on the shelf, that is, the distance between the crest of the wave depression and the bottom, and the waves break when $k_{\text{int}} > 0.4$.

Analysis of the performed experiments concerning the interaction of internal solitary waves with underwater obstacles shows that three scenarios of wave interaction with topographic features can be distinguished. They can be classified according to the value of the parameter k_{int}. In this section, attention will be concentrated on an obstacle in the form of a thin vertical plate of finite length.

Scenario 1. Transformation. This scenario is characterized by a comparatively weak influence of the bottom obstacle on the propagation and spatial structure of internal solitary waves. The distance from the interface to the top of the obstacle, $h_i = H - h_1$, is appreciably larger than the wave amplitude. In this case, the wave is adjusted to the change of the local ambient conditions, and it is accordingly transformed. In experiment 2802, the interaction is studied between the internal solitary wave with amplitude $a = 3.6\,\text{cm}$ and the extended obstacle ($H_{\text{ob}} = 16\,\text{cm}$; $L_{\text{ob}} = 52.5\,\text{cm}$), whose effect on the wave is considerably stronger when compared with the thinness of the obstacle. The salinity profile (before run 1) is presented in Fig. 3.8. This profile is described by equation (3.7) with the parameters $z_c = 29\,\text{cm}$ and $\delta = 0.62\,\text{cm}$. Therefore, the thickness of the lower layer is $h_2 = 29\,\text{cm}$ and $h_i = h_2 - H_{\text{ob}} = 13\,\text{cm}$. The primary parameter determining the degree of interaction between the internal solitary wave and the topographic features is the ratio between the distance from the interface to the obstacle top and the wave amplitude (Vlasenko and Hutter, 2002a). In the considered case, this ratio was equal to 0.27, i.e., the interaction was weak. In Fig. 3.9, a series of photos is presented which show the transformation of the internal solitary wave. Only little changes of the back face of the wave are observed when the wave moves (from the right) and passes over the obstacle. The back face of the wave is undisturbed when the wave is ahead of the obstacle (frame 2), and it is only weakly deformed when the

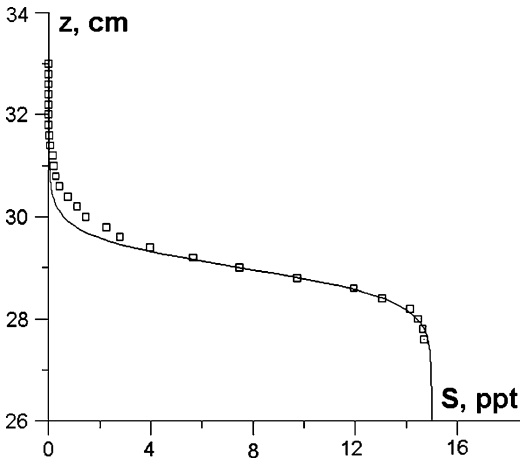

Fig. 3.8 Salinity profile for experiment 2802

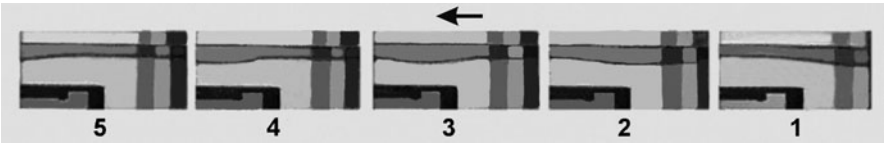

Fig. 3.9 Transformation of an internal solitary wave on an extended obstacle ($H_{ob} = 16$cm; $L_{ob} = 52.5$cm, experiment 2802). The arrow indicates the direction of the wave motion

wave moves above the obstacle (frame 4). This is so even though the obstacle is elongated and its influence increases along its length. The distortions of the back face are caused by the intensification of the inverse flow under the effect of the obstacle and the development of a Kelvin–Helmholtz instability. The influence of the obstacle is reduced if its length is decreased. Moreover, the amplitude of the transmitted wave decreases slightly as compared with the amplitude of the incident wave.

Scenario 2. Interaction. As the coefficient of interaction k_{int} increases, the scenario of interaction of the solitary internal wave with the topographic feature is changed. We consider the character of the change of this process with a successive increase of the coefficient k_{int}. Attention will be focused on the obstacle which is a thin vertical plate.

In experiment 0104, a wave of moderate intensity was created. Its amplitude was $a = 3.5$ cm. The salinity profile before run 1 is presented in Fig. 3.10. The parameters of the experiments are listed in Table 3.1. The coefficient of interaction is equal to $k_{int} = a/(h_2 - H_{ob}) = 0.39$, that is, close to the upper boundary of the regime of wave transformation; nevertheless, the character of the interaction is substantially changed.

With the water of the upper layer being dyed, we could see the change of the wave shape in the process of its interaction with the plate. In Fig. 3.11, a series of photographs showing the transformation of the internal solitary wave is illustrated.

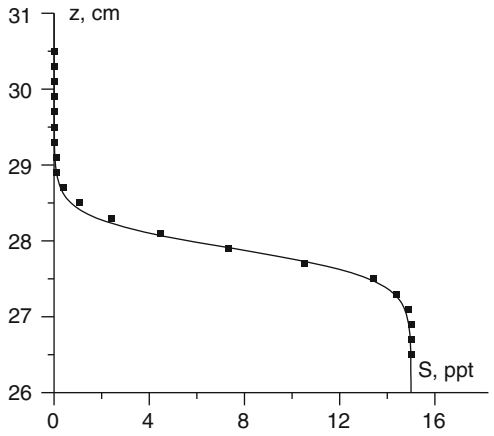

Fig. 3.10 Profile of salinity in experiment 0104

Table 3.1 Parameters of the experiments with the thin plate

No.exp.	H, [cm]	z_c, [cm]	δ, [cm]	h_2, [cm]	H_{ob}, [cm]	a, [cm]	$k_{int.}$
0104	30.5	27.9	0.4	27.9	19	3.5	0.39
3003	30.5	27.7	0.7	27.7	19	5.1	0.59
2203	30.5	27.8	0.5	27.8	22	5.8	1.0

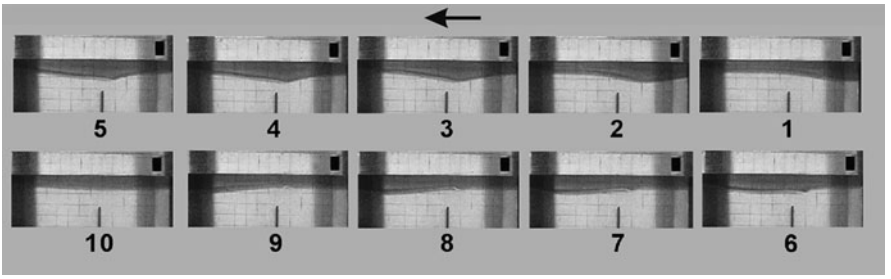

Fig. 3.11 Interaction of internal solitary waves with a thin plate shown in the middle of the frames when $k_{int} = 0.39$ (experiment 0104). Frames are consecutively numbered with times when they were shot in parentheses as follows: 1 (3.8 s), 2 (5,4 s), 3 (6.8 s), 4 (7.4 s), 5 (7.8 s), 6 (8.8 s), 7 (9.8 s), 8 (10.8 s), 9 (11.4 s), and 10 (17.2 s). (Camera was switched on at time $t = 0$ s.) The *arrow* indicates the direction of wave motion

To appreciate the rate of change of the shape of the wave during its passage across the obstacle, consecutive frames are numbered from 1 to 10 and times (in sec) at which they were shot are listed in the figure caption. The plate is seen as a thin vertical line on each frame above the number of the frame.

Changes of the shape of the wave that moves from the right and passes across the obstacle are appreciable. At first, shoaling of the leading face occurs (frame 2), which is immediately followed by a shoaling of the back face (frame 3). Sharpening of the wave occurs when the top of the wave is positioned above the plate (frames 4

and 5). As the wave continues to move and the wave crest passes the position above the plate end, a sharp peak is formed. Its location relative to the plate remains unchanged with time (frames 3–7). Then the wave leaves the obstacle but the interface level stays locally above the initial level; however, as time proceeds, it again restores its initial value (after approximately 6 s). Most likely, the appearance of the sharp peak is connected with the formation of a vortex at the edge of the plate. To corroborate this inference, recall that in this pure baroclinic motion the volume transports in the upper and lower layers have the same magnitude, explicitly (Bogucki and Garrett 1993),

$$\bar{u}_1(x)\,(h_1 + \eta(x)\,) = \bar{u}_2(x)\,(h_2 - \eta(x)\,),$$

in which $\bar{u}_1(x)$ and $\bar{u}_2(x)$ are the averaged upper and lower horizontal velocities. Thus, the cross-sectional area in the lower layer above the obstacle is reduced. This leads to a considerable growth of the velocity near the top of the obstacle (plate). Due to the separation of the flow (separation with fix point at the top of the obstacle), a vortex is formed. Its origin is flow instability in the region with negative pressure gradient. On the other hand, an instability, caused by the retardation of the wave motion under the influence of the obstacle, occurs at the back face of the wave and a vortex of opposite rotation is formed. The combined effect of these vortical structures of opposite rotation results in the appearance of a sharp peak. The vortical structures are not visible at small intensity of the interaction between the wave and the obstacle. Note also that the experimental studies of wave propagation over a ridge showed that the geometry at the top of the ridge plays an important role in the generation of turbulence (Wessel and Hutter (1996)). If the top is made round, turbulence weakens and wave loss decreases.

A series of relatively small vortices could be seen on the back face of the wave; these vortices form owing to the instability of the flow in that region. These vortical structures are analogous to vortices that were found by Wessel and Hutter (1996) and Grue et al. (1999). In the considered situation, the formation of vortices is a characteristic feature of the interaction of internal solitary waves with an obstacle when the process of interaction follows scenario 2. Thus, we can verify that the generation and development of vortices are a result of the obstacle effect, which leads to wave instability and flow separation at the obstacle.

It should be noted that the reflected wave was not observed. This was confirmed by analysis of the data obtained by gauge G_1. The arrangement of gauges and probes relative to the obstacle is presented in Fig. 3.6. The amplitude of the transmitted wave was equal to 2.9 cm. The shapes of the incident and transmitted waves were also obtained. They are displayed in Fig. 3.12 normalized to unit maximum amplitude. Panel (a) shows the incident wave and panel (b) shows the transmitted wave. Here, the theoretical profile corresponds to the K–dV theory (3.8), represented by the smooth solid curves. It is seen that the profile of the incident wave differs somewhat from the profile described by (3.8). Considering that the profile of the nonlinear incident wave was more blunt than the theoretical profile and a small plateau was formed near the crest of the wave (the crest was

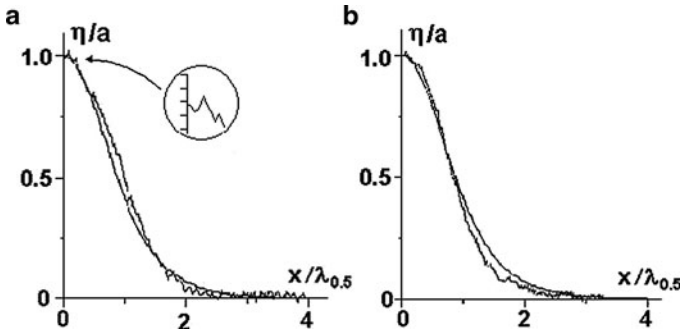

Fig. 3.12 Profiles of the incident (**a**) and transmitted (**b**) internal solitary waves (experiment 0104)

somewhat flattened), the value of the normalizing factor along the abscissa was estimated as the distance from the point where the data begin to differ from the value corresponding to the maximum amplitude down to the half-amplitude point. Note that the form of the soliton described by Gardner's equation had a similar plateau (Ostrovsky and Stepanyants 2005). This latter procedure was taken when the plateau was observed near the crest of the wave. Such a plateau was not observed for the transmitted wave; so, the normalizing factor was determined in the usual way. It can be seen that the profile of the transmitted wave is close to the theoretical profile.

The influence of the viscosity on the decay rate of the energy of the ISW should be determined to distinguish its contribution in the overall decay rate of the waves and to estimate separately the effect of the obstacle. The effect of viscosity was discussed in Sect. 3.1. A number of experiments were carried out to study the dissipation of internal solitary waves in the basin. For this series, gauges located along the basin were used. Detailed results of the experiments will be presented in Sect. 3.4. Here, we quote only the final result. The analysis showed that the energy of the wave decays according to the relation

$$E / E_0 = 10^{-bX}, \tag{3.14}$$

where $b = 0.021$ and $X = \left(x h_2 / H^2\right)$.

The energy of the incident wave is estimated using data of gauge G_1 and formula (3.13). Then, the energy loss connected with the viscosity effect is found according to formula (3.14) when the wave moves over the distance from gauge G_1 to the obstacle (see Fig. 3.6). Taking into account the energy loss, we can determine the energy of the wave when it is directly in front of the obstacle. A similar procedure is made to estimate the energy of the transmitted wave, namely the energy of the wave is estimated by using data of gauge G_2, thereby accounting for the energy loss caused by viscosity. The ratio between the energy of the transmitted wave and that of the wave which is incident on the obstacle is equal to 0.94. In other words, the

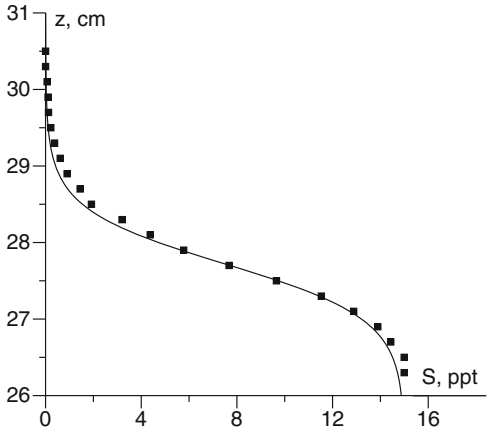

Fig. 3.13 Salinity profile in the water for experiment 3003 (before run 1)

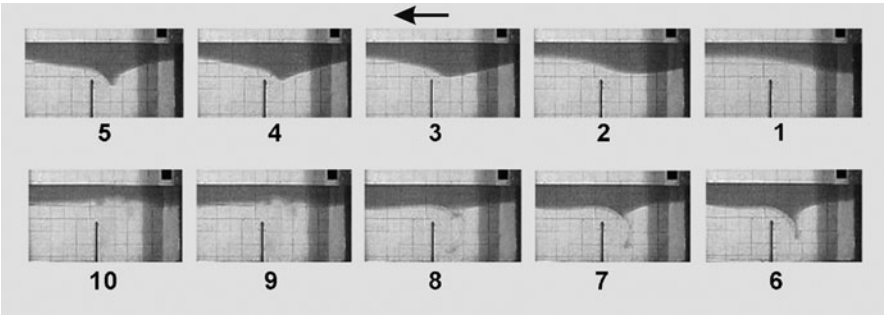

Fig. 3.14 Interaction of an internal solitary wave with a thin plate when $k_{\text{int}} = 0.59$ (experiment 3003). Frames are consecutively numbered and times when they were shot are given as follows: 1 (3.7 s), 2 (5.2 s), 3 (6.5 s), 4 (6.9 s), 5 (7.6 s), 6 (8.4 s), 7 (9.1 s), 8 (9.9 s), 9 (11.9 s), and 10 (12.8 s). (Camera was switched on at $t = 0$ s.) The *arrow* indicates the direction of the wave motion

energy loss acquired by the wave in passing the obstacle is approximately 6%. Such a loss of wave energy for weak wave interaction with the obstacle is small.

In experiment 3003, the overall depth is 30.5 cm. The salinity profile is depicted in Fig. 3.13. It is described by (3.7) with the parameters as listed in Table 3.1.

The pattern of the interaction of the internal solitary wave with the underwater obstacle (thin plate) can be inferred from the photo sequence in Fig. 3.14. Consecutive frames from 1 to 10 and times (in seconds) at which they were shot are listed in the figure caption. Scrutiny of the patterns shows that three stages of the scenario can be distinguished.

Stage 1. This stage extends from the beginning when the ISW is far from the obstacle to the instant when a deformation of the leading face can be observed (frames 1, 2).

Stage 2. Further steepening of the leading face of the wave and sharpening of the wave profile occur. First, the wave amplitude increases (frame 3), then steepening

of the back face sets in, followed by additional sharpening of the wave profile (frame 4), and, then, the wave crest begins to take on a shape of a sharp, slightly elongated peak (frame 5). On frame 6, we see that the peak is transformed into a thin jet oriented at a small angle to the vertical. The jet is caused by the formation of a vortex pair in front of the plate. The counter-flow velocity increases in the layer between the interface and the obstacle top. The flow separates at the sharp edge of the obstacle from it and a vortex sheet is formed. Subsequently, the sheet rolls up into a vortex in the vicinity of the leading edge of the obstacle. On the other hand, the counter flow intensifies and causes a growing instability at the back face of the wave and generates an additional vortex of opposite rotation. This can be seen on frame 6. Under the influence of the vortex pair, the thin jet of light water is injected into the heavy fluid.

Stage 3. The jet continues to move under the influence of the initial impulse but the flow becomes unstable in the central part of the jet as it is separated into two parts. Under the effect of the buoyancy forces, the main part quickly rises (frames 7, 8). This process is accompanied by elevation of the interface and the beginning of the formation of the reflected wave (frames 9, 10). A series of vortical structures, which in the transmitted wave are responsible for the appearance of a dispersive trail, can now be observed on the interface.

The weak haze, visible in front of the plate close to the interface (see frame 8), manifests that mixing of the fluids takes place. It is caused by turbulence of the flow. The leading part of the jet continues its movement under the influence of the vortex located near the sharp edge of the obstruction. Apparently, it keeps its identity at a long distance. The trajectory of its motion can be seen on frames 7–9. Note, however, that the location of the discussed sharp peak of the interface is practically the same as we can see in Fig. 3.11 when the coefficient of interaction was $k_{int} = 0.39$.

The reflected and transmitted waves were observed by analyzing data obtained by gauges $G_1$and G_2. The amplitude of the transmitted wave was equal to 3.4 cm, while the amplitude of the reflected wave was equal to 0.8 cm, and the shapes of the reflected and transmitted waves were obtained. They are displayed in Fig. 3.15 in normalized form [panel (a) corresponds to the incident wave, panel (b) to the transmitted wave, and panel (c) to the reflected wave]. Here, the theoretical profile corresponding to the K–dV theory (3.8) is the smooth sech^2-profile, whereas the rugged curves are taken from the measurements. The profile for the incident wave differs from that described by (3.8), but that of the transmitted wave is very close to the theoretical profile. The profile of the reflected wave is also close to the theoretical profile but appreciable pulsations of the data are observed. Note that the normalizing factor for the incident wave along the abscissa was taken as discussed for the data of experiment 0104 (see above).

The energy of the incident wave was measured by gauge G_1(see Fig. 3.6), and then, the energy loss caused by the influence of the viscosity was calculated using formula (3.14) when the wave had moved the distance between gauge G_1 and the obstacle. Thus, the energy of the wave which is incident on the obstacle was found. The ratio between the energy of the transmitted wave and that which is incident on

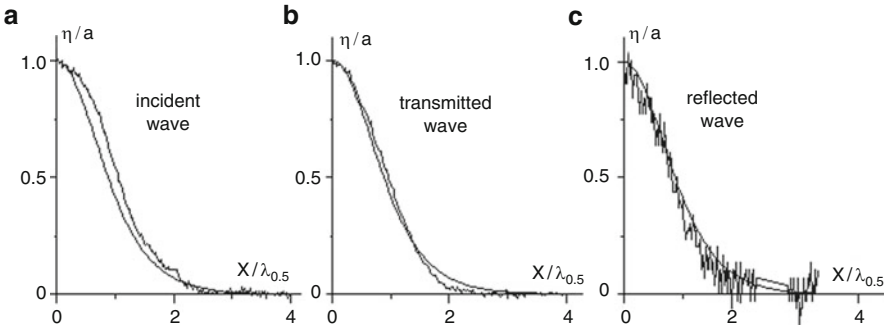

Fig. 3.15 Profiles of incident, transmitted, and reflected waves taken from measurements of experiment 3003 and the K–dV theory

the obstacle is approximately 52%. This ratio is a measure of the energy loss caused by the influence of the obstacle. An analogous procedure was followed to estimate the ratio between the energy of the reflected wave and that of the incident wave, $E_{\mathrm{ref}}/E_{\mathrm{inc}}$. It was equal to 4%, which is very small. We can say that a moderate interaction between the wave and obstacle (coefficient of interaction $k_{\mathrm{int}} = 0.59$) results in an appreciable reflection. Moreover, about half of the initial energy decays due to turbulence above the plate and subsequent mixing of the fluids.

Thus, the larger value of the coefficient k_{int} that is characterized by the extent of the interaction of internal solitary waves with an underwater obstacle leads to a significant change of the flow pattern. A jet directed downward is formed; light fluid entrained by the jet is transported into the lower layer with the heavier fluid and due to jet instability the fluids are mixed. Under the effect of buoyancy forces, the lighter fluid elevates and a reflected wave is generated.

Scenario 3. Wave Blockage. This scenario is characterized by the expression $k_{\mathrm{int}} \geqslant 1.0$.

In experiment 2203, the overall depth was 30.5 cm. The salinity profile is given in Fig. 3.16. It is described by equation (3.7) with the parameters presented in Table 3.1. The amplitude of the incident wave is 5.8 cm; so, the parameter of interaction $k_{\mathrm{int}} = a/(h_2 - H_{\mathrm{ob}}) \cong 1$.

The evolution of the pattern of the interaction of the solitary internal wave with the underwater obstacle (thin plate) is displayed in the photographs reproduced in Fig. 3.17. Consecutive frames are numbered from 1 to 10 and times (in seconds) at which they were shot are listed in the figure caption. Analysis of the patterns shows that again three stages can be distinguished.

Stage 1. This persists as long as the incident ISW does not suffer a deformation of its leading face that is induced by the effect of the plate.

Stage 2. Here, steepening of the leading face of the wave and sharpening of the wave profile occur. The wave crest is initially flat but as the wave approaches the plate a peak arises close to the plate (frame 2). The sharpening continues to develop and the peak transforms into a thin vertical downward jet. From this

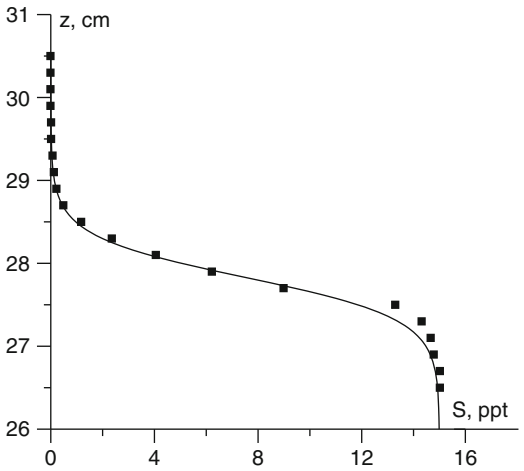

Fig. 3.16 Salinity distribution (experiment 2203, before run 1)

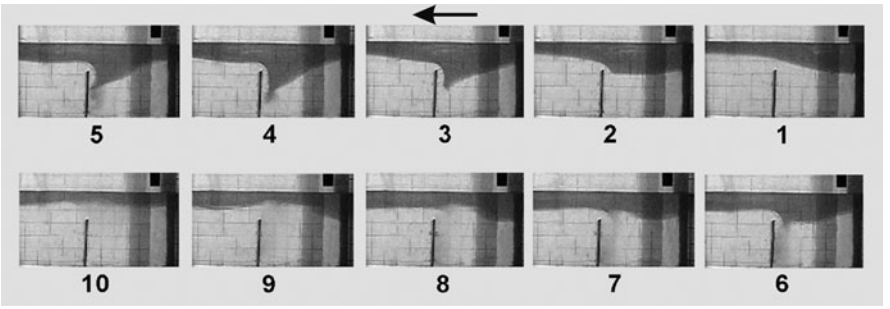

Fig. 3.17 Interaction of an internal solitary wave with a thin plate when $k_{\text{int}} \cong 1.0$ (experiment 2203). Frames are consecutively numbered and times when they were shot are shown in parentheses as follows: 1 (2.3 s), 2 (4.1 s), 3 (5.2 s), 4 (6.3 s), 5 (7.2 s), 6 (8.2 s), 7 (9.3 s), 8 (10.2 s), 9 (11.4 s), and 10 (15.6 s). (Camera was switched on at $t = 0$ s.) The *arrow* indicates the direction of the wave motion

jet, some dyed freshwater is transported a large distance downward along the plate. This differs from the scenario "interaction". The instability of the back face of the wave begins to develop when the jet hits the plate (frames 3, 4). The action of the buoyancy forces stops the jet from moving further down – it breaks. The breaking process leads to mixing of freshwater entrained by the jet with surrounding saltwater. This can be seen in frames 5 and 6 where the region of mixed fluid is observed as haze. In contrast to the previous scenario, the region of mixed fluid is wider and its boundary reaches the upstream lateral surface of the plate. The reason for such a behavior is connected with the appearance of the high intensity of the attached vortex, more intense than the vortex in the case of moderate k_{int}.

Stage 3. Once the jet is stopped, the lighter fluid rises under the action of the buoyancy forces and local elevation and deformation of the interface take place.

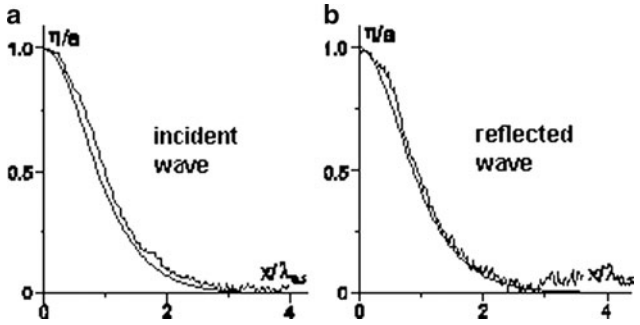

Fig. 3.18 Profiles of incident and reflected waves for experiment 2203

A mushroom-like structure can be observed (frames 7, 8). Then, the reflected wave is formed which quickly propagates away from the obstacle. The interface has a broken form that is caused by the newly arising vortical structures. When that occurs, the mixed fluid with intermediate density between the freshwater and saltwater moves slowly upward from the deeper horizons. A foggy cloud remains above and slightly in front and immediately above the top of the plate. Finally, an elongated perturbation moves across and above the obstacle; however, its amplitude is small. The main part of the energy is concentrated in the reflected wave; however, a substantial part of the energy also transfers to the dissipation region owing to the intense turbulence and mixing. Moreover, a thin region between the plate and the jet remains during the entire process of interaction.

It should also be noted that a transmitted wave was not measurable but reflected waves were observed. This was confirmed by analysis of data obtained by gauges G_1 and G_2. The amplitude of the reflected wave was equal to 2.5 cm. The shapes of the incident and reflected waves are shown in Fig. 3.18 in the usual scaled form [panel (a) displays the incident wave, panel (b) the reflected wave]; they are well reproduced. Their profiles were calculated with normalizing factors as quoted before; they correspond well with the theoretical sech^2-profile of the K–dV theory (3.8). Nevertheless, the profile of the measured incident wave differs from that described by (3.8): it possesses a larger area and is uniformly somewhat larger than the sech^2-profile. The profile of the reflected wave is close to the theoretical profile.

The ratio between the energy of the reflected wave and that of the incident wave was estimated using formula (3.14). The ratio is $E_{\mathrm{ref}}/E_{\mathrm{inc}} = 0.23$; that is, the main part of the energy of the internal solitary wave is spent on the generation of the vortex system and subsequent dissipation when the strong interaction with the underwater obstacle (thin plate) takes place. A reflected wave is generated in this process and its energy is 23% of the energy of the incident wave.

In summary, we may state that the influence of the obstacle height on the scattering of an incident solitary wave was studied in this section when the obstacle is a thin vertical plate. The analysis of the patterns of the flows induced by the interaction of internal solitary waves with the plate and estimated characteristics of the incident, transmitted, and reflected waves has shown that three scenarios of

interaction can be distinguished. The primary parameter determining the degree of interaction is the ratio between the wave amplitude and the distance from the interface to the top of the obstacle $k_{\text{int}} = a/(h_2 - H_{\text{ob}})$.

The scenario "*transformation*" is defined by the inequality $k_{\text{int}} < 0.3$ and corresponds to weak interaction between the wave and the obstacle (Helfrich and Melville 1986; Helfrich 1992; Vlasenko and Hutter 2002b). Only a small change of the leading and back faces of the wave is observed when it passes across the obstacle, incidentally even when the obstacle is elongated and its influence increases. The amplitude of the transmitted wave is slightly decreased as compared with that of the incident wave, and a reflected wave does not occur.

The scenario "*interaction*" is characterized by the interval relation $0.4 < k_{\text{int}} < 1$. A distinguished feature of this regime is the formation of a vortex pair due to the increase of the topographic effect caused by the obstacle. The vortex pair is responsible for the generation of a downward jet at a small angle with the vertical. Lighter fluid from the upper layer is entrained by the jet and is transported downward. Due to the development of a local instability, the jet is decomposed in two parts (1) the main part diffuses upward, and after stopping, causes the reflected wave and (2) the leading part separates from the main part and continues its motion under the influence of the vortex attached to the top of the obstacle, and is gradually mixed with a heavier fluid. Depending on the coefficient of interaction, part of the initial energy of the incident wave is transferred into energies of the transmitted and reflected waves, but the energy loss to dissipation (formation of vortical structures and mixing) is appreciable.

The third scenario "*blockage*" is defined by the expression $k_{\text{int}} \geq 1$. When the wave amplitude is close to, or larger than, a critical value determined by $k_{\text{int}} \cong 1$, a sharp wave steepening is observed. A peak arising near the wave crest caused by the generation of a vortex pair transforms into a vertical jet. It is stronger than the vortex pair in the previous case and it penetrates to a larger depth. Lighter fluid from the upper layer is entrained by a jet. Buoyancy forces acting on the jet lead to jet instability, induced turbulence, and mixing of fluid. In contrast to the "*interaction*" scenario, the region of mixed fluid is much larger, and it reaches the plate. Then, fluid moves upward but this process is quicker than the fluid elevation in the previous case. A reflected wave of appreciable intensity is generated in this elevation process but the main part of the energy of the incident wave is spent on the generation of vortical structures, mixing, and dissipation. Transmitted waves did not arise in the regime "*blockage*". Note that in the experiments performed by Sveen et al. (2002), the coefficient of interaction was $k_{\text{int}} < 0.6$ and the interaction of the solitary internal wave of depression was moderate. The process of interaction followed scenario 2 and a series of vortices arising due to flow instability was observed. In the experiments by Guo et al. (2004), the coefficient of interaction reached the value $k_{\text{int}} = 0.86$. The process of the development of interaction was close to scenario 3, and generated vortices were more intensive than in the previous work.

3.2.2 *Influence of the Obstacle Length on Internal Solitary Waves*

Increasing the length of the obstacle L_{ob} leads to a change of the process of interaction of internal solitary waves with the submerged obstacle. These changes have basically quantitative character. Basic distinctions are primarily observed for scenarios 2 and 3 when the movement of the freshwater over the obstacle is retarded in comparison to that of the thin obstacle. This process is still slower when the obstacle is long and its length is compared with the wavelength L_w. When the thin plate was used, the blockage was not high, and transmitted and reflected solitary waves could be generated. Analysis of the data in the various cases shows that the extent of interaction between a solitary internal wave and an extended obstacle is determined by the coefficient $k_{int} = a/(h_2 - H_{ob})$. As for thin obstacles, three scenarios of interaction can be distinguished. First, we consider an obstacle of length $L_{ob} = 17$ cm and then $L_{ob} = 52.5$ cm. Obstacle models were made of a plastic material and their form was rectangular. Note that the wavelength L_w was estimated following expression (3.11), and the values of L_w were in the interval from 30 to 45 cm. Main attention will be focused on scenarios 2 and 3. The differences to the case of using a thin plate are concerned with some quantitative changes, and there are no appreciable radical changes of the interaction processes.

Scenario 2. Interaction. To begin with, consider experiment 1503 in which the interaction was characterized by a moderately large coefficient k_{int}. The parameters of the experiments are presented in Table 3.2.

The amplitude of the incident wave was 2.05 cm; so, the parameter of the interaction is $k_{int} = a/(h_2 - H_{ob}) = 0.43$. The value of the parameter k_{int} is close to the value in experiment 0104 when it was equal to 0.39. The pattern of the interaction of the solitary internal wave with the extended underwater obstacle is displayed in Fig. 3.19. Scrutiny of the pattern shows that again three stages of the scenario can be distinguished. To appreciate the evolution of the change in shape of the wave when it passes over the extended obstacle, the correspondence of the number of frames and times of observations is shown in the caption to Fig. 3.19. Comparison with the results of experiment 0104 (see Fig. 3.11) shows that the process of wave interaction with the obstacle is appreciably retarded. We can see that a little peak is formed on the interface close to the leading edge of the obstacle as in experiment 0104. A small increase of the coefficient k_{int} and obstacle length led to a change in the flow pattern. The generation of a thin jet is observed (frames 4, 5); it is caused by a vortex pair, which consists of a vortex arising at the back face of the wave due to flow instability and another, attached, vortex that is formed close to the edge of

Table 3.2 Parameters of the experiments with the extended obstacle ($L_{ob} = 17$cm)

No. exp.	H, [cm]	z_c, [cm]	δ, [cm]	h_2, [cm]	H_{ob}, [cm]	L_{ob}, [cm]	a, [cm]	$k_{int.}$
1503	30	26.8	0.8	26.8	22	17	2.05	0.43
1703	30.5	27.4	0.5	27.4	19	17	5.8	0.69
0403	33	29.4	0.55	29.4	22	17	6.5	0.88

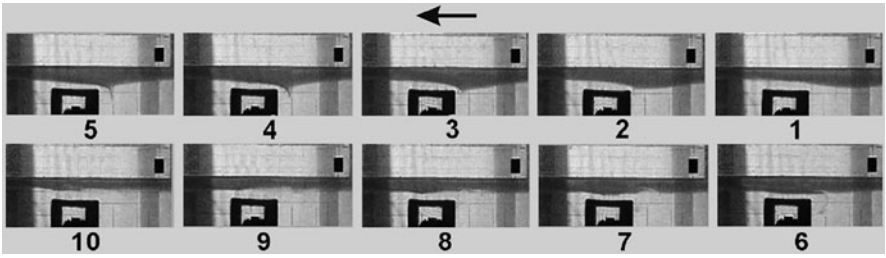

Fig. 3.19 Sequence of photographs showing various stages of the interaction of an internal solitary wave with the obstacle (experiment 1503). Frames are consecutively numbered with times when they were shot as follows: 1(3.8 s), 2 (5,1 s), 3 (5.5 s), 4 (7.4 s), 5 (8.0 s), 6 (9.2 s), 7 (11.0 s), 8 (12.2 s), 9 (14.2 s), and 10 (20.0 s). (Camera was switched on at $t = 0$ s.) The *arrow* indicates the direction of the wave motion

the obstacle (near the upstream side). They rotate in opposite directions. The dimensions of the jet are not large and neither is its intensity. This proves that the arising vortex pair is not strong because the extent of the interaction of the internal solitary wave with the obstacle is moderate. In contrast to experiment 0104, the interface form becomes rugged, and many bulges and troughs can be observed (frames 8, 9). Their formation is connected with the processes of jet generation, development of jet instability, and fluid turbulence. Reflected and transmitted waves were generated in the process of interaction of the wave with the extended obstacle. The energies of these waves were estimated using formula (3.13), and the energy dissipation due to viscosity was estimated with expression (3.14). The ratios $E_{\text{ref}}/E_{\text{inc}} = 0.16$ and $E_{\text{tran}}/E_{\text{inc}} = 0.33$ were obtained. It is evident that an appreciable part of the energy is dissipated.

An increase of the coefficient k_{int} leads to an intensification of the process of interaction of the internal solitary wave with the obstacle. The conclusion, formulated in the previous section, also applies here when the interaction of the more intensive internal solitary wave with the elongated obstacle is considered. The parameters of such an experiment, here 1703, are presented in Table 3.2. The amplitude of the incident wave was 5.8 cm and, so, the parameter of interaction is $k_{\text{int}} = a/(h_2 - H_{\text{ob}}) = 0.69$.

The value of the parameter k_{int} in experiment 1703 is close to the value in experiment 3003 (see Fig. 3.14) in which it was equal to 0.59. The changes of the patterns of interaction of solitary internal waves with a long underwater obstacle can be seen in Fig. 3.20. Here, consecutive frames are numbered from 1 to 10 and times (in seconds) at which they were shot are listed in the figure caption. The pattern again suggests that three stages of the scenario can be distinguished.

Comparison with the data obtained in experiment 3003, in which a thin plate was used as an obstacle, shows that the processes of interaction are analogous. We see again the formation of a thin jet caused by a vortex pair (frame 5). This jet is decomposed in two parts (frame 6). The jet head continues its movement downward at some angle to the vertical. Its intensity decreases, and it is entrained in the circular motion by the vortex attached to the upwind sharp edge of the obstacle (frame 7). The other remainder of the jet loses stability, and turbulent mixing takes

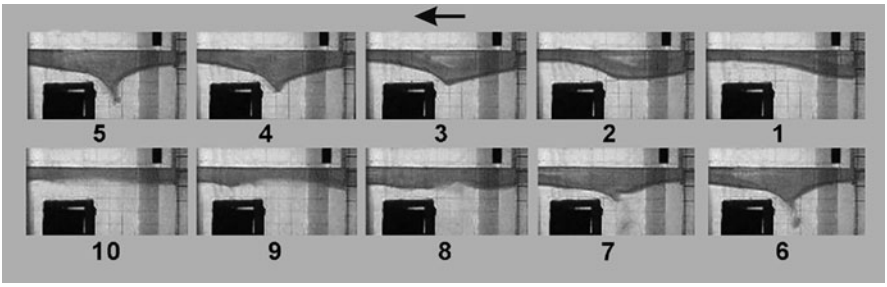

Fig. 3.20 Sequence of photographs, showing various stages of the interaction of an internal solitary wave with the obstacle (experiment 1703). Frames are consecutively numbered with times when they were shot as follows: 1(2.5 s), 2 (4.4 s), 3 (5.1 s), 4 (5.8 s), 5 (6.7 s), 6 (7.1 s), 7 (8.4 s), 8 (10.2 s), 9 (12.6 s), and 10 (15.8 s). (Camera was switched on at $t = 0$ s.) The *arrow* indicates the direction of the wave motion

place. Then, the mixed fluid moves upward under the effect of the buoyancy forces. This motion deforms the interface (frame 8) and a reflected wave is generated. We can see the intermittent structure of the interface and hazy regions caused by turbulence and mixing of the fluids. As a whole, the process of interaction of the internal solitary wave with an extended obstacle is similar to that of the interaction with a thin plate. Differences are observed in quantitative characteristics (the jet is stronger; the process of passage of the wave over the obstacle is slower).

The energies of the reflected waves were estimated using formula (3.13). The energy dissipation due to the viscosity effect was taken into account by using expression (3.14); the ratio $E_{\text{ref}}/E_{\text{inc}} = 0.09$ was obtained. If we compare this ratio with the analogous value obtained in experiment 3003 ($E_{\text{ref}}/E_{\text{inc}} = 0.04$), we can see that the greater part of energy of the incident wave is spent on the generation of the reflected wave. This proves that an extended obstacle leads to a more effective blocking of the flow over the obstacle, and a larger part of energy of the incident wave is spent on the generation of the reflected wave.

Scenario 3. Wave Blockage. This scenario is characterized by the expression $k_{\text{int}} \geq 1.0$.

In this experiment, Nr 0403, the interaction is characterized by a large value of the coefficient k_{int}. The parameters of the experiments are presented in Table 3.2. The amplitude of the incident wave was 6.5 cm; so, the parameter of interaction is $k_{\text{int}} = a/(h_2 - H_{\text{ob}}) \approx 0.88$ (close to 1.0). The evolution of the shape of the internal solitary wave in the process of its interaction with the extended underwater obstacle is reproduced in Fig. 3.21. Here, consecutive frames are numbered from 1 to 10 and times (in sec) at which they were shot are listed in the figure caption.

Again, three stages of the scenario can be distinguished. The flow pattern displayed in Fig. 3.21 is similar to that presented on Fig. 3.17 for experiment 2203. As in Fig. 3.17, the instability onset, the formation of the strong jet, and the generation of the turbulence and mixing of the fluids can be identified in Fig. 3.21. The character of the differences to the two former cases is quantitative. However, there are some notable peculiarities. First, we can see the location of the vortices composing the

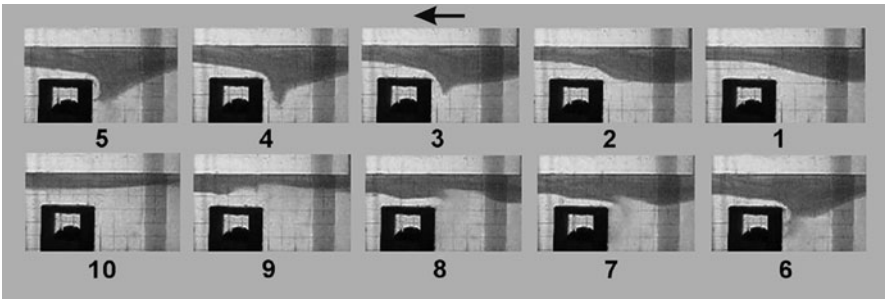

Fig. 3.21 Sequence of photographs showing the process of wave blockage by an extended obstacle (experiment 0403). Frames are consecutively numbered with times when they were shot as follows: 1 (4.2 s), 2 (5.3 s), 3 (6.2 s), 4 (6.9 s), 5 (8.2 s), 6 (9.1 s), 7 (11.7 s), 8 (12.6 s), 9 (15.7 s), and 10 (24.7 s). (Camera was switched on at $t = 0$ s). The *arrow* indicates the direction of the wave motion

vortex pair. After cessation of the downward movement of the jet and the commencement of its lifting under the buoyancy effect, the vortices survive. They continue the rotation and the generation of the jet. The latter appears as a thin streak of dyed fluid over the upstream side of the obstacle (frames 7, 8). Salt fluid is above and beneath the streak. Evidently, the first vortex is above the obstacle edge and the other at the lower boundary of the interface. The interface bulge in front of the obstacle (frames 7, 8) cannot penetrate downstream because blocking of flow takes place. Second, if the jet is strong, it can penetrate to large depths in the heavy fluid. Under such conditions, its movement into the opposite direction (upwards) is very quick. In other words, the greater the penetration depth of the jet is, the larger will be the jet velocity when it moves upward. This leads to a conspicuous thinning of the upper layer (frame 9) and the generation of a comparatively strong reflected wave.

The energy of the reflected wave is estimated by using formula (3.13). The wave energy dissipation due to the viscosity effect is taken into account by using expression (3.14). The ratio $E_{\text{ref}}/E_{\text{inc}} = 0.16$ was obtained. If we compare these results with the results obtained in experiment 1703 in which the extended obstacle was also used, it is seen that an increase of the interaction coefficient results in an amplification of the reflected wave. The obstacle elongation also leads to an amplification. This can be concluded from a comparison of experiments 3003 and 1703 whose values of the coefficient k_{int} were close to one another.

As remarked above, a series of experiments was conducted when the obstacle length increases to more than the characteristic length of the internal solitary waves. The length of the obstacle was equal to 52.5 cm. Attention will also be focused on scenarios 2 and 3. We begin with scenario 2.

Scenario 2. Interaction. The results of experiment 0203 in which the interaction is characterized by a moderate value of the coefficient k_{int} are considered here. The parameters of the experiments are presented in Table 3.3.

The pattern of the interaction of a solitary internal wave with the extended underwater obstacle is shown in the 10 frames of Fig. 3.22. Frames are numbered

Table 3.3 Parameters of the experiments with the extended obstacle ($L_{ob} = 52.5$cm)

No. exp.	H, [cm]	z_c, [cm]	δ, [cm]	h_2, [cm]	H_{ob}, [cm]	L_{ob}, [cm]	a, [cm]	$k_{int.}$
0203	33	29.7	0.55	29.7	16	52.5	6.7	0.49
2412	32.5	30.7	0.57	30.7	22	52.5	7.3	0.84
0604	30.5	27.6	0.55	27.6	22	52.5	5.9	1.05

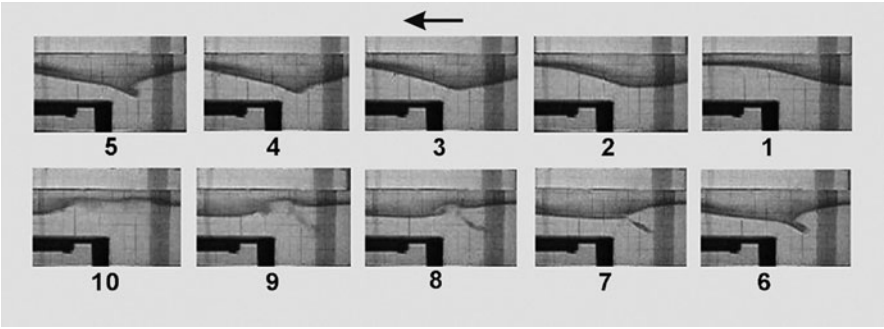

Fig. 3.22 Sequence of photographs showing the process of wave interaction with an extended obstacle (experiment 0203). Frames are consecutively numbered with times when they were shot as follows: 1 (8.9 s), 2 (10.6 s), 3 (11.2 s), 4 (11.8 s), 5 (13.0 s), 6 (13.8 s), 7 (14.7 s), 8 (15.6 s), 9 (16.7 s), and 10 (19.4 s). (Camera was switched on at $t = 0$ s.) The *arrow* indicates the direction of the wave motion

with times when they were shot (see caption to the figure). As before, three stages of the scenario can be distinguished.

The main difference between this and the case, when a thin plate was used as obstacle (see Fig. 3.14), lies in the fact that the arising jet is directed at some angle with respect to the horizon (frames 5–7). An increase of the obstacle length results in the formation of flow in the lower layer above the obstacle top; it is directed upstream. The pattern of the flow separation is similar to that over a backward step when an extended separation zone prevails. This causes the inclination of the jet. We can see that lighter fluid from the upper layer entrained by the jet is not translated to large depth because the attached vortex is not strong. So, the mechanism of the generation of the reflected wave is not "switched on" and a reflected internal solitary wave is not formed. Another characteristic feature of the flow pattern that is connected with the large length of the obstacle is the appearance of a bulge on the interface (frame 9). The jet still exists and the bulge is caused by the generation of another vortex pair due to flow instability. These results confirm the already-formulated conclusion about the influence of the obstacle length on the process of interaction of the internal solitary wave with the extended obstacle, namely, the greater the obstacle length is, the larger will be its blocking effect. The influence of an increase of the length manifests itself in the fact that the topographic effect of the obstacle becomes more pronounced, and the dissipative losses of the energy rise.

Scenario 3. Wave Blockage. A larger value of the coefficient k_{int} was reached in experiment 2412. The parameters of the experiment are presented in Table 3.3. The

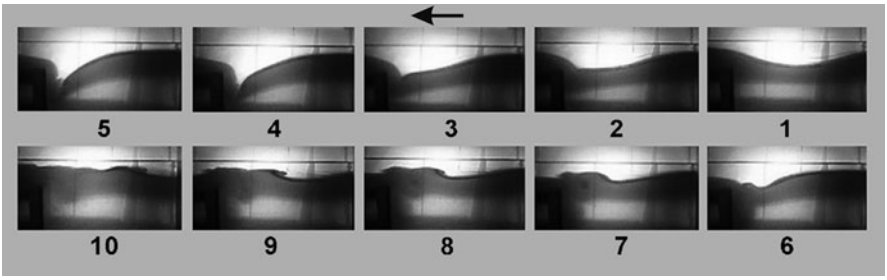

Fig. 3.23 Sequence of photographs showing the process of wave blockage of internal solitary wave by an extended obstacle [The right end of the obstacle is seen on the very left of each frame.] (experiment 2412). (Note the different dyeing of the layers.) Frames are consecutively numbered with times when they were shot as follows: 1 (11.5 s), 2 (12.6 s), 3 (13.0 s), 4 (13.9 s), 5 (14.8 s), 6 (16.4 s), 7 (18.5 s), 8 (20.5 s), 9 (19.3 s), and 10 (23.3 s). (Camera was switched on at $t = 0$ s.) Wave motion is from right to left (see *arrow*)

amplitude of the incident wave was 7.3 cm; so, the parameter of interaction is $k_{\text{int}} = 0.84$, that is, it is taken to be close to 1.0. Fig. 3.23 shows ten snapshots of the wave when passing the long obstacle in consecutive order as before with corresponding times when they were shot (see caption to figure). It is significant that the lower layer was dyed. This allows one to consider some peculiarities of the pattern of the flow.

Evidently, shoaling and sharpening of the leading face occur and a sharp peak appears on the interface before the upstream side of the obstacle (frame 2). This peak further develops and a thin vertical jet is generated as before (frames 3, 4). On frame 5, one can observe the development of a jet instability. After cessation of the motion of the jet, lighter fluid rises (frame 6) and a mushroom-like structure is formed on the interface (frame 7, 8). The left part of the structure moves downstream over the obstacle and, due to flow instability above the obstacle, a series of bulges and troughs arises (frames 9, 10). Their origin is likely connected with the development of Kelvin–Helmholtz instabilities. These perturbations move slowly downstream. They are responsible for the formation of the wave train. Notice that fission and disintegration of internal solitary waves can be described by the K–dV equation as these waves propagate to regions of decreasing depth on the shelf zone (Djordjevic and Redekopp 1978). The right part of the mushroom-like structure quickly moves upstream. The formation of a baroclinic bore can be seen which moves more rapidly than the lower layers of the fluid. The fluid in the bore is heavier than the surrounding fluid. Then the bore is broken, heavier fluid falls down and is mixed with the surrounding fluid (frame 9). We conclude from this analysis of the frames that a transmitted wave cannot be generated in such a situation. Indeed, the gauge records only a wave train. However, the reflected wave must be seen.

The estimation of the ratio between the energy of the incident wave and reflected wave is $E_{\text{ref}}/E_{\text{inc}} = 0.27$. Hence, an appreciable part of energy of the incident wave is spent on the generation of the reflected wave. Of the entire signal, only a wave train passes over the extended obstacle. The wave energy contained in the train is not high. We conclude this from consideration of the shape of the train. In Fig. 3.24,

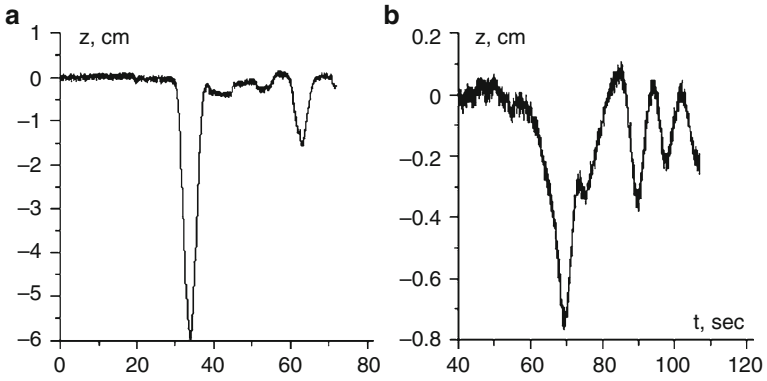

Fig. 3.24 (**a**) Displacement of the interface caused by the incident wave and (**b**) dispersive train behind the extended obstacle (experiment 0604)

as an example, the interface displacements caused by the incident internal solitary wave (panel a) and by the dispersive train of the wave (panel b) behind the obstacle are presented. The parameters of experiment 0604 are presented in Table 3.3. We see that the wave amplitude in the train is fairly small; so, the wave energy is even smaller and negligible. It should be noticed that dissipation in the process of interaction of a strong internal solitary wave with an extended obstacle, whose length is of the same order as the wavelength, is significant.

As a conclusion, we state that:

1. The process of interaction of an internal solitary wave with an extended obstacle is similar to the process of its interaction with a thin plate. Differences are in the quantitative characteristics.
2. It is shown that for an extended obstacle, blocking the flow over the obstacle is more effective, and an appreciable part of energy of the incident wave is spent on the generation of a reflected wave.
3. At moderate coefficients of interaction, the main distinction from the case, when a thin plate was used as an obstacle, lies in the fact that the arising jet is directed at some angle with respect to the horizontal; it does not penetrate to a large depth; so, the lighter fluid from the upper layer is not displaced into larger depths. The mechanism of generation of a reflected wave is not "switched on" and a weak reflected internal solitary wave is formed. Another characteristic feature of the flow pattern connected with the large length of the obstacle is the appearance of the bulge on the interface. We can see that a jet still exists and a bulge, caused by the generation of another vortex pair forming above the obstacle due to the instability of the flow, continues to develop because the obstacle length is large.
4. At high coefficient of interaction, after cessation of the motion of the jet, a lighter fluid moves upward and a mushroom-like structure is formed on the interface. The downstream part of the structure moves over the obstacle and, due to the

instability of the flow above the obstacle, a series of bulges and troughs arises. These perturbations slowly move downstream, which cause the formation of the dispersive wave train. The other part of the mushroom-like structure quickly moves upstream. This is likely the cause for the formation of a baroclinic bore that moves more rapidly than the lower layers of the fluid. The fluid in the bore is heavier than the surrounding fluid. The bore breaks when the heavier fluid falls down and mixes with the surrounding fluid. We conclude that a transmitted wave cannot be generated in such a situation. Indeed, the gauge records only a train of waves. However, the reflected wave is evident.

5. Dissipation in the process of interaction of a strong internal solitary wave with an extended obstacle is much larger than for an interaction with a narrow obstacle.

3.3 Internal Wave Transformation Caused by Lateral Constrictions

The spectrum of the internal wave field in lakes is continuous ranging from low-frequency basin scale to the buoyancy frequency (Wüest and Lorke 2003). Field observations show that the rate of decay of basin-scale internal waves is appreciably greater than that by internal dissipation (Horn et al. 2001). The nonlinear energy transfer from the basin-scale internal waves to the short-period motions is an important mechanism to enhance mixing and dissipation. The overturning and breaking of internal waves in the process of their interaction with lake boundaries and topographic features are the major mechanisms. Sills play a dominant role in enhancing the vertical exchange and dissipation of wave energy in multibasin lakes. Other mechanisms resulting in an increase of mixing and dissipation are concerned with the intensification of currents and the growth of shear stresses in constrictions. Besides, large-scale displacements of the water masses in the constrictions intensify the local diapycnal mixing due to the increased internal shear and bottom friction (Kocsis et al. 1998). Evidently, transformation, shoaling, and breaking of internal waves can be caused by constrictions. Breaking internal waves, which propagate through a constriction, were studied by Troy and Koseff (2005). The planar laser-induced fluorescence technique was used to produce calibrated images of the wave-breaking process. Experiments were made in a channel with a weakly constricted section. The width decreased from 30 cm to 11 cm over a distance of 1.3 m. It was demonstrated that the waves break due to the strongly modified shear stress distribution and associated instability originating from the high-shear regions of wave crests and troughs. The shear instability closely resembled Kelvin–Helmholtz instability, with a row of billows rolling up into well-known structures (“cat’s eye”) and disintegrating the wave that passed. Note that the influence of sills on a two-layer flow differs from the effect of constrictions, since a submerged sill is only in direct contact with the lower layer, and its influence on the upper layer is indirect. Alternatively, the constriction is in direct contact with both layers. The two-layer

fluid flow through constrictions was analyzed by Wood and Simpson (1984) and Armi (1986). Hydraulic analyses of Boussinesq and non-Boussinesq types in two-layer flows were conducted by Lawrence (1990). Nevertheless, the interaction of nonlinear internal waves in basins with constrictions has so far not been adequately studied.

From simple continuity arguments written in the reference frame moving with the internal solitary wave, we obtain

$$c\,h_1 = (c - u_1(x))\,(h_1 + \eta(x)), \tag{3.15}$$

$$c\,h_2 = (c + u_2(x))\,(h_2 - \eta(x)). \tag{3.16}$$

Here, h_1 and h_2 are the thicknesses of the upper and lower layers, respectively, $\eta(x)$ is the displacement of the interface (wave profile), $u_1(x)$and $u_2(x)$ are the velocities in the upper and lower layers, and c is the speed of the internal solitary wave. It was assumed that the inequality $a/L^* << 1$ is obeyed, where $L^*$is the wave half-length (see Bogucki and Garrett 1993). Equations (3.15) and (3.16) can be also written in the form

$$c\,\eta(x) = u_1(x)\,(h_1 + \eta(x))\,, \tag{3.17}$$

$$c\,\eta(x) = u_2(x)\,(h_2 - \eta(x)), \tag{3.18}$$

or

$$c\,a = u_1(h_1 + a), \tag{3.19}$$

$$c\,a = u_2(h_2 - a), \tag{3.20}$$

if we consider the cross section coinciding with the wave crest having amplitude a. Consider the Froude number $Fr = u/\sqrt{gH}$. It represents the parameter determining the existence of subcritical and supercritical flow regimes. Traditionally, it is equal to the ratio of the velocity to the speed of infinitesimally small disturbances. It was proposed by Wood and Simpson (1984) and Armi (1986) to consider the composite Froude number for two-layer flows, $G^2 = Fr_1^2 + Fr_2^2$, in order to determine the critical regime. Here, $Fr_i^2 = u_i^2/(g'\,h_i)$ for each layer where h_i is the thickness of layer i. Moreover, $g' = (\Delta\rho/\rho)g$, and $\sqrt{g'\,h_i}$ is the speeds of long internal waves.

Scrutiny of equations (3.15) and (3.16) shows that they are invalid when $u_1 > c$ or $|u_2| > c$; so, in these cases, a solitary wave does not exist. In a given situation, it is reasonable to consider the speed of the solitary wave as a characteristic parameter instead of the velocity of infinitesimally small disturbances. So, we also introduce the analogs for the Froude numbers $Fr_1^* = u_1/c$, $Fr_2^* = u_2/c$. It is shown by Bogucki and Garrett (1993) that the phase speed of an infinitely long, infinitesimally small wave in a two-layer system is

$$c_0 = \left(g' \frac{h_1 h_2}{h_1 + h_2} \right)^{1/2}. \tag{3.21}$$

Evidently, if $h_2 >> h_1$, this becomes $(g' h_1)^{1/2}$. If we consider finite amplitude waves, then we can take this speed instead of c_0 as characteristic parameter. So, we then consider the Froude number $Fr_i^* = u_i/c$, where c is the wave speed which accounts for the nonlinearity effects. For example, for shallow water and weakly nonlinear waves

$$c = c_0 \left(1 + \frac{1}{2} \frac{a(h_2 - h_1)}{h_2 h_1} \right), \tag{3.22}$$

whereas Ostrovsky and Grue (2003) proposed

$$c^2 = \frac{g'(h_1 + a)(h_2 - a)}{H} \tag{3.23}$$

for the calculation of the speed of strongly nonlinear waves, provided the density difference, $\Delta\rho \ll \rho_1$, is small.

Comparison of (3.23) with (3.21) shows that this formula differs from the linear long-wave model speed only by the fact that the actual depths at the wave peak $(h_1 + a)$ and $(h_2 - a)$ are taken instead of the nonperturbed depths h_1 and h_2. It was found that results obtained by using (3.23) are in complete agreement with observations of strongly nonlinear waves.

From (3.19) and (3.20), we deduce

$$\mathrm{Fr}_1^* = \frac{u_1}{c} = \frac{a}{h_1 + a}, \quad \mathrm{Fr}_2^* = \frac{u_2}{c} = \frac{a}{h_2 - a}. \tag{3.24}$$

Thus, the analog of the composite Froude number G_a is

$$\mathrm{G}_a^2 = \left(\mathrm{Fr}_1^*\right)^2 + \left(Fr_2^*\right)^2 = \left(\frac{u_1}{c}\right)^2 + \left(\frac{u_2}{c}\right)^2 = \left(\frac{a}{h_1 + a}\right)^2 + \left(\frac{a}{h_2 - a}\right)^2. \tag{3.25}$$

If the composite Froude number is larger than unity, waves cannot propagate in such systems and the considered flow cannot exist.

We can also estimate the energy contained in internal solitary waves. According to Bogucki and Garrett (1993) and Michallet and Ivey (1999), the total energy of a long wave is estimated as

$$E = g\Delta\rho \int_0^{\lambda} \eta^2(x) dx = cg\Delta\rho \int_{t_0}^{t_1} \eta^2(t) \mathrm{d}t.$$

Here, λ is the wavelength and t_1 and t_2 are the times of the passage of the front and end of the wave at fixed position x. Hence, $E \approx Cg\Delta\rho a^2\lambda$, where C is a constant. Let L_c be the length of the constriction and assume that its extension is not large; so, we take it to be justified to neglect the dissipation at such a short distance. Then, the energy is conserved, implying that

$$a^2\lambda B = a_0^2\lambda_0 B_0. \tag{3.26}$$

Here, a, λ, B and a_0, λ_0, B_0 are amplitude, wavelength, and channel width at the constriction and at a reference cross section distant from the constriction. When the width decreases, the wave amplitude increases, and the energy per unit length (this is the energy density) increases, but the total energy is not changed. Approximately, $E \cong Cg\Delta\rho a^2\lambda$, where C is a constant. For example, for the K–dV theory, $C = 4/3$. If we suppose that the energy flux is uniform across the flow in the horizontal direction, then, the total energy of the internal solitary wave in the basin is given by $E \cong Cg\Delta\rho a^2\lambda \cdot B$ and the energy density (per unit length) is $e \cong Cg\Delta\rho a^2 B$. Analysis of the experimental data shows that the wavelength is changed in the constriction but these wavelength changes are not large. So, a rough estimation shows that the change of the wave amplitude in the constriction is basically defined by the variation of the basin width.

Experimental investigations of the interaction of strongly nonlinear internal waves with constrictions of sinusoidal shape were carried out. The methodologies described in Sect. 3.2 were used for the creation of the two-layer salt stratification, the generation of internal solitary waves, the measurement of the parameters of waves by gauges, and for processing the experimental data. The boundary between the layers (or the upper layer) was dyed. Use of a digital camera allowed estimation of the parameters of internal solitary waves (measurement of the amplitude) and, subsequently, comparison with data obtained by the gauges.

Experiments were carried out with two types of constrictions of the sinusoidal shape which is described by the formula

$$f(x) = \frac{B_c}{2}\left[1 + \sin\left(\frac{2\pi x}{L_c} - \frac{\pi}{2}\right)\right].$$

Here, B_c is the minimum horizontal dimension of the constriction transverse to the wave propagation and L_c is the constriction length. Such a shape was used in order to ensure smooth coupling with the lateral wall of the channel. The first model (panel *a* in Fig. 3.25) has $L_c = 120$ cm and $B_c = 19.5$ cm which is close to the half-width of the channel, $B_0 = 40$ cm. The second model (panel *b* in Fig. 3.25) has $L_c = 97$ cm and $B_c = 32$ cm.

The basin geometry and equipment employed are presented in Fig. 3.26 (side view *a* and top view *b*). Locations of the gauges are shown schematically. The distances between them can be varied. Sometimes gauges are located in the cross section of the constriction. In a number of cases, two gauges were at the same long-

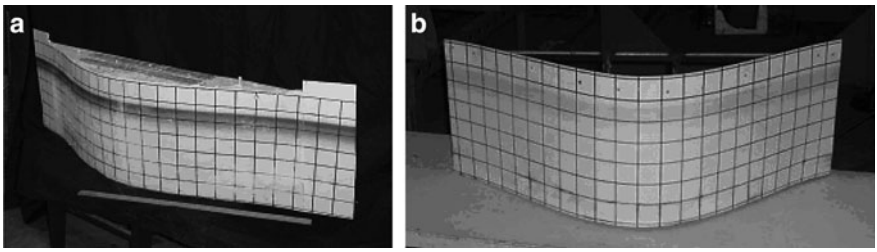

Fig. 3.25 Models of constrictions: (**a**) moderate thickness, (**b**) model of large thickness

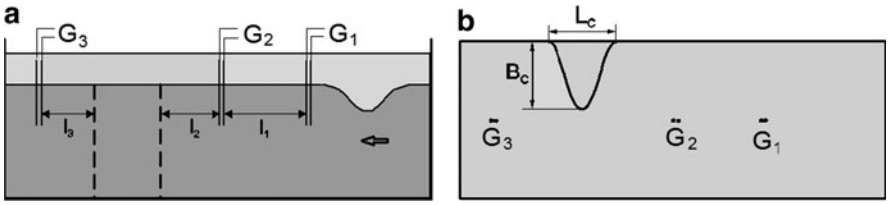

Fig. 3.26 Principal sketch of the channel flume for the two-layer wave experiments, (**a**) view from the side and (**b**) from the top. G_1, G_2, G_3 show double wire capacity gauges with distances l_1, l_2, l_3 as indicated. Cylindrical sinusoidal constriction with length L_c and breadth B_c is as indicated. The double arrow shows the direction of wave propagation

Table 3.4 Parameters of the experiments with the first model of the constriction

No. exp.	H, [cm]	z_c, [cm]	δ, [cm]	h_2, [cm]	a, [cm]
2610	30	27.2	0.54	27.2	6.2
0211	30	27.8	0.45	27.8	5.3
0411	30	27.9	0.3	27.9	8.2

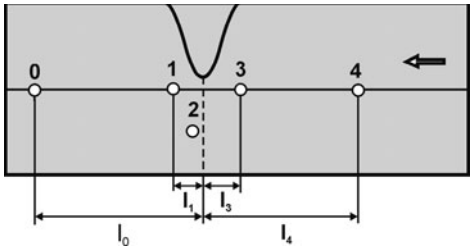

Fig. 3.27 Top view of the wave channel with placements of gauges G_0, G_1, G_2, G_3, G_4 in the basin with relative distances equal to $l_0 = 92$cm, $l_1 = 31$ cm, $l_3 = 29$cm, and $l_4 = 103$ cm (experiment 2610).

axis position but shifted in the lateral direction. In the experiment 2610, the model shown in Fig. 3.25a was used. The parameters of the experiments are listed in Table 3.4.

The arrangement of the gauge locations relative to the constriction is displayed in Fig. 3.27. Here, gauges G_0, G_1, G_3, G_4 are positioned along the mid-axis of the basin. Distances are as shown in the figure caption. Gauge 2 was located in the middle of the distance between the lateral wall and the top of the constriction, shifted by 1 cm downstream. The double arrow indicates the direction of wave

propagation. The measured amplitudes of the solitary wave, recorded by the gauges, are listed in Table 3.5.

It is evident from these registrations that the wave amplitude experiences appreciable changes. Gauge G_3 is located immediately before the constriction and, obviously, an influence of the wave profile can already be recognized. The flow is delayed at this place which is exemplified by the growth of the wave amplitude from gauge G_4 to gauge G_3. This proves that the flow is blocked. In the central part of the constriction, the flow accelerates and the amplitude decreases. Gauge G_1, as gauge G_3, is located at the half-slope position in the region of flow widening and the wave amplitude has further decreased. The wave energy is distributed over a larger width. Unfortunately, determination of the wave speed in this inhomogeneous regime has not been possible; we had to limit measurements to the recording of wave amplitudes. Estimation of the analog of the composite Froude number shows that $G_a = 0.57$. Hence, a certain flow blocking occurs but no reflected wave was discernable that would have been recorded by gauges, neither by gauge G_3 nor by gauge G_4. Note that we estimate the value of the composite Froude number by using information about the wave amplitude before the constriction. To consider the regime within the constriction, it is reasonable to use the wave amplitude within the constriction, for example, the value measured by gauge G_3 located on the axis of the basin. Then, the composite Froude number becomes $G_a = 0.85$. In Fig. 3.28, a series of photographs showing the wave transformation is displayed. The corresponding times when the shots were taken are listed in the figure caption. It can be seen that there is no shoaling of the leading face of the wave. When the back face of the wave enters the constriction, it steepens (frames 3, 4). Moreover, when the wave is close to the throat of the constriction its crest is flattened and a tendency to wave splitting can be observed on frames 3 and 4. Once the wave has passed the constriction, the upper layer becomes thinner. This thinning is concerned with the uneven passing of the wave through the constriction. The photos show that the back face of the wave steepens a little. This is likely the result of the appearance of flow instability.

In experiment 0211, an internal solitary wave of smaller intensity was generated. The parameters of the experiments are collected in Table 3.4. Antecedent experience has shown that the reconstruction of the flow field is observed when the wave enters and passes through the constriction. To capture the main features of this process, the locations of the gauges were changed. The arrangement of the gauge locations relative to the constriction is presented in Fig. 3.29. Here, gauges G_0 and G_4 are on the axis of the basin. Gauge $G_1$is located at the middle of the distance

Table 3.5 Amplitudes measured by gauges in experiments with the first model of constriction

No. exp.	Amplitude [cm]				
Gauge	0	1	2	3	4
2610	3.4	5.1	6.4	7.3	6.2
0211	3.5	3.9	5.3	7.9	5.3
0411	4.2	8.0	8.1	>10.0	8.2

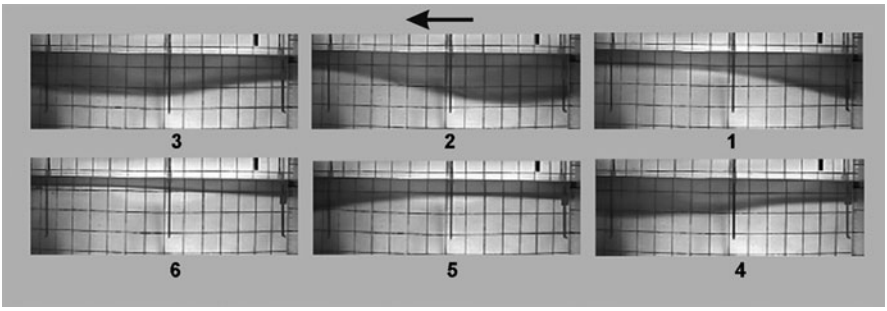

Fig. 3.28 (Experiment 2610). Six consecutive side video snapshots (from 1 to 6) of the interaction of an internal solitary wave with a constriction at moderate composite Froude number. The *arrow* indicates the direction of the wave propagation. The shots have been taken as follows:

Frame	1	2	3	4	5	6
Time of shot (sec)	61	64	67	68	70	76
Time difference (sec)	3	3	1	2	6	

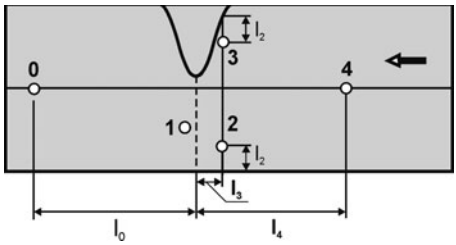

Fig. 3.29 Top view of the wave channel with placements of gauges G_0, G_1, G_2, G_3, G_4 with relative distances equal to $l_0 = 61$ cm, $l_2 = 5$ cm, $l_3 = 26$ cm, and $l_4 = 100$ cm. The *double arrow* indicates the direction of wave propagation (experiment 0211)

between the lateral wall and the maximum of the constriction, shifted by 2 cm downstream. Gauges G_2 and G_3 are located at some distance from the maximum constriction and shifted from the basin axis to measure the change of the interface displacement across the basin. Distances between gauges and the cross section of the constriction peak and boundaries are listed in the figure caption.

The measured amplitudes of the solitary waves recorded by the gauges are listed in Table 3.5. Evidently, the wave amplitudes measured by the various gauges differ substantially from one another. The table shows that the amplitude of the wave passing the constriction (gauge G_2) is the same as that of the incident wave measured by gauge G_4. This coincides with results of experiment 2610. On the other hand, the wave amplitude measured before the constriction (gauge G_3) is substantially greater than that of the incident wave (gauges G_2 and G_3 are located close to the cross section where the constriction has half its maximum value). This proves that the flow is blocked. So, the flow field reconstruction occurs when the

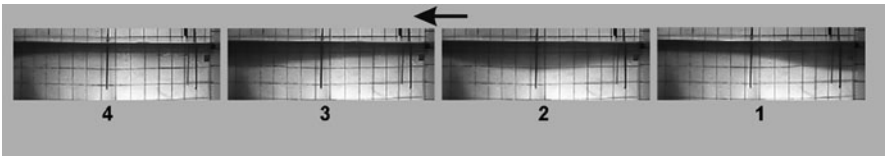

Fig. 3.30 Four consecutive snapshots (from 1 to 4) of the interaction of an internal solitary wave with constriction at moderate composite Froude number (experiment 0211). The *arrow* indicates the direction of the wave motion

internal solitary wave goes through the constriction. This manifests itself as a change of the wave amplitude in the crosswise direction before the constriction. Comparison with the results of experiment 2610 demonstrates that the wave amplitude grows with the removal of the gauge from the central axis. Incidentally, in experiment 2610, the amplitude of the incident wave was larger and that at the central axis was equal to 7.3 cm. In experiment 0211, the incident wave was weaker but the wave amplitude measured by gauge G_3 located close to the constriction was nevertheless as large as 7.9 cm. Note that gauge G_4 did not record the reflected wave; so, in this regime the reflected wave is not generated. This is confirmed by the photographs of Fig. 3.30. Indeed, no steepening of the back face of the wave is discernable. Moreover, the thickness of the upper layer is not changed after the wave passes the constriction when compared with experiment 2610 in which thinning of the upper layer in the region occurred somewhat downstream of the maximum constriction (Fig. 3.28, frame 6). The composite Froude number for this regime is equal to 0.55. This is only a little smaller than $G_a = 0.57$ at which a small trace of instability at the steepening of the back face of the wave was observed. To consider the regime within the constriction, as in experiment 2610, the wave amplitude within the constriction on the axis of the basin is estimated by using the data of gauges G_2 and G_3 under the assumption that the distribution of the amplitude in the cross section varies linearly. With $a \approx 6.6$ cm, we obtain $G_a = 0.65$.

The increase of the amplitude of the incident internal solitary wave leads to appreciable changes in the pattern of the wave passing through the constriction. In experiment 0411, the amplitude of the incident wave was equal to 8.2 cm. The parameters of the experiments are shown in Table 3.4. The distribution of the gauges was the same as in experiment 0211, as shown in Fig. 3.29. The measured amplitudes of the solitary wave recorded by the gauges are listed in Table 3.5. As in the previous experiment with the same distribution of the gauges, it can be seen that the amplitude of the wave measured by the gauges is considerably changed. As the data of Table 3.5 show, the amplitude of the wave, measured by gauge G_2 in the constriction, is close to the amplitude of the incident wave measured by gauge G_4. This is analogous to the results obtained in experiment 2610. On the other hand, the amplitude of the wave, measured ahead of the constriction (gauge G_3), is considerably greater than that of the incident wave. An intensive growth of the amplitude measured by gauge G_3 leads to the conclusion that considerable blocking of the flow must take place. The flow field is radically changed when the internal

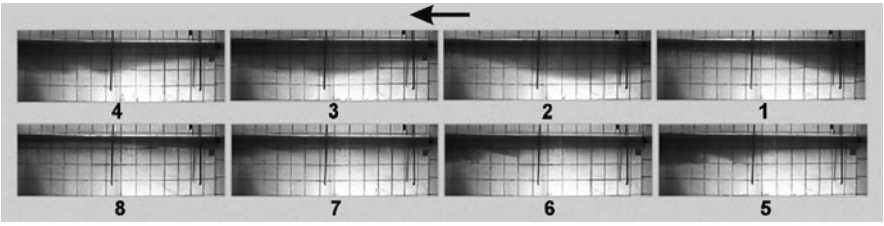

Fig. 3.31 (Experiment 0411). Eight consecutive side view snapshots (from 1 to 8) of the interaction of an internal solitary wave with a constriction at the critical composite Froude number. The *arrow* indicates the direction of the wave motion. The shots have been taken as follows:

Frame	1	2	3	4	5	6	7	8
Time of shot (sec)	6	9	11	12	13	14	15	23
Time difference (sec)	3	2	1	1	1	1	8	

solitary wave goes through the constriction. A comparison with the results of experiment 0211 demonstrates that the wave amplitude conspicuously grows with the shift of the gauge away from the central axis. The growth was so large that the amplitude was no longer indicated by the gauge; it was estimated from the digital photographs and approximately equal to 11.5 cm. We see again that the interface in the cross section before the constriction is tilted relative to the basin axis. An analog to the composite Froude number was estimated with value $G_a = 0.8$. If we estimate the composite Froude number within the constriction, that is, in the cross section where gauges 2 and 3 are located, and use the average amplitude, then $G_a = 0.97$. This means that the flow is critical somewhere in the considered cross section and the wave characteristics should radically change when it passes through the constriction. This is confirmed by the analysis of the series of photographs, displayed in Fig. 3.31, which also states details when shots were taken in the figure caption.

It can be seen that shoaling of the leading face of the wave occurs when the wave crest is close to the maximum constriction (frame 3). Fission of the solitary wave into two parts occurs. It is caused by the growth of the velocities in the upper and lower layers and the development of a Kelvin–Helmholtz instability. A vortex with horizontal axis is formed at the interface (frame 4). Then, the first part of the wave continues to move but the motion of the remainder is considerably retarded, its top slowly moves upward, and is then slightly translated downstream. A new vortex with horizontal axis is formed on the back face of the second part (frame 5). As a consequence, the interface takes a rugged form (frame 6) caused by the formation of turbulent vortices or boluses. A similar system of boluses was observed in Helfrich's (1992) experiments which were devoted to studying internal solitary waves breaking on a uniform slope. There, it was demonstrated that shoaling of a single solitary wave resulted in wave breaking on a slope due to developing instabilities and production of multiple turbulent boluses that propagated upward the slope. An important role of boluses is in transporting sub-pycnocline water upslope past the pycnocline–bottom intersection (Bourgault et al. 2005). It can be seen that due to the boluses sub-pycnocline water transport takes place in the given experiments.

Note that thinning of the upper layer is observed as a consequence of the existence of a supercritical regime of the flow. Thus, instabilities develop and result in breaking of this solitary wave. Fission into two parts occurs, the first (smaller) part continues its motion in the downstream direction while the remainder is trapped and degenerates.

Increase of the amplitude of the internal solitary waves results in the development of flow instability when the wave passes through the constriction. The criterion defining the flow regime is the analog of the composite Froude number. As indicated earlier, conservation of energy of the solitary wave can be expressed by the relationship $a^2\lambda B_c = a_0^2\lambda_0 B_0$. For this to hold true it is assumed that if the length of the constriction is not large, dissipation can be neglected. When the width is varied, the amplitude and energy per unit length, that is, the energy density $e \cong Cg\Delta\rho a^2 B$, are varied too but the total energy is not changed. Scrutiny of the experimental data shows that the wavelength changes in the constriction: changes in the length of waves are comparatively small, especially when compared with the change of the amplitude to the second power. On the other hand, determination of the wavelength is a rather sophisticated problem if the wave propagates under unsteady conditions. Nevertheless, to improve the estimation, the relationship between the wave amplitude and length based on a balance between steepening and dispersion effects (Bogucki and Garrett 1993), obtained for long waves, $a(L^*)^2 \cong const$, can be used. So, the character of the amplitude variation with a change in the width of the channel can roughly be described by the formula

$$a = \frac{a_0}{(1-r)^{2/3}}, \tag{3.27}$$

where r is the ratio between the remaining opening width at the position of maximum narrowing of the channel, $(B_0 - B_c)$, and the reference width of the basin B_0, $r = (B_0 - B_c)/B_0$. This is analogous to the degree of blocking introduced earlier by Wessel and Hutter (1996). We can approximately estimate the change of the Froude number with the variation of the width of the channel by substituting expression (3.27) into (3.25).

As is evident from the above, a critical value of the analog of the composite Froude number can be achieved not only by the growth of the amplitude of the internal solitary wave but by variations of the basin constriction as well. This leads to a critical regime for waves of moderate amplitude. In experiment 1312, the amplitude of the incident wave is equal to 3.9 cm. The parameters of the experiments are presented in Table 3.6. The chosen arrangement of the locations of the gauges relative to the constriction is sketched in Fig. 3.32. The measured amplitudes of the solitary waves recorded by the gauges are listed in Table 3.7.

A principal distinction of this experiment from the previous ones is to use the second model of the constriction (Fig. 3.25b). The length is somewhat shorter than in the first model but the transverse size is substantially larger. The gap between the maximum of the constriction and the lateral wall of the basin is 8 cm. Note that in experiment 0211, the amplitude of the wave was equal to 5.3 cm, that

Table 3.6 Parameters of the experiments when the second constriction is applied

No. exp.	H, [cm]	z_c, [cm]	δ, [cm]	h_2, [cm]	a, [cm]
1312	30	28.4	0.3	28.4	3.9
0712	30	27.8	0.4	27.8	8.0
0501	30	26.9	0.55	26.9	7.0

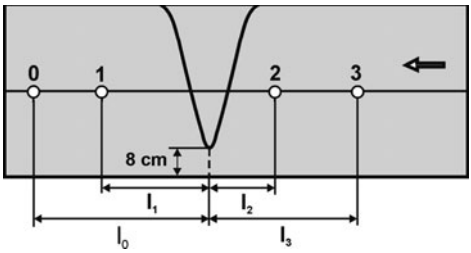

Fig. 3.32 Top view of the arrangement of the placements of the gauges with distance $l_0 = 92.5$ cm, $l_1 = 24.5$ cm, $l_2 = 57$ cm, and $l_3 = 100$ cm in experiment 1312 with large constriction. The *double arrow* indicates direction of wave propagation

Table 3.7 Amplitudes measured by gauges in experiments when the second constriction model is applied

No. exp.	Amplitude [cm]			
Gauge	0	1	2	3
1312	1.1	3.0	3.8	3.9
0712	2.6	3.8	6.3	8.0
0501	2.7	3.2	6.7	6.95

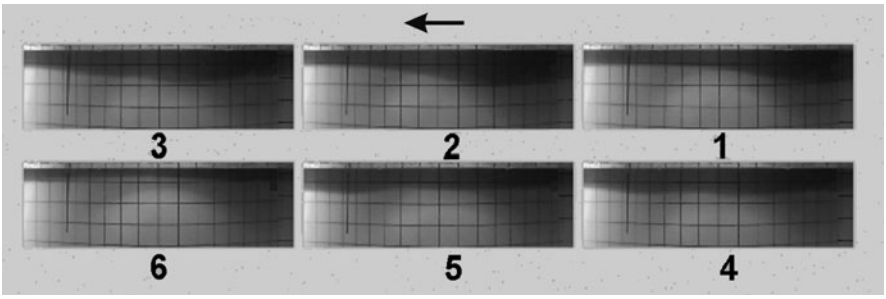

Fig. 3.33 (Experiment 1312). Six consecutive side view shots (from 1 to 6) of the interaction of the internal solitary wave with large constriction at high composite Froude number. The *arrow* indicates the direction of the wave propagation. The shots have been taken as follows:

Frame	1	2	3	4	5	6
Time of shot (sec)	5	7	9	10	11	21
Time difference (sec)	2	2	1	1	10	

is, appreciably greater than in this experiment. However, in experiment 0211, we did not observe visible changes in the form of the wave during its passing through the constriction; by contrast here, appreciable changes of the form of the wave can be observed (see Fig. 3.33). We see that the solitary wave is fissioned into two parts (frames 3–5). At the end of the process, the upper layer is thinned (frame 6). The

estimation of the composite Froude number at the section, where gauge G_3 is located, shows that the flow is stable ($G_a = 0.74$). Using formula (3.27), an estimate for the amplitude change can be found. The estimation of the composite Froude number in the zone of maximum constriction yields $G_a > 1$, that is, the flow is unstable in the constriction. This is evident from Fig. 3.33 where wave fission can clearly be identified.

A series of additional experiments confirms that an increase of the amplitude of the internal solitary wave leads to an increased development of instability, yielding fission of the wave into two parts, and subsequent thinning of the upper layer. The reconstruction of the flow field is more pronounced when the amplitude of the internal solitary wave is large. In experiment 0712, the wave amplitude was 8.0 cm. The same model of the constriction as in Fig. 3.25b was used. The parameters of the experiments are presented in Table 3.6. The arrangement of the gauge locations relative to the constriction is sketched in Fig. 3.34. Gauge G_2 was located 10 cm downstream from the largest constriction in the middle of the section. Measured amplitudes of solitary waves are presented in Table 3.7.

The displacement time series of the interface recorded by gauges G_3, G_2, G_1 are displayed in Fig. 3.35a–c, respectively. Gauge G_3 is located at the upstream end of the constriction. After the passage of the conspicuous incident wave through this section, the motion of the interface displacement is reduced to a state of only 3 cm. This can be seen in Fig. 3.35a, when the reading of gauge G_3 shows only weak oscillations during approximately 7 s. This occurs close to the time of the passage of

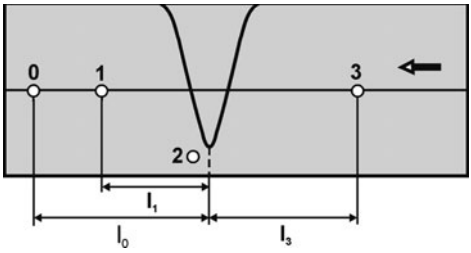

Fig. 3.34 Top view of a scheme of placement of gauges with distances $l_0 = 87$ cm, $l_1 = 31$ cm, and $l_3 = 51$ cm in experiment 0712. The *double arrow* indicates the direction of wave propagation

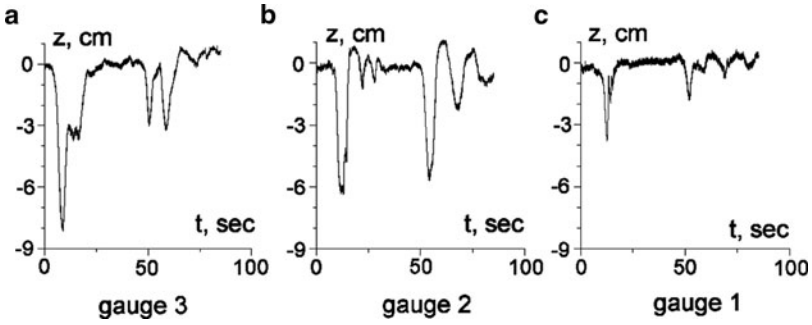

Fig. 3.35 Displacements of interfaces recorded by gauges: (**a**) – gauge G_3, (**b**) – gauge G_2, (**c**) – gauge G_1 (experiment 0712)

a solitary wave recorded by the gauge. It was shown earlier that at this moment the wave amplitude before the constriction (somewhat downstream of the location of gauge G_3) suddenly increased because the flow became unstable in the constriction. Actually, the analog of the composite Froude number corresponding to the section where gauge G_3 is located is 0.77. The estimation of G_a close to the largest constriction yields $G_a > 1$. The development of the instability leads to the generation of the wave train recorded by gauge G_2 as oscillations of the interface after the solitary wave had passed the position of maximum constriction (see Fig. 3.35b). Then, the wave amplitude decreases (down to 3.8 cm, see Fig. 3.35c) in the section in which gauge G_1 is located because the wave propagates into the diffuser part of the constriction.

A reflected wave is generated when the amplitude of the solitary wave is large. The peak recorded by gauge G_3 at $t = 50.5$s corresponds to this wave (see Fig. 3.35a). Note that the second peak (see Fig. 3.35a) at $t = 58.7$s is caused by the transmitted wave, which was reflected from the downstream wall of the channel and passed back through the constriction. The large amplitude, recorded by gauge G_2 at $t = 54.5$, corresponds to the collision of the solitary wave which passed through the constriction and is reflected from the downstream wall of the tank with the wave signal that reflected from the constriction and then reflected from the upstream wall of the tank. The small elevation of the displacement time series above the line $z = 0$ and beyond $t = 54.5$ s in Fig. 3.35b is connected with the thinning of the upper layer as discussed above. It should be noted that the flow pattern is appreciably more complicated than that discussed earlier. This is so because of the three-dimensionality of the flow patterns, and pointwise measurements cannot reproduce all the flow structures. These results of the measurements of the interface displacements at the gauges are confirmed by inspection of the photographs displayed in Fig. 3.36.

It can be seen that a flow instability is the triggering mechanism of the fission of the solitary wave into two parts (frame 2). After this splitting, the leading part

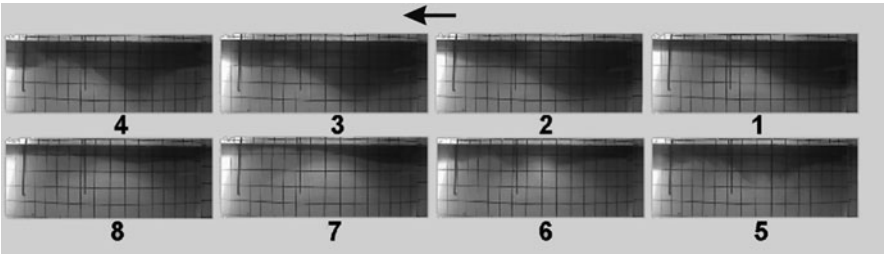

Fig. 3.36 (Experiment 0712). Eight consecutive snapshots of photographs (from 1 to 8) demonstrating the fission of an internal solitary wave. The *arrow* indicates the direction of the wave propagation. The shots have been taken as follows:

Frame	1	2	3	4	5	6	7	8
Time of shot (sec)	58	60	61	62.5	64	66	72	75
Time difference (sec)		2	1	1.5	1.5	2	6	3

continues to propagate downstream, while the remainder (the larger part) is trapped (frame 3). In the region of wave fission, a series of vortices with horizontal axes are generated. This is due to the development of a Kelvin–Helmholtz instability. The remainder of the wave does not move downstream as a movement to higher elevation (frame 4). The process of fission continues and the stagnant remaining part is broken up again; consequently, a new series of bulges (or boluses Helfrich (1992)) can be seen on frames 4 and 5. These boluses move downstream. Thinning of the upper layer sets in after the passage of boluses through the throat. This is recorded by gauge G_2 (see Fig. 3.35). As time proceeds, new perturbations pass through the constriction. They are also recorded by gauge G_2 as a wave train.

The three-dimensional character of the process of the internal solitary-wave passage through the constriction is especially evident when analyzing the surface flow pattern in the extending diffuser part of the constriction. Experiment 0501 was carried out to study features of surface flow in this region. The parameters of the experiments are presented in Table 3.6. A sketch of the gauge locations relative to the constriction is shown in Fig. 3.32 (experiment 1312), but the distances between the gauges and cross section of the largest width of constriction are now $l_0 = 170$ cm, $l_1 = 96$ cm, $l_2 = 57$ cm, and $l_3 = 76$ cm. The measured amplitudes of the interface displacements recorded by the gauges are listed in Table 3.7 and their time series are displayed in panels (a) to (c) of Fig. 3.37.

After the passage of the incident wave a conspicuous reduction of the motion is recorded at gauge G_3; it is similar to experiment 0712. At this instance, an increase of the wave amplitude takes place close to the constriction (at some distance from gauge G_3). The reason is a flow instability that occurs in the constriction. Indeed, the composite Froude number for the section where gauge G_3 is located is 0.6.

The estimate for G_a close to the maximum constriction yields $G_a > 1$. The wave amplitude decreases considerably when the wave propagates in the diffuser part of the constriction. A reflected wave is generated when fission of the solitary wave occurs, and its rear part slowly rises. The beginning of its formation can be seen in Fig. 3.37b where an extended zone of small displacement of the interface is observed. In the course of time, this depression zone propagates upstream, and a reflected wave, which is later recorded by gauge G_3 (see Fig. 3.37a), is formed.

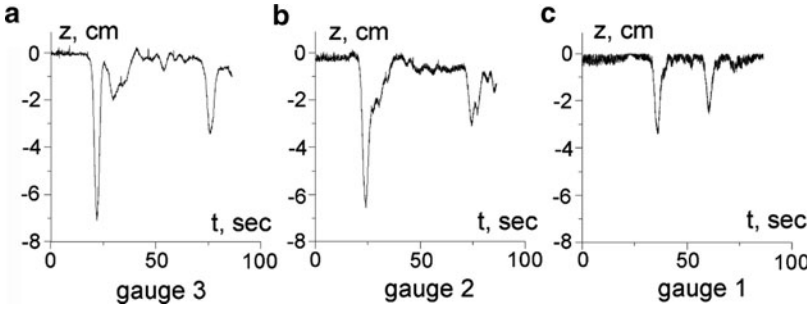

Fig. 3.37 Displacement of interface recorded in experiment 0501: (**a**) gauge 3, (**b**) gauge 2, and (**c**) gauge 1

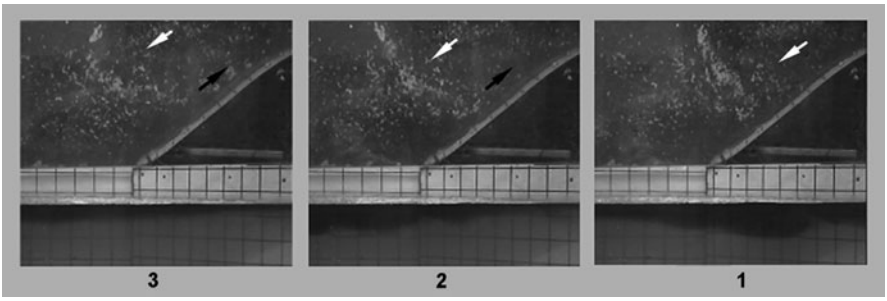

Fig. 3.38 (Experiment 0501). Surface flow caused by the interaction of the internal solitary wave with the constriction in the diffuser part of the constriction. The *top* row shows snapshots from above, the *white* and *black arrows* indicate the direction of the flow on the top free surface, and the *bottom* row series shows the associated shots from the side. The top layer is dyed. The shots are taken at $t = 35.5$ s (1), $t = 39.7$ s (2), and $t = 105.2$ s (3)

The flow was visualized by dyeing the upper layer. Small plastic particles were placed on the free surface in the diffuser part of the constriction. To observe the behavior, these particles were used as markers; a mirror was installed above the free surface at an angle of 45° with respect to the horizontal. This allows observation of the interface displacement and the motion of the markers simultaneously. Thus, we can obtain the information about the motion from the top and the side. The photographs of the divergent part of the constriction are shown in Fig. 3.38.

In the lower part of the photographs, the interface displacements are recorded. In the upper part, the positions of the markers are seen. The direction of the motion is indicated by black and white arrows. It can be seen that at the beginning (frame 1 corresponds to $t = 35.3$s after the camera has been turned on) the motion in the upper layer is directed downstream at a certain angle relative to the axis of the basin. It is typical for the flow in a diffuser. In the lower part, we can see the propagation of the wave train caused by breaking the solitary wave. In the course of time (frame 2, $t = 39.7$s), reverse flow is formed near the curved wall in the surface layer (black arrows in Fig. 3.38). It is caused by the onset of flow instability in the region with negative pressure gradient. A vortex with vertical axis is formed in the diffuser part of the constriction. Its boundary is shown by black and white arrows. It can be seen that thinning of the upper layer sets in at this moment.

Then, the vortex intensity grows (frame 3, $t = 105.2$s). At the same time, the wave train is translated downstream and the upper layer becomes thinner at a larger distance. Then, new smaller vortices are generated which gradually decay. However, the flow near the curved wall persists at all time until the reflected wave takes over in this region in spite of the fact that the motion of the dyed fluid displayed in the lower part of the frame is directed downstream. Analysis of the character of the flow caused by the passing and breaking of the internal solitary waves through the high constriction confirms that the flow is of three-dimensional character.

In summary, we may state that the transformation and breaking of internal solitary waves were studied for the cases when the characteristic constriction length

was close to the wavelength. It is shown that the interaction of solitary internal waves with a constriction is determined by the wave amplitude and the value of the minimum gap of the channel generated by the constriction. The formation of a vortex or vortices with horizontal axis on the back face of the wave is observed when the wave moves through the constriction. It is shown that a critical regime is characterized by a sharp wave steepening, an amplitude growth in the narrow part and subsequent breaking, and the formation of a vortex on the back face of the wave. At strong interaction, fission of an internal solitary wave into two waves occurs: the leading part progresses through the constriction, but the last part is trapped and forms a reflected wave and the 'tail' of the leading part. A system of turbulent boluses can be formed. They move downstream and are responsible for the transport of sub-pycnocline water.

The motion of internal solitary waves in the passage through the constriction is of three-dimensional character. This is exhibited by the formation of a system of vortices with vertical axes that arise in the diffuser part of the constriction. The motion of the vortices is seen for quite some time after the passage of the waves, and their appearance is the effective mechanism of energy dissipation. These vortices cause motions in the upper layer, as dye translation by vortices is seen on the photographs. Another important feature of the process of the passage of solitary waves through a constriction is the distribution of the amplitude irregularity in the cross section in front of the constriction. In other words, a reconstruction of the flow takes place. This is the main reason for the transformation of the flow near the constriction, fission of strongly nonlinear internal waves, and trapping of the rear part. The influence of the constriction on the internal solitary wave passage through the constriction results in a substantial transformation of the flow that may develop instabilities and strong dissipation. A large constriction causes wave breaking. It is demonstrated that the flow regime is determined by the fact that the composite Froude number depends on the wave amplitude and the value of the constriction when an internal solitary wave passes through the constriction.

3.4 Laboratory Study of the Dynamics of Internal Waves on a Slope

3.4.1 Reflection and Breaking of Internal Solitary Waves from Uniform Slopes at Different Angles

The major source of energy responsible for the appearance of fields of waves and currents in lakes is connected with wind effects on the free surface. This energy influx is responsible for the setup of surface water and the generation of internal waves in the form of basin-scale standing waves or propagating nonlinear waves. Field observations indicate that the decay rate of wind-forced basin-scale waves is larger than it may simply be estimated by internal dissipation (Stevens and

Imberger 1996; Horn et al. 2001). Other mechanisms governing the energy transfer from basin-scale waves to either smaller waves or turbulent scales must therefore be considered to provide an explanation for such a high value of decay rates. Among possible mechanisms that are responsible for the above-mentioned energy transfer, the following can be distinguished: (1) nonlinear steepening and disintegration of long internal waves into packets of short-period waves and solitons; (2) shear instability caused by the energy transfer from the mean flow to the small-scale motions; (3) shoaling and reflection from slopes; (4) effects of localized constrictions stimulating the development of wave instability; and (5) interaction with topography (Horn et al. 2001; Vlasenko and Hutter 2002b). Traveling short-period internal waves and solitons are relevant for small-scale processes, but their energy content is minor compared to that of the large-scale waves. However, this energy reservoir is an important intermediary between the energetic large-scale motions and small dissipative pulsations.

Important mechanisms of energy transformation in lakes from short-period (internal waves) to small-period motions are concerned with the shoaling of waves and their transformation, overturning, and breaking over sloping boundaries. These processes lead to the generation of turbulence and water mixing. Laboratory experiments were performed (Kao et al. 1985) to study the propagation of internal solitary waves of depression on a slope and shelf geometry. Authors considered breaking of internal waves, especially when interacting with a slope. It was found that the onset of wave breaking was governed by shear instability, which was initiated when the local Richardson number became less than ¼. Existence of a strong shear layer causes the development of instability of Kelvin–Helmholtz type and further wave breaking. The geometrical configuration of the bottom contributes considerably to this process owing to the intensification of the reverse flow in the lower layer to satisfy mass conservation during the wave propagation up the slope. Notice that the influence of the topography on the interaction of an internal wave with an obstacle described earlier causes shear intensification in the lower layer, leading to the formation of vortices. It was shown that before breaking the shape of the wave is deformed so that its leading front becomes milder and roughly parallel to the slope. In the process of wave adjustment to the slope, the back front of the wave steepens considerably with large-scale breaking and possible overturning in the lee of the wave. The propagation of long, weakly nonlinear interfacial waves in a two-layer fluid of slowly varying depth was theoretically studied by Helfrich et al. (1984). The cubic nonlinearity was included in the governing equation in order to investigate the wave behavior in the vicinity of a "turning point" that is approximately determined by equality of the layer thicknesses. It was found that more than one wave of reverse polarity may emerge as the incident wave passes through the mentioned "turning point". Theoretical and experimental investigations of the evolution of weakly nonlinear solitary waves in a two-layer fluid over bottom topography were carried out by Helfrich and Melville (1986). It was demonstrated that the incident wave amplitude and stratification influenced the development of the observed weak shearing; moreover, strong breaking instabilities were demonstrated. The regions of instabilities, which depend on the wavelength and

the ratio between the wave amplitude and the depth of the lower layer on the shelf, are identifiable if the difference between the densities of the upper and lower layers is given. Zones of strong overturning and second-mode wave generation, shearing, and stability are distinguished. To investigate the evolution of the incident waves, the K–dV equation was solved numerically and asymptotic solutions were determined. Particular attention was focused to a situation when a turning point (point of equal layer depths) is encountered on the slope.

Run-up of internal waves on a gentle slope was experimentally studied by Wallace and Wilkinson (1988). The waves were generated continuously at the interface of two miscible layers of different densities. As each wave in the periodic train propagated onto the slope, it steepened and developed into a solitary-like wave before finally overturning. The surrounding fluid was entrained into the wave at its overturning, and the resulting gravitational instability produced considerable turbulence and mixing. The broken wave took the form of a discrete bolus that propagated up the slope. It was noticed that the pattern of the overturning process was similar to the pattern that was previously considered experimentally (Kao et al. 1985; Helfrich and Melville 1986) in spite of some differences of the run-up phase of the waves on the slope. Principal attention was devoted to the determination of the bulk parameters of the dense fluid, which characterize the nature of the bolus, and ascertain the dependence of these parameters on the characteristics of the incident wave. A numerical simulation of the process of interaction of internal solitary waves of depression with the slope-shelf topography was conducted by Vlasenko and Hutter (2002b). The Reynolds-averaged equations, parametrized with vertical diffusivities, were solved. The solutions provide a detailed analysis of the evolution of the flow field during the process of interaction of strongly nonlinear waves with the bottom topography. It was demonstrated that at the beginning of the process, wave adjustment of the chosen initial wave profile takes place: generally, the leading front of the wave becomes more gently sloping, and the back front becomes steeper. Such behavior of the wave is concerned with the fact that the velocity of the trough is smaller than the velocity of the crest in shallow water when a wave depression is considered. The cumulative effect of the nonlinearity causes a steepening and eventually overturning of the back front of the wave over the slope. The authors found that just before breaking the horizontal orbital velocity at the site of instability exceeds the phase speed of the internal solitary wave. The results clearly show that the breaking is primarily due to kinematic overturning of the back front of the wave.

Laboratory experiments were made by Helfrich (1992) to observe the interaction of an internal solitary wave of depression with a uniform slope. The fission of the incident solitary wave into several solitary-like waves of elevation (boluses) and their development on the slope were considered. It was demonstrated that the shoaling of an internal solitary wave results in wave breaking and production of multiple turbulent surges (or boluses) that propagate up the slope. Significant mixing occurs everywhere inshore of the breaking zone. A breaking criterion is proposed. Amplitudes of waves were up to 3.5 cm. Only one configuration of the layer thickness ratio was considered. The author estimated that for the considered

series of slopes (0.034; 0.050; 0.067) the energy of the reflected wave is less than 25% of the energy of the incident wave.

Theoretical investigations, including comparison with field observations of the run-up of interfacial solitary waves, were performed by Bourgault et al. (2005). These authors interpreted the sharp fluctuations of the density on the background of the slowly varying density field, which were recorded by CTD (conductivity–temperature–depth) profilers, to be caused by internal solitary wave breaking and run-up on a uniform slope. Similar patterns of the density field were also observed in experiments by Helfrich (1992) when the slow variation of the density was accompanied by a sequence of isolated bursts of increased density. These variations of the density were generated during breaking and subsequent run-up of internal solitary waves on the slope and directly connected with the boluses translating up the slope. It was observed that the boluses exhibit the shape of internal solitary waves of elevation, but other bolus-like structures exhibit more irregular-shaped structures (Bourgault et al. 2005). An important role of the boluses is in transporting the sub-pycnocline water in the upslope direction past the intersection between the pycnocline and the bottom. An important feature of the process of interaction of internal solitary waves with the slope, considered in the paper, is the formation of an intrusive layer extending from the mixing zone back into the water column (Vlasenko and Hutter 2002b).

The shoaling and breaking of an internal solitary wave of depression on a uniform slope were studied experimentally by Michallet and Ivey (1999). Various bottom slopes, ratios of layer thicknesses, and density differences between the layers were investigated. The mechanism that led to wave breaking was examined with flow visualization and particle image velocimetry. It was shown that at an early stage because of the interaction of the internal solitary wave with a slope, the leading front becomes parallel to the slope, while the back front is steepening. The flow associated with the incoming wave is characterized by shear: it is directed up the slope in the upper layer and down in the lower layer. Then, behind the wave, close to the inclined boundary, some velocities are directed upward. These velocities, which are caused by the separation of the lower-layer flow from the boundary, are likely induced by an adverse pressure gradient. As the wave shoals, the vertical velocity increases, the back front of the wave becomes unstable, and the vortex reaches its maximum size and a bolus is formed. The slope reflectance relative to the incident internal solitary waves was also studied. It was found that the ratio between the length of the solitary wave, L_w, and the characteristic length of the slope, L_S, determines the amount of energy reflected from the slope. For small ratios L_W/L_S, the reflection coefficient (relative to the energy of the waves) increases linearly with the growth of the ratio. Beyond $L_W/L_S \approx 0.5$, the rate of increase begins to slow down and the reflection coefficient asymptotically approaches the limiting value 1.0. The authors suggested that strong reflection of an incident wave from the slope at $L_W/L_S > 0.5$ is due to the small timescale of interaction between the wave and the slope. It was found that the mixing efficiency of the breaking event has its peaks at a maximum of 25% when $L_W/L_S = 0.5$, and its value decreases on either side of this peak value. It is also noteworthy that all

estimates of energy of internal solitary waves were made by taking into account the energy loss caused by the effect of viscosity. For this purpose, a special series of experiments was designed to obtain a graphical relationship of the nondimensional wave energy against nondimensional distance.

Numerical simulations of the process of reflection of internal solitary waves from a slope and comparison of the results with experimental data by Michallet and Ivey (1999) were performed by Bourgault and Kelley (2007). A two-dimensional numerical model was used. It was proposed to use the Iribarren slope parameter (Boegman et al. 2005) instead of the ratio L_W/L_S to analyze the processes of wave reflection from the slope. The Iribarren slope parameter is the ratio between the slope of the inclined boundary and the wave amplitude divided by the wavelength. Viscous dissipation was taken into account (Bourgault and Kelley 2007). It was concluded that the underestimation of the reflectance from a uniform slope for normally incident interfacial waves occurred in the experiments (Michallet and Ivey 1999), although the theoretical model did not take into account the three-dimensional character of the turbulence generated by wave breaking.

Experimental investigations of the propagation of internal waves and their reflection from a smooth uniform slope were conducted by Chen et al. (2007a, b). They showed that the K–dV theory is suitable for internal solitary waves with small to moderate amplitudes. Alternatively, for waves of larger amplitude, the EK–dV equation corresponded more adequately to the obtained data. For a uniform slope, the amplitude-based and energy-based coefficients of reflection of internal solitary waves were obtained. It was shown that at sufficiently small and moderate slopes, the reflection coefficients increase linearly with the growth of the bottom inclination, and, at larger slopes, the coefficients approach a constant value asymptotically. Wave attenuation caused by viscosity effects during the propagation along the channel was taken into account by estimations of the amplitude and energy of the incident and reflected waves. The reflected wave amplitude calculated from experimental data agrees with those reported by other authors. Experiments with inverse slopes were also made. A mirror-image model is hypothesized to provide a generic description of the physical consequences leading to wave breaking and mixing on a wide range of uniform slopes.

Mention should also be made of experimental studies regarding the interaction of internal waves with a slope. Features of the process of reflection of internal waves from a slope were studied experimentally by Cacchione and Wünch (1974), Ivey and Nokes (1989), and Dauxious et al. (2004). Particular interest was focused on the case of near-critical reflection of internal waves when the inclination of the group velocity vector is close to the topographic slope. In this case, the reflected waves are trapped along the slope and their energy is concentrated into a narrow zone over the slope. It was found that interfacial mixing is a result of wave breaking for long-period waves and energy dissipation through viscous losses in the bottom boundary layer along the slope for shorter-period waves. Interfacial mixing increases considerably when the slope approaches the critical angle. The mixing rate caused by internal wave breaking was estimated. Experimental investigations of the run-up of internal waves and mixing of fluids on a uniform slope were made

(Umeyama and Shintani 2004). The image-processing technique was used to illustrate the run-up of the internal waves and the mixing of the freshwater and saltwater. It was shown that the entrainment of the upper-layer water into the lower-layer water by boluses played a major role during the run-up of the internal waves. It was concluded that the interaction of the internal waves with the slope can lead to instability and wave breaking, which results in strong mixing close to the boundaries. Such mechanisms of energy transfer from large to small (or dissipative) scales play a certain role in lake dynamics along with more energetic processes of the interaction of large internal solitary waves with bottom topography.

After this brief introduction into previous work of internal waves on a sloping bottom, let us now give an account of our own attempts in this regard. A series of experiments to study the process of interaction of strongly nonlinear internal solitary waves with uniform slopes (gentle and steep) were carried out. The same methodologies were used as those developed for the investigations described above for the creation of a two-layer salt stratification, generation of internal solitary waves, measurement of wave parameters by gauges, and processing of the experimental data. The boundary between the layers (or the upper layer) was dyed. The use of a digital camera allows estimation of the parameters of the internal solitary waves, and these can be compared with data obtained by the gauges. Experiments were carried out with two types of slopes of different angles relative to the horizontal, $\beta_1 = 12.5^\circ$ and $\beta_1 = 60^\circ$ (gentle and steep slopes). The slope model was installed at the end of the basin. In experiment 0404 (run 1), a gentle slope ($\beta_1 = 12.5^\circ$) was installed. The slope length, L_S, was equal to 135.5 cm. A sketch of the locations of the gauges relative to the slope is presented in Fig. 3.39. The gauges G_0, G_1, G_2, G_3, and G_4 are positioned at the axis of the basin. Distances from the end wall of the basin and between the gauges are as shown in the figure caption. The arrow indicates the direction of wave propagation.

The overall depth was equal to 30 cm, and the salinity profile before run 1 was described by equation (3.7) with $\delta = 0.55$ cm. The thickness of the lower layer was $h_2 = 27.55$ cm. Amplitudes of the incident waves and reflected waves (with identifier "r") are listed in Table 3.8. The displacement time series of the interface, recorded by the gauges G_4, G_2,G_0, are displayed in Fig. 3.40a–c, respectively.

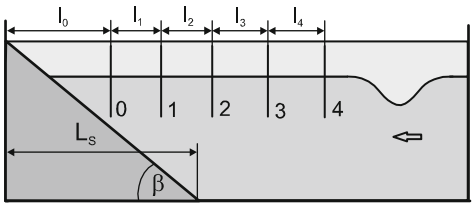

Fig. 3.39 Sketch of the side view of the placement of gauges with distances $l_0 = 82.5$ cm, $l_1 = 59.5$ cm, $l_2 = 55.5$, $l_3 = 40$ cm, and $l_4 = 49.5$ cm in experiments with slopes (experiment 0404, run 1)

Table 3.8 Amplitudes measured by the gauges in experiment 0404, run 1

Gauge	4	3	2	1	0	4r	2r
Amplitude	4.5 cm	4.4 cm	4.3 cm	4.3 cm	4.0 cm	1.6 cm	1.3 cm

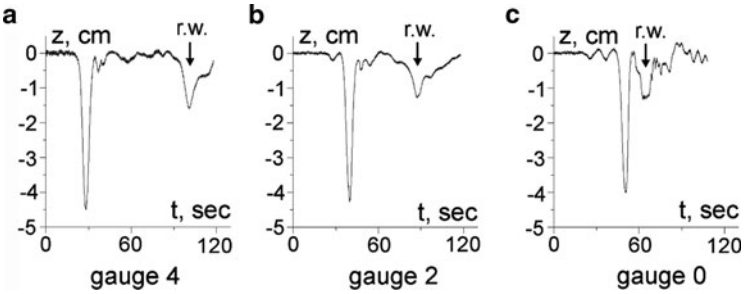

Fig. 3.40 Time series of the displacements of the interface caused by incident and reflected internal solitary waves: (**a**) gauge G_4, (**b**) gauge G_2, (**c**) gauge G_0(experiment 0404, run 1)

Table 3.9 Amplitudes measured by gauges in experiment 0604

Gauge	4	3	2	1	0	4r
Amplitude	5.9 cm	5.75 cm	5.7 cm	5.6 cm	5.0 cm	2.3 cm

The speeds of the incident and reflected waves were obtained using the data of recordings at different gauges. We see that the amplitude of the incident wave decays weakly with the traveled distance. From Fig. 3.40c we infer that the formation of the reflected wave (r.w.) takes about 6 s (time interval from 62 to 68 s). Otherwise, the reading at gauge G_0 is practically constant with small oscillations only. This gauge is located above the slope (distance from the end wall of basin is $0.6\,L_S$); all processes of wave steepening and wave breaking over the slope were recorded here. The peak of the reflected wave arises at gauge G_2 (Fig. 3.40b) at $t = 88$s and at gauge G_4 at $t = 101$s (Fig. 3.40a). The form of the leading front of the reflected wave is similar to that of a solitary wave.

When the incident wave is stronger, formation of the reflected wave is equally more conspicuous. In experiment 0604 (run 1), the amplitude of the incident wave was equal to 5.6 cm. The locations of the gauges relative to the slope were the same as in experiment 0404 as displayed in Fig. 3.39, and the gauges G_0, G_1, G_2, G_3, and G_4 are positioned at the axis of the basin, but distances from the end wall of the basin and between gauges were different as follows: $l_0 = 72\,\text{cm}$, $l_1 = 51\,\text{cm}$, $l_2 = 52.5\,\text{cm}$, $l_3 = 57.5\,\text{cm}$, and $l_4 = 54.5\text{cm}$. The overall depth was equal to 30 cm, and the salinity profile was described by (3.7) with $\delta = 0.57\,\text{cm}$. The thickness of the lower layer was $h_2 = 27.1\,\text{cm}$. Amplitudes of the incident waves and the reflected wave (with identifier 'r') are listed in Table 3.9.

The displacement time series of the interface recorded by gauges G_4,G_2, and G_0 are shown in Fig. 3.41a–c. It can again be seen that the amplitudes of the incident waves decay slightly with the traveled distance. The reflected wave (r.w.) propagates backward from gauge G_0 over gauge G_2 to gauge G_4 and is characterized by the formation of a clean signal from gauge G_0 to gauge G_4. Then this wave (r.w.) is reflected from the wall of the basin, and this re-reflected wave (r.r.w.) is shown as a yet small signal that is again seen in panels (a) and (b) of Fig, 3.41, but not in panel (c) since it is outside the plotted range.

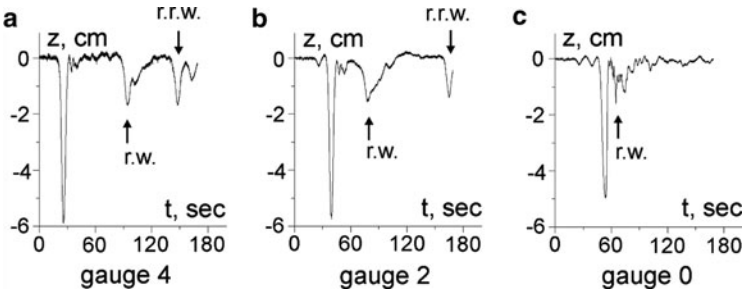

Fig. 3.41 Displacement time series of the interface caused by incident and reflected internal solitary waves at gauges G_4, G_2, and G_0(experiment 0604, run 1)

Gauge G_0 is located approximately at the half-length of the slope L_S (0.53%), that is, closer to the end wall than gauge G_0 in experiment 0404. In contrast to experiment 0404, where the reflected wave is seen as a sufficiently long displacement of the interface (see Fig. 3.40c), in experiment 0604, the signal oscillates with sharp peaks (see Fig. 3.41c). Apparently, this is caused by steepening, wave breaking, and the formation of boluses which can run up on the slope, and mixing processes.

Subsequently, the displacement signal moves in the opposite direction and a reflected wave is gradually formed. This formation is nearly complete in Fig. 3.41b. Its perfection continues as it leaves the slope region. This wave, at least its leading front, has been formed in the region where gauge G_4 is installed (Fig. 41a), and its energy can be estimated. Moreover, in Fig. 41a the wave is displayed, which is re-reflected (r.r.w) from the upstream end (at the inclined gate) of the basin. The form of this re-reflected wave is close to the solitary wave shape, and its amplitude is nearly the same as that recorded by gauge G_4 at the first wave passage.

A series of experiments was performed when the gentle uniform slope ($\beta_1 = 12.5°$) was installed. Solitary waves of different intensities were generated in the experiments.

Some evolutionary stages of the process of interaction of the solitary wave with the gentle uniformly sloping bottom can be seen in series of photographs reproduced in Fig. 3.42 and obtained in experiment 1104 (run 1), where only the interface was dyed. The exact times and temporal differences between the photographs are listed in the figure caption and the parameters of the stratification and the solitary waves for six experiments are summarized in Table 3.10. It can be seen that when the leading face of the wave reaches gauge G_0 that is located at the half-length of the slope, the back face steepens (frame 2). Note that recordings of gauge G_0 are similar to those presented in Fig. 3.41c; that is, it takes some time until the perturbations pass the gauge, where sharp changes of the recordings may be observed. The wave adjusts to the slope form: the leading front becomes milder and its inclination tends to coincide with that of the slope. The back front steepening gradually increases, and, at a certain stage of the evolution, the back face of the wave transforms into a baroclinic bore (frame 3), which is destroyed upward along

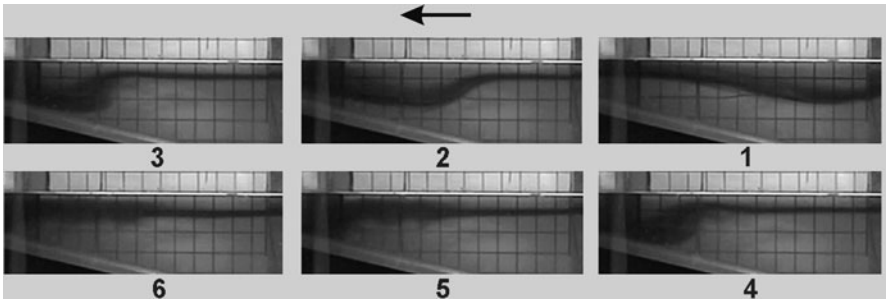

Fig. 3.42 (Experiment 1104, run1). A series of photographs demonstrating the run-up of an internal solitary wave on a gentle slope. The *arrow* indicates the direction of the propagation of the wave. The frames are numbered in consecutive order and times when they were shot are as follows:

Frame	1	2	3	4	5	6
Time of shot (sec)	69.9	75.0	78.5	80.1	83.3	85.2
Time difference (sec)	5.1	3.5	1.6	3.2	1.9	

Table 3.10 Summary of parameters of incident and reflected waves (uniform slope, $\beta_1 = 12.5^0$)

No. exp.	No. run	Parameters [cm]	Type of wave	No. gauge	Distance [cm]	Amplitude a, [cm]	c, [cm/s]
0404	run1	$H = 30;\ h_1 = 2.45;\ \delta = 0.55$	Inc.	4	277	4.5	7.6
			Inc.	2	197.5	4.3	7.6
			Refl.	4	277	1.6	6.8
			Refl.	2	197.5	1.3	6.8
	run2	$H = 30;\ h_1 = 2.6;\ \delta = 0.6$	Inc.	4	277	4.1	7.4
			Inc.	2	197.5	4.0	7.4
			Refl.	4	277	1.16	6.6
			Refl.	2	197.5	1.24	6.6
0604	run1	$H = 30;\ h_1 = 2.9;\ \delta = 0.57$	Inc.	4	287.5	5.9	8.43
			Inc.	2	175.5	5.7	8.43
			Refl.	4	287.5	1.7	7.0
			Refl.	2	175.5	1.55	7.0
	run2	$H = 30;\ h_1 = 3.1;\ \delta = 0.67$	Inc.	4	287.5	5.5	8.13
			Inc.	2	175.5	5.3	8.13
			Refl.	4	287.5	1.6	-
			Refl.	2	175.5	1.6	-
1104	run1	$H = 30;\ h_1 = 3.2;\ \delta = 0.52$	Inc.	4	256	5.4	8.4
			Inc.	2	148	5.2	8.4
			Refl.	4	256	1.9	7.8
			Refl.	2	148	1.9	7.8
	run2	$H = 30;\ h_1 = 3.3;\ \delta = 0.6$	Inc.	4	256	4.35	7.9
			Inc.	2	148	4.1	7.9
			Refl.	4	256	1.4	7.1
			Refl.	2	148	1.6	7.1

the slope (frame 4). Heavier fluid penetrates into the light fluid and falls down on the wave trough. Due to the development of the breaking process, the flow becomes turbulent, and fluids are mixed. On the photographs, the wash-out of the dyed interface and its thickening (frames 5, 6) can be clearly seen. Then, this comparatively lighter water rises and formation of the reflected wave begins. A substantial part of the initial energy of the solitary wave is spent on the turbulization and mixing of fluids. An intrusive layer is formed above the slope (frames 5, 6) which gradually extends backward into the upstream region.

Close inspection of the experimental data shows that the speeds of the incident waves were lower than those described by the K–dV theory, and the wave profile is wider than the K–dV profile. This problem was encountered already earlier. The reason for the discrepancy lies in the fact that the K–dV theory adequately describes solitary waves with comparatively small amplitudes. When the amplitude increases, the application of the EK–dV theory or fully nonlinear theory should be employed. The frequency–amplitude relationship was analyzed by Michallet and Barthelemy (1998). The experimental data, recording the interface displacements in time at a given point, are used to test this. So, it is reasonable to use the integral scale of the frequency as the principal characteristic of the waves (or the characteristic frequency). It is determined by the relation

$$\omega_k = \frac{2a}{\int\limits_{-\infty}^{\infty} \eta(t, x_0)\mathrm{d}t} = \frac{c_k}{\lambda}, \tag{3.28}$$

where $\eta\,(t,\ x_0\,)$ is the interface displacement as a function of time, c_k is the phase velocity, and λ is the characteristic length (Koop and Butler 1981).

Next, consider the conception of critical depth h_c. If the interface position in a layered fluid coincides with h_c, then the K–dV theory predicts that solitary waves do not exist. This is concerned with the fact that the nonlinear terms in the K–dV equation disappear. This configuration is called “turning point”. In a two-layered system, this critical level is approximately equal to half of the overall depth. In the general case, the value h_c is determined by the following equation due to Kakutani and Yamazaki (1978):

$$\frac{h_c^2(H - h_c)}{(H' - h_c)^3} = \frac{\rho_2}{\rho_1}, \tag{3.29}$$

where $H' = H - c_0^2/g$, and

$$c_0^2 = \frac{gH}{2}\left[1 - \left(1 + \frac{4h_1(h_1 - H)(\rho_2 - \rho_1)}{\rho H^2}\right)^{1/2}\right], \tag{3.30}$$

or approximately (Michallet and Barthelemy 1997)

$$c_0 = \sqrt{\frac{g(\rho_2 - \rho_1)h_1 h_2}{\rho_1 h_2 + \rho_2 h_1}}. \tag{3.31}$$

When the difference of the densities is small (Bogucki and Garrett 1993)

$$c_0 = \sqrt{g' \frac{h_1 h_2}{H}}, \quad g' = \frac{\rho_2 - \rho_1}{\rho_2}. \tag{3.32}$$

If the free surface is replaced by a rigid lid (this is permissible only for small density differences), we obtain $H = H'$, and equation (3.29) can be shown to take the form (Michallet and Barthelemy 1998)

$$\frac{h_c^2}{(H - h_c)^2} = \frac{\rho_2}{\rho_1}. \tag{3.33}$$

For strongly nonlinear solitary waves, Michallet and Barthelemy (1998) compared experimental data with results of numerical calculations following the K–dV–mK–dV theory developed earlier by Funakoshi (1985) and Funakoshi and Oikawa (1986) (see also Gardner's equation or extended K–dV equation (Ostrovsky and Stepanyants 2005)). The K–dV and modified K–dV theories are combined in a new theory through incorporation in the equation of cubic nonlinear terms. The theory is designed to consider waves of which the amplitudes are in the interval from 0 to $\bar{h}$, where $\bar{h} = h_2 - h_c$ is the distance between the interface and critical level; thus, $\bar{h}$ is an upper bound of the amplitude of the internal solitary waves. The main assumption lies in the fact that the amplitude and $\bar{h}$ are of the same order of magnitude and small in comparison with the overall depth. When the free surface is replaced by a rigid lid, then the displacement of the interface caused by the solitary wave can, according to Michallet and Barthelemy (1997), be written as

$$\eta(x,t) = a \frac{\operatorname{sech}^2[\kappa(x - C_m t)]}{1 - \mu \tanh^2[\kappa(x - C_m t)]}, \tag{3.34}$$

where the expressions for κ, μ, and C_m are

$$\kappa = \sqrt{\frac{4}{3} \frac{H}{h_c(H - h_c)} \cdot \frac{(-a) \cdot (a + 2\bar{h})}{(H - h_c)^3 + h_c^3}}, \tag{3.35}$$

$$\mu = \frac{-a}{a + 2\bar{h}}, \tag{3.36}$$

$$C_m = c_0 \left[1 + \frac{(a + \bar{h})^2}{2h_c(h_c - H)}\right]. \tag{3.37}$$

The sign of $\bar{h}$ determines the polarity of the solitary wave, i.e., $a \leq 0$ if $\bar{h} \geq 0$ and $a \geq 0$ if $\bar{h} \leq 0$.

The expression to compute the frequency ω_k that is equivalent to equation (3.28) for large-amplitude waves, can be written as

$$\omega_k = \frac{2a}{\int\limits_{-\infty}^{\infty} \eta(t, x_0)\mathrm{d}t} = \frac{C_m \kappa \sqrt{\mu}}{\operatorname{arctanh}\sqrt{\mu}}. \tag{3.38}$$

It was shown that the frequency–amplitude characteristics of large internal solitary waves tend to be predicted asymptotically by the K–dV–mK–dV theory (Michallet and Barthelemy 1998).

A comparison of the data of our experiments with the frequency–amplitude relations (3.38) is accomplished in Fig. 3.43. The two graphs in panels (a) and (b) show values for ω_k as functions of a/H for moderate and large amplitudes. In panel (a), the results correspond to moderate amplitudes ($3.0 \div 4.5$ cm) of internal solitary waves. Curves 1 and 2 fit the K–dV theory for $h_1 = 2.45$ cm and $h_1 = 3.3$ cm, respectively. The relationship described by formula (3.38) is presented as curves 3 ($h_1 = 3.3$cm) and 4 ($h_1 = 2.45$ cm). Full circles correspond to the incident waves and crosses to the reflected waves. It is seen that the characteristics of strongly nonlinear internal solitary waves studied in the experiments agree well with the mK–dV theory. A still better agreement with the mK–dV theory is achieved for even stronger waves for which the amplitudes are in the interval 5.0–5.9 cm. These data are presented in Fig. 3.43b again as full circles for the incident waves and crosses for the reflected waves. Here, curves 1 and 2 fit the K–dV theory for

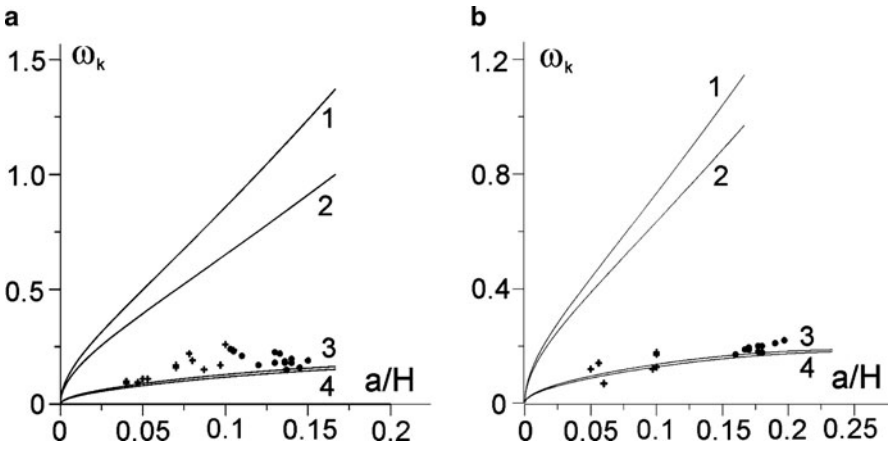

Fig. 3.43 Frequency–amplitude relations for incident and reflected internal solitary waves: (**a**) moderate amplitudes, (**b**) large amplitudes. Curves labeled "1" and "2" are obtained with the K–dV theory and curves "3" and "4" with the mK–dV theory as explained in the main text

$h_1 = 2.9$ cm and $h_1 = 3.4$ cm, respectively. Curves 3 ($h_1 = 3.4$ cm) and 4 ($h_1 = 2.9$ cm) are described by the mK–dV theory.

Experiments 2606 and 2906 with the second model ($\beta_1 = 60°$) were carried out to study the reflection of internal solitary waves from a steep slope. The slope length L_S was equal to 17.3 cm. A sketch of the gauge locations relative to the slope is presented in Fig. 3.39. Here, gauges G_0, G_1, G_2, G_3, and G_4 are at the axis of the basin. In experiment 2906, distances from the end wall of the basin and between the gauges are equal to $l_0 = 10$cm, $l_1 = 41.5$ cm, $l_2 = 55.5$ cm, $l_3 = 19.5$ cm, and $l_4 = 54.5$ cm. The overall depth is 30 cm and the salinity profile before the run is described by equation (3.7) with $\delta = 0.55$ cm. The thickness of the lower layer before run 1 is $h_2 = 27.0$ cm and the amplitudes of the incident and reflected waves (with identifier 'r') are listed in Table 3.11.

In this experiment, the initial forward-moving wave travels from right to left, encountering gauge G_4 (1) first, gauge G_2 (1) second and gauge G_0 (1) last (for numbers in parentheses, see Fig. 3.44). After reflection gauge G_0 is encountered first, gauge G_2 and gauge G_4 follow consecutively afterward. Then, the wave signal is reflected at the wave generator and seen at gauge G_4 (3) followed by gauge G_2 (3) and gauge G_0 (3). After yet another reflection gauge G_0 (4) is encountered first followed by gauge G_2 (4) and gauge G_4 (4). The displacement time series of the interface recorded by gauges G_4, G_2, and G_0 are displayed in Fig. 3.44a–c. Evidently, the reflection of strongly nonlinear internal solitary waves from a steep slope is considerably more efficient than that from a gentle slope and the shapes of the reflected waves are clearly identified. We also see the reflection of a solitary wave from the opposite end of the basin, i.e., from the inclined gate of the wave generator. Information from photographs (experiment 2906) in Fig. 3.45 is consistent with the gauge data.

Table 3.11 Amplitudes measured by gauges in experiment 2906

Gauge	4	3	2	1	3r	4r
Amplitude	4.6 cm	4.5 cm	4.5 cm	4.35 cm	3.7 cm	3.5 cm

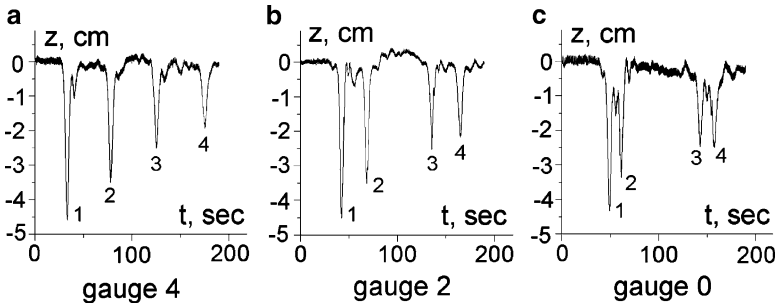

Fig. 3.44 (Experiment 2906). Displacements of the interface caused by incident and reflected internal solitary waves. The following identifications are made: "1" corresponds to the first forward-moving signal. "2" is the first reflection and backward-moving wave, "3" is the re-reflected signal moving forward, while "4" is reflected again at the steep plane and moves backward

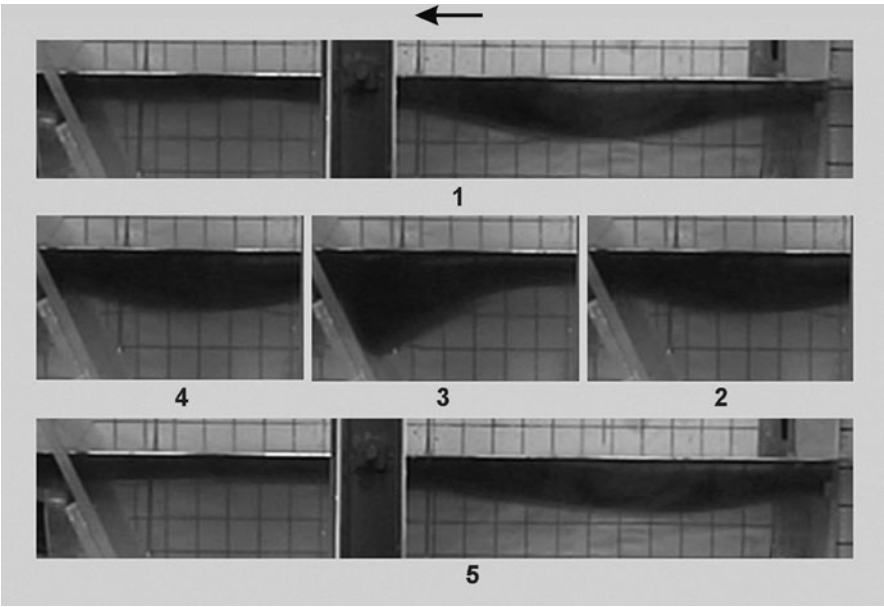

Fig. 3.45 (Experiment 2906). Photographs of interaction of an internal solitary wave with steep slope. The *arrow* indicates the direction of the propagation of the wave. The frames are consecutively numbered and times when they were shot are as follows:

Frame	1	2	3	4	5
Time of shot (sec)	61.1	67.6	70.1	73.1	80.1
Time difference (sec)	6.6	2.5	2.0	7.0	

The processes of the formation of a reflected wave from steep and gentle slopes differ from each other. For a gentle slope, the level of the wave trough is practically unchanged. At the beginning, the wave is adjusted to the sloping surface and its leading front and trough are adjusted to the same inclination as the slope. However, a steepening of the back face of the wave occurs. Then, a baroclinic bore is formed. It runs up on the slope and is destroyed, and fluids are mixed. The elevation of lighter fluid causes formation of a reflected wave. Because of all these intermediary mechanisms, the energy of the reflected wave is not very high and the time of the interaction process following this scenario is long. Similar processes are realized for waves with different amplitudes if the slope is gentle. On the other hand, the reflection process is more effective when the incident wave encounters a steep slope. When a wave collides with a steep slope, its trough quickly dives to an even larger depth.

In Fig. 3.45, the depth of the trough submersion is approximately two amplitudes of the wave far from the steep slope. The wavelength is radically decreased. A rapid transformation of the kinetic energy in potential energy occurs in this process. Due to the buoyancy effect, the submerged fluid moves upward and the reflected wave is formed. The stored potential energy transforms into kinetic energy of the reflected wave. When the reflected wave leaves the given region, a thinning of the upper

layer can be seen that is restored later. The characteristic time of the interaction process is short. Note that dissipation is not large in the process of reflection as is evidenced from Fig. 3.45 where the regions of mixed fluid are very small. Evidently, different mechanisms of reflection of strongly nonlinear internal solitary waves from gentle and steep slopes determine the ratio between the reflection coefficient and the slope value.

Before studying the energetic characteristics of the wave reflection from a slope, we consider the loss of energy of the internal solitary waves caused by dissipation. The main reasons for energy decrease have been elucidated earlier in another section. The integral estimation of energy loss of solitary waves moving in the basin can be made by using experimental information obtained from gauges located along the basin.

The energy dissipation of internal solitary waves of depression propagating at a constant depth in a channel was estimated by Michallet and Ivey (1999). The authors consider the change of the ratio between the instantaneous energy $E$and the initial wave energy E_0 as a function of the normalized traveled distance $x\ h_2/H^2$. Data were obtained for the case when waves were free to reflect from each end of the basin. The data analysis shows that they can be approximated by the following relationship:

$$\frac{E}{E_0} = 10^{-bx}, \tag{3.39}$$

where b is *constant*. An optimal fit of the data from an experimental investigation by Michallet and Ivey (1999) is $b = 0.023$. Our own determination of the energy loss by solitary waves when they propagate along the basin led to a similar result, namely, $b = 0.021$ (somewhat less). The results are given in Fig. 3.46.

The use of relation (3.39), describing the dependence of the energy loss of the wave on the distance x, enables us to estimate the coefficient of reflection of internal solitary waves from a slope. Amplitude-based reflection coefficients $R_a = a_r/a_i$ on a uniform slope versus the slope angle, β, are displayed in panel a) of Fig. 3.47 as circles. Here, a_r and a_i are the amplitudes of the reflected and incident waves,

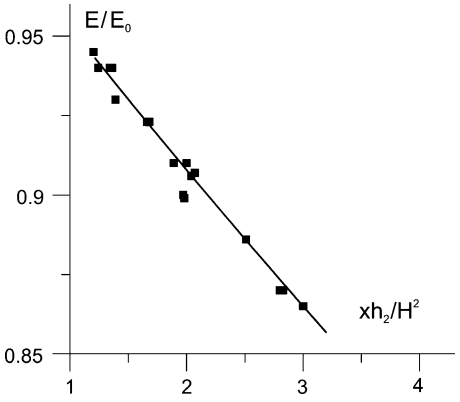

Fig. 3.46 Decay of the energy of internal solitary waves with distance when traveling along a channel of constant depth. The *filled squares* are taken from our own experiments

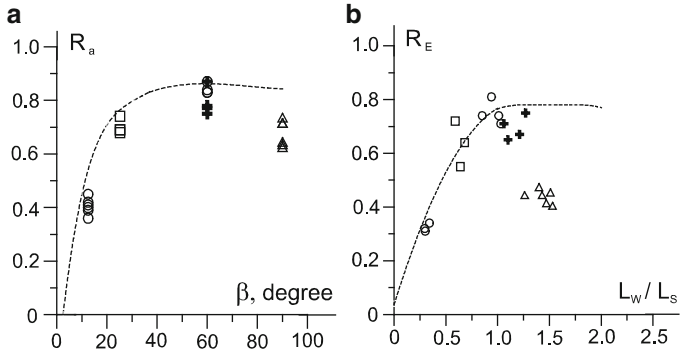

Fig. 3.47 Reflection coefficient of ISW from slopes: (**a**) amplitude-based coefficient versus slope, (**b**) energy-based coefficient versus ratio lengths of wave and slope. Circles correspond to a uniform slope; symbols (squares, crosses, and triangles) refer to experimental results discussed in Sect. 3.4.2

respectively. The dashed curve is the curve which generalizes the experimental data by Chen et al. (2007b). The dependence of the energy-based reflection coefficient R_{E} on the characteristic length ratio L_{w}/L_S is presented in panel (b) of Fig. 3.47. Here, $R_{\mathrm{E}} = E_r/E_i$, where E_r and E_i are the energies of the reflected and incident waves, and $L_{\mathrm{w}}$is the characteristic wavelength, while L_S is the slope length. The dashed curve represents the combined experimental data by Michallet and Ivey (1999) and Chen et al. (2007a, b).

It can be seen that data points are situated somewhat below the curve. Alternatively, the curve can be divided into two main parts which correspond to a gentle slope and a steep slope. There is an intermediate part between the two. As noted above, there are two main mechanisms of wave reflection from slopes. The topographic effect is weak for a gentle slope and energy reflection takes place due to instability of the back of the wave, its steepening, breaking, and subsequent generation of turbulence causing fluid mixing. Then, the lighter fluid moves upward and wave reflection occurs. The mechanism is characterized by considerable mixing of light and heavy fluids; so, the process is governed by high-energy dissipation and a small reflection coefficient. It is realized at gentle slopes. On the other hand, the topographic effect is strong for steep slopes. The wave amplitude highly increases near the slope. When its growth is stopped, rapid elevation of the lighter water sets in and an intensive reflected wave is generated. The reflection process on a steep slope is fast as compared with the case of a gentle slope, and dissipation is weak.

Note that the ratio of the slope S to the wave slope a/λ is commonly used to classify the breaking of surface waves. This ratio can be expressed as the offshore form of the Iribarren number (Boegman et al. 2005)

$$\xi = \frac{S}{(a/\lambda)^{1/2}}. \tag{3.40}$$

Substituting the characteristic wavelength L_w instead of the wavelength, the Iribarren number can be used to study the reflection of internal solitary waves from slopes (Bourgault and Kelley (2007)). The Iribarren number ξ was estimated for experiments with uniform slopes. It was found that this number ranges from 0.58 to 0.72 for a gentle slope (model 1) and varies between 3.2 and 3.4 for a steep slope (model 2). The ratio of the slope steepness to the wave steepness is determined by the Iribarren number that can be used as a parameter which characterizes the regimes of reflection. In our own experiments, strongly internal solitary waves were generated and the wave steepness did not vary in a wide interval. When the Iribarren number is less than 1, the increase of the reflection coefficient differs little from a linear law (the first regime, panel b) of Fig. 3.47). The changes of the reflection coefficient are small for a large value of the Iribarren number (> 3). In panel (b) of Fig. 3.47, this regime corresponds to reflections from a steep slope (the second regime). It may be called the saturation regime. A situation with weak solitary waves certainly calls for further study.

As conclusion, we state that there are two principal mechanisms of wave reflection from slopes. They can be distinguished as gentle and steep slopes. This leads to different dependences of reflection coefficients on the topographic parameters. The topographic effect is weak for a gentle slope and the reflection of energy takes place due to instability on the back of the wave, its steepening, breaking, and subsequent generation of turbulence. Then, lighter fluid rises under the action of buoyancy forces with the subsequent onset of the reflected wave. The mechanism is characterized by considerable mixing of light and heavy fluids. The reflection coefficients grow with amplification of topographical effects. The distinctive properties of this process are high-energy dissipation and small reflection coefficients. It is realized at gentle slopes. On the other hand, the topographic effect is strong for steep slopes. The amplitude of the wave highly increases near the slope. When the growth stops, rapid elevation of lighter water sets in under the influence of buoyancy forces and an intensive reflected wave is generated. The reflection process at steep slope is fast. Processes leading to energy dissipation have no time to develop; so, the energy loss to dissipation is small. The reflection coefficients are only slightly changed with the amplification of the topographic effects. The mechanism of the generation of the reflected wave is governed by the transformation of kinetic energy of the incident wave into potential energy associated with the submergence of light fluid into heavier fluid, and, similarly, the inverse process of potential energy transformation into kinetic energy of the reflected waves! Thus, the process of reflection of internal solitary waves from a steep slope is characterized by small dissipation and high reflection.

3.4.2 Influence of Slope Nonuniformity on the Reflection and Breaking of Waves

A series of experiments was performed to study the reflection of strongly nonlinear internal solitary waves at nonuniform slopes. It is known that slopes in lakes, as a

rule, are nonuniform. The coastal zone depth grows slightly with an increase of the distance from a shoreline. Then, the depth sharply increases and the slope angle becomes large. This feature must be taken into account when considering the interaction of internal waves with a slope. The peculiarities of the topography can appreciably influence the character of the wave reflection. Moreover, the development of the instability and breaking of waves, the occurrence of turbulent mixing, and the amount of energy loss by the incident wave can depend on the slope nonuniformity. Its influence is especially important when the level of thermocline in a lake is not far from the depth where the topography sharply changes.

Three models of slopes were studied in the experiments. The models consisted of a small smooth "insert" 1 ($\alpha = 12.46°$) in the upper part of the slope and the main part 2 with different angles ($\beta = 25.2°; 60°; 90°$). The end edge of the "insert" was submerged to $h^* = 5.2$ cm from the free surface in all experiments. Note that the depth of the interface was approximately $h_1 \cong 3$ cm in the experiments. The shape of the model with nonuniform slope is schematically sketched in Fig. 3.48.

In experiments 1505 and 1705, the first model of the nonuniform slope was studied ($\beta = 25.2°$). Table 3.12 lists the parameters of the incident and reflected waves including amplitudes recorded by the gauges: overall thickness H; thickness of the upper layer h_1; value of δ characterizing the thickness of the intermediate layer; and calculated speed of waves. Estimates of the amplitude-based reflection coefficient $R_a = a_r/a_i$ on the nonuniform slope versus the slope angle β are presented in panel a) of Fig. 3.47 as hollow squares.

We see that the difference between the experimental data corresponding to the uniform slope and the current results is small. The reflection coefficient is an integral parameter; so, certain features of the process of the formation of wave reflection are not well represented by this value, for example, the thickening of the intermediate layer due to mixing of fluids. Estimates of energy-based reflection coefficients $R_E = E_r/E_i$ versus L_w/L_S are presented in panel (b) of Fig. 3.47 as hollow squares. The results differ slightly from those obtained from uniform slope experiments as in panel a). It should be noted that it is not evident what value should be used as slope length in the case of nonuniform slope. In panel (b) of Fig. 3.47, the overall length of the slope is used. A similar problem appears when considering

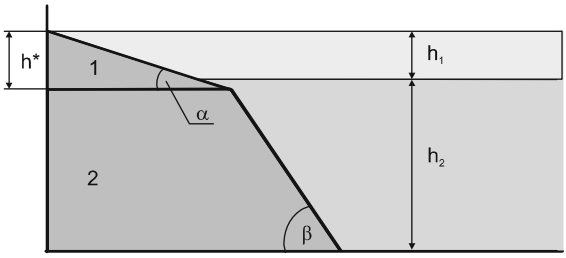

Fig. 3.48 Shape of the model of nonuniform slope. The boundary slope consists of two elements, 1 and 2, with slope angles α and β, respectively. h^*, the 1st element depth is larger than h_1, the depth of the two-layer interface: $h^* = 5.2$ cm, $h_1 \cong 3$ cm, $\alpha = 12.46^0$, and $\beta = 25.2^0, 60^0, 90^0$

Table 3.12 Summary of parameters of incident and reflected waves (nonuniform slope, $\alpha = 12.46°$, $\beta = 25.2°$) in experiments 1505 and 1705

No. exp.	No. run	Parameters [cm]	Type of wave	No. gauge	Distance [cm]	Amplitude a, [cm]	c, [cm/s]
1505	run 1	$H = 30$	Inc.	4	203.0	4.2	7.7
		$h_1 = 3.0$	Inc.	2	128.5	4.1	7.8
		$\delta = 0.4$	Refl.	4	203.0	2.6	7.4
			Refl.	2	128.5	2.9	7.4
	run 2	$H = 30$	Inc.	4	203.0	3.5	7.6
		$h_1 = 3.2$	Inc.	2	128.5	3.4	7.6
		$\delta = 0.48$	Refl.	4	203.0	2.2	7.2
			Refl.	2	128.5	2.1	7.2
1705	run 1	$H = 30$	Inc.	4	201.5	5.3	8.6
		$h_1 = 3.2$	Inc.	3	149.0	5.1	8.5
		$\delta = 0.43$	Refl.	4	201.5	3.04	7.3
			Refl.	3	149.0	3.06	7.3
	run 2	$H = 30$	Inc.	4	201.5	5.0	8.5
		$h_1 = 3.4$	Inc.	3	149.0	4.9	8.5
		$\delta = 0.56$	Refl.	4	201.5	3.0	7.8
			Refl.	3	149.0	2.9	7.8

the dependence of the reflection coefficient on the slope angle. The angle, β, of the main part of the slope is used as abscissa in panel (a) of Fig. 3.47.

A series of photographs of the process of reflection of an internal solitary wave from a nonuniform slope are shown in Fig. 3.49 and times when shots were taken are listed in the figure caption (experiment 1705). It can be seen that the leading face of the wave is already adjusted in frame 1 to the form of the "insert", but the form of the remainder is practically unchanged (frame 1). At this time slice, the flow is still in a transient stage. The leading face continues to run on the upper slope, but the heavier fluid moves down rapidly on the main slope and the back face of the wave is considerably steepened (frame 2). A vortex is formed in the region of the steepened back front, and heavier fluid moving down the slope entrains lighter (dyed) fluid in the motion. Under these effects, a tongue-like near-wall flow is formed (frame 3). In the region with negative pressure gradient, this flow becomes unstable and separation occurs.

A second vortex of opposite rotation is generated. Similar vortices arising at separation of an inverse flow in the region with negative pressure gradient were discussed in other sections. Under the influence of the vortex pair, a jet is formed (frame 4). Then, the upper vortex shifts toward left, and lighter fluid remains under the effect of the second vortex. We see that the fluid moves along streamlines corresponding to the motion caused by the vortex (frames 5, 6). Then, the flow becomes unstable and fluids are mixed locally. In frame 7, a hazy region underneath the wave appears, which is caused by these processes (frame 7). Immediately afterward, lighter (dyed) fluid begins to move upward under the buoyancy effect, and formation of the reflected wave sets in (frame 8). In short, the appearance of a vortex pair results in the formation of a jet and subsequent mixing of fluids.

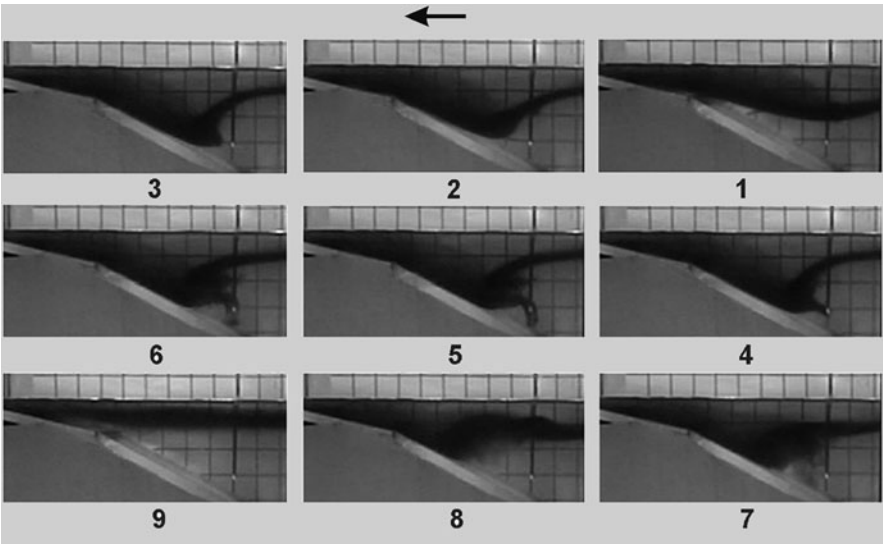

Fig. 3.49 (Experiment 1705). Photographs of the interaction of internal solitary waves with nonuniform slope. The arrow shows the direction of the propagation of the wave. The frames were consecutively numbered and times when the shots were taken are:

Frame	1	2	3	4	5	6	7	8	9
Time of shot (sec)	65.8	67.8	68.5	69	69.8	70.2	71.2	72.5	80.5
Time difference (sec)		2.0	0.7	0.5	0.8	0.4	1.0	1.3	8.0

An increase of the angle of the main slope, β, leads to the generation of more intensive reflected waves. This is evident from the analysis of the results presented in Fig. 3.47 (displayed as crosses). The reflection coefficients are estimated here by processing data of experiments 1406 and 2006 in which the second slope model ($\beta = 60^\circ$) was studied (see Fig. 3.48).

The parameters of the incident and reflected waves are listed in Table 3.13. They indicate the amplitudes recorded by the gauges; overall thickness H; thickness of upper layer h_1; value of δ characterizing the thickness of the intermediate layer; and calculated speeds of the waves.

Scrutiny of the results shows that the estimated reflection coefficient is consistent with the results obtained earlier. Some features of the process of interaction of the internal solitary wave with the steep slope with "insert" are displayed in Fig. 3.50. The first conclusion is that the speed of the process of solitary wave interaction with the steep slope is higher than for the gentle slope. In frame 1, a weakly dyed zone close to the edge of the "insert" was washed out at the creation of the two-layer system; it is displaced under the flow effect as a tracer. After the approach of the incident wave onto the slope, the wave trough dives rapidly (frame 2). A fast flow directed down the slope arises. Dyed particles (frame 1) entrained by the flow move in the same direction (frames 2 and 3). Once this process is stopped, the form of the lower part becomes more filled (frame 4), likely due to the increased potential of flow instability and the formation of vortical structures that are

Table 3.13 Summary parameters of incident and reflected waves (nonuniform slope, $\alpha = 12.46°$, $\beta = 60°$)

No. exp.	No. run	Parameters [cm]	Type of wave	No. gauge	Distance [cm]	Amplitude a, [cm]	c, [cm/s]
1406	run 1	$H = 29.5$	Inc.	4	201.5	5.2	8.5
		$h_1 = 3.5$	Inc.	2	132.0	5.2	8.6
		$\delta = 0.45$	Refl.	4	201.5	3.75	8.05
			Refl.	2	132.0	3.8	8.05
	run 2	$H = 30$	Inc.	4	201.5	4.3	7.9
		$h_1 = 3.7$	Inc.	2	132.0	4.2	8.0
		$\delta = 0.57$	Refl.	4	201.5	2.8	7.9
			Refl.	2	132.0	3.2	7.9
2006	run 1	$H = 30$	Inc.	4	203.5	3.3	7.7
		$h_1 = 3.1$	Inc.	2	134.0	3.2	7.8
		$\delta = 0.52$	Refl.	4	203.5	2.16	7.2
			Refl.	2	134.0	2.5	7.2
	run 2	$H = 30$	Inc.	4	203.5	2.9	7.4
		$h_1 = 3.3$	Inc.	2	134.0	2.8	7.5
		$\delta = 0.58$	Refl.	4	203.5	2.8	7.5
			Refl.	2	134.0	2.7	-

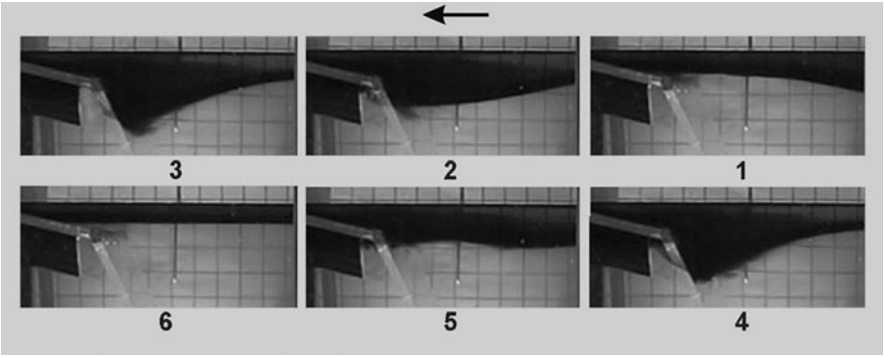

Fig. 3.50 (Experiment 1406). Sequence of six photographs of the interaction of an internal solitary wave with nonuniform slope. The arrow shows the direction of the propagation of the wave. The frames were consecutively numbered and times when the shots were taken are:

Frame	1		2		3		4		5		6
Time of shot (sec)	60.0		64.3		65.5		67.0		70.0		78.8
Time difference (sec)		4.3		1.2		1.5		3.0		8.8	

substantially weaker than for the gentle slope. As this lower wave part rises, the reflected wave is generated (frame 5). This process ends with a restored upper layer (frame 6). An upper layer thinning is not observed. The reason is the presence of the "insert" that functions as an additional sink of wave energy.

A further increase of the slope angle does not only result in a change of the pattern of the flow but reflection coefficients are changed as well. In experiments

Table 3.14 Summary of parameters of incident and reflected waves (non-uniform slope, $\alpha = 12.46°$, $\beta = 90°$)

No. exp.	No. run	Parameters [cm]	Type of wave	No. gauge	Distance [cm]	Amplitude a, [cm]	c, [cm/s]
0407	run 1	$H = 30$	Inc.	4	214.0	4.35	7.2
		$h_1 = 2.5$	Inc.	2	140.0	4.2	7.4
		$\delta = 0.39$	Refl.	4	214.0	2.3	6.8
			Refl.	2	140.0	2.7	6.8
	run 2	$H = 30$	Inc.	4	214.0	3.7	7.2
		$h_1 = 2.7$	Inc.	2	140.0	3.6	7.0
		$\delta = 0.42$	Refl.	4	214.0	2.0	6.5
			Refl.	2	140.0	2.4	6.5
0507	run 1	$H = 30$	Inc.	4	204.5	5.05	8.0
		$h_1 = 2.7$	Inc.	3	150.5	4.9	7.9
		$\delta = 0.43$	Refl.	4	204.5	3.05	7.2
			Refl.	3	150.5	2.9	7.2
	run 2	$H = 30$	Inc.	4	204.5	4.5	7.7
		$h_1 = 2.9$	Inc.	2	143.5	4.4	7.7
		$\delta = 0.48$	Refl.	4	204.5	2.55	6.9
			Refl.	2	143.5	2.7	6.9
0307	run 1	$H = 30$	Inc.	4	210.0	5.8	8.3
		$h_1 = 2.9$	Inc.	2	140.0	5.6	8.2
		$\delta = 0.59$	Refl.	4	210.0	3.6	7.2
			Refl.	2	140.0	3.7	7.1
	run 2	$H = 30$	Inc.	4	210.0	4.4	7.5
		$h_1 = 3.0$	Inc.	2	140.0	4.2	7.4
		$\delta = 0.66$	Refl.	4	210.0	2.7	6.9
			Refl.	2	140.0	3.0	7.0

0407 and 0507, the third slope model was studied ($\beta = 90°$, see Fig. 3.48). The parameters of the incident and reflected waves are listed in Table 3.14. They include the amplitudes recorded by the gauges; overall thickness H; thickness of upper layer h_1; value of δ characterizing the thickness of the intermediate layer; and calculated speeds of the waves. Estimated amplitude-based and energy-based coefficients of reflection, $R_a = a_r/a_i$ and $R_E = E_r/E_i$, are displayed in Fig. 3.47 as hollow triangles. As can be seen, the values of the coefficients are substantially smaller than the data obtained for uniform slope. Here, once more the question arises about which value of the slope angle that must be plotted on the abscissa. In panel (a) and panel (b) of Fig 3.47, the angle of the main part of the slope, β, and the characteristic length ratio, L_w/L_S, where L_S is the slope length, are plotted on the abscissas, respectively.

In Fig. 3.51, a series of photographs is presented. The flow pattern is similar to the pattern discussed above when the reflection of the solitary waves from the steep slope ($\beta = 60°$) was considered. The important feature of the pattern in this case is to generate vortical structures that are formed near the sharp edge of the "insert". The downward motion of the wave crest is stopped (frame 2), and then it begins to elevate.

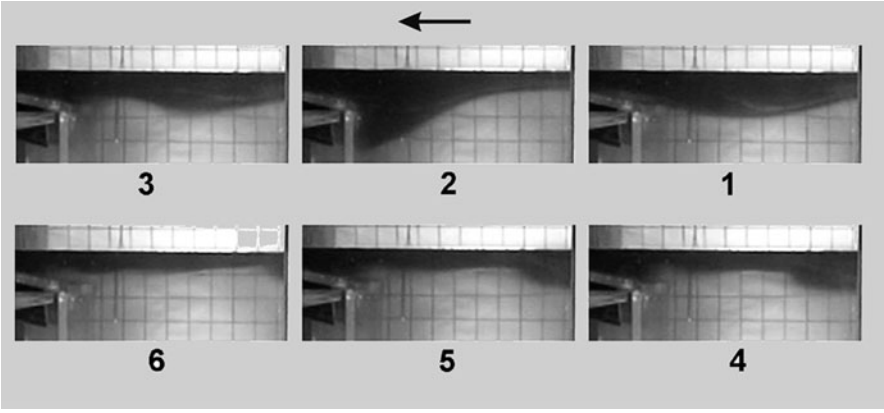

Fig. 3.51 (Experiment 0307). Sequence of photographs of the interaction of an internal solitary wave with nonuniform slope. The arrow shows the direction of the propagation of the wave. The frames were consecutively numbered and times when the shots were taken are:

Frame	1		2		3		4		5		6
Time of shot (sec)	68.0		70.9		74.9		77.3		78.0		79.7
Time difference (sec)		1.9		4.0		2.4		0.7		1.7	

Part of the energy flux is directed into the "insert" where it is dissipated. When fluid rises, the flow is separated at the sharp edge and an attached vortex is generated. Its influence can be seen in frame 4 where a strong local elevation of the interface takes place. The vortex causes a local deformation of the interface and subsequent turbulization and mixing of the fluids due to the development of a flow instability. Results of its influence are displayed in frame 5 where deformation of the upper layer close to the 'insert' edge occurs. As a result, the interface form is intermittently meandering, and its boundary is washed out (frame 6), which is a consequence of the formation and breakdown of vortical structures. An appreciable part of the incident wave energy is spent on irregular deformation of the interface and generation of turbulence through the destruction of the arising vortical structures, and on mixing of the fluids. This results in a decrease of the reflected wave energy. Such a conclusion is confirmed by estimates of reflection coefficients that are calculated by processing of data recorded by the gauges. These coefficients are smaller than those concerned with uniform slopes (see Fig. 3.47). It can be concluded that the "insert" is an effective dissipater of energy of incident waves.

In summary, we may state:

1. Interaction of strongly nonlinear internal solitary waves was considered with a nonuniform slope containing a more gentle "insert" as compared with the main part of the slope. This "wedge" was located in the upper region of the slope. It was shown that the influence of the "insert" is small at a gentle main slope but its effect is high at a steep main slope.

2. Nonuniformity of the slope as a gentle “insert” affects the reflection coefficient only weakly. If the main slope is sufficiently steep ($\beta \approx 90^\circ$), its effect increases substantially. Due to the formation of vortical structures close to the edge between ‘insert’ and main slope, the interface is appreciably deformed, and flow instability leads to turbulization and mixing of fluids. As a result, the reflection coefficient decreases.

3.5 Conclusions

Field observations show that the rate of decay of basin-scale internal waves due to the formation of small-scale waves is appreciably greater than that by internal dissipation (Horn et al. 2001). The nonlinear energy transfer from basin-scale internal waves to short-period motions is an important mechanism to enhance mixing and dissipation. Among possible mechanisms which are responsible for the above-mentioned energy transfer, the following subprocesses can be distinguished: (1) nonlinear steepening and disintegration of long internal waves into packets of short-period waves and solitons; (2) shear instability caused by energy transfer from the mean flow to the small-scale motions; (3) shoaling and reflection from slopes; (4) effects of localized constrictions stimulating the development of wave instability; and (5) interaction with topography (Horn et al. 2001; Vlasenko and Hutter 2002b).

Experimental investigations have been conducted under controlled conditions when the required parameters of the medium and generated waves which can be produced are of specific interest. They can be realized when experiments in laboratory tanks are conducted. Data obtained in laboratory experiments possess a high degree of reliability and permit considering the different features of the dynamical processes concerning the propagation of the internal solitary waves. The investigated results allow extending our knowledge and understanding the character of the nonlinear wave propagation in the stratified medium.

Our experimental focus deals with the propagation and interaction of internal waves with underwater obstacles, slopes, and the effect of localized constrictions of the channel. The underwater obstacles are considered to be of rectangular form. The study is a natural continuation of works devoted to the interaction of internal solitary waves with topographic features such as triangles (Wessel and Hutter, 1996, Hüttemann and Hutter, 2001, Vlasenko and Hutter, 2001, Maurer et al., 1996, Sveen et al., 2002, Guo et al. 2004). It has become evident that the degree of wave interaction with a rectangular obstacle is stronger than with a triangular obstruction. The principal attention of our experiments was also focused on strongly nonlinear internal solitary waves. Such more complicated experimental conditions are not only useful from a viewpoint of examination of extreme situations of wave interaction with obstacles, but also essential in verification attempts of numerical models to calculate the scattering of internal solitary waves by topographic features, when the point of separation is on the obstacle.

The analysis of the patterns of the flows induced by the interaction of internal solitary waves with the underwater obstacle as a plate and estimated characteristics of the incident, transmitted, and reflected waves has shown that three scenarios of interaction can be distinguished. The primary parameter determining the degree of interaction is the ratio between the wave amplitude and the distance from the interface to the top of the obstacle $k_{\text{int}} = a/(h_2 - H_{\text{ob}})$. The scenario *transformation* is defined by the inequality $k_{\text{int}} < 0.3$. The scenario *interaction* is characterized by the interval relation $0.4 < k_{\text{int}} < 1$. A distinguished feature of this regime is the formation of a vortex pair due to the increase of the topographic effect caused by the obstacle. This vortex pair is responsible for the generation of a downward jet at a small angle with the vertical direction. Lighter fluid from the upper layer is entrained by the jet and is transported downward. The third scenario *blockage* is defined by the inequality $k_{\text{int}} \geq 1$. A peak arising near the wave crest caused by the generation of a vortex pair transforms into a vertical jet. It is stronger than the vortex pair in the previous case, and it penetrates to larger depth.

Analysis of experimental data showed that the process of interaction of an internal solitary wave with an extended obstacle is similar to the process of its interaction with a thin plate. Differences are in the quantitative characteristics. It is shown that for a large obstacle, blockage of the flow by the obstacle is more effective, and an appreciable part of the energy of the incident wave is spent for the generation of a reflected wave. At moderate coefficients of interaction, the major difference to the case, when a thin plate was used as obstacle, lies in the fact that the arising jet is directed more horizontally; so, it does not penetrate to large depth, and, consequently, the lighter fluid from the upper layer is not much displaced to lower levels.

Other mechanisms resulting in an increase of mixing and dissipation are connected with the intensification of currents and the growth of shear stresses in constrictions. Besides, large-scale displacements of the water masses in the constrictions intensify the local diapycnal mixing due to the increased internal shear and bottom friction. Evidently, transformation, shoaling, and breaking of internal waves can be caused by constrictions. The transformation and the breaking of internal solitary waves were studied for the cases when the characteristic length of the constriction was close to the wavelength. It is shown that the interaction of solitary internal waves with a constriction is determined by the wave amplitude and the value of the minimum gap of the channel generated by the constriction. A formation of a vortex (or vortices) with horizontal axis on the back face of the wave is observed when the wave moves through the constriction. It is shown that the critical regime is characterized by a sharp wave steepening, an amplitude growth in the narrow part and subsequent breaking, and the formation of a vortex on the back face of the wave. At strong interaction, fission of the internal solitary wave into two occurs: the leading part progresses through the constriction but the last part is trapped and forms a reflected wave plus a tail of the leading part. Here, a system of turbulent boluses can be formed. They move downstream and are responsible for the transport of sub-pycnocline water.

The motion of internal solitary waves in the passage through the constriction is of three-dimensional character. This structure is exhibited by the formation of a system of vortices with vertical axes which arise in the diffuser part of the constriction. The motion of the vortices is seen for quite some time after the passage of the waves, and their appearance is the effective mechanism of energy dissipation. These vortices cause motions in the upper layer, as is evidenced on the photographs of dye translation due to vortices. Another important feature of the process of the passage of solitary waves through a constriction is the distribution of the amplitude irregularity in the cross section in front of the constriction.

Important mechanisms of energy transformation in lakes from short-period (internal waves) to small-period motions are concerned with the shoaling of waves and their transformation, overturning, and breaking over sloping boundaries. These processes lead to the generation of turbulence and water mixing. Analysis of the results of the performed experiments and data obtained by other authors showed that there are two principal mechanisms of wave reflections from slopes. They can be distinguished by gentle and steep slopes. This leads to different dependences of reflection coefficients on the topographic parameters. The topographic effect is weak for a gentle slope and the reflection of energy takes place due to instability on the back of the wave, its steepening, breaking, and subsequent generation of turbulence. Then lighter fluid rises under the action of buoyancy forces with subsequent onset of the reflected wave. The mechanism is characterized by considerable mixing of light and heavy fluids. The reflection coefficients grow with amplification of the topographic effects. The distinctive properties of this process are high-energy dissipation and small reflection coefficients, which are realized at gentle slopes. On the other hand, the topographic effect is strong for steep slopes. The amplitude of the wave highly increases near the slope. When the growth stops, rapid elevation of lighter water sets in under the influence of buoyancy forces and an intensive reflected wave is generated. This reflection process at steep slopes is fast. Processes leading to energy dissipation have no time to develop; so, the energy loss to dissipation is small. The reflection coefficients are slightly changed with the amplification of the topographic effects. The mechanism of generation of the reflected wave is concerned with the transformation of kinetic energy of the incident wave into potential energy associated with the submergence of light fluid in heavier fluid, and the inverse process of potential energy transformation into kinetic energy of the reflected waves. Thus, the process of reflection of internal solitary waves from a steep slope is characterized by small dissipation and high reflection.

The interaction of strongly nonlinear internal solitary waves was considered with a nonuniform slope consisting of a steep slope at lower depth and shallower sloping element – called "insert" – close to the shore. It was shown that the influence of the insert is small at a gentle main slope but its effect is high at a steep main slope. If the main slope is sufficiently steep ($\beta \approx 90^\circ$), the effect of the insert increases substantially. Due to the formation of vortical structures close to the edge between insert and main slope the interface is appreciably deformed; flow instability leads to turbulization and mixing of fluids. As a result, the reflection coefficient decreases.

An important role of data of laboratory experiments is also to provide detailed quantitative and qualitative information that is often inaccessible under natural conditions when performing field observations. Qualitative improvement of the numerical models and corroboration of their validity are achieved by verification using the data of the laboratory measurements obtained under well-defined circumstances. Integration of numerical models and laboratory experiments are fruitful approaches to improve the predictions of specific features of the dynamical processes of energy transformation in lakes.

Acknowledgments The authors thank their colleagues from IHM NASU: Dr. Oleksandr Stetsenko for fruitful discussions and for assisting with the experiments; we also thank Dr. Vitaliy Oleksiuk, Mr. Oleksiy Kulik, and Mr Sergey Pihur for help when conducting the experiments.

This research was supported by INTAS Grant No. 03-51-3728.

References

Ablowitz M.J., Segur H. Solitons and the Inverse Scattering Transform. SIAM, 1981, 438 p.

Armi, L.: The hydraulics of two flowing layers with different densities. J. Fluid Mech. **163**, 27–58 (1986)

Benjamin, T.B.: Internal waves of permanent form in fluid of great depth. J. Fluid Mech. **29**, 559–592 (1967)

Boegman, L., Ivey, G.N., Imberger, J.: The degeneration of internal waves in lakes with sloping topography. Limnol. Oceanogr. **50**, 1620–1637 (2005)

Bogucki, D., Garrett, C.:A simple model for the shear-induced decay of an internal solitary wave. J. Phys. Oceanogr. **8**, 1767–1776 (1993)

Bourgault, D., Kelley, D.E.: On the reflectance of uniform slopes for normally incident interfacial solitary nwaves. J. Phys. Oceanogr. **37**, 1156–1162 (2007)

Bourgault, D., Kelley, D.E., Galbraith, P.S.: Interfacial solitary wave run-up in the St. Lawrence estuary. J. Mar. Res. **63**, 1001–1015 (2005)

Bukreev, V.I., Gavrilov, N.V.: Experimental investigation of solitary internal waves in a two-layer fluid. Zh. Prikl. Mekh. Tekhn. Fiziki (PMTF) **N.5**, 51–56 (1983) (in Russian) 1983 [English translation: Sov. Phys. J. Appl. Mech. Tech. Phys. **n.5** (1983)].

Cacchione, D., Wünch, C.: Experimental study of internal waves over a slope. J. Fluid Mech. **66**, 223–239 (1974)

Carr, M., Davies, P.A.: The motion of an internal solitary wave of depression over a fixed bottom bouddary in a shallow, two-layer fluid. Phys. Fluids **18**, 016601 (2006)

Chen, C.-Y., Hsu, J.R.-C., Chen, H.-H., Kuo, C.-F., Cheng, M.-H.: Laboratory observations on internal solitary wave evolution on steep and inverse uniform slopes. Ocean Eng. **34**, 157–170 (2007a)

Chen, C.-Y., Hsu, J.R.-C., Chen, H.-H., Kuo, C.-F., Cheng, M.-H.: An investigation on internal solitary waves in a two-layer fluid: Propagation and reflection from steep slope. Ocean Eng. **34**, 171–184 (2007b)

Dauxious, T., Didier, A., Falcon, E.: Observations of near-critical reflection of internal waves in a stably stratified fluid. Phys. Fluids **16**, 1936–1941 (2004)

Diebels, S., Schuster, B. & Hutter, K.: Nonlinear internal waves over variable bottom topography. *Geophys. Astrophys. Fluid Dyn.* **76**, 165–192 (1994)

Djordjevic, V.D., Redekopp, L.G.: The fission and disintegration of internal solitary waves moving over two-dimensional topography. J. Phys. Oceanogr. **8**, 1016–1024 (1978)

Drazin P.G., Reid W.H. Hydrodynamic stability. Cambridge University Press, 2004, 605 p.

Evans, W.A.B., Ford, M.J.: An integral equation approach to internal (2-layer) solitary waves. Phys. Fluids **8**, 2032–2047 (1996)
Funakoshi, M.: Long internal waves in a two-layer fluid. J. Phys. Soc. Japan **54**, 2470–2476 (1985).
Funakoshi, M., Oikawa, M.: Long internal waves of large amplitude in a two-layer fluid. J. Phys. Soc. Japan **55**,128-144 (1986)
Gavrilov, N.V.: Viscous damping of solitary internal waves in two-layer fluid. Zh. Prikl. Mekh. i Tekhn. Fiziki **N.4**, 51–54 (1988)(in Russian)
Gear, J., Grimshaw, R.: A second-order theory for solitary waves in shallow fluids. Phys. Fluids **26**, 14–29 (1983)
Grue, J., Jensen, P.O., Rusas, P.-O., Sveen, J.K.: Properties of large-amplitude internal waves. J. Fluid Mech. **380**, 257–278 (1999)
Grue J. Generation, propagation, and breaking of internal waves. Chaos, **15**, 037110 (2005)
Guo, Y., Sveen, J.K., Davies, P.A., Grue, J., Dong, P.: Modelling the motion of an internal solitary wave over a bottom ridge in a stratified fluid. Environ. Fluid Mech. **4**, 415–441 (2004)
Helfrich, K.R.: Internal solitary wave breaking and run-up on a uniform slope. J. Fluid Mech. **243**, 133–154 (1992)
Helfrich, K.R., Melville, W.K.: On long nonlinear internal waves over slope-shelf topography. J. Fluid Mech. **167**, 285–308 (1986)
Helfrich, K.R., Melville, W.K., Miles, J.W.: On interfacial solitary waves over slowly varying top [pgraphy. J. Fluid Mech. **149**, 305–317 (1984)
Horn, D.A., Redekopp, L.G., Imberger, J., Ivey, G.N.: Internal wave evolution in a space- time varying field. J. Fluid Mech. **424**, 279–301 (2000)
Horn, D.A., Imberger, J., Ivey, G.N.: The degeneration of large-scale interfacial gravity waves in lakes. J. Fluid Mech. **434**, 181–207 (2001)
Hüttemann, H.: Modulation interner Wasserwellen durch Variation der Bodentopographie. Diploma Thesis, Department of Mechanics, Darmstadt University of Technology, 110 p. (1997)
Hüttemann, H., Hutter, K.: Baroclinic solitary water waves in two-layer fluid system with diffusive interface. Exp.Fluids **30**, 317–326 (2001)
Ivey, G.N., Nokes, R.I.: Vertical mixing due to the breaking of critical internal waves on slope boundaries. J. Fluid Mech. **204**, 479–500 (1989)
Joseph R.I. Solitary waves in a finite depth fluid. J.Fluid Mech., **10**, L225-L227 (1977)
Kakutani, T., Yamazaki, N.: Solitary waves on a two-layer fluid. J. Phys. Soc. Japan **45**, 674–679 (1978)
Kao, T.W., Pan, F.S. Renouard, D.: Internal soliton on the pycnocline : Generation, propagation, and shoaling and breaking over a slope. J. Fluid Mech.**159**, 19–53 (1985)
Keulegan, G.H.: Gradual damping of solitary waves. J. Res. Natl. Bur. Stand. **40**, 480–487 (1948)
Keulegan, G.H.: Characteristics of internal solitary waves. J. Res. Natl. Bur. Stand. **51**, 133–140 (1953)
Koop, C.G., Butler, G.: An investigation of internal solitary waves in a two-fluid system. J. Fluid Mech. **112**, 225–251 (1981)
Kocsis, O., Mathis, B., Gloor, M., Schurter, M., Wüest, A.: Enhanced mixing in narrows: A case study at the Mainau sill (Lake Constance). Aquat.sci. **60**, 236–252 (1998)
Kubota, T., Ko, D.R.S., Dobbs, L.D.: Weakly-nonlinear, long internal gravity waves in stratified fluids of finite depth. J. Hydronautics **12**, 157–165 (1978)
Lawrence, G.A.: On the hydraulics of Boussinesq and non-Boussinesq two-layer flows. J. Fluid Mech. **215**, 457–480 (1990)
Lee, C.-Y., Beardsley, R.C.: The generation of long nonlinear internal waves in a weakly stratified shear flow. J. Geophys. Res. **79**, 453–457 (1974)
Leone, C., Segur, H., Hammack, J.L.: Viscous decay of long internal solitary waves. Phys. Fluids **25**, 942–944 (1982)

Maurer, J.: Skaleneffekte bei internen Wellen im Zweischichten-Fluid mit topographischen Erhebungen. Diploma Thesis, Department of Mechanics, Darmstadt University of Technology, 112 p (1993)

Maurer, J., Hutter, K., Diebels, S.: Viscous effects in internal waves of a two-layered fluid with variable depth. Eur. J. Mech., B/Fluids **15**, 445–470 (1986)

Michallet, H., Barthelemy, E.: Ultrasonic probe and data processing to study interrfacial solitary waves. Exp.Fluids **22**, 380–386 (1997)

Michallet, H., Barthelemy, E. Experimental study of interfacial solitary waves. J. Fluid Mech. **366**, 159–177 (1998)

Michallet, H., Ivey, G.N.: Experiments on mixing due to internal solitary waves breaking on uniform slopes. J. Geophys. Res.**104**, 13467–13477 (1999)

Ono, H.: Algebraic solitary waves in stratified fluids. J. Phys. Soc. Japan **39**, 1082–1091 (1975)

Ostrovsky, L.A., Grue, J.: Evolution equations for strongly nonlinear waves. Phys. Fluids **15**, 2934–2948 (2003)

Ostrovsky, L.A., Stepanyants, Y.A.: Internal solitons in laboratory experiments: Comparison with theoretical models. Chaos **15**, 037111 (2005)

Segur, H., Hammack, J.L.: Soliton models of long internal waves. J. Fluid Mech. **118**, 285–304 (1982)

Schuster, B.: Experimente zu nicht-linaren Wellen grosser Amplitude in einem Rechteckkanal mit variabler Bodentopographie. Ph. D. Dissertation, Department of Mechanics, Darmstadt University of Technology, 165 p (1992)

Stevens, C., Imberger, J.: The initial response of a stratified lake to a surface shear stress. J. Fluid Mech. **342**, 39–66 (1996)

Sveen, J.K., Guo, Y., Davies, P.A., Grue, J.: On the breaking of internal solitary waves at a ridge. J. Fluid Mech. **469**, 161–188 (2002)

Troy, C.D., Koseff, J.R.: The generation and quantitative visualization of breaking internal waves. Exp. Fluids **38**, 549–562 (2005)

Troy, C.D., Koseff, J.R.: The viscous decay of progressive interfacial waves. Phys. Fluids **18**, 026602 (2006)

Turner J.S. Buoyancy effects in fluids. Cambridge University Press, 1973, 367 p.

Umeyama, M,: Experimental and theoretical analyses of internal waves of finite amplitude. J. Waterway, Port, Coastal and Ocean Eng. **128**, 133–141 (2002)

Umeyama, M, Shintani, T.: Visualization analysis of runup and mixing of internal waves on an upper slope. J. Waterway, Port, Coastal and Ocean Eng.**130**, 89–97 (2004)

Vlasenko, V.I., Hutter, K.: Generation of second mode solitary waves by the interaction of a first mode soliton with a sill. Nonlinear Proc. Geophys. **8**, 223–239 (2001)

Vlasenko, V.I., Hutter, K.: Transformation and disintegration of strongly nonlinear internal waves by topography in stratified lakes. Ann.Geophys. **20**, 2087–2103 (2002a)

Vlasenko, V.I., Hutter, K.: Numerical experiments on the breaking of solitary internal waves over a slope-shelf topography. J. Phys. Oceanogr. **32**, 1779–1793 (2002b)

Walker, S.A., Martin, A.J., Easson, W.J., Evans, W.A.B.: Comparison of laboratory and theoretical internal solitary wave kinematics. J. Waterway, Port, Coastal and Ocean Eng. **129**, 210–218 (2003)

Wallace, B.C., Wilkinson, D.L.: Run-up of internal waves on a gentle slope in a two-layered system. J. Fluid Mech. **191**, 419–442 (1988)

Wessel, F.: Wechselwirkung interner Wellen im Zweischichtenfluid mit topographischen Erhebungen. Diploma Thesis, Department of Mechanics, Darmstadt University of Technology, 69 p. (1993)

Wessel, F., Hutter, K.: Interaction of internal waves with topographic sill in a two-layer fluid. J. Phys. Oceanogr. **26**, 5–20 (1996)

Wood, I.R., Simpson, J.E.: Jumps in layered miscible fluids. J. Fluid Mech.**140**, 329–342 (1984)

Wüest, A., Lorke, A.: Small-scale hydrodynamics in lakes. Ann. Rev. Fluid Mech. **35,** 373–412 (2003)

Chapter 4
Numerical Simulations of the Nonhydrostatic Transformation of Basin-Scale Internal Gravity Waves and Wave-Enhanced Meromixis in Lakes

V. Maderich, I. Brovchenko, K. Terletska, and K. Hutter

Abstract The processes of the transformation of basin-scale internal waves are simulated by a numerical three-dimensional nonhydrostatic model that is applied to a sequence of idealized problems, namely the transformation and degeneration of basin-scale internal waves in a rectangular basin, in a basin with a sloping bottom, in a basin with a sill and a cross-section constriction, and finally in a small, elongated lake. The results of the simulations are compared with laboratory experiments and with field observations, when they are available.

4.1 Introduction

4.1.1 Physical Processes Controlling the Transfer of Energy Within an Internal Wave Field from Large to Small Scales

In stratified media, internal waves provide an important mechanism for energy transfer. In a stably stratified lake, wind is one of the principal sources of mechanical energy, which is spent on turbulent mixing in the epilimnion, generation of barotropic and baroclinic circulation and generation of basin-scale surface and internal waves. Wind-induced currents in the epilimnion create the tilt of the thermocline (metalimnion). The corresponding established potential energy is a source for basin-scale internal waves. The Coriolis force somewhat complicates the behavior of the system, and it is significant in long-wave dynamics if the lateral dimension of the lake is larger than the internal Rossby radius $L_R = c_{IW}/f$, where c_{IW} is the phase velocity of long internal waves and f is the Coriolis parameter. Topographic Rossby waves (Stocker and Hutter 1987) and Kelvin and Poincaré-

V. Maderich (✉)
Institute of Mathematical Machine and System Problems of National Academy of Sciences of Ukraine, Kiev, Ukraine

K. Hutter (ed.), *Nonlinear Internal Waves in Lakes*,
Advances in Geophysical and Environmental Mechanics and Mathematics,
DOI 10.1007/978-3-642-23438-5_4,

type waves are excited in these lakes (Hutter 1983). When the lateral dimension of the lake is smaller than L_R, the dominant response of the tilting of the thermocline is a basin-scale gravitational standing internal wave (internal seiche). Field studies indicate, however, that large-scale internal waves transform into an internal surge that may disintegrate into a sequence of solitary waves via nonlinear steepening and interaction with the bottom topography (Hunkins and Fliegel 1973; Thorpe 1977; Farmer 1978; Filatov 2012, Chap. 2 this volume). The ensuing wave evolution then leads to the formation of a continuous spectrum of waves, ranging from basin-scale waves to waves with frequencies approaching the maximum buoyancy frequency. Shear instability (Thorpe 1977), wave reflection (Thorpe 1997), and shoaling on the bottom slope then cause turbulent mixing in the lake interior and benthic boundary layer and result in an enhanced dissipation of the large-scale motion (Wuest and Lorke 2003). In turn, turbulent mixing (meromixis) then alters the background stratification and the transport of momentum, heat, and matter in the lake. Whereas large-scale circulation in a lake is hydrostatic, small-scale processes describing the formation of the internal wave spectrum are fundamentally nonhydrostatic. To understand the mechanisms of the energy transfer between different scales, it is necessary to parametrize the internal wave-enhanced meromixis. The use of analytical methods to describe such processes is restricted to cases of small and moderate amplitude motions. However, internal seiching is often governed by large amplitude phenomena. In this chapter, the processes of the transformation of basin-scale internal waves are simulated by a numerical three-dimensional nonhydrostatic model. In Sect. 4.2 we describe the modified model (Kanarska and Maderich 2003) used in the simulations. Classification of the degeneration regimes of basin-scale internal gravity waves in a lake is considered in Sect. 4.3. In this section, the numerical model is applied to a sequence of idealized problems: the transformation and degeneration of basin-scale internal waves in a rectangular basin, in a basin with sloping boundary, in a basin with a sill and narrowing cross-section and finally in a small elongated lake. Most of these problems are of laboratory scale; this allows to compare results of the simulations with well-controlled laboratory experiments to verify a numerical model and to separate the effects of interest (see also Berntsen et al. 2006). The simulations were also compared with observations when they are available.

4.1.2 Nonhydrostatic Modeling

In the past few decades, great progress has been made in developing methods for the solution of the unsteady three-dimensional Navier–Stokes (NS) equations for incompressible fluids, starting from seminal papers by Harlow and Welch (1965) and Chorin (1968). These methods (see the review by Fletcher (1991)) were implemented in computational fluid dynamics (CFD) codes developed mainly for industrial applications. However, many motions in the ocean and lakes are characterized by important peculiarities (1) the aspect ratio of the fluid containers,

i.e., the ratio of the vertical to the horizontal scales is small; (2) motions are free surface flows; and (3) flows are stratified. Therefore, the pressure distribution is close to hydrostatic and this hydrostatic component can be easily calculated as a function of the atmospheric pressure, free surface elevation, depth, and density. In stably stratified basins, fast surface waves and slow internal waves coexist. A straightforward numerical solution scheme for the NS equations to determine the unsteady three-dimensional fields of velocity, pressure, and scalars (e.g., temperature) and a two-dimensional field of free surface elevation is computationally much too expensive for these flows. Therefore, in almost all models (except the models of surface wave breaking), the free surface position is calculated from the depth-integrated continuity equation instead of the sophisticated marker-and-cell (MAC) method (Harlow and Welch 1965) or the volume-of-fluid (VOF) method (Hirt and Nichols 1981). The family of the so-called "projection methods" of solution of the NS equations was developed following Chorin (1968). In the original work, the solution of the problem was split into two steps. In the first step, the provisional velocity field is advanced in time using the momentum equation without taking the pressure gradients into account. The full pressure field and final divergence-free velocity are found in the second (projection) step. To improve the efficiency of this method in the nonhydrostatic models, the pressure is decomposed into hydrostatic and nonhydrostatic parts (Mahadevan et al. 1996a, b; Marshall et al. 1997a, b; Casulli and Stelling 1998). In the first step, the hydrostatic pressure gradients are retained in the momentum equations, neglecting the contribution of the nonhydrostatic pressure. The surface elevation and provisional velocity field are obtained simultaneously by an implicit time-stepping method. At the second step, the provisional velocity is corrected by including the nonhydrostatic pressure terms in such a fashion that the resulting velocity field is nondivergent. Further improvements include nonhydrostatic corrections of the surface elevation (Casulli 1999; Casulli and Zanolli 2002) and using the "pressure correction" method by Jankowski (1999), Fringer et al. (2006), and Kanarska et al. (2007) in which, at the first step, the nonhydrostatic pressure from the previous time step is also retained, whereas at the second step, a pressure correction is computed. The major characteristics of the nonhydrostatic baroclinic models with pressure decomposition are given in Table 4.1.

Most of the developed approaches are not compatible with a large class of hydrostatic models that use mode-splitting and terrain-following coordinates (e.g., POM: Blumberg and Mellor 1987; BOM: Berntsen 2000; ROMS: Shchepetkin and McWilliams 2005; and THREETOX: Maderich et al. 2008). In these models, the vertically integrated equations of continuity and momentum (external mode) are separated from the equations for the vertical structure of the flow (internal mode). The two-dimensional equations for the external mode variables are solved explicitly, using a short external time step, whereas three-dimensional velocity and scalar fields are computed semi-implicitly with a larger internal step. Most of these models use terrain-following or hybrid vertical coordinates, which allow accurate description of the complicated bottom relief of coastal seas or lakes. Only recently, a few nonhydrostatic algorithms with mode

Table 4.1 Nonhydrostatic free-surface baroclinic models using pressure decomposition

Reference	Vertical coordinate	Horizontal coordinate	Mode splitting	Hydrostatic part
Mahadevan et al. (1996a,b)	Mixed σ/z	Orthogonal curvilinear	No	
Marshall et al. (1997a, b)	z	Orthogonal curvilinear	No	
Casulli and Stelling (1998)	z	Cartesian	No	
Jankowski (1999)	σ	Unstructured	No	TELEMAC
Casulli and Zanolli (2002)	z	Unstructured	No	
Kanarska and Maderich (2003)	s	Orthogonal curvilinear	Yes	POM
Wadzuk and Hodges (2004)	z	Cartesian	No	ELCOM
Heggelund et al. (2004)	σ	Cartesian	Yes	BOM
Fringer et al. (2006)	z	Unstructured	No	
Kanarska et al. (2007)	s	Orthogonal curvilinear	Yes	ROMS

splitting were developed for POM (Kanarska and Maderich 2003), BOM (Heggelund et al. 2004), and ROMS (Kanarska et al. 2007) to convert these codes into nonhydrostatic models or to embed nonhydrostatic submodels into large-scale hydrostatic models. In this chapter, a modified model of Kanarska and Maderich (2003) is described and used for modeling internal waves in lakes.

4.2 Description of the Nonhydrostatic Model

4.2.1 Model Equations

Stably stratified flows in lakes include large-scale currents, internal waves, and turbulence. In general, three approaches can be used to describe these flows (Pope, 2000): (1) Direct numerical simulation (DNS), when the Navier–Stokes equations supplemented by transport equations for temperature are solved; (2) Reynolds averaged Navier–Stokes (RANS) equations supplemented by a closure model of turbulence are solved; and (3) Large-eddy simulation (LES) in which large eddies in resolved scales are computed, whereas small-scale turbulence in small non-resolved scales is parametrized. The aim of this study is to gain more insight into the energy transfer between processes of different scales in the lake; so, the LES approach was chosen as compromise between computationally expensive DNS and complicated RANS models. In the used LES model, the turbulent transports of mass, momentum, and a scalar are parametrized in terms of resolved-scale flow. The 3D equations of continuity, momentum, and scalar transport in the Boussinesq approximation for resolved-scale variables are

$$\frac{\partial U_\alpha}{\partial x_\alpha} = 0, \tag{4.1}$$

$$\frac{\partial U_\alpha}{\partial t} + U_\beta \frac{\partial U_\alpha}{\partial x_\beta} - \varepsilon_{\alpha\beta\gamma} f_\beta U_\gamma = -\frac{1}{\rho_0}\frac{\partial P}{\partial x_\alpha} - \frac{\partial \tau_{\alpha\beta}}{\partial x_\beta} + \nu \frac{\partial}{\partial x_\beta}\left(\frac{\partial U_\alpha}{\partial x_\beta} + \frac{\partial U_\beta}{\partial x_\alpha}\right) - g_\alpha \frac{\rho}{\rho_0}, \tag{4.2}$$

$$\frac{\partial \phi}{\partial t} + U_\alpha \frac{\partial \phi}{\partial x_\alpha} = -\frac{\partial \psi_\alpha}{\partial x_\alpha} + \chi_\phi \frac{\partial^2 \phi}{\partial x_\alpha \partial x_\alpha}. \tag{4.3}$$

Here t denotes time, $U_\alpha = (U, V, W)$, P, and ϕ are the resolved-scale velocity, pressure, and scalar (potential temperature T and salinity S) in Cartesian coordinates $x_\alpha = (x, y, z)$, with z directed vertically upward; ρ is density; ρ_0 is undisturbed density; $f_\alpha = (0; 0; f)$ is the Coriolis parameter, $\varepsilon_{\alpha\beta\gamma}$ is the permutation symbol, $g_\alpha = (0, 0, g)$, g is the gravitational acceleration; $\tau_{\alpha\beta}$ is the tensor of the subgrid-scale turbulent stress and ψ_α is a vector of subgrid-scale turbulent flux of the scalar; and ν and χ_ϕ are kinematic viscosity and diffusivity, respectively. System (4.1)–(4.3) is closed by the equation of state for the density ρ of water $\rho = \rho(S,T,P)$, according to Mellor (1991). Note, that in (4.2) the acceleration due to the Coriolis force is taken in the "traditional approximation" and $f = 2\Omega_z$, where Ω_z is the vertical component of the angular velocity of the rotation of the Earth.

The tensor of turbulent subgrid-scale stresses (SGS), $\tau_{\alpha\beta}$ and flux of scalar, ψ_α are parametrized in terms of the resolved scale variables (U and ϕ) using the eddy viscosity model of SGS:

$$\tau_{\alpha\beta} = -K_M\left(\frac{\partial U_\alpha}{\partial x_\beta} + \frac{\partial U_\beta}{\partial x_\alpha}\right) + \frac{2}{3}k_s\delta_{\alpha\beta}, \tag{4.4}$$

$$\psi_\alpha = -K_H \frac{\partial \phi}{\partial x_\alpha}, \tag{4.5}$$

where $\delta_{\alpha\beta}$ is the Kronecker symbol, K_M the eddy viscosity, K_H the eddy diffusivity, and $Pr_t = K_M/K_H$the turbulent Prandtl number. The subgrid-scale kinetic energy $k_s = (1/2)\tau_{\alpha\alpha}$ is included in the resolved scale pressure P. The eddy viscosity K_M is calculated using the Smagorinsky (1963) model, modified for stratified flows (e.g., Siegel and Domaradzki 1994). In this model, K_M is parametrized as

$$K_M = (C_s\delta)^2\sqrt{S'^2(1 - Ri_t/Ri_{cr})}, \tag{4.6}$$

where $Ri_t = N'^2/S'^2$ is the Richardson number:

$$S'^2 = \frac{1}{2}\left(\frac{\partial U_\alpha}{\partial x_\beta} + \frac{\partial U_\beta}{\partial x_\alpha}\right)^2, \quad N'^2 = -\frac{g}{\rho_0 Pr_t}\frac{\partial \tilde{\rho}}{\partial z}.$$

The critical value of the Richardson number $Ri_{\mathrm{cr}} = 0.25$ (Miles, 1961), C_{s} is the Smagorinsky constant, and $\delta = \min(l, l_\Delta)$, where l_Δ is the scale of the subgrid turbulence. In the finite-difference representation, l_Δ is usually the nominal grid spacing:

$$l_\Delta = (\mathrm{d}x \cdot \mathrm{d}y \cdot \mathrm{d}z)^{1/3}, \tag{4.7a}$$

whereas l is the distance to the solid boundary or to the free surface. Here, $\mathrm{d}x$ and $\mathrm{d}y$ are horizontal mesh sizes and $\mathrm{d}z$ is the vertical mesh size. However, when the horizontal scales of processes are much larger than the vertical ones, another representation of l_Δ can be used, namely,

$$l_\Delta = \frac{3 \cdot \mathrm{d}x \cdot \mathrm{d}y \cdot \mathrm{d}z}{\mathrm{d}x \cdot \mathrm{d}y + \mathrm{d}y \cdot \mathrm{d}z + \mathrm{d}z \cdot \mathrm{d}x}. \tag{4.7b}$$

When $\mathrm{d}x \approx \mathrm{d}y \approx \mathrm{d}z$, then $l_\Delta \approx \mathrm{d}x$ and when $\mathrm{d}x \approx \mathrm{d}y \gg \mathrm{d}z$, then $l_\Delta \approx \mathrm{d}z$. The vertical gradient of the potential density $\tilde{\rho}$ is defined by

$$\frac{\partial \tilde{\rho}}{\partial z} = \frac{\partial \rho}{\partial z} - \frac{1}{c_{\mathrm{s}}^2}\frac{\partial P}{\partial z}$$

where c_{s} is the speed of sound. The value $K_M = 0$ is chosen when $Ri_t \geqslant Ri_{\mathrm{cr}}$. Finally, the turbulent Prandtl number is given by $Pr_t = 1$.

The kinematic boundary condition at the free surface $z = \eta$ is

$$W = \frac{\partial \eta}{\partial t} + U\frac{\partial \eta}{\partial x} + V\frac{\partial \eta}{\partial y}, \tag{4.8}$$

and the pressure equals $P = P_a$, where P_a is the atmospheric pressure. The fluxes of momentum and scalar (heat and salinity) are approximately prescribed as

$$K_M \frac{\partial (U, V)}{\partial z} = \frac{(\tau_{0x}, \tau_{0y})}{\rho_0}, \quad K_H \frac{\partial (\phi)}{\partial z} = F_\phi, \tag{4.9}$$

where τ_{0x} and τ_{0y} are the components of the surface wind stress vector; F_ϕ are surface heat and freshwater fluxes. Note that (4.9) assumes $(|\partial W/\partial x|, |\partial W/\partial y|) \ll (|\partial U/\partial z|, |\partial V/\partial z|)$, which expresses the shallowness property. At solid boundaries, the no-slip and no-flux boundary conditions are used. At an open boundary, a set of open boundary conditions can be used (Mellor 2004).

Integrating the continuity equation (4.1) over depth from the bottom, $z = -H(x, y)$, to the free-surface, $z = \eta$, and applying the kinematic condition (4.8) and the no-slip condition on the bottom yields the equation

$$\frac{\partial \eta}{\partial t} + \frac{\partial}{\partial x}\int_{-H}^{\eta} U \mathrm{d}z' + \frac{\partial}{\partial y}\int_{-H}^{\eta} V \mathrm{d}z' = 0, \tag{4.10}$$

that will be used to determine the elevation of the free surface.

The pressure P can be decomposed into the sum of atmospheric P_a, hydrostatic P_h, and nonhydrostatic Q components as $P = P_\mathrm{a} + P_\mathrm{h} + Q$. The hydrostatic pressure component is determined from the vertical momentum equation by neglecting the convective, the Coriolis, and the viscosity terms as

$$P_\mathrm{h}(x, y, z, t) = g\rho_0\eta(x, y, t) + g\int_{z}^{0} \rho(x, y, z', t)\mathrm{d}z' \tag{4.11}$$

We assume that at the free surface, $z = \eta$, the nonhydrostatic component of the pressure equals to zero ($Q = 0$). This does not mean, however, that effects of nonhydrostatic pressure disappear at the surface because they persist in the momentum equations and therefore in (4.10) that govern the free surface evolution.

4.2.2 Model Equations in Generalized Vertical Coordinates

The nonhydrostatic numerical algorithm was implemented using a horizontal curvilinear orthogonal coordinate system (Mellor 2004) and general vertical coordinates (Mellor et al. 2002). Transformation from the Cartesian coordinates into general vertical coordinates allows flexible and accurate description of the bottom topography. For the sake of simplicity, Cartesian horizontal coordinates are considered.

Transformation from the Cartesian coordinate system (x,y,z,t) to the s-coordinate system (x^*, y^*, k, t^*) is

$$\begin{aligned} x &= x^*, \quad y = y^*, \quad t = t^* \\ z_k &= \eta(x^*, y^*, t^*) + s(x^*, y^*, k, t^*) \end{aligned} \tag{4.12}$$

where k is a vertical variable. The top numerical level at $k = 1$ follows the water surface ($s = 0$ at $k = 1$) and the lowest numerical level $k = k_\mathrm{b}$ follows the bottom surface ($s = -(H + \eta)$ at $k = k_\mathrm{b}$). The transformation includes as limiting cases the standard sigma system: $s = \sigma(k)(H(x, y) + \eta(x, y, t))$ and quasi-z-level system: $s = \sigma(k)(H_\mathrm{max} + \eta(x, y, t))$, where H_max is the maximum depth (Fig. 4.1). In the quasi-z-level system, s is still a function of time and the z-levels change in time according to changes of the free surface elevation. The quasi z-level system is most

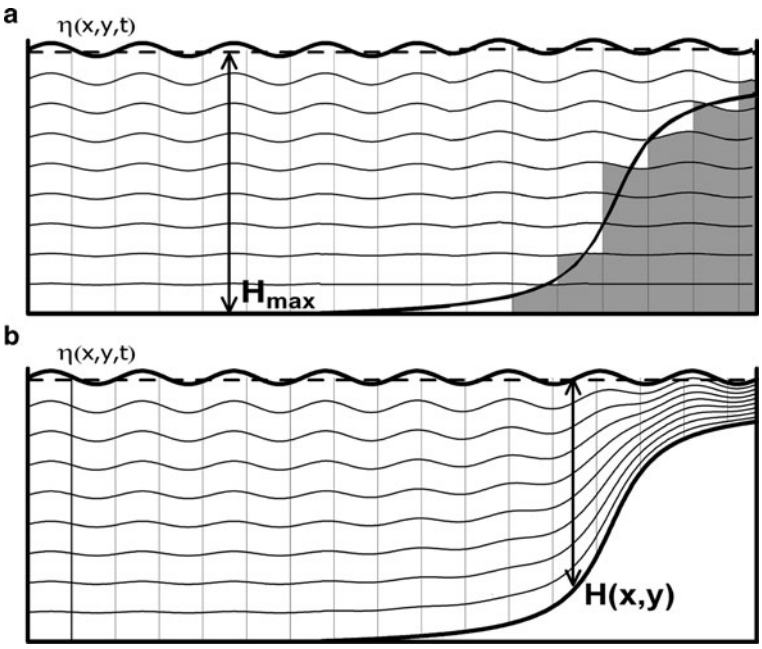

Fig. 4.1 Vertical coordinate system: (**a**) quasi-z levels and (**b**) sigma levels

appropriate for steep bottom topography with underwater structures, whereas the sigma system is best for smooth topography.

It is well known that terrain-following ocean models have difficulties in simulating baroclinic flows over steep topography because of the pressure gradient errors. Two parameters describe the steepness of the bottom topography (Ezer et al. 2002): "slope parameter" $s_{\mathrm{H}} = |\delta H|/2H$ and "hydrostatic consistency parameter" $r_{\mathrm{H}} = \sigma \delta H/(H\delta\sigma)$, where $\delta H$and $\delta\sigma$ are grid cell variations of H and σ. When $s_{\mathrm{H}} \ll 1$ and $r_{\mathrm{H}} \leq 1$, then the sigma-system can be applied but elsewhere quasi-z-level system should be used. With (4.12), the transformation of the governing equations (4.1)–(4.3) from the Cartesian coordinates into the s-vertical coordinate system (Kanarska and Maderich 2003) is as follows (asterisks are now omitted):

$$\frac{\partial U s_k}{\partial x} + \frac{\partial V s_k}{\partial y} + \frac{\partial U A_1}{\partial k} + \frac{\partial V A_2}{\partial k} + \frac{\partial W}{\partial k} = 0, \tag{4.13}$$

$$\begin{aligned}
&\frac{\partial U s_k}{\partial t}+\frac{\partial U^2 s_k}{\partial x}+\frac{\partial UV s_k}{\partial y}+\frac{\partial U\omega}{\partial k}-fVs_k\\
&=-gs_k\frac{\partial \eta}{\partial x}-g\frac{s_k}{\rho_0}\int_k^1\left[s_k\frac{\partial \rho}{\partial x}+A_1\frac{\partial \rho}{\partial k'}\right]\mathrm{d}k'-\left(\frac{\partial s_k Q}{\partial x}+\frac{\partial QA_1}{\partial k}\right)\\
&+\frac{\partial}{\partial k}\left[\frac{(K_M+\nu)}{s_k}\frac{\partial U}{\partial k}\right]+\mathrm{Dif}(U),
\end{aligned}\tag{4.14}$$

$$\begin{aligned}
&\frac{\partial V s_k}{\partial t}+\frac{\partial UV s_k}{\partial x}+\frac{\partial V^2 s_k}{\partial y}+\frac{\partial V\omega}{\partial k}+fUs_k\\
&=-gs_k\frac{\partial \eta}{\partial y}-g\frac{s_k}{\rho_0}\int_k^1\left[s_k\frac{\partial \rho}{\partial y}+A_2\frac{\partial \rho}{\partial k'}\right]\mathrm{d}k'-\left(\frac{\partial s_k Q}{\partial y}+\frac{\partial QA_2}{\partial k}\right)\\
&+\frac{\partial}{\partial k}\left[\frac{(K_M+\nu)}{s_k}\frac{\partial V}{\partial k}\right]+\mathrm{Dif}(V),
\end{aligned}\tag{4.15}$$

$$\frac{\partial W s_k}{\partial t}+\frac{\partial WU s_k}{\partial x}+\frac{\partial WV s_k}{\partial y}+\frac{\partial W\omega}{\partial k}=-\frac{\partial Q}{\partial k}+\frac{\partial}{\partial k}\left[\frac{K_M}{s_k}\frac{\partial W}{\partial k}\right]+\mathrm{Dif}(W),\tag{4.16}$$

where, $s_k=\delta s$ is the distance between levels and

$$A_1=-\left(\frac{\partial s}{\partial x}+\frac{\partial \eta}{\partial x}\right),\quad A_2=-\left(\frac{\partial s}{\partial y}+\frac{\partial \eta}{\partial y}\right),\quad A_3=-\left(\frac{\partial s}{\partial t}+\frac{\partial \eta}{\partial t}\right).$$

The transformed vertical velocity ω is given by

$$\omega=W+A_1U+A_2V+A_3.\tag{4.17}$$

The equation for the scalar ϕ (4.3) is written as

$$\frac{\partial \phi s_k}{\partial t}+\frac{\partial U\phi s_k}{\partial x}+\frac{\partial V\phi s_k}{\partial y}+\frac{\partial W\phi}{\partial k}=\frac{\partial}{\partial k}\left[\frac{(K_H+\chi_\phi)}{s_k}\frac{\partial \phi}{\partial k}\right]+\mathrm{Dif}(\phi).\tag{4.18}$$

while the terms of the horizontal diffusion of momentum and scalar are

$$\mathrm{Dif}(U)=\frac{\partial \hat{\tau}_{xx}}{\partial x}+\frac{\partial}{\partial k}\frac{A_1}{s_k}\hat{\tau}_{xx}+\frac{\partial \hat{\tau}_{xy}}{\partial y}+\frac{\partial}{\partial k}\frac{A_2}{s_k}\hat{\tau}_{xy},$$

$$\mathrm{Dif}(V)=\frac{\partial \hat{\tau}_{yy}}{\partial y}+\frac{\partial}{\partial k}\frac{A_2}{s_k}\hat{\tau}_{yy}+\frac{\partial \hat{\tau}_{xy}}{\partial x}+\frac{\partial}{\partial k}\frac{A_1}{s_k}\hat{\tau}_{xy},$$

$$\mathrm{Dif}(W) = \frac{\partial \hat{\tau}_{zx}}{\partial x} + \frac{\partial}{\partial k}\frac{A_2}{s_k}\hat{\tau}_{zx} + \frac{\partial \hat{\tau}_{zy}}{\partial y} + \frac{\partial}{\partial k}\frac{A_1}{s_k}\hat{\tau}_{zy},$$

$$\mathrm{Dif}(\phi) = \frac{\partial \hat{q}_x}{\partial x} + \frac{\partial}{\partial k}\frac{A_1}{s_k}\hat{q}_x + \frac{\partial \hat{q}_y}{\partial y} + \frac{\partial}{\partial k}\frac{A_2}{s_k}\hat{q}_y,$$

where

$$\hat{\tau}_{xx} = 2K_M\left(s_k\frac{\partial U}{\partial x} + \frac{\partial}{\partial k}A_1U\right),$$

$$\hat{\tau}_{xy} = \hat{\tau}_{yx} = K_M\left(s_k\frac{\partial U}{\partial y} + \frac{\partial}{\partial k}A_2U + s_k\frac{\partial V}{\partial x} + \frac{\partial}{\partial k}A_1V\right),$$

$$\hat{\tau}_{yy} = 2K_{_M}\left(s_k\frac{\partial V}{\partial y} + \frac{\partial}{\partial k}A_2V\right),$$

$$\hat{\tau}_{xz} = 2K_M\left(s_k\frac{\partial W}{\partial x} + \frac{\partial}{\partial k}A_1W\right), \quad \hat{q}_x = K_H\left(s_k\frac{\partial \phi}{\partial x} + \frac{\partial}{\partial k}A_1\phi\right),$$

$$\hat{\tau}_{yz} = 2K_M\left(s_k\frac{\partial W}{\partial y} + \frac{\partial}{\partial k}A_2W\right), \quad \hat{q}_y = K_H\left(s_k\frac{\partial \phi}{\partial y} + \frac{\partial}{\partial k}A_2\phi\right).$$

Note that the metric of the coordinate system x, y, k, t [with asterisks x^*, y^*, t^* in (4.12)] is not orthogonal, and the unknown velocity components (U, V, W) are not those of the original Cartesian system.

Apart from topographic Rossby waves, the above equations describe fast external gravity waves and slow internal gravity waves. In many circulation models (e.g., POM, BOM, ROMS, and THREETOX), the vertically integrated equations of motion and continuity (external mode) are separated from the equations for the vertical structure (internal mode). The 2D equations for the external mode are solved then explicitly, using a short external time step Δt_{E} to satisfy the Courant–Friedrichs–Lewy condition for fast barotropic long waves. The 3D equations for the internal mode are solved semi-implicitly with a larger internal step Δt_{I}. This approach was recently implemented in nonhydrostatic algorithms (Kanarska and Maderich 2003; Heggelund et al. 2004; Kanarska et al. 2007). The vertically averaged barotropic velocities and nonhydrostatic pressure are given by

$$\bar{U} \equiv \int_{\mathrm{kb}}^{1} U\mathrm{d}k, \quad \bar{V} \equiv \int_{\mathrm{kb}}^{1} V\mathrm{d}k, \quad \bar{Q} \equiv \int_{\mathrm{kb}}^{1} Q\mathrm{d}k,$$

in which integration is from the basal to the free surface. With these, the equations for the surface elevation (4.10) can be written as

$$\frac{\partial \eta}{\partial t} + \frac{\partial \overline{U} s_k}{\partial x} + \frac{\partial \overline{V} s_k}{\partial y} = 0. \tag{4.19}$$

The depth-averaged horizontal momentum equations take the forms

$$\begin{aligned}
&\frac{\partial \bar{U} s_k}{\partial t} + \frac{\partial \bar{U}^2 s_k}{\partial x} + \frac{\partial \bar{U}\bar{V} s_k}{\partial y} - f\bar{V} s_k + g s_k \frac{\partial \eta}{\partial x} \\
&\quad = -\tau_{0x} + \tau_{bx} + \overline{Dif}(\bar{U}) - g\frac{s_k}{\rho_0}\int_{\mathrm{kb}}^{1}\int_{k}^{1}\left[s_k\frac{\partial \rho}{\partial x} + A_1\frac{\partial \rho}{\partial k'}\right]\mathrm{d}k'\mathrm{d}k \\
&\qquad - \left(s_k\frac{\partial \bar{Q}}{\partial x} + A_1\frac{\partial \bar{Q}}{\partial k}\right) + G_x,
\end{aligned} \tag{4.20}$$

$$\begin{aligned}
&\frac{\partial \bar{V} s_k}{\partial t} + \frac{\partial \bar{U}\bar{V} s_k}{\partial x} + \frac{\partial \bar{V}^2 s_k}{\partial y} + f\bar{U} s_k + g s_k \frac{\partial \eta}{\partial y} \\
&\quad = -\tau_{0y} + \tau_{by} + \overline{\mathrm{Dif}}(\bar{V}) - g\frac{s_k}{\rho_0}\int_{\mathrm{kb}}^{1}\int_{k}^{1}\left[s_k\frac{\partial \rho}{\partial y} + A_2\frac{\partial \rho}{\partial k'}\right]\mathrm{d}k'\mathrm{d}k \\
&\qquad - \left(s_k\frac{\partial \bar{Q}}{\partial y} + A_2\frac{\partial \bar{Q}}{\partial k}\right) + G_y,
\end{aligned} \tag{4.21}$$

where G_x, G_y are the so-called dispersion terms (Blumberg and Mellor 1987), which are the result of the integration over depth of the advective and diffusive terms; and τ_{bx}, τ_{by} are the bottom shear stresses, that can be determined from the internal mode solution. The terms $\overline{\mathrm{Dif}}(\bar{U})$ and $\overline{\mathrm{Dif}}(\bar{V})$ are depth-averaged horizontal viscosity. For depth-independent kinematic viscosity, $\overline{\mathrm{Dif}}(\,) = \mathrm{Dif}(\,)$.

4.2.3 Numerical Algorithm

The model equations are solved on an Arakawa-C grid with the scalars located at the center of the cell, while the velocity components are defined at the center of the cell faces. The numerical solution of the governing equations is based on the modified algorithm by Kanarska and Maderich (2003), with the following four-stage procedure: (1) calculation of the free surface level and the depth-integrated velocity field; (2) calculation of the provisional hydrostatic components of velocity; (3) calculation of the nonhydrostatic components of the velocity and pressure fields; and (4) calculation of scalar fields. The procedure of the solution of the model equations on the time interval $[n-1; n+1]$ with external time step Δt_{E} and internal time step $\Delta t_{\mathrm{I}} = M\Delta t_{\mathrm{E}}$ is summarized as follows:

First Stage. Following the POM algorithm (Blumberg and Mellor 1987), the 2D equations for the external mode are solved explicitly with a short external time step $\Delta t_{\mathrm{E}} = \Delta t_{\mathrm{I}}/M$ to determine the free surface elevation and depth-averaged velocities:

$$\frac{\eta^{m+1}-\eta^{m-1}}{2\Delta t_{\mathrm{E}}}+\frac{\partial(\bar{U}s_k)^m}{\partial x}+\frac{\partial(\bar{V}s_k)^m}{\partial y}=0, \tag{4.22}$$

$$\begin{aligned}&\frac{(\bar{U}s_k)^{m+1}-(\bar{U}s_k)^{m-1}}{2\Delta t_E}+\frac{\partial\left(\bar{U}^2s_k\right)^m}{\partial x}+\frac{\partial(\bar{U}\bar{V}s_k)^m}{\partial y}-\overline{\mathrm{Dif}}\left(\bar{U}^{m-1}\right)\\&+gs_k\frac{\partial\eta^m}{\partial x}-f(\bar{V}s_k)^m\\&=-\left(s_k\frac{\partial\bar{Q}^n}{\partial x}+A_1\frac{\partial\bar{Q}^n}{\partial k}\right)-\frac{gs_k{}^n}{\rho_0}\int_{\mathrm{kb}}^1\int_k^1\left(s_k{}^n\frac{\partial\rho^n}{\partial x}+A_1\frac{\partial\rho^n}{\partial k'}\right)\mathrm{d}k'\mathrm{d}k\\&+G_x^n-\frac{\tau^{(x)}}{\rho_0}+\tau_{bx}^n,\end{aligned} \tag{4.23}$$

$$\begin{aligned}&\frac{(\bar{V}s_k)^{m+1}-(\bar{V}s_k)^{m-1}}{2\Delta t_E}+\frac{\partial(\bar{V}\bar{U}s_k)^m}{\partial x}+\frac{\partial\left(\bar{V}^2s_k\right)^m}{\partial y}-\overline{\mathrm{Dif}}\left(\bar{V}^{m-1}\right)\\&+gs_k\frac{\partial\eta^m}{\partial y}+f(\bar{U}s_k)^m\\&=-\left(s_k\frac{\partial\bar{Q}^n}{\partial y}+A_2\frac{\partial\bar{Q}^n}{\partial k}\right)-\frac{gs_k{}^n}{\rho_0}\int_{\mathrm{kb}}^1\int_k^1\left(s_k{}^n\frac{\partial\rho^n}{\partial y}+A_2\frac{\partial\rho^n}{\partial k'}\right)\mathrm{d}k'\mathrm{d}k\\&+G_y^n-\frac{\tau^{(y)}}{\rho_0}+\tau_{by}^n.\end{aligned} \tag{4.24}$$

The index $m=1,\ldots,M$ marks the external time stepping, while the index n refers to the internal time stepping. The Courant–Friedrichs–Levy (CFL) computational stability condition limits the external mode time step Δt_{E}. All terms on the right-hand side of (4.22)–(4.24) are evaluated at the internal time step and kept constant during the external time steps. The advective and horizontal diffusion terms in the external mode are calculated by vertical integration of the corresponding internal terms. To retain the nonhydrostatic dynamics in the free surface field, (1) the terms involving the nonhydrostatic pressure are retained in equations (4.23)–(4.24) following Kanarska et al. (2007) and (2) the initial 2D velocity fields on each external stage are determined by direct integration of the general nonhydrostatic 3D velocity fields of the previous internal step. According to the POM algorithm, the obtained M fields of the free surface elevation are averaged at the interval $[n;n+1]$. This averaged value η is used in the internal mode equations at the following stage. Thus, two modes are directly coupled at each internal step.

Second Stage. The 3D equations for the internal mode are solved by the projection method at the second and third stages. At first, the momentum equations without the nonhydrostatic component of the pressure ($Q=0$) are solved semi-explicitly with a large internal time step Δt_{I} to determine the provisional velocities (U,V,W). In semi-discrete form, they are

$$\frac{\left(\tilde{U}s_k\right)^{n+1}-(Us_k)^{n-1}}{2\Delta t_{\mathrm{I}}}+\frac{\partial(U^2s_k)^n}{\partial x}+\frac{\partial(UVs_k)^n}{\partial y}+\frac{\partial(U\omega s_k)^n}{\partial k}$$
$$=-gs_k\frac{\partial\tilde{\eta}}{\partial x}-g\frac{{s_k}^n}{\rho_0}\int_k^1\left[{s_k}^n\frac{\partial\rho^n}{\partial x}+A_1\frac{\partial\rho^n}{\partial k'}\right]\mathrm{d}k'+\frac{\partial}{\partial k}\left[\frac{(K_M+\nu)}{{s_k}^{n+1}}\frac{\partial\tilde{U}^{n+1}}{\partial k}\right]$$
$$+\mathrm{Dif}\left(U^{n-1}\right)+f(Vs_k)^n, \tag{4.25}$$

$$\frac{\left(\tilde{V}s_k\right)^{n+1}-(Vs_k)^{n-1}}{2\Delta t_{\mathrm{I}}}+\frac{\partial(UVs_k)^n}{\partial x}+\frac{\partial(V^2s_k)^n}{\partial y}+\frac{\partial(V\omega)^n}{\partial k}$$
$$=-gs_k\frac{\partial\tilde{\eta}}{\partial y}-g\frac{{s_k}^n}{\rho_0}\int_k^1\left[{s_k}^n\frac{\partial\rho^n}{\partial y}+A_2\frac{\partial\rho^n}{\partial k'}\right]\mathrm{d}k'+\frac{\partial}{\partial k}\left[\frac{(K_M+\nu)}{{s_k}^{n+1}}\frac{\partial\tilde{V}^{n+1}}{\partial k}\right]$$
$$+\mathrm{Dif}\left(V^{n-1}\right)-f(Us_k)^n, \tag{4.26}$$

$$\frac{\left(\tilde{W}s_k\right)^{n+1}-(Ws_k)^{n-1}}{2\Delta t_{\mathrm{I}}}+\frac{\partial(UWs_k)^n}{\partial x}+\frac{\partial(VWs_k)^n}{\partial y}+\frac{\partial(W\omega s_k)^n}{\partial k}$$
$$=\frac{\partial}{\partial k}\left[\frac{(K_M+\nu)}{{s_k}^{n+1}}\frac{\partial\tilde{W}^{n+1}}{\partial k}\right]+\mathrm{Dif}\left(W^{n-1}\right). \tag{4.27}$$

At this stage, all boundary conditions for the velocity field are satisfied. As evident from (4.25)–(4.27), the vertical viscosity terms are treated implicitly. When these equations are discretized, the three-diagonal matrices are solved by the direct method.

Third Stage. At this step, the solution for the provisional velocity field is corrected with the gradient of the nonhydrostatic pressure Q to satisfy the continuity equation. In semi-discrete form, the momentum equations are

$$\frac{(Us_k)^{n+1}-\left(\tilde{U}s_k\right)^{n+1}}{2\Delta t_{\mathrm{I}}}=-\left(\frac{\partial(s_kQ)^{n+1}}{\partial x}+\frac{\partial(QA_1)^{n+1}}{\partial k}\right), \tag{4.28}$$

$$\frac{(Vs_k)^{n+1}-\left(\tilde{V}s_k\right)^{n+1}}{2\Delta t_{\mathrm{I}}}=-\left(\frac{\partial(s_kQ)^{n+1}}{\partial y}+\frac{\partial(QA_2)^{n+1}}{\partial k}\right), \tag{4.29}$$

$$\frac{(Ws_k)^{n+1}-\left(\tilde{W}s_k\right)^{n+1}}{2\Delta t_{\mathrm{I}}}=-\frac{\partial Q^{n+1}}{\partial k} \tag{4.30}$$

and the continuity equation is

$$\frac{\partial (Us_k)^{n+1}}{\partial x} + \frac{\partial (Vs_k)^{n+1}}{\partial y} + \frac{\partial (UA_1)^{n+1}}{\partial k} + \frac{\partial (VA_2)^{n+1}}{\partial k} + \frac{\partial W^{n+1}}{\partial k} = 0. \tag{4.31}$$

Substitution of the expressions for the velocities into (4.31) results in the Poisson equation for the nonhydrostatic pressure component Q as follows:

$$\begin{aligned}
&\left[\frac{\partial}{\partial x}\left(s_k \frac{\partial Q}{\partial x}\right) + \frac{\partial}{\partial x}\left(A_1 \frac{\partial Q}{\partial k}\right) + \frac{\partial}{\partial k}\left(A_1 \frac{\partial Q}{\partial x}\right) + \frac{\partial}{\partial y}\left(s_k \frac{\partial Q}{\partial y}\right) + \frac{\partial}{\partial y}\left(A_2 \frac{\partial Q}{\partial k}\right)\right. \\
&\left. + \frac{\partial}{\partial k}\left(A_2 \frac{\partial Q}{\partial y}\right) + \frac{\partial}{\partial k}\left(\frac{1}{s_k}\frac{\partial Q}{\partial k}\right) + \frac{\partial}{\partial k}\left(\frac{{A_1}^2}{s_k}\frac{\partial Q}{\partial k}\right) + \frac{\partial}{\partial k}\left(\frac{{A_2}^2}{s_k}\frac{\partial Q}{\partial k}\right)\right]^{n+1} \\
&= \frac{1}{2\Delta t_{\mathrm{I}}}\left[\frac{\partial (\tilde{U}s_k)}{\partial x} + \frac{\partial (\tilde{V}s_k)}{\partial y} + \frac{\partial (\tilde{U}A_1)}{\partial k} + \frac{\partial (\tilde{V}A_2)}{\partial k} + \frac{\partial \tilde{W}}{\partial k}\right]^{n+1}.
\end{aligned} \tag{4.32}$$

The discretization of the Poisson equation for Q in the s-coordinate system leads to a linear system of equations with a diagonal band matrix of width equal to 15[1] for the nonhydrostatic pressure $Q_{i,j,k}$:

$$\begin{aligned}
&a_1 Q_{i+1,j,k} + a_2 Q_{i-1,j,k} + a_3 Q_{i+1,j,k+1} + a_4 Q_{i-1,j,k+1} + a_5 Q_{i,j+1,k} + a_6 Q_{i,j-1,k} \\
&+ a_7 Q_{i,j+1,k+1} + a_8 Q_{i,j-1,k+1} + a_9 Q_{i+1,j,k-1} + a_{10} Q_{i-1,j,k-1} + a_{11} Q_{i,j+1,k-1} \\
&+ a_{12} Q_{i,j-1,k-1} + a_{13} Q_{i,j,k+1} + a_{14} Q_{i,j,k-1} + a_{15} Q_{i,j,k} = R_Q,
\end{aligned} \tag{4.33}$$

where

$$a_1 = \frac{\mathrm{d}z_{ijk}(s_k)_{i+1/2,j}}{\mathrm{d}x_{ij}\mathrm{d}xx_{ij}}, \quad a_2 = \frac{\mathrm{d}z_{ijk}(s_k)_{i-1/2,j}}{\mathrm{d}x_{ij}\mathrm{d}xx_{i-1,j}},$$

$$a_3 = -\frac{\mathrm{d}z_{ijk}}{\mathrm{d}x_{ij}}\left(\frac{A_1^{i+1,j,k}}{\mathrm{d}z_{i+1,j}} + \frac{A_1^{i,j,k+1}}{\mathrm{d}z_{i,j}}\right), \quad a_4 = \frac{\mathrm{d}z_{ijk}}{\mathrm{d}x_{ij}}\left(\frac{A_1^{i-1,j,k}}{\mathrm{d}z_{i-1,j}} + \frac{A_1^{i,j,k+1}}{\mathrm{d}z_{i,j}}\right),$$

$$a_5 = \frac{\mathrm{d}z_{ijk}(s_k)_{i,j-1/2}}{\mathrm{d}y_{ij}\mathrm{d}yy_{ij}}, \quad a_6 = \frac{\mathrm{d}z_{ijk}(s_k)_{i,j-1/2}}{\mathrm{d}y_{ij}\mathrm{d}yy_{i,j-1}},$$

$$a_7 = -\frac{\mathrm{d}z_{ijk}}{\mathrm{d}y_{ij}}\left(\frac{A_2^{i,j+1,k}}{\mathrm{d}z_{i,j+1}} + \frac{A_2^{i,j,k+1}}{\mathrm{d}z_{i,j}}\right), \quad a_8 = \frac{\mathrm{d}z_{ijk}}{\mathrm{d}y_{ij}}\left(\frac{A_2^{i,j-1,k}}{\mathrm{d}z_{i,j-1}} + \frac{A_2^{i,j,k+1}}{\mathrm{d}z_{i,j}}\right),$$

$$a_9 = \frac{\mathrm{d}z_{ijk}}{\mathrm{d}x_{ij}}\left(\frac{A_1^{i+1,j,k}}{\mathrm{d}z_{i+1,j}} + \frac{A_1^{i,j,k-1}}{\mathrm{d}z_{i,j}}\right), \quad a_{10} = -\frac{\mathrm{d}z_{ijk}}{\mathrm{d}x_{ij}}\left(\frac{A_1^{i-1,j,k}}{\mathrm{d}z_{i-1,j}} + \frac{A_1^{i,j,k-1}}{\mathrm{d}z_{i,j}}\right),$$

[1] For brevity, this will be called a "15-diagonal" matrix.

$$a_{11} = \frac{\mathrm{d}z_{ijk}}{\mathrm{d}y_{ij}}\left(\frac{A_2^{i,j+1,k}}{\mathrm{d}z_{i,j+1}} + \frac{A_2^{i,j,k-1}}{\mathrm{d}z_{i,j}}\right), \quad a_{12} = -\frac{\mathrm{d}z_{ijk}}{\mathrm{d}y_{ij}}\left(\frac{A_2^{i,j-1,k}}{\mathrm{d}z_{i,j-1}} + \frac{A_2^{i,j,k-1}}{\mathrm{d}z_{i,j}}\right),$$

$$a_{13} = -\frac{1 + \left(A_1{}^{i,j,k+1/2}\right)^2 + \left(A_2{}^{i,j,k+1/2}\right)^2}{(s_k)_{ij} \cdot \mathrm{d}zz_{ij,k}},$$

$$a_{14} = -\frac{1 + \left(A_1{}^{i,j,k-1/2}\right)^2 + \left(A_2{}^{i,j,k-1/2}\right)^2}{(s_k)_{ij} \cdot \mathrm{d}zz_{ij,k-1}},$$

$$a_{15} = -\frac{\mathrm{d}z_{ijk}(s_k)_{i+1/2,j}}{\mathrm{d}x_{ij}\mathrm{d}xx_{ij}} - \frac{\mathrm{d}z_{ijk}(s_k)_{i-1/2,j}}{\mathrm{d}x_{ij}\mathrm{d}xx_{i-1,j}} - \frac{\mathrm{d}z_{ijk}(s_k)_{i,j+1/2}}{\mathrm{d}y_{ij}\mathrm{d}yy_{ij}} - \frac{\mathrm{d}z_{ijk}(s_k)_{i,j-1/2}}{\mathrm{d}y_{ij}\mathrm{d}yy_{i,j-1}}$$
$$- \frac{1}{(s_k)_{ij}}\left(\frac{1 + \left(A_1{}^{i,j,k-1/2}\right)^2 + \left(A_2{}^{i,j,k-1/2}\right)^2}{\mathrm{d}zz_{ijk-1}} + \frac{1 + \left(A_1{}^{i,j,k+1/2}\right)^2 + \left(A_2{}^{i,j,k+1/2}\right)^2}{\mathrm{d}zz_{ijk}}\right),$$

$$R_Q = \frac{1}{2\Delta t_{\mathrm{I}}}\left[\frac{\tilde{U}_{i+1,j,k}(s_k)_{i+1/2,j} - \tilde{U}_{i,j,k}(s_k)_{i-1/2,j}}{\mathrm{d}x_{i,j}} + \frac{\tilde{V}_{i+1,j,k}(s_k)_{i+1/2,j} - \tilde{V}_{i,j,k}(s_k)_{i-1/2,j}}{\mathrm{d}y_{i,j}}\right.$$
$$+ \left(\tilde{U}_{i,j,k-1}A_1^{i,j,k-1} - \tilde{U}_{i,j,k+1}A_1^{i,j,k+1}\right)$$
$$\left. + \left(\tilde{V}_{i,j,k-1}A_2^{i,j,k-1} - \tilde{V}_{i,j,k+1}A_2^{i,j,k+1}\right) + \left(\tilde{W}_{i,j,k} - \tilde{W}_{i,j,k+1}\right)\right]^{n+1},$$

where

$$\mathrm{d}xx_{i,j} = \frac{\mathrm{d}x_{i,j} + \mathrm{d}x_{i+1,j}}{2}; \quad \mathrm{d}yy_{i,j} = \frac{\mathrm{d}y_{i,j} + \mathrm{d}y_{i,j+1}}{2},$$

$$\mathrm{d}z_{i,j,k} = z_{i,j,k} - z_{i,j,k+1}; \quad \mathrm{d}zz_{i,j,k} = zz_{i,j,k} - zz_{i,j,k+1}.$$

The generalized coordinate system is not orthogonal and it results in the appearance of cross-terms in (4.33), whereas in the z-system, which is orthogonal, the corresponding matrix is 7-diagonal (see Fig. 4.2). The linear system (4.33) is solved by us using the bi-conjugate gradient method with incomplete LU decomposition pre-conditioning (Seager 1988). Heggelund et al. (2004) used an iterative approach when the simpler system of linear equations with a 7-diagonal matrix was solved at each iteration step, whereas the cross-terms were calculated explicitly. Berntsen and Furnes (2005) proposed modeling the nonhydrostatic pressure directly in the σ-coordinates to simplify the system of linear equations. For a set of numerical experiments, Bergh and Berntsen (2009a, b) and Keilegavlen and Berntsen (2009) showed that the difference with using the full system (4.33) and its simplified counterpart leads to the minor errors.

In quasi-z-system coordinates, it is acceptable to use a simplified form of equation (4.33) with a corresponding seven-diagonal matrix in which the

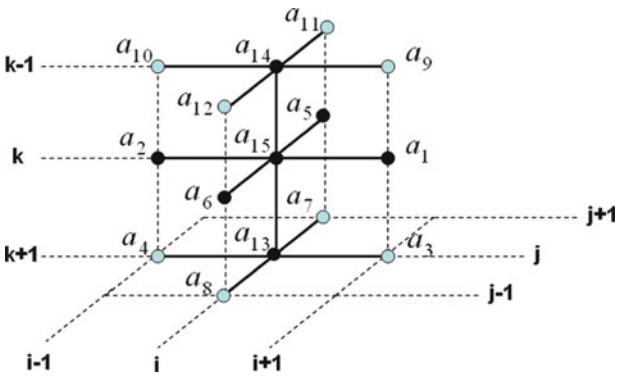

Fig. 4.2 Spatial scheme of finite-difference representation of the Poisson equation for the nonhydrostatic component of the pressure in generalized vertical coordinates. *Black balls* correspond to nodes used in the z-system of coordinates

coefficients a_3, a_4, a_7, a_8, a_9, a_{10}, a_{11}, and a_{12} are set equal to zero due to their smallness. The possibility of such a simplification in the general case should be studied for given parameters of the generalized vertical coordinate.

The condition of zero normal flow is imposed at the solid boundaries. It results in a Neumann-type boundary condition for the nonhydrostatic pressure component Q (Fletcher 1991). At the free surface and at open boundaries $Q = 0$. However, it does not mean that the dynamics in the vicinity of the free surface is close to hydrostatic because free surface dynamics is nonhydrostatic (see discussion in first stage description). An alternative boundary condition of Neumann-type is considered by Bergh and Berntsen (2009b). It was shown that the difference between solutions using the Dirichlet and the Neumann boundary conditions was significant for coarse vertical resolution. Once the nonhydrostatic pressure is computed, the corresponding velocity field $(U^{n+1}, V^{n+1}, W^{n+1})$ is determined from (4.28)–(4.30).

Fourth Stage. The scalar fields (temperature and salinity) are computed using a semi-implicit numerical scheme. In semi-discrete form, the scalar transport equation is

$$\frac{(\phi_i s_k)^{n+1} - (\phi_i s_k)^{n-1}}{2\Delta t_i} + \frac{\partial (U\phi_i s_k)^n}{\partial x} + \frac{\partial (V\phi_i s_k)^n}{\partial y} + \frac{\partial (W\phi_i s_k)^n}{\partial k}$$
$$= \frac{\partial}{\partial k}\left[\frac{(K_H + \chi_\phi)}{s_k}\frac{\partial \phi_i^{n+1}}{\partial k}\right] + \mathrm{Dif}\left(\bar{\phi}_i^{n-1}\right) \tag{4.34}$$

The advective terms in the equations for the scalar function are approximated by total variation diminishing (TVD) schemes (Van Leer 1979). Implicit treatment of the vertical diffusion terms is used. The three-diagonal matrix obtained after spatial discretization is solved by the direct method.

4.3 Regimes of Degeneration of Basin-Scale Internal Gravity Waves

4.3.1 Linearized Ideal Fluid Problem

Consider an idealized two-layer model of an elongated stratified lake. The rectangular basin of length L, breadth B ($B \ll L$), and depth H ($H \ll L$) is filled with two layers of undisturbed thicknesses $h_1$and h_2, with densities ρ_1 and $\rho_2 > \rho_1$. These layers are divided by an interface layer with thickness δ_ρ. The motions in the basin can be caused by an initial tilt of the interface η_i, with amplitude η_{i0}, and by a tilt of the free surface, with amplitude η_0 (Fig. 4.3). In the absence of rotation, the initially tilted interface and free surface cause long surface and internal waves that form standing surface and internal wave patterns.

The simple ideal fluid problem for the two-layer stratification ($\delta_\rho \equiv 0$) in a narrow basin of constant depth and width can be formulated for small interface and surface disturbances in the hydrostatic and Boussinesq approximations (e.g., Gill 1982). The seiching along the basin ($V \equiv 0$) is described by a system of equations for continuity and momentum in layers as

$$\frac{\partial(\eta - \eta_i)}{\partial t} + h_1 \frac{\partial U_1}{\partial x} = 0, \tag{4.35}$$

$$\frac{\partial U_1}{\partial t} + g \frac{\partial \eta}{\partial x} = 0, \tag{4.36}$$

$$\frac{\partial \eta_i}{\partial t} + h_2 \frac{\partial U_2}{\partial x} = 0, \tag{4.37}$$

$$\frac{\partial U_2}{\partial t} + g \frac{\partial \eta}{\partial x} + g' \frac{\partial \eta_i}{\partial x} = 0, \tag{4.38}$$

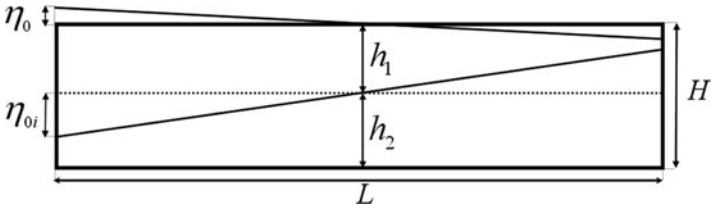

Fig. 4.3 Schematics of a two-layer basin

where U_1 and U_2 are velocities in the upper and lower layers and the reduced gravity is $g' = g(\rho_2 - \rho_1)/\rho_2 \approx g(\rho_2 - \rho_1)/\rho_0$.

Combining (4.35), (4.37), and (4.36), (4.38) yields equations for the barotropic mode

$$\frac{\partial \eta}{\partial t} + H\frac{\partial \bar{U}}{\partial x} = 0, \tag{4.39}$$

$$\frac{\partial \bar{U}}{\partial t} + gH\frac{\partial \eta}{\partial x} + g'h_1\frac{\partial \eta_i}{\partial x} = 0, \tag{4.40}$$

in which the depth-independent barotropic component of the velocity is $\bar{U} = (h_1U_1 + h_2U_2)/H$. The last term in (4.40) can be dropped, because in the Boussinesq approximation $g' \ll g$ and (4.39)–(4.40) reduce to the wave equation for η

$$\frac{\partial^2 \eta}{\partial t^2} = c_0^2\frac{\partial^2 \eta}{\partial x^2}, \tag{4.41}$$

where $c_0 = \sqrt{gH}$ is a speed of linear long surface waves. The solution of (4.41) with boundary conditions of no flux ($\bar{U} = 0$) on the walls at $x = \{0; L\}$ describes long standing waves (surface seiche) with period $T^{(m)} = 2L/mc_0,\ m = 1, 2, 3, \ldots$. The equations describing the baroclinic mode are derived for $\Delta U = U_2 - U_1$. With the rigid lid approximation ($\eta \ll \eta_i$), these equations are

$$-\frac{\partial \eta_i}{\partial t} + \frac{h_1h_2}{H}\frac{\partial \Delta U}{\partial x} = 0, \tag{4.42}$$

$$\frac{\partial \Delta U}{\partial t} + g'\frac{\partial \eta_i}{\partial x} = 0, \tag{4.43}$$

and reduce to the equation for the interface elevation

$$\frac{\partial^2 \eta_i}{\partial t^2} = c_{0i}^2\frac{\partial^2 \eta_i}{\partial x^2}, \tag{4.44}$$

where

$$c_{0i} = \sqrt{g'h_1h_2/H} \tag{4.45}$$

is the linear speed of long interface internal waves. The boundary conditions of no-flux ($U_1 = U_2 = 0$) on the walls at $x = \{0; L\}$ can be rewritten using (4.43) as

$$\frac{\partial \eta_i}{\partial x} = 0. \tag{4.46}$$

The solution of (4.44) with boundary conditions (4.46) describes long internal standing waves (internal seiche) with period $T^{(m)} = 2L/mc_{0i}$, $m = 1, 2, 3, \ldots$. In particular, the analytical solution can be obtained (Boegman et al. 2005a, b) for an initial motionless linearly tilted interface and no motion as

at

$$\eta_i(x,0) = \left(\frac{2}{L}x - 1\right)\eta_{i0}, \quad \frac{\partial \eta_i(x,0)}{\partial t} = 0. \tag{4.47}$$

This solution is the Fourier cosine series $(n = 1, 3, 5, ...)$

$$\eta_i = -\sum_{n=1}^{\infty} \frac{8\eta_{0i}}{(n\pi)^2} \cos\left(\frac{n\pi}{L}x\right) \cos\left(\frac{c_{0i}n\pi}{L}t\right). \tag{4.48}$$

The linear solution shows that, in the spatial–temporal evolution of the interface, the basin-scale baroclinic disturbances dominate. However, the linear solution of the problem cannot describe the formation of internal bores and their subsequent decomposition into the packets of internal solitary waves, which are observed in lakes.

4.3.2 *Nonlinear Models of Internal Waves*

The detailed overviews of nonlinear models of the internal waves are given by Ostrovsky and Stepanyants (1989, 2005) and Helfrich and Melville (2006). The unidirectional propagation of internal solitary waves (ISW) of weak and moderate amplitude can be described by the extended Korteweg–de Vries (eK–dV or Gardner) equation (e.g., Grimshaw et al. 2002). In the rigid lid approximation and in a basin of constant depth, it is given by

$$\frac{\partial \eta}{\partial t} + (c_{0i} + \alpha\eta + \alpha_1\eta^2)\frac{\partial \eta}{\partial x} + \beta\frac{\partial^3 \eta}{\partial x^3} = 0, \tag{4.49}$$

where the nonlinear α and α_1 and dispersive β coefficients are parameters in the Boussinesq approximation $(\Delta\rho/\rho_0 \ll 1)$ given by

$$\alpha = \frac{3c_{0i}}{2}\frac{h_1 - h_2}{h_1 h_2}, \quad \beta = \frac{c_{0i}h_1 h_2}{6}, \tag{4.50}$$

and α_1 is the cubic nonlinear coefficient

$$\alpha_1 = -\frac{3c_{0i}}{8h_1^2 h_2^2}(h_1^2 + h_2^2 + 6h_1 h_2), \tag{4.51}$$

which is always negative for interfacial waves (Kakutani and Yamasaki 1978). When, $\alpha_1 = 0$ Eq. (4.49) is reduced to the K–dV equation with the steady-state solitary wave solution

$$\eta(x,t) = a\,\mathrm{sech}^2\left[\sqrt{\frac{3a}{4}\frac{(h_1-h_2)}{h_1^2h_2^2}}(x-(c_{0i}+\alpha a/3)t)\right]. \tag{4.52}$$

The amplitude a is positive (elevation wave) if $h_1-h_2 > 0$ ($\alpha > 0$) and negative (depression wave) if $(h_1-h_2) < 0$ ($\alpha < 0$). If $h_1-h_2 = 0$, the interfacial solitons do not exist.

The steady-state solitary wave solution of the Gardner equation also can be found explicitly (see e.g., Grimshaw et al. 2008),

$$\eta(x,t) = \frac{6\beta\gamma^2}{\alpha[1+\sqrt{1+6\alpha_1\beta\gamma^2/\alpha^2}\cosh(\gamma(x-\beta\gamma^2 t))]}, \tag{4.53}$$

where γ is a parameter characterizing the inverse width of the soliton. The soliton amplitude is

$$a = 6\beta\gamma^2/\alpha(1+\sqrt{1+6\alpha_1\beta\gamma^2/\alpha^2}),$$

and its sign coincides with the sign of the coefficient of quadratic nonlinearity α. The soliton amplitude varies from small values, when the Gardner soliton (4.53) coincides with the K–dV soliton (4.52), to the limiting value

$$a_{\mathrm{lim}} = -4h_1h_2\frac{h_2-h_1}{h_1^2+h_2^2+6h_1h_2}, \tag{4.54}$$

when the soliton has a "table-top" shape.

The theory for long waves with large nonlinearity in a two-layered basin also predicts a steady-state solitary wave solution (Miyata 1985; Choi and Camassa 1999). This solitary wave is called the Miyata–Choi–Camassa (MCC) solitary wave. In the Boussinesq approximation, it can be calculated from the nonlinear ordinary differential equation

$$\left(\frac{\mathrm{d}\eta}{\mathrm{d}X}\right)^2 = \left[\frac{3g\Delta\rho}{c_{0i}^2\rho_0(h_1^2-h_2^2)}\right]\times\frac{\eta^2(\eta-b_1)(\eta-b_2)}{(\eta-b_*)}, \tag{4.55}$$

where $X = x - ct$,

$$b_* = \frac{h_1h_2}{h_2-h_1}, \quad c = c_{0i}\sqrt{\frac{(h_1-a)(h_2+a)}{h_1h_2}}.$$

Here, c_{0i} is the speed of the linear interface wave (4.45). The parameters b_1 and b_2 are the roots of the quadratic algebraic equation

$$b^2 + q_1 b + q_2 = 0,$$

$$q_1 = -\frac{c^2}{g} - h_1 + h_2, \quad q_2 = h_1 h_2 \left(\frac{c^2}{c_{0i}^2} - 1 \right).$$

Equation (4.55) can be solved, and the wave form $\eta(x)$ is obtained implicitly by an integral $x = \hat{X}(\eta)$.

The solution (4.55) and solutions of the Euler equations for steady solitary waves (Grue et al. 1999) predict that in the Boussinesq approximation these waves exist for amplitudes less than the maximum value

$$A_{\text{lim}} = \frac{h_1 - h_2}{2}. \tag{4.56}$$

However, these solutions for solitary waves of large amplitude suffer from the Kelvin–Helmholtz (KH) instability caused by a jump in the tangential velocity across the interface (Camassa et al. 2006; Fructus et al. 2009).

4.3.3 Energy Equations

In this section, we consider the equations of energy transformations. In the Boussinesq approximation, the equation of state is linearized and instead of (4.3), a single equation for the density evolution emerges:

$$\frac{\partial \rho}{\partial t} + U_\alpha \frac{\partial \rho}{\partial x_\alpha} = \text{Diffusion terms}. \tag{4.57}$$

Multiplying the momentum equation (4.2) with U_α and (4.57) with gz and, subsequently, summing these resulting equations yields the evolution equation for the density of the total mechanical energy E as

$$\frac{\partial E}{\partial t} + \frac{\partial f_E}{\partial x_\alpha} = \text{Diffusion} + \text{Dissipation}. \tag{4.58}$$

Here, E is the sum, $E = E_{\text{K}} + E_{\text{P}}$, of the kinetic energy, $E_{\text{K}} = \rho_0 U_\alpha^2/2$, and the potential energy, $E_{\text{P}} = \rho g z$, per unit of volume, respectively. The flux of energy f_E is

$$f_E = U_\alpha (P + E_{\text{K}} + E_{\text{P}}) \tag{4.59}$$

where P is pressure. The right-hand side of equation (4.58) represents diffusion of energy and viscous dissipation (Venayagamoorthy and Fringer 2005; Lamb and Nguyen 2009).

The potential energy of finite volume of fluid PE can be subdivided into the available potential energy (APE), which is available for transformation into turbulent kinetic energy, and the background potential energy (BPE), defined as the minimum potential energy attainable through adiabatic redistribution of the density in a given volume of fluid (Shepherd 1993; Winters et al. 1995). The APE of finite volume V is the difference between the potential energy and BPE

$$\mathrm{APE} = \mathrm{PE} - \mathrm{BPE} = g\int_V z\rho \mathrm{d}V' - g\int_V z\bar{\rho}_r(z,t)\mathrm{d}V', \tag{4.60}$$

where $\bar{\rho}_r(z,t)$ is a background monotonic reference density profile. The horizontally uniform background density is obtained by sorting the density field within the flow volume V(Winters et al. 1995). The potential energy of the sorted density field is the BPE. For example, for the two-layer stratification with constant density difference between the layer densities in a narrow basin of constant depth and width, the APE of seiching along the basin is

$$\mathrm{APE} = \frac{gB\Delta\rho}{2}\int_0^L \eta^2(x,t)\mathrm{d}x. \tag{4.61}$$

The available potential energy density E_A is defined as

$$E_\mathrm{A} = g\int_z^{z^*} (\bar{\rho}(z',t) - \rho)\mathrm{d}z', \tag{4.62}$$

where the reference profile $\bar{\rho}(z,t)$ is invertible with inverse $z^*(\bar{\rho},t)$. The corresponding hydrostatic pressure is $\bar{P}(z,t)$. The value of E_A is the work done to move a fluid parcel from height z^* to height z against buoyancy forces in the fluid with reference profile $\bar{\rho}(z,t)$ (Lamb 2007). In the closed system, $\bar{\rho}(z,t)$ can be obtained by sorting, and $\bar{\rho} = \bar{\rho}_r$. In an open system, like a propagating solitary wave, the undisturbed far-field density distribution also can be used as reference profile (Lamb and Nguyen 2009). The sum of E_K and E_A is called the pseudo-energy density E_PSE (Shepherd 1993). Equation (4.58) can be rewritten in terms of the pseudo-energy as

$$\frac{\partial E_\mathrm{PSE}}{\partial t} + \frac{\partial f_{E\alpha}}{\partial x_\alpha} = g\int_z^{z^*} \frac{\partial \bar{\rho}(z',t)}{\partial t}\mathrm{d}z' + \mathrm{Diffusion} + \mathrm{Dissipation}. \tag{4.63}$$

The flux of energy is rewritten as

$$f_{E\alpha} = U_\alpha(p + E_\mathrm{K} + E_\mathrm{A}), \tag{4.64}$$

where $p = P - \bar{P}(z,t)$. Integrating (4.64) over the depth yields, in the rigid lid approximation,

$$F_\alpha = \mathrm{PWF}_\alpha + \mathrm{KEF}_\alpha + \mathrm{APEF}_\alpha, \tag{4.65}$$

where

$$\mathrm{PWF}_\alpha = \int_{-H}^{0} U_\alpha p \mathrm{d}z, \tag{4.66}$$

is the rate of work done by the pressure perturbations, while the quantities

$$\mathrm{KEF}_\alpha = \int_{-H}^{0} U_\alpha E_\mathrm{K} \mathrm{d}z, \tag{4.67}$$

$$\mathrm{APEF}_\alpha = \int_{-H}^{0} U_\alpha E_\mathrm{A} \mathrm{d}z \tag{4.68}$$

are the fluxes of the kinetic and available potential energies. Integrating (4.63) over the volume V spanning the entire depth yields

$$\frac{\mathrm{d}}{\mathrm{d}t}\mathrm{PSE} = F^{(n)}|_\Sigma + \int_V \left(g \int_z^{z^*} \frac{\partial \bar{\rho}(z',t)}{\partial t} \mathrm{d}z' + \mathrm{Diffusion} + \mathrm{Dissipation} \right) \mathrm{d}V', \tag{4.69}$$

where $\mathrm{PSE} = \mathrm{APE} + \mathrm{KE}$,

$$\mathrm{KE} = \int_V E_\mathrm{K} \mathrm{d}V', \tag{4.70}$$

$F^{(n)}$ is the total flux of the pseudo-energy normal to the horizontal boundary Σ of the volume.

4.3.4 *Classification of the Degeneration Regimes of Basin-Scale Internal Gravity Waves in a Lake*

Depending on the amplitude of the initial disturbance and the depth of the layers, there is a wide spectrum of possible flow regimes in a basin, which essentially differ from the solutions of the linear problem. Similar to Sect. 4.3.1, consider a rectangular basin filled with two layers of fluid divided by an interfacial layer

(see Fig. 4.3). Following Horn et al. (2001), we determine the characteristic time scales of the main processes, and then the main regimes, which are characterized by particular dominating mechanisms.

The period of the gravest mode $T_i = T_i^1$ is the first characteristic time scale. The maximum values of the layer velocities at the center of the basin occur when $t = T_i/4; 3T_i/4; 5T_i/4; \ldots$ Before the flow reverses at $t = T_i/4$, the layer velocities at the center of the tank are (Horn et al. 2001)

$$\hat{U}_1 = g' \frac{h_2}{H} \frac{2\eta_{i0}}{L} t, \quad \hat{U}_2 = -g' \frac{h_1}{H} \frac{2\eta_{i0}}{L} t. \tag{4.71}$$

The interfacial shear ΔU_i is also periodic and has a maximum at the same time as the velocities, i.e., $\Delta U = \hat{U}_1 - \hat{U}_2 = 2g'\eta_{i0}t/L$. The local Richardson number in the interface layer is

$$Ri = \frac{g'\delta_\rho}{(\Delta U)^2}. \tag{4.72}$$

In steady shear flow, the Kelvin–Helmholtz instability develops at $Ri < 1/4$; else, the flow is stable. The critical shear corresponding to $Ri = 1/4$ is

$$\Delta U = 2\left(g'\delta_\rho\right)^{1/2}. \tag{4.73}$$

The second characteristic time T_{KH} can be estimated from (4.72), using (4.71) with $t = T_{\mathrm{KH}}$ and (4.73). This yields

$$T_{\mathrm{KH}} = \frac{L}{\eta_{i0}} \left(\frac{\Delta\rho}{g'}\right)^{1/2}. \tag{4.74}$$

The flow will remain stable if $T_{\mathrm{KH}} > T_i/4$.

Two kinds of nonlinear effects can be essential for a finite value of the tilted interface. In the first case, the nonlinear steepening is developed because the phase velocity of long waves depends on the disturbed thickness of the layer (Whitham 1974). Balancing the unsteady and nonlinear terms in (4.49) at $\alpha_1 = 0$ leads to the steepening time scale (Horn et al. 2001)

$$T_s \approx \frac{L}{\alpha\eta_{i0}}. \tag{4.75}$$

The time scale for dispersion effects can be estimated by balancing the unsteady and dispersion terms in (4.49) as $T_{\mathrm{disp}} = L^3/\beta$. Nonlinear steepening dominates over dispersion when $T_s/T_{\mathrm{disp}} \ll 1$. For small interface shifts

$$\eta_{0i} \ll \frac{1}{9} \frac{h_1^2 h_2^2}{(h_1 - h_2)L^2},$$

dispersion effects prevent development of fronts.

Another nonlinear mechanism of wave transformation manifests itself as formation of internal bores when flows in layers achieve a supercritical state. The critical composite Froude number is

$$Fr^2 = \hat{U}_1^2/g'h_1 + \hat{U}_2^2/g'h_2 = 1, \tag{4.76}$$

where $\hat{U}_1$ and $\hat{U}_2$ are given by (4.71). The flow may be supercritical ($Fr>1$) in the center of the basin where the velocities are largest. An internal bore links the supercritical region with the downstream (relative to the fast-flowing thin layer) subcritical region. The characteristic time of the formation of an internal bore T_b was estimated by substituting (4.71) in (4.76) (Horn et al. 2001),

$$T_\mathrm{b} = \frac{T_i h_1 h_2}{4\eta_{i0}} \left[\frac{H}{h_1^3 + h_2^3}\right]^{1/2}. \tag{4.78}$$

The dissipative time scale T_d is the e-folding time scale for the amplitude decay of the initial internal standing wave,

$$T_\mathrm{d} = T_\mathrm{i}/\gamma_\mathrm{d}, \tag{4.79}$$

where γ_d is the decay modulus such that $2\gamma_\mathrm{d} = \mathrm{d}E/E$, whereas E is the seiche energy (Keulegan 1959). Horn et al. (2001) estimated the dissipation for waves in the laboratory basin, taking into account bottom, upper lid, and sidewall friction as well as friction in the interface layer. The resulting relation is

$$\gamma_\mathrm{d} = \frac{\pi\delta_\mathrm{b}A_\mathrm{b}}{2V} + \frac{\nu H T_\mathrm{i}}{2\delta_\rho h_1 h_2}, \tag{4.80}$$

where $\delta_\mathrm{b} = (\nu T_\mathrm{i}/\pi)^{1/2}$ is the thickness of the laminar boundary layer, ν is the kinematic viscosity, A_b is the total area of the solid boundaries, and V is the total volume.

The relation between the time scales (T_i, T_KH, T_s, T_b, and T_d) determines characteristic regimes of degeneration of basin-scale waves. Equating time scales, Horn et al. (2001) calculated regime boundaries in terms of η_{i0}/h_1 and h_1/H for given characteristics of the basin (L, g', δ_ρ). The regime boundaries for the basin-scale seiche are shown in Fig. 4.4 following Horn et al. (2001), with the difference that the diagram includes also regimes with $0.5 \leqslant h_1/H \leqslant 1$ to distinguish the difference between the wave transformation near the bottom and near the free surface (Kanarska and Maderich 2004). The solid curve ($T_\mathrm{d} = T_\mathrm{s}$) in Fig. 4.4 separates regime I of damped linear waves ($T_\mathrm{d} < T_\mathrm{s}$) from regime II of solitary wave generation ($T_\mathrm{d} > T_\mathrm{s}$). The supercritical regime III is formed at $T_\mathrm{b} < T_\mathrm{i}/4$. The curves $T_\mathrm{KH} = T_\mathrm{i}/4$ and $T_\mathrm{b} = T_\mathrm{i}/4$ separate regime IV of Kelvin–Helmholtz billows. The curves $T_\mathrm{b} = T_\mathrm{i}/4$ and $T_\mathrm{KH} = T_\mathrm{i}/4$ separate regime V, when flows are supercritical and the Richardson number falls below the value 1/4 (regime of supercritical flows

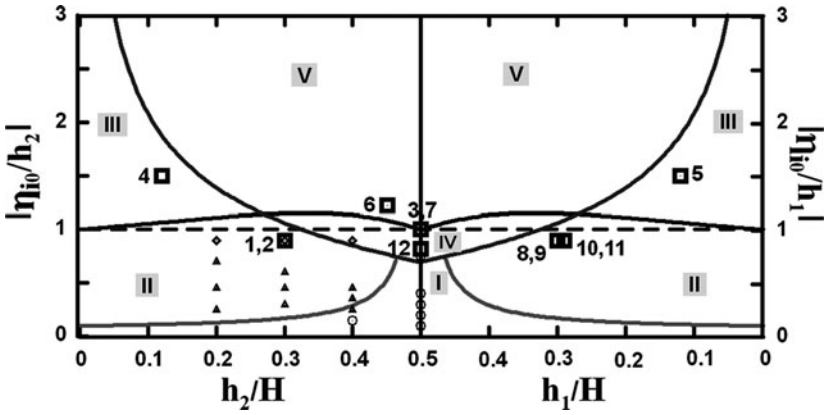

Fig. 4.4 Regime diagram. Roman numbers identify regimes. *Solid lines* show regime boundaries, where the *dashed line* (connecting the ordinate points 1 on either side) separates regimes with gravitational currents. The *circles* and *triangles* show laboratory experiments by Horn et al. (2001), while *numbered boxes* identify numerical runs given in Tables 4.2 and 4.4

and Kelvin–Helmholtz billows). Note that ratios $\eta_{i0}/h_1 > 1$ and $h_1/H < 0.5$ correspond to an initial distribution of the density when the interface crosses the bottom, whereas ratios $\eta_{i0}/h_1 > 1$ and $h_1/H > 0.5$ correspond to an initial distribution of the density when the interface crosses the upper boundary of the basin. In both cases, the flows form gravitational currents, so regime V can be named also "the regime of gravity currents" (Kanarska and Maderich 2004). In the limit $\eta_{i0}/h_1 \to \infty$, this regime is "lock exchange flow".

Laboratory experiments and observations in some lakes (Horn et al. 2001) generally support this classification. However, the scaling presented above was derived for basins of simple form based on assumptions on weak nonlinearity and two-layer stratification. In the following sections, the regimes of degeneration of basin-scale internal waves will be considered numerically using the nonhydrostatic model described in the previous section.

4.4 Numerical Simulation of Degeneration of Basin-Scale Internal Gravity Waves

4.4.1 Degeneration of Basin-Scale Internal Waves in Rectangular Basins

First, we consider the case of degeneration of basin-scale internal waves in a rectangular basin using data of the laboratory experiments by Horn et al. (2001) and results of numerical simulations. Several numerical studies have been carried out to simulate these experiments (Kanarska and Maderich 2004; Wadzuk and

Table 4.2 Parameters of numerical experiments

Run	h_2/H	η_{i0}/h_2	h_1/H	η_{i0}/h_1	Regime	Resolution (x × y × z)
1	0.3	0.9	–	–	Hydrostatic	$2,000 \times 300 \times 5$
2	0.3	0.9	–	–	II	$2,000 \times 300 \times 5$
3	0.5	1	0.5	1	IV–V	$2,000 \times 300 \times 5$
4	0.12	1.5	–	–	III	$2,000 \times 300 \times 5$
5	–	–	0.12	1.5	III	$2,000 \times 300 \times 5$
6	0.45	1.22	–	–	V	$2,000 \times 300 \times 5$
7	0.5	1	0.5	1	IV–V	$800 \times 80 \times 25$
8	–	–	0.3	0.9	II	$2,000 \times 300 \times 5$
9	–	–	0.3	0.9	II	$2,000 \times 300 \times 5$

Hodges 2004; Staschuk et al. 2005; Kanarska et al. 2007; Bergh and Berntsen 2009b). Here, these studies are complemented by using the model described in Sect. 4.2. The experiments performed by Horn et al. (2001) were carried out in a fully enclosed tank with length $L = 600\,\text{cm}$, height $H = 29\,\text{cm}$, and width $B = 30\,\text{cm}$. The tank was filled with water exhibiting a two-layer salt stratification. The density difference between the layers was $\Delta\rho = 20\,\text{kg m}^{-3}$. The thickness of the interface, δ_ρ, was approximately 1–2 cm. The tank could be rotated about a horizontal axis to tilt the initial position of the interface. Prior to the experiment, it was inclined to a prescribed angle. At the beginning of the experiment, the tank was quickly rotated into the horizontal position. The inclined interface produced seiching.

The parameters of the numerical runs are given in Table 4.2. The initial conditions of these runs are identified also by boxes in Fig. 4.4. They were carried out with molecular values of viscosity $K_\text{M} = 10^{-6}\text{m}^2\text{s}^{-1}$ and diffusivity of salt $K_\text{H} = 10^{-9}\,\text{m}^2\text{s}^{-1}$. The no-slip boundary condition at the bottom was used and at the free surface, the shear stresses were set to zero. Runs 1–6 and 8–9 were carried out in the "quasi-two-dimensional mode" in a narrow tank of width $B = 9\,\text{cm}$ with free-slip conditions on the sidewall and resolution $1,000 \times 80 \times 5$, while run 7 was carried out with a resolution $800 \times 80 \times 25$ and the no-slip condition on the sidewalls to verify the two-dimensional character of the flows.

The position of the interface calculated from the linear analytic solution (4.48) and density snapshots from Run 1 (hydrostatic model) at the same time are shown in Fig. 4.5. Figures 4.5 and 4.6 show the distribution of the density snapshots of the interface position at the same dimensionless times t/T_s in the corresponding laboratory experiment and the nonhydrostatic Run 2. As seen in Fig. 4.5b, the nonlinearity in the hydrostatic model causes a steepening basin-scale wave and bore formation contrary to the linear hydrostatic solution (Fig. 4.5a). However, the hydrostatic approximation cannot predict disintegration of the bore on a sequence of solitary waves observed in the experiment (Horn et al. 2001), as seen in Fig. 4.5a. As shown in Fig. 4.5, the initial tilt of the interface produced as a consequence of a basin-scale wave, the formation of an internal surge and fission of a surge on a sequence of internal solitary waves (ISWs). These processes correspond to Regime II (Horn et al. 2001). The studied solitary wave generation in the experiment was

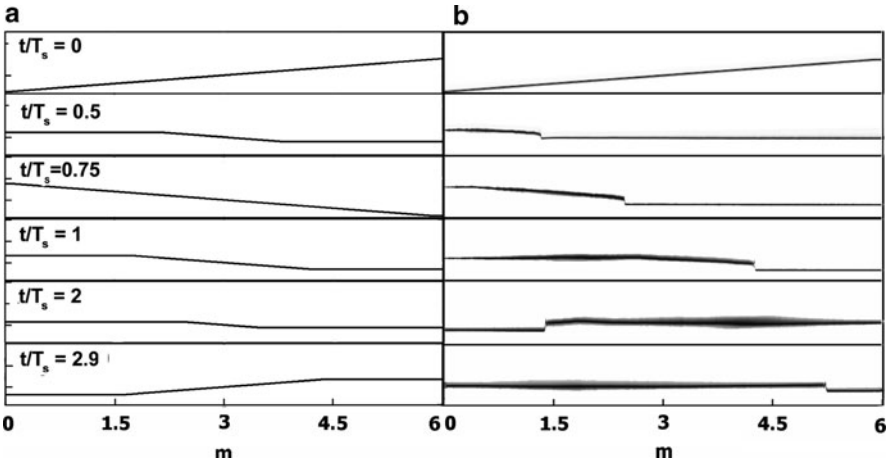

Fig. 4.5 Time series of the interface according to the linear hydrostatic solution (**a**) and simulation of nonlinear hydrostatic case (**b**) for parameters of Run#1

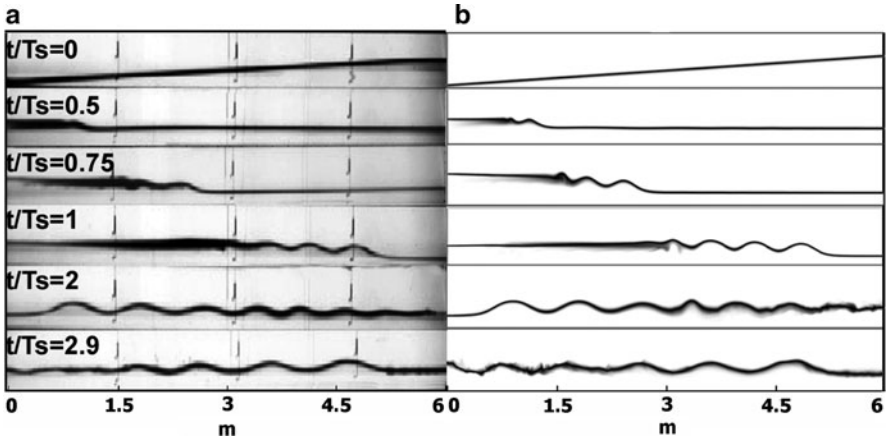

Fig. 4.6 Time series of photographs of the experiment of Horn et al. (2001) (**a**) versus simulation. © J. Fluid Mech Cambridge University Press, reproduced with permission. (**b**) for parameters of Run#2

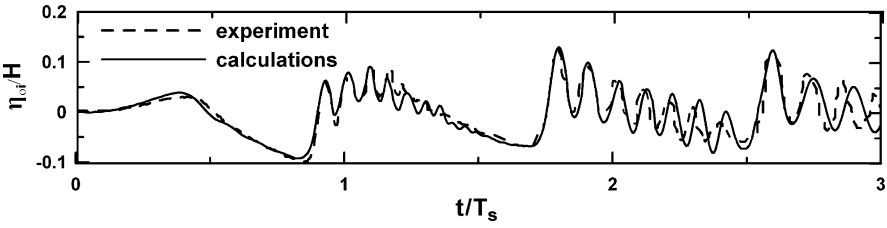

Fig. 4.7 Measured (Horn et al. 2001) and computed-by-model temporal variations of depth of the interface in the center of the tank in Run#2

quite well simulated in the nonhydrostatic Run 2. The model predicts amplitude and number of generated ISWs (Fig. 4.6). The amplitude of the leading ISW a was smaller than the upper level depth $h_1 (a/h_1 \approx 0.3)$.

Therefore, the evolution and propagation of an ISW packet can be described by the nonlinear Korteweg–de Vries (K–dV) equation. However, this evolution takes place in a time–space-varying stratification and is subject to currents caused by basin-scale seiching. An extended K–dV equation with time–space variable coefficients was derived by Horn et al. (2000) and compared with their experiment (Horn et al. 2001). It was shown that energy could be transferred either to or from the evolving wave packet, depending on the relative phases of the evolving waves and the background variation. The experiment in Fig. 4.6a as well as simulations in Fig. 4.6b for $T/T_S = 0.5, 0.75, 1$ show a pycnocline broadening following an internal surge and solitons (see also Kanarska and Maderich 2004; Staschuk et al. 2005; Kanarska et al. 2007). The same effect is also visible in the hydrostatic model (Fig. 4.5b). It was concluded by Staschuk et al. (2005) that this broadening was caused by strong interaction of the nonlinear wave with the wall.

The power spectral density (PSD) of the spatial variations of the interface for Run 1 and Run 2 is shown in Fig. 4.8. Figure 4.8b shows a shift of spectra to shorter wavelengths $(\lambda/2L = 0.1 - 0.2)$ with time that corresponds to the transfer of energy from basin-scale waves to the solitary waves.

The frequency analysis of the temporal interface variation was carried out at the center of the tank to exclude large-scale standing odd modes. The continuous wavelet transformation with the Morlet basis function (Torrence and Compo, 1998) was used. Figure 4.9 shows that the major part of the energy consists of nonlinear traveling waves with periods in the range $T/T_i = 0.25 \div 1$. They were disintegrated on the chain of short-period $(T/T_i \approx 1/16)$ solitary waves. These findings agree with the frequency spectral analysis at the center of the laboratory tank by Boegman et al. (2005b).

Figure 4.10 shows the computed density distribution of Run 3 in comparison with the laboratory experiment. The parameters of this run correspond to the boundary between regime IV (KH billows of Fig. 4.4) and V (supercritical flow and KH billows). In this run initially, the interface coincides with the tank diagonal line and the undisturbed depths of the upper and lower layers are equal, a condition which prevents formation of ISW. Two almost symmetrical bores are formed and the flows between them are accelerated up to the KH instability and the appearance of billows and consequent mixing. Figure 4.11 shows the evolution of the interface in the 3D case for Run 7. In the early stages of the instability, the growing disturbances are two-dimensional, whereas in the next stages the structure of the KH billows is three-dimensional.

Two cases that correspond to regime III (supercritical flow) are shown in Fig. 4.12. The first is initially a shallow layer near the bottom, whereas the second case is the same shallow layer cropping on the surface. In both cases initially, a gravitational current was formed, and then a high-amplitude solibore appeared which disintegrated into a chain of ISW. However, bottom friction in Run 4 is important and it resulted in a slow-down of the flow and relatively early formation

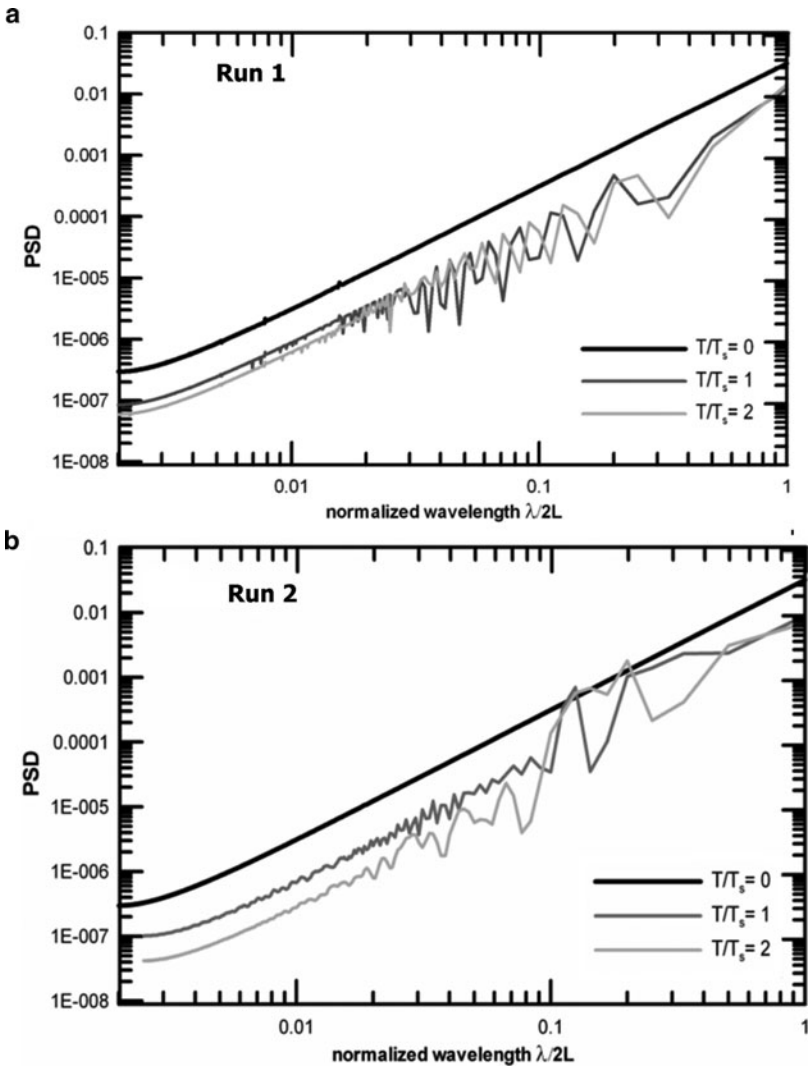

Fig. 4.8 Power spectral density of the spatial variations of the interface at different times in Run#1 (**a**) and Run#2 (**b**)

of ISW. Therefore, care should be observed when extending results of laboratory experiments with rigid lid to free surface flows in lakes.

Figure 4.13 shows results for Run 6 corresponding to regime V (supercritical flow and KH instability). This regime corresponds to a higher initial slope and some asymmetry of the undisturbed upper- and lower-layer thicknesses that resulted in the development of instability and KH billows with intense mixing and solibore.

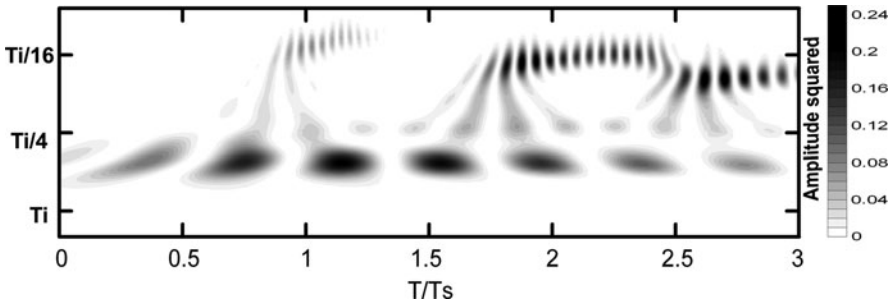

Fig. 4.9 Continuous wavelet transform of the computed depth of the interface at the center of the tank for Run#2 using the Morlet basis function

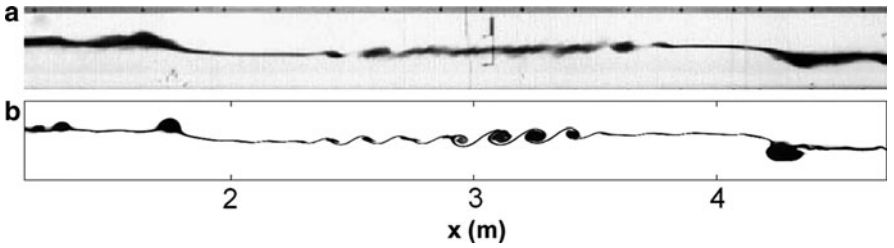

Fig. 4.10 Photograph of the experiment of Horn et al. (2001) (**a**) versus simulation. © J. Fluid Mech Cambridge University Press, reproduced with permission. (**b**) for parameters of Run#3

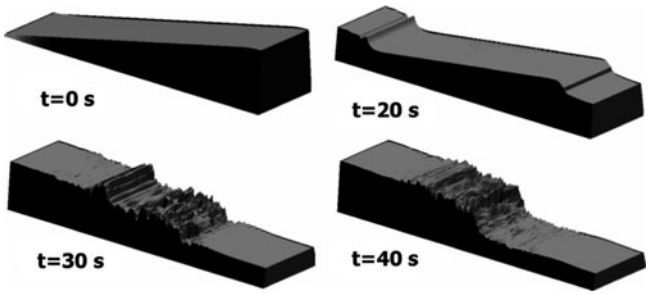

Fig. 4.11 The computed evolution of interface for Run#7

Wind acting on the surface of a lake causes both external and internal seiches. Both types of standing waves do not interact in the linear approximation at $g' \ll g$. Compare now the interface time series for Run 8 without initial free surface tilt caused by external force and Run 9 with linear tilt of the free surface $\eta_0 = 0.05 \cdot \eta_{0i}$. As seen in Fig. 4.14, temporal variations of the interface in the basin of constant depth depend only weakly on the barotropic seiche.

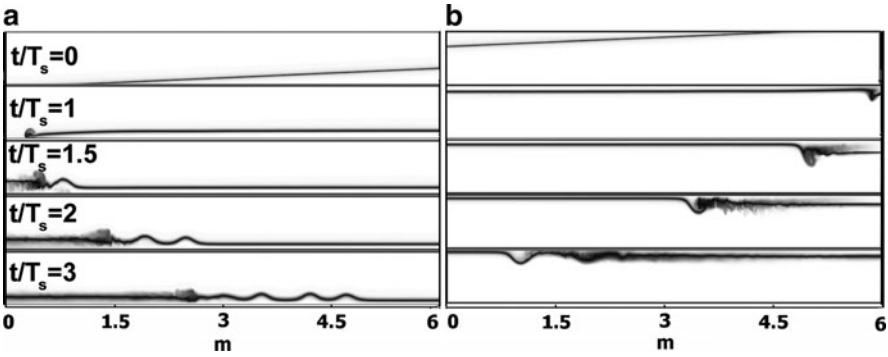

Fig. 4.12 The simulated density field for parameters of Run #4 (**a**) and Run#5 (**b**)

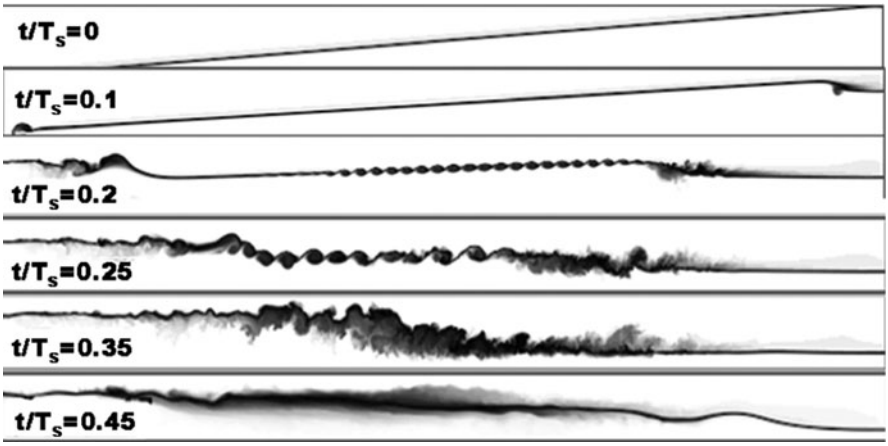

Fig. 4.13 Simulated density field for parameters of Run#6

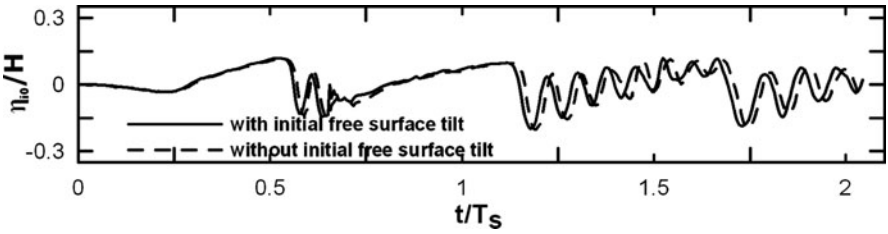

Fig. 4.14 The computed temporal variations of depth of the interface in the center of the tank in Run#7 and Run#8

4.4.2 *Modeling of Breaking of Internal Solitary Waves on a Slope*

It was pointed out in the Introduction that energy is supplied to a lake by wind at basin scales and then it is transferred to the small-scale motions. Horn et al. (2001) categorized regimes corresponding to different pathways of energy transfer. Their laboratory experiments and numerical simulations by Kanarska and Maderich (2004), Wadzuk and Hodges (2004), Staschuk et al. (2005), and Kanarska et al. (2007) as well as modeling results described in the previous paragraphs confirm this classification. However, the classification includes only mixing processes related to *shear instability* of flows and with bore or solibore formation, whereas in a lake an important process of mixing is also *internal wave shoaling* on the bottom slope. Internal wave breaking results in kinetic energy dissipation and mixing in the metalimnion on the perimeter of the lake.

ISW depressions dominate a typical lake situation when the metalimnion is closer to the surface $(h_1 - h_2 < 0)$; however, during winter, due to convection, the pycnocline can be closer to the bottom $(h_1 - h_2 > 0)$, supporting ISW elevations. The breaking process of an ISW depression over slopes was intensively studied experimentally and theoretically in the context of ocean and lake boundary mixing. Field observations show a variety of processes of ISW transformation in the shallow water column, including fission of ISW depression and transition into ISW elevation on a slope (Zhao et al. 2003; Orr and Mignerey 2003; Moum et al. 2003; Klymak and Moum 2003; Bourgault et al. 2007b; Shroyer et al. 2008). The laboratory experiments performed by Helfrich (1992) and Michallet and Ivey (1999) also showed that at small slope angles the incident wave depression was changed into a wave elevation, forming a turbulent surge or 'bolus'. A set of experiments was carried out by Chen et al (2007a, b) for a full range of slopes and ISWs of both depressions and elevations. Breaking over slopes was numerically studied by Vlasenko and Hutter (2002c), Bourgault and Kelley (2007), and Lamb and Nguyen (2009). The experiments on seiching in a rectangular basin (Horn et al. 2001) were extended by Boegman et al. (2005a, b) for the case of basin-scale wave degeneration in a rectangular basin with one sloping side. It was shown that initially, an ISW packet was formed from an initial basin-scale wave, and these waves of depressions were shoaled as waves of elevations. However, theoretical studies of dynamics and energetics of internal seiching are still not known.

In this section, breaking of large-amplitude ISWs of depression at the whole range of bottom slopes is simulated and compared with laboratory experiments, including some that are presented in Chap. 3. We compare results of simulations of ISW breaking on a slope with experiments by Michallet and Ivey (1999) and Gorodetska et al. (2012) to validate the model and to obtain a full set of data necessary for the calculation of energetics of breaking. Additional runs were carried out to analyze new aspects of ISW shoaling. Except for details, the set-up of many laboratory experiments is similar. It is sketched schematically in Fig. 4.14. The brine stratification is in two layers, separated by a thin intermediate layer. The waves are generated by a gravitational spreading (collapse) of a mixed volume of water with density of the upper layer at the end of the flume ("step pool" technique

(Kao et al. 1985)). The sign of the difference of the position of the interface η_{0i} between this volume and the remainder of the flume determines what kind of wave (depression or elevation) will be generated.

The collapse generates a leading ISW traveling along the flume and shoaling on the sloping bottom at the opposite side of the flume causing mixing and a reflected wave. In the simulations, we mimic this approach to generate an ISW of very large amplitude (Fig. 4.15). The ISW is described by the wave amplitude a and characteristic length L_W of the ISW that is defined, following Koop and Butler (1981), as

$$L_W = \frac{1}{a}\int_{-\infty}^{\infty} \eta_i \mathrm{d}x, \tag{4.81}$$

The experiments on ISWs of depression can be characterized by five nondimensional parameters (1) normalized density difference $(\rho_2 - \rho_1)/\rho_2$; (2) thickness ratio between layers h_2/h_1; (3) nonlinearity parameter a/L_w; and (4) ratio of height to length of sloping side H/L_s.The nonlinearity parameter a/L_w and the ratio of the height to the length of the sloping side H/L_s, as suggested by Boegman et al. (2005a, b), can be combined in one parameter, the so-called Iribarren number

$$\xi = (H/L_s)/(a/L_w)^{1/2}. \tag{4.82}$$

Numerical values of these parameters of the experiments and simulations are given in Table 4.3.

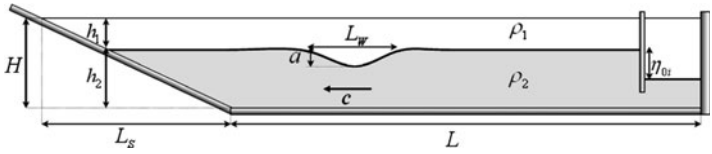

Fig. 4.15 Schematic diagram of the experiments (Michallet and Ivey 1999; Gorodetska et al. 2012) for ISW propagation and reflection from a slope

Table 4.3 Parameters of runs with breaking of ISW on slope

Experiment	Run	h_2/h_1	H/L_s	$\Delta\rho/\rho_0$	a/h_1	a/L_w	ξ	Resolution (x × y × z)
Michallet and Ivey (1999)	MI 2 (3D)	4.56	∞	0.04	1.07	0.103	∞	800 × 100 × 32
	MI 2 (2D)	4.56	∞	0.04	1.07	0.11	∞	800 × 100 × 5
	MI 8(3D)	4.88	0.169	0.04	1.06	0.106	0.52	800 × 100 × 32
	MI 8(2D)	4.88	0.169	0.04	1.1	0.11	0.5	800 × 100 × 5
	MI 12(3D)	4.25	0.214	0.012	1.19	0.105	0.66	800 × 100 × 32
	MI 12(2D)	4.25	0.214	0.012	1.22	0.108	0.65	800 × 100 × 5
	MI 15(3D)	3.35	0.214	0.047	0.74	0.07	0.8	800 × 100 × 32
	MI 15(2D)	3.35	0.214	0.047	0.78	0.08	0.76	800 × 100 × 5
Gorodetska et al. (2012)	1104	8	0.22	0.01	1.63	0.134	0.6	1,100×350×5
	2906	9	1.73	0.01	1.5	0.155	4.4	1,100 × 350 × 5
	A1	4.1	0.04	0.022	1.4	0.08	0.143	1,200 × 500 × 5
	A2	4.1	0.15	0.022	1.4	0.08	0.53	1,200 × 500 × 5
	A3	4.1	0.04	0.022	0.95	0.08	0.139	1,200 × 500 × 5

Most simulations were carried out in the "quasi-two-dimensional mode" with free-slip conditions on the sidewalls and free surface, whereas no-slip boundary conditions were used at the bottom. Some experiments in Table 4.3 were performed in three dimensions to estimate the effect of sidewalls on the wave transformations. All runs were done using molecular values of the viscosity and salt diffusivity.

Consider the formation of large amplitude ISWs in the well-documented laboratory experiments of Grue et al. (1999). These experiments were carried out in a tank of length $L = 21.4$ m, width $B = 0.5$ m, and total depth of the water $H = 0.77$ m. The brine stratification was established in two layers with thicknesses of the upper and bottom layers $h_1 = 0.15$ m and $h_2 = 0.62$ m, respectively. The density difference was 0.023 kg m^{-3} and the interface thickness was 0.02 m. We emulated experiment C of Grue et al. (1999), where a wave of almost maximum amplitude A_{lim} was created. The formation of ISWs was simulated in the quasi-two-dimensional mode with resolution of 1,200 $\times$ 500 $\times$ 5 in a computational tank of length 25 m. When the ISWs approached the end of the tank, they were moved to the beginning of a new tank of the same length, so the total distance traveled by the wave can be much larger in the "computational tank" than in the real tank.

Figure 4.16 shows the process of ISW formation. It can be separated into three stages. In the first stage, the head of the gravity current is formed with intensive mixing in the rear part (Fig. 4.16a). In the second stage, the head of the gravitational current transforms into a strongly nonlinear wave, which cannot transport the matter contrary to the gravitational current (Fig.4.16b, c). The profile of the interface in Fig. 4.16b and the vertical profile of the velocity at the maximum displacement of the wave in Fig. 4.17b in the simulation and in experiment C (Grue et al. 1999) agree well with one another. However, both simulation and experiment show that this signal is not a solitary wave, as suggested by Grue et al. (1999). The leading part of the wave profile is stable, and it can be described by the MCC solution (see Sect. 4.3.2) with amplitude $a = 0.225$ m that is close to the maximum value $A_{\text{lim}} = 0.235$ m. However, the rear part of the wave is transformed into a secondary wave of smaller amplitude (Fig. 4.16c), which is not revealed by Grue et al. (1999) because this process is relatively slow. The strong shear results in a K–H instability, which arises at the maximum displacement of the wave (Fig. 4.16b and c). The corresponding Richardson number,

$$Ri = -\frac{g}{\rho_0}\frac{\partial \rho}{\partial z}\Bigg/\left(\frac{\partial U}{\partial z}\right)^2, \tag{4.83}$$

is also given in Fig. 4.17b. The minimum Richardson number is 0.08, which is so much less than the critical value 0.25 that linear stability of parallel stratified flow is guaranteed (Miles 1961; Howard 1961; Miles and Howard 1964). The computed value of the interfacial Richardson number, $Ri_\delta = g'\delta_\rho/(\Delta U)^2$ (4.72) is $Ri_\delta = 0.09$, also much less than the critical value 0.24. Here, δ_ρ is the thickness of the interface layer with assumed linear distribution of the density, and ΔU is the shift of the horizontal velocity on the interface. The value of δ_ρ was estimated from the profile of the density in Fig. 4.17a as $\delta_\rho = 0.025$ m. The characteristic scale of

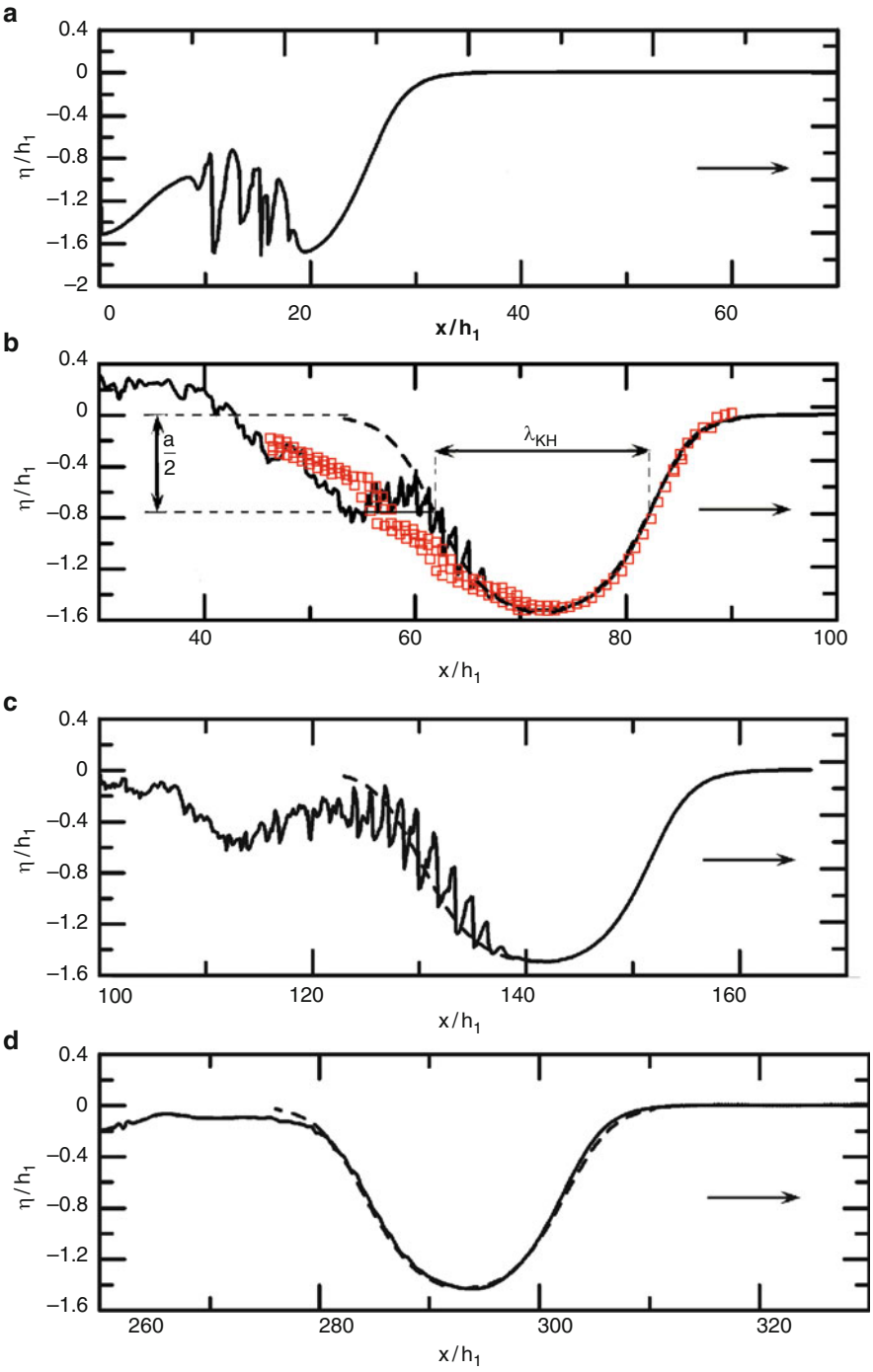

Fig. 4.16 Formation of ISW depression by collapse mechanism, as shown by interface η_i evolution. The *dashed line* corresponds to the MCC solitary wave. *Boxes* in (**b**) represent experiment C (Grue et al. 1999) and λ_{KH} is the size of the KH billow. The *arrow* gives the direction of wave propagation

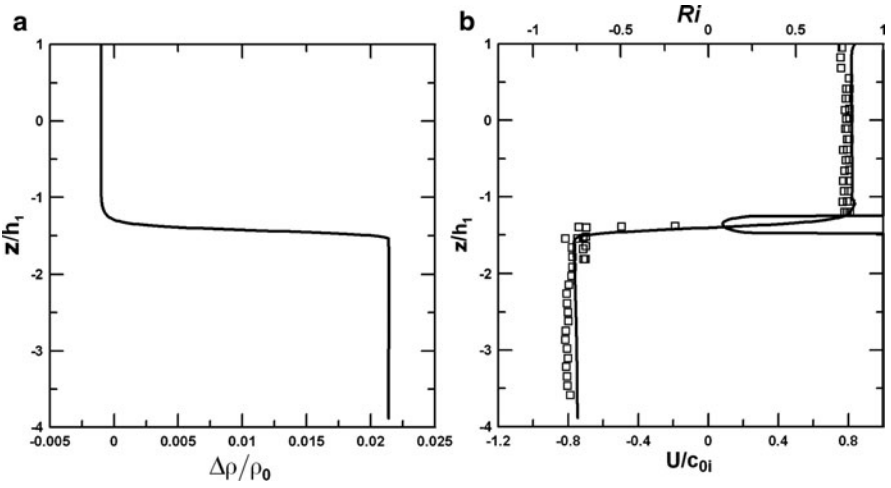

Fig. 4.17 Computed density profile (**a**) and vertical profile of velocity and Richardson number (**b**) at the maximal displacement of the wave at $x = 10.5$ m. *Boxes* represent experiment C (Grue et al. 1999)

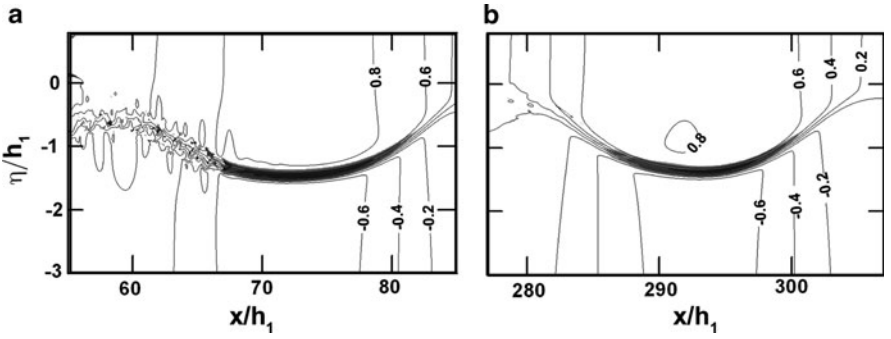

Fig. 4.18 The normalized horizontal velocity U/c_0 and potentially unstable region ($Ri < 0.25$) shown as shaded area in (**a**) unstable wave (see Fig. 4.16b) and in (**b**) stable wave (see Fig. 4.16d). The scythes approximately mark the locations of the troughs in Fig. 4.16b,d

the Kelvin–Helmholtz billows λ_{KH} in Fig. 4.16b is about 20 cm. The ratio of the unstable billow scale to the interface thickness $\lambda_{KH}/\delta_\rho = 8$ agrees well with the theoretical estimate $\lambda_{KH}/\delta_\rho = 7.5$ from stability analysis and results of laboratory experiments with interfacial solitary waves of large amplitude (Fructus et al. 2009), where the ratio $\lambda_{KH}/\delta_\rho = 7.9$. However, nonuniformity of flows in the solitary wave makes use of the Richardson number as an indicator of instability and for analysis of stability of parallel stratified flows insufficient. Figure 4.18 shows potentially unstable regions or "pockets" (Fructus et al. 2009) with $Ri < 0.25$ in the process of solitary wave formation (Fig. 4.16b) and in the steady solitary wave (Fig. 4.16d). The horizontal length L_x of pockets with $Ri < 0.25$ is a helpful

predictor of K–H instability (Fructus et al. 2009) because this length characterizes the horizontal extent where unstable motion can grow. The empirical relation

$$L_x/\lambda_{0.5} = 0.86, \tag{4.84}$$

separates potentially stable ($L_x/\lambda_{0.5} < 0.86$) and unstable pockets. Here, $\lambda_{0.5}$ is the wavelength defined as the width of the solitary wave at the level of the half-amplitudes $|a|$ (see Fig. 4.16b). The computed values are $L_x/\lambda_{0.5} = 0.9$ and 0.78 for pockets in Fig. 4.16b, d, respectively. They confirm the visual observation of the wave state: unstable in Fig. 4.16b and stable in Fig. 4.16d. As a result of mixing, the wave amplitude decreases due to the loss of mass caused by the Kelvin–Helmholtz instability, and the interfacial Richardson number grows to 0.11 in Fig. 4.16c. At the third stage, the wave amplitude and shear decrease and the wave is stabilized (Fig. 4.16d). The amplitude of the stable wave is $a = 0.21$ m and the interfacial Richardson number is 0.14. This wave is described well by the MCC solution (4.55), and it slowly decays by the viscous effects.

Consider now breaking of the ISW depression of large amplitude on the slope. The kinematics and dynamics of the breaking depend on the slope, stratification, wave amplitude, and the wavelength. At first, consider the effect of moderate and large slope. Two experiments of Gorodetska et al. (2012) (Runs 1104 and 2906 in Table 4.3) were simulated. The set-up of these experiments is described in detail in Chap. 3 of this book. The parameters of the corresponding runs are given in Table 4.3.

Figures 4.19 and 4.20 show a sequence of snapshots of experiment 1104 and sections of the computed salinity and vorticity at different stages of shoaling of the ISWs in Run 1104 for moderate slope ($H/L_s = 0.22$) and $a/h_1 = 1.63$. The first frames ($t = 0$; 5 s) show that the incoming wave is deformed since the rear front is steepened. The next frame ($t = 10$ s) shows that the mass of the water in the wave depression retards near the coast and water from the lower layer pushes the rear front with compensating flow at the lower part of the upper layer: this process is clearly visible in the vorticity distribution. The overturning in the rear part of the wave causes mixing and "bolus" formation ($t = 10$ s). The "bolus" (Helfrich 1992)

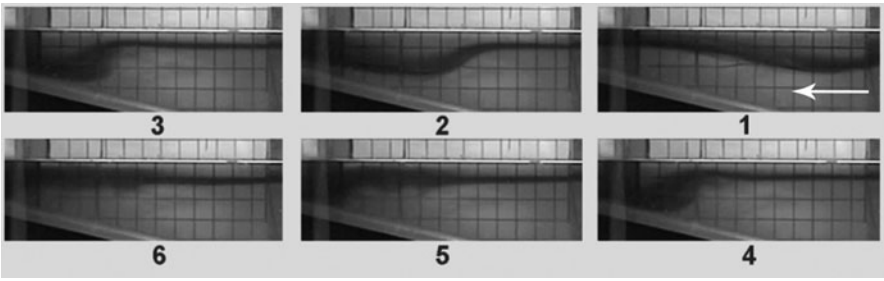

Fig. 4.19 Photographs of the wave breaking of ISW at the moderate slope in the laboratory experiment 1104 (Gorodetska et al. 2012)

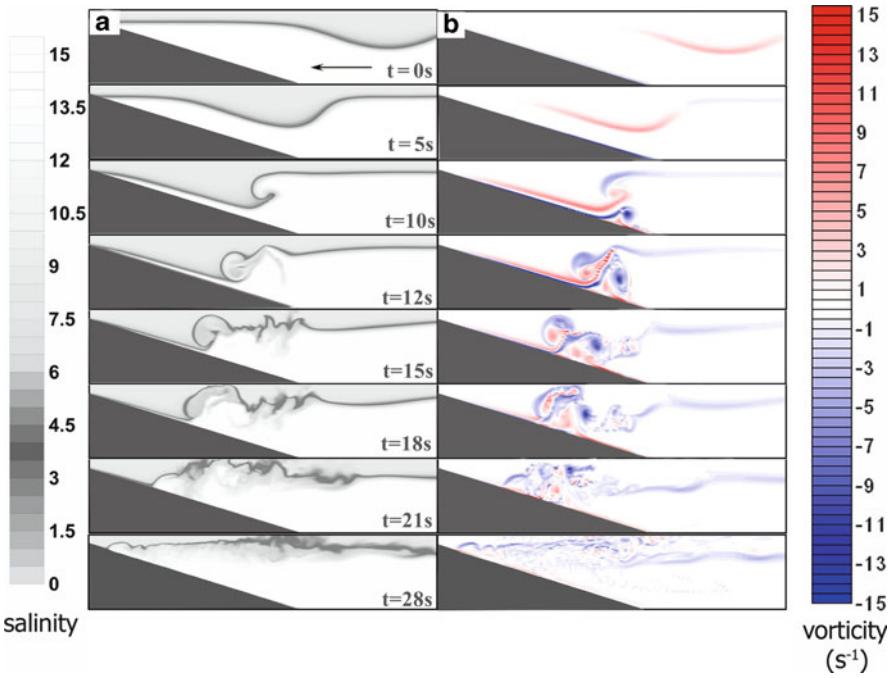

Fig. 4.20 Wave breaking and run-up of ISW depression in Run 1104: (**a**) salinity field, (**b**) vorticity

is a vortex pair formed by the momentum pulse in the rear of a breaking wave. It entrains water from both layers and propagates to the coast as wave elevation (t = 12–28 s). This process is qualitatively the same as in experiment (MI 8) (Michallet and Ivey 1999). It was numerically studied in detail by Vlasenko and Hutter (2002c).

Figures 4.21 and 4.22 show a sequence of snapshots from experiment 2906 and of sections of salinity in Run 2906 for a large slope $(H/L_s = 1.73)$ and large amplitude of the ISW $(a/h_1 = 1.5)$. In this case, the bolus did not form. However, similar to a reflection of an ISW from a vertical wall (Fig. 4.6), some mixing results in a broadening of the interface layer. The measured (Gorodetska et al. 2011) and computed temporal variations of the depth of the interface at the position of gauge G2 agree well (Fig. 4.23).

The breaking of an ISW on a gently sloping bottom needs more detailed consideration. Vlasenko and Hutter (2002c) showed that for a stratified lower layer, the transformation of an ISW was governed not only by nonlinear effects that dominated at the mild slope and resulted in overturning, but also by dispersion effects. Over the gently sloping bottom, a secondary wave tail is formed due to dispersion. According to Vlasenko et al. (2005), three possible scenarios of the behavior of large-amplitude ISWs are possible when at some point along the inclined bottom, the critical amplitude A_{lim} (4.56) is approached. If the inclination

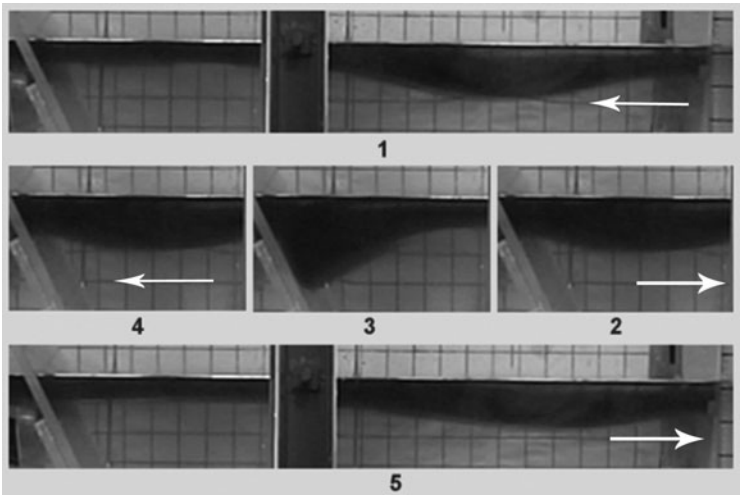

Fig. 4.21 Photographs of wave breaking of the ISW at the steep slope in experiment 2906 (Gorodetska et al. 2012, Chap. 3, this volume)

of the slope is moderate (like in Run 1104) and the wave overturns, then the first scenario is realized. The second scenario is an adiabatic transformation when the ISW amplitude is close to the local value of A_{lim}. The ISW adjusts to the almost critical wave shape following the depth variation. The third scenario is the above-mentioned nonadiabatic "dispersive" evolution when the wave radiates a dispersive wave tail.

However, our numerical experiments demonstrated the possibility of one more nonadiabatic scenario of breaking of large amplitude ISW on a gentle slope. We considered the transformation processes in greater detail and carried out three additional runs (A1–A3), given in Table 4.3. The numerical flume parameters are close to those in the experiments by Grue et al. (1999).

In Run A1, the ISW of large amplitude $(a/h_1 = 1.4)$ was exactly as generated in experiment C of Grue et al. (1999), shown in Fig. 4.16. The slope is small $(H/L_{\mathrm{s}} = 0.04)$. The wave transformation is shown in Fig. 4.24. In this case, when the ISW approaches the critical amplitude the KH instability arises at the trough of the wave. KH billows merge to large-scale vortices, which efficiently mix the interface and diminish the wave amplitude. The wave moves on to the shore without overturning and with formation of a weak bolus. In this case, shear instability is the dominating mechanism of the wave transformation.

In Run A2, the ISW approaching the slope is the same as in Run A1 but bottom slope is larger $(H/L_{\mathrm{s}} = 0.15)$. Figure 4.25 shows that the wave evolution follows an intermediate scenario between the case of moderate slope (Run 1104) and gentle slope (Run A1). As in Run A1 the KH instability appears, but at shallow water the overturning mechanism is dominant as in Run 1104 and the wave is transformed into a sequence of wave elevations with strong mixing in the lower layer. Consider

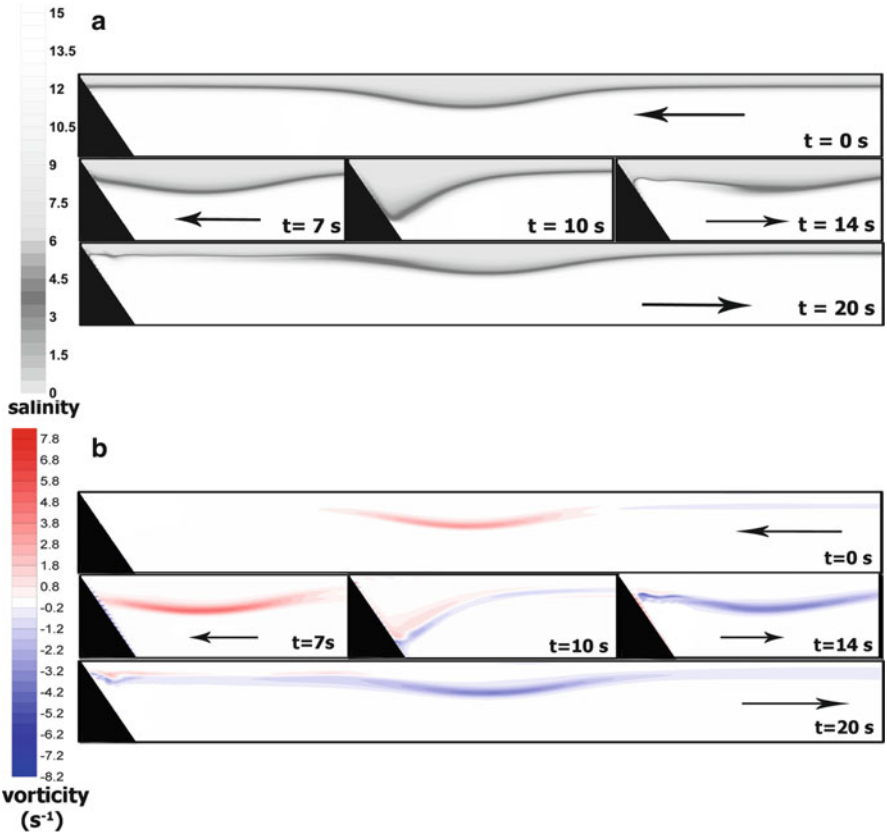

Fig. 4.22 Wave breaking and run-up of ISW depression in Run 2906: (**a**) salinity field (**b**) vorticity

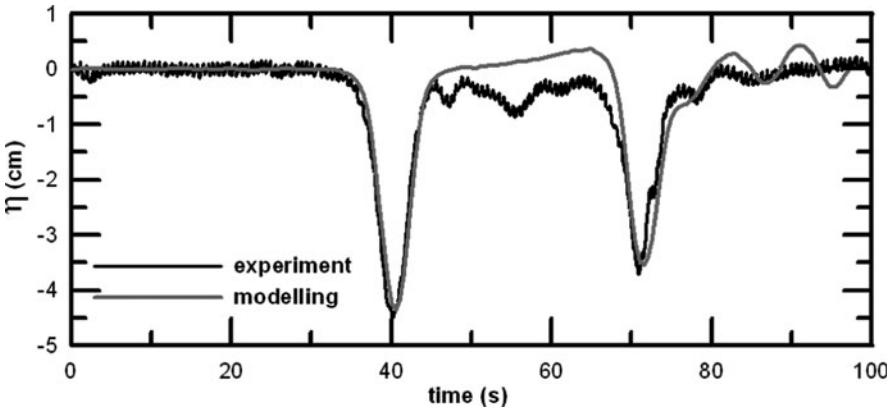

Fig. 4.23 The measured (Gorodetska et al. 2012, Chap. 3, this volume) and computed temporal variations of depth of the interface in the position of gauge G2 in Run 2906

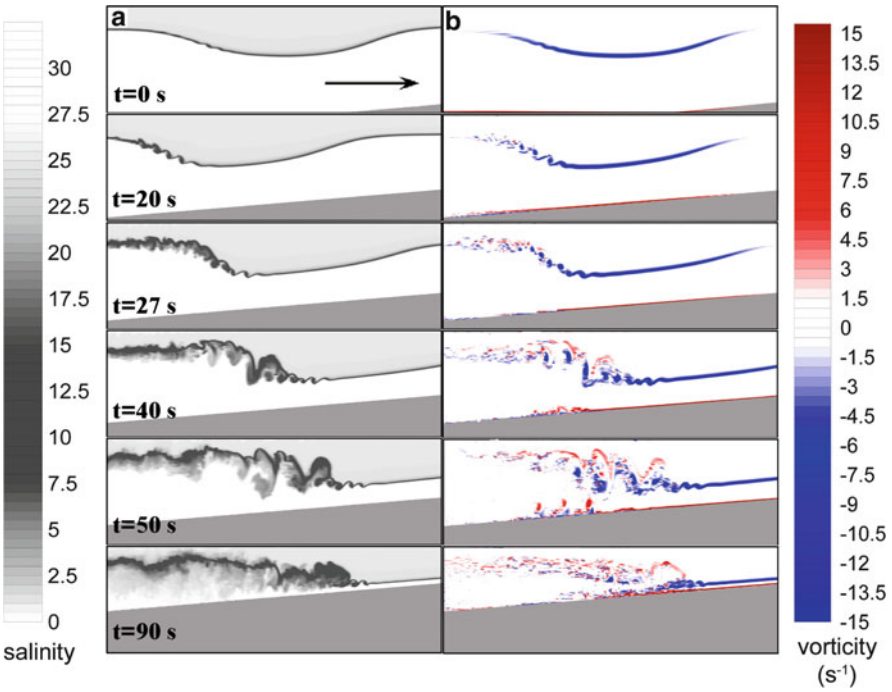

Fig. 4.24 Wave breaking and run-up of ISW depression in Run A1: (**a**) salinity field (**b**) vorticity. The *arrow* shows the direction of wave propagation

now Run A3 where the slope is gentle $(H/L_s = 0.04)$ as in Run A1 but the ISW amplitude $(a/h_1 = 0.95)$ is less than in Run A1. Figure 4.26 shows that the ISW evolved without shear instability and without wave overturning. Behind the wave depression, a wave hump arises which surges onto the shallow water. We can conclude that at gentle slopes, large-amplitude ISWs transform according to the fourth nonadiabatic scenario in which at first shear instability dominates, and then the wave changes the polarity without overturning. Field observations in the South China Sea (Orr and Mignerey 2003) confirm the existence of such a scenario of ISW breaking (compare Figs. 4.24 and 4.27). In all cases, the sign of the vorticity was changed in the approaching waves, which are transformed from wave depression to wave elevation.

Let us next consider an energy transformation in the breaking of an ISW on the slope. For comparison of the energetics of breaking in 2D simulations and in field observations with the laboratory experiments, it is important to estimate effects of energy loss due to wall friction in laboratory tanks. A number of theoretical and experimental studies (Leone et al. 1982; Maurer et al. 1996; Michallet and Ivey, 1999) were carried out to study this effect. They showed that the energy decays exponentially with distance traveled by the ISWs. Bourgault and Kelley (2007) parametrized side-wall effects in their 2D model using a quadratic friction law and adjusting the drag coefficient C_D to the measurement data of Michallet and

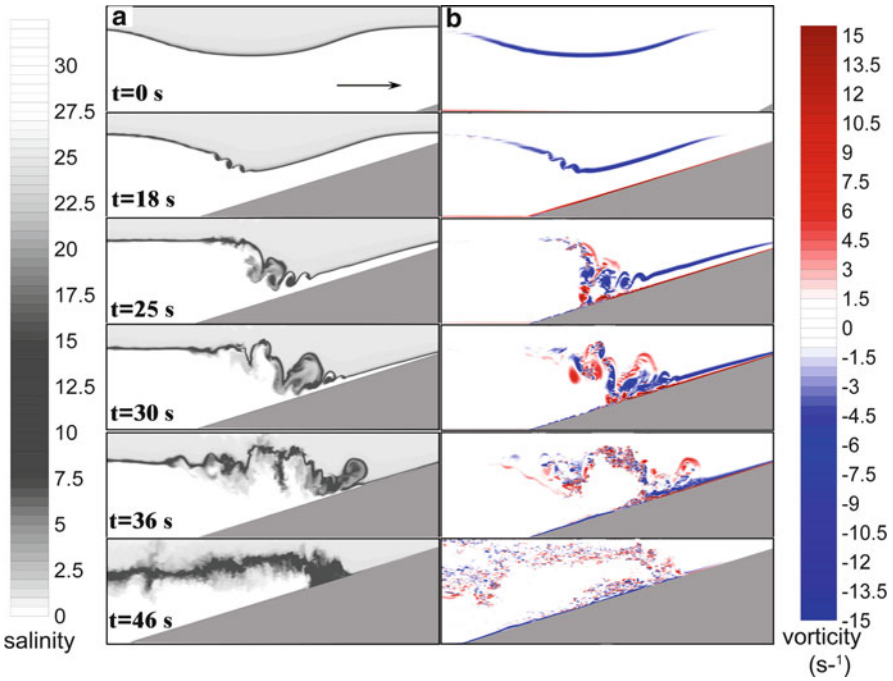

Fig. 4.25 Wave breaking and run-up of ISW depression in Run A2: (**a**) salinity field (**b**) vorticity. The *arrow* shows direction of wave propagation

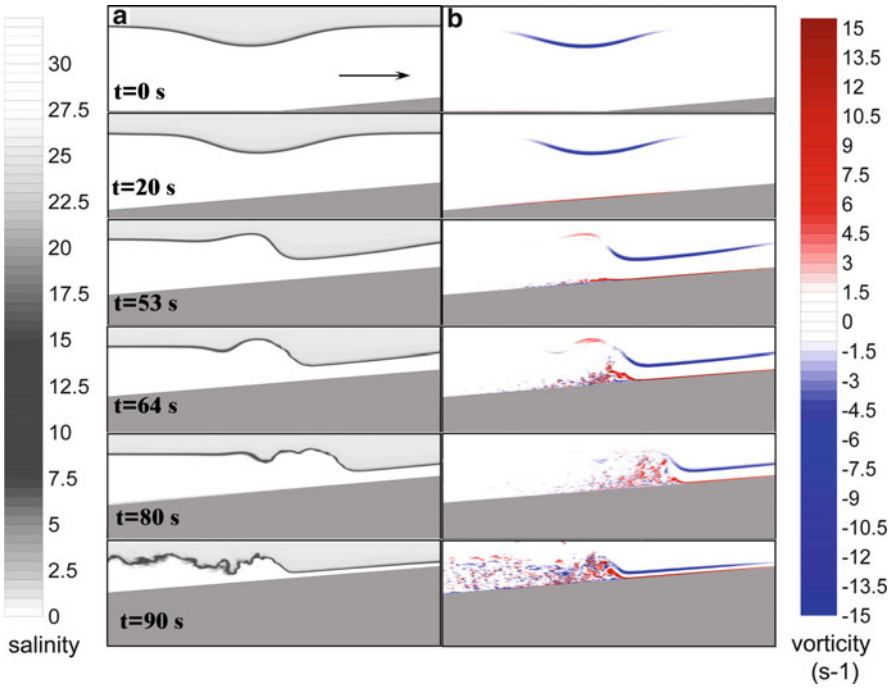

Fig. 4.26 Wave breaking and run-up of ISW depression in Run A3: (**a**) salinity field (**b**) vorticity

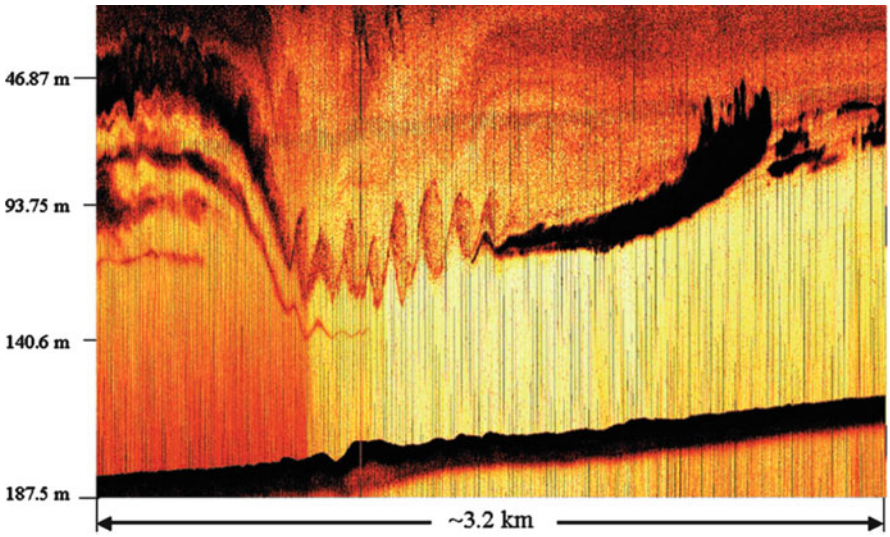

Fig. 4.27 Wave breaking and runup of ISW-depression in Run A3: (**a**) salinity field (**b**) vorticity

Ivey (1999). Then they compared simulated reflectance characteristics with those of Michallet and Ivey (1999) and Helfrich (1992) and concluded that side-wall friction in the laboratory experiments was an important factor in the energy transformation for ISW shoaling.

Here we check this suggestion using fully 3D simulations. At first, we compare 2D and 3D simulations with the observed decay of ISWs in the laboratory tank of Michallet and Ivey (1999) without slope (Table 4.3, Exp MI2). In Fig. 4.28, the simulated pseudo-energy PSE, normalized with its initial value is plotted against the traveled distance weighted by the layer thickness ratio. To compare results with Michallet and Ivey (1999), the pseudo-energy was calculated using the weakly nonlinear estimate (Bogucki and Garrett, 1993; Lamb, 1994) for a two-layer fluid

$$\mathrm{PSE} = \mathrm{APE} + \mathrm{KE} \approx g\Delta\rho B \int_0^L \eta_i^2 \mathrm{d}x, \tag{4.85}$$

where the available potential energy APE is equal to the kinetic energy KE.

The straight line in Fig. 4.28 fits experiment MI2 (Michallet and Ivey 1999). As seen from the figure, the simulations correctly describe the PSE decay. Our 2D simulation agrees well with results of the 2D modeling (Bourgault and Kelley 2007). We conclude that the 3D model correctly describes ISW dynamics in the laboratory flume and shows dominance of side-wall friction over interface and bottom friction in the energy dissipation in the laboratory flume of constant width and depth.

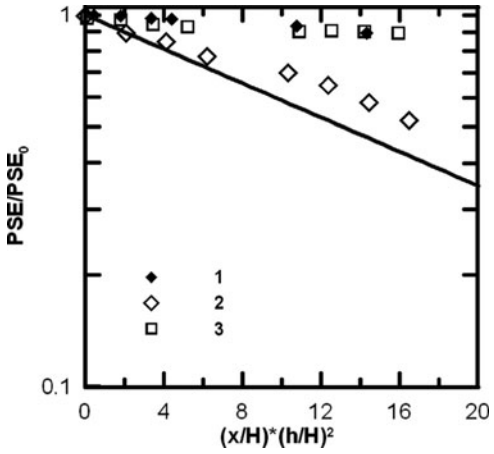

Fig. 4.28 Computed versus measured (Michallet and Ivey, 1999) decay of pseudo-energy. Solid line fits the experiments of Michallet and Ivey (1999). 1:2D simulation, 2: 3D simulation, and 3: 2D simulation by Bourgault and Kelley (2007)

Consider now the budget of the energy of ISW breaking at the slope. The pseudo-energy of the incoming ISW, $\mathrm{PSE_i}$, is transformed into wave energy reflected from the slope, $\mathrm{PSE_r}$; this energy is dissipated in the bottom boundary layer, in the sidewall boundary layers (in the laboratory experiments), in the interface layer, and in breaking events, and it is transferred to the potential energy by mixing caused by wave breaking. The pseudo-energy E of waves passing through a given cross section of a computational flume at the time interval $t_2 - t_1$ is given by

$$\mathrm{PSE} = \int_{t=t_1}^{t=t_2} \int_{y=0}^{y=B} F_x \mathrm{d}y' \mathrm{d}t', \tag{4.86}$$

where $F_x = F_1$ is the flux (4.65). For weakly nonlinear ISWs in a two-layer fluid, $F_x \approx \mathrm{PWF}_x$, and the PSE is approximately (Helfrich 1992)

$$\mathrm{PSE} \approx c_{0i} g \Delta\rho B \int_{t_1}^{t_2} \eta_i^2 \mathrm{d}t. \tag{4.87}$$

With the assumption that APEF and KEF in (4.65) are approximately equal, the following simplified relation is obtained (Helfrich 1992; Bourgault and Kelley 2007):

$$F_x = \int_{-H}^{0} \left[Up + \rho(U^2 + W^2)\right] \mathrm{d}z \approx \int_{-H}^{0} \left[Up + \rho U^2\right] \mathrm{d}z. \tag{4.88}$$

Figure 4.29a shows the dependence of the reflectivity of ISWs on the Iribarren number for laboratory experiments (Michallet and Ivey 1999) and numerical

modeling (Bourgault and Kelley 2007). Note that Michallet and Ivey (1999) calculated the pseudo-energy of waves using the weakly nonlinear relation (4.85), whereas Bourgault and Kelley (2007) used for the flux of the pseudo-energy approximation, (4.86). The reflection coefficient $R = \mathrm{PSE_r}/\mathrm{PSE_i}$ depends on the Iribarren number ξ (4.82). The solid curves in the figure show an exponential fit (Bourgault and Kelley 2007),

$$R = 1 - \exp(-\xi/\xi_0), \tag{4.89}$$

where $\xi_0 = 0.78 \pm 0.02$. As seen in this figure, the 2D simulations show a trend similar to the experiment, but they overestimate the reflectance when compared with the experiment. It can be explained by (1) an effect of sidewalls in the laboratory experiment and (2) a difference in the methods of estimation of the pseudo-energy. Consider both possibilities. Figure 4.29b shows results of computations of reflection coefficients using 3D (1) and 2D (2) models and using the full relation (4.65) for PSE. In this figure, the computed reflection coefficients using 3D (3) and 2D (4) models and using relations (4.88) for the flux of the pseudo-energy are given. Lastly, in the figure the computed reflection coefficients are shown using 3D (5) and 2D (6) models and using relations (4.87) for PSE.

At first, compare results obtained by using 3D and 2D models. There are no large differences between the 2D and 3D case; at least, the difference is much less than that between the laboratory experiment and the computations in (a). Compare next the results of computations of the reflection coefficient using relation (4.88) for the flux of the pseudo-energy and using relations (4.87) for PSE. As panel (b) suggests, the difference between these cases is almost the same as in panel (a) for 2D as well as for 3D simulations. We conclude that the discrepancy in panel (a) between computations and laboratory experiment can be explained by the difference between methods of calculation of the pseudo-energy rather than friction on the sidewalls of the laboratory flume. Compare now the computed reflection coefficient using the full relations (4.65) with approximate relations (4.88) and (4.87). As seen in panel (b), relation (4.88) overestimates the reflection coefficient. This result agrees with conclusions of Lamb and Nguyen (2009) that are based on 2D modeling. At the same time, relation (4.88) underestimates the reflectivity when compared with the full relation (4.65). The three conclusions are evident from an intercomparison of modeling and experiment (1) The friction on the sidewalls does not strongly effect the experimental data on wave breaking in the laboratory flumes, contrary to long-time ISWs traveling along the flumes (see Fig. 4.28); (2) the approximate relation (4.87) for the flux of the pseudo-energy overestimates the reflection coefficient, whereas relation (4.88) somewhat underestimates it; and (3) the laboratory experiment data can be used for field comparison without wall corrections because the main part of the dissipation is related with the fiction and mixing on the slope area.

Figure 4.30 shows the dependence of the reflectance coefficient on the Iribarren number plotted on the basis of 2D simulations, given in Table 4.3 (except Run MI2), with the use of the full relation (4.65) for the pseudo-energy. As seen in the

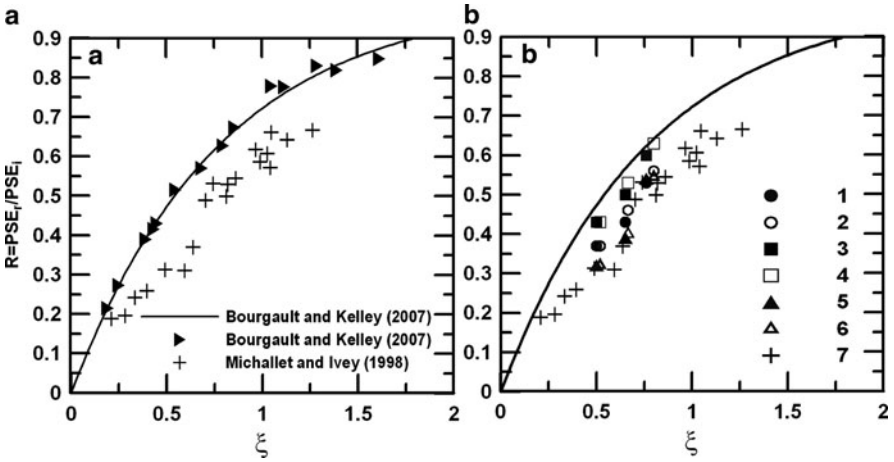

Fig. 4.29 Reflection coefficient R versus Iribarren number. (**a**) Comparison of 2D simulations (Bourgault and Kelley 2007) with laboratory experiments (Michallet and Ivey 1999); (**b**) Comparison of reflection coefficients using 3D (1) and 2D (2) modeling and full relations (4.65) for PSE with computations using 3D (3) and 2D (4) modeling and relation (4.86) and with computations using 3D (5) and 2D (6) modeling and relations (4.85) and with laboratory experiments (Michallet and Ivey 1999), where relation (4.85) was used

figure, the simulated dependence agrees well with the experiment. Note that curve (4.89) overestimates the reflectivity at large slope. As experiments in Sect. 4.3.4 show, even reflection of ISWs from a vertical wall results in some mixing in the interface layer.

Compare results of modeling using LES model (4.6) with observations of an ISW train impacting the beach. The simulation reproduces conditions of a field experiment (Bourgault et al. 2007) on the flank of Ile-aux-Lievres Island in the St. Lawrence Estuary on 26 August 2004 (Fig. 4.31). The dashed line in Fig. 4.31a shows an average transect where measurements were collected, black squares mark moorings (A, B, and C), and the triangles mark thermistor and CT chains. The open arrow indicates the direction of the leading ISW and the solid and dashed black arrows show directions of the surface current and the current at depth 13 m, respectively. Panel (b) in this figure shows the measured density profile and associated squared buoyancy.

The model was used in the 2D configuration along the wave direction in Fig. 4.31a. Like numerical experiments given in Bourgault et al. (2007), the profile of density was used in accordance with Fig. 4.31b. The initial ISW was generated in such way to agree with observed parameters of the wave: length $L_w = 62$ m and amplitude $a = 6.5$ m. The ratio $a/h_1 \approx 0.8$, the slope s is approximately 0.05, and the corresponding Iribarren number is ,$\xi = 0.16$ which is close to the parameters of Run A3 in Table 4.3. The echogram of the wave transformation is shown in Fig. 4.32, whereas results of simulation are presented in Fig. 4.33. In the process of transformation, the rear part of the wave becomes steeper ($t = 360$ s). Then, wave elevation is formed ($t = 500$ s). This wave propagates to shore as decaying

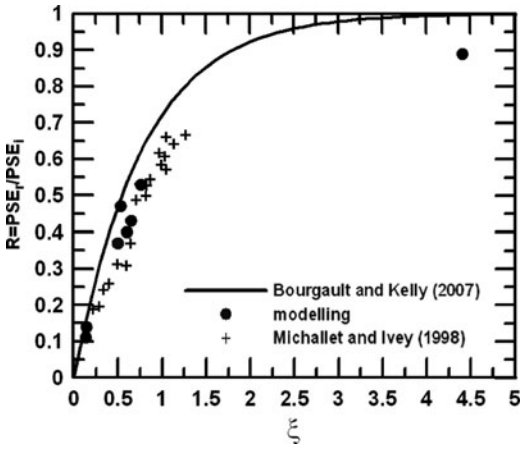

Fig. 4.30 Reflection coefficient R versus Iribarren number ξ

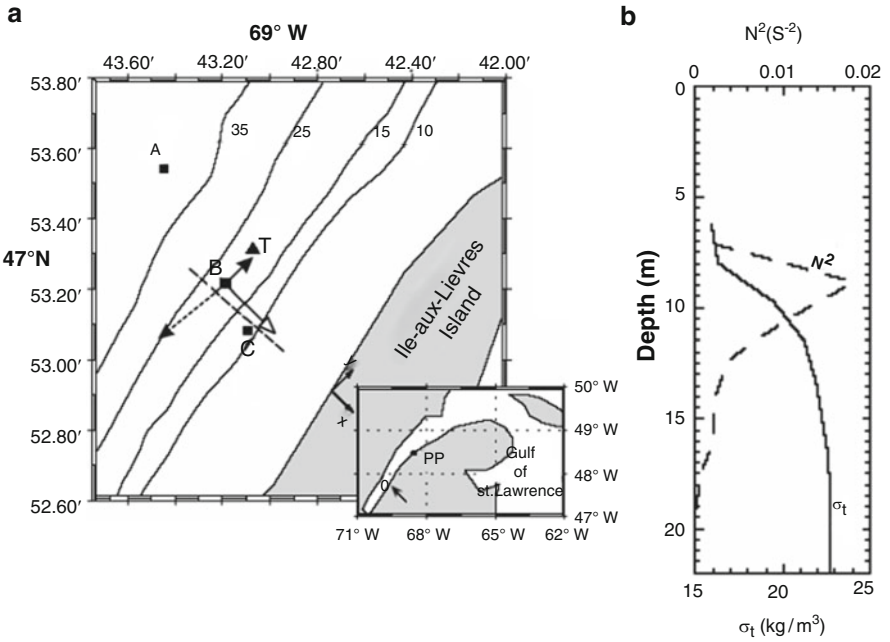

Fig. 4.31 (**a**) Chart of the field site and (**b**) Mean density anomaly σ_t and squared buoyancy N^2 (Bourgault et al. 2007)

"bolus" (t = 680–1,100 s). Like Run A3 in Fig. 4.34, the leading wave depression was transformed into wave elevation without breaking. The next secondary wave was transformed with mixing (t = 680 s). The secondary bolus dissipated moving onshore (t = 880–1,400 s). The process of wave transformation is again repeated when the next wave approaches the shore. Unlike many laboratory experiments and

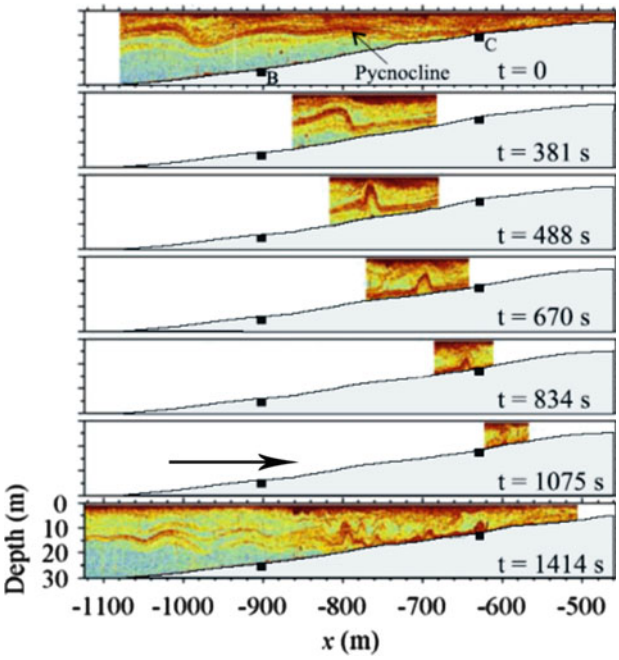

Fig. 4.32 Echogram showing the wave impacting the flank of Ile-aux-Lievres Island (Bourgault et al. 2007)

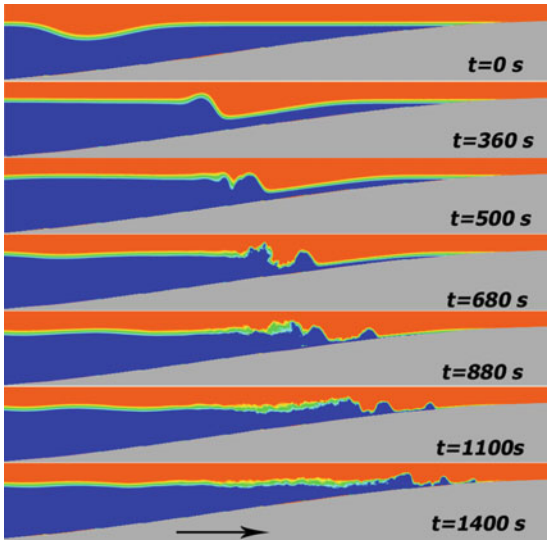

Fig. 4.33 The simulated density cross sections corresponding to Fig. 4.31

observations, the first wave elevation is formed without wave overturning (cf. Fig. 4.19) and without shear instability (cf. Fig. 4.33). It can be explained by the small bottom slope ($s = 0.05$) and moderate wave steepness that allowed smooth transformation of the wave depression into wave elevation (cf. Fig. 4.33). Comparing this simulation of a large-scale event using LES parametrization with DNS simulation in Run A3 confirms that details of the dissipation mechanism do not play an important role in the wave breaking on the sloping bottom and that results of laboratory experiments can be used to interpret field observations.

4.4.3 *Degeneration of Basin-Scale Internal Waves in Basins with Bottom Slopes*

As discussed in previous sections, in lakes the source for progressive high-frequency ISWs is often a nonlinear internal surge that forms in the process of seiching. The sloping topography of lakes results in internal wave shoaling. Here, we consider degeneration of internal waves in a laboratory-scale basin with sloping bottom at one of the basin ends. These numerical simulations reproduce some of the laboratory experiments of Boegman et al. (2005a). These experiments were conducted in a rectangular tank (the same as discussed in previous sections). A uniform slope was created at one end of the tank. The tank was filled with a two-layer salinity stratification. The density difference between the layers was $\Delta\rho = 20\,\mathrm{kg\ m^{-3}}$. The tank was covered by a lid, which allows inclining into the required interfacial tilt. Rapid rotation of the tank to its original horizontal position results in an initial inclination of interface and subsequent seiching. The parameters of the simulated experiments are given in Table 4.4. Initial conditions can be characterized as either upwelling on the slope (Run 10) or downwelling on the slope (Run 12). The initial configuration of the experiments is shown in Fig. 4.34. According to the classification given in Sect. 4.3.4, Run 10 corresponds to Regime

Table 4.4 Parameters of the numerical experiments on the degeneration of basin-scale internal waves in basins with bottom slopes

Run\Experiment	h_1/H	η_{0i}/h_1	Regime	Slope	Resolution (x × y × z)
10\BO 6	0.29	−0.90	II	0.15	1,100 × 350 × 5
11\BO 6A	0.29	−0.90	II	∞	1,100 × 350 × 5
12\BO 18	0.50	+0.82	IV	0.15	1,100 × 350 × 5

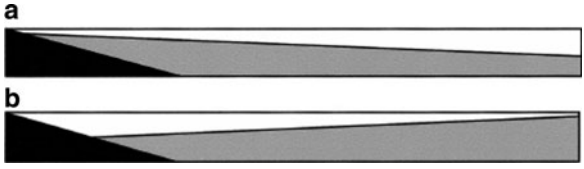

Fig. 4.34 Initial conditions in the experiments of Boegman et al. (2005a, b). (**a**) Upwelling on the slope (Run 10). (**b**) Downwelling on the slope (Run 12)

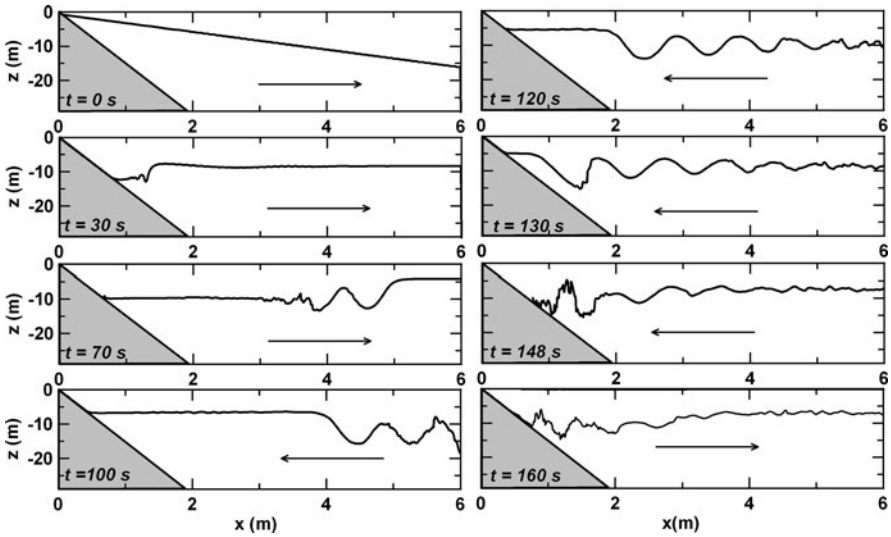

Fig. 4.35 Computed variations of depth of the interface in Run 10

II (solitary wave generation) whereas Run 12 corresponds to Regime IV (KH billows); it can be compared with Run 3 in Table 4.2. Run 11, with parameters of Run 10, was performed in a rectangular tank to clarify the effects of sloping bottom.

Consider the processes of high-frequency wave formation and shoaling in Run 10 (upwelling at slope). Figure 4.35 shows a sequence of positions of the interface between layers. At first a bore is formed ($t = 30$ s), which is transformed into a chain of ISWs propagating to the end of tank with slope ($t = 70$ s). These waves are reflected, as in the case of the rectangular tank (cf. Fig. 4.5), and shoaled on the slope. The presence of bottom slope in Run 10 essentially changes the evolution of the ISW chain. Breaking of the sequence of solitary waves results in mixing and energy dissipation. The amplitude of the reflected waves is half of the incident wave amplitude. The temporal variations of the depth of the interface in the center of the tank for Run 11 and in Run 10 and corresponding continuous wavelet transforms are given in Figs. 4.36 and 4.37, respectively. The formation and evolution of a solitary wave chain in a rectangular tank (Fig. 4.36) are similar to Run 2 (Fig. 4.6). A time–frequencies wavelet analysis in Fig. 4.36b shows that at $t/T>1$, the high-frequency ISW chain persists for a long time and is decaying under viscosity effects. However, the sloping bottom effectively damps the short waves, as seen in Fig. 4.37b.

The kinematics of breaking in Run 10 at the given slope 0.15 is similar in the laboratory and numerical experiments (Runs 1104 and A2) considered above in detail. The ratio of the amplitude of the leading solitary wave to the thickness of the upper layer $a/h_1 \approx 2$ at $t = 120$ s, and it is described well by the MCC model. Figure 4.38 shows that in both experiment and simulation, a rear part of incident wave is steepened; this results in the wave overturning and formation of boluses.

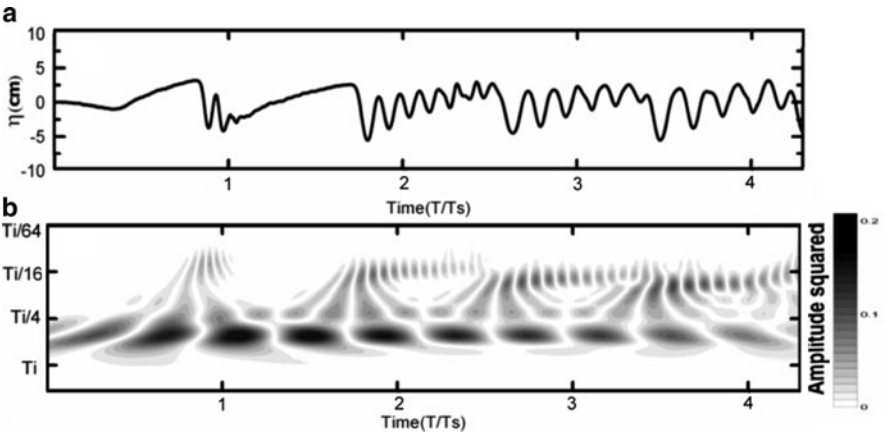

Fig. 4.36 Computed temporal variations of depth of the interface in the center of the tank in Run 11 (**a**). Continuous wavelet transform of the computed depth of the interface at the center of the tank for Run 11 using Morlet basis function (**b**)

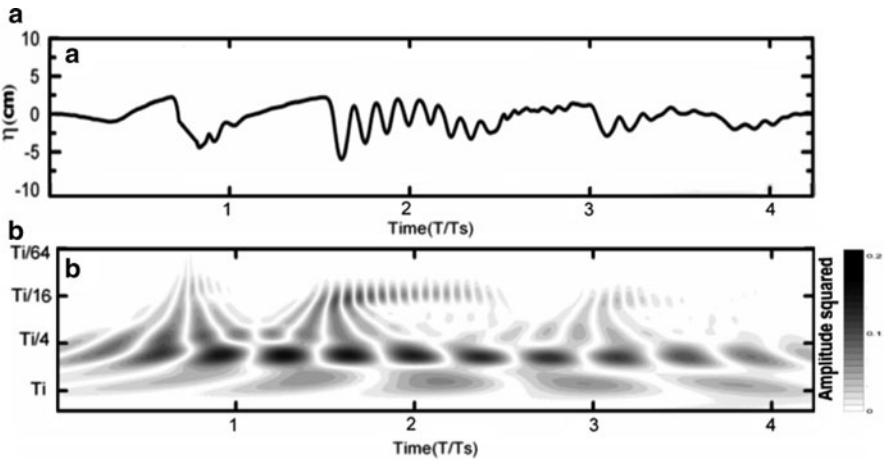

Fig. 4.37 Computed temporal variations of depth of the interface in the center of the tank in Run 10 (**a**). Continuous wavelet transform of the computed depth of the interface at the center of the tank for Run 10 using Morlet basis function (**b**)

The overturning mechanism is dominating; however, some effects of shear instability are also visible at $t = 130$ s (cf. Fig. 4.35).

Consider the case of downwelling at slope (Run 12). Figure 4.39 shows the sequence of positions of interface between layers. This run is close to Run 3 from Table 4.2. However, the presence of slope results in differences between them even in initial stages of seiching. Instead of formation of two bores in Run 3, only one bore arose in Run 12 ($t = 30$ s). This bore was transformed into a solibore ($t = 40$–60 s). Like Run 3 (see Fig. 4.10), strong shear across the interface caused instability and formation of KH billows ($t = 30$–40 s). These billows are well

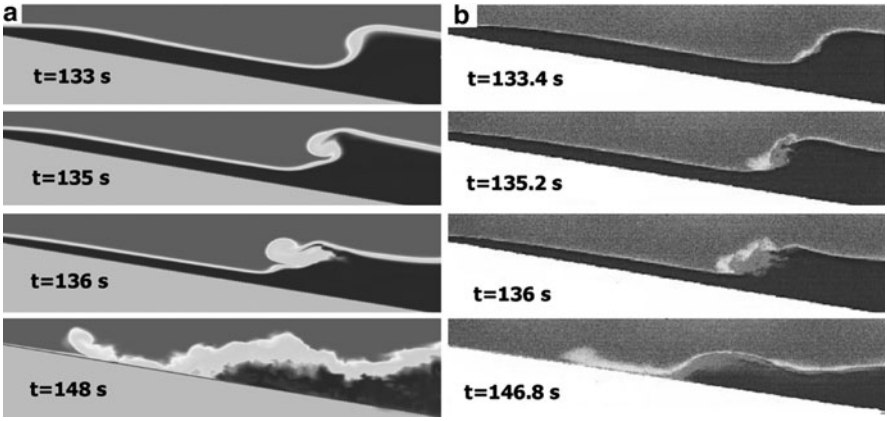

Fig. 4.38 Comparison of wave sequence breaking at the slope 3/20 with laboratory experiment (Boegman et al. 2005a, b). (**a**) – Calculations (Run 10), (**b**) – Laboratory experiment 6. (© 2005 by the Association for the Sciences of Limnology and Oceanography, Inc, reproduced with permission)

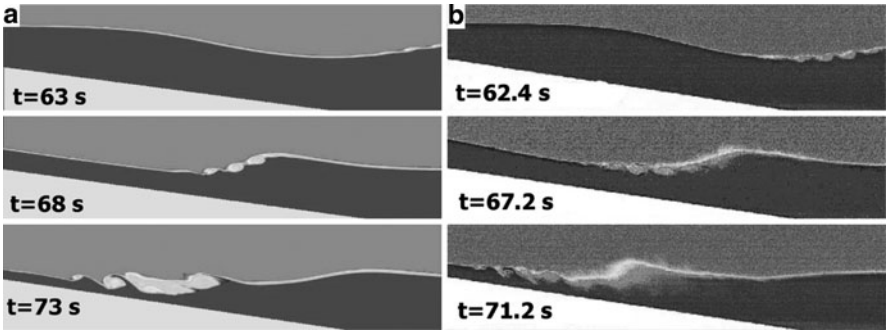

Fig. 4.39 Comparison of sequence of wave breaking at the slope 3/20 in simulations and laboratory experiment (Boegman et al. 2005a, b). (**a**) – Calculations (Run 12). (**b**) – Laboratory experiment 18. (© 2005 by the Association for the Sciences of Limnology and Oceanography, Inc, reproduced with permission)

visible in the field of salinity and vorticity in Fig. 4.40, and they enhanced mixing between the layers. A moving bore destroys KH structure in the interface layer.

The kinematics of wave breaking on the slope in Run 12 differs from that in Run 10. The ratio of the amplitude of the leading wave in the solibore to the thickness of the upper layer $a/h_1 \approx 2$ at $t = 60$ s. Figure 4.41 shows that steepening of the rear part of the leading wave is accompanied by shear instability ($t = 65$ s). A sequence of frames with wave breaking from simulation and laboratory experiment is given in Fig. 4.39. Both simulations and laboratory experiments showed that a shear instability mechanism dominates in wave breaking, whereas overturning was not observed as bolus formation. This mechanism is similar to that observed in Run A2.

The results of modeling showed that two mechanisms (overturning and shear instability) determine the nature of ISW depression and solibore depression

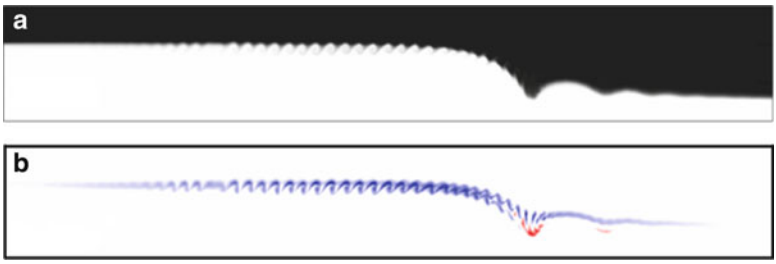

Fig. 4.40 Salinity (**a**) and vorticity (**b**) distributions at t =30 s in Run 12

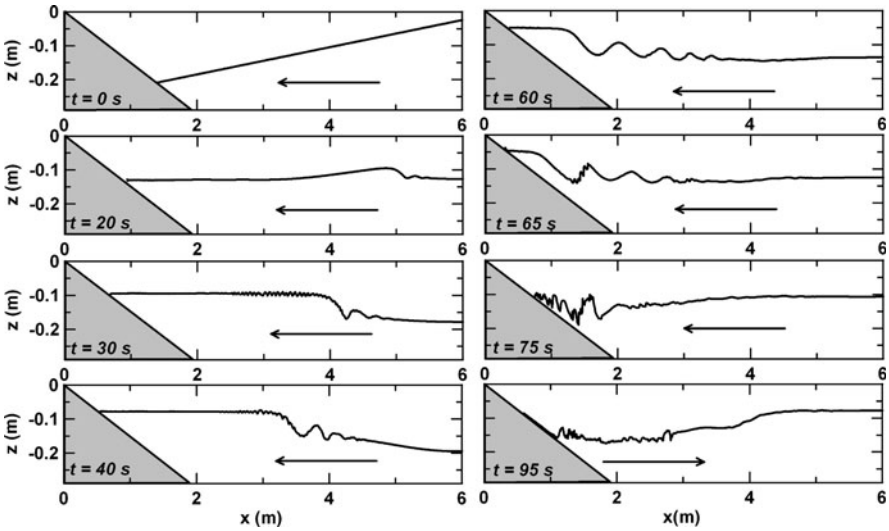

Fig. 4.41 The computed variations of depth of the interface in Run 12

breaking. By analogy with surface waves, Boegman et al. (2005a) classified internal wave breakers according to the Iribarren number ξ as spilling breakers, plunging breakers, collapsing breakers, and as Kelvin–Helmholtz breakers. Boegman et al. (2005a) suggests that Fig. 4.38 (Run 10) is an example of plunging breaker, whereas Fig. 4.39 presents an example of a KH breaker. Note that there is not a full analogy between internal and surface waves because air has a density thousand times smaller than that of water, whereas the density difference between layers of water is of the order 10^{-2} and therefore, the dynamics of flows in both layers is important for internal waves contrary to the surface wave counterpart. So, ISW breaking can be classified as "overturning" breakers and "KH breakers."

The computed energy transformations in Run 12 are given in Figs. 4.42–4.43. The evolution of kinetic energy (KE) and potential energy (PE) of the tank in Fig. 4.39 shows that shoaling of the wave chain at t = 60–75 s results in the fast suppression of the kinetic and potential energy. Figure 4.43 shows the evolution of

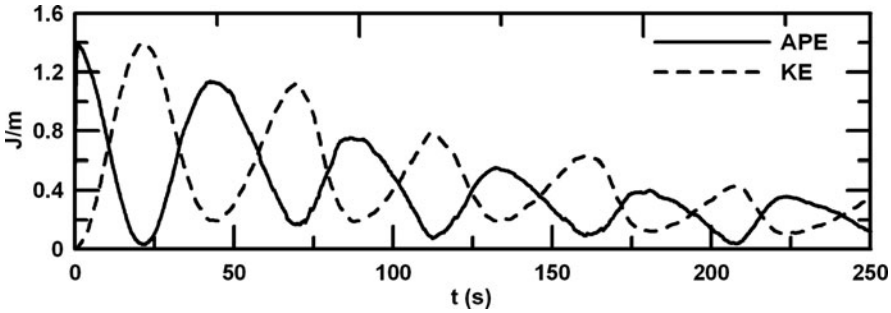

Fig. 4.42 Evolution of kinetic and available potential energy in Run 12

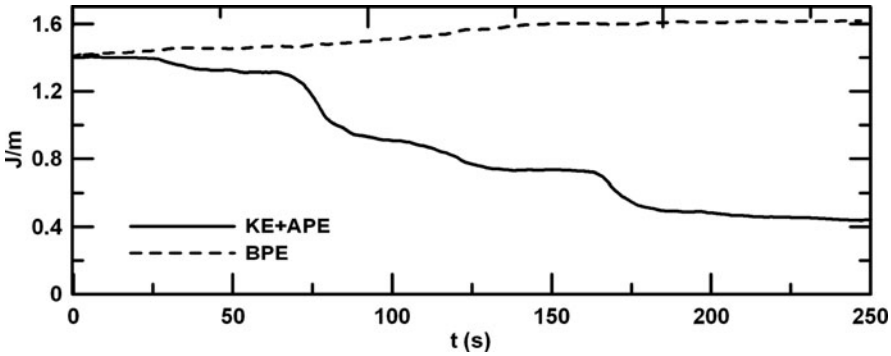

Fig. 4.43 Evolution of the pseudo-energy *PSE* and background energy *BPE* in Run 12

pseudo-energy PSE (sum of kinetic energy and available potential energy (APE)) and of background potential energy (BPE) calculated by adiabatic sorting of density field within volume (see Sect. 4.3.3 for details). This figure also shows that fast transfer of energy into the BPE took place at 60–80 s when the wave train was shoaled at the slope and mixing results in irreversible thickening of the pycnocline. Because of strong damping of the wave energy (Fig. 4.42), the next shoaling events at 120 s and 170 s are relatively weak in the energy transformation (Fig. 4.43). The thickening of pycnocline is shown in Fig. 4.44. Note that another process that results in thickening of pycnocline is a nonadiabatic background diffusion of temperature or salinity.

4.4.4 Modeling of Interaction of Internal Waves with Bottom Obstacles

Only a few field observations on ISW behavior over bottom obstacles are described in the literature (Sabinin 1992; Kocsis et al. 1998). The interaction of ISW elevation

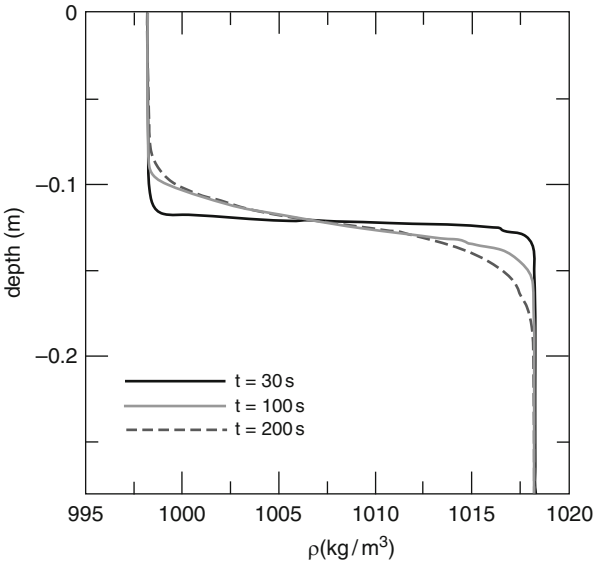

Fig. 4.44 Evolution of the reference density $\bar{\rho}_r(z,t)$profile in Run 12

with a triangular obstacle in a laboratory tank with two-layer stratification was studied by Wessels and Hutter (1996). Further, Hüttemann and Hutter (2001) in laboratory experiments and Vlasenko and Hutter (2002a, b) in numerical exercises found that the presence of the interface layer of finite thickness results in the generation of higher order baroclinic modes. The interaction of an ISW depression in a two-layer fluid using a triangular obstacle with rounded tip was investigated in the laboratory by Sveen et al. (2002) and Guo et al. (2004), whereas Brovchenko et al. (2007) modeled such interaction with rectangular obstacles both experimentally and numerically. Chen (2007b) conducted experiments and studied the transformation and breaking of both ISW depressions and elevations over obstacles in the form of triangles and semicircles of different heights. ISW breaking in a laboratory model of a double-ridge and double-ridge and shelf was studied by Chen et al. (2008) and Cheng et al. (2009), respectively. These studies were motivated by interest in large ISW behavior in the South China Sea (e.g., Orr and Mignerey 2003). Breaking of periodic progressive two-layer interfacial waves at a ridge was also investigated through laboratory experiments by Hult et al. (2009).

In this section, the processes of ISW transformation by rectangular obstacles will be our initial concern. In the next section, we consider the nonlinear impact of a sill on flow structure and mixing in the seiching. We compare results of simulations of ISW transformation and breaking over a rectangular obstacle with the laboratory experiments of Gorodetska et al. (2012, Chap. 3, this volume). The set-up of these experiments is represented schematically in Fig. 4.45. The stratification, established with brine, is two layers with thin intermediate transition layer. The ISWs were generated by collapse of a mixed volume at one end of tank (like the method described in Sect. 4.4.2). The height, H_{obst} and length, L_{obst} of the obstacle and the

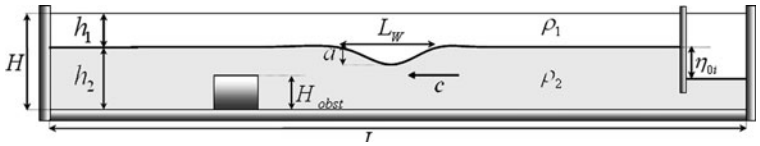

Fig. 4.45 Schematic diagram of experiments (Chen 2007; Nikishov and Gorodetska 2011) for ISW transformation by an obstacle

Table 4.5 Summary of computational runs in modeling ISW interaction with obstacle

Run	H_{obst} cm	L_{obst} cm	h_1 cm	h_2 cm	$\|a\|$ cm	L_w cm	$\|a\|/L_w$	L_w/L_{obst}	μ
2203	22	Plate	2.7	27.8	6.5	39	0.17	28	1.1
3003	19	Plate	2.8	27.7	5.6	33	0.17	23	0.64
0104	19	Plate	2.6	27.9	3.6	30	0.12	21.5	0.4
0104a	19	17	2.6	27.9	3.6	30	0.12	1.8	0.4
0104b	19	52.5	2.6	27.9	3.5	30	0.16	0.6	0.4
1503	22	17	3.2	26.8	2.1	30	0.07	1.8	0.43
1703	19	17	3.1	27.4	4.9	39	0.15	2.3	0.7
1703a	19	Plate	3.1	27.4	4.9	39	0.15	28	0.7
1703b	19	52.5	3.1	27.4	4.9	39	0.15	0.75	0.7
1703c	19	78	3.1	27.4	4.9	39	0.15	0.5	0.7
1703d	19	500	3.1	27.4	4.9	39	0.15	0.5	0.7
0403	22	17	3.6	29.4	6.2	42	0.15	2.5	0.84
0203	16	52.5	3.3	29.7	6.7	42	0.16	0.8	0.49

wave amplitude a were varied in these experiments. More experimental details are given in Sect. 3.2 of Chap. 3.

The simulations were carried out in the quasi-two-dimensional mode with free-slip conditions on the sidewalls and the free surface, whereas no-slip boundary conditions were used at the bottom and end walls. All runs were done using molecular values of the viscosity and salt diffusivity. The parameters of the numerical experiments are given in Table 4.5.

These runs were carried out for different heights, H_{obst} and lengths, L_{obst} of the rectangular obstacles and amplitudes of ISW a at the same background brine stratification, with upper- and bottom-layer salinities $S_{up} = 0$ and $S_{bot} = 15$, respectively, at a constant temperature of 20°C. As in the laboratory experiment, the obstacle was placed 2 m from the end wall of the computational tank with a total length of 7 m. Exceptions were Run 0104a and Runs 1703a–c, where the obstacle was placed 5 m from the end wall of the computational tank with a total length of 10 m. This was done to study wave transformation after the obstacle. The obstacle was varied in computations from a plate of thickness 1.4 cm to a step of 5 m length. The resolution was $1,000 \times 500 \times 5$ for a 7-m tank and $1,000 \times 500 \times 5$ for a 10-m tank.

The experiments can be characterized by several nondimensional parameters: (1) Thickness ratio between layers h_1/h_2; (2) nonlinearity parameter $|a|/L_w$; (3) ratio of the obstacle length to wavelength L_o/L_w; and (4) The blocking parameter $\mu = |a|/(h_2 - H_{obst})$. The last parameter was suggested by Wessels and

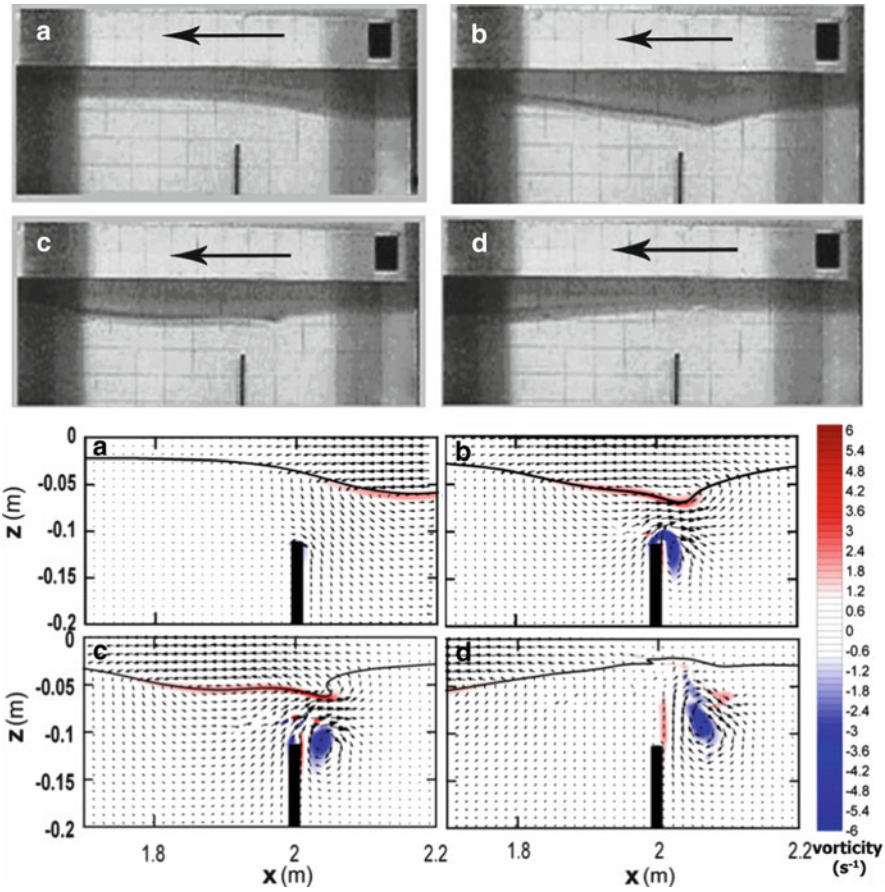

Fig. 4.46 The upper plates show the upper-layer evolution in the process of ISW transformation visualized in laboratory experiment 0104 and the lower plates show computed velocity and vorticity for the same times in Run 0104. The thick *black line* shows the computed interface position. The *arrow* shows direction of wave propagation

Hutter (1996) in a somewhat different form. The parameter $\mu = 1$ for small obstacles and for ISWs of small amplitude, whereas $\mu = 1$ when the interface in the ISW "touches" the obstacle.

Consider the effects of the degree of blocking on the wave transmission and reflection for the obstacle "plate". Figure 4.46 shows the ISW transformation visualized in laboratory experiment 0104 and the computed velocity and vorticity for the same times in Run 0104. This experiment is characterized by a moderate degree of blocking $(\mu = 0.4)$. As seen in the figure, the interaction process may be divided into several stages. In the first stage (b), the front of the incident wave is deformed by flow forming in the lower layer, which detaches from the plate. In the next stage, a strong eddy in the lower layer is formed in front of the plate (c).

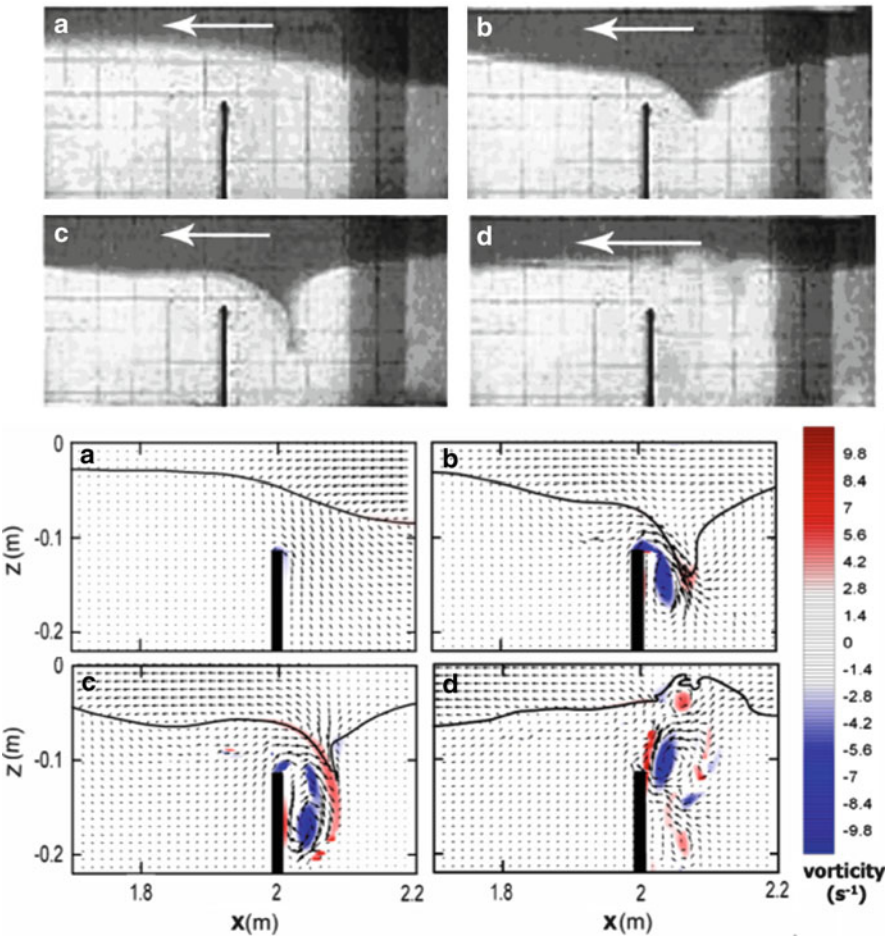

Fig. 4.47 The *upper plates* show the upper-layer evolution in the process of ISW transformation visualized in laboratory experiment 0303 and the lower plates show computed velocity and vorticity for the same times in Run 3003. The thick black line shows the computed interface position. The *arrows* show direction of wave propagation in the experiment

The interface is strongly deformed but entrainment of wave trough into the lower layer and mixing are weak. Then, this vortex and a much weaker vortex of baroclinic nature follow returning in equilibrium interface.

Figure 4.47 shows the transformation of the visualized upper layer in laboratory experiment 3003 and computed velocity and vorticity for the same times in Run 3003. This experiment is characterized by a stronger degree of blocking ($\mu = 0.64$). The interaction process is initially similar to the previous one. At the first stage (b), the front of the incident wave is strongly deformed by flow forming in the lower layer. This flow detached and formed a strong vortex. In the second stage (c), this jet-like flow entrains the wave trough into the bottom layer. Then at the third stage,

this eddy is reflected from the bottom step and together with weaker baroclinic vortex, causes intensive mixing of stratified water in the neighborhood of the step.

The transformation of the ISW in experiment 2203 for a large value of the degree of blocking ($\mu = 1.1$) is qualitatively similar to the previous experiment, but wave reflection is large and mixing in the jet formed in front of the plate is much higher. This case can be named "blocking" case. Whereas in the case of weak interaction ($\mu = 0.4$), the jet angle relative to the horizontal is 15°, for the blocking case ($\mu = 1.0$) this angle is around 80°.

The behavior of ISWs in the frontal part of a long obstacle is similar to the interaction with thin plate. Figure 4.48 shows ISW transformation in experiment 0203 in the case of a moderate value of the blocking parameter ($\mu = 0.49$). The novel feature is detachment of the bottom boundary layer over the front wall that feeds the big frontal vortex.

The flow regimes can be characterized by the composite Froude number:

$$Fr^2 = \frac{U_1^2}{g'(h_1 - \eta)} + \frac{U_2^2}{g'(h_2(x) + \eta)}, \tag{4.90}$$

where $g' = g\Delta\rho/\rho_0$ and $h_2(x)$is the thickness of the lower layer. The maximum values of the Froude number $Fr^2_{\max}$at the front of the obstacles of different height and length are given in Fig. 4.49. The values of $Fr^2_{\max}$ grow with an increase in the degree of blocking parameter. Note that the flow is supercritical at $\mu > 0.6$. It results in entrainment of upper-layer water through the interface into the lower layer and breaking of the interface and mixing, which agrees with experiments. In Run 0104 ($\mu = 0.4$), the value of $Fr_{\max}$ is 0.6, whereas in Run 3003 ($\mu = 0.64$), this value is 1.1. So, we can classify the interaction as weak when $Fr_{\max} < 1$ and strong when $Fr_{\max} > 1$.

Consider now a large-scale process of wave transformation. Several additional runs (0104a–b, 1703a–c) were carried out in the computational tank of length 10 m to simulate the wave evolution. Figure 4.50 shows the evolution of ISWs of the same amplitude over the obstacle of the same height but of different lengths: (a) plate (Run 1703a), (b) $L_{\text{ob}} = 52$ cm (Run 1703b), and (c) $L_{\text{ob}} = 500$ cm (Run 1703c). An incident solitary wave of large amplitude is well described by the MCC model. As noted above, the processes in the frontal zone of the obstacle are similar in the three cases. As seen in the figure, the leading reflected waves have almost the same amplitude. The main effect of the obstacle length is the different transformation of the transmitted wave. Figure 4.51 shows the profiles of the interface in the transmitted wave. The leading wave is also described by the MCC solution. The amplitudes of ISWs in the cases of the plate and the obstacle were almost the same, but for the obstacle with a length of approximately the length of the incident wave, a second solitary wave was formed whereas behind the thin plate, it is of very small amplitude. The transmitted wave over the step is propagated as a solitary wave with a high-frequency tail. These results qualitatively agree with the analytical theory of the solitary wave fission at the semi-infinite step and the simulation results (Grimshaw et al. 2008; Maderich et al. 2009, 2010).

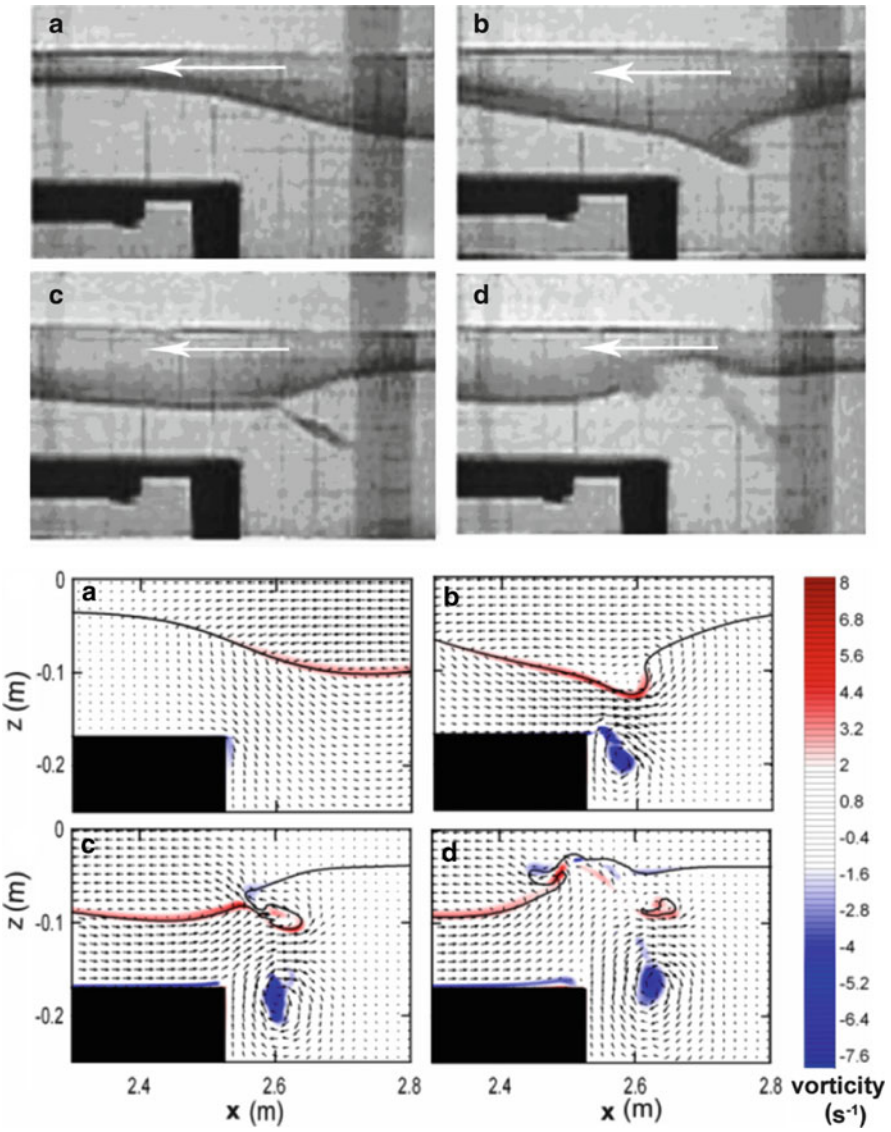

Fig. 4.48 The *upper plates* show the upper-layer evolution in the process of ISW transformation visualized in laboratory experiment 0203 and the lower plates show computed velocity and vorticity for the same times in Run 0203. The thick *black line* shows the computed interface position. The *arrows* in the upper panels show direction of wave propagation in the experiment

The pseudo-energy PSE of waves passing through a given cross section of a computational flume at the time interval $t_2 - t_1$ is calculated using (4.86). The fluxes of the incident wave and that reflected by the obstacle are computed in the cross section x_r, and the flux of the transmitted wave is computed in the cross-

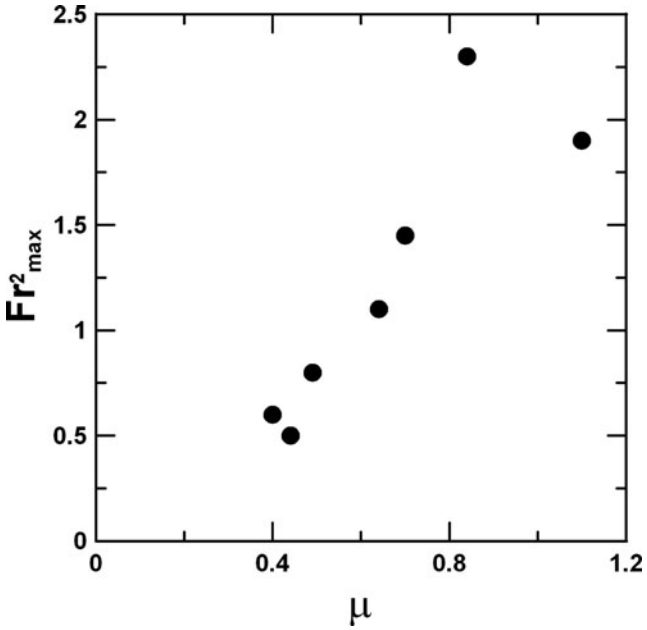

Fig. 4.49 The maximum Froude number $Fr_{\max}$at the front of the obstacle versus degree of blocking parameter μ

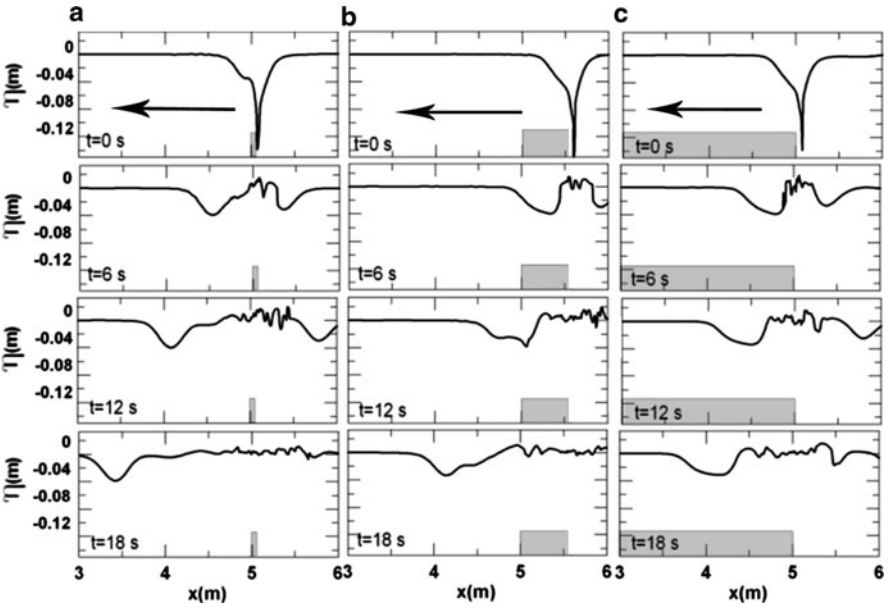

Fig. 4.50 Visualized numerical simulations of the upper layer for different lengths of the obstacle (**a**) plate (Run 1703a), (**b**) $L_{ob} = 52.5$ cm (Run 1703b), and (**c**) $L_{ob} = 500$ cm (Run 1703d). Waves propagate from right to left

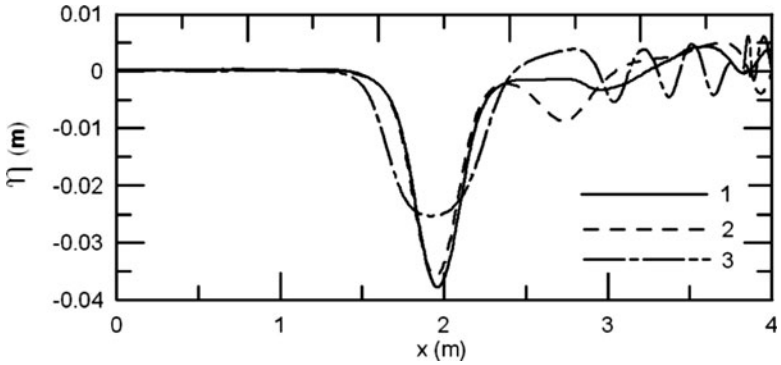

Fig. 4.51 The profile of interface in the leading ISW for 1-plate (Run 1703a), 2-long obstacle (Run 1703b), and 3-step (Run 1703d)

section x_l. The pseudo-energy of incident $(\mathrm{PSE_{in}})$, reflected $(\mathrm{PSE_{ref}})$, and transmitted $(\mathrm{PSE_{tr}})$ waves are calculated from relation (4.86):

$$\begin{aligned}
\mathrm{PSE_{int}} &= -\int_{t=t_1}^{t=t_2}\int_{y=0}^{y=B} F_x(x_r, y, t)\mathrm{d}y'\mathrm{d}t', \\
\mathrm{PSE_{tr}} &= -\int_{t=t_1}^{t=t_2}\int_{y=0}^{y=B} F_x(x_l, y, t)\mathrm{d}y'\mathrm{d}t', \\
\mathrm{PSE_{ref}} &= \int_{t=t_1}^{t=t_2}\int_{y=0}^{y=B} F_x(x_r, y, t)\mathrm{d}y'\mathrm{d}t'.
\end{aligned} \tag{4.91}$$

The relative difference of the transmitted and reflected energy δE and the relative energy loss due to dissipation and mixing δE_{loss} are estimated from the relations

$$\delta E = \frac{\mathrm{PSE_{in}} - \mathrm{PSE_{tr}}}{\mathrm{PSE_{in}}}, \tag{4.92}$$

$$\delta E_{\mathrm{loss}} = \frac{\mathrm{PSE_{in}} - \mathrm{PSE_{tr}} - \mathrm{PSE_{ref}}}{\mathrm{PSE_{in}}}. \tag{4.93}$$

Figure 4.52 shows the relative difference of transmitted and reflected energy δE plotted using computed data and laboratory experiments by Chen (2007) and Wessels and Hutter (1996). As seen in the figure, the difference of the transmitted and reflected energy falls with increase of the blocking parameter and for μ>0.8, reflection dominates. The energy loss δE_{loss} in Fig. 4.53 grows with an increase of the interaction parameter to some critical value at $\mu \approx 0.7 - 0.8$and then decreases. The maximum energy loss is around 50%. It agrees with the estimated energy loss at the step (Maderich et al. 2010) where $\delta E_{\mathrm{loss}} = 0.48$ at $\mu = 0.73$. Another effect

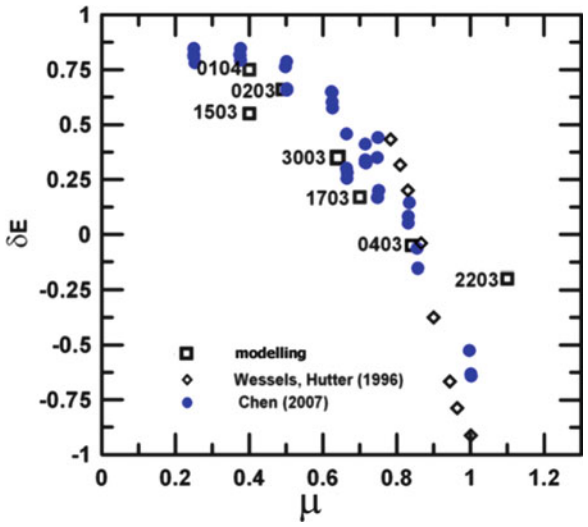

Fig. 4.52 The relative difference of transmitted and reflected energy δE

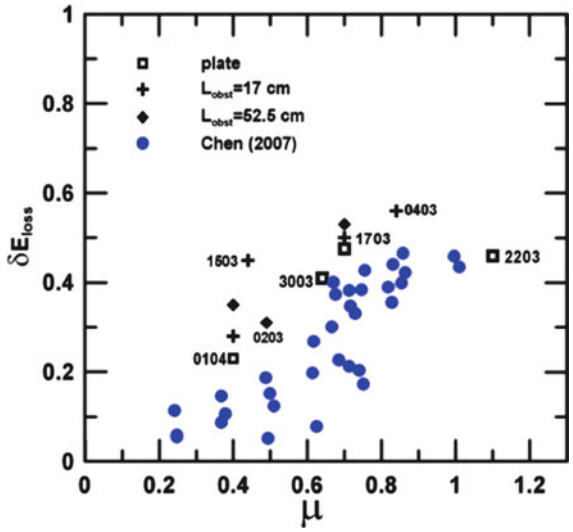

Fig. 4.53 The relative loss of energy δE_{loss} over obstacle

was revealed by Maderich et al. (2010) for ISW transforming at the step at a moderate value of $\mu = 0.44$. In that case, transformation of the transmitted wave after the step is accompanied by shear instability and the formation of Kelvin–Helmholtz billows like the adjustment of large-amplitude interfacial solitary waves to a stable state and transformation over the very mild slope studied in Sect. 4.3.

Note that energy transformation in experiments (Wessels and Hutter 1996; Chen 2007) was calculated using the simplified linear formula (4.87). The good

agreement between experiments and calculations with obstacles of different forms in Fig. 4.52 demonstrates that wave reflection depends mainly on the blocking rather than on the form of the obstacle. Similar to the wave dissipation on a slope, the energy loss calculated by (4.87) is less than when calculated with (4.86).

4.4.5 *Degeneration of Basin-Scale Internal Waves in Basin with Bottom Sill*

The glacially formed alpine lakes and fjords can consist of several basins separated from one another by sills and narrows. An example is Lake Constance where a sill (minimum depth around 100 m) in the Mainau Island area separates two deep basins: Obersee (maximum depth 252 m) and Überlinger See (maximum depth 184 m). The Mainau sill area (1% of the lake area) contributes 40% of the basin-scale diffusivity and dissipation rate of turbulent energy (Kocsis et al. 1998). The sill changes the structure of the internal modes and the largest scale mode shows strong currents above the sill (Münnich 1996). The enhanced mixing over the sill can be attributed to wind and density currents, basin-scale internal seiche pumping (Van Senden and Imboden 1989), and transformation and disintegration of nonlinear internal waves (Vlasenko and Hutter 2002b).

In this section, we focus on the dynamics of degeneration of large-scale waves in the basin with a sill, whereas effects of narrows and combinations of narrows and sills will be considered in the next section. Similar to the previous sections, the laboratory scale computational tank with two-layer salt stratification was used. The tank has length $L = 6$ m and height $H_\mathrm{m} = 0.29$ m (Horn et al. 2001), with a sill placed in the center.

The sill is assumed of the Gaussian form

$$H = H_\mathrm{m} - H_\mathrm{sill} \cdot e^{-\frac{(x-x_\mathrm{s})^2}{L_\mathrm{sill}}}, \tag{4.94}$$

where $H_\mathrm{m} = 0.29\,\mathrm{m}$, $H_\mathrm{sill} = 0.14\,\mathrm{m}$, $x_\mathrm{s} = 3\,\mathrm{m}$, and $L_\mathrm{sill} = 0.5\,\mathrm{m}$. The initial salinity distribution corresponds to Run 8 of Sect. 4.4.1, where nondimensional parameters are $h_2/H_\mathrm{m} = 0.7$ and $\eta_{i0}/h_2 = 0.39$. The simulations were carried out in the quasi-two-dimensional mode using molecular values of viscosity and salt diffusivity. Resolution was $1,300 \times 500 \times 5$ nodes.

Run 8 considered in Sect. 4.4.1 is in the regime of solitary wave generation (Regime II). However, the presence of the sill essentially affects the wave formation process and dissipation of the wave chain. The evolution of the salinity in this case is shown in Fig. 4.54. The initial tilt of the interface (Fig. 4.54a) produces, as in Run 8, two-way flow that results in a surge formation on the right side of the basin (Fig. 4.54b). The surge transforms into a chain of solitary waves (Fig. 4.54c).

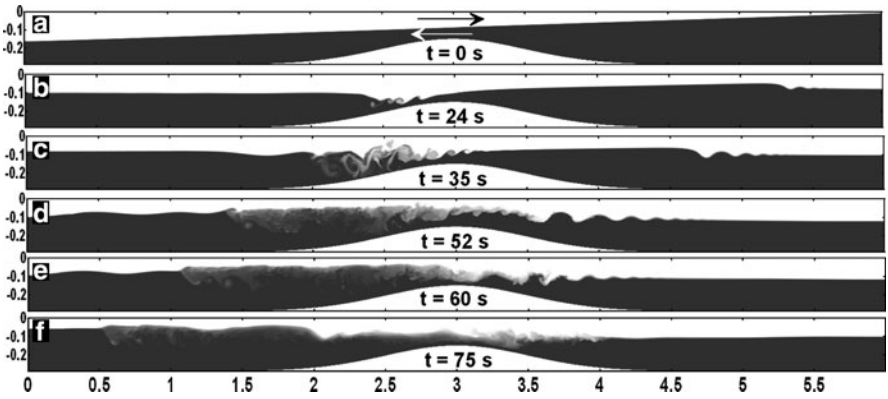

Fig. 4.54 The simulated salinity field in the case of tank with the sill Wave propagation is from *right* to *left*

Meanwhile, the two-way flow over the sill initially accelerates and becomes supercritical, as seen in Fig. 4.54. The theory of two-layer hydraulics predicts for steady flow in channel that the maximal exchange flow through a sill exists when flow is critical (composite Froude number $Fr^2 = 1$) at two control points: one is on the top of the sill and the other is at the exit of the channel (Armi and Farmer, 1986). The flow is subcritical $(Fr^2<1)$ between these two control points. However, in the case of unsteady exchange flows these conditions are not satisfied: a zone of supercritical flow arises at the lee side of the heavy fluid flow.

In more detail, flows over the sill are shown in Fig. 4.55. As seen in the sequence of snapshots of salinity and vorticity in this figure, this flow is unstable. The shear instability results in the appearance of KH billows ($t = 27$ s) and subsequent mixing ($t = 35$ s). Eventually, when exchange flow is weakened the KH billows shift to the right.

The next important event is formation of a chain of ISW depressions, which interact with the sill (Fig. 4.56). When waves approach the sill they are steepened, change polarity, and break. However, the breaking mechanism essentially differs from convective breaking (Fig. 4.38) and shear-induced breaking (Fig. 4.39) because waves interact with the sill on the background of the two-way exchange flow. The shear flow prevents front breaking of the wave elevation approaching the crest of the sill whereas in the lee wave crest, shear instability is enhanced resulting in "backward" instability. The backward instability was examined by Hult et al. (2009) in a laboratory study of breaking of periodic progressive two-layer interfacial waves at a Gaussian ridge. In these experiments, backward instability is only one of three types of instability: backward breaking, forward plunging breaking, and forward Kelvin–Helmholtz breaking. In our numerical simulation, only the first type was observed.

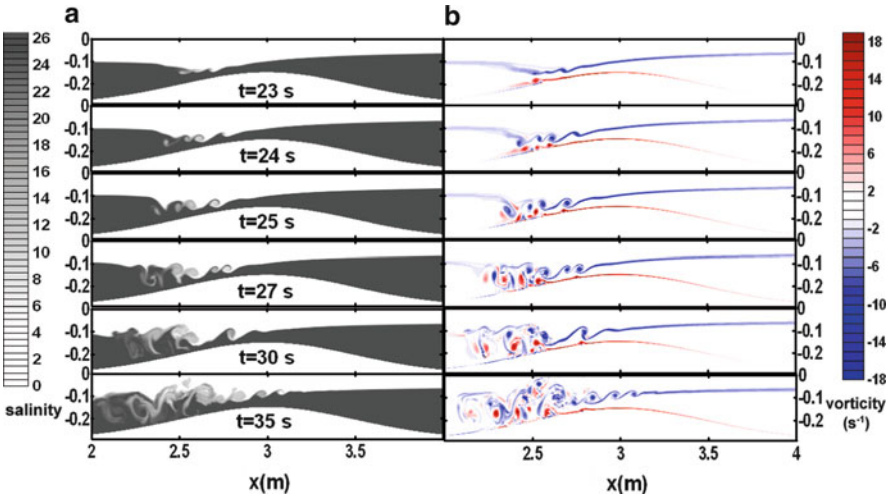

Fig. 4.55 Supercritical flow regime over the sill. *Left panels* show salinity field and right panels show vorticity

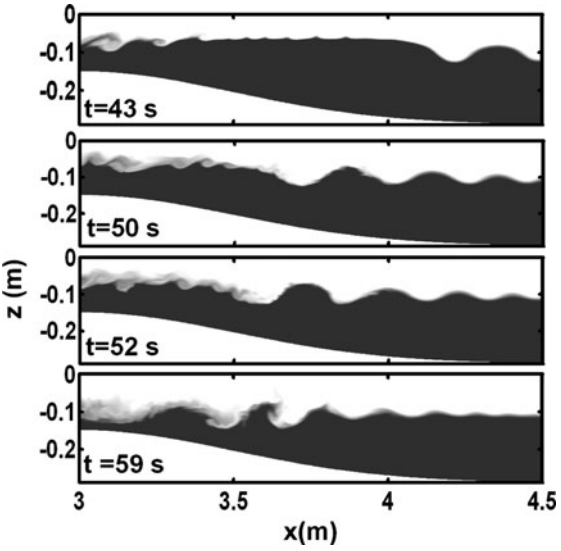

Fig. 4.56 Wave-breaking regime in the salinity field

The presence of a sill essentially changes the processes of the energy exchange between potential and kinetic energy (Fig. 4.57). This is so because the sill is blocking free seiching in the basin, which results in strong dissipation of supercritical flows over the sill and because the train of solitary waves breaks at the sill. Together, these effects result in the enhancement of mixing and growth of background energy (Fig. 4.58), whereas the available potential energy decays faster than in the case of seiching in the basin with slope (Fig. 4.43).

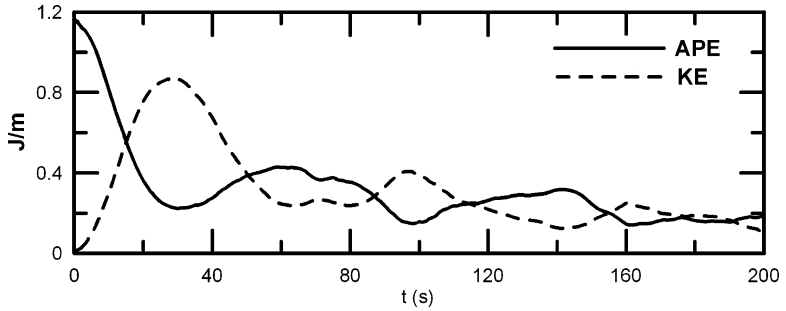

Fig. 4.57 Evolution of kinetic KE and available potential energy APE in the basin with the sill

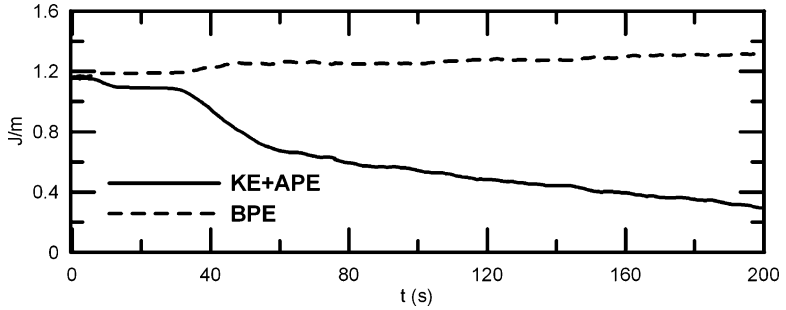

Fig. 4.58 Evolution of the total pseudo-energy PSE and background energy BPE in the basin with the sill

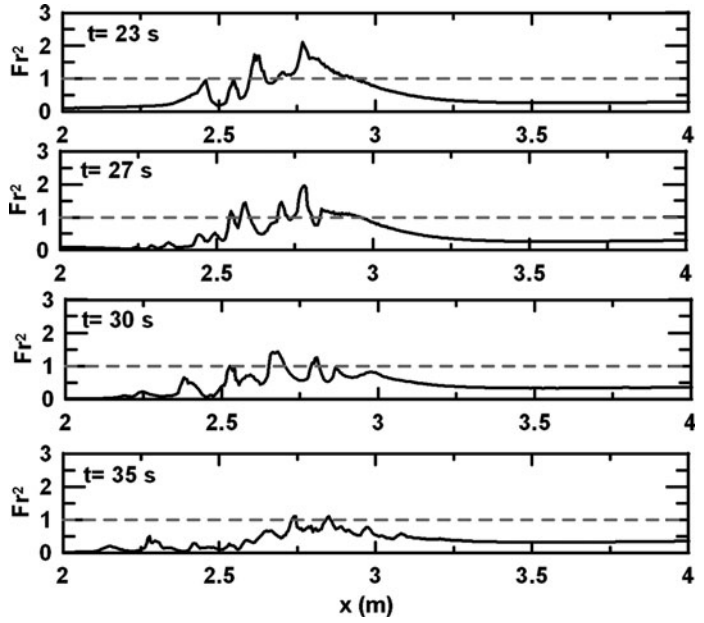

Fig. 4.59 The composite Froude number variations along the basin with the sill

4.4.6 *Degeneration of Basin-Scale Internal Waves in Basins with a Narrow*

The aim of this section is to study the dynamics of the degeneration of large-scale waves in the basin with a narrow and combination of a narrow and a sill. Only a few laboratory experiments were carried out to study the internal wave behavior in the lateral constriction. Troy and Koseff (2005) studied stability of progressive, periodic, lowest-mode internal waves traveling through a constriction. The wave amplitude in the constriction increases and the Kelvin–Helmholtz shear instability develops in the high-shear wave crest and trough regions. The laboratory experiment on propagation of ISWs through a narrow (Nikishov and Gorodetska 2011) showed also instability of the wave in the constriction. However, neither laboratory nor theoretical studies are known to date on the effect of narrows on seiching in the lake.

The laboratory scale computational tank with two-layer salt stratification was used in simulations. The tank has length $L = 6$ m and height $H_{\mathrm{m}} = 0.29$ m (as in the experiment by Horn et al. (2001)) and width $B = 0.5$ m with a narrows placed in the center of the tank (Fig. 4.60). The narrow is of symmetric form. It is also of Gaussian form,

$$B = B_{\mathrm{m}} - 2B_{\mathrm{narrow}} \cdot e^{-\frac{(x-x_{\mathrm{s}})^2}{L_{\mathrm{narrow}}}}, \tag{4.95}$$

where $B_m = 0.5\,\mathrm{m}$, $2B_{\mathrm{narrow}} = 0.28\,\mathrm{m}$, $x_{\mathrm{s}} = 3\,\mathrm{m}$, and $L_{\mathrm{narrow}} = 0.5\,\mathrm{m}$. The initial salinity distribution corresponds to Run 8 from Sect. 4.4.1, where nondimensional parameters are $h_2/H_{\mathrm{m}} = 0.7$ and $\eta_{i0}/h_2 = 0.39$. The simulations were carried out in the three-dimensional mode using molecular values of viscosity and salt diffusivity. The resolution of the grid was $600 \times 200 \times 23$ nodes.

At first, consider the effect of a narrow in the basin of constant depth. As pointed out in the previous section, the run considered in Sect. 4.4.1 (Run 8) is the regime of solitary wave generation (Regime II). The evolution of the simulated salinity field in the central part of the tank with narrow is shown in Fig. 4.61. Initial tilt of the interface (Fig. 4.61a) produces two-way flow that accelerates and become supercritical in the narrow, as seen in Fig. 4.62. Shear instability results, first, in the

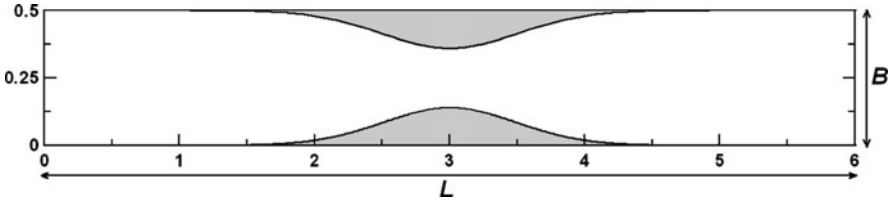

Fig. 4.60 Top view of the computational basin with narrow

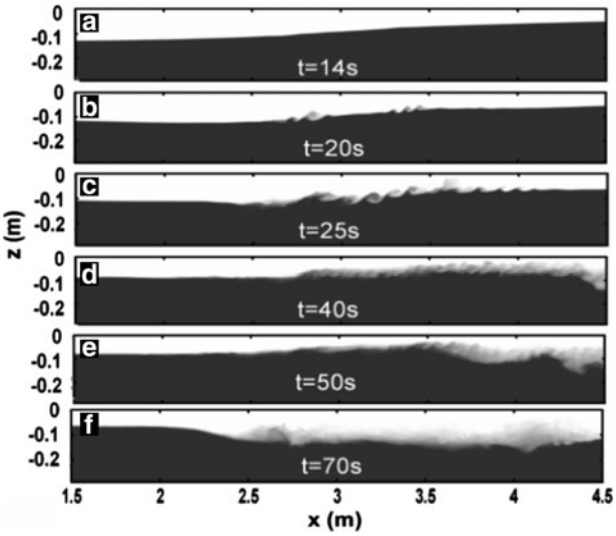

Fig. 4.61 The simulated salinity field in the central part of the tank with narrow

appearance of the KH billows in the constriction and upstream of the dense water current ($t = 20$ s). Next, KH billows spread on both sides of the constriction.

According to the theory of two-layer hydraulics, a steady exchange flow through a contraction in the channel is maximal when the flow is critical in the narrowest section of the contraction (Farmer and Armi 1986). However, as seen in Fig. 4.62, the zone of supercritical flow arises at the upwind side of the heavy fluid flow. The shear instability in the narrow results in the development of KH billows (Fig. 4.61). Meanwhile, tilt results in surge formation at the right side of basin (Fig. 4.61). The surge transforms into an undulating bore that propagates to the left side. However, strong dissipation and mixing in the narrows damp both large-scale seiche oscillations and formation of chain of solitary waves.

Consider the effect of a combination of narrow and sill. The form of the narrow is described by (4.95) and the form of the sill is given by (4.94). The resolution was also $600 \times 23 \times 200$ nodes. The evolution of the simulated salinity field in the central part of the tank with narrow and sill is shown in Fig. 4.63. The initial tilt of the interface produces two-way flow that accelerates and become supercritical in the narrow/sill, as seen in Fig. 4.64. The instability arises at the crest of the sill that coincides with the maximum constriction of the narrow. A strong mixing exists in the lee side of the combination of sill and constriction at $t = 20 - 70$s.

Armi and Riemenschneider (2008) in the frame of the theory of two-layer hydraulics found that steady exchange flow through a co-located sill and contraction in a channel is maximal when flow is critical at the crest/narrows and when the other control point is the virtual control on the dense side of the topographic control. As seen in Fig. 4.64, the critical point is placed initially ($t = 20$ s) at the lee side of the co-located sill and contraction, and supercritical flow is downstream of it. With

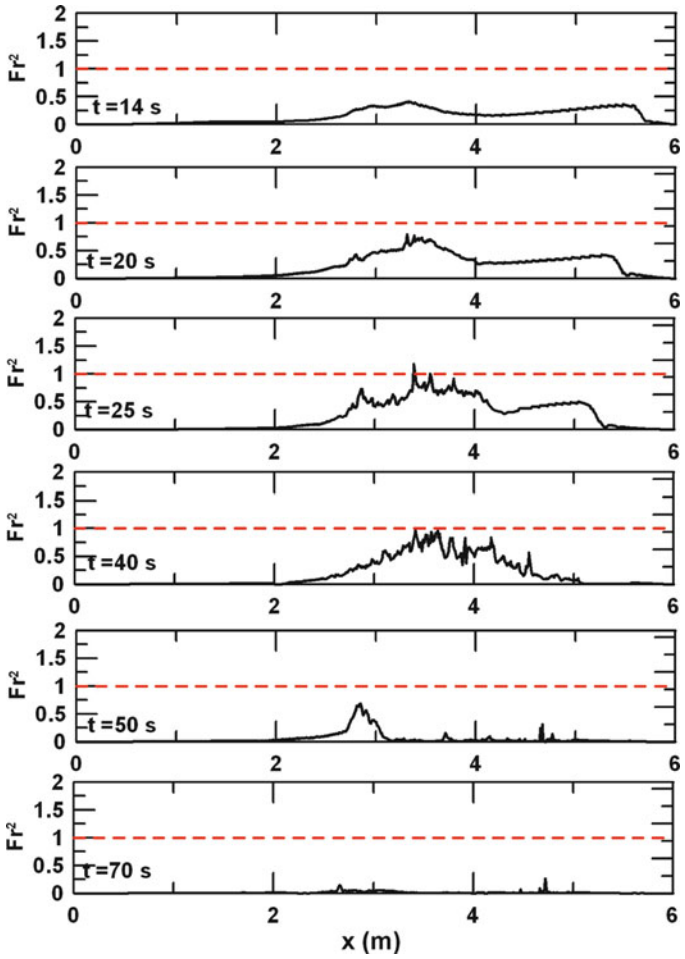

Fig. 4.62 The composite Froude number variations along the basin with narrow

time, the supercritical zone shifts upstream ($t = 40$ s) and exchange flow decreases at $t = 70$ s. The evolution of the composite Froude number in the case of a contraction/sill is similar to the sill case in Fig. 4.59. The differences with the hydraulic theory for the pure sill, pure contraction, and contraction/sill can be attributed to the unsteady character of the exchange flow when capacities of reservoirs of light and dense waters are limited and time varied, resulting in the submaximal exchange.

The chain of ISW is formed at the right side of the basin and when they approach the sill/constriction, they steepen and break. The strong mixing and dissipation result in the "absorption" of waves by the obstacle contrary to the case of pure contraction when strongly deformed waves transmit through the narrows.

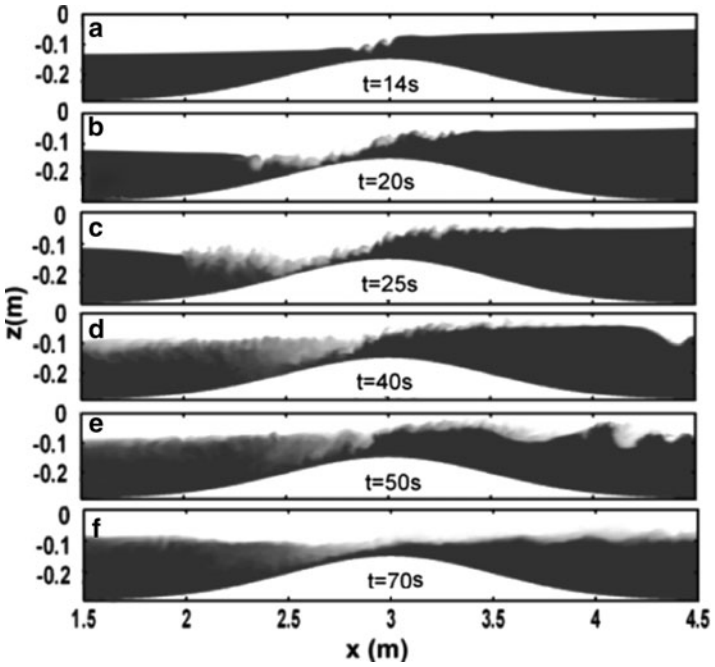

Fig. 4.63 The simulated salinity field in the central part of the tank with narrow and sill

4.4.7 Degeneration of Basin-Scale Internal Waves in a Small Elongated Lake

In the previous sections, we have considered a set of idealized problems in basins of laboratory scale: the transformation and degeneration of basin-scale internal waves in a rectangular basin, in a basin with sloping boundary, and in a basin with a sill and narrowing cross-section. Here, the transformation of large-scale waves in a small elongated lake with more realistic topography is studied where the above-mentioned effects are combined. The lake is of length 5 km, width 1 km, and maximal depth 30 m (Fig. 4.65). The bathymetry includes a relatively deep, proper, and shallow shelf. Examples of small- and medium-sized lakes are given by Filatov (2012, this vol.). The depth distribution is described by the formula

$$H(x,y) = 0.25H_{\max}\left(\sin\left(a_1\pi(x-x_s) - \frac{\pi}{2}\right) + \sin\left(b_1\pi(y-y_s) - \frac{\pi}{2}\right)\right)^2$$
$$\text{for } \frac{(x-x_s)^2}{{x_s}^2} + \frac{(x-y_s)^2}{{y_s}^2} < 1, \tag{4.96}$$

where $H_{\max} = 30\,\text{m}$, $x_s = 2,500\,\text{m}$, $y_s = 500\,\text{m}$, $a_1 = 0.0003\,\text{m}^{-1}$, and $b_1 = 0.001\,\text{m}^{-1}$. The undisturbed temperature profile is described as

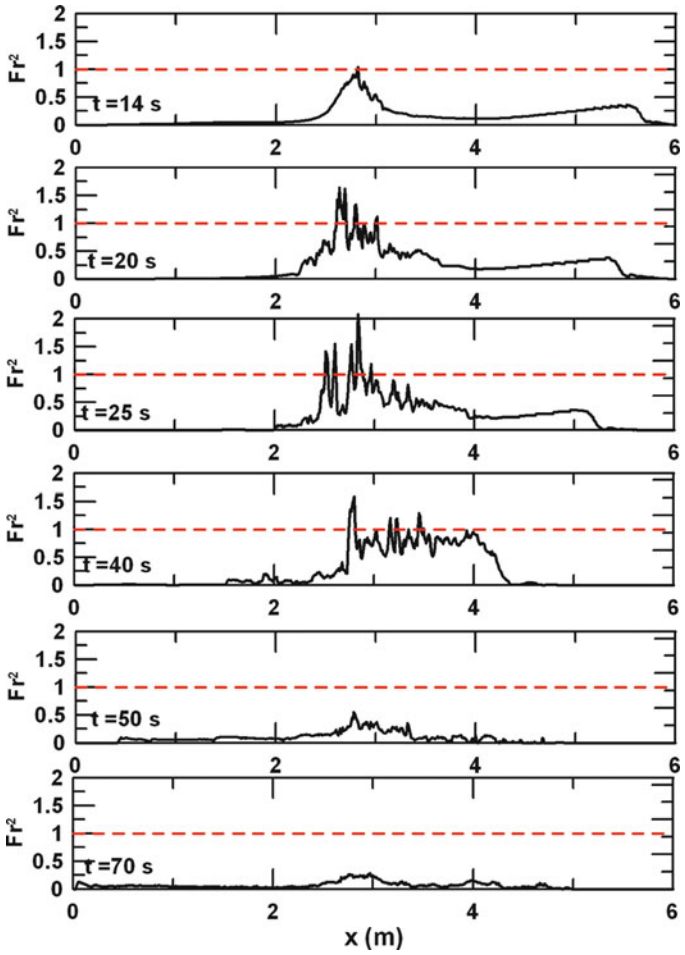

Fig. 4.64 The composite Froude number variations along the basin with narrow and sill

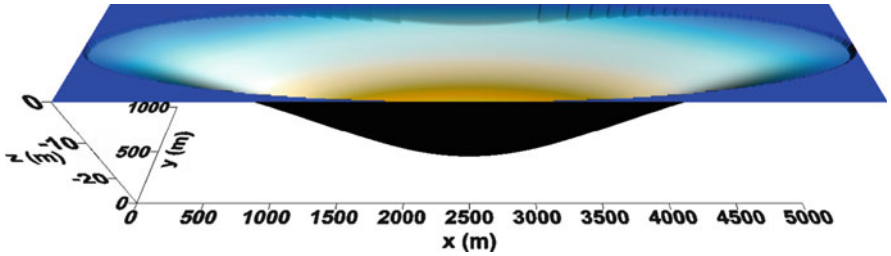

Fig. 4.65 The lake bathymetry

$$T(z) = \frac{T_{\text{up}} + T_{\text{bot}}}{2} + \frac{T_{\text{up}} - T_{\text{bot}}}{2} \tan h\left(\frac{z - h_1}{\mathrm{d}h}\right), \tag{4.97}$$

where $T_{up} = 25°\text{C}$, $T_{\text{bot}} = 15°\text{C}$, $h_1 = 4.5\text{m}$, and $\mathrm{d}h = 2.5\,\text{m}$. This profile is shown in Fig. 4.66 and corresponds to the lake temperature in the moderate latitudes. Initially, the thermocline in the lake was inclined along the lake with tilt $\eta_{oi}/h_1 = 1.7$, where η_{i0} is the maximal deviation from the undisturbed value of the depth of the isosurface of the maximal vertical gradient of the temperature. The corresponding cross-section of the temperature along the lake is shown in Fig. 4.67. Three runs were carried out to separate the effects of 3D geometry of the lake and the nonhydrostatic effects: 3D nonhydrostatic run (Run 3DNH), 3D hydrostatic run (Run 3DH), and 2D nonhydrostatic run (Run 2DNH). In all runs, the eddy viscosity and the diffusivity were calculated using the eddy viscosity model of SGS (4.4)–(4.5) with the nonisotropic length scale l_Δ (4.7b). Resolution in 3D and 2D modes is $500 \times 100 \times 60$ and $500 \times 100 \times 5$ nodes, respectively. The σ-system was used to describe the bottom topography smoothly.

Figure 4.68 shows the sequence of the vertical cross-sections of temperature along the lake for three runs (3DNH, 3DH, and 2DNH,). The parameters of these runs ($\eta_{oi}/h_1 = 1.7$and $h_1/H_{\max} = 0.15$) are close to the supercritical regime III, which was discussed in Sect. 4.3.4. In this regime, the internal bore is formed when flows in the layers achieve a supercritical state. The bottom topography, three-dimensional shape of the lake, and continuous stratification essentially affect this

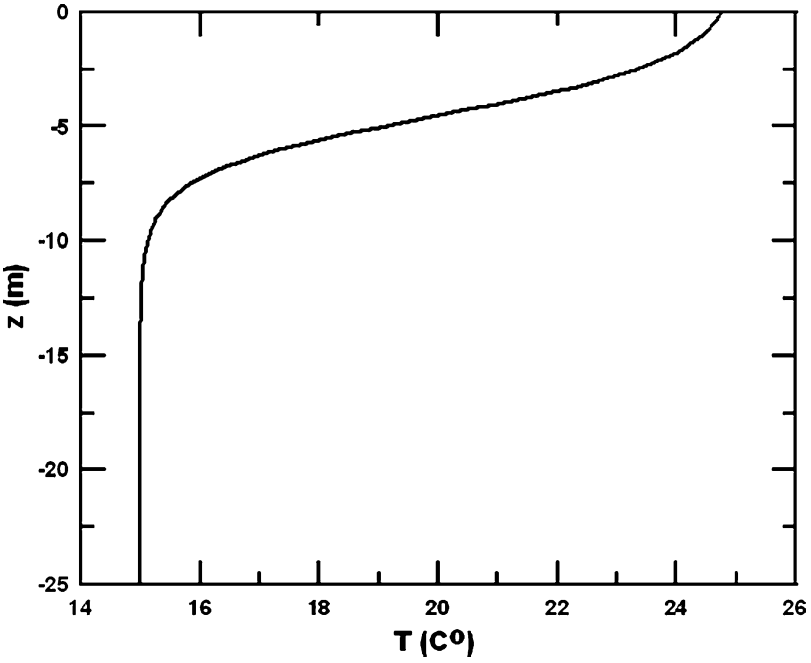

Fig. 4.66 The undisturbed temperature profile

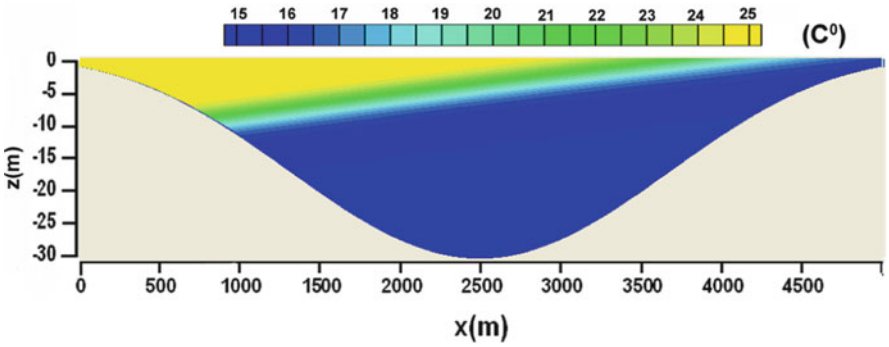

Fig. 4.67 The initial vertical cross section of temperature along the lake

regime. Like the simulations in the rectangular laboratory basin (Figs. 4.12b), nonlinearity results in bore formation at time $t = 3.5$ h. In the 2D case, this bore evolves into the solibore with a sequence of solitary waves ($t = 4.5$ h). Bore formation and evolution is accompanied by strong mixing and thickening of the lake thermocline. The three-dimensional shape of the lake results in the new effects. The interaction of basin-scale motions with the "spoon-like" end of lake in the 3D case results in formation of a large-amplitude bore earlier than in the 2D case (see Fig. 4.68b). Mixing is more intensive than in 2D case.

In the process of bore evolution, solitary waves appeared in the nonhydrostatic case (see Fig. 4.68b, c). Note that a "soliton-like" structure appeared also in the hydrostatic run with characteristics similar to the nonhydrostatic case. However, they are not true solitary waves because these waves arose due to nonlinear steepening balanced by numerical dispersion and therefore, wave characteristics depend on the numerical scheme and the grid resolution (Daily and Imberger 2003; Wadzuk and Hodges 2004). Bore formation and evolution in the 3D case also are accompanied by the generation of second mode waves in the rear part of moving solibores. This effect also occurs in the hydrostatic case, but waves are not presented here.

The spatial structure of the basin-scale wave transformation is also of interest. The time evolution of the isotherm 20°C and the elevation are shown in Fig. 4.69, whereas the near-bottom velocity field at $t = 3.5$ h is given in Fig. 4.70. As seen in Fig. 4.70, the "spoon-like" bottom topography at the ends of the lake results in the focusing of flow and formation of jet along the lake axis (see Fig. 4.69 at $t = 4.5$ h. This jet has maximum velocity around 0.8 m s^{-1}, whereas the bore propagates with velocity around 0.3 m s^{-1}. This flow can result also in the erosion of the bottom in the zone of high bottom velocity. This supercritical jet is visible for subsequent times as supercritical flow causing the internal wave wake. This wake is also visible at the surface of lake as distortions of the elevations. Then, the waves radiated by the jet propagate in front of the solibore to the opposite end of the lake, where the solibore shoals.

We hypothesize that in some cases, this wave wake behind the source of disturbance is visible in the elongated lakes, and this physical phenomenon could be interpreted as a wake of a moving large animal. The legend of the Loch Ness

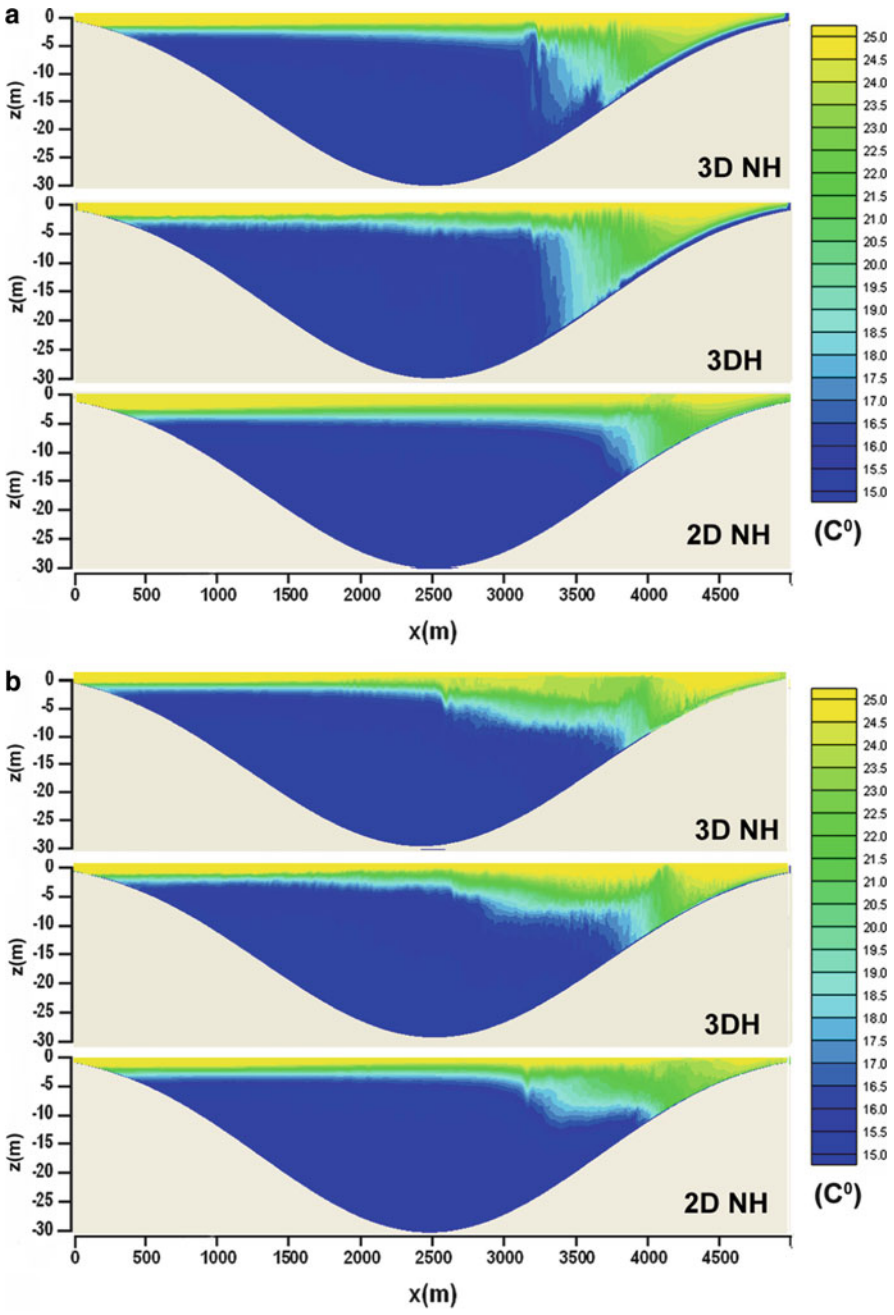

Fig. 4.68 (continued)

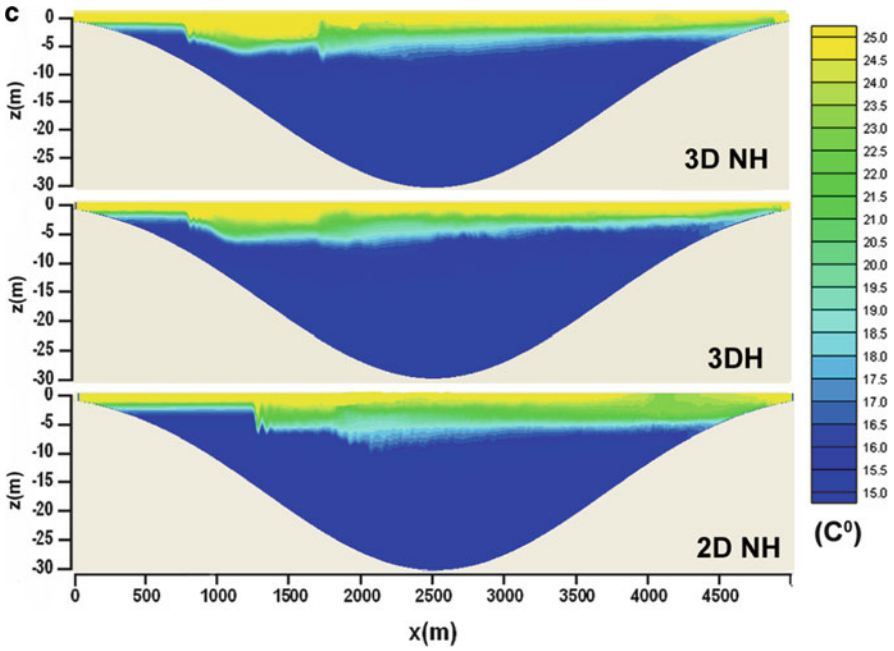

Fig. 4.68 The temperature cross-section along the lake at $t = 3.5$ h (**a**), $t = 4.5$ h (**b**), and $t = 7$ h (**c**)

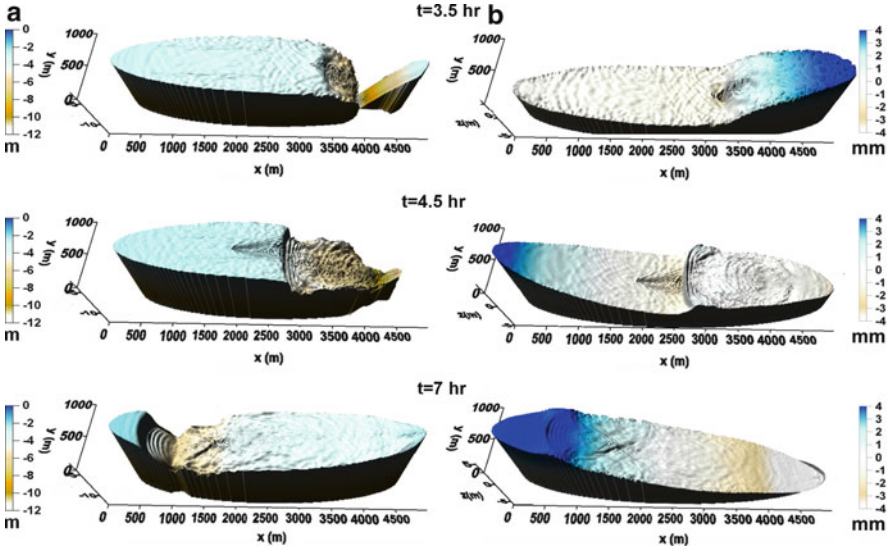

Fig. 4.69 The isosurface of temperature $T = 20°\text{C}$ (**a**) and elevation (**b**) in the lake

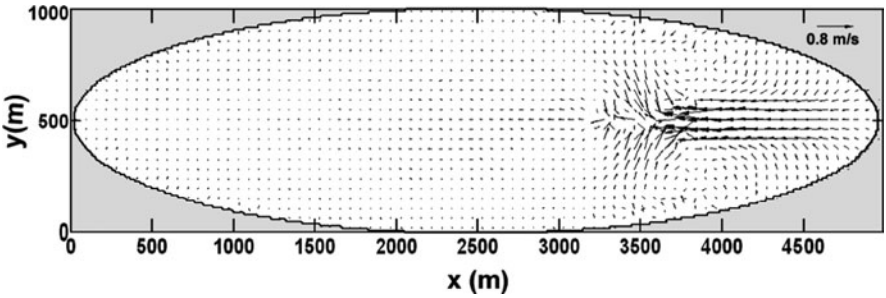

Fig. 4.70 The near-bottom velocity field at $T = 3.5$ h

monster can be based on such observations by local population. The Loch Ness is a long and deep lake (see Sect. 2.1.2 of this book) with length around 35 km, width 1.2 km, and maximal depth 250 m with strong summer stratification. The internal surges in the Loch Ness are well-known phenomenon (Thorpe et al. 1972; Thorpe 1974, 1977). They are generated by wind, and they have the character of an internal undular bore with a steep leading front followed by a train of internal undulations (compare Fig. 4.69 with Fig. 2.4). The size and geometry of Loch Ness differs from those considered in this section; therefore, it is necessary to extend modeling for conditions of this lake to verify if simulated phenomenon of the cumulative jet can be reproduced for the Loch Ness and for other elongated deep lakes.

4.5 Conclusions

The processes of the transformation of basin-scale internal waves in lakes were simulated by a numerical three-dimensional nonhydrostatic model. A detailed description of the model and numerical algorithm was given. The model is a modified nonhydrostatic extension of the free-surface primitive POM model (Kanarska and Maderich 2003). It was applied to a sequence of idealized problems of the transformation and degeneration of basin-scale internal waves in a basin of laboratory scale. The simulation results were compared with laboratory experiments (Horn et al. 2001) carried out in a rectangular basin. Numerical modeling confirmed classification of regimes proposed by Horn et al. (2001) and extended laboratory studies on the whole diapason of possible regimes.

The breaking mechanisms of internal solitary wave depressions were studied numerically. The analysis of laboratory experiments and numerical experiments showed that breaking of large-amplitude waves over a gently sloping bottom could follow different scenarios. Three scenarios were described by Vlasenko et al. (2005). According to the first scenario at a moderate slope, an overturning mechanism of wave dominates with formation of boluses. The second scenario is an adiabatic transformation when the ISW amplitude is close to the local limiting value of solitary waves. The third scenario is a nonadiabatic dispersive evolution.

Our experiments suggest a new scenario of breaking of large-amplitude internal waves at mild slopes, when shear instability is the dominating mechanism of the wave transformation and waves dissipate without overturning and with the formation only weak wave elevation. The simulation of basin-scale wave evolution in a basin with a sloping bottom and the laboratory experiments of Boegman et al. (2005a) showed that this mechanism was realized also in the shoaling of a chain of solitary waves. Intercomparison of 2D and 3D simulations and laboratory experiments showed that laboratory experiment data could be used for estimations of energy transformation caused by wave breaking on the bottom slope without corrections due to side-wall effects.

Modeling of internal wave depressions of large-amplitude transformation on the obstacles demonstrated the primary importance of the ratio of the wave amplitude to the thickness of the lower layer over the obstacle (blocking parameter μ). When $\mu \ll 1$the interaction is weak, whereas at $\mu \sim 1$ interaction is strong and it results in entrainment of a wave trough in the lower layer and in the mixing. The difference of the transmitted and reflected energy falls with an increase of the blocking parameter and for μ>0.8, reflection dominates. The energy loss δE_{loss} grows with the increase of the interaction parameter to some critical value at $\mu \approx 0.7 - 0.8$and then decreases. The maximum energy loss is around 50%. The main effect of the obstacle length is a different transformation of the transmitted wave. The amplitudes of ISWs in the case of a plate and an elongated obstacle were almost the same but, in the case of an obstacle with a length of approximately the length of the incident wave, a second solitary wave was formed, whereas after the thin plate it is of very small amplitude. The transmitted wave over the step is propagated as a solitary wave with a high-frequency tail.

The modeling of the dynamics of the degeneration of large-scale waves in a basin with a sill showed that the presence of the sill essentially affects the wave transformation process and dissipation of the wave chain. At the sill, two-way flow initially accelerates and become supercritical. Then, the chain of the ISW depression interacts with the sill. The breaking mechanism ("backward instability") differs considerably from convective breaking and shear-induced breaking because waves interact with the sill in the background of the two-way exchange flow. The processes of the wave transformation in the basin with narrows and a combination sill/constriction are qualitatively similar. The two-way exchange flow in all considered cases was submaximal.

The presence of sill, narrows, and combinations of sill/constriction essentially change the processes of the energy transformation because sills and narrows block free seiching in the basin and result in strong dissipation of supercritical flows over the sill and narrow and because the train of solitary waves breaks at the sill and narrow. Together, these effects result in the enhancement of mixing, whereas kinetic and available potential energies decay faster than in the case of seiching in the basin without sills and narrows.

Most simulations in this chapter were carried out for 2D geometry that allowed studying the thin structure of the waves and instability processes in detail. However, the geometry of real lakes can essentially impact the regimes of the nonlinear

degeneration of large-scale internal waves. The 3D simulations of the seiching of the small, elongated lake showed a new effect of focusing flow by "spoon-like" topography at the end of the lake and generation of a supercritical jet in front of the surge propagating as a solibore. These 3D geometrical peculiarities need further, more detailed, study for real lakes, using nonhydrostatic models. For medium-sized lakes, the rotation effects also must be included.

References

Armi L, Farmer DM (1986) Maximal two-layer exchange through a contraction with barotropic net flow. J Fluid Mech 164: 27–51

Armi L, Riemenschneider U (2008) Two-layer hydraulics for a co-located crest and narrows. J Fluid Mech 615: 169–184

Bergh J, Berntsen J (2009a) Numerical studies of wind forced internal waves with a nonhydrostatic model. Ocean Dynamics 59:1025–1041

Bergh J, Berntsen J (2009b) The surface boundary condition in nonhydrostatic ocean models. Ocean Dynamics DOI 10.1007/s10236-009-0242-1

Berntsen J (2000) Users guide for a mode-split σ- coordinate numerical ocean model. Tech. Rep. 135, Dept. of Applied Mathematics, University of Bergen, Bergen, Norway

Berntsen J, Furnes G (2005) Internal pressure error in sigma-coordinate ocean models-sensitivity of the growth of the flow to the time stepping method and possible nonhydrostatic effects. Cont Shelf Res 25: 829–848

Berntsen J, Xing J, Alendal G (2006) Assessment of non-hydrostatic ocean models using laboratory scale problems. Cont Shelf Res 26: 1433–1447

Blumberg AF, Mellor GL (1987) A description of a three-dimensional coastal ocean circulation model, In: Heaps N. (ed) Three-Dimensional Coastal Ocean Models, Am Geoph Union, New York

Boegman L, Ivey GN, Imberger J (2005a) The degeneration of internal waves in lakes with sloping topography. Limnol Oceanogr 50: 1620–1637

Boegman L, Ivey GN, Imberger J (2005b) The energetics of large-scale internal wave degeneration in lakes. J Fluid Mech 531: 159–180

Bogucki D, Garrett C (1993) A simple model for the shear-induced decay of an internal solitary wave. J Phys Oceanogr 8: 1767–1776

Bourgault D, Kelley DE (2007) On the reflectance of uniform slopes for normally incident interfacial solitary waves. J Phys Oceanogr 37: 1156–162

Bourgault D, Blokhina MD, Mirshak R, Kelley DE (2007) Evolution of a shoaling internal solitary wavetrain. Geoph Res Letters 34, L03601, doi:10.1029/2006GL028462

Brovchenko I, Gorodetska N, Maderich V, Nikishov V, Terletska K (2007) Interaction of internal solitary waves of large amplitude with obstacle. Applied Hydromechanics 9(81): 3-7

Camassa R, Choi W, Michallet H, Rusas P, Sveen JK (2006) On the realm of validity of strongly nonlinear asymptotic approximations for internal waves. J Fluid Mech 549:1–23

Casulli V (1999) A semi-implicit finite difference method for non-hydrostatic, free-surface flows. Int J Numer Methods Fluids 30: 425–440

Casulli V, Stelling G (1998) Numerical simulation of 3D quasi-hydrostatic free-surface flows. J Hydraul Eng 124: 678–686

Casulli V, Zanolli P (2002) Semi-implicit numerical modeling of non-hydrostatic free-surface flows for environmental problems. Math Comput Model 36: 1131–1149

Chen CY (2007) An experimental study of stratified mixing caused by internal solitary waves in a two-layered fluid system over variable seabed topography. Ocean Eng: 34: 1995–2008

Chen CY, Hsu JRC, Chen HH, Kuo CF, Cheng MH (2007a) Laboratory observations on internal solitary wave evolution on steep and inverse uniform slopes. Ocean Eng 34: 157–170
Chen CY, Hsu JRC, Cheng MH, Chen HH, Kuo CF (2007b) An investigation on internal solitary waves in a two-layer fluid: Propagation and reflection from steep slopes. Ocean Eng 34: 171–184
Chen CY, Hsu JRC, Cheng MH, Chen CW (2008) Experiments on mixing and dissipation in internal solitary waves over variable ridges. Environ Fluid Mech 8(3): 199–215
Cheng MH, Hsu JRC, Chen CY, Chen CW (2009) Modelling the propagation of an internal solitary wave across double ridges and a shelf-slope. Environ Fluid Mech 9: 321–340
Choi W, Camassa R (1999) Fully nonlinear internal waves in a two-fluid system. J Fluid Mech 396: 1–36
Chorin AJ (1968) Numerical solution of the Navier–Stokes equations. Math Comput 22:745–762
Daily C, Imberger J (2003) Modelling solitons under the hydrostatic and Boussinesq approximations. Int J Num Methods Fluids 43: 231–252
Ezer T, Arango H, Schepetkin AF (2002) Developments in terrain-following ocean models: intercomparisons of numerical aspects. Ocean Modelling 4: 249–267
Farmer DM (1978) Observations of long nonlinear internal waves in a lake. J Phys Oceanogr 8: 63–73
Farmer DM, Armi L (1986) Maximal two-layer exchange over a sill and through the combination of a sill and contraction with barotropic flow. J Fluid Mech 164: 53–76
Filatov NN (2012, this volume) Field studies of non-linear internal waves in lakes on the globe, Chap. 2. Nonlinear Internal Waves in Lakes. Springer, Heidelberg
Fletcher CAJ (1991) Computational techniques for fluid dynamics, 2nd Edn, vol 2. Springer-Verlag, Berlin
Fringer OB, Street RL (2003) The dynamics of breaking progressive interfacial waves. J Fluid Mech 494: 319–353
Fringer OB, Gerritsen M, Street RL (2006) An unstructured-grid, finite-volume, nonhydrostatic, parallel coastal ocean simulator. Ocean Modelling 14: 139–173
Fructus D, Carr M, Grue J, Jensen A, Davies PA (2009) Shear-induced breaking of large internal solitary waves. J Fluid Mech 620: 1–29
Gill AE 1982 Atmosphere–ocean dynamics. Academic Press, London
Gorodetska N, Nikishov V (2012, this vol.) Laboratory modelling on transformation of large amplitude internal waves by topographic obstructions, Chap. 3. Nonlinear Internal Waves in Lakes. Springer, Heidelberg.
Grimshaw R, Pelinovsky E, Poloukhina O (2002). Higher-order Korteweg-de Vries models for internal solitary waves in a stratified shear flow with a free surface. Nonlinear Processes in Geophysics 9, 221–235
Grimshaw R, Pelinovsky E, Talipova T (2008) Fission of a weakly nonlinear interfacial solitary wave at a step. Geophys Astrophys Fluid Dyn 102: 179–194
Grue J, Jensen PO, Rusas P-O, Sveen JK (1999) Properties of large-amplitude internal waves. J Fluid Mech 380: 257–278
Guo Y, Sveen JK, Davies PA, Grue J, Dong P (2004) Modelling the motion of an internal solitary wave over a bottom ridge in a stratified fluid. Env Fluid Mech 4: 415–441
Harlow FH, Welch JE (1965) Numerical calculation of time-dependent viscous incompressible flow of fluid with free surface. Phys Fluids 8: 2182–2189
Heggelund Y, Vikebo F, Berntsen J, Furnes G (2004) Hydrostatic and non-hydrostatic studies of gravitational adjustment over a slope. Cont Shelf Res 24: 2133–2148
Helfrich KR 1992 Internal solitary wave breaking and run-up on a uniform slope. J Fluid Mech 243: 133–154
Helfrich KR, Melville WK (2006) Long nonlinear internal waves. Ann Rev Fluid Mech 38: 395–425
Hirt C, Nichols B (1981) Volume of Fluid (VOF) method for the dynamics of free boundaries. J Comp Physics 39: 201–225

Horn DA, Redekopp LG, Imberger J, Ivey GN (2000) Internal wave evolution in a space-time varying field. J Fluid Mech 424: 279–301
Horn DA, Imberger J, Ivey GN (2001) The degeneration of large-scale interfacial gravity waves in lakes. J Fluid Mech 434: 181–207
Howard LN (1961) Note on a paper by John W. Miles. J Fluid Mech 10: 509–512
Hult E, Troy CD, Koseff JR (2009) The breaking of interfacial waves at a submerged bathymetric ridge. J. Fluid Mech 637: 45–71
Hunkins K, Fliegel M (1973) Internal undular surges in Seneca Lake: A natural occurrence of solitons. J Geophys Res 78: 539–548
Hüttemann H, Hutter K (2001) Baroclinic solitary water waves in two-layer fluid system with diffusive interface. Exp Fluids 30: 317–326
Hutter K (1983) Hydrodynamics of lakes. Springer–Verlag, Berlin
Jankowski, JA (1999) A non-hydrostatic model for free surfaces flows. PhD thesis, University of Hannover, Germany
Kakutani T, Yamasaki N (1978) Solitary waves on a two-layer fluid. J Phys Soc Japan 45: 674-679
Kanarska Y, Maderich V (2003) A non-hydrostatic numerical model for calculating free-surface stratified flows. Ocean Dynamics 53: 176–185
Kanarska Y, Maderich V (2004) Strongly non-linear waves and gravitational currents in rectangular basin. Applied Hydromechanics, 6(78) No 2: 75–78
Kanarska Y, Shchepetkin A, McWilliams JC (2007) Algorithm for non-hydrostatic dynamics in the Regional Oceanic Modeling System. Ocean Modelling 18: 143–174
Kao TW, Pan FS, Renouard D (1985) Internal solitons in the pycnocline: Generation, propagation, and shoaling and breaking over a slope. J Fluid Mech 159: 19–53
Keilegavlen E, Berntsen J (2009) Non-hydrostatic pressure in σ-coordinate ocean models. Ocean Modelling 28: 240–249
Keulegan GH (1959) Energy dissipation in standing waves in rectangular basins. J Fluid Mech 6: 33–50
Klymak JM and Moum J (2003) Internal solitary waves of elevation advancing on a shoaling shelf. Geophys Res Let doi:10.1029/2003GL017706
Kocsis O, Mathis B, Gloor M, Schurter M, Wüest A (1998) Enhanced mixing in narrows: A case study at the Mainau sill (Lake Constance). Aquat Sci 60: 236–252
Koop CG, Butler G (1981) An investigation of internal solitary waves in a two-fluid system. J Fluid Mech 112: 225–251
Lamb KG (1994) Numerical experiments of internal wave generation by strong tidal flow across a finite amplitude bank edge. J Geophys Res 99: 843–864
Lamb KG (2007) Energy and pseudoenergy flux in the internal wave field generated by tidal flow over topography. Cont Shelf Res 27: 1208–1232
Lamb KG, Nguyen VT (2009) On calculating energy flux in internal solitary waves with an application to reflectance. J Phys Oceanogr 39: 559–580
Leone C, Segur H, Hammack JL (1982) Viscous decay of long internal solitary waves. Phys Fluids 25: 942–244
Maderich V, Heling R, Bezhenar R, Brovchenko I, Jenner H, Koshebutskyy V, Kuschan A, Terletska K, (2008) Development and application of 3D numerical model THREETOX to the prediction of cooling water transport and mixing in the inland and coastal waters. Hydrological Processes 22: 1000–1013
Maderich V, Grimshaw R, Talipova T, Pelinovsky E, Choi B, Brovenchko I, Terletska K, Kim D (2009) The transformation of an interfacial solitary wave of elevation at a bottom step. Nonlinear Processes in Geophysics 16: 1–10
Maderich V, Talipova T, Grimshaw R, Brovenchko I, Terletska K, Pelinovsky E, Choi B (2010) Interaction of a large amplitude interfacial solitary wave of depression with a bottom step. Phys Fluids. doi:10.1063/1.3455984
Mahadevan A, Oliger J, Street R, (1996a) A nonhydrostatic mesoscale ocean model. Part I: Implementation and scaling. J Phys Oceanogr 26: 1860–1879

Mahadevan A, Oliger J, Street R (1996b) A nonhydrostatic mesoscale ocean model. Part II: Numerical implementation. J Phys Oceanogr 26: 1880–1900

Marshall J, Hill C, Perelman L, Adcroft A (1997a) Hydrostatic, quasi-hydrostatic, and nonhydrostatic ocean modeling. J Geophys Res 102: 5733–5752

Marshall J, Adcroft A, Hill C, Perelman L, Heisey C (1997b) A finite-volume, incompressible Navier–Stokes model for studies of the ocean on parallel computers. J Geophys Res 102: 5753–5766

Maurer J, Hutter K, Diebels S. (1996) Viscous effects in internal waves of two-layered fluids with variable depth. Eur J Mech, B/Fluids 15: 445–470

Mellor GL (1991) An equation of state for numerical models of ocean and estuaries. J Atmos Ocean Tech 8: 609–611

Mellor G (2004) Users guide for a three-dimensional, primitive equation, numerical ocean model. Tech. rep. Princeton University, Princeton

Mellor GL, Hakkinen S, Ezer T, Patchen R. (2002) A generalization of a sigma coordinate ocean model and an intercomparison of model vertical grids. In: Pinardi N, Woods JD (eds.), Ocean Forecasting: Conceptual Basis and Applications, Springer, Berlin

Michallet H, Ivey GN (1999) Experiments on mixing due to internal solitary waves breaking on uniform slopes. J Geophys Res 104: 13467–13477

Miles JW (1961) On the stability of heterogeneous shear flows. J Fluid Mech 10: 496–508

Miles JW, Howard LN (1964) Note on a heterogeneous shear flow. J Fluid Mech 20: 331–336

Miyata, M. 1984. An internal solitary wave of large amplitude. La Mer 23, 43–48

Moum JN, Farmer DM, Smyth WD, Armi L, Vagle S (2003) Structure and generation of turbulence at interfaces strained by internal solitary waves propagating shoreward over the continental shelf. J Phys Oceanogr 33: 2093–2112

Münnich M (1996) The influence of bottom topography on internal seiches in stratified media. Dyn Atmos Ocean 23: 257–266

Orr MH, Mignerey PC (2003) Nonlinear internal waves in the South China Sea: observation of the conversion of depression internal waves to elevation internal waves. J Geophys Res. doi:10.1029/2001JC001163

Ostrovsky LA, Stepanyants YA (1989). Do internal solitons exist in the ocean? Rev Geophys 27: 293–310

Ostrovsky LA, Stepanyants YA. (2005) Internal solitons in laboratory experiments: Comparison with theoretical models. Chaos, doi: 10.1063/1.2107087

Pope S (2000) Turbulent flows. Cambridge University Press, Cambridge

Sabinin KD (1992) Internal wave train above the Mascarene Ridge. Izvestiya, Atmos Ocean Phys 28:625–633

Seager V (1988) A SLAP for the masses. LLNL Tech Rep. UCRL-100267, Livermore, CA.

Shchepetkin AF, McWilliams JC (2005) The Regional Ocean Modeling System: A split-explicit, free-surface, topography-following coordinate oceanic model. Ocean Modelling 9: 347–404

Shepherd TG (1993) A unified theory of available potential-energy. Atmos - Ocean 31: 1–26

Shroyer EL, Moum JN, Nash JD (2008) Observations of polarity reversal in shoaling nonlinear internal waves. J Phys Oceanogr 39: 691–701

Siegel DA, Domaradzki JA (1994) Large-eddy simulation of decaying stably stratified turbulence. J Phys Oceanogr 24: 2353–2386

Smagorinsky J (1963) General circulation experiments with the primitive equations. Mon Weather Rev 91: 99–164

Staschuk N, Vlasenko V, Hutter K (2005) Numerical modelling of disintegration of basin-scale internal waves in a tank filled with stratified water. Nonlinear Proc Geoph 12: 955–964

Stocker T, Hutter K (1987) Topographic waves in channels and lakes on the f-plane. Springer, Berlin.

Sveen JK, Davies PA, Grue J (2002) On the breaking of internal solitary waves at a ridge. J Fluid Mech 469: 161–188

Thorpe SA (1974) Near-resonant forcing in a shallow two-layer fluid: a model for the internal surge in Loch Ness? J Fluid Mech 63: 509–527.
Thorpe SA (1977) Turbulence and mixing in a Scottish loch. Phil Trans R Soc Lond A 286: 125–181
Thorpe SA, Hall A, Crofts I (1972) The internal surge in Loch Ness. Nature 237: 96–98.
Thorpe SA (1997) On the interaction of internal waves reflecting from slopes. J Phys Oceanogr 27:2072–2078
Torrence C, Compo GP (1998) A practical guide to wavelet analysis. Bull Amer Meteor Soc 79: 61–78
Troy CD, Koseff JR (2005) The instability and breaking of long internal waves. J Fluid Mech 543: 107–136
Van Leer B (1979) Toward the ultimate conservative difference scheme. V: A second order sequel to Godunov's method. J Comput Phys 32: 101–136
Van Senden, DC, Imboden DM (1989) Internal seiche pumping between sill-separated basins. Geophys Astrophys Fluid Dyn 48: 135–150
Venayagamoorthy SK, Fringer OB (2005) Nonhydrostatic and nonlinear contributions to the energy flux budget in nonlinear internal waves. Geophys Res Lett. doi:10.1029 / 2005GL023432
Vlasenko VI, Hutter K (2002a) Generation of second mode solitary waves by the interaction of a first mode soliton with a sill. Nonlinear Processes in Geophysics 8: 223–239
Vlasenko VI, Hutter K (2002b) Transformation and disintegration of strongly nonlinear internal waves by topography in stratified lakes. Annales Geophys 20: 2087–2103
Vlasenko V, Hutter K (2002c) Numerical experiments on the breaking of solitary internal waves over a slope-shelf topography. J Phys Oceanogr 32: 1779–1790
Vlasenko V, Ostrovsky L, Hutter K (2005) Adiabatic behaviour of strongly nonlinear internal solitary waves in slope-shelf areas. J Geophys Res. doi: 10.1029/2004JC002705
Wadzuk M, Hodges BR (2004) Hydrostatic and non-hydrostatic internal wave models. Final report to ONR. CRWR Online Report 04-09, U. Texas, Austin. Available from: http://www.crwr.utexas.edu/online.shtml
Wessels F, Hutter K (1996) Interaction of internal waves with topographic sill in a two-layer fluid. J Phys Oceanogr 26: 5–20
Whitham GB (1974) Linear and nonlinear waves. Wiley, New York
Winters KB, Lombard PN, Riley JJ, D'Asaro EA (1995) Available potential energy and mixing in density stratified fluids. J Fluid Mech 289: 115–128
Wuest A, Lorke A (2003) Small-scale hydrodynamics in lakes. Ann Rev Fluid Mech 35: 373–425
Zhao Z, Klemas V, Zheng Q, Yan X (2003) Satellite observation of internal solitary waves converting polarity. Geophys Res Let. doi:10.1029/2003GL018286

Lake Index

K. Hutter (ed.), *Nonlinear Internal Waves in Lakes*,
Advances in Geophysical and Environmental Mechanics and Mathematics,
DOI 10.1007/978-3-642-23438-5, © Springer-Verlag Berlin Heidelberg 2012